Composites Science and Technology

Shamsher Bahadur Singh
Muthukumar Gopalarathnam
Venkatesh Kumar R. Kodur
Vasant A. Matsagar *Editors*

Fiber Reinforced Polymeric Materials and Sustainable Structures

Springer

Composites Science and Technology

Series Editor

Mohammad Jawaid, Laboratory of Biocomposite Technology, Universiti Putra Malaysia, INTROP, Serdang, Malaysia

This book series publishes cutting edge research monographs comprehensively covering topics in the field of composite science and technology. The books in this series are edited or authored by top researchers and professional across the globe. The series aims at publishing state-of-the-art research and development in areas including, but not limited to:

- Conventional Composites from natural and synthetic fibers
- Advanced Composites from natural and synthetic fibers
- Chemistry and biology of Composites and Biocomposites
- Fatigue damage modelling of Composites and Biocomposites
- Failure Analysis of Composites and Biocomposites
- Structural Health Monitoring of Composites and Biocomposites
- Durability of Composites and Biocomposites
- Biodegradability of Composites and Biocomposites
- Thermal properties of Composites and Biocomposites
- Flammability of Composites and Biocomposites
- Tribology of Composites and Biocomposites
- Applications of Composites and Biocomposites

Review Process

The proposal for each volume is reviewed by the main editor and/or the advisory board. The chapters in each volume are individually reviewed single blind by expert reviewers (at least two reviews per chapter) and the main editor.

Ethics Statement for this series can be found in the Springer standard guidelines here - https://www.springer.com/us/authors-editors/journal-author/journal-author-helpdesk/before-you-start/before-you-start/1330#c14214

Shamsher Bahadur Singh ·
Muthukumar Gopalarathnam ·
Venkatesh Kumar R. Kodur · Vasant A. Matsagar
Editors

Fiber Reinforced Polymeric Materials and Sustainable Structures

Springer

Editors
Shamsher Bahadur Singh
Department of Civil Engineering
Birla Institute of Technology and Science (BITS) Pilani
Pilani, Rajasthan, India

Muthukumar Gopalarathnam
Department of Civil Engineering
Birla Institute of Technology and Science (BITS) Pilani
Pilani, Rajasthan, India

Venkatesh Kumar R. Kodur
Department of Civil and Environmental Engineering
Michigan State University
East Lansing, MI, USA

Vasant A. Matsagar
Department of Civil Engineering
Indian Institute of Technology (IIT) Delhi
New Delhi, India

ISSN 2662-1819 ISSN 2662-1827 (electronic)
Composites Science and Technology
ISBN 978-981-19-8978-0 ISBN 978-981-19-8979-7 (eBook)
https://doi.org/10.1007/978-981-19-8979-7

This Springer imprint is published by the registered company Springer Nature Singapore Pte Ltd.
The registered company address is: 152 Beach Road, #21-01/04 Gateway East, Singapore 189721, Singapore

Preface

At the outset, it was our great privilege to extend a hearty welcome to all participants and invited speakers to the US2020 Partnership Workshop on "FRP Materials and Sustainable Structures," organized by the Department of Civil Engineering, Birla Institute of Technology and Science, Pilani, Pilani Campus (Rajasthan), India, on March 4th, 2022, leading to the creation of this book.

As we know that the COVID-19 pandemic has engulfed the whole world and the big question is whether the world population have enough sustainable resources and strategies in place to safeguard themselves from COVID-19 and similar infectious diseases. The entire scientific community is worried about the sustainability of resources for the future generations to come which includes sustainable civil engineering infrastructure systems in the post-COVID conditions.

The infrastructure in the form of buildings, bridges, roads, railways, airports, power plants needs to satisfy all the requirements of safety while being cost-effective and sustainable. The greater awareness of the world's limited natural resources and the desire for state-of-the-art systems necessitate new materials to be adopted in design and retrofitting of structural systems. Also, the ever-increasing world population coupled with the movement of people toward urban world has resulted in an unprecedented demand in terms of new infrastructure systems being built in a place that is likely to experience multiple natural hazards such as earthquakes, hurricanes, wind storms, flooding, and fire. Many new fields with innovative materials are born in the civil engineering domain such as structural health monitoring that essentially reflects the need for continuous monitoring of structures for sustainability, and advanced composite materials such as FRPs and development of design approaches to cater for the new construction materials.

In recent years, advent of advanced composite materials such as carbon fiber reinforced polymer (CFRP), glass fiber reinforced polymer (GFRP), aramid fiber reinforced polymer (AFRP), and basalt fiber reinforced polymer (BFRP) systems has provided solutions to the many problems related to deteriorating health of civil engineering infrastructures such as reduced strength, stiffness, and most importantly durability. Furthermore, the development of natural fiber-based composites has led to the cost-effective as well sustainability-based design of FRP reinforced and/or

FRP strengthened concrete infrastructures. These advanced and natural fiber-based composites have great potential for upgrading the strength, stiffness, and resilience of the structural systems in particular and civil engineering infrastructures in general.

Thus, this book is based on presentations made at one-day international workshop at BITS Pilani on the development of innovative FRP materials using different types of fibers and polymeric systems/resins for structural applications. In addition, this book also deals with current design practice for using different kinds of FRP materials for improving strength, stiffness, durability, resilience, and sustainability of structural systems. Further, emphasis is placed on the use of agricultural waste-based fibers for developing green composites for civil engineering infrastructures. Moreover, FRP material characteristics, manufacturing techniques, background and history of its use with its advantages and disadvantages along with design of retrofitting and rehabilitation of structures using FRP are presented in detail. Hence, researchers and the practicing engineers working in the broad field of design of civil infrastructures can significantly gain by keeping abreast of the latest trends and developments in the field of FRP materials for design of high-performance structural systems with adequate sustainability and durability. We are thankful to all speakers and authors who have contributed their valuable chapters for bringing out this wonderful book.

Finally, we do hope that all the valuable chapters from eminent speakers and authors will be beneficial to the researchers, practitioners, and academicians and will create further opportunities to enrich their knowledge in the field of FRP materials and sustainable structures with primary aim of fabricating the structures with lowest carbon footprint and reduced greenhouse gas emissions.

Pilani, India — Prof. Shamsher Bahadur Singh
Pilani, India — Dr. Muthukumar Gopalarathnam
East Lansing, USA — Prof. Venkatesh Kumar R. Kodur
New Delhi, India — Prof. Vasant A. Matsagar

Contents

Fire Resistance Requirements for Bio-Based Fiber-Reinforced Polymer Structural Members

Venkatesh Kumar R. Kodur, S. Venkatachari, Vasant A. Matsagar, and Shamsher Bahadur Singh

Abstract In this chapter, the fire resistance requirements for structural components incorporating bio-based fiber-reinforced polymer composites are presented. The factors that are to be accounted for in evaluating the performance of fiber-reinforced polymer (FRP) structural members at elevated temperatures are discussed. In addition, the various steps associated with evaluating the fire resistance, both experimental and numerical, are outlined. The application of a numerical procedure for evaluating the fire performance of a typical bio-based FRP-strengthened concrete beam is illustrated through a case study. It is shown that the fire resistance of the bio-based FRP-strengthened beam can be much lower than a similar concrete beam strengthened using conventional glass- or carbon-based FRP. Further, it is shown that the fire resistance of bio-based FRP-strengthened concrete members can be enhanced through the application of supplementary fire insulation.

1 Introduction

The use of sustainable material alternatives is gaining significant attention in various sectors due to rising environmental concerns on carbon-di-oxide (CO_2) emissions

V. K. R. Kodur (✉) · S. Venkatachari
Department of Civil and Environmental Engineering, Michigan State University, East Lansing, USA
e-mail: kodur@egr.msu.edu

S. Venkatachari
e-mail: venkat28@msu.edu

V. A. Matsagar
Department of Civil Engineering, Indian Institute of Technology (IIT) Delhi, Hauz Khas, New Delhi 110 016, India
e-mail: matsagar@civil.iitd.ac.in

S. B. Singh
Department of Civil Engineering, Birla Institute of Technology & Science (BITS) Pilani, Vidya Vihar, Pilani, Rajasthan 333 031, India
e-mail: sbsingh@pilani.bits-pilani.ac.in

S. B. Singh et al. (eds.), *Fiber Reinforced Polymeric Materials and Sustainable Structures*, Composites Science and Technology, https://doi.org/10.1007/978-981-19-8979-7_1

arising from the use of petroleum-based products, depletion of non-renewable resources, and increasing waste generation. Natural fibers, derived from agricultural waste (or by-products) are being considered as a potential alternative, in place of petroleum-based synthetic fibers (such as glass or carbon-based fibers), for the development of bio-based composite materials for use in civil engineering applications. Natural (or bio-based) fiber-reinforced polymers (NFRP) offer several advantages over traditional FRP materials, including cost savings, relatively lightweight, appreciable strength and stiffness properties, and environment friendly benefits. Furthermore, finding such applications for agricultural waste will lead to reduced carbon emissions, energy savings, and economy in the construction sector.

NFRP composites are currently being used in some engineering applications. Table 1 shows the properties of various traditional FRP and NFRP fibers and their composites at room temperature as reported in published literature [1–5]. NFRP composites incorporating jute, hemp, kenaf, and bamboo fibers are used in the manufacture of automotive parts, packaging, and to a limited extent in structural components (such as wall panels, bricks, window frames, etc.) [4, 6]. In addition, NFRP composites are also finding increasing applications in the fabrication of electrical and electronic components, sports equipment, and aerospace components. The use of NFRP composites in these applications is due to their low specific weight, low cost, locally sourced materials, and resistance to corrosion and fatigue. However, the high moisture absorption, poor thermal performance, and variable quality of the NFRP composites limit their wider use [7–9].

While the use of NFRPs is, at present, mainly in non-structural applications, there is enormous potential for its use in buildings, especially in strengthening and retrofitting applications, where the span of structural members is small and the required strengthening requirements are low to moderate. When used in buildings, structural members must be designed to satisfy the appropriate fire resistance requirements, in addition to other requirements such as flammability and smoke development criteria specified in building codes [1]. These fire resistance requirements are included in the codes on the premise that when other measures of controlling fire fail, structural integrity is the last line of defense. Currently, one of the main impediments to using bio-based FRPs in buildings is the lack of knowledge about the fire performance of bio-based FRP composites.

In this paper, the fire resistance requirements for bio-based FRP composites are discussed. The factors that differentiate the performance of NFRP at elevated temperatures, as compared to that of traditional materials, such as concrete, steel, and conventional FRP are discussed. The general procedures associated with evaluating the fire resistance, both experimental and numerical, are outlined. Through a case study, the application of the numerical procedure for evaluating the fire performance of a NFRP-strengthened concrete beam is illustrated.

Table 1 Room temperature material properties of synthetic and natural fibers and their composites

Fiber or composite	Density (g/cm^3)	Tensile strength (MPa)	Elastic modulus (GPa)	Elongation at break (%)
Carbon	1.7	4000	230–240	1.4–1.8
E-glass	2.5	2000–3500	70	2.5
S-glass	2.5	4570	86	2.8
Aramid	1.4	3000–3150	63–67	3.3–3.7
Cotton	1.5–1.6	287–800	5.5–12.6	7.0–8.0
Jute	1.3–1.45	393–773	13–26.5	1.16–1.5
Flax	1.5	345–1100	27.6	2.7–3.2
Hemp	1.48	550–900	70	1.6
Sisal	1.45	468–640	9.4–22	3–7
Coir	1.15	131–175	4–6	15–40
Carbon/epoxy	1.5–2.1	1050–1500	180	0.5–1.8
Glass/epoxy	1.25–2.5	700–1050	42–55	1.2–5
Aramid/epoxy	1.25–1.45	1400	76	1.4–4.4
Jute/unsaturated polyester	–	50	8	–
Flax/epoxy	–	132–160	15–27	–
Hemp/polypropylene	–	52	4	
Sisal/epoxy	–	330–410	6–10	–
Kenaf/polypropylene	–	46	5	–

2 Need for Fire Resistance in Bio-Based FRP Composites

For structural applications, conventional FRP composites offer several advantages over traditional construction materials like steel and concrete [1]. However, unlike steel and concrete, the FRP composites are highly combustible and burn when exposed to fire. Flame spread and toxic smoke generation are two major issues that limit the application of FRP composites in building applications, and the extent of flame spread largely depends on the type and composition of the specific FRP material.

Owing to their combustible nature, the FRP composites begin to decompose even at low to moderate temperatures in a fire scenario. In addition, the strength and stiffness properties of the FRP undergo rapid degradation with a moderate temperature rise of 200 to 300 °C. Further, the interfacial bond properties of the FRP composites also experience drastic degradation with temperature rise that affects the load (or stress) transfer between the FRP and concrete. Due to these issues concerning the high-temperature behavior, the FRP composites demonstrate poor fire resistance properties.

Much like the traditional FRP composites, NFRP composites are also highly susceptible to flaming, charring, material degradation, and rapid loss of strength and stiffness properties when exposed to elevated temperatures [8, 10, 11]. NFRP composites also have lower initial strength and stiffness at ambient conditions in comparison to traditional FRPs. In addition, the degradation in material properties in the case of NFRPs can be more drastic since the NFRPs incorporate natural fibers (such as hemp, jute, rice husk, etc.) in place of synthetic fibers (such as carbon or glass).

To illustrate the difference in the behavior of FRP at elevated temperatures, the variation of strength and stiffness with temperature for conventional and bio-based FRP are presented in Fig. 1 along with other traditional construction materials. In the figure, the ratio of strength at elevated temperature to that at room temperature is plotted. As is the case with steel, concrete, and wood, the strength of FRP also decreases with increasing temperature. While the data for concrete, steel, wood, and conventional FRP is well documented in the literature [1], there is no reliable data for the properties of NFRP at elevated temperatures. Based on the limited information available at room temperature conditions, the NFRPs have much lower strength and stiffness as compared to conventional FRPs, such as CFRP, GFRP, etc. Also, since the NFRPs incorporate plant-based fibers, the drop in strength and stiffness is likely to occur early (at a lower temperature rise) and at a more rapid pace than conventional FRPs. With these considerations, the probable trends for strength and stiffness degradation of NFRP are shown in Fig. 1. As can be seen in the figure, the rate of strength and stiffness loss is much greater for FRP than that of concrete and steel. In the case of concrete, the 50% strength loss does not occur until about 600 °C whereas for steel the corresponding temperature is 500 °C. The critical temperatures (50% strength loss) of CFRP and GFRP are 250 °C and 325 °C, respectively [12]. The critical temperature of NFRPs is expected to be much lower than that of conventional FRP. In addition, the strength and stiffness characteristics of the NFRP can vary significantly depending on the type and composition of the FRP, and the quality of the natural fibers used in the composite.

3 Fire Resistance Requirements

Structural members are to be designed to satisfy the requirements of serviceability and safety limit states. One of the major safety requirements in building design is the provision of appropriate fire resistance to structural members. Structural members are required to meet the criteria for flammability, smoke development, and fire resistance ratings prescribed in building codes and standards.

Since the FRP materials are highly combustible, a large extent of toxic gases, heat, and flame spread can get generated during the burning of the FRP. The emitted smoke and flame spread can hinder the occupant evacuation and firefighting operations during a fire incident. For these reasons, construction materials are classified based on flame spread index (FSI) and smoke-developed index (SDI) for use in

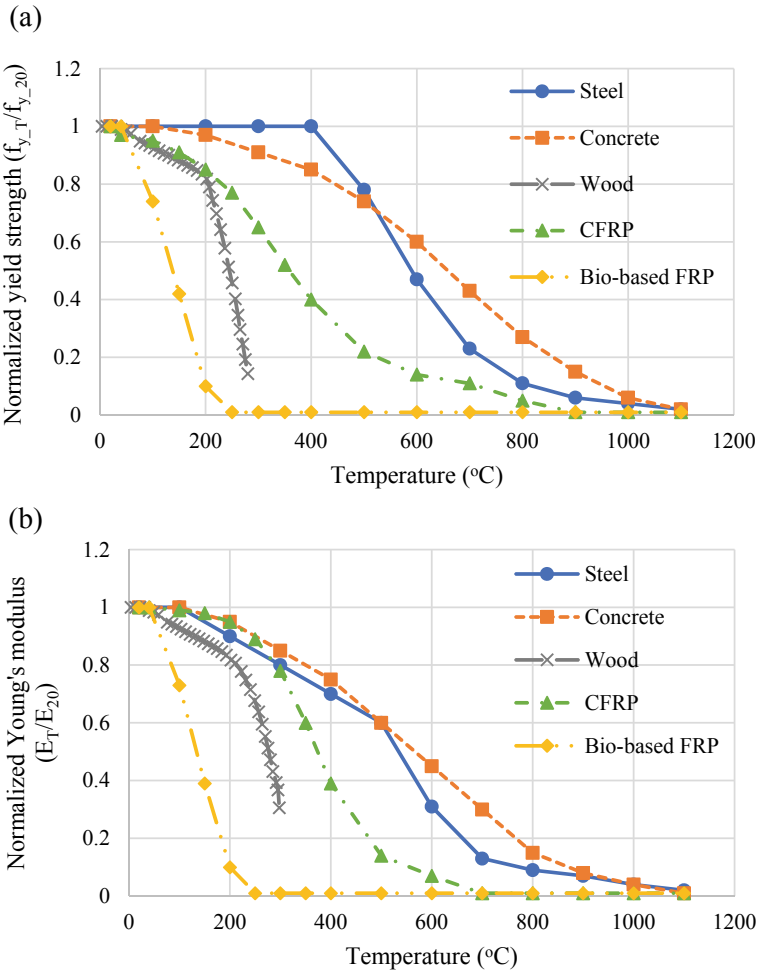

Fig. 1 Variation of **a** strength and **b** stiffness with temperature for different materials

building applications. Evaluation of flame spread and smoke development is undertaken through standard tests as per test procedures recommended in different standards such as the American Society for Testing and Materials (ASTM) and National Fire Protection Association (NFPA) standards. The test procedures for measuring FSI and SDI for different building materials are specified in ASTM E84 [13] and NFPA 255 [14] standards. In these test methods, the surface burning behavior of a material is evaluated using a Steiner Tunnel setup, which is available in certain laboratories such as the Underwriters Laboratories (UL) in Northbrook, IL, USA. Additional characteristics such as specific optical density of smoke generated and surface flammability of building materials can be obtained using ASTM E662 [15] and ASTM E162 [16] testing protocols. Typically, the FSI and SDI classifications

for FRP materials are provided by the manufacturer in directories such as UL and also in some building codes based on the standard testing protocols discussed above. Currently, such classifications are not available for NFRP materials and need to be generated for their use in buildings.

In addition to the above requirements for flammability and smoke development, the structural members in buildings are also required to satisfy minimum fire resistance ratings. Fire resistance is defined as the ability of a structural member to carry its service loading at elevated temperatures that could be encountered in a fire. It is the time during which a structural member exhibits resistance to failure. On the other hand, building codes specify a minimum time for which a structural member has to withstand the effect of fire, without experiencing failure. These times are expressed in hours (1, 1.5, 2, 3, and 4 h) and are referred to as fire resistance ratings. Typical fire resistance rating requirements for specific structural members in a building are specified in building codes, such as the International Building Code (IBC) 2021 [17] and National Building Code of India 2016 [18]. Generally, the fire resistance rating of a structural member is a function of applied load, member type (e.g., column, beam, wall), member dimensions, probable fire intensity, and type of construction material (concrete, steel, or wood). In addition, the ratings also depend on the type of occupancy, the number of stories, and the floor area in a building. For instance, the fire resistance ratings required for columns in multi-story buildings vary from 1 to 4 h while primary beams are required to have a fire resistance rating of 1 to 3 h (IBC 2021 [17]).

The fire resistance of a structural member depends, in part, on the materials used in its construction. Structural components made of bio-based FRP should also satisfy the fire resistance requirements. While the commonly used fire protection techniques for concrete and steel can also be adapted for achieving the required ratings of NFRP structural members, in general, there are some major differences associated with FRP as a material. In steel-reinforced and prestressed concrete structural members, the concrete cover thickness requirements, for the steel reinforcement, are complemented, to a certain extent, by the requirements for corrosion control. For FRP-reinforced concrete structural members, no special concrete cover thickness provisions are required for corrosion control. However, the size of the concrete section, cover thickness, and insulation (if any) needs to be determined based on the strengthening requirements and limiting the temperature rise in the FRP reinforcement. Since the NFRP composites have lower initial strength and stiffness as compared to conventional FRPs, a larger thickness (or more number) of NFRP reinforcement may be needed to achieve similar performance as that of conventional FRP composite members.

Also, where NFRP sheathing or externally bonded NFRP sheets are used as external reinforcement in the repair or rehabilitation of a structural member, fire performance characteristics of the concrete member might be affected due to the flammable nature of the FRP composite. In this case, the building codes also require that the overall structural assembly satisfy appropriate fire safety requirements. This can be achieved by applying a layer of fire insulation to the FRP-strengthened member.

4 Fire Resistance Assessment

The fire resistance of structural members can be determined through standardized fire resistance tests; however, such tests are costly and time-consuming. Alternatively, rational methods can be applied to evaluate the fire resistance of structural members. These methods can be carried out at a simplified level or an advanced level through numerical analysis. In these methods, the sectional temperatures that develop in a fire-exposed member and the degradation in the structural behavior are traced to evaluate the fire resistance of the member. In this section, the steps associated with evaluating fire resistance, both testing and numerical methods, are outlined.

4.1 Testing

A common method to assess fire resistance is by subjecting building elements, such as beams, slabs, or walls to a standardized fire test. Data from these tests can be used to develop fire resistance ratings of different structural members. The fire resistance of bio-based FRP composite structural members (or components) can be evaluated through fire tests as per specifications in codes and standards in a particular country such as ASTM E119 [19], NFPA 251 [20], ISO 834 [21], etc.

During a test, the specimen is exposed to a standard fire in specially built test furnaces. Figure 2 shows the standard time–temperature curve as per ASTM E119 specifications [19]. The test furnace is designed to reproduce conditions that a member might be exposed to during a fire, which includes temperature, structural loads, and heat transfer. In addition, the test specimen needs to be fabricated to ensure normal quality and condition at the time of testing. Depending on the size of the furnace, the dimensions of the FRP composite member that can be tested can vary.

Several fire tests have been carried out on conventional FRP-strengthened concrete members to develop fire resistance ratings [22–26]. In these tests, FRP-strengthened concrete members with different types of strengthening methods, insulation schemes,

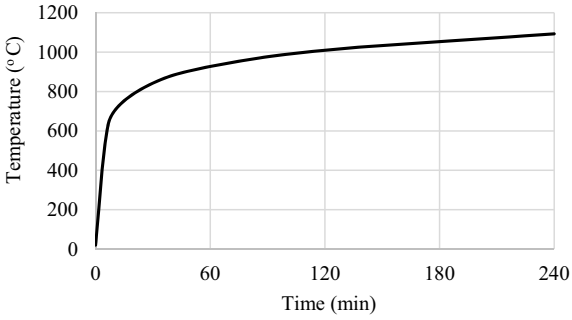

Fig. 2 ASTM E-119 standard fire time–temperature curve for testing building elements

and fire scenarios have been tested. These tests indicate that FRP-strengthened reinforced concrete members with supplemental fire protection can achieve the required fire resistance ratings (up to 4 h) under standard fire exposure. However, such fire test data is unavailable for NFRP composite members.

In the fire test method, the fire resistance rating is expressed as the time that the specimen reaches specified limiting criteria of performance during exposure to a standard fire. There are three performance criteria in the standard test method. These are related to load-bearing capacity (strength), insulation, and integrity criteria [1]:

Load-bearing capacity: For load-bearing constructions, the test specimen shall not collapse in such a way that it no longer performs the load-bearing function for which it was constructed.

Insulation: For constructions such as floors and walls that have the function of separating two parts of a building, the average temperature rise at the unexposed face of the specimen shall not exceed 139 °C, the maximum temperature rise at the unexposed face of the specimen shall not exceed 181 °C.

Integrity: For constructions such as walls, floors, and roofs, the formation in the test specimen of openings through which flames or hot gases can pass shall not occur. Failure of integrity is deemed to have occurred when a specified cotton wool pad applied to the unexposed face is ignited.

In many cases, not all criteria have to be satisfied. Beams, for example, are required only to demonstrate the load-bearing capacity criteria; the ability to carry loads for the fire resistance period. Non-load-bearing walls, if used as fire separations, have only to meet the requirements of integrity and insulation. Load-bearing fire separations, however, have to meet all three criteria of performance.

Results, obtained from the standard tests, can be used as a basis for developing fire resistance ratings for NFRP-strengthened concrete members. These ratings are given in the tabulated form in terms of minimum dimensions to obtain specific fire resistance ratings. For concrete walls, for example, the minimum thickness of the concrete to obtain specific fire resistance is given. For concrete floors, the minimum thickness of the floor and the minimum thickness of the concrete cover to the reinforcing steel are given.

4.2 Numerical Modeling

Evaluating the fire resistance ratings through fire tests is quite expensive, complicated, and time-consuming. Numerical modeling, on the other hand, is an effective alternative to evaluating the fire performance of bio-based FRP composite members. In addition, the numerical model also allows quantifying the effect of various governing parameters, such as the type and composition of the FRP composite, different types of strengthening methods and fire insulation schemes.

Numerical models, capable of simulating the behavior of structural members under fire conditions, have been developed for predicting the fire resistance of conventional FRP-strengthened concrete members [27, 28]. Such models can be applied

for evaluating the fire resistance of bio-based FRP-strengthened concrete members through appropriate material properties, discretization, and fire limits for the natural fiber-based composite members. A flow chart, illustrating the calculation procedure employed in such models, is shown in Fig. 3. The calculation of fire resistance is performed in three steps:

1. calculation of the fire temperature,

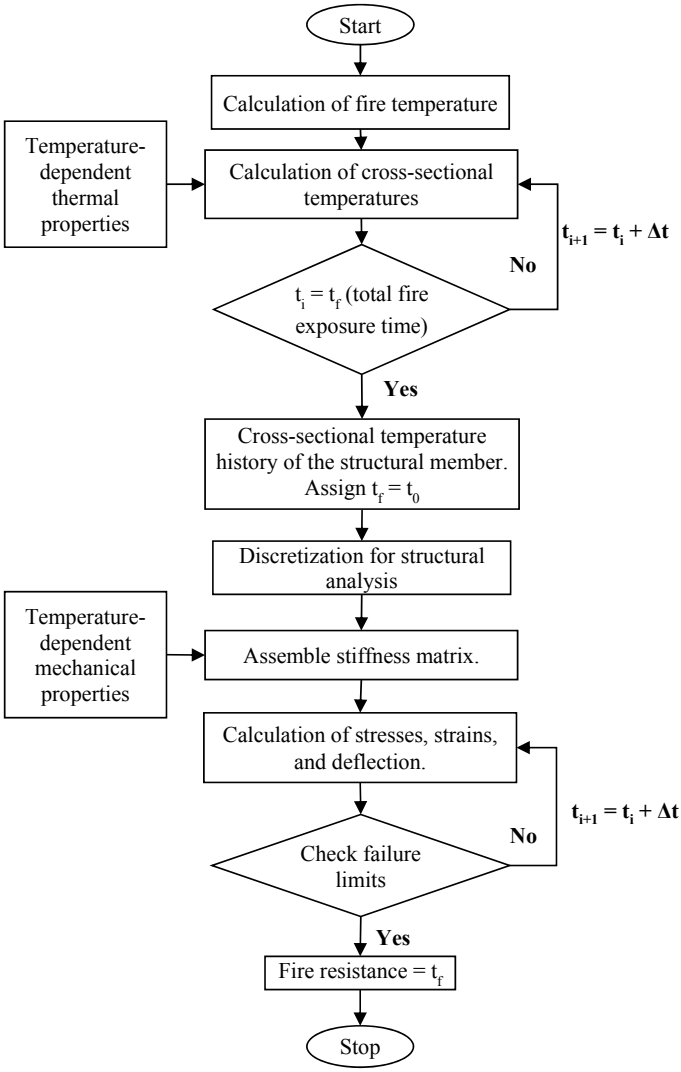

Fig. 3 Flowchart showing numerical procedure for evaluating fire resistance of structural members incorporating bio-based FRPs

2. calculation of temperature in the fire-exposed FRP-strengthened member, and
3. calculation of capacity and deformations of the FRP-strengthened member during the exposure to fire.

Fire Temperature: At present, in calculations of fire resistance of NFRP-strengthened concrete members, the fire temperature course is assumed to follow the ASTM E119 standard or equivalent temperature–time relation. For evaluating the performance of the structural member under more realistic fire severities, other design temperature–time relationships such as the parametric fire curves in Eurocode 1 [29] or design fire scenarios generated as per the recommendations in the SFPE Handbook [30] can be utilized.

Structural Member Temperature: The next step in the procedure is the calculation of the temperatures of the fire-exposed member. These temperatures are calculated using a 2-D heat transfer analysis. In this method, the cross-section of the member is divided into a number of elemental regions, which may have various shapes such as squares or rectangles, depending on the geometry of the member. For each element or layer, a heat balance is made. By solving the heat balance equations for each element or layer, the temperature history of the member can be calculated.

Strength: In the third step, a structural analysis is conducted to determine the capacity and deformations in the member during exposure to fire. The FRP-strengthened member is discretized into several segments along the length of the member, and the cross-section at the center of each segment is divided into several elements (same as the heat-transfer analysis). Moment–curvature relations are derived for various segments of the member by applying force equilibrium and strain compatibility. These time-dependent moment–curvature relations are used to generate the moment and deflection at different segments as a function of fire exposure time.

The response parameters obtained from the numerical analysis include the cross-sectional temperatures, stress and strains, moment capacity, and deflections. These response parameters are compared with the different failure limits, as prescribed in ASTM E119 [19]. The fire resistance is obtained by determining the time at which the failure limit states are reached. The temperature, strength, and deflection-based failure limits are given below.

1. The temperature in the tensile reinforcing steel reached 593 °C.
2. The average temperature on the unexposed surface of the slab exceeds 139 °C or the temperature at any one point on the unexposed surface exceeds 181 °C above the initial temperature (applicable only to slabs and walls).
3. The moment carrying capacity of the structural member falls below the moment due to applied loading.
4. The mid-span deflection exceeds $L^2/400d$ (mm), and the rate of deflection exceeds $L^2/9000d$ (mm/min), where L and d are the span (mm) and effective depth (mm) of the structural member.

To calculate the fire resistance of the FRP-reinforced structural members, knowledge of the relevant thermal and mechanical properties of the constituent materials

at elevated temperatures is essential. Thermal and mechanical properties of various traditional materials, such as concrete and steel rebar at elevated temperatures, are given in codes and standards such as Eurocode [31] and ASCE manual [32] and also in various published papers [33]. Only limited high-temperature material property data is available for FRP composite, and even these are for conventional FRPs [34, 35]. Methods to determine the high-temperature properties of FRP composites, including those of bio-based FRPs, are discussed in a recent publication (Kodur et al. [36]).

5 Case Study

To assess the fire performance of bio-based FRP concrete structural members, a feasibility study is undertaken with the main emphasis on the fire resistance of NFRP-strengthened concrete beams. The numerical model developed by Kodur and Ahmed [27] using the FORTRAN program and further extended by Kodur and Bhatt [28] is applied to evaluate the fire resistance of NFRP-strengthened concrete beams. Using the model, the temperature gradients in the cross-section of the member, available moment capacity, and mid-span deflections, as functions of fire exposure time, and the fire resistance of the beam can be computed. Realistic strength and deflection-based limit states are used to determine the failure of the beam. The numerical model has been validated previously against fire test data on conventional FRP-strengthened concrete members and complete details of the validation studies can be found in [27, 28, 37].

The model is applied to compare the fire performance of a NFRP strengthened concrete beam with that of a conventional FRP-strengthened beam. Two beams, one strengthened with carbon fiber-reinforced polymer (CFRP) (B1), and the other strengthened with hemp-based FRP (B2), are analyzed. Figure 4 shows the details of the beam considered for this study. The FRP reinforcement for strengthening is selected to achieve a 25% increase in the moment capacity of the beams. The tensile strength and elastic modulus of the CFRP strip are taken as 1170 MPa and 96.5 GPa, respectively and the corresponding values for the NFRP strip are taken as 52 MPa and 6.8 GPa, respectively. The strength and modulus properties of NFRP are taken based on the room temperature values reported for hemp-based FRP composites [38]. No fire insulation is applied to these beams. The beams are exposed to standard ASTM E119 fire temperatures for 240 min or until failure occurs.

The results from the thermal analysis are shown in Fig. 5 where the temperatures in the steel reinforcement, mid-concrete layer (evaluated at the mid-point of the concrete section), and FRP reinforcement are plotted against time. The critical temperature at which failure is assumed to occur, for the steel and FRP reinforcement, is also shown in the figure. For NFRP, the critical temperature is assumed as 150 °C, which corresponds to 50% tensile strength loss in hemp-based FRP. Based on the limited studies reported in the literature for NFRP composites, it is expected that the natural fiber-based composite will degrade at a faster pace than conventional FRPs and the

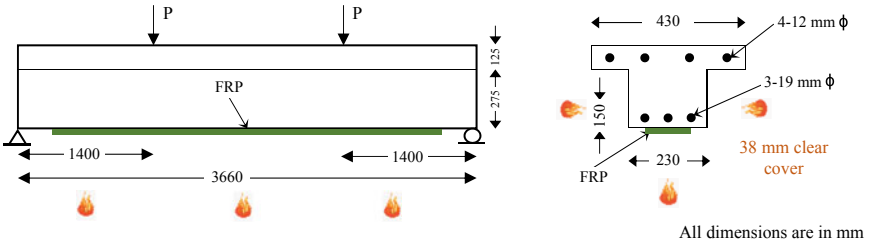

Fig. 4 Elevation and cross-section of reinforced concrete beam strengthened with CFRP or NFRP reinforcement

critical temperature can range anywhere between 125 °C and 200 °C depending on the type and composition of these composites. The critical temperature of 150 °C chosen in this study can result in a conservative estimate of the fire resistance of NFRP-strengthened concrete members. The critical temperatures for reinforcing steel and the CFRP strip are taken as 593 °C and 250 °C, respectively. The temperatures in the beam section increase rapidly with fire exposure time as can be seen from Fig. 5. The temperature in the NFRP strip is slightly lower than the CFRP strip due to the higher thickness of the NFRP (10 mm) used in comparison to that of CFRP (1 mm).

To illustrate the variation of the structural response during fire exposure, the moment capacity degradation and enhanced mid-span deflections of the beams are plotted in Fig. 6. It is seen that both beams experience rapid degradation in the moment capacity and increased deflection right from the start of fire exposure time, with the trends being more rapid for the NFRP beam. The failure or the fire resistance of the CFRP-strengthened beam is 165 min, while that for the NFRP-strengthened beam is 140 min based on the deflection limit state. The NFRP beam loses much

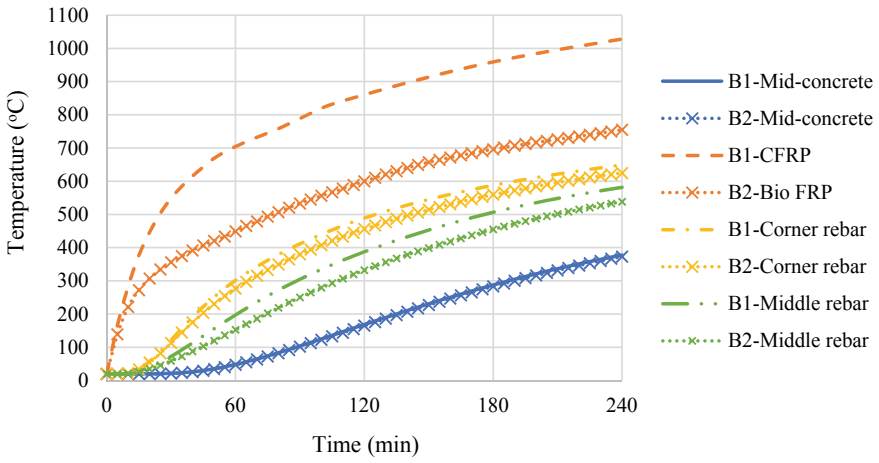

Fig. 5 Thermal response of concrete beams strengthened with CFRP or NFRP reinforcement

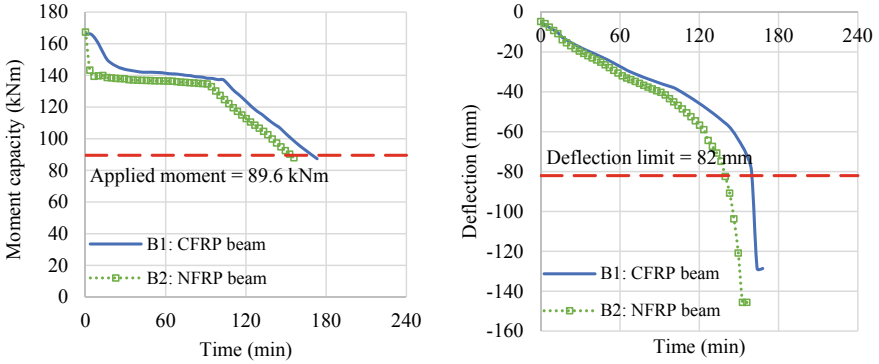

(a) Moment capacity (b) Mid-span deflection

Fig. 6 Structural response of concrete beams strengthened with CFRP or NFRP reinforcement

of the strengthening within 5 min of fire exposure, whereas it takes about 25 min for the CFRP beam to lose its strengthening as seen from Fig. 6. This is because of the faster degradation of strength and stiffness properties of the bio-based FRP with temperature rise as compared to the CFRP strip. Beyond these times, the FRP-strengthened beams act like regular concrete beams without any contribution from the FRP reinforcement. The fire resistance times of 140 min and 165 min in the NFRP and CFRP-strengthened beams are obtained mainly due to the resistance of the concrete section.

Application of fire insulation can delay the temperature rise in the FRP, steel rebar, and the overall concrete section, and thus increase the fire resistance of the FRP-strengthened member. When a layer of fire insulation of 19 mm thickness is applied to the NFRP-strengthened beam, it was observed that the fire performance improved significantly. The NFRP beam was able to retain its strengthening for about 40 min and experienced a more gradual increase in deflections with fire exposure time. The beam did not undergo failure for the entire duration of fire exposure of 240 min. Currently, these numerical studies are being refined and expanded to evaluate the effect of various factors including the presence of fire insulation, strengthening method, and type of FRP on the fire resistance of FRP-strengthened concrete members.

6 Research Needs

As discussed earlier, there is a lack of data on the fire performance of structural members incorporating bio-based FRPs. The fire resistance performance of NFRP structural members can be established through fire tests and calculation methods. Existing test methods and numerical models can be extended to assess the effect of fire on NFRP members. However, for evaluating the fire resistance of NFRP structural

members, high-temperature material properties and material models for NFRP are required as part of the input data. While the material properties of conventional FRPs at elevated temperatures are available in the literature [39], very little information is available on the properties of NFRP composites at room and elevated temperatures.

For bio-based FRP, the effect of temperature on the following properties must be determined as a function of temperature:

- Flammability properties: Flammability index and smoke development classification
- Thermal properties: thermal conductivity, specific heat, and glass transition temperature
- Mechanical properties: tensile strength, compressive strength, modulus of elasticity, stress–strain relations, bond strength, and bond-slip relations
- Deformation properties: thermal expansion and creep

The properties of the bio-based FRP composite together with those of the steel reinforcement and concrete, as a function of temperature, can be used as input data for the numerical model. Through numerical studies, the main variables influencing the fire performance of the NFRP-reinforced concrete members can be established.

The main factors influencing the fire performance of the NFRP-reinforced concrete members, as obtained from the preliminary numerical studies, can be taken into account in designing specimens, such as beams and slabs, for fire tests. The specimens, after sufficient curing, can be tested in a specially built furnace by subjecting them to fire, according to specified time–temperature relations, under design loads. The data recorded during the fire tests will include the history of temperatures along the cross-sections, deflections, and the ultimate fire resistance of the structural members.

Data obtained from the fire tests can be used to establish the validity of the numerical model for the NFRP structural members. These numerical methods can then be used to carry out detailed parametric studies to determine the extent of influence of different parameters, such as the dimensions of structural members and concrete cover, the number (and thickness) of NFRP reinforcement, the thickness and type of fire insulation, etc. on the fire performance of the NFRP structural members.

Results from these studies can be used to make design recommendations, including optimum fire protection measures, for improving the fire performance of NFRP structural members. In addition, data obtained from the parametric studies can be used to develop simple design equations or design charts for calculating the fire resistance ratings, which can be incorporated into the building codes. Such a study on NFRP structural members, which is in progress at Michigan State University, will result in cost-effective, sustainable, and fire-safe construction, and lead to its application in buildings.

7 Summary

Based on the information presented in this paper, the following points can be drawn:

- Very limited information is available on the high-temperature properties of bio-based FRPs and fire performance of bio-based FRP structural components.
- Data on the variation of properties of bio-based FRP (thermal, mechanical, and deformation) at elevated temperatures is required for evaluating the fire resistance of structural members incorporating bio-based FRPs.
- The bio-based FRP-strengthened concrete members exhibit lower fire resistance in comparison to concrete members strengthened with conventional FRP composites.
- Supplementary fire insulation is to be applied on the bio-based FRP-strengthened members to meet the required fire resistance ratings for their use in building applications.

Acknowledgements The study presented in this paper is part of a joint research project between Michigan State University (MSU), USA, Indian Institute of Technology (IIT) Delhi, India, and Birla Institute of Technology & Science (BITS) Pilani, India. The authors appreciate the support of Partnership 2020: U.S.-India Higher Education Cooperation, a collaborative initiative between the U.S. Department of State and the University of Nebraska at Omaha (https://partnership2020.org/).

References

1. Kodur V, Naser M (2020) Structural fire engineering, McGraw Hill Professional, New York, NY, USA
2. Mohanty M, Misra G (2000) Hinrichsen, biofibres, biodegradable polymers and biocomposites: an overview. Macromol Mater Eng 276:1–24. https://doi.org/10.1002/(SICI)1439-2054(20000301)276:1%3C1::AID-MAME1%3E3.0.CO;2-W
3. Ahmed S, Guo Z, Zhang C, Shi D (2020) Zhu, A review on durability of fiber reinforced polymer (FRP) bars reinforced seawater sea sand concrete. Constr Build Mater 256:119484. https://doi.org/10.1016/j.conbuildmat.2020.119484
4. Pickering KL, Efendy MA, Le TM (2016) A review of recent developments in natural fibre composites and their mechanical performance. Compos A Appl Sci Manuf 83:98–112. https://doi.org/10.1016/j.compositesa.2015.08.038
5. Wang YC, Wong P, Kodur V (2007) An experimental study of the mechanical properties of fibre reinforced polymer (FRP) and steel reinforcing bars at elevated temperatures. Compos Struct 80:131–140. https://doi.org/10.1016/j.compstruct.2006.04.069
6. Mochane MJ, Mokhena TC, Mokhothu TH, Mtibe A, Sadiku ER, Ray SS, Ibrahim ID, Daramola OO (2019) Recent progress on natural fiber hybrid composites for advanced applications: a review. http://researchspace.csir.co.za/dspace/bitstream/handle/10204/10871/Mochane_22244_2019.pdf?isAllowed=y&sequence=1.
7. Pandey J, Nagarajan V, Mohanty A, Misra M (2015) Commercial potential and competitiveness of natural fiber composites. In: Biocomposites E (ed) New York. USA, NY, pp 1–15
8. Bachtiar EV, Kurkowiak K, Yan L, Kasal B, Kolb T (2019) Thermal stability, fire performance, and mechanical properties of natural fibre fabric-reinforced polymer composites with different fire retardants. Polymers 11:699. https://doi.org/10.3390/polym11040699

9. Lau K, Hung P, Zhu M-H, Hui D (2018) Properties of natural fibre composites for structural engineering applications. Compos B Eng 136:222–233. https://doi.org/10.1016/j.compositesb.2017.10.038
10. Arrakhiz FZ, El Achaby M, Malha M, Bensalah MO, Fassi-Fehri O, Bouhfid R, Benmoussa K, Qaiss A (2013) Mechanical and thermal properties of natural fibers reinforced polymer composites: Doum/low density polyethylene. Mater Des 43:200–205. https://doi.org/10.1016/j.matdes.2012.06.056
11. Parameswaranpillai J, Krishnasamy S, Siengchin S, Radoor S, Joy R, George JJ, Muthukumar C, Thiagamani SMK, Salim NV, Hameed N (2022) Thermal properties of the natural fiber-reinforced hybrid polymer composites: an overview, natural fiber-reinforced composites: thermal properties and applications 31–51. https://doi.org/10.1002/9783527831562.ch3.
12. Wang YC, Kodur V (2005) Variation of strength and stiffness of fibre reinforced polymer reinforcing bars with temperature. Cement Concr Compos 27:864–874. https://doi.org/10.1016/j.cemconcomp.2005.03.012
13. ASTM (American Society for Testing and Materials) (2021) Standard test method for surface burning characteristics of building materials. ASTM E84–21, West Conshohocken, PA, USA
14. NFPA (National Fire Protection Association) (2006) Standard method of test of surface burning characteristics of building materials. NFPA 255, Quincy, MA, USA
15. ASTM (American Society for Testing and Materials) (2019) Standard test method for specific optical density of smoke generated by solid materials. ASTM E662–19, West Conshohocken, PA, USA
16. ASTM (American Society for Testing and Materials) (2016) Standard Test Method for Surface Flammability of Materials Using a Radiant Heat Energy Source, ASTM E162–16, West Conshohocken, PA, USA
17. ICC (International Code Council) (2018) International Building Code, IBC 2021, Country Club Hills, IL, USA, 2021. https://codes.iccsafe.org/public/document/toc/542/ (Accessed 25 June 2018)
18. Bureau of Indian Standards (2016) National building code of India 2016, SP 7: 2016. New Delhi, India
19. ASTM (American Society for Testing and Materials) (2019) Standard methods of fire test of building construction and materials, ASTM E119–19, West Conshohocken, PA, USA
20. NFPA (National Fire Protection Association) (2006) Standard Methods of Tests of Fire Resistance of Building Construction and Materials, NFPA 251, Quincy, MA, USA
21. ISO (International Organization for Standardization) (1999) Fire resistance tests-elements of building construction, ISO-834, Geneva, Switzerland
22. Williams V, Kodur MF, Green L (2008) Bisby, fire endurance of fiber-reinforced polymer strengthened concrete T-beams. ACI Struct J 105:60
23. Yu VK (2014) Fire behavior of concrete T-beams strengthened with near-surface mounted FRP reinforcement. Eng Struct 80:350–361. https://doi.org/10.1016/j.engstruct.2014.09.003
24. Chowdhury EU, Bisby LA, Green MF, Kodur VK (2007) Investigation of insulated FRP-wrapped reinforced concrete columns in fire. Fire Saf J 42:452–460
25. Kodur VK, Bisby LA, Green MF (2006) Experimental evaluation of the fire behaviour of insulated fibre-reinforced-polymer-strengthened reinforced concrete columns. Fire Saf J 41:547–557
26. Bhatt PP, Kodur VK, Shakya AM, Alkhrdaji T (2021) Performance of insulated FRP-strengthened concrete flexural members under fire conditions. Frontiers Struct Civil Eng 15:177–193. https://doi.org/10.1007/s11709-021-0714-z
27. Kodur V, Ahmed A (2010) Numerical model for tracing the response of FRP-strengthened RC beams exposed to fire. J Compos Constr 14:730–742. https://doi.org/10.1061/(ASCE)CC.1943-5614.0000129
28. Kodur V, Bhatt P (2018) A numerical approach for modeling response of fiber reinforced polymer strengthened concrete slabs exposed to fire. Compos Struct 187:226–240. https://doi.org/10.1016/j.compstruct.2017.12.051

29. CEN (European Standards Committee) (2002) Eurocode 1: Actions on structures - Part 1–2: General actions—actions on structures exposed to fire, EN 1991–1–2, Brussels, Belgium
30. SFPE (Society of Fire Protection Engineers) (2011) Calculating fire exposures to structures, S.01, Gaithersburg, MD, USA
31. CEN (European Standards Committee) (2004) Eurocode 2-Design of Concrete Structures, Part 1–2: General Rules for Structural Fire Design, EN 1992-1-2, Brussels, Belgium, 2004
32. Lie TT(1992) Structural fire protection, ASCE (American Society of Civil Engineers), Reston, VA, USA
33. Kodur V (2014) Properties of concrete at elevated temperatures. International Scholarly Research Notices. 2014
34. Bisby LA, Green MF, Kodur VK (2005) Response to fire of concrete structures that incorporate FRP. Prog Struct Mat Eng 7:136–149. https://doi.org/10.1002/pse.198
35. Griffis RM, Chang C (1981) Thermal response of graphite epoxy composite subjected to rapid heating. J Composite Mater 15:427–442. https://doi.org/10.1177/002199838101500503
36. Kodur VKR, Venkatachari S, Matsagar V, Singh SB (2022) Test methods for characterizing the properties of fiber-reinforced polymer composites at elevated temperatures. Polymers 14(9):1734. https://doi.org/10.3390/polym14091734
37. Yu B, Kodur V (2014) Effect of high temperature on bond strength of near-surface mounted FRP reinforcement. Compos Struct 110:88–97. https://doi.org/10.1016/j.compstruct.2013.11.021
38. Wambua P, Ivens J, Verpoest I (2003) Natural fibres: can they replace glass in fibre reinforced plastics? Compos Sci Technol 63:1259–1264. https://doi.org/10.1016/S0266-3538(03)00096-4
39. Kodur V, Bhatt P, Naser M (2019) High temperature properties of fiber reinforced polymers and fire insulation for fire resistance modeling of strengthened concrete structures. Compos B Eng 175:107104. https://doi.org/10.1016/j.compositesb.2019.107104

Methodologies for Evaluating FRP-Concrete Interfacial Bond Strength at Elevated Temperatures

P. P. Bhatt and Venkatesh Kumar R. Kodur

Abstract The strength of interfacial bond between fiber reinforced polymer (FRP) and concrete substrata influences the capacity of FRP-strengthened concrete structure both at ambient and fire conditions. Evaluation of bond strength is a challenging task at elevated temperatures and requires specialized test setup and a complex set of procedures. In this chapter an innovative test setup and procedure for evaluating the FRP-concrete interfacial bond strength at elevated temperature is proposed, wherein double lap shear tests are conducted on concrete blocks strengthened with FRP sheet. The applicability of the procedure is illustrated by testing the concrete prisms strengthened with carbon FRP sheet at four different temperature levels. The results from the test indicated that the bond strength decreases by 35% at temperatures close glass transition temperature of bonding adhesive.

Keywords FRP-concrete bond strength · Fire resistance · High temperature properties · Bond strength test methods

1 Introduction

The potential of fiber reinforced polymer (FRP) as a strengthening and repair material in retrofitting of concrete structures is well established. Use of FRP offers advantages such as, high strength-to-weight ratio, corrosion resistance, and ease of application, over other traditional strengthening systems [1]. In majority of strengthening and retrofitting applications, FRP sheets or laminates are externally applied to the surface of concrete member using an organic polymer based bonding adhesive such as epoxy resin. The bonding adhesive serves as a medium for transfer of stresses from concrete

P. P. Bhatt
Pacific Structural Forensics, Jersey City, NJ 07310, USA

V. K. R. Kodur (✉)
SAFE-D Center, Department of Civil and Environmental Engineering, Michigan State University, East Lansing, MI 488823, USA
e-mail: kodur@egr.msu.edu

S. B. Singh et al. (eds.), *Fiber Reinforced Polymeric Materials and Sustainable Structures*, Composites Science and Technology, https://doi.org/10.1007/978-981-19-8979-7_2

to FRP, and therefore, the FRP-concrete interfacial bond is critical for effectively carrying the load on the member.

At ambient conditions current design procedures account for interfacial bond by premature debonding through limiting the tensile and shear strains at the level of FRP-concrete interface. However, under fire conditions the bond starts degrading rapidly due to softening of bonding adhesives at temperatures close to the glass transition temperature (T_g), which is in the range of 60–82 °C [2]. The rapid degradation of bond reduces the structural effectiveness of the strengthening system at a faster rate, which in turn leads to rapid reduction of the moment (or shear) capacity of the strengthened structural member, thereby resulting in earlier failure under fire conditions [3, 4]. Thus, temperature induced bond degradation has significant influence on the fire performance of FRP-strengthened concrete structural members. In fact, several experimental studies [5–10] on fire response of FRP-strengthened concrete beams have identified temperature induced bond degradation as a primary reason for early failure of FRP-strengthened beams under fire conditions. Therefore, knowledge of FRP-concrete interfacial bond behavior at elevated temperatures is a key factor in the fire design of strengthened concrete structures and must be evaluated.

Despite the severity of the issue, limited studies have been reported in the literature evaluating the behavior of FRP-concrete interfacial bond at elevated temperatures [11–17]. Different test setups were used in these studies to determine the FRP-concrete bond strength at elevated temperatures. For instance, Gamage et al. [14] and Carlos et al. [16] conducted single lap shear tests, whereas all the other studies conducted a double lap shear test (DST) on concrete blocks strengthened with FRP sheets or strips to evaluate the bond behavior at elevated temperatures. Further, these studies were conducted with different FRP materials and bonding adhesives with T_g ranging from 47 to 85 °C (measured using different methods). Additionally, due to lack of standard test procedures different types of specimens, heating rates, and load levels were considered in these studies. As a result, there exists a wide variation in the reported results, as shown in Fig. 1.

In each of the aforementioned studies, the authors reported a high scatter in the bond strength measured at same temperature level. Moreover, the bond behavior

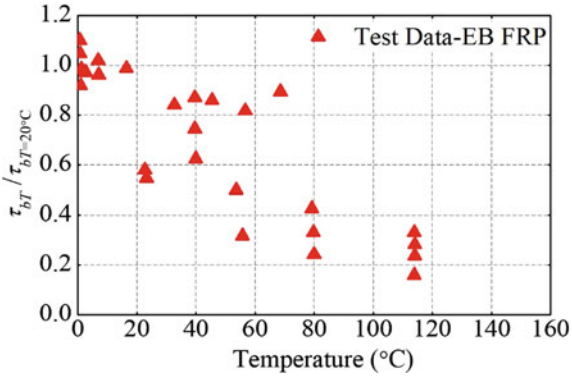

Fig. 1 Variation of bond strength with temperature as reported in various studies

reported in each of these studies was also significantly different. For instance, Blontrock [11] and Klamer et al. [12] reported an increase in the bond strength until the T_g of the adhesive followed by a sharp decrease at temperatures beyond T_g. Whereas Wu et al. [13], Gamage et al. [14], Firmo et al. [16], and Carlos et al. [17] reported a consistent decrease in the bond strength with increase in temperatures below or above T_g of the adhesives. On the other hand, Leone et al. [15] reported a decrease in bond strength until T_g of adhesive followed by an increase in bond strength beyond T_g of adhesive. Thus, it is evident from the above discussion that the results reported in the above-mentioned studies do not provide a clear understanding of the FRP-concrete interfacial bond behavior at elevated temperatures. Further, there are no recommended standardized test methods and procedure for undertaking bond strength tests at elevated temperatures [18]. To address this concern and to evaluate the bond behavior at elevated temperatures a unique test procedure is proposed in this chapter.

2 Limitations of Current Test Method

The FRP-concrete bond behaviour is primarily evaluated using direct shear test methods involving single lap shear test or double lap shear test setup. In a single lap shear test, a portion of FRP sheet is bonded to one side of the concrete block, which is held in position using a steel frame, while the other end of the FRP sheet is clamped and pulled by means of testing machine. In case of double lap shear tests, two concrete prisms are joined by an FRP sheets on two opposing faces and moved apart by means of steel rebar anchored within the blocks or through steel plates connected by bars clamped in wedges of testing machine.

The single lap shear test although easier to implement requires specific attention to maintain the alignment for ensuring pure shear stress in the bonded region. Further, the inherent eccentricity between the tensile load in FRP sheet and restraint provided by the concrete substrate often results in normal stresses in the bonded region which in turn affect the failure mode of the bond. Moreover, due to the direct clamping of the FRP sheet by the testing machine, premature failure of sheet prior to failure of bond is often observed. The double lap shear test removes the disadvantages of load eccentricity and clamped grips, but the specimen is too heavy to handle, and requires specialized equipment for measuring slip at bonded region. Moreover, the symmetrical geometry doesn't guarantee equal load distribution on either side resulting in unrealistic predictions. To address these limitations, an innovative double lap shear test method is proposed here.

3 Proposed Test Method

An innovative test setup and procedure is proposed to characterize the FRP-concrete interfacial bond behaviour at elevated temperatures. The proposed test procedure involves a series of double lap shear tests on specially fabricated test specimens comprising of concrete prism strengthened with a continuous FRP sheet. The FRP sheet is applied on two opposing faces of the prism and is wrapped over a half-cylinder plate, which is clamped to the wedges of the testing machine. The concrete prism is placed in the test frame and is fixed at the bottom, while the half-cylinder plate is pulled upward to generate shear stresses at the FRP-concrete interface. The details of a typical specimen assembly, equipment used, test setup, and procedure followed are described here.

3.1 Typical Specimen

The test specimen used in the proposed test method comprises of four different components, namely a concrete prism, a steel rebar with threads cut on one end, a carbon fiber sheet, and an aluminium plate (in shape of half-cylinder) with smooth semi-circular surface on the top and a rectangular base at the bottom, as shown in Fig. 2a. The concrete prism is strengthened with an inverted U-shaped continuous FRP sheet on two opposing faces and is provided with a concentric steel rebar with unthreaded end flushed with the top surface of the prism, while the threaded end protruding outside the bottom end of prism. The inverted U-shaped FRP sheet is wrapped over the semi-circular half-cylinder placed on the top surface of the prism. The diameter of the half-cylinder is equal to the width of the concrete prism to ensure that a pure shear stress is applied to the FRP-concrete interface. A schematic layout of the assembled specimen is shown in Fig. 2b. The assembled specimen is placed in a specially designed and fabricated test set up as shown in Fig. 3a and described in following section.

3.2 Test Equipment, Setup, and Procedure

The test equipment comprises of a tension testing machine, a loading device, a heating device, and instruments for measuring temperature, load, and deformation of the specimen as well as a data acquisition system for recording the measurements. The testing machine comprises of two heavy steel beams laid horizontally and connected through a high strength extension rod on each end. A steel plate is rigidly connected using high tension bolts at the mid-span of the top and bottom beams each. These steel plates are in turn rigidly connected with two steel plates (connector plates) at

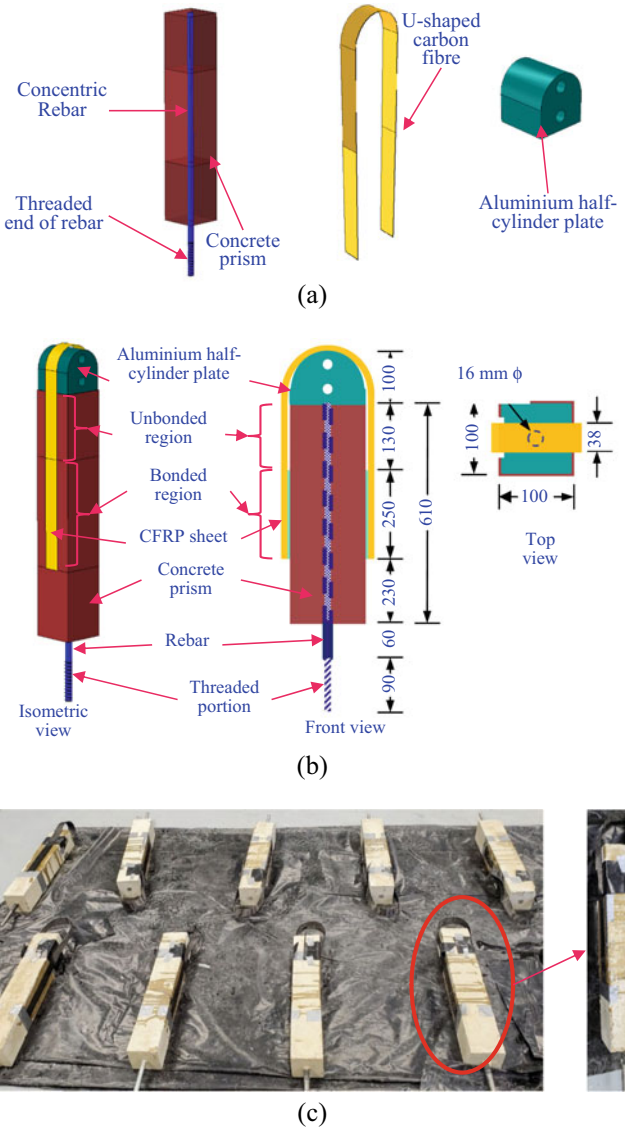

Fig. 2 Specimens for bond strength tests: **a** components of specimen, **b** schematic layout, **c** typical test specimens

the top and a U-shaped bracket at the bottom, using high tension bolts, as shown in Fig. 3a. Two washer plates are provided between the connector plates and either side of anchor plate to ensure sufficient space is available for placing the half-cylinder between the anchor plates. This arrangement creates a clamping bracket for anchoring the top end of the specimen.

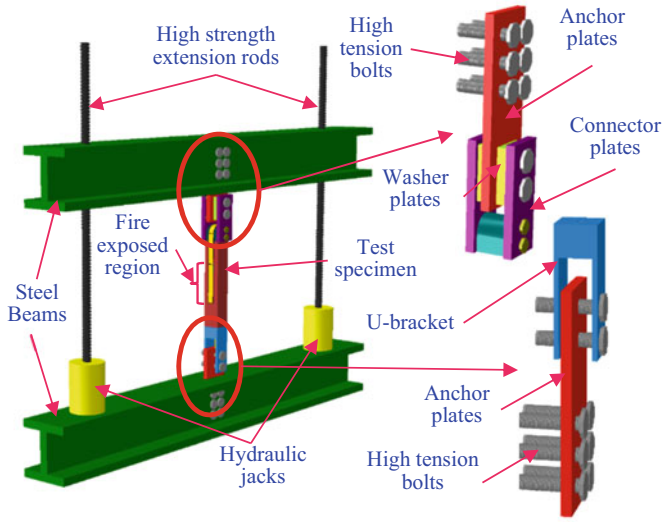

(a)

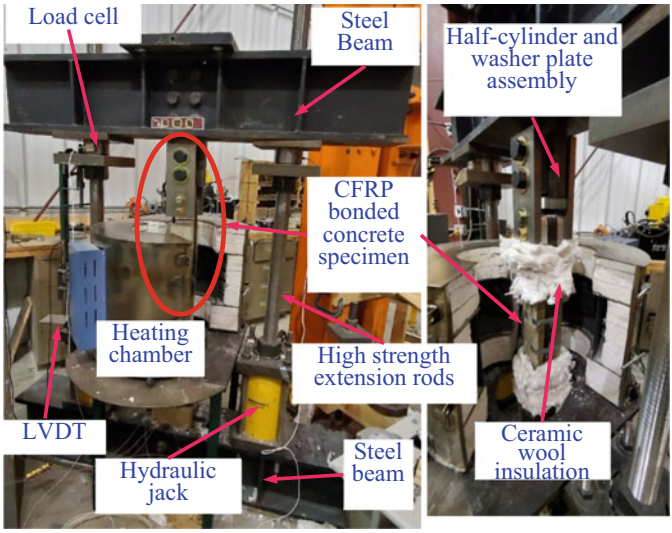

(b)

Fig. 3 Test set up for high temperature bond strength tests **a** schematic view, **b** experimental setup

The loading device comprises of two hydraulic jacks placed on the bottom steel beam, as shown in Fig. 3b, which moves the top beam upward through the high strength extension rods. The heating device comprises of a small-scale electric furnace which is placed on a tabletop between the top and bottom steel beams, as

shown in Fig. 3b. The furnace can heat the test specimen to a desired target temperature, which can be as high as 1000 °C. The electric furnace comprises of cylindrical chamber with an inner diameter of 203 mm and an inner height of 254 mm. The target temperature, heating rate, and stabilization duration can be programmed into the furnace through a control module.

The load applied to the specimen is measured by a pair of load cells attached to extension rods and the axial deformation of the specimen is measured through a linear variable displacement transducer (LVDT), attached to the top loading frame through a rigid steel bracket assembly. The furnace temperature is measured by taking the average of three internal thermocouples mounted on the interior walls of furnace which monitor the furnace temperature at upper, middle, and lower zones. In addition, four thermocouples (two on each bonded face) are directly attached to the specimen to monitor the actual specimen temperature during high temperature tests. The load cells, LVDT, and specimen thermocouples are connected to a data acquisition system, wherein applied load, displacement as well as furnace and specimen temperatures can be recorded. Through this setup, double lap bond strength test can be conducted on FRP-strengthened concrete prism as per following procedure.

First the specimen is mounted in the testing machine and is anchored at the top end by tightly bolting the half-cylinder plate, placed at top surface of prism, to the connector plates. The tight connection allows for a rigid body movement of the half-cylinder plate with the top beam. The bottom end of the specimen is anchored by tightly bolting the steel rebar to the U-shaped steel bracket, which keeps the prism fixed at the bottom. After anchoring the specimen, the unbonded region at top and bottom of the prism is covered with insulation (*cf*. Fig. 3b) to prevent direct exposure to heat and subsequent temperature rise in those regions. The furnace door is then closed, and heating is turned-on to attain a target temperature at a pre-determined heating rate. Once the target temperature in the bonded region is reached it is maintained at that level for five minutes to ensure uniform temperature along the entire bonded region. Upon stabilization of temperature, hydraulic pumps, attached to loading jacks, are turned-on and loading is applied on the specimen. When hydraulic jacks apply an increasing load, the top beam along with the half-cylinder plate (on the top of the specimen) moves upward, which in turn pulls the CFRP sheet. Since the prism is tightly anchored at the bottom, the entire tensile force (pull on CFRP) is carried by the bonded region through shear. During the test, the top beam is always maintained in a perfectly horizontal position to minimize eccentric loading during the test and ensure equal loading on both the bonded regions. The load is applied continuously until one or both the bonded region fails, while the temperature, displacement, and load applied are recorded.

4 Bond Strength Test

To illustrate the applicability of the above-described test method, eight different specimens were tested at Civil Infrastructure Laboratory of Michigan State University. The dimensions of each component of the specimen are shown in Fig. 2b. The concrete prisms were 610 mm long and 100 mm × 100 mm in cross-section, the concentric steel rebar was 16 mm in diameter and 760 mm long with threads cut on one end for a length of 90 mm. The carbon fiber sheet was 38 mm wide and 1100 mm long, of which 250 mm was bonded to the concrete prism on two opposing sides, while loosely passing over the half-cylinder plate. The bond between carbon sheet and concrete started at 230 mm from bottom end of the prism while the top 130 mm portion of the sheet was left unbonded as shown in Fig. 2b.

The carbon fiber sheet was applied using a two-component epoxy V-wrap 770 epoxy through wet-layup procedure, as described by the manufacturer. Prior to application of the carbon sheet, the concrete surface on either side of the prism was roughened using a belt sander and thoroughly clean using compressed air. The bond length on either side of the specimen was 250 mm, which was higher than the minimum anchorage length (111.2 mm), determined as per ACI 440.2R-17 [2] guidelines.

The concrete prisms were cast from a batch of pre-mixed concrete which comprised of Type I Portland cement, sand, and carbonate based coarse aggregates. The batch mix yielded an average cylindrical compressive strength of 37 MPa and a split tensile strength of 3.5 MPa, measured through testing of 3 cylinders each for tension and compression, after 28-days of casting. The rebars had an average yield strength of 430 MPa, determined from the tensile test of three rebar coupons. The dry carbon fiber sheet and the laminate had a tensile strength of 4830 MPa, and 1240 MPa, and elastic modulus of 227.5 GPa and 73.77 GPa, respectively, as reported by manufacturer, while the epoxy resin used for bonding the carbon fiber sheet had glass transition temperature of 82 °C. These properties are summarized in Table 1.

The double lap bond strength tests were conducted at four target temperatures, i.e., 20, 40, 60, and 80 °C. The last target temperature being the closest to the T_g of the adhesive. The heating rate in the furnace was set to 2–5 °C per minute depending on the target temperature (higher rate for higher target temperature). All tests were

Table 1 Material properties of the carbon fabric, epoxy and CFRP laminate (as per manufacturer)

Material	Ultimate tensile strength (MPa)	Elastic modulus (GPa)	Ultimate strain (%)	Glass transition temperature T_g (°C)
V-wrap C200H dry carbon sheet	4830	22.75	2.1	–
V-wrap 770 epoxy	60.7	2.76	4.4	82
V-wrap C200H cured laminate	1240	73.77	1.7	Not available

conducted under steady state condition. The loading was applied on the specimen at a rate of 2 mm/min until failure occurred. The temperature rise at the interface, the load applied, and the resulting deflection were recorded through a data acquisition system which are then analyzed to evaluate the load–displacement response of the bonded joint.

5 Results and Discussion

Data recorded in the above tests is utilized to evaluate the bond strength of CFRP-concrete interface at elevated temperatures. It was observed that at lower temperatures i.e., 20 and 40 °C, failure of the specimens occurred in cohesive mode, while at 60 and 80 °C, failure occurred in mixed cohesive-adhesive pattern, with a thin layer of concrete attached to the disbanded CFRP sheet. These failure patterns are shown in Fig. 4a. The bond performance of CFRP-concrete system is evaluated using the average bond stress along the bonded length of the specimen [19]. The peak value of the average bond stress defined as the ratio of failure load to bonded area is taken as the bond strength of the specimen. At each target temperature two specimens were tested and the average of two values is taken as the bond strength of the CFRP-concrete interface. The load applied when the failure is reached and the computed bond strength of each specimen, as well as the average bond strength of the interface at each temperature, are summarized in Table 2.

It can be seen from the table that at same temperature level, the failure load from two tested specimen is nearly same indicating a minute scatter in the results. The average failure load of the specimens tested at room temperature (i.e., 20 °C), is 26.13 kN, which is in close agreement with the theoretical value of failure load (27.10 kN) computed using the relation proposed by Chen and Teng [20]. Since the difference between the experimentally measured and theoretically computed failure load is only 3.3%, the measured failure load is taken as the actual failure load of the CFRP-concrete interface. At 40 °C, the average failure load of the CFRP-concrete interface decreases slightly to 24.96 kN. At elevated temperatures, i.e., 60 °C and 80 °C, the failure load of the CFRP-concrete interface further decreases to 21.68 kN and 17.03 kN, respectively.

The load versus displacement response of a representative specimen tested at each target temperature is shown in Fig. 4b. At each target temperature the load increases linearly with displacement till failure occurs in an abrupt pattern. It can be seen from the figure that at lower temperatures, the initial stiffness of the CFRP-concrete interface is nearly same, however, with increases in temperature the stiffness of the interface decreases at a faster rate. This can be attributed to the fact that with increase in temperature, the epoxy loosens which reduces the load transferring capability of the bonded joint thereby reducing the stiffness of the joint.

The bond strength of each specimen normalized with respect to average bond strength at 20 °C, are summarized in Table 2 and the average of normalized bond strength at each temperature are plotted in Fig. 4c. It can be seen from the Table 2 and

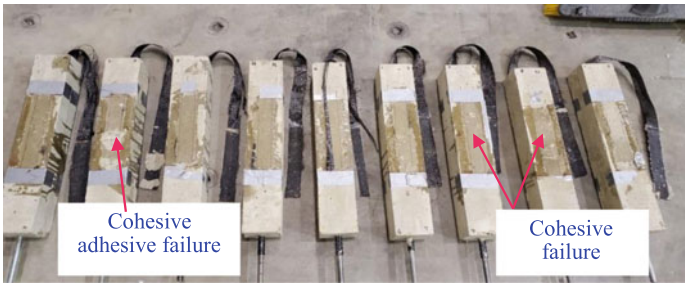

(a)

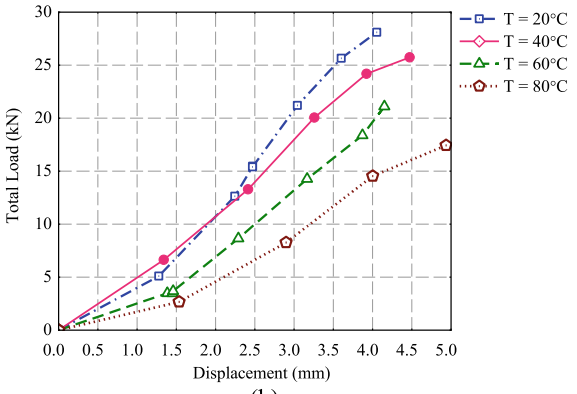

(b)

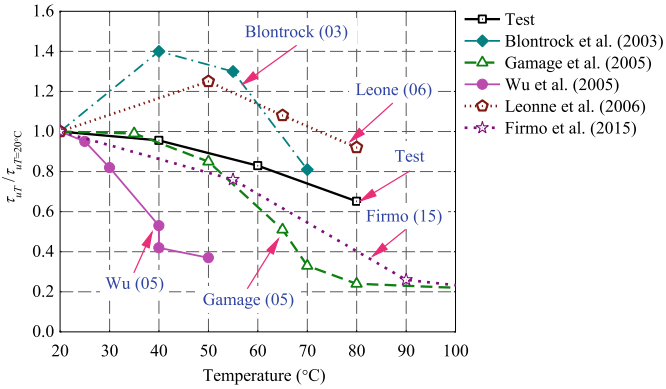

(c)

Fig. 4 Results from the double lap shear test on FRP-concrete specimens at elevated temperature **a** load displacement response of CFRP-concrete interface, **b** comparison of bond strength variation with temperature, **c** tested specimens

Table 2 Summary of bond strength tests results

S. No.	Test temperature (°C)	Failure load (kN)	Bond strength (MPa)	Average strength (MPa)	Retained strength ratio	Normalized strength ratio
1	20	28.10	1.45	1.35	1.08	1.00
2	20	24.16	1.25		0.92	
3	40	24.19	1.25	1.29	0.93	0.96
4	40	25.73	1.33		0.98	
5	60	21.10	1.09	1.12	0.81	0.83
6	60	22.26	1.15		0.85	
7	80	17.43	0.90	0.88	0.67	0.65
8	80	16.63	0.86		0.64	

Fig. 4c that the CFRP-concrete bond strength decreases progressively with increase in temperature. The decrease in bond strength is marginal (only 4%) at 40 °C, but there is rapid decrease in bond strength to 83% and 65% of the room temperature strength at 60 °C and 80 °C, respectively. This deteriorating pattern in bond strength follows the same trends as reported in previous studies. Further, the bond strength retention factors reported in the previous studies are also plotted in Fig. 4c. It can be seen from the figure that the bond strength retention factors measured in the current tests compare well with the previously reported trends.

6 Practical Implications

FRP-concrete interfacial bond strength is a major factor influencing the fire resistance of FRP-strengthened concrete structural members. Like other properties the bond strength degrades with increase in temperature. Research till date indicates that the degradation in bond strength is much higher than the degradation in tensile strength of FRP at the same temperature level [3, 4]. Therefore, it is necessary to evaluate the FRP-concrete bond behaviour strength at elevated temperatures specifically up to a temperature range of 300–350 °C [4]. At present, there is no guidance for characterizing the bond behavior of elevated temperature. Moreover, the available studies have several limitations as explained earlier. The standardized test procedure described in this chapter can be easily adopted for undertaking interfacial bond strength of different FRP types at various temperature levels.

7 Summary

The FRP-concrete interfacial bond strength degrades rapidly with rise in temperature. The rapid degradation leads to significant decrease in the capacity of the strengthened structural member and often lead to abrupt failure. Therefore, it is necessary to account for the temperature dependent interfacial bond strength in determining fire response of FRP-strengthened concrete members. Currently, there are no standardized test procedures and methods provided in test standards for evaluating the high temperature FRP-concrete interfacial bond strength. Therefore, an innovative test setup and procedure is proposed here to evaluate the bond strength of FRP-concrete interface. This method involves conducting a double lap shear test on a concrete prism strengthened with FRP on two opposing faces. The applicability is illustrated by measuring the FRP-concrete bond strength at four different temperature levels. The results indicate that the bond strength decreases by 35% at temperature close to T_g of the bonding adhesive. The trends measured in the current study agree with those reported in open literature.

Acknowledgements The authors wish to acknowledge the support of Structural Technologies LLC and Michigan State University for providing the materials and infrastructure for undertaking this research. Any opinions, findings, conclusions, or recommendations expressed in this paper are those of the author and do not necessarily reflect the views of the sponsoring institutions.

References

1. CE Bakis LC Bank VL Brown E Cosenza JF Davalos 2002 Fiber-reinforced polymer composites for construction-state-of-the-art review J Comp Const 6 2 73 87
2. ACI 440.2R-17 (2017) Guide for the design and construction of externally bonded FRP systems for strengthening concrete structures, ACI
3. Bhatt PP, Kodur VKR, Hawileh R, Al-Nuaimi N, Abdalla J (2019) Effect of temperature induced bond degradation on fire performance of FRP-strengthened concrete beams. In: 7th international colloquium performance, protection & strength structure und. external load. & eve. (PROTECT 2019), Whistler
4. Bhatt PP (2021) Fire performance of FRP-strengthened concrete flexural members. Ph.D. thesis, Michigan State University, East Lansing
5. Blontrock H, Taerwe L, Vandevelde P (2000) Fire tests on concrete beams strengthened with fiber composite laminates. In: Third Ph.D. symposium in civil engineering, institute of structural engineering, University of Agricultural Science, Vienna, pp 151–161
6. B Williams VKR Kodur MF Green LA Bisby 2008 Fire endurance of fiber-reinforced polymer strengthened concrete T-beams ACI Struct J 105 1 60 67
7. A Ahmed VKR Kodur 2011 The experimental behavior of FRP-strengthened RC beams subjected to design fire exposure Eng Struct 33 7 2201 2211
8. Firmo JP, Correia JR, França P (2012) Fire behaviour of reinforced concrete beams strengthened with CFRP laminates: protection systems with insulation of the Anchorage Zones. Comp Part B Eng 43(3):1545–1556
9. JP Firmo JR Correia 2015 Fire behaviour of thermally insulated RC beams strengthened with EBR-CFRP strips: experimental study Comp Struct 122 144 154

10. TB Carlos JPC Rodrigues RCA Lima de D Dhima 2018 Experimental analysis on flexural behaviour of RC beams strengthened with CFRP laminates and under fire conditions Comp Struct 189 516 528
11. Blontrock H (2003) Analysis and modeling of the fire resistance of concrete elements with externally bonded FRP reinforcement. Ph.D. thesis, Ghent Univ., Belgium
12. Klamer EL, Hordijk DA, Janssen HJM (2005) The influence of temperature on the debonding of externally bonded CFRP, ACI: SP 230, pp 1551–1570
13. ZS Wu K Iwashita S Yagashiro T Ishikawa Y Hamaguchi 2005 Temperature effect on bonding and debonding behavior between FRP sheets and concrete J. Soc Mat Sci Jap 54 5 474 480
14. JCPH Gamage R Al-Mahaidi MB Wong 2006 Bond characteristics of CFRP plated concrete members under elevated temperatures Comp Struct 75 1–4 199 205
15. Leone M, Matthys S, Aiello MA (2009) Effect of elevated service temperature on bond between FRP EBR systems and concrete. Comp Part B Eng 40(1):85–93
16. JP Firmo D Pitta JR Correia C Tiago MRT Arruda 2015 Experimental characterization of the bond between externally bonded reinforcement (EBR) CFRP strips and concrete at elevated temperatures Cem Conc Comp 60 44 54
17. TB Carlos JPC Rodrigues 2018 Experimental bond behavior of a CFRP strengthening system for concrete elements at elevated temperatures Const Build Mat 193 395 404
18. VKR Kodur MZ Naser 2020 Structural fire engineering 1 Mc Graw-Hill Professional New York
19. B Yu VKR Kodur 2014 Effect of high temperature on bond strength of near-surface mounted FRP reinforcement Comp Struct 110 88 97
20. JF Chen JG Teng 2001 Anchorage strength models for FRP and steel plates bonded to concrete J Struct Eng 127 7 784 791

Durability of FRP Composites for Use in Civil Infrastructure—From Materials to Application

Vistasp M. Karbhari

Abstract Although fiber reinforced polymer (FRP) composite materials have found acceptance for use in civil infrastructure applications such as in reinforcement, in rehabilitation, and in new structural systems there are still concerns related to long-term durability in harsh and changing environmental conditions and after exposure to heat in the form of fire and elevated temperatures seen in some industrial applications. This paper presents examples of carbon-epoxy composites used in civil infrastructure. Results are discussed from both materials and applications perspectives addressing some long-standing myths and providing guidance for field use and design, emphasizing that if processed and used in appropriate fashion these materials can provide tremendous advantages with relatively low concern regarding degradation below threshold values used in design.

Keywords Composites · Durability · Infrastructure · Deterioration

1 Introduction

A nation's prosperity and progress depend intrinsically on the state of its built infrastructure. Structural concrete and steel have been used successfully over the ages but suffer from the effects of degradation and deterioration ranging from effects of corrosion of steel to those of deterioration of concrete. Some examples of this are shown in Fig. 1. Such deterioration not only results in significant cost related to maintenance and repair but also economic and operational losses due to posting and even closure of roads/bridges, reduced load capacity and usage of buildings, and lower pressures and flow in pipelines. As an example, the American Road and Transportation Builders Association estimated that in 2021 there were 223,972 bridges (or 36% of the inventory) that needed replacement or rehabilitation with an estimated cost of replacement exceeding $58 billion [1]. Statistics in other countries are similar in most cases. As infrastructures ages the issues related to its continued operation

V. M. Karbhari (✉)
Department of Civil Engineering and Department of Mechanical & Aerospace Engineering, University of Texas, Arlington, TX 76006, USA
e-mail: vkarbhari@uta.edu

S. B. Singh et al. (eds.), *Fiber Reinforced Polymeric Materials and Sustainable Structures*, Composites Science and Technology, https://doi.org/10.1007/978-981-19-8979-7_3

Fig. 1 Deterioration in infrastructure components

at the highest levels of effectiveness increase often leading to deficiencies that may be functional in addition to structural. For these reasons, among others, there is a constant search for new materials and methods that can effectively meet the demands of the built infrastructure.

Fiber reinforced polymer (FRP) composites have been used extensively in civil infrastructure applications in forms ranging from reinforcement in concrete to bonded components for strengthening and retrofit and as new structural components and systems. The light weight, high specific performance attributes, ease of use in the field, tailorability, and potential high durability make these materials and the structural components/systems extremely attractive for use especially when considering long periods of use in harsh and changing environments with minimal inspection. Their use has been proven in areas such as seismic retrofit (Fig. 2) [2], where the ability to place reinforcement primarily in the hoop direction for confinement without increasing axial stiffness has significant structural advantages, and in the strengthening of deteriorated/damages and/or understrength elements such as beams and slabs through the external bonding of prefabricated strips or placement of fabric through wet layup in the field (Fig. 3) [3, 4].

In addition, these materials have been shown to be extremely effective in blast hardening of structures and elements (Fig. 4) [5], and in the development of new structural systems such as pylons [6] and entire bridge systems [7, 8] (Fig. 5) that incorporate a combination of FRP and conventional materials or FRP alone. In all these the inherent tailorability, high performance attributes, lightweight and ease of placement in the field, and potential long-term durability are significant advantages over conventional materials.

Fig. 2 Application of composites for seismic retrofit of columns

Fig. 3 External bonding of composites for strengthening of decks

While the long-term durability of FRP composites is often stated as one of the attractive features for use in civil infrastructure it must be noted that these materials do degrade and age with time, albeit not at the same rate and through the same processes as conventional materials. The durability depends intrinsically on the choice of constituents (fiber, filler, matrix/resin), the processing methods used, degree of cure attained, and the environment to which the material and resulting structural system are exposed. It has to be kept in mind that although there is a very large database on FRP materials used in the aerospace sector, the materials used in

Fig. 4 Use of composites for blast hardening

Carbon/Epoxy Pylon System FRP Bridge System

Fig. 5 Composites in new infrastructure systems

civil infrastructure often differ based on process and standards and hence the characteristics and durability cannot be directly applied to civil infrastructure applications. The lack of understanding about these materials among civil engineers as well as the paucity of long-term validated data has resulted in these materials being afforded extremely high factors of safety, that could better be described as factors of "ignorance," resulting in very high inefficiencies. While the topic of durability of FRP materials in civil infrastructure and the development of appropriate design factors is a fairly complex topic [9–11] there is a strong basis for this to be addressed in a comprehensive fashion keeping in perspective the nuances and variations of this class of materials. Since there are several myths about the durability of these materials the paper is structured around a set of these with the intention of using data to address misconceptions and dispel myths, while providing a better understanding of key aspects as related to carbon/epoxy composites based on research conducted by the author's research group.

2 Materials Durability

Although carbon fibers are inert to most environmental conditions likely to be faced by civil infrastructure components except for elevated temperatures at the level that initiate surface oxidation and degradation, carbon fiber reinforced composites can deteriorate through degradation at the level of the resin and/or the fiber-matrix bond. This can be seen through exposures as simple as immersion in an aqueous solution to the more complicated mechanisms seen in freeze–thaw cycling. In general, the degradation in properties is more pronounced for characteristics that are dependent on the resin and bond rather than those that are fiber dominated. Thus, while degradation in tensile strength and modulus can be seen over periods of time and types of exposure the deterioration is likely to be significantly higher in off-axis and resin dominated modes.

Figure 6, for example, shows the deterioration in tensile strength and modulus over an extended period due to exposure in water, concrete leachate and saltwater solution for specimens consisting of two layers of unidirectional fabric similar to that used for the strengthening of concrete through external bonding using the wet layup process. As can be seen there is minimal change in the modulus over the extended period of exposure and strength is seen to decrease by a maximum of 21% when immersed in the saltwater solution.

In comparison, unidirectional composites are more susceptible to crack propagation and interlayer separation under flexural/shear loading. Interlaminar properties are dependent on resin characteristics which show greater susceptibility to moisture induced deterioration when processed using wet layup due to varying interlayer thicknesses, and higher void contents. Deterioration is at the fiber matrix interface level through debonding and microcrack coalescence as well as in the resin rich zone between fabric layers, resulting in the two layered composites showing a higher level of shear strength deterioration than the single layered composite specimens. As can

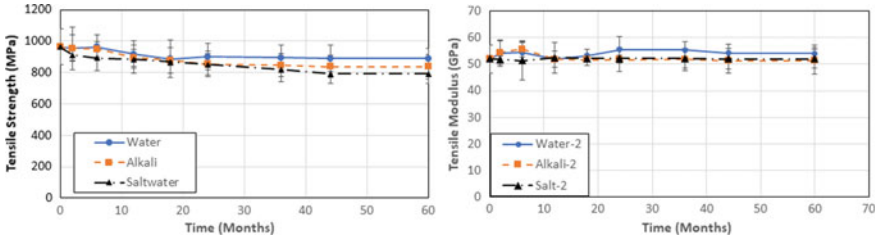

Fig. 6 Change in tensile characteristics as a function of solution and time of immersion [12]

be seen in Fig. 7 in all cases there is rapid degradation for an initial period followed by a slower rate of deterioration with longer time periods of immersion resulting in near asymptotic or extremely slow duration rate regimes, with overall deterioration being significantly greater than that noted in tension.

The difference in response can be elucidated further through assessment of in-plane shear strength as shown in Figs. 8 and 9. As noted in [13] the large drops in strength can be directly related to deterioration at both the inter-ply and fiber–matrix interphase levels, which due to the ±45° configuration results in a direct effect on modulus as well.

The effect of moisture uptake on the deterioration of the bond between the fiber and matrix can be clearly seen from a comparison of micrographs in Fig. 9 wherein the one on the left shows good bond development in an unexposed specimen as against less hackling in the resin and cleaner fiber surfaces after 32 weeks of immersion in deionized water at 60 °C as seen in the micrograph on the right.

Most design guidelines emphasize the tensile characteristics of materials as related to strengthening since those are the mechanical attributes used in design. However, the crucial failure mechanisms are at the interfacial and fiber-matrix debond level, as well as those related to the interfaces between layers of fabric laid up (often in a vertical or overhead configuration) sequentially. These interfaces are the weakest zone in the composite and can be significantly deteriorated by environmental exposure since these are based on the resin. As discussed, earlier moisture exposure results in significant deterioration in interlaminar and intralaminar characteristics, often at rates significantly higher than those determined for fiber direction tensile properties.

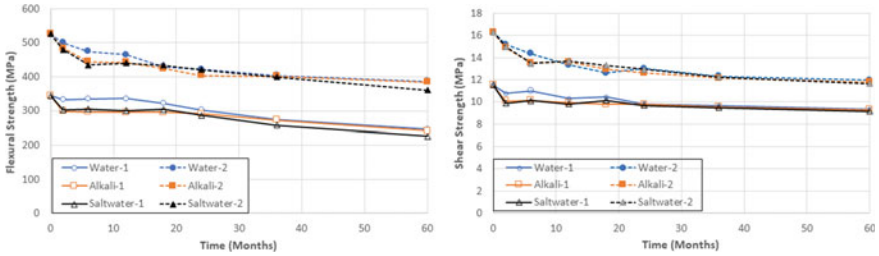

Fig. 7 Change in flexural characteristics as a function of solution and time of immersion [12]

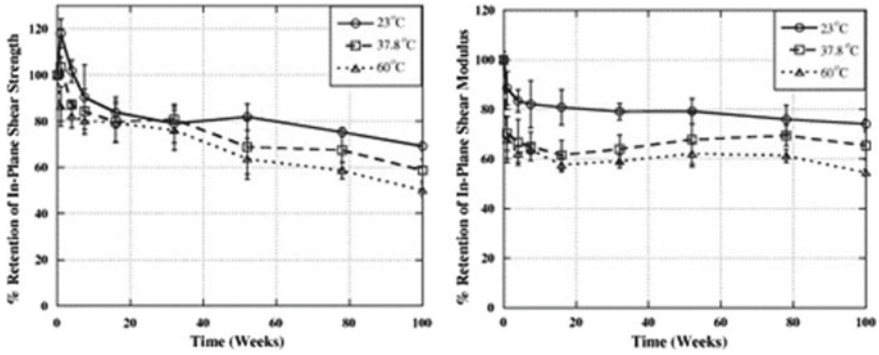

Fig. 8 Change in in-plane shear characteristics as a function of temperature and time of immersion [13]

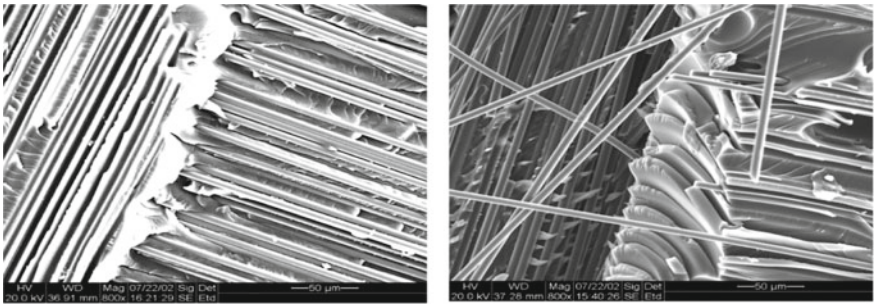

Fig. 9 Micrographs showing a comparison of fiber-matrix bond [13]

Degradation in these characteristics can lead to premature failure due to mechanisms such as fiber–matrix debonding and layer delamination/separation. And hence it is critical that changes in these properties are not only evaluated, but also considered in the design process.

To predict the change in performance attributes over time, degradation is often accelerated using time–temperature superposition principles. At the simplest level this entails exposing specimens in the laboratory to conditions of elevated temperature immersion. A caution related to this process, although widely used, is that extrapolation of short-term results to predict long-term effects can result in significant over estimation of deterioration as depicted schematically in Fig. 10, leading to unrealistic estimates for degradation and overly conservative thresholds for performance attributes. The actual degradation of carbon-epoxy composites over time is significantly lower than that predicted through acceleration in short-term tests as can be seen through results obtained for strength and stiffness over an extended period of time.

Figure 6, as stated earlier, depicts the actual change in tensile strength and stiffness of a two-layered carbon/epoxy composite fabricated using the wet layup process

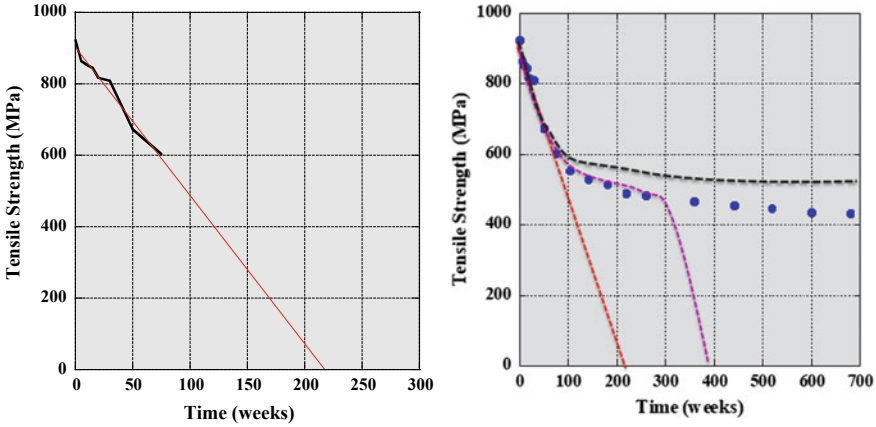

Fig. 10 Extrapolation from short-term data

immersed in solutions emphasizing not just the low level of deterioration but also the asymptotic behaviour over the longer time period. It is of interest to note that strength retention at the end of the 60-month period of immersion in water is 92.3% and that for modulus is 104.05% (with the increase being due to post-cure effects) whereas the predicted values based on an Arrhenius method of acceleration are 76.2% and 97%, respectively [14] emphasizing the differences between prediction based on short-term data and actual behaviour.

It should also be stressed that unless the structure is underwater it is rare that the strengthening system will remain immersed in the solution over the extended period of time. As has been pointed out by a number of investigators previously, based on the mechanisms in the resin, drying of a composite can result in significant regain in mechanical characteristics [15], again making the experimental tests far more aggressive as related to deterioration than the effects of field exposure.

3 Application to Structures

Carbon fiber reinforced polymer composites have been used to great effect for the strengthening of deteriorating bridge infrastructure ranging from beams to slabs, caps, and columns. In these applications the focus of materials selection and design needs to be not just on the composite but also on the bond between the composite and the concrete substrate requiring close attention to surface preparation, environmental conditions during placement and cure, and exposure conditions in addition to the expected structural considerations [16, 17]. Substrate surface characteristics are a major consideration in the overall durability of the system and to this end due focus needs to be given to the "effect of defects" on overall response and life-cycle prediction. Results of studies on these topics as related to carbon/epoxy bridge strengthening

systems are given in [18, 19]. Effectively, the data needs to be brought to bear under a damage tolerance methodology as depicted schematically in Fig. 11, providing a direct correlation between damage/defect size/extent to the residual design characteristics and remaining service life. Examples of defect type of fracture energy release rate are shown in Fig. 12 as examples.

The incorporation of materials level data along with the interaction between the strengthening system and the structure to be strengthened under a reliability framework such as shown schematically in Fig. 13 provides the basis for the assessment of service-life of a rehabilitated structure [20]. In this model a structure having a reliability, β_c, lower than desired can be rehabilitated using FRP composites to increase reliability to a level β_{rehab} after which the change in reliability with time is predicted based on an interactive materials-structure health monitoring scheme. The incorporation of materials durability data provides the basis for service-life prediction under a range of exposure and use conditions. Such tools provide the owner/operator of a structural system such as a bridge the ability to not just predict remaining service life but also provide condition-based assessments for maintenance.

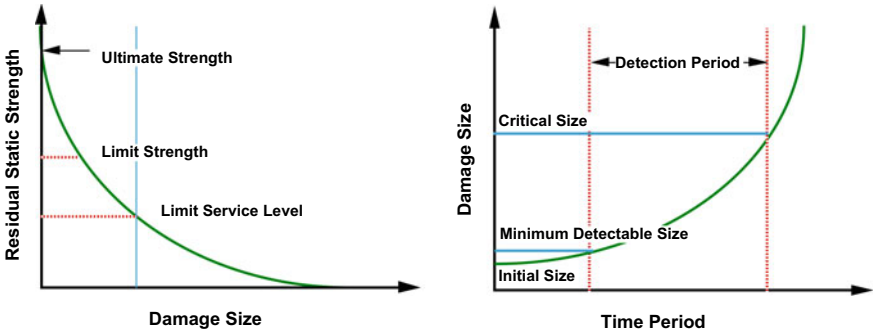

Fig. 11 Schematic of an effect of detects damage tolerance methodology

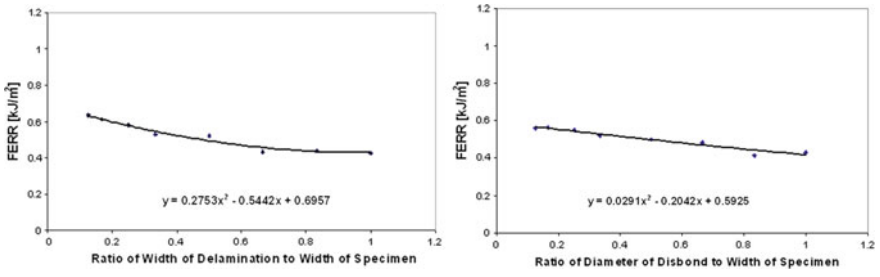

Fig. 12 Effect of defects

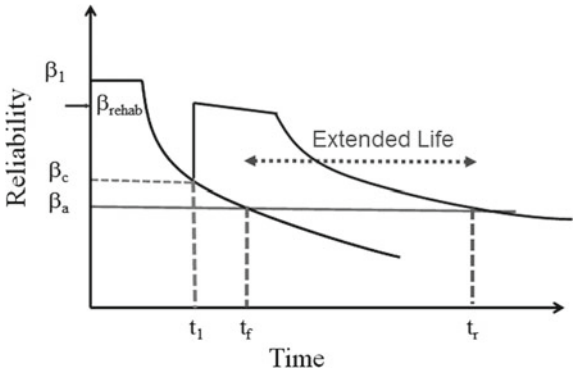

Fig. 13 Schematic of reliability based life-extension model

4 Summary and Conclusions

Fiber reinforced polymer matrix composites provide significant advantages over conventional materials as related to the retrofit and rehabilitation of deterioration and understrength infrastructure systems. However, these systems should not be regarded as a panacea for the serious issues facing the built infrastructure. Rather they are an addition to the palette available to the designer in selecting the method that is the most appropriate for a specific situation. In many cases due to their light weight, high performance attributes, ease of placement in the field, ability for use with minimal added dimensions to the original structure, and potential long-term durability carbon fiber reinforced polymer composites prove to be effective choices. In using these materials, however, specific aspects need to be kept in kind, among which are the following:

- While FRP composites do not corrode (as in rusting of steel) they undergo physical and chemical changes including those due to oxidation and can be degraded due to environmental exposure. The type and level of degradation depends on the constituents (fiber and resin), processing details including the degree of cure, and the presence of defects. In general, appropriately designed FRP materials can show extremely good durability.
- FRP composites used in civil infrastructure applications have different characteristics from those used in the commercial/defense aerospace sectors based on processing method and level of materials specification. Thus, data bases from the aerospace sector are not directly applicable to the civil sector.
- Carbon fibers are relatively inert to most environmental influences likely to be faced in civil infrastructure applications. However, their incorporation into FRP composites results in the potential of degradation of the composite at the level of the resin and/or the fiber-matrix interface.
- As with grades of steel and concrete, composites also differ based on constituents and processing method and hence it is critical to specify these details for design, and not assume that all composites have the same characteristics and durability.

- The processing method used to fabricate FRP composites has a significant effect on both short-term and long-term characteristics. The use of the wet layup process will result in lower fiber volume fractions and a higher void content than pultrusion. However, it provides greater flexibility for use in the field especially when conformance to the structural profile is necessitated.
- Damage mechanisms can be complex with competing mechanisms related to progression of cure over time and deterioration.
- The glass transition temperature is a key characteristic of long-term durability and can be used to set operational limits.
- The intrinsic effectiveness of a the FRP material in effecting structural rehabilitation is the bond between the FRP material and the original substrate (steel or concrete) and hence surface preparation and details of field installation are important to both structural effectiveness and life-cycle durability.

While databases for FRP materials used in civil infrastructure are being developed and there is a significant body of evidence demonstrating the durability of these materials there are still concerns related to the long-term performance characteristics primarily due to the lack of sufficient historical data. In addition, the variability of the material based on constituents selected and the processing method used can result in levels of concern. To address these comprehensive investigations spanning extended periods of exposure with well defined material systems need to be undertaken ensuring the use of an integrated approach that takes into account the differences between laboratory and field settings, the effects of structural level interactions that may not be apparent at the level of isolated materials tests, and the development and use of mechanistic and phenomenological models that need to be validated for future use at the materials and structural systems levels. This is shown schematically in Fig. 14.

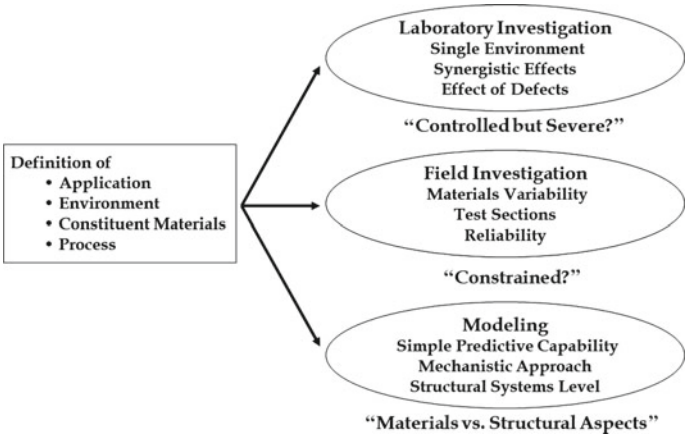

Fig. 14 Schematic of levels of investigation needed

Acknowledgements The author gratefully acknowledges the contributions of members of his research group whose efforts led to the results summarized in this paper. The primary contributors are also acknowledged through the cited references. Funding for the research was provided by several agencies including the California Department of Transportation, the Civil Engineering Research Foundation, the Federal Highway Administration, the National Science Foundation, and the Advanced Research Projects Agency.

References

1. American Road & Transportation Builders Association, https://artbabridgereport.org/. Accessed on April 21, 2022
2. Seible F, Karbhari VM Seismic retrofit of bridge columns using advanced composite materials, the national seminar on advanced composite material bridges, Washington, D.C., 1–29 pp, May 5–7, 1997
3. VM Karbhari L Zhao 2000 Use of composites for 21st century civil infrastructure Comput Methods Appl Mech Eng 185 433 454
4. VM Karbhari F Seible 2000 Fiber reinforced composites—advanced materials for the renewal of civil infrastructure Appl Compos Mater 7 2/3 95 124
5. F Seible G Hegemier VM Karbhari J Wolfson K Arnett R Conway JD Baum 2008 Protection of our bridge infrastructure against man-made and natural hazards Struct Infrastruct Eng 4 6 415 429
6. Y Einde Van den VM Karbhari F Seible 2007 Seismic performance of a FRP bridge pylon connection Composites B 38 5/6 685 702
7. Seible F, Karbhari VM, Burgueno R (1999) Kings stormwater channel and I-5/Gilman bridges. Struct Eng Int 9(4):250–253
8. VM Karbhari F Seible R Burgueno A Davol M Wernli L Zhao 2000 Structural characterization of fiber-reinforced composite short- and medium-span bridge systems Appl Compos Mater 7 2/3 151 182
9. VM Karbhari MA Abanilla 2007 Durability characteristics of wet layup carbon/epoxy used in external strengthening: design factors, reliability, and durability prediction Composites B 38 1 10 23
10. RA Atadero VM Karbhari 2008 Calibration of resistance factors for reliability-based design of externally-bonded FRP Composites B 39 4 665 679
11. Karbhari VM, Li Y A review of durability based safety factors for the use of FRP composites in civil infrastructure. In: Proceedings of the 10th US-Japan conference on composite materials, pp 291–300. Stanford, CA, September 16–18, 2002
12. Karbhari VM, Hassanpour B (2022) Water, saltwater, and concrete leachate solution effects on durability of ambient temperature cure carbon-epoxy composites. J Appl Polymer Scien 139(27):e52496, 16
13. MA Abanilla VM Karbhari Y Li 2006 Interlaminar and intralaminar durability characteristics of wet layup carbon/epoxy used in external strengthening Composites B 37 7/8 650 661
14. Karbhari VM, Abanilla MA (2007) Design factors, reliability, and durability prediction of wet layup carbon/epoxy used in external strengthening. Composites: B 38:10–23
15. W Chu VM Karbhari 2005 Effect of water sorption on performance of pultruded E-glass/vinylester composites ASCE J Mat Civil Eng 17 1 63 71
16. Mirmiran A, Shahawy M, Nanni A, Karbhari VM (2004) Bonded repair and retrofit of concrete structures using FRP composites: recommended construction specifications and process control manual. NCHRP 514, Transportation Research Board of the National Academies

17. Mirmiran A, Shahawy M, Nanni A, Karbhari VM, Yalim B, Kalayci AS (2008) Recommended construction specifications and process control manual for repair and retrofit of concrete structures using bonded FRP composites, NCHRP 609, Transportation Research Board of the National Academies
18. VM Karbhari R Navada 2008 Investigation of durability and surface preparation associated defect criticality of composites bonded to concrete Composites A 39 6 997 1006
19. VM Karbhari K Ghosh 2009 Comparative durability evaluation of ambient temperature cured externally bonded CFRP- and GFRP composite systems for repair of bridges Composites A 40 9 1353 1363
20. Lee LS, Atadero R, Karbhari VM Remaining life of FRP rehabilitated bridge structures. In: Proceedings of the 4th Asian-Australasian conference on composite materials, Sydney, July 6–9, 2004, pp 1012–1017

Fabrication and Mechanical Characterization of Glass/Epoxy and Carbon/Epoxy Fiber-Reinforced Composite Laminates

A. S. Mehra and Shamsher Bahadur Singh

Abstract The paper discusses the procedure followed for the fabrication of fiber-reinforced polymer composite laminates from unidirectional glass and carbon fiber, using the classical hand-layup technique. The mechanical properties of these laminates were determined through a series of standard characterization tests, conducted on specimens drawn out in the form of coupons. To understand the material response, stress-vs.-strain curves till failure are plotted and analyzed. The test results showed that except for the longitudinal tensile strength and modulus, glass fiber-reinforced polymer (GFRP) laminates possess better mechanical properties than carbon fiber-reinforced polymer (CFRP) laminates. The obtained strength and stiffness properties can be utilized for the analysis and design of composite structural elements fabricated from such laminates.

Keywords CFRP · GFRP · Hand layup · Mechanical characteristics · Off-axis test

Nomenclature

σ_1	Longitudinal tensile/compressive stress acting on a ply, along principal material axis-1.
σ_2	Transverse tensile/compressive stress acting on a ply, along principal material axis-2.
σ_{xu}	Ultimate tensile stress generated in the laminate subjected to 10° off-axis tension test.
σ_{mu}	Tensile strength of the epoxy matrix.
τ_{12}	In-plane shear stress acting on a ply in principal material plane1-2.
ϵ_{mu}	Tensile strain in the epoxy matrix at failure.

A. S. Mehra (✉) · S. B. Singh
Department of Civil Engineering, BITS Pilani, Pilani 333031, India
e-mail: p20190440@pilani.bits-pilani.ac.in

S. B. Singh
e-mail: sbsingh@pilani.bits-pilani.ac.in

S. B. Singh et al. (eds.), *Fiber Reinforced Polymeric Materials and Sustainable Structures*, Composites Science and Technology, https://doi.org/10.1007/978-981-19-8979-7_4

ν_{12}	Poisson's ratio of a ply for principal material plane 1–2
v_m, v_f	Volume of the matrix, and fibers, respectively.
ρ_m, ρ_f, ρ_c	Mass density of the matrix, fibers, and composite laminate, respectively.
θ	Orientation of the fibers of a laminate measured from the loading axis.
E_1, E_2	Elastic modulus of a ply along principal material axes 1 and 2, respectively
E_m	Elastic modulus of the epoxy matrix.
E_x	Elastic modulus of the laminate subjected to 45° off-axis tension test.
G_{12}, G_{23}	Shear modulus of a ply corresponding to principal material planes 1–2 and 2–3, respectively
S	In-plane shear strength of a ply, in principal material plane 1–2.
V_m, V_f	Volume fraction of the matrix, and fibers, respectively
v_m, v_f	Volume of the matrix, and fibers, respectively.
W_m, W_f	Weight fraction of the matrix, and fibers, respectively.
w_m, w_f, w_c	Weight of the matrix, fibers, and composite laminate, respectively.
X_T, X_C	Longitudinal tensile and compressive strengths of a ply, along principal material axis-1, respectively.
$X_{\epsilon T}$, $X_{\epsilon C}$	Longitudinal tensile and compressive strain at failure, of a ply, along principal material axis-1, respectively.
Y_T, Y_C	Transverse tensile and compressive strengths of a ply, along principal material axis-2, respectively.
$Y_{\epsilon T}$, $Y_{\epsilon C}$	Transverse tensile and compressive strain at failure, of a ply, along principal material axis-2, respectively

1 Introduction and Research Significance

Composite laminae are the basic building blocks of a structural element fabricated from a composite laminate. The prerequisite for the analysis and design of any composite structure is to have knowledge about the strength and stiffness properties of each and every constituting lamina along their respective principal material directions and planes, as applicable.

A unidirectional fiber-reinforced lamina (or ply) is an orthotropic material, however, due to the random distribution of fibers in the cross-section, the transverse plane 2–3 acts as the plane of isotropy. Figure 1 shows a schematic representation of a unidirectional fiber-reinforced lamina and its principal material axes 1, 2, and 3.

Therefore the complete material response of a unidirectional fiber-reinforced lamina can be defined through five independent elastic constants: E_1, E_2, G_{12}, G_{23}, ν_{12}, and five strength parameters: X_T, X_C, Y_T, Y_C, S. These properties can be determined analytically from the apparent or in-situ properties of the constituents (fibers and the matrix) depending on their orientation, distribution, and relative volume fractions present in the composite; using several known micromechanics formulations

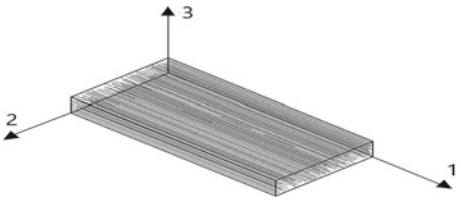

Fig. 1 Schematic representation of a unidirectional fiber-reinforced lamina and its principal material axes

[1]. However, only the bulk properties of these constituents are made available to the designer by the manufacturer. These bulk properties are generally found to be unreliable and several times higher than the apparent (or in-situ) properties [2]. Such discrepancies can be primarily attributed to the surface damage of fibers caused by the abrasion occurring between the fibers during transportation, handling, and storage operations; degradation of the material due to environmental factors; variation in the quality of precursors; and variation in the manufacturing process, etc. [3]. Hence, the most rational way of determining these properties is to conduct a series of experimental tests as per the provisions and norms of the established testing standards and guidelines [4–9].

This study is an attempt to obtain the apparent (or in-situ) strength and stiffness properties of unidirectional glass fiber-reinforced polymer laminates and carbon fiber-reinforced polymer laminates, through a series of experimental characterization tests as per the recommendations of the relevant American Society of Testing Material (ASTM) testing standards. In addition, the various modes of failure as observed during the testing are also analyzed. The obtained strength and stiffness properties and the analyzed failure characteristics will be utilized by the authors for the analysis and design of composite structural elements, to be fabricated from such laminates in the near future.

2 Fabrication Process

The characterization tests were conducted on coupons, machined from composite plates, to dimensions as required by the corresponding testing standards and/or guidelines [4–9]. The glass fiber-reinforced polymer (GFRP) laminated plates and the carbon fiber-reinforced polymer (CFRP) laminated plates were fabricated using the classical hand-layup technique. To ensure that the matrix properly wets and bonds the fibers together, and the cured laminate contains a sufficient volume of fibers so as to significantly enhance the mechanical characteristic of the unreinforced matrix, the fiber volume fraction was fixed at 0.6. Prior to the fabrication of the laminates, the unidirectional mats of glass and carbon fiber were cut to the required dimensions and weighted independently. The required quantity of the two-part epoxy matrix (Part-I: Epoxy resin; Part-II: Reactive polyamide hardener) as a function of the measured weight of the fiber mats, the density of fiber and epoxy, and the assumed value of fiber volume fraction, was estimated using Eq. (1), derived from the rule of mixtures

(ROM) approach. To account for the possible wastage of epoxy during the fabrication process, the calculated weight was increased by 10%. The required quantity of resin and hardener (to be mixed in a ratio of 9:1 by weight, as per the supplier) were calculated using Eq. (2).

$$w_m = w_f \times \frac{V_m}{V_f} \times \frac{\rho_m}{\rho_f} \tag{1}$$

$$w_{m,\text{resin}} = 0.9 \times w_m;\ w_{m,\text{hardener}} = 0.1 \times w_m \tag{2}$$

The various steps followed in the fabrication of GFRP laminates are shown in Fig. 2. Identical steps were followed for the fabrication of CFRP laminates also.

To provide a smooth surface finish, the wetted fiber mats were placed over thin aluminum sheets(~1 mm thick) and stacked together to the required lamination scheme. Though the objective of the study is to determine the apparent strength and stiffness properties of a single unidirectional GFRP ply, and a single unidirectional CFRP ply, the plates were fabricated as laminates instead of laminae, since a single-ply would have been too fragile to test [1]. In a particular composite plate, all laminae had the same fiber type and orientation, and the number of plies to be stacked was decided as per the thickness requirements of the corresponding testing standard.

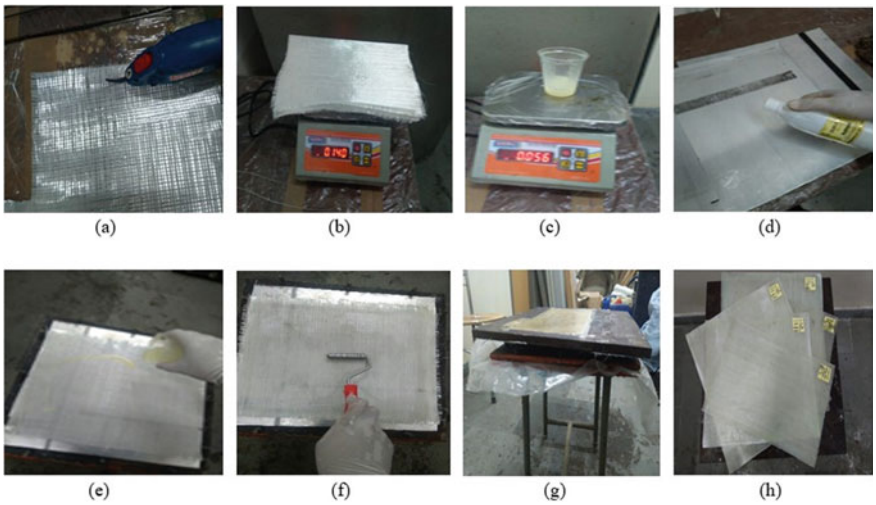

Fig. 2 Fabrication of GFRP composite laminates: **(a)** cutting of unidirectional glass fiber mats; **(b)** weighting of the glass fiber mats; **(c)** weighting of the epoxy resin; **(d)** cleaning of aluminum sheets with acetone; **(e)** pouring and spreading of epoxy resin with steel putty knife; **(f)** removal of air bubbles with steel washer roller; **(g)** pressing the laminate with steel plates; **(h)** finished GFRP laminates

Before placing the fibers, the surfaces of aluminum sheets were first cleaned with acetone to remove dirt and other contaminants and then greased with a thin layer of wax to prevent them from bonding to the surface of the composite laminate. To obtain a uniform thickness, the entire assembly was sandwiched between two 12 mm thick mild steel plates (having in-plan dimensions slightly larger than that of the laminate) and pressed with an additional 16 mm thick mild steel plate from the top. The mild-steel plates were removed after 24 h. of fabrication and after that, the laminates were left undisturbed to self-cure for at least 14 days, at room temperature (30 °C).

After 15 days of curing, the aluminum sheets were also removed and the actual weight of the composite laminates was measured, corresponding to which, the actual weight of the matrix was calculated using Eq. (3); the weight fractions of fiber and matrix were calculated using Eq. (4); the density of the composite laminates was calculated using Eq. (5), derived from the inverse rule of mixture (IROM) approach; the actual volume fraction of the constituents present in a laminate were obtained using Eq. (6), derived from the rule of mixture (ROM) approach. The presence of air voids in the cured laminates was not taken into consideration in the present study.

$$w_m = w_c - w_f \tag{3}$$

$$W_f = \frac{w_f}{w_c};\ W_m = \frac{w_m}{w_c} \tag{4}$$

$$\rho_c = \frac{1}{\frac{W_f}{\rho_f} + \frac{W_m}{\rho_m}} \tag{5}$$

$$V_f = W_f \times \frac{\rho_c}{\rho_f};\ V_m = 1 - V_f \tag{6}$$

The average fiber volume fraction in the GFRP laminates was obtained as 0.590, and as 0.588 in the CFRP laminates. The average mass density of GFRP laminates was found to be around 2.01 gm/cc, and around 1.55 gm/cc for CFRP laminates. The measured properties of the laminates are listed in Table 1.

In addition, for determining the strength and stiffness properties of the epoxy matrix, a neat sheet of epoxy having thickness as required by the respective testing standard [8, 9] was also cast. The mixture of resin and hardener was poured over a flat toughened glass surface and the wet epoxy pool was leveled using a spirit level to obtain a uniform thickness. The specimen was left undisturbed to self-cure for at least 15 days at room temperature (30 °C).

3 Experimental Investigation

The experimental tests were carried out on coupons machined from the previously fabricated fully cured GFRP and CFRP composite plates, and epoxy sheet. The

Table 1 Measured properties of CFRP and GFRP composite laminates

Laminate	GFRP						CFRP					
Specimen Id[+]	T-0-G	T-10-G	T-45-G	T-90-G	C-0-G	C-90-G	T-0-C	T-10-C	T-45-C	T-90-C	C-0-C	C-90-C
No. of plies stacked[*]	2	3	3	4	5	5	4	6	6	8	10	10
t_c (mm)	1.0	1.5	1.5	1.7	2.3	2.3	1.0	1.6	1.4	2.0	2.3	2.3
ρ_c (gm/cc)	1.99	2.00	2.03	2.03	2.00	2.00	1.55	1.54	1.56	1.55	1.56	1.56
V_f	0.57	0.61	0.58	0.61	0.59	0.59	0.59	0.58	0.56	0.60	0.61	0.61

[+]**First letter (type of loading)**-T: tension loading; C: compression loading. **Second letter (orientation of fibers)-**0: fibers aligned along the loading direction; 10: fibers oriented at an angle of 10° from the loading direction; 45: fibers oriented at an angle of 45° from the loading direction; 90: fibers oriented at an angle of 90° from the loading direction. **Third letter (type of laminate)**-G: GFRP; C: CFRP

[*] A single-ply of GFRP had a thickness of 0.5 mm, and that of CFRP had a thickness of 0.25 mm

various steps followed in the preparation of GFRP test coupons are shown in Fig. 3. Identical steps were followed for the preparation of test coupons from the CFRP plates and the epoxy sheet also.

Depending on the type of test, the coupons were subjected to either a tensile loading or a compressive loading from the two ends, through a displacement-controlled hydraulic actuator of the 100 kN capacity universal testing machine (UTM). Before the load was applied, both ends of the coupon were clamped to the actuator using serrated hydraulic wedge grips by applying a constant grip pressure of 2 MPa (maintained throughout the tests and kept as the same for all the specimens and tests). To increase the friction and prevent the coupons from getting crushed at the grips, before clamping, both ends of the coupon were covered with a single folded sheet of emery cloth (with the abrasive surface facing towards the laminate) as shown in Fig. 3f. The load resisted by the coupon and the corresponding deformation were periodically measured using the inbuilt load cells and extensometers of the UTM. The testing setup is shown in Fig. 4.

For the fiber-reinforced laminates, the longitudinal tensile strength (X_T), the corresponding strain ($X_{\epsilon T}\%$), and the longitudinal elastic modulus (E_1) were measured from the *0° Tension test* [4]. The test was carried out on flat rectangular specimens having fibers parallel to the loading direction as shown in Fig. 5a. The specimen had a gage length of 108 mm, a width of 15 mm, a thickness of 1 mm, and a grip length of 56 mm. The tensile load was applied in the form of extension, occurring at a rate of 2 mm/min till failure.

The in-plane shear strength (S) was indirectly measured from the *10° Off-axis tension test* [5]. The test was carried out on flat rectangular specimens having fibers

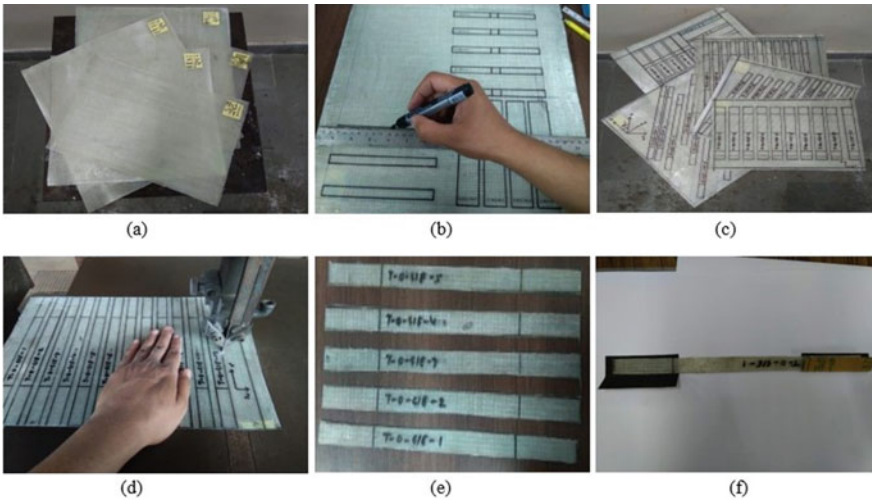

Fig. 3 Preparation of GFRP test coupons**: (a)** cured GFRP laminates; **(b)** marking of coupons; **(c)** marked GFRP laminates; **(d)** machining of a GFRP laminate; **(e)** machined coupons; **(f)** strengthening, and enhancement of friction at grips using folded emery cloth strips

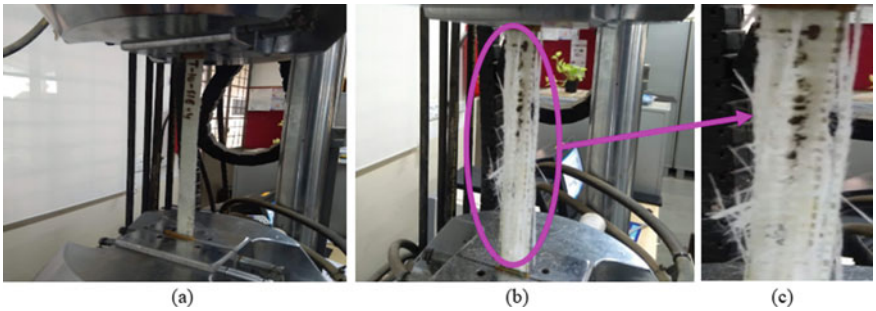

Fig. 4 Testing of 0° GFRP coupon in tension: **(a)** tensile load being applied to the coupon through end grips of a displacement controlled hydraulic actuator; **(b)** delamination type failure mode observed at ultimate load; **(c)** a zoomed-in view of the laminate delamination

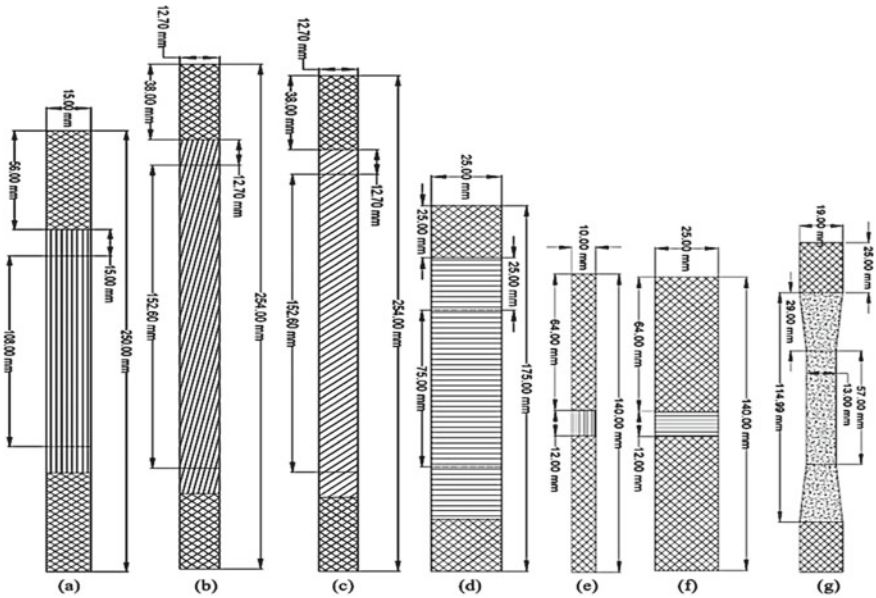

Fig. 5 Details of coupons tested in: **(a)** 0° tension test; **(b)** 10° tension test; **(c)** 45° tension test; **(d)** 90° tension test; **(e)** 0° compression test; **(f)** 90° compression test; **(g)** epoxy tension test

inclined at an angle of 10° from the loading direction as shown in Fig. 5b. The specimen had a gage length of 152.6 mm, a width of 12.7 mm, a thickness of 1.5 mm, and a grip length of 38 mm. The tensile load was applied at a rate of 2 mm/min till failure. The in-plane shear modulus (G_{12}) was indirectly measured from the *45° Off-axis tension test* [6]. The test was carried out on flat rectangular specimens having fibers inclined at an angle of 45° from the loading direction as shown in Fig. 5c. The dimensions of the specimen and the loading rate were identical to that of the

10° Off-axis tension test. The transverse tensile strength (Y_T), the corresponding strain ($Y_{\epsilon T}\%$), and the transverse elastic modulus (E_2) were measured from the *90° Tension test* [4]. The test was carried out on flat rectangular specimens having fibers perpendicular to the loading direction as shown in Fig. 5d. The specimen had a gage length of 75 mm, a width of 25 mm, a thickness of 2 mm, and a grip length of 25 mm. The tensile load was applied at a rate of 2 mm/min till failure. The longitudinal compressive strength (X_C) and the corresponding strain ($X_{\epsilon C}\%$) were measured from the *0° Compression test* [7]. The test was carried out on flat rectangular specimens having fibers parallel to the loading direction as shown in Fig. 5(e). The specimen had a gage length of 12 mm, a width of 10 mm, a thickness of 2.4 mm, and a grip length of 64 mm. The compressive load was applied in the form of a compression, occurring at a rate of 1.5 mm/min till failure. The transverse compressive strength (Y_C) and the corresponding strain ($Y_{\epsilon C}\%$) were measured from the *90° Compression test* [7]. The test was carried out on flat rectangular specimens having fibers perpendicular to the loading direction as shown in Fig. 5f. The specimen had a gage length of 12 mm, a width of 25 mm, a thickness of 2.4 mm, and a grip length of 64 mm. The compressive load was applied at a rate of 1.5 mm/min till failure.

The tensile strength (σ_{mu}), the corresponding strain (ϵ_{mu} %) at failure, and the elastic modulus (E_m) of the epoxy matrix were measured from the *Tension test* [8, 9]. The test was carried out on dog-bone-shaped specimens as shown in Fig. 5(g). The specimens had a gage length of 57 mm, a width of 13 mm, a thickness of 3.2 mm, and a grip length of 25 mm. The tensile load was applied at a rate of 5.0 mm/min till failure. The description of the above-mentioned characterization tests is summarized in Table 2.

The respective strength values were calculated by dividing the maximum load before failure with the undeformed cross-section area of the gage region. The corresponding strain values were calculated by dividing the total longitudinal deformation of the gage region till the ultimate load, with the undeformed gage length. The elastic modulus was taken equal to the chord modulus of the stress-vs.-strain curve for the strain range of 0.1–0.3%. Stress transformation relations given by Eq. (7) were written for the *10° Off-axis tension test* specimens at failure (σ_{xu} being the ultimate stress sustained by the 10° off-axis tension specimen), from which the in-plane shear strength of the laminates was indirectly calculated using Eq. (8).

The accuracy of using the *10° Off-axis tension test* for obtaining the in-plane shear strength of the unidirectional composite laminate was investigated by Charmis and Sinclair [5]. From their extensive experimental and numerical study, they concluded that when a 10° off-axis tension coupon fails, among the stresses generated along the principal material axes σ_1, σ_2, and τ_{12} it is only the τ_{12} which is closest to its critical value (i.e., the in-plane shear strength of the laminate (S)), and hence causes the shearing of the specimen along a plane inclined at 10° with the longitudinal axis.

$$\begin{pmatrix} \sigma_1 \\ \sigma_2 \\ \tau_{12} \end{pmatrix} = \begin{bmatrix} cos^2 10 & sin^2 10 & 2sin10cos10 \\ sin^2 10 & cos^2 10 & -2sin10cos10 \\ -sin10cos10 & sin10cos10 & cos^2 10 - sin^2 10 \end{bmatrix} \begin{pmatrix} \sigma_{xu} \\ 0 \\ 0 \end{pmatrix} \quad (7)$$

Table 2 Description of characterization tests

Test	Laminates	Properties determined	Specimen id$^{\Delta}$	No. of specimens	Displacement rate (mm/min)	Grip pressure (MPa)	References
0° tension	GFRP; CFRP	E_1; X_T; $X_{\epsilon T}$	T-0-G-E; T-0-C-E	5	2.0	2.0	ASTM D3039 [4]
10° off-axis tension	GFRP; CFRP	S	T-10-G-E; T-10-C-E	5	2.0	2.0	ASTM D3039 [4]; Charmis and Sinclair [5]
45° off-axis tension	GFRP; CFRP	G_{12}	T-45-G-E; T-45-C-E	5	2.0	2.0	ASTM D3039 [4]; Pindera and Hearkovich [6]
90° tension	GFRP; CFRP	E_2; Y_T; $Y_{\epsilon T}$	T-90-G-E; T-90-C-E	5	2.0	2.0	ASTM D3039 [4]
0° compression	GFRP; CFRP	X_C; $X_{\epsilon C}$	C-0-G-E; C-0-C-E	5	1.5	2.0	ASTM D3410 [7]
90° compression	GFRP; CFRP	Y_C; $Y_{\epsilon C}$	C-90-G-E; C-90-C-E	5	1.5	2.0	ASTM D3410 [7]
Tension	Epoxy	E_m; σ_{mu}; ϵ_{mu}	T-E	5	5.0	2.0	ASTM D3013 [8]; ASTM D638 [9]

Δ First letter (type of loading)—T: Tensile loading; C: Compression loading. **Second letter (orientation of fibers)—**0: fibers aligned along the loading direction; 10: fibers oriented at an angle of 10° from the loading direction; 45: fibers oriented at an angle of 45° from the loading direction; 90: fibers oriented at an angle of 90° from the loading direction; E(for neat expoxy test): type of material, epoxy. **Third letter (type of fibers)**—G: Glass; C: Carbon. **Fourth letter (type of matrix)—**E: Epoxy

$$\therefore S = |\tau_{12}| = 0.171\sigma_{xu} \tag{8}$$

Modulus transformation relations given by Eq. (9) were written for the *45° Off-axis tension test* specimens (E_x being the elastic modulus of the 45° off-axis tension specimen), from which the in-plane shear modulus of the laminates was indirectly calculated using Eq. (10), (the in-plane Poisson's ratio ν_{12} was calculated from the rule of mixtures approach and stiffness properties E_1 and E_2 were taken as that obtained from the respective experimental tests). The explanation behind using the *45° Off-axis tension test* for obtaining the in-plane shear modulus (G_{12}) of the unidirectional composite laminate is provided by Pindera and Hearkovich [6], that the error induced in the calculation of G_{12} from the off-axis tension tests due to the presence of end restrains is a multiple of the expression: $cos^2\theta - sin^2\theta$, ($\theta$ is the angle of inclination of fibers measured from the loading axis) and hence vanishes when the fibers are aligned at an angle of 45°.

$$\frac{1}{E_x} = \frac{cos^4 45}{E_1} + \frac{sin^4 45}{E_2} + \frac{1}{4}\left(\frac{1}{G_{12}} - \frac{2\nu_{12}}{E_1}\right) sin^2(2 \times (45)) \tag{9}$$

$$\therefore G_{12} = \frac{1}{\frac{4}{E_x} - \frac{1}{E_1} - \frac{1}{E_2} + \frac{2\nu_{12}}{E_1}} \tag{10}$$

4 Results and Discussions

The failure modes as experienced by the GFRP and CFRP laminates when subjected to various loading configurations are shown in Fig. 6 and Fig. 7, respectively; the corresponding stress-vs.-strain curves are plotted in Fig. 8 and Fig. 9, respectively.

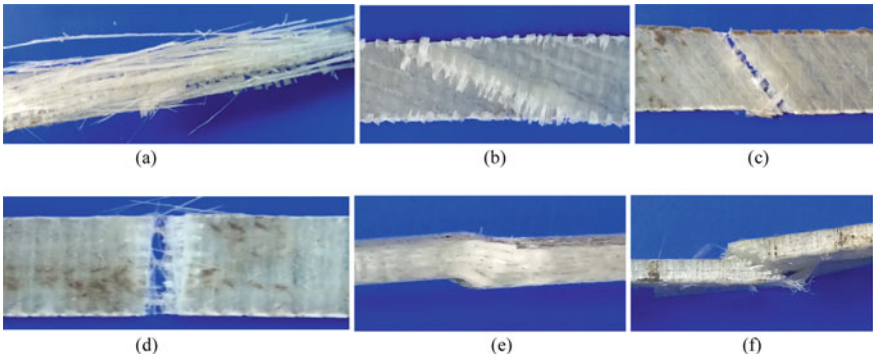

Fig. 6 Failure modes observed in GFRP laminates: **(a)** 0° tension test, **(b)** 10° tension test, **(c)** 45° tension test, **(d)** 90° tension test, **(e)** 0° compression test, **(f)** 90° compression test

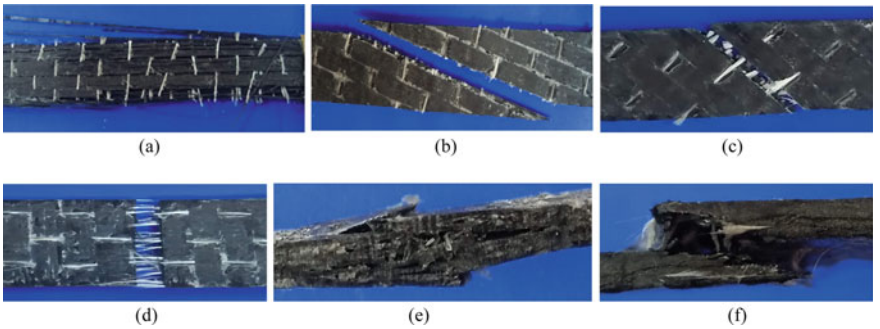

Fig. 7 Failure modes observed in CFRP laminates: **(a)** 0° tension test; **(b)** 10° tension test; **(c)** 45° tension test; **(d)** 90° tension test; **(e)** 0° compression test; **(f)** 90° compression test

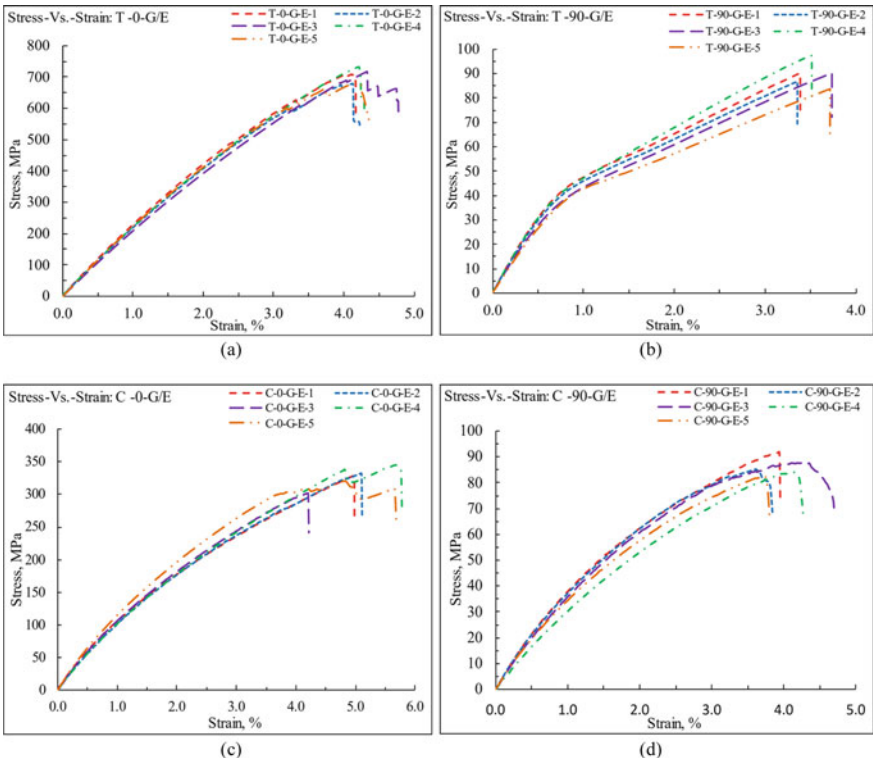

Fig. 8 Stress-versus-strain curves of GFRP laminates: **(a)** 0° tension test; **(b)** 90° tension test; **(c)** 0° compression test; **(d)** 90° compression test

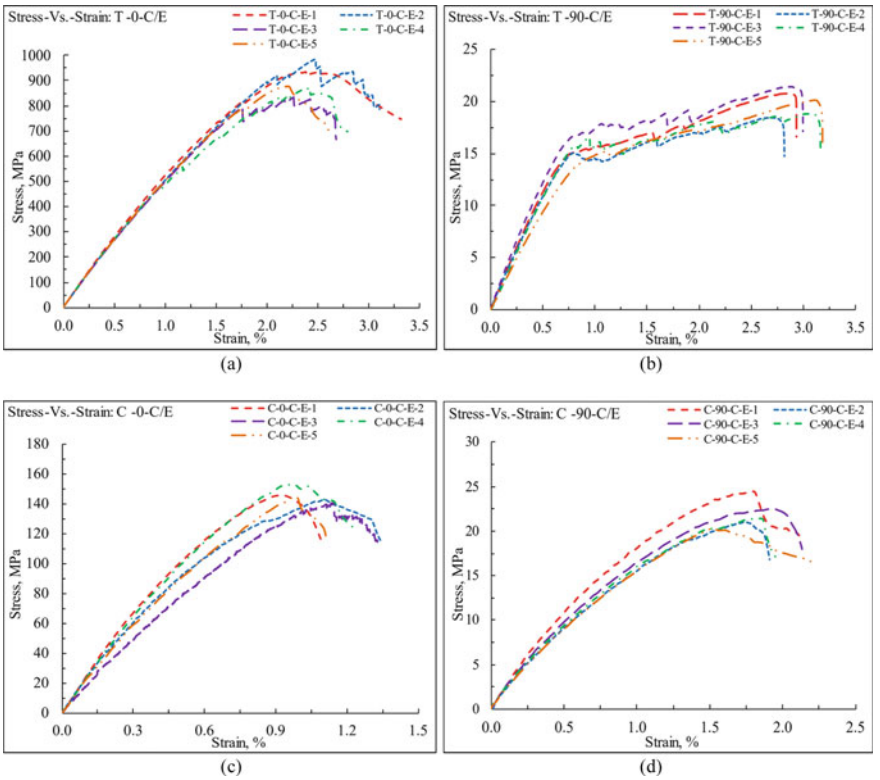

Fig. 9 Stress-versus-strain curves of CFRP laminates: **(a)** 0° tension test; **(b)** 90° tension test; **(c)** 0° compression test; **(d)** 90° compression test

The test results are summarized in Table 3, and the stiffness and strength properties of the composite laminates and epoxy resin as obtained from the experimental investigation are compiled in Table 4.

In the longitudinal tension test, both GFRP and CFRP coupons failed in a brittle mode with fiber pullout and debonding of the constituents. From the corresponding load-vs.-deflection curves, it can be inferred that compared to CFRP laminates, the GFRP laminates possess a lower tensile strength and elastic modulus but a higher value of failure strain. The failure of GFRP was much more sudden and brittle, whereas CFRP showed a ductile material response, attributed to the progressive failure of plies that started at around one-half of the ultimate load.

When the tensile load was applied to the laminates in the direction transverse to that of the fibers, both GFRP and CFRP laminates failed due to the rupture of the matrix in tension. The ductility observed in both laminates was found to be much more prominent than that in the longitudinal tension test. This could be due to the debonding of the constituents and splitting of fibers at the microscopic level, caused by the development of high-stress concentration at the fiber-matrix interface [3].

Table 3 Summary of test results

Specimen	Laminate	Failure mode*#	Ultimate load	Ultimate stress,	Strain at ultimate stress	Maximum strain$	Maximum in-plane shear stress	Elastic modulus+	Shear modulus
			kN	MPa	%	%	MPa	GPa	GPa
T-0-G-E	GFRP	DGM	10.70	703.82	4.20	4.38	–	22.95	–
T-10-G-E		AGM	1.71	86.14	0.89	1.00	14.73	15.02	–
T-45-G-E		AGM	0.57	30.22	1.92	2.09	–	4.01	1.23
T-90-G-E		LGB	3.70	89.07	3.50	3.50	–	6.11	–
C-0-G-E		HGM	6.67	326.20	4.96	5.16	–	12.14	–
C-90-G-E		HGM	4.68	86.24	3.94	4.11	–	4.08	–
T-0-C-E	CFRP	DGM	13.52	900.48	2.35	2.90	–	55.46	–
T-10-C-E		AGM	0.95	53.08	0.29	0.30	9.08	17.73	–
T-45-C-E		AGM	0.26	14.05	0.55	0.59	–	3.10	1.19
T-90-C-E		LGB	1.01	19.92	2.91	3.02	–	2.26	–
C-0-C-E		DGM	3.14	145.29	1.03	1.22	–	19.10	–
C-90-C-E		HGM	1.25	21.94	1.77	2.06	–	1.97	–
T-E	Epoxy	-	1.39	34.36	4.06	4.07	–	1.11	0.40

* ASTM three-part failure mode code for failure in tension. **First letter (failure type)—**D: edge delamination; A: angled; L: lateral. **Second letter (failure area)-** G: gage. **Third letter (failure location)—**M: middle; B: bottom

ASTM three-part failure mode code for failure in compression. **First letter (failure type)—**H: through thickness; D: delamination. **Second letter (failure area)—**G: gage. **Third letter (failure location)—**M: middle.

$ At 80% of ultimate stress, on the falling branch(the portion of the stress-vs.-strain curve after the ultimate stress).

+ Chord modulus at 0.1–0.3% strain range

Table 4 Experimentally determined strength and stiffness properties of composite laminates and epoxy resin

Property	SI unit	GFRP laminate	CFRP laminate	Epoxy
X_T	MPa	703.82	900.48	–
X_C	MPa	326.20	145.29	–
Y_T	MPa	89.07	19.92	–
Y_C	MPa	86.24	21.94	–
S	MPa	14.73	9.08	–
$X_{\epsilon T}$ %	mm/mm	4.20	2.35	–
$Y_{\epsilon T}$ %	mm/mm	3.50	2.91	–
$X_{\epsilon C}$ %	mm/mm	4.96	1.03	–
$Y_{\epsilon C}$ %	mm/mm	3.94	1.77	–
E_1	GPa	22.95	55.46	–
E_2	GPa	6.11	2.26	–
G_{12}	GPa	1.23	1.19	–
σ_{mu}	MPa	–	–	34.36
ϵ_{mu}%	mm/mm	–	–	4.06
E_m	GPa	–	–	1.11

Under longitudinal compressive loads, delamination occurred in the CFRP laminates, possibly due to the microbuckling of fibers, followed by the debonding of the constituents, Fig. 7e. On the other hand, the GFRP laminated failed in the gross shear failure mode, resulting from the localized rotation of the fibers just before the failure load, Fig. 6e.

When the compressive load was applied in the direction perpendicular to the orientation of fibers, a single through-thickness crack inclined at an angle of 45° from the loading direction got generated at the middle of the gage sections of both the GFRP and CFRP laminates, Fig. 6f and Fig. 7f, respectively. Such a failure occurred due to the shear failure of the matrix, accompanied with the debonding of the constituents, under the action of compressive loads.

The in-plane shear failure of the unidirectional composite laminates generally takes place due to the shearing-off of the matrix along the direction of fibers [3]. Such a failure mode is observed because the accompanying complementary in-plane shear stresses acting perpendicular to the fibers are not high enough to shear-off the fibers [2]. As, per this criterion, both the tested GFRP and CFRP laminates must have possessed nearly equal in-plane shear strength, which, however, was not observed in the present study. The in-plane shear strength of GFRP laminates was found to be around 1.6 times higher than that of the CFRP laminates. A possible explanation could be the relatively high interfacial bond developed by the epoxy resin with the glass fibers as compared to that with carbon fibers. The high interfacial bond strength forced the fibers to jointly participate with the matrix in resisting the in-plane shear stresses acting along the fiber direction. This can be confirmed from

the visual inspection of coupons at failure. In the case of GFRP, pull-out of fibers occurred along the shearing plane at failure and prevented the complete separation of the laminate, Fig. 6b, however, in the case of CFRP, no fiber pull-out occurred along the failure plane that passed purely through the matrix and led to a complete separation of the coupon Fig. 7b. The tests results show that the in-plane shear modulus takes almost the same value for both the GFRP and the CFRP laminates.

The poor performance of CFRP laminates, except that in the longitudinal tensile test, can be attributed to the poor bonding of fibers with the epoxy matrix; the type and quality of precursor used for the manufacturing of the fibers; the manufacturing process followed for the production of fibers; and most predominantly the anisotropic nature of the carbon fibers. In the longitudinal direction of the fiber, the carbon atoms are arranged as densely packed hexagonal layers resulting in the high strength and modulus, whereas, in the transverse direction these layers are bonded by weak Van der Walls forces resulting in lower strength and stiffness in the direction perpendicular to fibers [3, 10].

5 Conclusion

The paper presented the results of an experimental investigation carried out for determining the apparent (or in-situ) strength and stiffness properties of unidirectional carbon fiber-reinforced composite laminates and unidirectional glass fiber-reinforced composite laminates. The characterization tests were carried out on coupons drawn from laminates that were fabricated using the hand-layup process and cured at room temperature. To analyze the material response and the corresponding failure characteristics, stress-vs.-strain curves up to the ultimate failure of the laminates were plotted. The test results show that under the action of tensile loads, failure in CFRP laminates is much more ductile as compared to GFRP laminates. Under compressive loads, GFRP laminates with fibers aligned along the loading direction suffer localized rotation of the fibers before the failure load, whereas, in CFRP laminates failure occurs due to the longitudinal splitting of the fibers. The joint participation of fibers and matrix in resisting the in-plane shear stresses increases the in-plane shear capacity of GFRP laminates by around 1.6 times as compared to that of CFRP laminates. The anisotropic material characteristic of the fiber, poor bonding with epoxy resin, and large variability in the manufacturing process and precursors significantly affect the material response of CFRP laminates, especially if the property under consideration is controlled by the interfacial fiber-matrix bond.

The symbols are used in this paper are treated as Nomenclature.

Acknowledgements The technical support provided to the authors through US-India Partnership 2020 project was instrumental in the successful execution of the presented work. Also, the financial support provided by the Council of Scientific and Industrial Research (CSIR), New Delhi through Scheme no. (22(0781)/19/EMR-II) sanctioned to the second author is highly appreciated for helping in the successful execution of the presented study.

References

1. RM Jones 1999 Mechanics of composite materials 2 Taylor and Francis Group New York
2. EJ Barbero 2018 Introduction to composite materials design 3 CRC Press Taylor and Francis Group, New York
3. BD Agarwal LJ Broutman K Chandrashekhara 2006 Analysis and performance of fiber composites 3 Wiley New Jersey
4. ASTM International (2014) Standard Test Method for Tensile Properties of Polymer Matrix Composite Materials, ASTM D3039, West Conshohocken
5. Chamis CC, Sinclair JH 10° Off-axis tensile test for intralaminar shear characterization of fiber composites, Report No. NASA TN D-8215, Lewis Research Center, National Aeronautics and Space Administration, Washington DC, April 1976
6. Pindera MJ, Herakovich CT (1985) Shear characterization of unidirectional composites with the off-axis tension test. Experimental Mech 103–111
7. ASTM International (2003) Standard test method for compressive properties of polymer matrix composite materials with unsupported gage section by shear loading, ASTM D3410, West Conshohocken
8. ASTM International (2013) Standard specification for epoxy molding compound, ASTM D3013, West Conshohocken
9. ASTM International (1999) Standard test method for tensile properties of plastics, ASTM D638, West Conshohocken
10. IM Daniel O Ishai 2006 Engineering mechanics of composite materials 2 Oxford University Press New York

Mechanical Characterization of Natural Fiber Reinforced Polymer Composites

P. Siva Sankar and Shamsher Bahadur Singh

Abstract Natural fibers, especially flax, jute and hemp fibers have gained more interest in the recent years due to their promising mechanical properties such as low cost, a high percentage of cellulose, easy availability and biodegradability. This research work aims to determine the elastic and strength properties of flax fiber-reinforced polymer (FFRP), jute fiber reinforced polymer (JFRP) and hemp fiber-reinforced polymer (HFRP) composites. These composites were fabricated by hand lay-up technique with the fiber volume fraction limited to 50%. The material characterization was performed by conducting tensile and compressive tests as per ASTM standards to evaluate the elastic and strength properties such as tensile strength, young's modulus, compressive strength and shear modulus. The mercerization process is also considered to treat the surface of the fiber with NaOH solution to identify the effects on the mechanical properties of the composite. From the obtained results, it was observed that HFRP composites have better tensile and compressive strength, whereas FFRP composites have better stiffness. The mercerization process on the fiber's surface had mixed effects on the elastic and strength properties of the natural fiber reinforced polymer (NFRP) composites.

Keywords Jute fiber · Hemp fiber · Flax fiber · Mercerization · Mechanical properties

Notations

E_1	Young's modulus of elasticity in the principal direction -1 (fiber direction)
E_2	Young's modulus of elasticity in direction transverse to the fiber direction
G_{12}	Shear moduli in the plane 1–2

P. S. Sankar (✉) · S. B. Singh
Department of Civil Engineering, Birla Institute of Technology and Science, Pilani 333031, India
e-mail: p20190444@pilani.bits-pilani.ac.in

S. B. Singh
e-mail: sbsingh@pilani.bits-pilani.ac.in

S. B. Singh et al. (eds.), *Fiber Reinforced Polymeric Materials and Sustainable Structures*, Composites Science and Technology, https://doi.org/10.1007/978-981-19-8979-7_5

ν_{12}	Major Poisson's ratios in the planes 1–2
X_t, X_c	Tensile and compressive strength of lamina in fiber direction, respectively
Y_t, Y_c	Tensile and compressive strength of lamina in direction transverse to the fiber direction
S	Shear strength of lamina in plane 1–3
T	Shear strength of lamina in plane 1–2

1 Introduction

In the past few decades, the progress of using plant fiber-reinforced polymer composites has increased due to their mechanical properties and environmentally friendly nature. Remarkably, lignocellulosic fibers such as flax, hemp, sisal, abaca and jute fibers have been proposed as an alternative for synthetic fibers, especially glass fibers, owing to their easy availability and cost [18]. The use of natural fibers is increased remarkably because the field of application is enhanced daily, especially in the construction and automotive industries. Natural fibers possess many benefits compared to synthetic fibers, such as low cost, low weight, low density, and acceptable specific properties and these fibers are biodegradable and recyclable. The natural fibers are available from renewable sources, have high stiffness and strength, and cause no skin irritations while using these fibers in manufacturing polymer reinforced composites [22]. The disposal method of synthetic fiber-reinforced composites and the recycling process is also a serious issue to consider the synthetic fibers. Natural fiber composites play a significant role in the environmental situation and various applications [16].

Natural fiber-reinforced polymer composites have many applications in automotive industries, construction, aviation, sports, goods packaging, and other engineering applications. The selection of natural fiber-reinforced composite is based on the availability of the material and mechanical properties of the composite. The engineers consider a particular set of natural fiber reinforced polymer composite based on the required strength and application. The composite material's elastic and strength properties are essential and act as inputs for the analysis and design of any composite-based structure through simulations. Before applying a manufactured composite to different applications, the evaluation of the mechanical properties of the composite is critical.

The mechanical properties of the natural fiber reinforced polymer composites are greatly influenced by several factors such as fiber content, matrix nature, fiber length, molding process and the interface between fiber and matrix [9]. Alavudeen et al. [1] have identified a significant change in the strength of the composites while reinforcing the natural fibers by using fiber surface treatments and hybridization with synthetic fibers. Flynn et al. [6] have investigated the impact of hybridization with the carbon and flax fibers by changing the flax fiber volume fractions. They found that the hybridization of carbon and flax fibers significantly improves mechanical

properties. Zhang et al. [24] have studied the hybridization effect of natural fibers with glass fibers. Their study observed that increase in the content of glass fiber results in the improvement of the tensile properties of the composite. Sarawar et al. [17] have evaluated the mechanical characterization of hybridized kevlar/flax/epoxy composite and they have identified that resistance to failure of flax/epoxy composite is doubled by the addition of 25% kevlar fibers. Singh et al. [19] identified the effect of curing temperature on the elastic and strength properties of the jute fiber reinforced polymer composites. Tensile strength values are increased until the curing temperature reaches 100^0 C and drastically, it reduces with the further increase up to 130 °C.

The hydrophilic nature of the plant-based fibers lowers the compatibility with the matrix due to its hydrophobic nature and results in poor mechanical properties of the composite. Chemical treatment helps reduce the fiber's hydrophilic nature and improves the fiber-matrix interface adhesion [10]. Sometimes, treating the fiber with more chemical amounts also damages the fiber's texture. During the mercerization process, if more NaOH is used, the fibers appear more and more yellowish [14]. However, the chemical treatments used to treat the fiber surface do not always lead to increased performance of composites. In contrast, sometimes, they can lead to a significant reduction in eco-sustainability [5].

This research work aims to evaluate the mechanical behavior of pure flax, pure hemp, pure jute, and pure treated flax fiber-reinforced polymer composites. The hand lay-up method has been used to manufacture the FFRP, HFRP and JFRP composites. The elastic properties of the unidirectional composite such as young's modulus in fiber and transverse direction, shear modulus and the strength properties such as tensile and compressive strength along the fiber direction as well as transverse direction, as shown in Fig. 1, are determined by the ASTM standards and the evaluation of the mechanical properties are presented in detail.

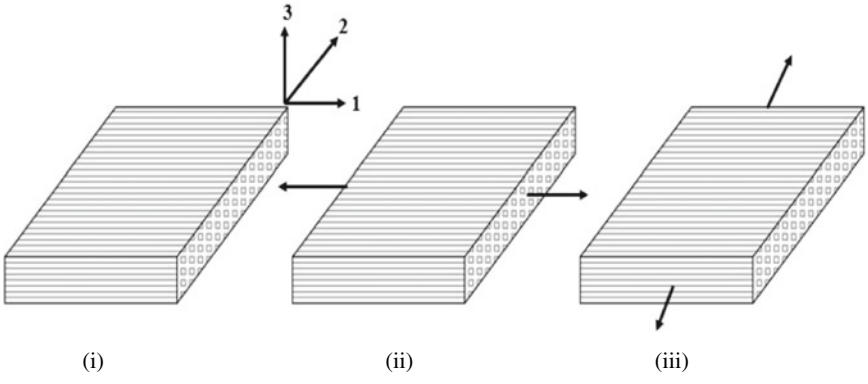

Fig. 1 Loading orientation of material property testing in unidirectional composites (i) Unidirectional laminate; (ii) Fiber direction; (iii) Transverse direction

2 Materials

Natural fibers considered in this experimental work are hemp, jute and flax, whose properties are given in Table 1. The matrix was prepared by considering epoxy resin of grade 'Resin 691' and the hardener of type 'Reactive Polyamide 140' with the mixing ratio of 90:10 concentration by weight, respectively. The mechanical properties of the resin are also presented in Table 1. Mercerization has been used to modify the fiber surface chemically, and it involves treating the fibers with sodium hydroxide (NaOH) solution. In this study, the volume fraction of the fibers in the composite was limited to 50% (± 3).

2.1 Surface Modification of Natural Fibers

The fiber-matrix interface in a composite is a reaction zone where two phases are combined mechanically and chemically. To characterize the mechanical properties of the composite, interfacial adhesion plays an important role. Poor adhesion across the phase boundary leads to weak force dispersion and affects the mechanical properties [7]. The main problem in the natural fiber composite is due to the fiber's hydrophilic nature and the matrix's hydrophobic nature [10]. At the interface, the weakening bond develops due to the fiber and matrix incompatibility phases. To improve matrix compatibility with the fiber, the hydrophilic nature of the fiber is to be reduced by using chemical treatments [8]. There are different types of methods available to treat the fibers chemically such as silane [2], alkaline [7], acetylation [13], maleated coupling [12], to name a few. The selection of suitable chemical treatment is based on the type of fiber and the constituents of cellulose, hemicellulose, and other substances present in the fiber.

Based on an extensive literature review, this work considers the alkaline chemical treatment method to treat the natural fibers with the sodium hydroxide (NaOH) solution and when the fibers are treated with the alkali, which directs fibrillation and develops rough surface topography over the fiber [11]. Developed rough surface helps to improve the adhesion property between fiber and matrix. The changes in the

Table 1 Mechanical properties of natural fibers and resin [15]

Fiber type	Mechanical properties of natural fibers and resin					
	Density (g/cm^3)	Tensile strength (MPa)	Young's modulus (GPa)	Specific modulus (GPa)	Elongation (%)	Specific gravity
Flax	1.40	340–1600	25–81	16.7–54	1.1–3.3	1.5
Hemp	1.48	550–900	70	47	0.8–3	1.5
Jute	1.46	385–850	9–31	6.9–20.7	1.4–2.1	1.3–1.5
Resin	1.16	70–85	3.5	2.5–3.8	3.5–4.1	1.34

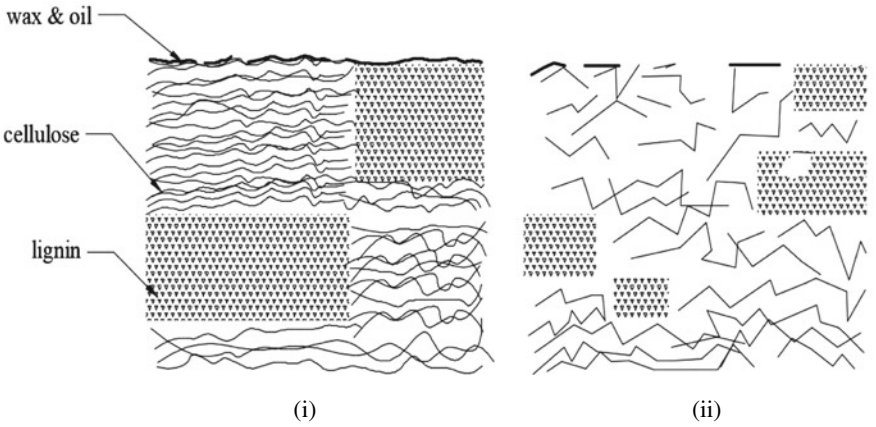

Fig. 2 Typical structure of (i) untreated and (ii) alkalized cellulose fiber

fiber cellulose structure before and after the chemical treatment of mercerization are presented schematically in Fig. 2. Treated fibers have distension of cellulose bonds and partial removal of oil and wax. The mercerization or alkaline treatment process includes the removal of hydrogen bonding in the network structure, which is why fiber absorbs the moisture and the reaction during the treatment are mentioned in Eq. (1).

$$\text{Fiber} - \text{cell} - \text{OH} + \text{NaOH} \rightarrow \text{Fibercell} - \text{O}^{-} + \text{H}_2\text{O} + \text{impurities} \quad (1)$$

In this work, to identify the suitable percentage of NaOH solution for the mercerization process, the fibers were treated with two different rates, such as 6% of NaOH and 2% NaOH. The results showed that the chemical treatment with 2% NaOH solution exhibited better results compared to 6% of NaOH solution. To identify the suitable rate of NaOH solution, flax fiber is considered for the sample testing. Flax fiber has been treated with NaOH solution for a 1 h duration at 2% and 6% percentages. The preparation of specimens and testing of the specimens has been mentioned in the next part of this paper under the preparation of the composite specimen.

The results show that soaking fibers in a 6% NaOH solution negatively affects the fiber's mechanical properties due to the high concentration of NaOH, making the fiber texture rougher and developing voids between the fibers. From Fig. 3, it is identified that the 2% of NaOH solution treatment has better results in terms of tensile strength when compared to the 6% of NaOH solution treatment. Based on this observation, for further work in this research, the 2% of NaOH solution treatment is considered to evaluate the elastic properties and strength properties.

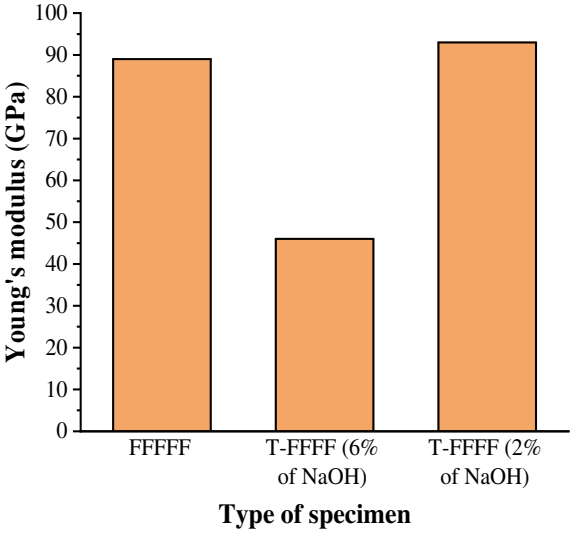

Fig. 3 Influence of alkaline treatment on tensile strength of FFRP composites

2.2 Preparation of Composite Specimen

The fabrication of the composite material was carried out by the hand lay-up method in this research work. Samples are fabricated by repeatedly stacking the jute/flax/hemp fiber layers as per the required laminate stacking sequence. The matrix was applied in between each layer of the fiber. The matrix is prepared by gently mixing the appropriate percentage of resin and hardener with proper care to not to develop any bubbles in the resin. Creating of bubbles in the matrix will result in voids in the laminate. In this study, the volume fraction was limited to 50% ($\pm$ 3).

Before placing the natural fibers in the composite fabrication process, they are treated with sodium hydroxide (NaOH) to improve their compatibility with the matrix. In this work, the natural fibers are treated using 2% sodium hydroxide solution to modify the fiber's surface and eliminate the wax and oils. The natural fibers are immersed in the 2% of NaOH solution for 1 h at room temperature. After that, the fibers are removed from the NaOH solution and washed with distilled water 3–4 times to eliminate the residue of the NaOH solution on the fibers [23]. After thoroughly cleaning the fibers, the fibers are kept at the temperature of 40 °C for 24 h. The thickness of the end laminate is based on the pressure applied to the laminate while casting.

This work incorporates a novel technique to apply uniform pressure on all the laminates [20]. Initially, the fiber layers are placed between two aluminum foils to get a smooth finish on the surface. To apply the uniform pressure on the fiber layers, the fiber stacked aluminum foil is placed in between the two mild steel plates of a thickness of 12 mm. The bolts and nuts are used to connect the plates and

maintain uniformity over applying pressure; the bolts are tightened using the bolt tightening machine with a torque of 250 Nm. During applying pressure on laminates, the extra resin will escape from the sides of the plate and the amount of loss is directly proportional to the magnitude of the pressure.

To compensate for the loss of the resin in the laminate, the extra 3% is added to the total matrix. Later for the curing process, the whole setup of mild steel plates is kept at an elevated temperature of 80 °C for a 6 h duration.

The laminates are removed from the steel plates after the curing period and kept at room temperature till the time of testing. To predict the material's longitudinal, transverse and in-plane shear characteristics, samples were cut from the laminate in the direction of 0°, 90° and 45° with respect to the fiber direction. For each test, three samples are considered from the laminate to predict the material properties by conducting tensile and compression tests.

The fabrication and testing of the composite specimen involve the steps of fiber cutting, chemical treatment of fiber, drying, manufacturing of composite plate, marking and cutting the specimens from the composite plate and testing the specimens. The entire process is mentioned in Fig. 4.

3 Testing of Composite Specimen

This work investigated the mechanical behaviour of natural fiber reinforced polymer composites by conducting various tests. Tensile and compressive tests were conducted to determine the composite's elastic and strength properties as per ASTM D3039 and ASTM D3410, respectively. The description of specimen ID's presented in Table 2.

3.1 Tensile Test

Tensile characteristics such as stiffness and strength of the natural fibers are determined by conducting a tensile test as per the guidelines by ASTM D3039. A universal testing machine with a capacity of 100 kN is used to perform the tensile test. The pressure was maintained at 3.5 MPa in the edge grips to prevent slippage and failure at the grips during the time of applying tensile load. The cross head displacement rate is applied as per the ASTM D3039 with a rate of 2 mm/min. The dimensions of the specimens when the fibers are parallel to the loading direction i.e., fibers are oriented at 0^0 direction was $250 \times 25 \times 4 \pm (0.3)$ mm (length x width x thickness). When the fibers are perpendicular to the loading direction, i.e., fibers are oriented at 90° direction was $175 \times 25 \times 4 \pm (0.3)$ mm (length x width x thickness), and for the fibers oriented at 45° direction was $195 \times 25 \times 4 \pm (0.3)$ mm (length x width

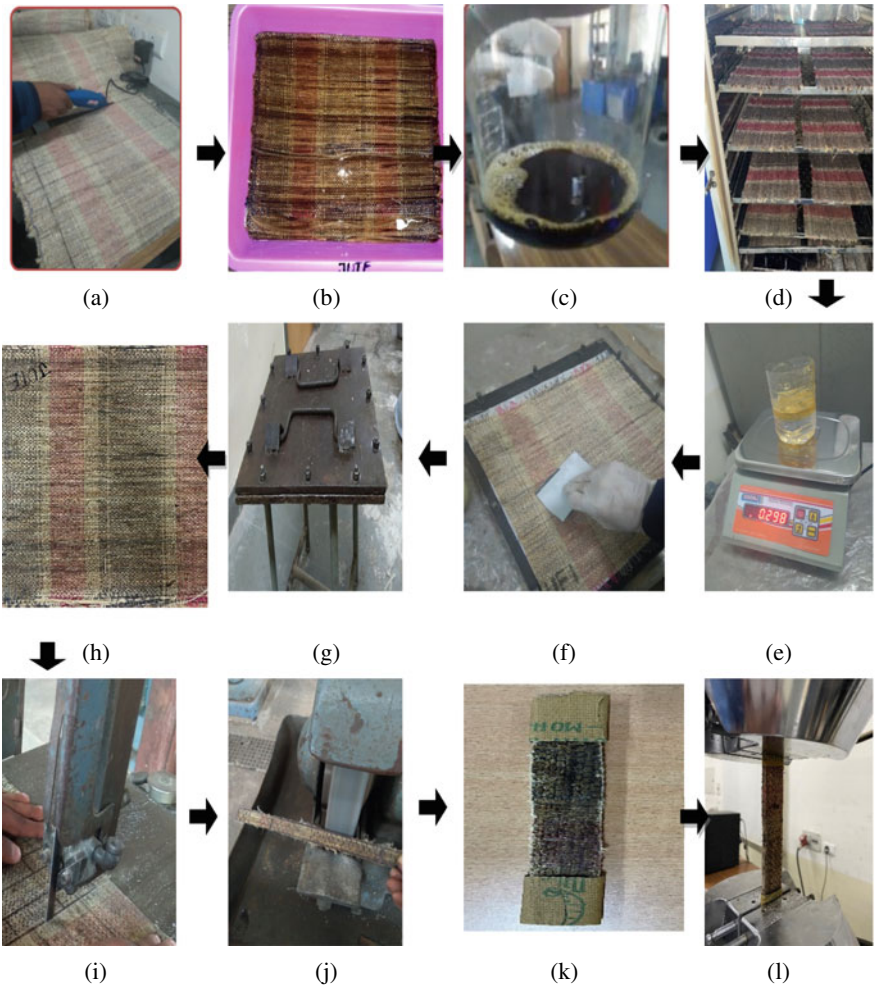

Fig. 4 Fabrication process of composites and preparation of specimens for testing: **a** Fiber cutting, **b** Soaking of fibers in NaOH solution **c** Washing of fibers with distilled water to remove the NaOH residue on fiber **d** Drying the fiber at 80 °C for 24 h **e** Considering epoxy resin with respect to fiber volume ratio **f** Applying epoxy to fibers **g** Drying the laminate at 80 °C for 6 h Final laminate after removing from oven **i** Machining of specimens **j** Smoothing of specimens **k** Strengthening of grip **l** Testing of the specimen

x thickness). For all the specimens in the tensile test, the grip length on either side is 50 mm. The properties of young's modulus (E1, E2) and tensile strength(Xt, Yt) have been evaluated by conducting the tensile test along with the fiber and transverse directions. The detailed dimensions and codes for the tensile tests are presented in Table 3.

Table 2 Description of laminates

Laminate type	Tensile test specimen ID	Compressive test specimen ID
Plain FFRP	T—FFFF	C—FFFF
Plain HFRP	T—HHHH	C—HHHH
Plain JFRP	T—JJJJ	C—JJJJ
Plain treated FFRP	T—T-FFFF	C—T-FFFF

Notes 'T' stands for tensile test, 'C' stands for the compressive test, and the second letter 'T' in the plain treated FFRP stands for a treated specimen

Table 3 Codes and dimensions of test specimens

Test	Code	Length (mm)	Width (mm)	Thickness (mm)	Gauge length (mm)
Tensile—0°	ASTM-D 3039	250	25	4 ± 0.3	150
Tensile—90°		175	25	4 ± 0.3	75
Tensile—45°		190	25	4 ± 0.3	90
Compressive—0°	ASTM-D 3410	105	10	4 ± 0.3	25
Compressive—90°		105	25	4 ± 0.3	25

3.2 Compressive Test

Compressive characteristics such as failure strain and compressive strength are determined by conducting the compressive tests as per the guidelines by ASTM D3410. A universal testing machine with a capacity of 100 kN is used to perform the compressive test. The pressure was maintained at the wedge grips to prevent the slippage of specimens is 4.15 MPa and the cross head displacement rate was 1.5 mm/min. The dimensions of the specimens when the fibers are parallel to the loading direction i.e., fibers are oriented at 0° direction was $105 \times 10 \times 4 \pm (0.3)$ mm (length x width x thickness). When the fibers are perpendicular to the loading direction, i.e., fibers are oriented at 90° direction was $105 \times 25 \times 4 \pm (0.3)$ mm (length x width x thickness). For all the specimens in the tensile test, the grip length on either side is 40 mm. The compressive strength (Xc, Yc) of the fiber in both directions has been evaluated by conducting the compressive test along with the fiber and transverse directions. The detailed dimensions and codes for the compressive tests are presented in Table 3.

3.3 Shear Modulus

The shear modulus in the composite was calculated when the fibers were placed at 45° and the test was conducted using a universal testing machine by applying a

uniaxial tensile load on the specimen [21]. During the tensile test, the specimen is failed by the cause of shear failure along 45° direction to the x-axis. In this case, the shear modulus (G_{12}) was calculated using Eq. (2).

$$G_{12} = \frac{1}{\frac{4}{E_x} - \frac{1}{E_1} - \frac{4}{E_2} + \frac{2\nu_{12}}{E_1}} \tag{2}$$

where G_{12} is the shear modulus of the specimen, E_x is the modulus of elasticity along the loading direction, E_1 is the modulus of elasticity along the fiber direction, E_2 is the modulus of elasticity along the transverse direction of the fiber, ν_{12} is the Poisson's ratio of the specimen in the plane 1–2. The in-plane shear strength is also calculated using the stress transformation relations written for the 45° off-axis tensile test using Eq. (3).

$$\begin{pmatrix} \sigma_1 \\ \sigma_2 \\ S \end{pmatrix} = \begin{bmatrix} \cos^2 45 & \sin^2 45 & 2\sin 45\cos 45 \\ \sin^2 45 & \cos^2 45 & -2\sin 45\cos 45 \\ -\sin 45\cos 45 & \sin 45\cos 45 & \cos^2 45 - \sin^2 45 \end{bmatrix} \begin{pmatrix} \sigma_x \\ 0 \\ 0 \end{pmatrix} \tag{3}$$

By conducting the tensile test along 45° to the fiber direction, the specimens' properties of shear modulus and in-plane shear strength are determined. The detailed dimensions and codes for the 45^0 tensile tests are presented in Table 3.

4 Results and Discussion

The main aim of this study is to investigate the elastic and strength properties of the natural fiber reinforced polymer-based composites. The properties such as tensile strength, compressive strength, young's modulus, shear strength, shear modulus of the FFRP, HFRP, JFRP, and treated FFRP laminates are determined. The detailed description of the mechanical characteristics of these laminates is explained in the following sections:

4.1 Tensile Characteristics

The comparison of tensile strength and young's modulus values are presented in the bar chart as shown in Fig. 5. The figure observed that the tensile strength along the fiber direction of the HFRP composite is higher than the remaining composites. Tensile strength along the fiber direction of HFRP composite w.r.t FFRP, JFRP and treated FFRP composites is 25%, 47% and 23% higher, respectively. Tensile strength along the transverse direction of FFRP composite w.r.t Treated FFRP, HFRP and JFRP is 40%, 49% and 80%, respectively. Failure modes of the NFRP specimens

under tension and compressions are shown in Fig. 6. During the time of testing under tension, it was noted that NFRP specimens failed catastrophically. From the stress–strain graphs of Fig. 7, it was observed that the FFRP and JFRP specimens have higher failure strain than the HFRP and treated FFRP specimens. The strain at 80% of the peak load in the post-peak region is assumed as failure strain. In the 0° tension test, the type failure is observed as splitting gage middle failure mode, and in the 90° tension test, the failure occurred as lateral gage middle failure and in the case of 45° tension test, the failure is aligned middle gage failure as shown in Fig. 6. Fig. 5 compares the young's modulus of different composites obtained from the tensile testing of coupons under the 0° and 90° w.r.t fiber direction. The figure observed that the young's modulus of the HFRP composite along the fiber direction is higher than the remaining composites and w.r.t FFRP, JFRP and treated FFRP composites are 26%, 21% and 13% higher, respectively. The figure observed that the young's modulus of the FFRP composite along the transverse direction is higher than the remaining composites. Young's modulus of FFRP composite w.r.t treated FFRP, HFRP and JFRP and composites is 42%, 53% and 61% higher, respectively.

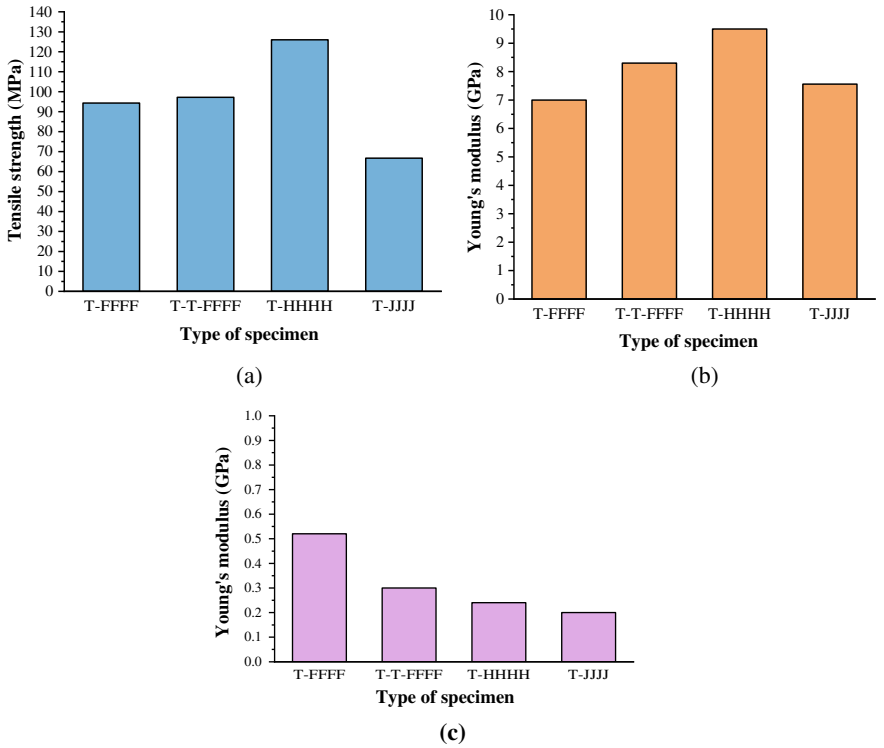

Fig. 5 Tensile behavior of composites: **a** Tensile strength; **b** Longitudinal young's modulus; **c** Transverse young's modulus

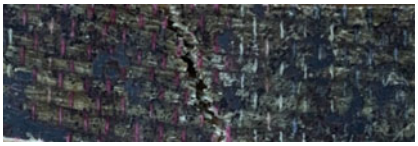

(i) 0° Tension- Splitting gage middle failure

(ii) 90° Tension- Lateral gage middle failure

(iii) 45° Tension- Aligned middle gage failure

(iv) 0° compression- brooming gage middle failure

(v) 90° Compression- Thickness gage middle failure

Fig. 6 Failure modes of NFRP composites

4.2 Compressive Characteristics

The comparison of compressive strength values is presented in the bar chart as shown in Fig. 8. The figure observed that the compressive strength along the fiber direction of the HFRP composite is higher than the remaining composites. Compressive strength along the fiber direction of HFRP composite w.r.t FFRP, JFRP and treated FFRP composites is 24%, 51% and 58% higher, respectively. Compressive strength along the transverse direction of HFRP composite w.r.t Treated FFRP and FFRP and JFRP is 44%, 22% and 50%, respectively. Failure modes of the NFRP specimens under tension and compressions are shown in Fig. 6. During the compression test, it was noted that NFRP specimens failed catastrophically and from the stress–strain graphs of Fig. 9, it was observed that the FFRP and HFRP specimens had high failure strain than the JFRP and treated FFRP specimens. The strain at 80% of the peak load in the post-peak region is assumed as failure strain. In the 0^0 compression test, the type failure is observed as brooming gage middle failure mode due to crushing, and in the 90^0 compression test, the failure occurred through-thickness gage middle failure.

From the tensile and compression tests as per the ASTM standards, the elastic and strength properties of the different types of NFRP composites are determined and tabulated in Table 4.

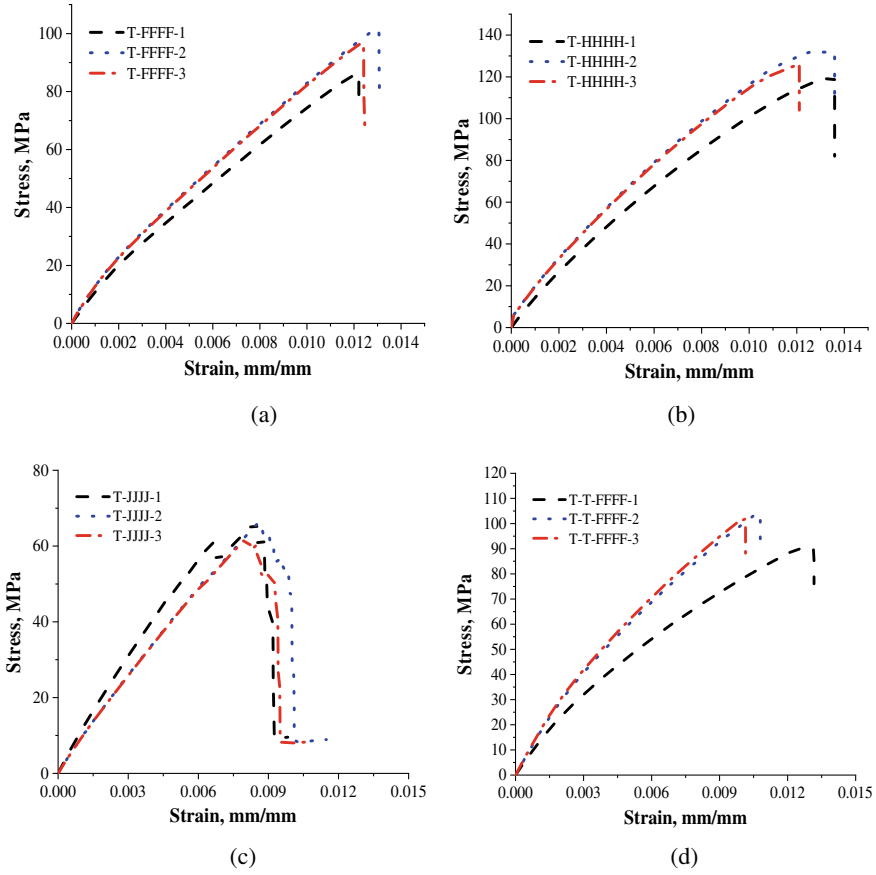

Fig. 7 Stress–strain graphs of plain NFRP specimens under tension test **a** T-FFFF **b** T-HHHH **c** T-JJJJ **d** T-T-FFFF

5 Conclusions

In this study, the elastic and strength properties of FFRP, HFRP and JFRP composites are determined experimentally by conducting the tensile and compression tests. Based on this experimentally work, the following concluding remarks are made:

- The results indicated that hemp fiber reinforced polymer composite has the maximum tensile strength along the direction of the fiber and maximum compressive strength along the fiber direction and in the transverse direction.
- The results showed that hemp fiber-reinforced polymer composite has the maximum stiffness along the direction of the fiber. The flax fiber-reinforced polymer composite has higher stiffness and compressive strength along the transverse direction of the fiber.

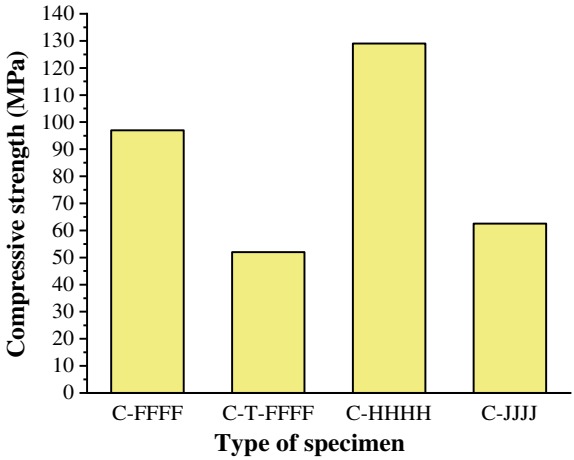

Fig. 8 Compressive strength of NFRP composites

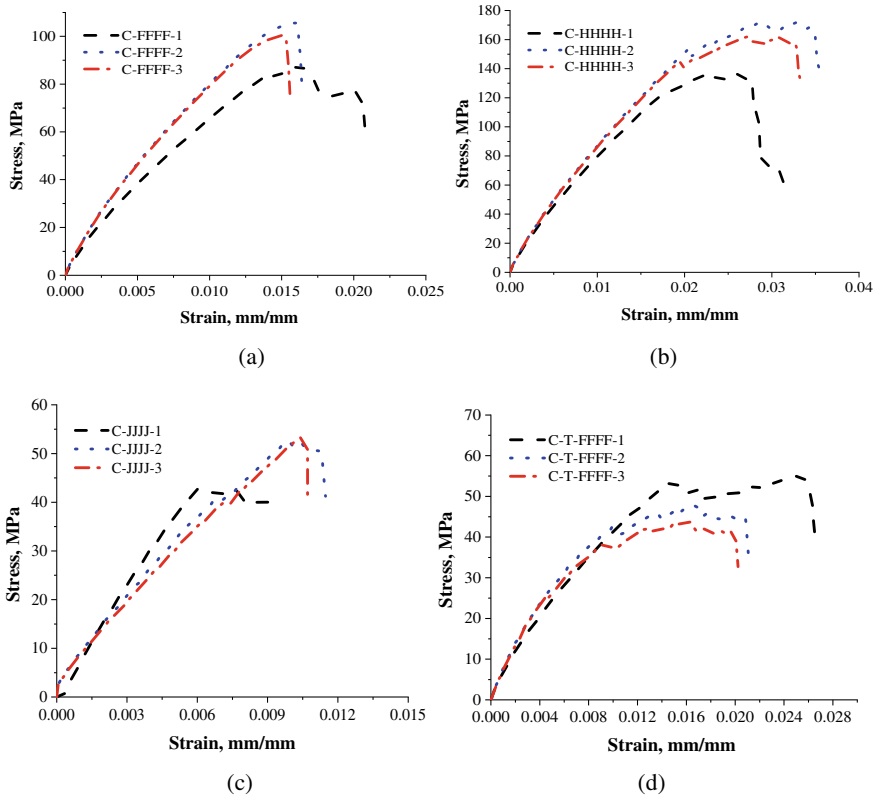

Fig. 9 Stress–strain graphs of plain NFRP specimens under compression test **a** T-FFFF **b** T-HHHH **c** T-JJJJ **d** T-T-FFFF

Table 4 Material properties of the NFRP composite

Laminate type	E_1	E_2	G_{12}	X_t	X_c	Y_t	Y_c	S = T
	(GPa)			(MPa)				
Flax-epoxy	7.02	0.52	0.010	94.3	97	10.5	5.6	5.1
Treated flax(2% NaOH)-epoxy	8.30	0.3	0.33	97.2	52	6.2	4.0	4.7
Hemp-epoxy	9.50	0.24	0.014	126	129	5.4	7.2	1.0
Jute-epoxy	7.56	0.2	0.010	66.7	62.5	2.03	3.6	2.2

Notes E_1 = young's modulus of elasticity in the principal direction −1 (fiber direction); E_2 = young's modulus of elasticity in direction transverse to the fiber direction; G_{12} = shear moduli in the planes 1–2; X_t, X_c = tensile and compressive strength of lamina in fiber direction; Y_t, Y_c = tensile and compressive strength of lamina in direction transverse to the fiber direction; S = shear strength of lamina in plane 1–3; T = shear strength of lamina in plane 1–2

- The chemical treatment improved the flax fiber-reinforced polymer composite properties along the fiber direction and in the case of the transverse direction, it showed negative results. Chemical treatments do not always lead to a remarkable increase in the composite performance but can significantly reduce the eco-sustainability.
- The natural fiber-reinforced composites manufactured by hand lay-up process provide an alternative to replace the existing synthetic fibers, mainly glass fibers, with high strength, low-cost and environmentally friendly nature.
- Future work should concentrate on hybridizing natural fibers with synthetic as well as natural fibers to enhance a composite's mechanical properties.

Acknowledgements Financial support provided by the Council of Scientific & Industrial Research (CSIR), New Delhi through Scheme no. (22(0781)/19/EMR-II) sanctioned to the second author is highly appreciated for helping in the execution of the project. The technical suggestions and discussion from the US-2020 partnership project are acknowledged to be helpful.

References

1. Alavudeen A, Rajini A, Kaarthikeyan S, Thiruchitrambalam M, Venkateshwaren N (2015) Mechanical properties of banana/kenaf fiber-reinforced hybrid polyester composites: effect of woven fabric and random orientation. Mater Des 66:246–257
2. Asim Md, Jawaid Md, Abdan K, Ishak Md. R (2016) Effect of alkali and silane treatments on mechanical and fiber-matrix bond strength of kenaf and pineapple leaf fibers. J Bionic Eng 13:426-435
3. ASTM D 3039 (2008) Standard test method for compressive properties of polymer matrix composite materials unsupported gauge sections by shear loading. American society of testing and materials. Philadelphia, USA
4. ASTM D 3410 (2008) Standard test methods for compressive properties of polymer matrix composite materials unsupported gauge sections by shear loading. American society of testing and materials. Philadelphia, USA

5. Cavalcanti DKK, Banea MD, Neto JSS, Lima RAA, Filva da LFM, Carbas RJC (2019) Mechanical characterization of intralaminar natural fiber reinforced hybrid composites. Composites Part B, 175. https://doi.org/10.1016/j.compositesb.2019.107149
6. Flynn J, Amiri A, Ulven C (2015) Hybridized carbon and flax fiber composites for tailored performance. Mater Des 102:21–29
7. Gieparda W, Rojewski A, Wustenhagen S, Jakubowska AK, Krobholz A (2021) Chemical modification of natural fibers to epoxy laminate for lightweight constructions. Compos A. https://doi.org/10.1016/j.compositesa.2020.106171
8. Ismail NF, Radauan AM, Slong AB, Muhamad N, Haron che H che (2021) The effect of alkali treatment on physical, mechanical and thermal properties of kenaf fiber and polymer epoxy composites. Polymers . https://doi.org/10.3390/polym13122005
9. Junior JHSA, Amicp SC, Botelho, Amado FDR (2013) Hybridization effect on the mechanical properties of curaua/glass fiber composites. Compos: Part B 55:492–497
10. Kabir MM, Wang H, Lau KT, Cardona F (2012) Chemical treatments on plant-based natural fiber reinforced polymer composites: an overview. Compos: Part B 43:2883–2892
11. Koohestani B, Darban AK, Mokhtari P, Yilmaz E, Darezereshki (2017) Comparison of different natural fiber treatments: a literature review. Int J Environ Sci Technol. https://doi.org/10.1007/s13762-018-1890-9
12. Nechifor M, Tanasa F, Teaca AA, Sulea D (2022) Maleated coupling agents for the surface treatment of natural fibers. Surf Treat Methods Nat Fibers Eff Biocompos. https://doi.org/10.1016/B978-0-12-821863-1.00005-3
13. Oladele IO, Michael OS, Adediran AA, Balogun OP, Ajagbe O (2020) Acetylation treatment for the batch processing of natural fibers: e_ects on constituents, tensile properties and surface morphology of selected plant stem fibers. Fibers. https://doi.org/10.3390/fib8120073
14. Ouarhim W, Zari N, Bouchfid R, Qaiss A, El K (2019) Mechanical performance of natural fibers-based thermosetting composites. Surf Treat Methods Nat Fibers Eff Biocompos. https://doi.org/10.1016/B978-0-08-102292-4.00003
15. Pickering KL, Efendy MGA, Le TM (2016) A review of recent developments in natural fiber composites and their mechanical performance. Composites: Part A 83, 98–112
16. Ramesh M, Palanikumar K, Reddy KH (2013) Mechanical property evaluation of sisal–jute–glass fiber reinforced polyester composites. Composites: Part B 48, pp 1–9
17. Sarawar A, Mahboob Z, Zdero R, Bougherara H (2020) Mechanical characterization of a new Kevlar/flax/epoxy hybrid composites in a structure. Polym Testing. https://doi.org/10.1016/j.polymertesting.2020.106680
18. Seghini MC, Touchard F, Sarasini F, Arnault AL, Ricciardi MR, Antonuucci V, Tirillo J (2020) Fatigue behavior of flax-basalt/epoxy hybrid composites in comparison with non-hybrid composites. Int J Fatigue. https://doi.org/10.1016/j.ijfatigue.2020.105800
19. Singh JIS, Singh S, Dhawan V (2017) Effect of curing temperature on mechanical properties of natural fiber reinforced polymer composites. J Natural Fibers 5:687–696
20. Singh SB, Vummadisetti S (2020) Development and characterization of novel functionally graded hybrid of carbon-glass fibers. Int J Mater Eng Innov 11:212–243
21. Singh SB, Vummadisetti S, Chawla H (2018) Influence of curing on the performance of FRP laminates. J Build Eng 16:01–19
22. Venkateshwaran N, Elayaperumal A, Sathiya GK (2012) Prediction of tensile properties of hybrid-natural fiber composites. Compos B 43:793–796
23. Vinod A, Vijay R, Singaravelu DL, Sanjay MR, Siengchin., Moure M.M. (2019) Characterization of untreated and alkali-treated natural fibers extracted from the stem of Catharanthus roseus. Mater Res Express. https://doi.org/10.1088/2053-1591/ab22d9
24. Zhang Y, Li Y, Ma H, Yu T (2013) Tensile and interfacial properties of unidirectional flax/glass fiber reinforced hybrid composites. Compos Sci Technol 88:172–177

Effect of Layer Thickness and FRP Reinforcement Ratio on the Load Carrying Capacity of ECC Composite Beams

Preethy Mary Arulanandam, Madappa V. R. Sivasubramanian, and Shamsher Bahadur Singh

Abstract In recent years, Fibre-Reinforced Polymer (FRP) bars have been used as reinforcement in concrete beams. However, the ductility of the beams is highly dependent on the properties of concrete since the failure mode of concrete is due to crushing. Substitution of concrete with Engineered Cementitious Composite (ECC) can avoid the ductility and durability problems associated with the concrete. In this paper, the flexural behaviour of FRP reinforced ECC-Concrete composite beams is numerically investigated through the Finite Element (FE) platform. To verify the robustness of the FE model of the composite beams, the simulation results were compared against the experimental results available in the literature and good agreements were achieved. An extensive parametric study was then conducted to examine the effect of the FRP reinforcement ratio against ECC layer thickness. It was observed that the load-carrying capacity of the composite beams is improved with the increase in ECC height replacement and Basalt Fibre Reinforced Polymer (BFRP) reinforcement ratios. In addition, composite beams show enhanced load-carrying capacity of 40% and 2%, of ECC layer thickness and FRP reinforcement ratio, respectively.

Keywords ECC · FRP · Layer thickness · Reinforcement ratio

1 Introduction

Reinforced concrete (RC) structures exposed to corrosive environments, such as deicing salts, chemical treatment plants, structures built in or close to seawater, etc., are suitable to be reinforced with Fiber-Reinforced Polymer (FRP) bars to eliminate durability problems [1]. Over the past two decades, FRP materials have been used

Present Address:
P. M. Arulanandam · M. V. R. Sivasubramanian (✉)
Department of Civil Engineering, National Institute of Technology Puducherry, Karaikal 609602, India
e-mail: madappa@nitpy.ac.in

S. B. Singh
Department of Civil Engineering, BITS Pilani, Pilani 333031, India
e-mail: sbsingh@pilani.bits-pilani.ac.in

S. B. Singh et al. (eds.), *Fiber Reinforced Polymeric Materials and Sustainable Structures*, Composites Science and Technology, https://doi.org/10.1007/978-981-19-8979-7_6

as an alternative for steel reinforcement in concrete structures [2, 3]. However, FRP reinforcement has low elastic modulus and linear deformation properties, leading to large deflections and crack widths which leads to brittle failure, which has prevented FRP structures from being widely used [4].

Engineered Cementitious Composite (ECC) is a cement-based composite material exhibiting superior ductility (typically >3%, 300 times that of normal concrete or FRC), tight crack width (less than 80 μm), and relatively low fiber content (2% or less of short randomly oriented fibers) [5, 6]. ECC's ultimate tensile strength and tensile strain capacities are 5–8 MPa and 3–5%, respectively. ECC's compressive strength and compressive strain capacity range from 30 to 90 MPa and 0.45–0.65%, respectively [7]. ECC exhibits superior tensile strain hardening and multiple cracking behaviors by systematically tailoring the fiber, matrix, and interface properties, guided by micromechanics principles [8].

In order to enhance both the ductility and durability of structures, researchers proposed FRP reinforced ECC-Concrete composite beams. The excellent crack control ability and durability of ECC materials have encouraged the use of ECCs in the tensile zone around longitudinal steel reinforcement [9, 10]. The results showed that the flexural capacity and deformation ability slightly improve, but the crack width before yielding of steel reinforcement significantly decreases to just 20% of that in conventional RC beams [11, 12]. ECC-concrete composite beams reinforced with FRP bars were also to solve cracking and deflection problems associated with the brittleness of FRP-reinforced beams [13, 14].

2 Research Significance

Strength and ductility are critical parameters in the design of concrete structures. It is anticipated that utilizing FRP bars and ECC at strategic locations in the RC beam elements will give promising results in high strength and ductility. However, the successful utilization of ECC requires robust analysis and design procedures. Studies available in the literature deal only with modelling and analysis of FRP reinforced composite beam against particular ECC layer thickness and FRP reinforcement ratio. Hence, in this study, the numerical analysis of FRP reinforced ECC-Concrete composite beams with different reinforcement ratios against ECC layer thickness are investigated and presented the effects on the flexural capacity of the composite beams.

3 Finite Element Analysis

This research study is conducted on the nonlinear analysis, and the response of FRP reinforced ECC-Concrete composite beams under monotonic loading through FE analysis on the ABAQUS platform. The numerical investigation for the response

of FRP reinforced ECC-Concrete composite beams under monotonic loading was performed in ABAQUS finite element software. For this purpose, three Basalt Fibre Reinforced Polymer (BFRP) reinforced ECC-Concrete composite beams chosen from the literature [13, 14] were modelled and analysed. The numerical results are obtained in terms of load–deflection response and compared with the experimental results.

Constitutive Model and Plasticity Parameters

In the present study, ECC and concrete are modelled using the damage plasticity model available in the ABAQUS nonlinear program to define the damage and failure mechanisms [15]. Uniaxial tensile and compression stress–strain responses (Fig. 1) are employed to develop the constitutive behaviour of the materials. The input parameters needed to model the constitutive behaviour of composite beams is presented in Table 1.

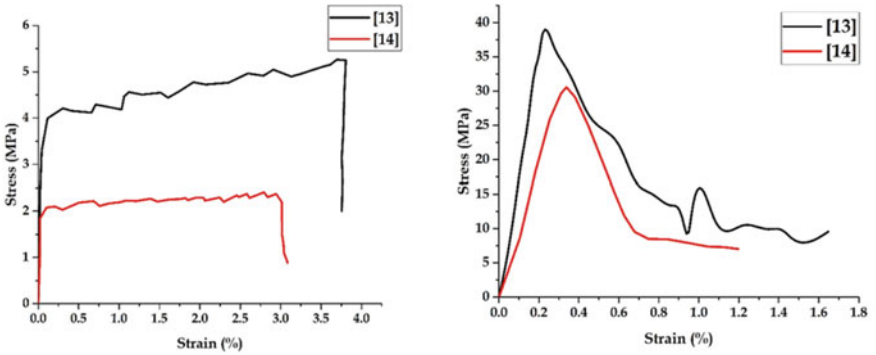

(a) Tension *(b) Compression*

Fig. 1 Stress–strain behaviour of ECC

Table 1 Input parameters required for FE analysis

Properties	ECC		BFRP	
	[13]	[14]	[13]	[14]
First cracking strength (MPa)	2.8	2.0	Not applicable	Not applicable
First cracking strain (%)	3.20×10^{-4}	0.023	Not applicable	Not applicable
Tensile strength* (MPa)	4.6	2.4	907	1250
Ultimate tensile strain	0.018	0.025	0.0196	0.026
Young's modulus (GPa)	15.50	16.15	46.2	50
Compressive strength# (MPa)	38.3	31.4	Not applicable	Not applicable

*Tensile test values are taken from the uniaxial test of ECC coupons and dogbone specimens
#Compressive test values are taken from the compression test of ECC cubes and cylinders

This model incorporates two main failure mechanisms in the form of tensile cracking and compressive crushing. Thus, damage parameters, strain hardening, and strain-softening rules for ECC and concrete materials are duly incorporated in this study. The compressive and tensile damage parameters (d_c and d_t) are calculated based on Eqs. (1), (2), respectively,

$$d_c = 1 - \frac{\sigma_c E_c^{-1}}{\varepsilon_c^{pl}(1/b_c - 1) + \sigma_c E_c^{-1}} \tag{1}$$

$$d_t = 1 - \frac{\sigma_t E_c^{-1}}{\varepsilon_t^{pl}(1/b_t - 1) + \sigma_t E_c^{-1}} \tag{2}$$

where σ_c and σ_t are compressive and tensile stresses, respectively, E_c is the modulus of elasticity, ε_c^{pl} and ε_t^{pl} are plastic strains corresponding to compressive and tensile strengths, respectively. $b_c = \frac{\varepsilon_c^{pl}}{\varepsilon_c^{in}}$, ε_c^{in}—compressive inelastic strain, $b_t = \frac{\varepsilon_t^{pl}}{\varepsilon_t^{cr}}$, ε_t^{cr}—tensile cracking strain. b_c and b_t are the constant parameters that can vary from 0 to 1, whereas 1 means no damage and 0 means total damage.

The plasticity parameters following the Drucker-Prager criteria are employed to define the failure of ECC and concrete materials, which are present in [16] (Table 2).

Details of the Experimental Study

The details of the composite beam specimens available in the literature, which are used in this study, are presented in Table 3. During the experimental study, all the beam specimens were tested under vertical monotonic loading and the mid-point load–deflection response was measured. The loading patterns of the beam specimens are shown in Fig. 2.

Modelling of Composite Beams

The modeling procedure for the selected composite beams in the ABAQUS platform is discussed in this section. ECC and concrete are modeled using 8-noded linear hexahedral solid elements with reduced integration (C3D8R). A 2-noded nonlinear truss element (T3D2) is used for steel reinforcement. The embedded

Table 2 Details of plasticity parameters

Parameter	Value	Description
Ψ (°)	20 (ECC) 36 (Concrete)	Dilation angle
$\mathfrak{E}$	0.1	Eccentricity
σ_{b0}/σ_{c0}	1.16	The ratio of biaxial compressive ultimate strength to uniaxial ultimate compressive strength
K_C	0.67	A ratio of the second stress invariant on the tensile meridian to that on the compressive meridian
μ	0.01	Viscosity parameter

Table 3 Details of beam specimens

S. No.	Beam ID	Dimensions ($b \times d \times l$)* (mm)	FRP type	Reinforcement ratio (%)	ECC layer thickness (mm)
1	EC-1 [13]	200 × 300 × 2350	BFRP	1.05	90
2	EC-2 [14]	150 × 200 × 1500	BFRP	0.57	50.75
3	EC-3 [14]	150 × 200 × 1500	BFRP	0.57	99.75

*(b = breadth, h = height, l = span)

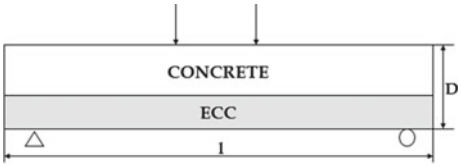

Fig. 2 Loading pattern of composite beams

method with the perfect bond between reinforcement and the surrounding material is adopted to simulate the reinforcement-material bonding interaction properly. In addition to this, for composite beams, a perfect bond was assumed between concrete and ECC since experimentally, no debonding was observed between the materials. Hence, tie constraint (surface-to-surface property) generates the composite action. The boundary (simply supported ends) and loading conditions (two-point loading) were specified in the analysis. The geometry, reinforcement, boundary conditions and loading pattern of the composite beam simulated are shown in Fig. 3. The meshing of the beam element is performed by employing fine mesh (i.e., 30 × 30 mm mesh size) to attain an accurate response with the experimental results. An incremental displacement-control program was adopted to analyze the selected FRP reinforced composite beams.

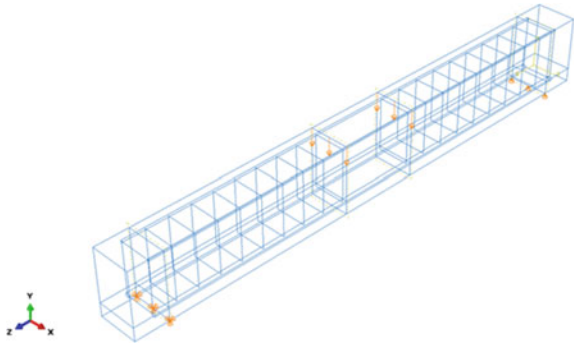

Fig. 3 Composite beam simulated in ABAQUS

4 Verification of Numerical Models

In this section, the load–deflection response of all the composite beams has been evaluated numerically and compared against the experimental results. The verification and discussion of the obtained results were discussed as follows.

Load–Deflection Response

To understand the effectiveness of the procedure adopted for the numerical simulation, the load–deflection response of the composite beams obtained from the FE analysis were compared against the results from the experimental study (Fig. 4).

In general, from Fig. 4 it can be seen that the numerical response shows good agreement with the experimental response. From Table 4, it can be observed that the difference between the numerical and experimental responses of the composite beams is less than 5% for all composite beams. This shows the robustness of the numerical procedure adopted for the analysis of the FRP reinforced composite beams.

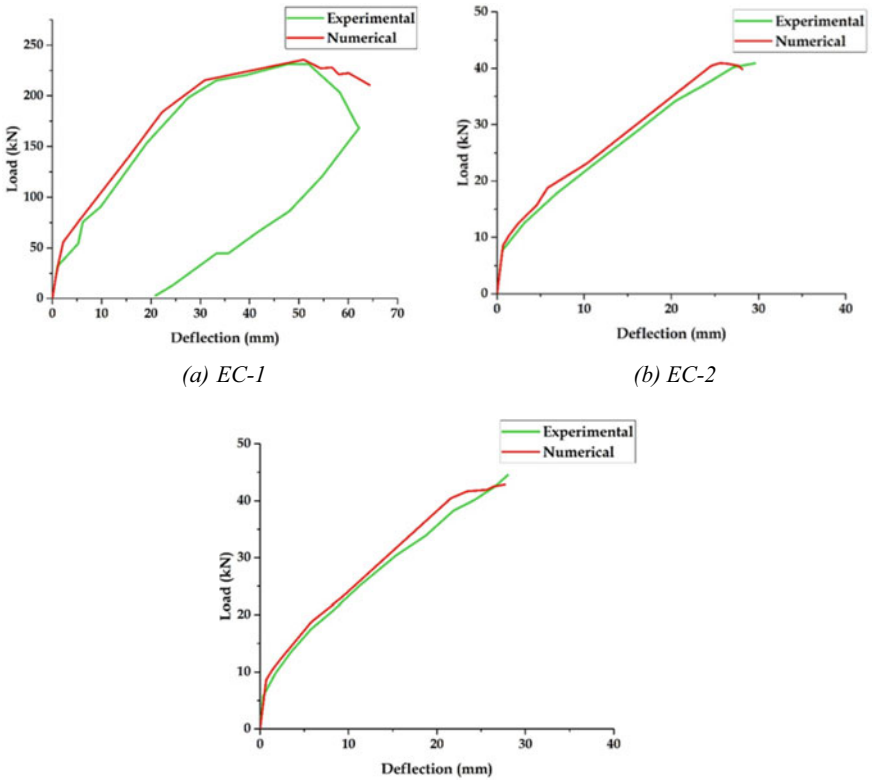

(a) EC-1 *(b) EC-2*

(c) EC-3

Fig. 4 Load–deflection response of composite beams

Table 4 Comparison of results

S. No.	Specimen ID	Ultimate deflection (mm)		Ultimate load (kN)		% difference in load
		Experimental	Numerical	Experimental	Numerical	
1	EC-1 [13]	51.9	50.9	231.2	235.7	1.93
2	EC-2 [14]	29.7	26.1	40.9	41.2	0.73
3	EC-3 [14]	28.1	27.6	44.5	42.8	3.82

5 Parametric Study

As is stated above, the numerical load–deflection behaviour agrees well with the experimental behaviour which shows the robustness of the employed numerical procedure. Hence, it is appropriate to adopt the same procedure for the parametric study. The parametric study includes:

- Effect of ECC layer thickness against various FRP reinforcement ratio
- Effect of FRP reinforcement ratio against various ECC layer thickness.

The parametric study is done to understand the effect of ECC layer thickness and BFRP reinforcement in the composite beam. For this purpose, a constant cross-section of the beam is used whereas the ECC layer thickness and BFRP reinforcement ratio are varied. The cross-section of the composite beam along with ECC layer thickness and BFRP reinforcement ratio is shown in Fig. 5.

Effect of ECC layer thickness against various FRP reinforcement ratio

In this section, the selected FRP reinforcement ratios are analysed for five different ECC layer thicknesses (i.e., 0, 20, 40 and 60% of the beam depth) to investigate the effect of various ECC layer thickness against each reinforcement ratio in composite beams.

The effect of the load-carrying capacity of the ECC-Concrete composite beams with different ECC layer thicknesses is shown in Fig. 6. It is observed that an increase in ECC layer thickness increases the load-carrying capacity of the beam, after a peak load is achieved, the load-carrying capacity decreases as an increase in ECC layer thickness. This behavior is observed in all composite beams employed in this study, irrespective of the reinforcement ratio. For a composite beam of a particular cross-section, 40% ECC layer thickness exhibits enhanced load carrying capacity

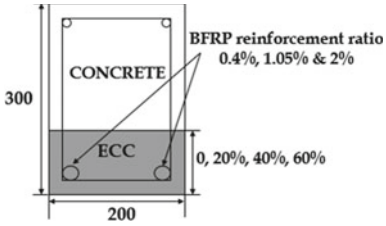

Fig. 5 Cross-section detail of composite beam

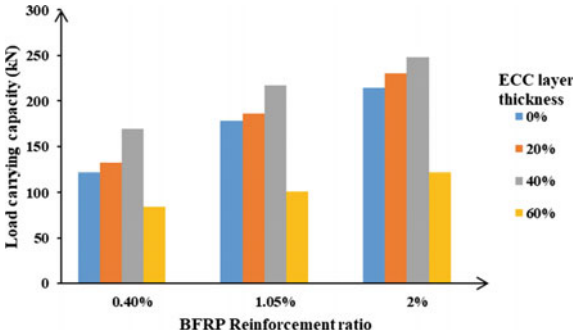

Fig. 6 Load versus FRP reinforcement ratio

for all reinforcement ratios used. However, with a further increase of the ECC layer thickness, the ultimate load carrying capacity of the composite beams were reduced to some extent. This was mainly because as the height of the ECC in the cross-section increased, and extent above the neutral axis where ECC materials are participated in the compressive zone. The incorporation of PVA fibres increases the porosity of the cement-based materials, which leads to internal structural damage, which in turn affects the compressive capacity of the beams. As the load increased, the overall load bearing capacity decreased. Therefore, there was an optimal range for cross-section replacement ratios. Hence, for this study the 40% ECC height replacement of the composite beams could obtain better mechanical properties and economic benefits.

Effect of FRP reinforcement ratio against various ECC layer thickness

In this section, the selected ECC layer thickness is analyzed for various FRP reinforcement ratios (0.4, 1.05 and 2%) to investigate the effect of reinforcement ratio for each ECC layer thickness in composite beams.

The effect of the load-carrying capacity of the ECC-Concrete composite beams with different FRP reinforcement ratios is shown in Fig. 7. It is understood that an increase in FRP reinforcement ratio increases the load-carrying capacity of full concrete and for all ECC-Concrete composite beams irrespective of the ECC layer thickness. Further, it is observed that the highest reinforcement ratio of 2%, showed enhanced load carrying capacity for the composite beam with 40% ECC layer thickness.

6 Conclusion

This study is conducted on the numerical analysis of BFRP reinforced ECC-Concrete composite beams and the obtained results are verified against the experimental studies. Upon analysis, the load–deflection response was generated. Based on the numerical and experimental results, the following conclusions are drawn:

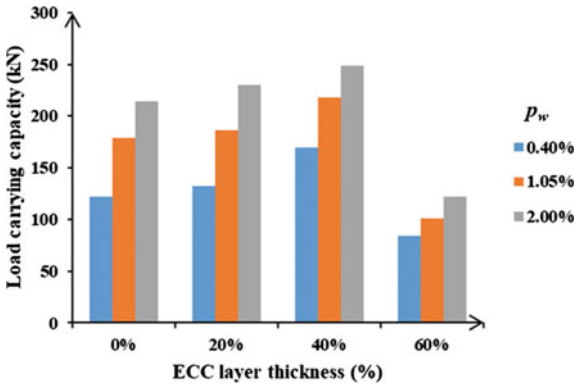

Fig. 7 Load versus ECC layer thickness

- The material constitutive model and plasticity parameters in the damage plasticity model are effectively used to define the behavior of ECC, concrete and FRP in the analysis.
- Close agreement between the numerical and experimental results is observed. In addition, the difference between the peak load of the numerical and experimental responses of all the reinforced beams is within the range of 5%, which shows the robustness of the procedure adopted for FE models.
- Generally, the load-carrying capacity of the composite beams is improved with the increase of the ECC height replacement and BFRP reinforcement ratios.
- Composite beams of a particular cross-section exhibit enhanced load carrying capacity of 40 and 2%, of ECC layer thickness and FRP reinforcement ratio, respectively.

Acknowledgements This paper is the part of the author's Ph.D. study enrolled at the National Institute of Technology Puducherry, India which is being supervised by the corresponding author.

References

1. AE Naaman 2003 FRP reinforcements in structural concrete: assessment, progress and prospects Fibre-Reinf Polym Reinf Concr Struct 2 July 3 24
2. Wang H, Belarbi (2005) A flexural behavior of fiber-reinforced-concrete beams reinforced with FRP rebars
3. M Pecce G Manredi E Cosenza 2000 Experimental response and code models of gfrp rc beams in bending J Compos Constr 4 November 182 190
4. M Theriaule B Benmokrane 1998 Effects of FRP reinforcement ratio and concrete strength on flexural behavior of concrete beams J Compos Constr 2 February 7 16
5. VC Li 2003 On engineered cementitious composites (ECC) a review of the material and its applications J Adv Concr Technol 1 3 215 230
6. T Kanda VC Li 1999 New micromechanics design theory for pseudostrain hardening cementitious composite J Eng Mech 125 4 373 381

7. PM Arulanandam SB Singh T Kanakubo MVR Sivasubramanian 2020 Behavior of engineered cementitious composite structural elements—a review Indian Concr J 94 6 5 28
8. SB Singh MVR Sivasubramanian 2013 Performance of ductile fibre-reinforced cementitious composite concrete frames under flexural loading Proc Inst Civ Eng Constr Mater 166 1 34 44
9. VC Li S Wang C Wu 2001 Tensile strain-hardening behavior or polyvinyl alcohol engineered cementitious composite (PVA-ECC) ACI Mater J 98 6 483 492
10. F Yuan J Pan Y Wu 2014 Numerical study on flexural behaviors of steel reinforced engineered cementitious composite (ECC) and ECC/concrete composite beams Sci China Technol Sci 57 3 637 645
11. J Zhang CKY Leung YN Cheung 2006 Flexural performance of layered ECC-concrete composite beam Compos Sci Technol 66 11–12 1501 1512
12. M Maalej ST Quek SFU Ahmed J Zhang VWJ Lin KS Leong 2012 Review of potential structural applications of hybrid fiber Engineered Cementitious Composites Constr Build Mater 36 216 227
13. F Yuan J Pan CKY Leung 2013 Flexural behaviors of ECC and concrete/ECC composite beams reinforced with basalt fiber-reinforced polymer J Compos Constr 17 5 591 602
14. W-J Ge 2018 Flexural behavior of ECC-concrete hybrid composite beams reinforced with FRP and steel bars J Compos Constr 23 1 04018069
15. Systèmes SD (2012) ABAQUS user's manual. Version 6.12. Simulia Corp. Johnston
16. AEH Khalil E Etman A Atta M Essam 2016 Nonlinear behavior of RC beams strengthened with strain hardening cementitious composites subjected to monotonic and cyclic loads Alexandria Eng J 55 2 1483 1496

Fibers and Polymers in Fiber Reinforced Polymer Composites: A Review

Ajay Vasudeo Rane and Sabu Thomas

Abstract A composite material is made up of a chemically and/or physically unique phase spread inside a continuous phase that has qualities that are distinct from both of these materials. The high specific strength (stress/density) and modulus (stress/stiffness) of composites, as well as their low density (mass/volume), make them particularly appealing. Fibers of varied diameters are the most important component of composite materials. Since antiquity, fibres, in particular, have been employed to strengthen considerably weaker materials. The potential of such reinforcement for boosting the fabrication of composites of engineering significance has only lately been scientifically examined. The content in this chapter is devoted to a variety of fibres that are now generating a lot of attention among researchers and engineers due to their structural and functional benefits.

1 Introduction

A composite material is made up of a chemically and/or physically unique phase spread inside a continuous phase that has qualities that are distinct from both of these materials. The high specific strength (stress/density) and modulus (stress/stiffness) of composites, as well as their low density (mass/volume), make them particularly appealing [1, 2]. This has sparked a lot of interest in their study and development in recent decades, especially for aviation applications that require more cargo capacity

A. V. Rane · S. Thomas (✉)
School of Energy Materials, Mahatma Gandhi University, Kottayam, Kerala 686560, India
e-mail: sabuthomas@mgu.ac.in

S. Thomas
School of Chemical Sciences, Mahatma Gandhi University, Kottayam, Kerala 686560, India

International and Interuniversity Centre for Nanoscience and Nanotechnology, Mahatma Gandhi University, Kottayam, Kerala 686560, India

A. V. Rane
Materials Research Laboratory, Department of Mechanical Engineering, KMEA Engineering College, Cochin, Kerala, India

S. B. Singh et al. (eds.), *Fiber Reinforced Polymeric Materials and Sustainable Structures*, Composites Science and Technology, https://doi.org/10.1007/978-981-19-8979-7_7

and engine efficiency. Although the consequences of exhaust emissions on the environment have provided the motivation for the future low weight vehicle, the automobile industry has showed interest in structural composite materials (i.e., for major load carrying components) in recent times for comparable reasons [3, 4].

Composites provide a number of advantages over traditional materials such as metals, including decreased density, improved corrosion resistance, and temperature stability. Fibers of varied diameters are the most important component of composite materials. Since antiquity, fibres, in particular, have been employed to strengthen considerably weaker materials. The potential of such reinforcement for boosting the fabrication of composites of engineering significance has only lately been scientifically examined. The content in this chapter is devoted to a variety of fibres that are now generating a lot of attention among researchers and engineers due to their structural and functional benefits [3, 5].

When fibres are employed as reinforcements, the fibre reinforcement can be aligned in the desired direction to produce a composite with directional properties. This sort of composite is ideal for constructions that require a variety of properties in various orientations. Fiber-reinforced polymers are a type of composite material that consists of a polymer matrix and another fibrous material for support. The polymer matrix is often a thermoset resin or a thermoplastic resin with chemical and abrasion resistance. It is, however, usually not mechanically robust. The fibre component creates a new compound with much improved performance. The fibre utilised keeps its shape but shares its unique properties with the matrix, resulting in a lighter, stiffer, and mechanically stronger new composite. Banana, coconut, kenaf, oil palm, sugarcane, pineapple, glass, carbon, polyethylene, aramid, ceramics, and whiskers are some of the most often utilised fibres. Natural fibres are less expensive, have a less environmental impact, and can be recycled. They provide great thermal and acoustic insulation, are less polluting, and cause less occupational skin and respiratory complaints. Synthetic fibres are more durable, less costly, and more widely accessible; they can handle big loads without breaking; they absorb little water and dry rapidly; they are wrinkle resistant, very light, and incredibly fine; and they are not affected by moths. Incorporating fibres into a polymer reduces weight while also improving elastic modulus and mechanical strength. As a result, these materials may be utilised to create components with precise tolerance limits, low fatigability, high impact tolerance, and superior compression characteristics. They make component design easier, resulting in increased manufacturing and operational efficiency. Fiber reinforced polymers also provide good thermal and acoustic insulation, as well as resistance to corrosive chemicals, sea wave impact, humid environments, and storm winds/waters. When compared to their 2D counterparts, certain 3D printing procedures and the incorporation of nanoparticles can boost strength [6–10].

1.1 Classification of Composites

Based on the matrix material, composite materials are classed as polymer matrix composites (PMC), metal matrix composites (MMC), and ceramic matrix composites (CMC). Polymer matrix composites are the most prevalent of these three composites because of their low manufacturing temperature and inexpensive cost. The majority of PMCs are made at room temperature. PMCs, on the other hand, can only be utilised at or slightly above room temperature. PMC has a maximum service temperature of around 300 °C. MMCs can withstand temperatures of up to 1200 °C. When compared to PMCs, MMC manufacturing is a little more challenging. Beyond 1200 °C, the CMCs can be employed. They do, however, need a very high production temperature or unique fabrication procedures. As a result, CMCs are extremely costly materials [8, 11].

1.2 Classification of Reinforcements Used in Fabrication of Fiber Reinforced Composites

Composites are characterized as particle composites or fibre reinforced composites depending on the kind of reinforcement. When compared to particle composites, the performance level of fibre reinforced composites is quite high. Short fibre reinforced composites and continuous fibre reinforced composites are two types of fibre reinforced composites. Based on the orientation of the fibres, short fibre reinforced composites are divided into two groups. They're short fibre reinforced composites that are both aligned and randomly orientated. Whiskers can be thought of as short fibres, yet each fibre is made up of a single crystal. Depending on the orientation of the fibres, continuous fibre reinforced composites can be classed as unidirectional, bidirectional, or multidirectional composites [9, 12–14].

Laminates and sandwich composites are the two forms of structural composites. The laminates are multilayered composites in which the fibres in each layer are orientated in the same or opposite directions. Sandwich composites are made up of composite skin layers and a light-weight core. Depending on the use, the core might be foam or a honeycomb structure. Sandwich composites are low in weight and rigid in nature. The term "hybrid composite" refers to a composite that has more than one form of reinforcement [3, 7, 15, 16].

The composites can also be divided into macro, micro, and nanocomposites based on the size of the reinforcement. More than millimeter-sized reinforcements are used in macro composites. In micro composites, micrometer-sized reinforcements are employed. Micro composites include glass and carbon fibre reinforced composites, for example.

Fiber reinforced composites make up the majority of today's composites. Because of the following qualities, fibres are superior to particles as reinforcements.

1. Extremely strong
2. Aspect ratio that is large (length to diameter ratio)
3. Extreme flexibility.

1.3 Classification of Polymers Used in Fabrication of Fiber Reinforced Composites

As previously said, matrix materials are divided into three categories. Polymeric, metallic, and ceramic matrix materials are among them. Polymer matrices are used in the majority of composites nowadays because they are reasonably inexpensive and easy to process.

A polymer is a macromolecule made up of one or more units that are repeated in a high number of times. A polymeric substance is made up of a large number of polymeric molecules with the same chemical structure. In a polymeric substance, the polymeric chains are either randomly organized or randomly arranged with some chain orientation. Depending on the processing parameters, the polymer might be formed in an amorphous or semi-crystalline state. The thermosetting and thermoplastic polymers are the two types of polymers.

The polymer molecules in a thermosetting polymer create a three-dimensional network structure with strong covalent connections between them. It is extremely difficult to distort the material after this sort of network structure has been developed. It's comparable to how cement sets. Thermoset polymers have several benefits over thermoplastics in the context of composites, and as a result, they are commonly employed [3, 17–20].

The following are some of the benefits:

- effective wetting with the reinforcements
- high thermal stability
- good creep resistance
- good chemical resistance
- facile production of composites because they are supplied in liquid form.

However, there are a few drawbacks, which include:

- brittleness is high
- production time is long
- storage life is limited.

The polymer molecules in a thermoplastic substance are kept together by weak van der Waals forces. As a result, deforming a thermoplastic material is simple when heat and pressure are applied. That is to say, it may be used again. As a result, a single stage of processing is not required to construct the final form. Some regular forms can be mass-produced and then distorted into the final shape at a later time. There are several more benefits in addition to this one. The fabrication time for thermoplastics is shorter, and they are more durable. Thermoplastic materials may be kept for a longer

period of time. Despite these benefits, thermoplastics are not widely employed due to the high processing temperatures, poor wettability to reinforcements, and high melt viscosity required. These issues have been partially overcome, and thermoplastic composites are becoming increasingly common [21–24].

2 Processing

2.1 Hand Lay Up

The 'hand layup' manufacturing technique is manually putting down individual layers or 'plies' of a type of reinforcement called 'prepreg.' This is made up of thousands of fibres that have been pre-impregnated with glue and bundled into tows before being woven together or organized in a single unidirectional ply [3, 12].

2.2 Resin Transfer Molding

Resin transfer moulding is a closed-molding production technique in which polymer resin is transferred over reinforcing fibres that have previously been deposited on the mold's surface [12].

2.3 Resin Infusion/Vacuum Bagging

Vacuum infusion is a technique for injecting resin into a laminate using vacuum pressure. Dry materials are deposited into the mould and a perforated release film is applied over the dry reinforcement after the mould has been gelcoated [25].

2.4 Autoclave Process

It's a method that involves forming both sides of the panel with a two-sided mould set. A flexible silicone or extruded polymer film such as nylon membrane is on the upper side, while a hard mould is on the lower side. Reinforcement materials can be manually applied or robotically placed. They are made up of continuous fibre shapes that are fashioned into textile structures. They're usually prepreg textiles or unidirectional tapes that have been pre-impregnated with resin. In other cases, a resin film is applied to the lower mould, and dry reinforcement is applied to the top. The upper mould is in place, and the vacuum is applied to the cavity of the mould. An

autoclave is used to seal the assembly. This procedure is usually carried out at a high pressure and at a high temperature. For maximal structural efficiency, enhanced pressure allows for a high fibre volume fraction and minimal void content [8].

2.5 Compression Molding

Compression moulding is a moulding technique that involves placing a feeding material into an open, heated mould chamber. After that, the mould is sealed with a top plug and compacted with massive hydraulic presses to ensure that the material reaches every part of the mould. In the heated mould, the charge cures [26].

2.6 Filament Winding

Filament winding is a fabrication method that is mostly used to create open (cylinders) or closed end structures (pressure vessels or tanks). The filaments are wound under tension around a revolving mandrel in this technique [15].

2.7 Pultrusion

Pultrusion is a composite synthesis technique that results in a consistent cross-section and manufacturing rate. The fibres are pulled through a heated die in this process. A steady pressure is supplied to the resin as it passes through the die, causing it to melt and impregnate the fibre reinforcement [8].

2.8 Injection Molding

Injection moulding is a manufacturing method that involves injecting molten material into a mould, to create components. Metals, glassware, elastomers, confections, and, most typically, thermoplastic and thermosetting polymers are among the materials used in injection moulding [4].

2.9 Reinforced Reaction Injection Molding

Two or more reactive resins are metered and impingement-mixed at high pressure to form a thermosetting polymer, injected into a mould, and then cured in the reinforced reaction injection moulding process [27, 28].

2.10 Thermoforming

Thermoforming is the process of softening a thermoplastic sheet by heating it to a certain temperature. The sheet is stretched and controlled across a single-sided mould. Then it cools to its final form [12].

3 Designing

To begin with, anisotropy's geometric and structural characteristics result in exceptional mechanical qualities. In the fibre direction, typical composite fibres have considerable strength and stiffness, but are weak and flexible perpendicular to it. Other physical parameters, like as electrical or thermal conductivity, may change significantly depending on whether they are tested parallel to or perpendicular to a fibre. These anisotropic qualities can be imparted to the fibre reinforced composite when implanted in a matrix. The mechanical and other physical qualities of the composite item may be customized in this situation based on the fibre positioning. Understanding the anisotropic characteristics of fibrous materials is critical for creating composites with customized features [3, 4].

Another distinguishing feature of fibres is their large surface area, which is due to their tiny diameter in comparison to their length. The interface to the matrix material is the fibre surface, which has topography and chemistry. First and foremost, the fibre surface controls the wetting behavior with matrix material, taking into consideration surface tension of the materials as well as capillary effects. Second, the load is transferred to the fibre via the contact between the fibre and the matrix. The failure of a composite item may be tailored to individual requirements by adjusting the adhesion between the two components. To build customized fibre reinforced composites, a thorough understanding of the interaction of fibre and matrix is required [3, 12].

4 Applications

4.1 Automotive Industry

The automobile industry's ultimate aim is a high strength-to-weight ratio. Fiber reinforced polymers are useful as metal alternatives in the bodywork of luxury vehicles and in the body sidings of trucks and trailers. These strong, stiff, and light materials, which have greater fracture points than steel, save fuel consumption while enhancing speed. They may also be readily moulded into the necessary shapes. This field accounts for over a third of all fiber reinforced polymers usage. Glass fibers reinforced polymers are used to reduce the weight and streamline the design of engine components such as the intake manifold by up to 60%. Several components can be merged to save money. In comparison to carbon fiber reinforced polymers, glass fiber reinforced polymers are weaker and more bendable. Instead of aluminium, gas and clutch pedals might be moulded as separate components from glass fiber reinforced polymers, allowing for faster production and reduced costs. For stress-specific strength, the fibres can be oriented in any direction, boosting component safety [2].

4.2 Construction Industry

The construction industry, which includes bridges and roads, presently uses over 20% of fiber-reinforced polymers. Fiber reinforced polymers can be used to improve the load-bearing capacity of existing structures (such as slabs, columns, or beams) or to repair damage. When it comes to retrofitting older structures that are facing loads considerably larger than they were meant to withstand, this is incredibly cost-effective and beneficial. Highway infrastructure such as guardrails, signboards, drainage systems, and bridge decks, as well as car skyways, utility poles, and pipes for gas, water, and sewage, are all made of fiber reinforced polymers. Fiber reinforced polymers are already widely used in domestic and corporate office furniture, household appliances, swimming pools, rain gutters, bathroom equipment, and pipe fittings and hoods [10, 29].

4.3 Aerospace Industry

Currently, just around 0.6 percent of fiber reinforced polymers are used in this field, but with future growth and decreased environmental costs, considerably more would be required. When compared to aluminium sheets, carbon fibres in fiber reinforced polymers lower weight by 25% while ensuring equivalent or higher strength. They have high tensile strength and can withstand severe conditions and temperature fluctuations. They have a high rigidity and do not expand much when heated. Although

initially costly, they save money for the aircraft industry, which values every gramme of extra weight because to its impact on fuel consumption, travel time and expenses, and aerodynamic safety. Carbon-fiber reinforced polymers also enables the manufacturing of complicated moulded components, decreasing the number of components by an incredible 95%. In comparison to other materials such as steel or cast aluminium, this simplifies, speeds up, and lowers the cost of manufacture. Many large contemporary airplanes are constructed up of more than 50% carbon-fiber reinforced polymers. Fiber reinforced polymers are also increasingly being used to make rotor blades for helicopters and high-end drones [30].

4.4 Consumer Goods Industry

Thanks to the widespread usage of carbon and other fiber reinforced polymers in sporting products, many athletes are finding it simpler to lift their gear. Musical instruments and their components, guns, camping tents, and camera tripods have all profited from these adaptable materials, which account for 6% of all fiber reinforced polymers utilized [4, 15].

4.5 Protective Equipment Industry

When aramids are employed in fiber reinforced polymers, they provide materials with remarkable thermal and impact resistance, as well as mechanical strength, making them perfect for use in bullet-proof and fire-resistant suits, as well as blast-protection vehicles and structures [31].

4.6 Marine Infrastructure Industry

In maritime shoreline situations or aboard ships, fiber reinforced polymers are appropriate substitutes for wood since they reduce structural weight and improve corrosion resistance. Other uses include rolling bridges, floating causeways, and platforms for maritime bases [11, 29].

4.7 Power Industry

Over the next decade, demand for fiber reinforced polymers in industry and energy applications is predicted to increase by more than 300%, mostly in electronic and electrical components. Most fiber reinforced polymers are electrically insulative,

can withstand harsh environmental chemicals (including corrosive ones), resist heat degradation, are largely non-flammable, have good structural integrity, and can withstand UV radiation. Glass-fiber reinforced polymers are non-magnetic and spark-resistant, making them suitable for use in power components. Reinforced polymers are also employed in the construction of wind turbine blades and gas tank storage modules [31, 32].

5 Conclusions

While the range of prospective applications is impressive, additional technical advancement is required to make the process cost-effective and maintain the finished fiber reinforced polymers component's high durability. To address the present challenges and make these composites the first choice for a wide variety of applications, materials research and industrial engineering must work together.

References

1. Alexopoulou E, Monti A (2013) Kenaf: a multi-purpose crop for several industrial applications, Springer, New York. https://doi.org/10.1007/978-1-4471-5067-1
2. Tucker N, Lindsey K (2002) An introduction to automotive composites, Rapra Technology Limited
3. Anastasios V, Thomas PK (2011) Fatigue of fiber-reinforced composites, Springer
4. Campilho RDSG (2016) Natural fiber composites, CRC Press, Taylor and Francis Group. Newyork. https://doi.org/10.1201/9781351050944-1
5. Syngellakis S (2015) Natural filler and fibre composites: development and characterisation, WIT Press, Boston. https://books.google.com/books?id=5f_SCQAAQBAJ&pgis=1
6. Rana S, Fangueiro R (2016) Fibrous and textile materials for composite applications. Springer, Singapore
7. Bai J (2013) Advanced fibre-reinforced polymer (FRP) composites for structural applications, 1st edn. Woodhead Publishers, Cambridge, UK
8. Susskind L, Jain R (2011) Strategies for sustainability—fiber reinforced polymer (FRP) composites for infrastructure applications, Springer. https://link.springer.com/book/https://doi.org/10.1007/978-94-007-2357-3
9. Bhatnagar A (2006) Lightweight ballistic composites: military and law-enforcement applications, Woodhead Publishers, Cambridge. https://doi.org/10.1533/9781845691554
10. Masuelli Mav (2013) Fiber reinforced technology applied polymers—the for concrete repair, InTech, Croatia
11. Müssig J (2010) Industrial applications of natural fibres: structure, properties and technical applications, Wiley. https://doi.org/10.1002/9780470660324
12. Sapuan SM, Jawaid M, Bin Yusoff N, Hoque ME (2015) Manufacturing of natural fibre reinforced polymer composites, Springer. https://doi.org/10.1007/978-3-319-07944-8_1
13. Karbhari VM (2013) Non-destructive evaluation (NDE) of polymer matrix composites. Woodhead Publishers, United Kingdom
14. Elmarakbi A (2013) Advanced composite materials for automotive applications: structural integrity and crashworthiness, Elmarakbi, Wiley. https://doi.org/10.1002/9781118535288.ch1
15. Tambyrajah D (2015) Indulge & explore natural fiber composites, Netherlands

16. Kinsey BL, Wu X (2011) Tailor welded blanks for advanced manufacturing. Woodhead Publishers, Cambridge, UK
17. Rao Y, Pochan JM (2007) Mechanics of polymer—clay nanocomposites, macromolecules, 40:290–296. https://doi.org/10.1021/ma061445w
18. Francois D, Andre P, Andre Z (2013) Mechanical behaviour of materials: fracture mechanics and damage, 1st edn. Springer, London
19. Altenbach H, Altenbach J, Kissing W (2004) Mechanics of composite structural elements, 1st edn. Springer, Berlin Heidelberg New York
20. Mark JE (2007) Physical properties of polymers handbook, 2nd ed. Springer
21. German RM (2016) Particulate composites: fundamentals and applications, 1st edn. Springer, Berlin Heidelberg New York
22. Pelleg J (2013) Mechanical properties of materials, 1st edn. Springer, Berlin Heidelberg New York
23. Francois D, Andre P, Andre Z (2012) Mechanical behaviour of materials: micro- and macroscopic constitutive behaviour, Springer
24. Lipatov YS (1995) Polymer reinforcement. Chem Tech Publishing, Canada, First
25. Salit MS (2014) Tropical natural fibre composites properties, manufacture and applications, Springer. https://doi.org/10.1007/978-981-287-155-8_1
26. Kozłowski RM (2012) Handbook of natural fibers—volume 2: processing and applications, Woodhead Publishing series in textiles, Philadelphia
27. Jinlian HU (2008) 3-D fi brous assemblies properties, applications and modelling of three-dimensional textile structures. Woodhead Publishers, USA
28. Wallenberger FT, Weston NE Natural fibers, plastics and composites, Kluwer Academic Press, p 2994
29. Fangueiro R (2011) Fibrous and composite materials for civil engineering applications, Woodhead Publishers, Cambridge. https://doi.org/10.1533/9780857095583
30. Irving PE, Soutis C (2015) Polymer composites in the aerospace industry, Woodhead Publishers, Kingston. http://www.sciencedirect.com/science/article/pii/B9780857095237000025
31. Elhajjar R, La Saponara V, Muliana A (2013) Smart composites: mechanics and design, CRC Press, Taylor and Francis Group, New York. https://doi.org/10.1201/b16257
32. Friedrich K, Breuer U (2015) Multifunctionality of polymer composites: challenges and new solutions, Woodhead Publishers. https://doi.org/10.1016/C2013-0-13006-1

Comparative Study of Long-Term Monitoring Systems and Introduction to Emerging Smart FRP Technology

Arghadeep Laskar, Sauvik Banerjee, Prashant Motwani, and Amer Iliyas Rather

Abstract This article presents feasibility and performance evaluation of three types of sensors systems, namely conventional wired sensor, wireless monitoring sensor and fibre optic sensor systems, to perform long term structural health monitoring of infrastructures. The short-term evaluation of the sensor systems showed comparable data. However, while all three systems were capable to record long-term continuous data, the fibre-optic system performed better than the conventional wired and wireless sensor technology. The article further reports the introduction of a novel smart fibre-reinforced material with an embedded fibre optic sensor for long term structural health monitoring of structures.

Keywords Fiber optic sensors · Fiber reinforced polymer · Long term structural health monitoring

1 Introduction

Structural Health Monitoring (SHM) is a technique to proactively manage structural health by diagnosing deterioration and damage at its onset and delivering an effective response to operational incidents, accidents, natural hazards, or other emergencies. A large number of studies are being conducted for the development of new sensors capable of acquisition of dynamic data [1]. Typically, sensor systems are classified under three major categories, namely, Conventional Wired Sensor (CWS) System, Wireless Monitoring Sensor (WMS) System and Fiber Optic Sensor (FOS) System.

A. Laskar (✉) · S. Banerjee · P. Motwani · A. I. Rather
Department of Civil Engineering, IIT Bombay, Bombay 400076, India
e-mail: laskar@civil.iitb.ac.in

S. Banerjee
e-mail: sauvik@civil.iitb.ac.in

P. Motwani
e-mail: pmotwani@iitb.ac.in

A. I. Rather
e-mail: 204040028@iitb.ac.in

S. B. Singh et al. (eds.), *Fiber Reinforced Polymeric Materials and Sustainable Structures*, Composites Science and Technology, https://doi.org/10.1007/978-981-19-8979-7_8

The present section provides a brief introduction, merits and demerits associated with each of the SHM systems.

1.1 CWS System

In the case of CWS Systems, different transduction mechanisms (e.g. piezo-electric, piezoresistive, capacitance) are designed to be used within a conventional wired network, and each individual sensor output voltage is transferred to a centralized data acquisition unit containing appropriate charge amplification, analog-to-digital converters, signal processing (e.g., anti-aliasing filtering), and demultiplexing. Traditional SHM often uses CWS systems but are usually expensive due to the necessity of continuous maintenance and are not always suitable for sensing remote structures. Moreover, power and wiring constraints imposed by these systems can increase the acquisition costs of such datasets, impose significant setup delays, and limit the number and location of sensors due to costs and installation logistics.

1.2 WMS System

Wireless sensors for SHM are an emerging new technology that promises to overcome many disadvantages pertinent to conventional wired sensors. WMS Systems are a possible alternative for traditional CWS systems since they enable dense in situ sensing and simplify the deployment of instrumentation. WMS acquisition is advantageous for enabling instrumentation in inaccessible places, reducing installation and maintenance costs while expanding its use in situations where large wired systems are not feasible. Batteries have historically powered WMS, and, as a result, the limiting factor in their overall lifespan has always been the battery lifetime. However, alternative solutions can be listed, such as the use of solar panels and the development of sensors that convert ambient vibrations into electromagnetic energy. Sazonov et al. [2] reported a field test in which the self-powered sensors were used on a rural highway. The sensors were shown to be self-powering even during periods of low traffic.

1.3 FOS System

FOS techniques and lasers have been under significant development in recent years and are now available in the market. They are characterized by an easy installation and data-collecting concept. These techniques often allow very delicate measuring in harsh conditions and in applications that were not possible in the past. FOS allows for

measurements that have been unpractical or too costly with the traditional sensor technology. Hundreds of measuring points along the same fibre, the distributed sensing, insensitivity to electromagnetic fields, and the fact that there is no need for protection against lightning are some of the advantages over the electrical-based counterparts [3, 4].

Table 1 provides a comprehensive comparison of CWS, WMS and FOS systems for their application in long-term SHM of infrastructures.

2 Selection of Sensor System

The selection of a CWS, WMS and FOS system requires to meet certain criteria before classifying it as a viable option for SHM applications. Many factors contribute to the selection process of a sensor node including, but not exclusively, the application, operational environment, the measurement type (strain, vibration, temperature, ultrasonic, etc.), sensor size and range, power consumption, robustness, and the lifetime of the sensing element [5].

In the CWS system, each node must contain several components for its efficient and reliable usage. The various components required include bus cables, sensing unit, signal processing unit, and ethernet connection with a Desktop/Laptop that is continuously powered. Power management/source system for the CWS system is mandatory for its reliable and efficient operation. With the presence of an energy source, powering the sensor will not be an issue despite the level of energy needed and the operation time. However, in the absence of an energy source, particularly when monitoring structures in remote areas, an alternative energy source must exist, or an alternate system such as WMS should be selected.

In WMS system, internal batteries are used to supply charge to the piezo-electric sensors, keeping in mind the limited lifetime that the batteries have before needing to be replaced. The energy consumption of the node, when an internal battery is used, affects the system outputs, such as the duration and frequency of data collection. A microcontroller can regulate the sleep and wake-up time for the sensor during or when an incident happens, such as traffic or crowd loading on a bridge, wind load on a high-rise building, or a bird strike on an aircraft nose. The WMS system relies on electrical and magnetic fields to convert the charge into measurements. It may not be effective in a highly electromagnetic environment, like metro lines or electric towers. WMS require the identification of network for data uploading and the positioning of sensors to cause minimum signal interception.

Thus, in cases where the sensors are to be multiplexed or placed close to each other, or the sensors are to be installed in a highly corrosive or electromagnetic environment, FOS system is preferred. FOS further provides the ability to perform direct embedment operations into construction materials to create ‘smart materials’ [3, 6].

Table 1 Comparison of CWS, WMS and FOS systems for long term SHM

Param	CWS	WMS	FOS
Data transmission	In CWS, a complex network of multiple sensors is brought to a single node/gateway. Thus, the sensors require continuous connection to the loggers, creating a complex wired network. The gateway is generally hard-powered and transmits data through ethernet or using IEEE communication	WMS sensors provide sensor-to-screen solutions with built-in transmitters within the sensor itself and can transmit data through radio frequency	In terms of data transmission, FOS is similar to the CWS system. The sensors are connected to a high-speed laser-based interrogator
Resistance to corrosion	In case of CWS and WMS system, the instrumentation is typically manufactured using metal wires and are susceptible to corrosion		FOS technology is non-metallic in nature and is not susceptible to corrosion
EM waves susceptibility	In case CWS, if the entire system is connected using bus cables/wires, the chances of EM waves susceptibility is limited	WMS technology transmits data using an unlicensed frequency band of 2.4 GHz. Thus, presence of high voltage electrical lines may cause interference issues	FOS technology is based on light-waves Thus, the presence of electromagnetic radiations does not contribute to signal loss
Multiplexing capability	In case of both CWS and WMS, each parameter to be measured (strain, acceleration, etc.) require independent communication to gateway whether using bus cables (CWS) or wireless (WMS). Thus, in CWS, the system requires a complex cable network and increases the chances of short-circuiting, while WMS may have interference issues		Multiple FOS can be multiplexed into a single array to record strain at several locations using a single channel of the optical interrogator
Embedding capability	CWS and WMS cannot be utilized to create smart materials since the morphological structure of such sensors are too big to be embedded		Unpackaged FOS can be embedded into construction materials to create smart materials to serve the dual purpose of taking load and measuring load

(continued)

Table 1 (continued)

Param	CWS	WMS	FOS
Electrical input	Most loggers in the CWS technology are hard-powered using an external DC supply	WMS have a built-in lithium-ion battery. The batteries can be replaced and the life of WMS can be extended for another 10 years	FOS systems utilizes laser interrogators. Thus similar to CWS, FOS systems also require hard-power
Installation	The sensors that operate on CWS technology require armoured jelly cables, nodes, and junction boxes. Thus, the installation is time-consuming and extremely difficult	WMS is based on self-adhesive or bracket mounts. Thus, the WMS can be mounted on a surface in a record time of 1–2 min	Installation of FOS system is comparatively faster than CWS but slower than WMS
Physical and environmental protection	Generally, CWS system comes with IP65 rating; however the bus cables connecting the gateway to sensors are not IP65 rating. Thus, the system becomes redundant after a few years	Typically, WMS has ingress protection with IP65 and above rating and are protected against rain, snow, and UV radiation	Similar to CWS, the sensors and gateway in the FOS system are IP65 and above. Although rodent-proof high-quality FOS cables are available to connect gateway and sensors, they are always at a greater risk of damage

3 Selection of Type of Sensor

Designing of the sensor network is crucial to select the type and number of sensors. The type of sensors highly depends on the application and the structure to be monitored. For instance, when using an accelerometer to measure the level of vibration, the interest will be more on understanding the global behaviour of the structure, i.e., the shift in the modal frequencies that may be used to identify the presence of damage. Vibration-based methods have been implemented already on many structures, mainly civil infrastructure, albeit these methods are not effective in providing a qualitative assessment about the health state of the structure. On the other hand, when strain sensors or ultrasonic transducers are considered, the focus is more on the local assessment of any damage that may be present within the structure. These techniques can detect small surface and embedded defects such as corrosion, fatigue cracking, impact damage, etc.

4 Research Significance

The present study reports a pilot investigation conducted to examine the capabilities and challenges of three different sensor systems but not mutually exclusive approaches to monitor a column specimen.

In this study, the intended functionality of different systems has been evaluated on its ability to identify potential changes in the structure and to provide decision-making support. Furthermore, to advance the research in the field of FOS system, a novel technique of potential embedment of Fibre Bragg Gating (FBG) based fibre optic strain sensors into the fibre-reinforced polymer (FRP) has been briefly discussed.

5 Specimen Identification

The instrumented specimen was essentially a part of another study involving seismic evaluation of a periodic column under controlled dynamic loading. The column specimen was fabricated with alternate layers of rubber and concrete bonded together using engineering adhesives. Long term data analysis has been performed on the column specimen under intermittent dynamic loads. Figure 1 shows the instrumented column specimen with various sensors installed at pre-decided locations (as discussed in Sects. 5.1 through 5.3) and the associated logging system.

Fig. 1 Instrumented column specimen and associated data logging systems

5.1 Vibration Sensor

A single vibration sensor (single or multi-axis accelerometer) in some cases may provide the information needed, for instance, in the case of determining the global modal frequencies and damping on a bridge structure. However, more sensors are needed to determine the mode shapes. The main requirement for a successful application of vibration-based methods is to identify the range of the targeted natural frequencies and mode shapes and overcome spatial aliasing [7]. In the present study, three mutually exclusive vibration monitoring sensors have been installed at the top location of the specimen, as shown in Fig. 2.

First, a spring-mass damping based CWS has been installed and connected to CF2000 FFT analyzer through bus cables. Second, a WMS has been installed next to the CWS that communicates to a wireless gateway using an unlicensed band of 2.4 Ghz. Finally, a Fabry–Perot technology-based FOS has been attached at the

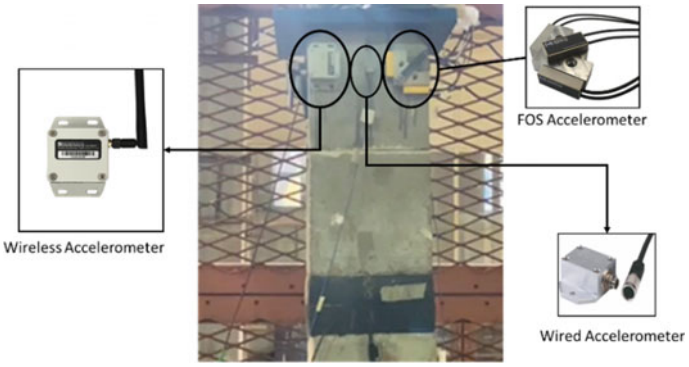

Fig. 2 Accelerometers installed on specimen

Fig. 3 Strain sensors installed on specimen

same location and connected to an optical interrogator using rodent-proof fibre optic cables.

5.2 Strain Sensor

Currently, the sensors used for SHM of civil engineering infrastructures mainly include vibrating wire sensors, resistance strain gauges and FBG sensors [8]. The measurement accuracy of the vibrating wire sensor is relatively low, and it is easily affected by the magnetic field and surrounding environment. The resistance strain gauge is characterized by high measurement accuracy, a wide measuring range and a simple structure. However, it has a distinct non-linearity when subjected to a large strain and weak signal. These shortcomings severely limit its application, especially in long-distance monitoring and harsh environments. FBG sensing technology has developed rapidly in recent years. It is characterized by high measurement precision, immunity to electromagnetic interference, stability of long-term sensing and so on. Therefore, the FBG sensing technology favours the long-term SHM.

In the present study, two commercially available FBG based strain sensors have been installed at the centre (front and back) of the column specimen between the two concrete cubes separated by a rubber layer. Additionally, a linear-potentiometer (LP) representing the CWS system has been attached next to the front FBG sensor to perform a comparative analysis of the recorded strain data.

5.3 Temperature Sensor

Long term continuous temperature measurement is typically used for continuous detection of leakage at pipelines, vessels and mass concrete structures. In the present study, an FBG based temperature sensor has been attached to the front surface of the column specimen. Additionally, a wireless resistance temperature detector (RTD) sensor has been attached at the back surface of the specimen as shown in Fig. 4.

6 Loading Protocol

The specimen has been mounted on a hydro-controlled uniaxial shake table. Two different types of loading protocol have been selected to investigate the sensor systems mounted on the specimen, namely, free vibration and forced controlled vibration**.**

In case of free vibration, the specimen has been manually displaced by providing a gentle push at the top of the specimen. The specimen has been allowed to vibrate

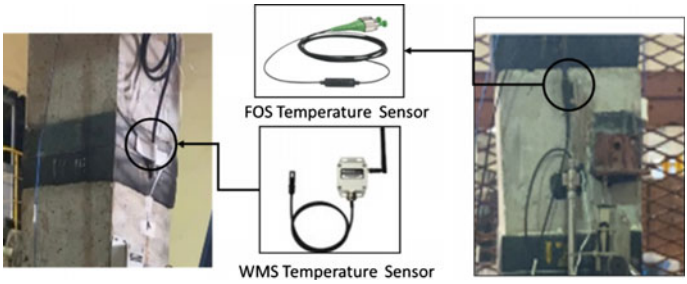

Fig. 4 Temperature sensors installed on specimen

freely under the applied load. The procedure of free vibration has been repeated four times a day in intervals of 2 h from 1100 and 1700 h.

The metamaterial-based concrete column has been designed to impede frequencies over a bandgap ranging between 5 and 10 Hz. Thus, the forced vibration tests have been conducted at a nominal frequency of 2.5 Hz and 0.1 g. In the case of the forced vibration test, the controlled load has been applied two times in a day from 1100 and 1700 h. However, in the present study, the data recorded only during the free vibration investigation has been reported.

7 Results and Discussion

The data from individual sensors and systems have been continuously monitored. However, the CWS system has been switched on only when the load has been applied. The present section briefly discusses the results obtained from the individual systems.

7.1 Free Vibration Long-Term Acceleration Data

During the free vibration investigation, the specimen has been first displaced manually along one of the transverse directions (Y-direction) and allowed to vibrate freely. Subsequently, after the specimen stabilized, it has been displaced along the orthogonal direction (X-direction) and allowed to vibrate freely. During the free vibration test, acceleration and strain information from the sensors have been automatically recorded in the respective logging systems.

Figure 5 reports the acceleration v/s time history recorded by FOS, WMS and CWS accelerometer. It can be observed from Fig. 5a, b that both FOS and CWS accelerometers appropriately recorded the acceleration response of the system during the free vibration investigation. However, the acceleration response recorded by WMS accelerometer (Fig. 5c) during the free vibration investigation has been observed to be negligible (varying between 993 and 994 μg). This indicates that the WMS

system failed to record the acceleration values during the free vibration test. This is essentially due to the fact that the WMS accelerometers are micro-electromechanical systems (MEMS) based accelerometers. These accelerometers get activated only when a particular threshold value is exceeded and is maintained for a particular duration. The concept of MEMS accelerometers is designed to be implemented in bridges so that minor vibrations due to vehicular movements are unaccounted and only meaningful data is stored in the server.

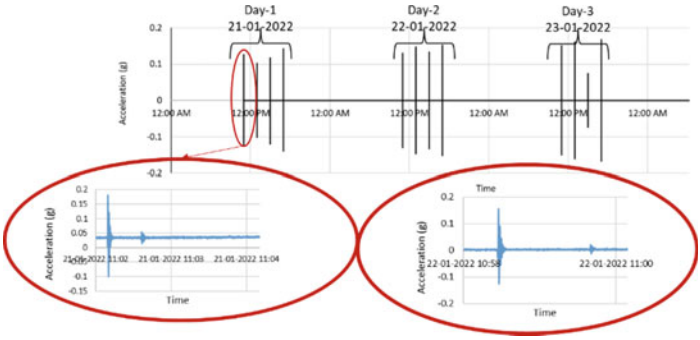

(a) Acceleration vs Time History from FOS System

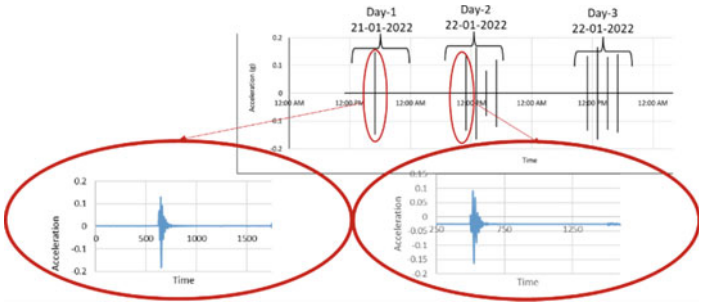

(b) Acceleration vs Time History from CWS System

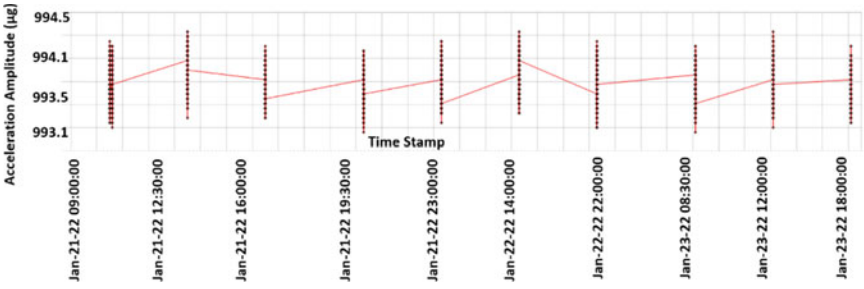

(c) Acceleration vs Time History from WMS System

Fig. 5 Acceleration versus time history from individual sensor systems

The acceleration data from the sensor systems has been post-processed to estimate the time period of the instrumented column (Table 2). The typical free vibration period for the column specimen has been estimated using the data obtained from the FOS system to be approximately 0.90 s along both X and Y directions.

Table 2 reports the peak 'g' value and 'time-period' obtained from the CWS accelerometers connected to the FFT analyzer. The FFT has been turned on only during the application of free vibration. The readings during first three-displacement cycles could not be recorded by the CWS accelerometers due to an instrument error. It can be observed from Table 2 that both FOS and CWS accelerometers reported almost identical values of time-period indicating the robustness of the two systems in sensing short-term vibrations.

7.2 Free Vibration Long Term Strain Data

Strain measurements have been performed in the present investigation by using FOS and CWS systems. FOS strain measurement system has been selected as a complementary solution to the resistance strain gauge, vibrating wire strain gauges and accelerometers. The combination of different types of technology, especially the combination of strain and acceleration measurement results, can facilitate the measurement of long-term deflection of bridges at inaccessible locations, allowing accurate analysis of the dynamic behaviour. The peaks in Fig. 6 shows the strain information from FOS and CWS system during each manual displacement. The front and back FOS strain sensor readings have been observed to be approximately equal and opposite in nature. The strain readings gradually reduced to zero as the system came to rest.

Table 3 compares FOS strain measurements with the peak strain values recorded by the LP connected through CWS technology. The displacement from LP has been utilized to estimate the peak strain readings. In most cases, the maximum front strain readings from the CWS system have been observed to be comparable to the maximum front strain readings from FOS.

7.3 Free Vibration Long Term Temperature Data

The temperature measurement plays a crucial role in structures constructed in extreme environments with a high-temperature variation. Further, massive concreting generates a high-temperature gradient that may affect the gain of concrete strength. Thus, it is paramount to monitor temperature of structural members and systems continuously for taking decisive actions.

Figure 7 shows the 24-h temperature variation recorded by FOS and WMS systems. The noisy data shown in Fig. 7a is due to the higher sampling rate which has

Table 2 Peak acceleration and time period from FOS and CWS systems

Day	Date	Time	Dir	Acceleration							
				FOS				CWS			
				X		Y		X		Y	
				Peak (g)	Time per. (s)	Peak accl. (g)	Time Per. (s)	Peak accl. (g)	Time per. (s)	Peak accl. (g)	Time per. (s)
Day 1	21-01-2022	11:00 AM	Y	0.01	0.93	0.18	0.87	Instrument error			
			X	0.20	0.93	0.05	0.90				
		01:00 PM	Y	0.20	0.87	0.30	0.84				
			X	0.29	0.90	0.20	0.80				
		03:00 PM	Y	0.34	0.87	0.45	0.83				
			X	0.43	0.90	0.33	0.90				
		05:00 PM	Y	0.39	0.95	0.52	0.87	0.03	0.85	0.18	0.85
			X	0.48	0.93	0.38	0.80	0.13	0.88	0.03	0.93
Day 2	22-01-2022	11:00 AM	Y	0.03	0.90	0.15	0.87	0.03	0.83	0.16	0.85
			X	0.11	0.87	0.02	0.90	0.16	0.85	0.03	0.87
		01:00 PM	Y	0.11	0.90	0.27	0.87	0.03	0.83	0.19	0.90
			X	0.23	0.90	0.13	0.83	0.19	0.92	0.02	0.85
		03:00 PM	Y	0.23	0.90	0.38	0.87	0.03	0.90	0.18	0.88
			X	0.33	0.90	0.25	0.90	0.14	0.92	0.10	0.90
		05:00 PM	Y	0.29	0.87	0.44	0.87	0.03	0.85	0.16	0.87
			X	0.37	0.93	0.29	0.83	0.13	0.88	0.04	0.92
Day 3	23-01-2022	11:00 AM	Y	0.09	0.90	0.16	0.87	0.03	0.83	0.16	0.85
			X	0.11	0.87	0.01	0.87	0.16	0.92	0.03	0.87

(continued)

Table 2 (continued)

Day	Date	Time	Dir	Acceleration							
				FOS				CWS			
				X		Y		X		Y	
				Peak (g)	Time per. (s)	Peak accl. (g)	Time Per. (s)	Peak accl. (g)	Time per. (s)	Peak accl. (g)	Time per. (s)
		01:00 PM	Y	0.08	0.90	0.24	0.90	0.03	0.83	0.19	0.90
			X	0.19	0.90	0.08	0.90	0.18	0.90	0.02	0.85
		03:00 PM	Y	0.18	0.90	0.23	0.90	0.02	0.87	0.18	0.88
			X	0.22	0.90	0.16	0.90	0.15	0.92	0.05	0.90
		05:00 PM	Y	0.14	0.90	0.30	0.90	0.03	0.90	0.16	0.90
			X	0.25	0.90	0.13	0.90	0.15	0.90	0.02	0.87

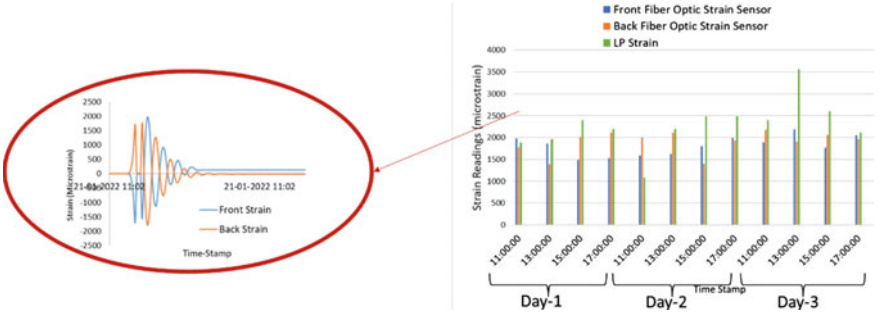

Fig. 6 Strain versus time history from FOS and CWS system

been selected to record the ambient temperature variations in the present investigation. Such high sampling rate is necessary to record the acceleration response from the FOS which is connected to the same interrogator through the same algorithm. The mean temperature variation recorded by both FOS and WMS on the column specimen has been observed to vary between 25 and 29 °C.

8 Introduction to Smart FRP

It has been observed in the present study that the FOS system can offer many potential advantages over the CWS and the WMS systems for SHM applications. The examination and comparison of the characteristics of the FOS system to conventional techniques reveal the dynamics of FOS systems in predicting minute disturbances in the column specimen. However, the current cost of access to customized FOS monitoring systems and services is exceptionally high. Hence, it is difficult to consider and include advanced SHM measures using the FOS system at this cost.

The primary motivation of using FOS in SHM is to benefit the future design of new buildings and protect the overall economics of building maintenance, as a consequence of better understanding of the assessment of existing buildings along with their adaptation and restoration protocols. With practising engineers, industry, and academia working in tandem, it is necessary to reduce the cost of the FOS system so that greater benefits can be accrued to society. While a commercially packaged FBG sensor consists of stainless-steel packing, a smart FRP packaged FBG sensor would cost significantly lower. This is due to the fact that the cost of FRP is substantially lower than the cost of stainless steel itself.

A novel manufacturing technology for the embedment of the FOS in pultruded FRP bars has been developed in an ongoing investigation in order to utilize them as the smart sensing element in concrete and steel structures. The finished product (referred to as ‘smart FRP bar’) has been manufactured by designing a FOS layout to be embedded into the FRP bar and subsequently modifying the open-resin pultrusion line that allows the sensor embedment within the composite bar and the subsequent

Table 3 Peak strain from FOS and CWS systems

Day	Date	Time	Dir	Strain					
				FOS				CWS	
				Front strain (με)		Back strain (με)			
				Max+	Max−	Max+	Max−	Max disp. (mm)	Max + Strain (με)
Day 1	21-01-2022	11:00 AM	Y	1980	1699	1776	1786	7.52	1880
			X	1710	2129	79	252	8.48	2120
		01:00 PM	Y	1864	1278	1387	1892	7.84	1960
			X	880	493	118	113	1.6	400
		03:00 PM	Y	1490	1932	2014	1407	9.6	2400
			X	1079	1316	162	170	1.12	280
		05:00 PM	Y	1529	1951	2106	1625	8.8	2200
			X	1267	782	81	0	1.28	320
Day 2	22-01-2022	11:00 AM	Y	1582	1976	2003	1739	4.32	1080
			X	742	608	124	103	1.6	400
		01:00 PM	Y	1629	2050	2107	1756	8.8	2200
			X	826	714	194	260	1.28	320
		03:00 PM	Y	1808	1488	1404	1689	9.92	2480
			X	1210	1854	462	333	0.64	160
		05:00 PM	Y	1986	1909	1931	1777	9.92	2480
			X	724	526	377	247	0.64	160
Day 3	23-01-2022	11:00 AM	Y	1888	1992	2181	1246	9.6	2400
			X	1050	934	0	400	1.28	320
		01:00 PM	Y	2190	2029	1903	1355	14.24	3560
			X	1082	381	309	381	0.64	160
		03:00 PM	Y	1768	2074	2064	1647	10.4	2600
			X	1368	1488	423	565	2.72	680
		05:00 PM	Y	2046	1841	1961	1405	8.48	2120
			X	1039	447	133	226	0.96	240

recovery of the associated fibre-optic leads. The present embedment technique has been validated by embedding a single optical fibre among 160,000 continuous reinforcing fibres impregnated with epoxy resin. The prototype sample has been subsequently tested using a FOS fault detector and by-passing a laser light through the FC/APC adaptor (as shown in Fig. 8).

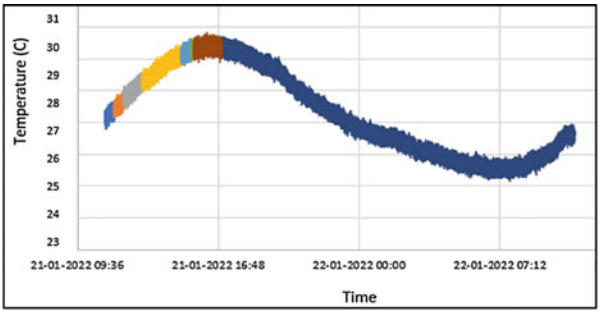

(a) FOS System

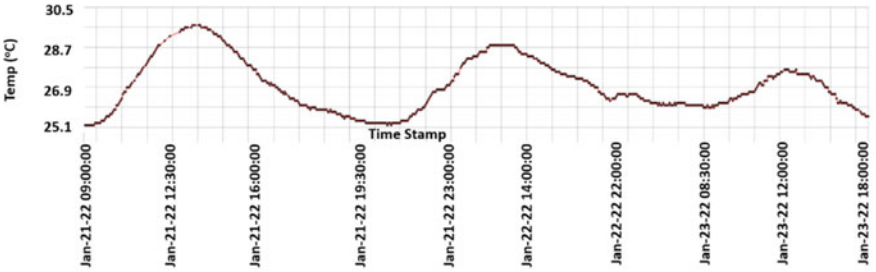

(b) WMS System

Fig. 7 Temperature versus time history

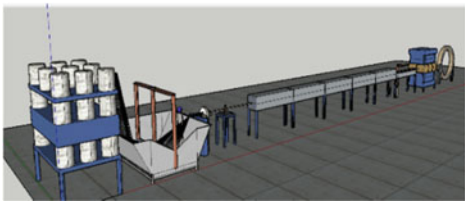

(a) Modified Pultrusion Line

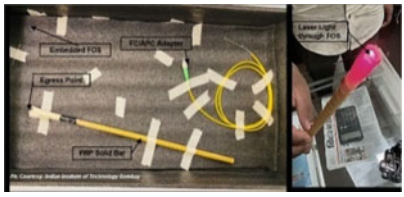

(b) Finished Smart FRP

Fig. 8 Smart FRP bar prototype

9 Summary and Conclusions

Preventive intervention using SHM is always efficient, less disruptive and economical than undergoing structural intervention by retrofitting. This is certainly true for the maintenance of ageing civil infrastructure where repair costs can become astronomical. With the increasing volumes and quality of data becoming available, intelligent monitoring of ageing assets is feasible. Insights from this data can be used to better

understand asset health and detect early warning signs so that proactive maintenance can be undertaken—saving time, money and improving worker and public safety.

The pilot investigation reported in this paper contributed towards testing three independent mutually exclusive sensor technologies, namely CWS, WMS and FOS to perform long-term continuous monitoring of infrastructure systems. The measured data can be used as an input for an in-time monitoring system which can be used for operational functions as well as for the management of the bridge maintenance, by complementing and targeting the information gathered with routine inspections.

The study concluded that although the FOS system showed satisfactory results for acquiring real-time data without any discrepancies, the commercial aspects of FOS system limit its feasibility in SHM applications. Thus, a detailed investigation has been undertaken to develop an FRP packaged FBG sensor that is cost-effective and technologically advanced.

Acknowledgements The authors would like to acknowledge Mr. Basava Choudhary from Medulla Soft Technologies Pvt Ltd for providing the fiber optic system and Prof. Su Taylor from Queens University Belfast for allowing the use of DataTaker for the pilot study. We would also like to acknowledge support from Mr. Neeraj Bubane and Quad Composite Pvt Ltd for allowing factory trials of embedment of FOS into FRP bars.

References

1. Mustapha S, Lu Y, Ng C-T, Malinowski P (2021) Sensor networks for structures health monitoring: placement, implementations, and challenges—a review. Vibration 4:551–584. https://doi.org/10.3390/vibration4030033
2. Sazonov E, Li H, Curry D, Pillay P (2009) Self-powered sensors for monitoring of highway bridges 9:1422–1429
3. R.M. Measures (2001) Structural monitoring with fibre optic technology, Academic Press
4. Bremer K, Wollweber M, Weigand F, Rahlves M, Kuhne M, Helbig R, Roth B (2016) Fibre optic sensors for the structural health monitoring of building structures. Proc Technol 26:524–529. https://doi.org/10.1016/j.protcy.2016.08.065
5. Ou J, Li H (2009) Structural health monitoring in the Mainland of China: review and future trends. In: Structure healing monitoring 2009 from system integration to autonomous system—proceeding 7th international working structuring healing and monitoring IWSHM 2009, vol 1, pp 29–41
6. Tang Y, Wang Z, Song M (2016) Self-sensing and strengthening effects of reinforced concrete structures with near-surfaced mounted smart basalt fibre-reinforced polymer bars. Adv Mech Eng 8:1–19. https://doi.org/10.1177/1687814016673499
7. Ostachowicz W, Soman R, Malinowski P (2019) Optimization of sensor placement for structural health monitoring: a review. Struct Heal Monit 18:963–988. https://doi.org/10.1177/1475921719825601
8. Torres B, Payá-Zaforteza Ignacio I, Calderón PA, Adam JM (2011) Analysis of the strain transfer in a new FBG sensor for structural health monitoring. Eng Struct 33:539–548. https://doi.org/10.1016/j.engstruct.2010.11.012

Experimental Investigation on Flexural Behaviour of RC Beams Strengthened with Various FRP Composite Configurations

Balla Taraka Malleswara Rao, Rahul Reddy Morthala, and S. Suriya Prakash

Abstract Strengthening the reinforced concrete (RC) beams in buildings and bridges is often needed to improve flexural performance. The various reasons for strengthening are (i) defective design or construction, (ii) deterioration due to the extreme weather conditions, (iii) to carry the additional storage or vehicular loading requirements, (iv) updating to the new code requirements, and (v) seismic strengthening and retrofitting. The fibre reinforced polymer (FRP) strengthening is proven to be very practical and advantageous compared to conventional methods like concrete jacketing and steel jacketing. The available literature mainly focuses on the flexural strengthening of RC beams with external bonding (EB) of pultruded laminates and is limited to laboratory scale specimens. Understanding the flexural behaviour of large-scale specimens consisting of various strengthening configurations is essential. In this study, an experimental investigation is carried out by testing RC beams of 300 × 300 × 3500 mm size. The test matrix consists of RC control beam; three other beams strengthened with CFRP precured laminates (EB-L), CFRP fabric (EB-F) and hybrid FRP strengthening (HYB). The hybrid FRP strengthening is the combination of CFRP pre-cured laminates at the soffit and EB CFRP fabric in the overall length of the beam. All the FRP strengthened specimens had improved flexural strength. However, HYB FRP strengthening was found to be very effective in enhancing flexural strength and ductility compared to other strengthening techniques. In HYB strengthening, the EB confinement provided by the CFRP fabric improves the compression strength of the concrete at the compression zone and prevents the debonding of CFRP laminates at the tension zone.

Keywords RC beam · CFRP laminates · CFRP fabric · HYB FRP strengthening · Flexural loading

B. T. M. Rao · R. R. Morthala · S. Suriya Prakash (✉)
Department of Civil Engineering, Indian Institute of Technology, Hyderabad, India
e-mail: suriyap@ce.iith.ac.in

B. T. M. Rao
e-mail: ce18resch11004@iith.ac.in

R. R. Morthala
e-mail: ce22resch01007@iith.ac.in

S. B. Singh et al. (eds.), *Fiber Reinforced Polymeric Materials and Sustainable Structures*, Composites Science and Technology, https://doi.org/10.1007/978-981-19-8979-7_9

1 Introduction

The strengthening of reinforced concrete (RC) members in the buildings and bridges are often required in various situations like (i) defective design or workmanship during the construction, (ii) structural deterioration due to the extreme weathering actions like carbonation, corrosion, (iii) to carried out the additional vehicular loads, (iv) updating the structure in accordance with new design standards, (v) seismic strengthening or retrofitting and (vi) maintaining the structural integrity [1–3]. The fiber reinforced polymer (FRP) strengthening has been widely adopted in the world over the last few decades [4–7]. The FRP strengthening is very efficacious when compared to the conventional techniques of steel [8, 9] and concrete jacketing [10]. However, choosing the correct strengthening configuration is very important for a particular type of loading. The external bonding (EB) technique of FRP wrapping in the transverse direction of concrete elements improves the performance of the compression members under axial loading [11–14]. However, the FRP wrapping is not effective in resisting the flexural loads. The various types of EB using FRP laminates [15–17] and the near-surface mounting (NSM) strengthening [18–20] in tension regions of RC beams are very effective in resisting the flexural loading. The de-bonding failure of the EB technique reduces the efficiency of the system [21, 22]. The hybrid combination (HYB) of CFRP laminates and FRP wrapping is a very effective solution for improving flexural enhancement in terms of strength and ductility.

In this experimental investigation, four full-scale specimens of 300 × 300 × 3500 mm size were cast, strengthened and tested. The test matrix consists of control RC beam, strengthened using CFRP laminates (EB-L), CFRP fabric (EB-F) and hybrid FRP strengthening (HYB). All the FRP strengthened specimens are found to be effectively improved the flexural strength. However, HYB specimens are found to be very effective in improving flexural strength and ductility compared to other strengthening systems. In HYB strengthening, the EB confinement provided by the CFRP fabric improves the concrete compression strength at the compression zone and prevents the delamination of CFRP laminates at the tension zone.

1.1 Motivation and Research Objectives

Existing research work has mainly focused on the flexural behaviour of laboratory-scale specimens [2, 23]. Also, the existing research work focused on RC beams strengthened using EB with FRP laminates [15–17] and NSM strengthening [18–20]. The de-bonding effect in the EB strengthened specimens will reduce the efficiency of the strengthening system. The prevention of the de-bonding effect and improving the efficiency of the strengthening system can be achieved using the HYB FRP technique. However, very limited research work in the past has focused on understanding the different FRP strengthening configurations and HYB FRP systems

on performance improvement [2, 23]. In this study, the flexural performance of the various FRP configurations on the RC specimens is experimentally investigated. The outcomes of the investigation are useful for understanding the flexural behaviour of FRP strengthened specimens.

2 Experimental Program

The experimental programme involves the casting, strengthening and testing of four RC beams of control and FFR strengthened specimens. The specifications of the control RC and FRP strengthened beams are presented in Table 1. The cross-sectional size of specimens is 300 × 300 mm with a total length of 3500 mm. The text matrix consists of a control RC beam, strengthened using CFRP laminates (EB-L), CFRP fabric (EB-F) and hybrid FRP strengthening (HYB). All the beam specimens are longitudinally reinforced with 8 bars of 12 mm diameter and transverse reinforced with 8 mm diameter stirrups at 150 mm c/c. The cross-section and longitudinal sectional details of the test matrix are presented in Fig. 1.

All the RC beams were cast, strengthened and tested at the structural lab at IIT Hyderabad. The mix design of the concrete is prepared to get the cylinder strength of 25 MPa in accordance with IS 10262 [24]. After 28 days of casting, the average cylinder strength of the concrete is found to be 28.4 MPa. The steel reinforcement of Fe 500 grade was used. CFRP fabric of 400 GSM was used for the strengthening of the EB-F specimen and wrapping of the HYB specimen. The pre-cured CFRP laminates of 50 × 1.74 mm were used for strengthening of EB-L and HYB specimens. The material properties of the steel rebar and FRP materials are presented in Table 2.

Table 1 Specification of the test matrix

S. No.	Specimen ID	Size of the specimen	Details of strengthening
1	RC	300 × 300 × 3500 mm	Control RC column without any strengthening
2	EB-L		EB with three CFRP laminates of size 50 × 1.75 mm at the soffit of the beam
3	EB-F		EB with two layers of 400 GSM CFRP fabric at the soffit of the beam
4	HYB		EB with three CFRP laminates of size 50 × 1.75 mm at the soffit of the beam + 2 layers of CFRP wrapping

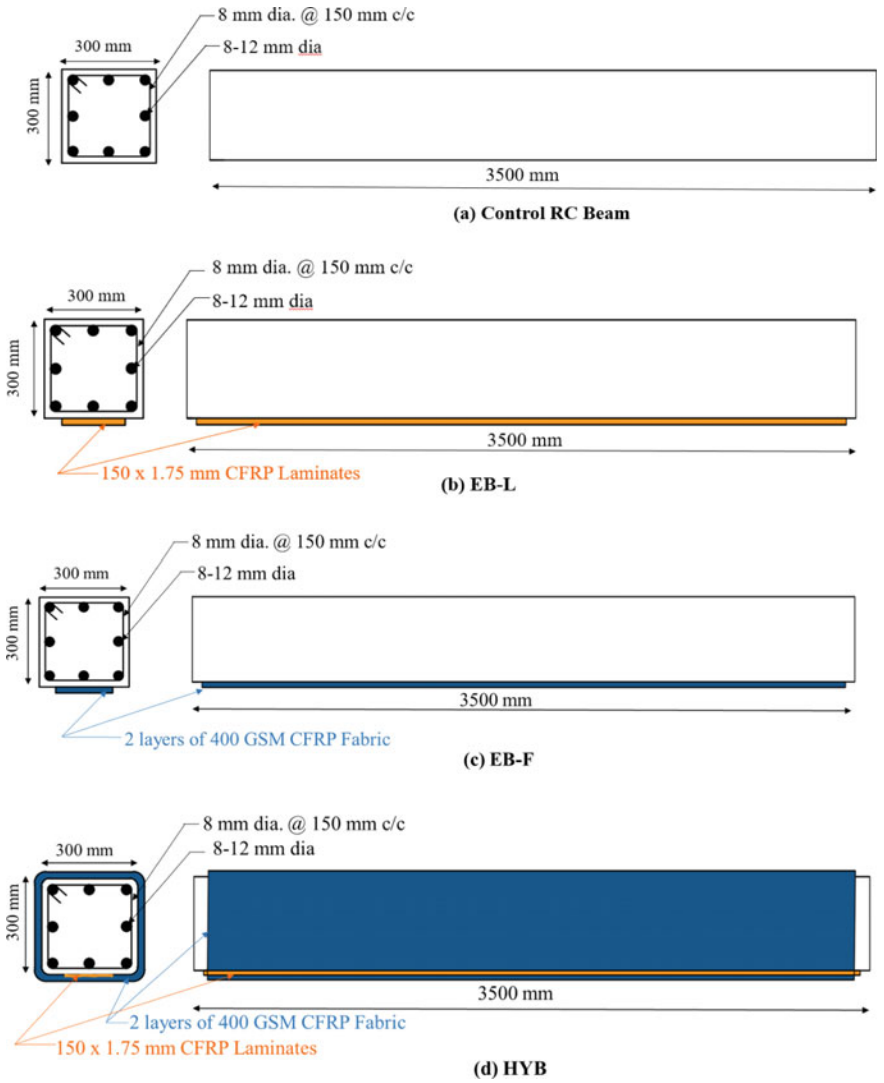

Fig. 1 Cross-sectional details of FRP strengthened beams

Table 2 Material properties

Material/properties	Steel rebar	CFRP laminate	CFRP fabric
Modulus of elasticity (GPa)	200	165	99.8
Tensile strength (MPa)	500	165	985

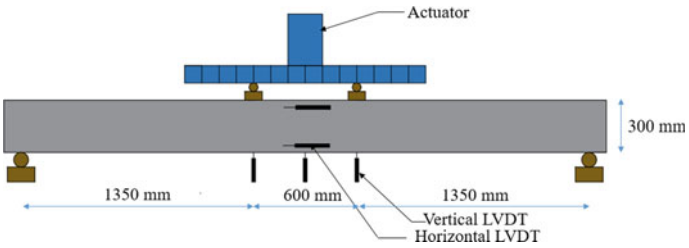

Fig. 2 Test setup for RC and FRP strengthened beams under flexural loading

2.1 Experimental Setup and Instrumentation

A 1000 kN capacity hydraulic actuator of MTS systems was used for testing the control RC and FRP strengthened beams. The beam specimens were tested under the displacement-controlled mode at a 0.03 mm/s loading rate. The beam specimens were tested under the four-point bending loading setup. The experimental test setup and the instrumentation are shown in Fig. 2. Linear variable differential transducers (LVDTs) were used to measure the displacements during the testing. The strain gauges are attached to the steel rebar and FRP materials to monitor the strain data during the test continuously. The LVDTs and strain gauges are connected to the data acquisition systems (DAQ) for continuous data monitoring.

3 Results and Discussion

The comparison of the load-deformation response of RC beam and strengthened with various FRP configurations are shown in Fig. 3. The comparison of the control and FRP strengthened beams results is shown in Table 3. The load value presented in Fig. 3 is the load value shown in the actuator, and deformation is measured using LVDT connected at the middle of the beam specimens. All the FRP strengthened configurations effectively improved the flexural capacity and stiffness. Improvement in the stiffness and strength is observed for the FRP strengthened beams using CFRP fabric (EB-F) compared to the EB-L and HYB strengthened RC beams. The strength improvement of 67.8 and 74.5% are observed for the EB-F and EB-L specimens compared to the control RC beam. A more brittle failure mode is observed for the FRP strengthened specimens and resulted in lesser ductility. The hybrid FRP strengthening led to the highest strength and ductility improvement when compared to both the EB-L and EB-F strengthened specimens. A strength enhancement of 97.3% is observed for the hybrid strengthened specimen compared to the control RC beam.

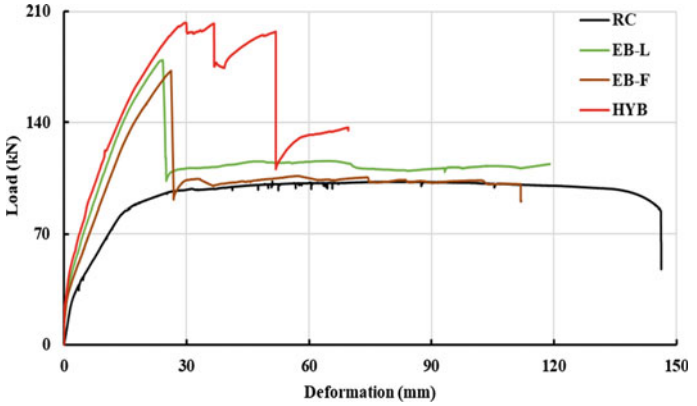

Fig. 3 Comparison of load-deformation response of control beam and FRP strengthened specimens with various configurations

Table 3 Summary of test results

S. No.	Specimen ID	Peak load (kN)	% increase
1	RC	102.8	–
2	EB-L	179.4	74.5
3	EB-F	172.5	67.8
4	HYB	202.9	97.3

4 Conclusions

RC beams strengthened with various FRP configurations were tested under flexural loading using a four-point bending test setup. The following conclusions can be made based on the results presented in this study:

- The flexural strengthening of RC beams using FRP is an effective solution for improving strength and stiffness.
- Displacement ductility reduced to FRP strengthening. FRP strengthened specimens failed in a brittle compared to the control RC beams.
- Hybrid FRP strengthening significantly enhances the strength and ductility compared to the externally bonded FRP (both fabric and laminates) strengthened systems.

Acknowledgements The authors would like to thank HEXACURE, a division of the BHOR chemicals and plastics Pvt. Ltd. for sponsoring the FRP materials used in the research work.

References

1. Hadi MNS (2006) Behaviour of FRP wrapped normal strength concrete columns unde eccentric loading. Compos Struct 72:503–511. https://doi.org/10.1016/j.compstruct.2005.01.018
2. Chellapandian M, Prakash SS, Sharma A (2019) Experimental and fi nite element studies on the flexural behavior of reinforced concrete elements strengthened with hybrid FRP technique. Compos Struct 208:466–478. https://doi.org/10.1016/j.compstruct.2018.10.028
3. Malleswara Rao BT, Prakash SS (2021) Shape effects on the behavior of hybrid FRP-strengthened rectangular RC columns under axial compression. J Compos Constr 25:04021042. https://doi.org/10.1061/(asce)cc.1943-5614.0001152
4. Chellapandian M, Prakash SS (2019) Axial compression-flexure interaction behavior of hybrid fiber-reinforced polymer-strengthened columns. ACI Struct J 116:125–38. https://doi.org/10.14359/51710877
5. Kadhim AMH, Numan HA, Özakça M (2019) Flexural strengthening and rehabilitation of reinforced concrete beam using BFRP composites: finite element approach. Adv Civ Eng. https://doi.org/10.1155/2019/4981750
6. Tobbi H, Farghaly AS, Benmokrane B (2012) Concrete columns reinforced longitudinally and transversally with glass fiber-reinforced polymer bars. ACI Struct J 109:551–558. https://doi.org/10.14359/51683874
7. Fitzwilliam J, Bisby LA (2010) Slenderness effects on circular CFRP confined reinforced concrete columns. J Compos Constr 14:280–288. https://doi.org/10.1061/(asce)cc.1943-5614.0000073
8. Parvin A, Brighton D (2014) FRP composites strengthening of concrete columns under various loading conditions. Polymers (Basel) 6:1040–1056. https://doi.org/10.3390/polym6041040
9. Chai YH, Priestley MJN, Seible F (2006) Analytical model for steel-jacketed RC circular bridge columns. J Struct Eng 120:2358–2376. https://doi.org/10.1061/(asce)0733-9445(1994)120:8(2358)
10. Júlio ES, Branco F, Silva VD (2003) Structural rehabilitation of columns with reinforced concrete jacketing. Prog Struct Eng Mater 5:29–37. https://doi.org/10.1002/pse.140
11. Chellapandian M, Prakash SS, Sharma A, Suriya Prakash S, Sharma A, Prakash SS et al (2017) Strength and ductility of innovative hybrid NSM reinforced and FRP confined short RC columns under axial compression. Compos Struct 176:205–216. https://doi.org/10.1016/j.compstruct.2017.05.033
12. Rao BTM, Prakash SS (2022) Numerical investigation on size and shape effects on hybrid FRP strengthened non-circular RC columns under axial compression, vol 198 LNCE. Springer International Publishing. https://doi.org/10.1007/978-3-030-88166-5_144
13. Mirmiran A, Shahawy M (1997) Behavior of concrete columns confined by fiber composites. J Struct Eng 123:583–590. https://doi.org/10.1061/(asce)0733-9445(1997)123:5(583)
14. Bisby LA, Dent AJ, Green MF (2005) Comparison of confinement models for FRP wrapped concrete. ACI Struct J 62–72
15. Deng L, Zhang P, Chen H (2011) Flexural behaviour of RC beams strengthened with prestressed CFRP plates: comparisons of bonded and unbonded method. Key Eng Mater 480–481:283–287. https://doi.org/10.4028/www.scientific.net/KEM.480-481.283
16. You YC, Choi KS, Kim J (2012) An experimental investigation on flexural behavior of RC beams strengthened with prestressed CFRP strips using a durable anchorage system. Compos Part B Eng 43:3026–3036. https://doi.org/10.1016/j.compositesb.2012.05.030
17. Ross CA, Jerome DM, Tedesco JW, Hughes ML (1999) Strengthening of reinforced concrete beams with externally bonded composite laminates. ACI Struct J 96:212–220. https://doi.org/10.14359/612
18. Khorramian K, Sadeghian P (2019) Performance of high-modulus near-surface-mounted FRP laminates for strengthening of concrete columns. Compos Part B Eng 164:90–102. https://doi.org/10.1016/j.compositesb.2018.11.064

19. Barros JAO, Varma RK, Sena-Cruz JM, Azevedo AFM (2008) Near surface mounted CFRP strips for the flexural strengthening of RC columns: experimental and numerical research. Eng Struct 30:3412–3425. https://doi.org/10.1016/j.engstruct.2008.05.019
20. Abdallah M, Al Mahmoud F, Boissière R, Khelil A, Mercier J (2020) Experimental study on strengthening of RC beams with side near surface mounted technique-CFRP bars. Compos Struct 234:111716. https://doi.org/10.1016/j.compstruct.2019.111716
21. Lu XZ, Teng JG, Ye LP, Jiang JJ (2007) Intermediate crack debonding in FRP-strengthened RC beams: FE analysis and strength model. J Compos Constr 11:161–174. https://doi.org/10.1061/(asce)1090-0268(2007)11:2(161)
22. Perrone M, Barros JAO, Aprile A (2009) CFRP-based strengthening technique to increase the flexural and energy dissipation capacities of RC columns. J Compos Constr 13:372–383. https://doi.org/10.1061/(asce)cc.1943-5614.0000031
23. Chellapandian M, Prakash SS, Rajagopal A (2018) Analytical and finite element studies on hybrid FRP strengthened RC column elements under axial and eccentric compression. Compos Struct 184:234–248. https://doi.org/10.1016/j.compstruct.2017.09.109
24. BIS. IS: 10262—2009 Indian Standard Guidelines for concrete mix design proportioning (2009)

Natural Fibres—A Potential Bio-reinforcement in Polymers for Fibre Reinforced Plastic (FRP) Structures—An Overview

Lakshmipriya Ravindran, M. S. Sreekala, and Sabu Thomas

Abstract Nature is the master source where we can locate several candidate materials for ecofriendly products. Natural fibres, cellulose nanofibres, cellulose nanocrystals and organic nano-silica are some examples only. Natural fibres being highly cellulosic exhibit attractive properties which can be effectively utilized to prepare ecofriendly and cost effective products which can replace many synthetic plastics. Utilization of biofibres will result in decreased emission, less wear to the processing tools, improve agricultural based economy and create rural jobs. The properties of these biomaterials vary much depending on the species, age, climate etc. of the plant source. Hence the reproducibility of the properties is less than the synthetic systems. Even though by sorting and giving appropriate treatments, can produce more reproducible result. The properties of natural fibres are dependent on the chemical composition of fibres. More cellulosic fibres exhibit excellent mechanical properties due to their more crystalline structure. The drawbacks of natural fibres like hygroscopic nature, lower mechanical performance etc. can be alleviated by hybridizing the same with other suitable biofibres or synthetic fibres. The interface properties of the composites can be improved by giving appropriate chemical and physical modifications. Strain compatibility is an important parameter in selecting hybrid fibres for reinforcement. It is reported earlier from our laboratory that hybridizing oil palm fibre with glass fibre in reinforcing phenol formaldehyde polymer resulted in very high improvement in properties of the system. As India a big producer of rice and wheat, we have much straw and rice husk unutilized in the paddy field which causes great environmental problems now a days. Presently it is used as cattle feed and as boiler fuel. Straw can be effectively utilized for reinforcement in cement for better properties. Both straw and rice husk are rich in silica content. It is possible to isolate organic nanosilica from these agricultural byproducts effectively. It can find enormous applications as a bionanomaterial in several systems. It is found to have many advantages as they exhibit antibacterial properties, self-cleaning

L. Ravindran
School of Energy Materials, Kottayam, Kerala 686560, India

M. S. Sreekala (✉) · S. Thomas
School of Chemical Sciences, Mahatma Gandhi University, Priyadarshini Hills P.O, Kottayam, Kerala 686560, India
e-mail: sreekalams@mgu.ac.in

S. B. Singh et al. (eds.), *Fiber Reinforced Polymeric Materials and Sustainable Structures*, Composites Science and Technology, https://doi.org/10.1007/978-981-19-8979-7_10

etc. The cellulosic natural fibres, wood etc. are good source for extracting cellulose nanofibres and nanocrystals. As they are cent percent cellulosic they will superior in reinforcing polymer matrices giving excellent barrier properties and thermal stability to the systems. The macro natural fibres, cellulose nanofibres and other bionanomaterials like nano-silica can find versatile applications as structural materials and in packaging industry.

Keywords Natural fibres · Polymer composites · Applications

1 Introduction

The rise in environmental awareness and societal interest, as well as new environmental restrictions and excessive petroleum demand, have prompted consideration of sustainable products. Natural fibre is one of the most biodegradable materials available, with superior characteristics than synthetic fibre. With considerable environmental benefits, biodegradable natural fibre composites are rapidly being researched for lightweight structural applications in the vehicle and construction industries. Poor interfacial bonding and manifestation of the hydrophilic feature of natural fibres are two drawbacks of natural fiber-composites. Natural fibres are hydrophilic because of their high concentration of hydroxyl groups, which makes them incompatible with polymer matrices. A lack of mechanical, thermal and physical qualities could result from this issue. This can be addressed by modifying fibres by chemical or physical means. In addition to the composite's stiffness and strength, additive fillers including MMT, CNT, nano-silica and nanocellulose can increase the stiffness, thermal insulation and electrical conductivity of the composite [1–3]. It is therefore possible to replace this solution with natural fibre (NF) instead of synthetic fibre (SF) to generate natural fiber-reinforced polymers (NFRP), which are also known as (biocomposites). Biocomposites can use lignocellulosic natural fibres like flax, jute, and hemp, as well as agricultural leftovers (agrofibres) like straw, as well as other industrial lignocellulosic fibres like flax, jute, and hemp. Biocomposites can be used to substitute wood in the building sector to enhance forest management and conserve a crucial slow renewable resource.

2 Natural Fibre Reinforced Polymer Composites (NFRP)

Green composites (GCs) have the potential to meet the growing demand for lightweight composite materials in various structural applications, as well as to reduce environmental footprint and ecological risk. GCs, as opposed to synthetic fiber-based polymer composites, can be easily disposed of or decomposed after they have served their purpose without harming the ecosystem. Natural fibre reinforced polymer composites have opened up new possibilities for value-added goods made

from renewable materials and for environmental sustainability. For structural and semi-structural applications, such as in aviation, transportation, electronics, sports equipment and household appliances, GCs have already proven their worth on the market. These sustainable composites are not only a replacement for conventional materials like wood and steel, but also challenge specific synthetic composites that have been around for decades. Natural Fibre Polymer Composites have shown to be more environmentally friendly in the automobile industry and are becoming a viable solution for aviation weight reduction. Polymer reinforced with natural fibre have recently demonstrated increased focus and interest in the creation of environmentally friendly materials, including the substitution of synthetic fibres frequently used in automotive applications. The influence of natural fibres derived for composite manufacture from milkweed, kusha grass, sisal, banana, and hay mixed with polypropylene (PP) 10:90 was investigated by Hariprasad et al. [4]. Different PP reinforced natural fibres are mechanically and acoustically examined and compared. When thicknesses are compared, natural fibre at 500 Hz is more efficient. In the frequency range 1500–2000 Hz, the change exhibits the least variance (0.25), and the maximum variation (0.5). Consequently, at higher frequencies, the increase in the thickness of sound absorption is no longer efficient.

Gomez-Campos et al. [5] compared the environmental performance of certain flax-based composite panels designed for aeroplane interior fitting parts to a glass fiber/epoxy composite with a honeycomb core using Life Cycle Assessment. Yan et al. [6] made fire retardants (FRs) from plant-based natural flax fabric-reinforced polymer (FFRP) composites. Ammonium polyphosphate (APP) and aluminium hydroxide (ALH) were utilised in varying mass concentrations as fire retardants. The results showed that the temperature of the thermal decomposition and the LOI values of the composites rose as the amount of fire retardant in the composites increased for both fire retardants. Under the UL-94 vertical test, FFRP composites containing 20% and 30% APP self-extinguished within 30 and 10 s, respectively, after the flame was extinguished. The mechanical tensile tests, on the other hand, revealed that the APP treated FFRP composites had lower elastic modulus and strength, with reductions of up to 24% and 18%, respectively. The FRs were efficiently coated onto the flax fibres, resulting in an enhancement in the flame retardancy of the treated composites. Natural fibres (bamboo, cotton, flax) and polylactic acid (PLA) fibres were combined, to develop a biocomposite [7]. These natural fibre composites were subjected to vibration damping and acoustic testing, and their performance was compared to that of a commercial panel comprised of a polypropylene (PP) matrix reinforced with hemp and kenaf fibres. The cotton/bamboo/PLA composite laminate showed the best acoustic performance (coincidence frequency of 2448 Hz) from both the coincidence frequency and wave number amplitude analyses, which is related to the fineness of cotton fibres, bending stiffness, natural frequency, and density of the composite panel.

Rice starch bioplastic films reinforced with untreated and treated pineapple leaf fibres (PALF) were fabricated by Mishra et al. [8]. In this study, the surface morphology, mechanical, and thermal properties were examined. Rice starch and PALF were combined in a 10:1 weight ratio to create three different films: Type A

(Pure rice starch), Type B (Rice starch reinforced with untreated PALF), and Type C (Rice starch reinforced with alkaline-treated PALF). The interfacial bonding between PALF and the rice starch matrix was improved after alkaline treatment of PALF, which in turn helped to increase the tensile strength of the films. After incorporating PALF into the rice starch matrix, dynamic mechanical analysis of films showed an increase in storage and loss modulus values. After treating PALF, the thermal stability of films was also enhanced. Biodegradability was also evidenced for bioplastic-composite films. Using the hand lay-up technique, the Calotropis Gigantea Fibre/ Areca Fine Fibres/ phenol formaldehyde (CGF/AFF/PF) hybrid composites were created by Sanjeevi et al. [9]. The effects of water absorption on the mechanical properties of CGF/AFF/PF hybrid composites have been investigated. As the percentage of fibre weight increases, so does the percentage of water absorption. This composite's water absorption behaviour follows the non- Fickian law. The mechanical properties of the hybrid composites were lower when they were wet than when they were dry. The hybrid composite with 35 wt.% fibre reinforcement showed the greatest strength in both wet and dry conditions. Fiber–matrix bonding was better in the composite with 35 wt.% fibre reinforcement than in the other two composites. Agglomeration reduced the strength of 45 wt.% composites when compared to 35 wt.% composites.

For the first time, Jirawattanasomkul et al. [10] investigated the development and use of water hyacinth wastes in the production of fibre-reinforced concrete composites as a green reinforcing material. The mechanical properties of the water hyacinth fibre-reinforced polymer composite are found to be suitable for concrete reinforcement. The mechanical properties of composite, such as tensile strength (137 MPa) and ultimate tensile strain (1.72%), are satisfactory for strengthening purposes from an engineering standpoint. Using water hyacinth fiber-reinforced polymer composites is more environmentally friendly because it uses less water during production and generates fewer natural wastes. The mechanical and thermal properties of single and hybrid natural fiber-reinforced composites made of polyester and epoxy were compared by Banea et al. [11]. Pure jute, jute curaua', and jute sisal composites were produced using two different thermoset polymer resins (an epoxy and a polyester). When compared to epoxy-based composites, epoxy matrix-based composites had higher tensile strength, while polyester-based composites had higher tensile and flexural stiffness. The impact energy of the polyester-based composites was significantly higher than that of the epoxy-based composites, which is a clear advantage. Among the composites tested, the jute sisal polyester-based composites had the best impact resistance. According to the findings of this study, polyester-based natural composites are better suited for impact-oriented applications. Finally, TGA testing revealed that epoxy-based hybrid composites are more thermally stable than polyester-based counterparts.

The physical, mechanical, and morphological properties of treated sugar palm fibre (SPF)/glass fibre (GF) reinforced poly(lactic acid) (PLA) hybrid composites were evaluated [12]. SPFs were subjected to alkaline and benzoyl chloride (BC) treatments. The best tensile and flexural strengths of 26.3 MPa and 27.3 MPa for SPF/GF/PLA hybrid composites were recorded after alkaline treatment of SPF, while the highest values of tensile and flexural moduli of 607 and 1847 MPa for

SPF/GF/PLA hybrid composites were recorded after BC treatment of SPF. The new SPF/GF/PLA hybrid composites could be used to make automotive components. The chemical interactions, mechanical, and thermal properties of alkali-treated and untreated hybrid fibres incorporated with bio phenolic matrix were investigated by Jawaid et al. [13]. Oil palm fibre (OPF) and pineapple fibre (PALF) were used as bio phenolic resin reinforcements. The results show that incorporating NaOH into hybrid composites (OPF/PALF) increases the tensile strength and modulus of all composites. In addition, when compared to other composites, the treated 50% PALF composite had the highest tensile strength and modulus. In comparison to other composites, the hybridisation of treated alkali (5% NaOH/50% PALF) fibre shows the best tensile strength and modulus with 33 and 7535 MPa, respectively. The hybrid composites treated with alkali (NaOH/1OPF.1PALF) had the highest flexural strength (99.8 MPa) and modulus (8813.1 MPa). The mercerization of OPF and PALF fibres reinforced composites improved the interfacial adhesion between pure and hybrid fibre composites and bio phenolic matrix, which was crucial in improving the mechanical properties of composites via alkali treatment with NaOH solution. It is also possible to develop new types of biodegradable and sustainable composites suitable for various industrial and engineering applications through the hybridization of bio-fiber composites.

Fouad et al. [14] treated date palm fibre with NaOH and used as reinforcement for phenolic bio-composites (DPF). When compared to untreated samples, the modified/treated fibres showed improved overall properties. In terms of tensile and flexural properties, the 50% DPF composites treated with DPF showed the highest tensile and flexural properties among all composites (Fig. 1). Three-point bending properties of DPF composites were reduced after fibre treatment. Treated 50% DPF showed better fibre distribution, 60% DPF showed void content, however 40% DPF showed poor fiber/matrix interfacial bonding. Treatment of DPF/Phenolic Composites found improved thermal stability due to good interfacial bonding. Rajamanickam et al. [15] prepared a natural composite by mixing the novel natural resin Vajram with natural banana fibre. Banana fibre properties were also improved by alkali treatment of the fibres with 5%, 10%, and 15% NaOH solution, respectively. 5% NaOH treated fibres have better physical, chemical, and mechanical properties. In terms of tensile, flexural, and impact strength, a banana fibre reinforced phenolic resin composite with 5% NaOH-treated fibres and a 30% weight ratio recorded the highest mechanical properties, with 22.62 MPa, 33.84 MPa and 5.87 kJ/m^2 recorded in each of these areas, respectively. The 80% Vajram mixed banana fiber-reinforced composite reduced tensile, flexural, and impact strength by 21.53%, 38.39%, and 44.63%, respectively. Bensalah et al. [16] introduced a new method for reinforcing phenolic resins with short alkali coir fibres (Bakelite). A study on thermal conductivity found that even though coir fibres have high thermal conductivity, the addition of coir fibres increased the thermal insulation of composites, and the removal of voids from the composites' structure reduced thermal conductivity. Adding coir fibres improved both the flexural modulus and total energy absorption capacity of composites, but 30 wt.% fibre loading shows the greatest improvement, attributed to the better dispersion, wetting of fibres, and interfacial bonding between the fibres and Bakelite, as compared to

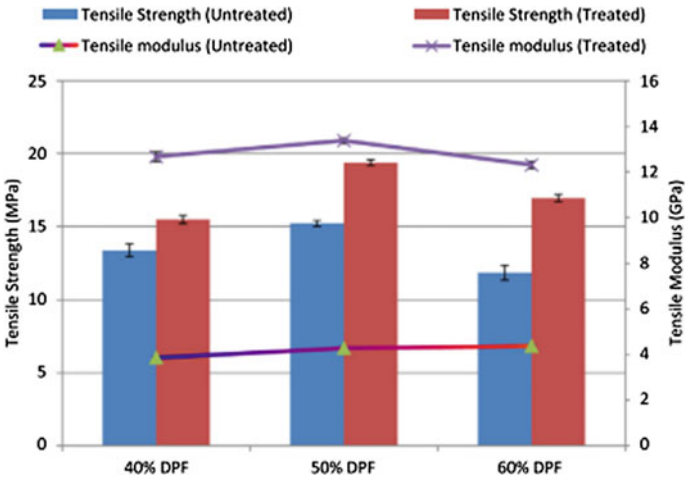

Fig. 1 Tensile strength and modulus of treated and untreated DPF/PF composites

the rest of composites. The results show that the damping factor is increased and the complex modulus values are reduced when temperature and fibre loading are combined.

3 Applications

There has been an explosion in the use of NFRP in a variety of engineering fields. Electrical and electronic, aerospace, sports, recreation, boats, machinery and office products are some of the industries where the applications of NFRP are found. To put it simply, NFRP are widely used in polymer composites because of their low specific weight and high strength, as well as their low production costs; their resistance to corrosion and fatigue; their completely biodegradable nature; their ability to improve the surface finish of moulded composite parts; and their relatively good mechanical properties. This physical disadvantage, which includes moisture absorption and limited processing temperature restrictions, has limited the NFRPs' performance [17]. The NFRP has exhibited improved ballistic resistance and energy absorption [18]. Pereira et al. [19] carried out a similar study for ballistics testing on polyester composites made from fique fibres. Fique fibres were tested in different volume fractions. Because of their high energy absorption and impact integrity, the polyester composites with 30% volume fractions of fibres are ideal candidates for multilayered armor system (MAS) and can also replace Kevlar. The hard armour system for ballistics protection is depicted schematically in Fig. 2. Filho et al. [20] looked at the ballistics of NFRPCs made of piassava fibre. 10–50% volume fractions were used to make the composites. The depth of penetration, which triggers the consistency with

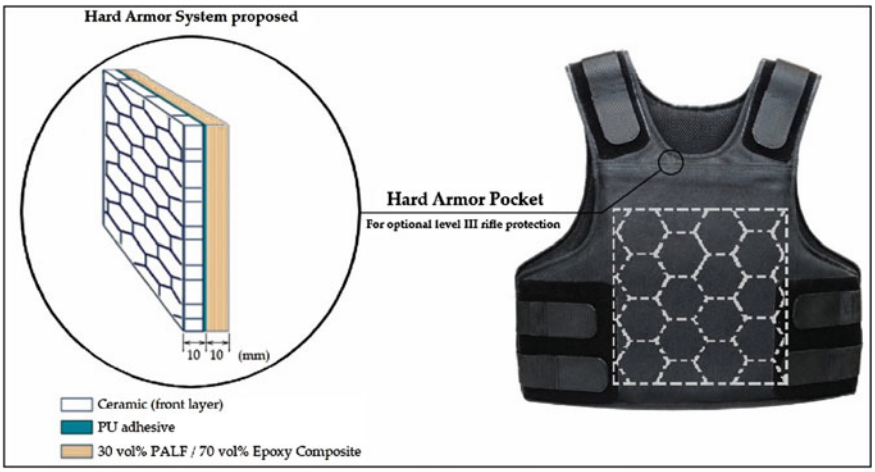

Fig. 2 Schematic diagram of the hard armor system for ballistics protection [20]

the human body, was used to assess the ballistic testing system in order to understand certain requirements of NIJ standard 0101.06.

4 Conclusions and Future Scope

In terms of strength to weight ratio, cost, and environmental impact, natural fibre reinforced composites outperform petroleum-based composites. There are numerous commercial and engineering applications for natural fibre composites. When compared to synthetic composites, natural fibre has less strength; however, when combined with synthetic composites, it provides high strength and lower environmental impact. Observation has shown that the alkaline treatment with an optimal concentration of 5–8 % is the best chemical treatment for natural fibres. Among the topics covered in this paper are the characteristics of natural fibres reinforced polymer composites, and their use in various applications. Due to their comparable mechanical strength to synthetic fibres and lower environmental impacts, NFRP's can be used in engineering applications. However, controlling and improving NFRPs' mechanical properties is a huge undertaking. The research community needs to support and encourage the use of novel NFs and new chemical techniques in the advancement of NFRP's. Finally, we can conclude that the development of NFRP's is rapidly expanding and is being envisioned as a future sustainable material for new and emerging uses. For the development of new natural fibre reinforced polymer composites, there are numerous natural fibres that can be used as reinforcement. It's possible that natural fiber-reinforced polymer composites could have a bright future in the field of thermal insulators. NFRPCs are currently seeing increased use, particularly in the automotive industry. Advances in materials science have led us to believe that

NFRP's will become more useful in the future because of these advancements. A large portion of the future market for electrical devices and sports equipment could be dominated by NFRP composites. To ensure long-term stability in outdoor applications, further research is needed to overcome obstacles such as moisture absorption. Extreme weather conditions, such as temperature, humidity, and UV radiation, all have an impact on the service life of NFRP.

References

1. Nurazzi NM, Asyraf MRM, Khalina A, Abdullah N, Sabaruddin FA, Kamarudin SH, Ahmad S, Mahat AM, Lee CL, Aisyah HA, Norrrahim MNF, Ilyas RA, Harussani MM, Ishak MR, Sapuan SM (2021) Fabrication, functionalization, and application of carbon nanotube-reinforced polymer composite: an overview. Polymers (Basel). 13:1047. https://doi.org/10.3390/polym13071047
2. Alias AH, Norizan MN, Sabaruddin FA, Asyraf MRM, Norrrahim MNF, Ilyas AR, Kuzmin AM, Rayung M, Shazleen SS, Nazrin A, Sherwani SFK, Harussani MM, Atikah MSN, Ishak MR, Sapuan SM, Khalina A (2021) Hybridization of MMT/lignocellulosic fiber reinforced polymer nanocomposites for structural applications: a review. Coatings 11:1355. https://doi.org/10.3390/coatings11111355
3. Nurazzi NM, Sabaruddin FA, Harussani MM, Kamarudin SH, Rayung M, Asyraf MRM, Aisyah HA, Norrrahim MNF, Ilyas RA, Abdullah N, Zainudin ES, Sapuan SM, Khalina A (2021) Mechanical performance and applications of CNTs reinforced polymer composites—a review. Nanomaterials 11:2186. https://doi.org/10.3390/nano11092186
4. Hariprasad K, Ravichandran K, Jayaseelan V, Muthuramalingam T (2020) Acoustic and mechanical characterisation of polypropylene composites reinforced by natural fibres for automotive applications. J Mater Res Technol 9:14029–14035. https://doi.org/10.1016/j.jmrt.2020.09.112
5. Gomez-Campos A, Vialle C, Rouilly A, Hamelin L, Rogeon A, Hardy D, Sablayrolles C (2021) Natural fibre polymer composites—a game changer for the aviation sector? J Clean Prod 286:124986. https://doi.org/10.1016/j.jclepro.2020.124986
6. Bachtiar EV, Kurkowiak K, Yan L, Kasal B, Kolb T (2019) Thermal stability, fire performance, and mechanical properties of natural fibre fabric-reinforced polymer composites with different fire retardants. Polymers (Basel) 11:699. https://doi.org/10.3390/polym11040699
7. Zhang J, Khatibi AA, Castanet E, Baum T, Komeily-Nia Z, Vroman P, Wang X (2019) Effect of natural fibre reinforcement on the sound and vibration damping properties of bio-composites compression moulded by nonwoven mats. Compos Commun 13:12–17. https://doi.org/10.1016/j.coco.2019.02.002
8. Bhadane P, Mishra A (2022) The effect of alkali treatment on pineapple leaf fibers (PALF) on the performance of PALF reinforced rice starch biocomposites. J Nat Fibers 1–15. https://doi.org/10.1080/15440478.2022.2060406
9. Sanjeevi S, Shanmugam V, Kumar S, Ganesan V, Sas G, Johnson DJ, Shanmugam M, Ayyanar A, Naresh K, Neisiany RE, Das O (2021) Effects of water absorption on the mechanical properties of hybrid natural fibre/phenol formaldehyde composites. Sci Rep 11:13385. https://doi.org/10.1038/s41598-021-92457-9
10. Jirawattanasomkul T, Minakawa H, Likitlersuang S, Ueda T, Dai J-G, Wuttiwannasak N, Kongwang N (2021) Use of water hyacinth waste to produce fibre-reinforced polymer composites for concrete confinement: mechanical performance and environmental assessment. J Clean Prod 292:126041. https://doi.org/10.1016/j.jclepro.2021.126041

11. Cavalcanti D, Banea M, Neto J, Lima R (2021) Comparative analysis of the mechanical and thermal properties of polyester and epoxy natural fibre-reinforced hybrid composites. J Compos Mater 55:1683–1692. https://doi.org/10.1177/0021998320976811
12. Sherwani SFK, Zainudin ES, Sapuan SM, Leman Z, Khalina A (2021) Physical, mechanical, and morphological properties of treated sugar palm/glass reinforced poly(lactic acid) hybrid composites. Polymers (Basel) 13:3620. https://doi.org/10.3390/polym13213620
13. Awad SA, Jawaid M, Fouad H, Saba N, Dhakal HN, Alothman OY, Khalaf EM (2022) A comparative assessment of chemical, mechanical, and thermal characteristics of treated oil palm/pineapple fiber/bio phenolic composites. Polym Compos 43:2115–2128. https://doi.org/10.1002/pc.26525
14. Asim M, Jawaid M, Fouad H, Alothman OY (2021) Effect of surface modified date palm fibre loading on mechanical, thermal properties of date palm reinforced phenolic composites. Compos Struct 267:113913. https://doi.org/10.1016/J.COMPSTRUCT.2021.113913
15. Rajamanickam SK, Manoharan M, Ganesan S, Natarajan P, Rajasekaran P (2021) Mechanical and morphological characteristics study of chemically treated banana fiber reinforced phenolic resin composite with Vajram Resin. J Nat Fibers 1–16. https://doi.org/10.1080/15440478.2020.1870622
16. Bensalah H, Raji M, Abdellaoui H, Essabir H, Bouhfid R, el kacem Qaiss A (2021) Thermo-mechanical properties of low-cost "green" phenolic resin composites reinforced with surface modified coir fiber. Int J Adv Manuf Technol 112:1917–1930. https://doi.org/10.1007/s00170-020-06535-9
17. Gallo E, Schartel B, Acierno D, Cimino F, Russo P (2013) Tailoring the flame retardant and mechanical performances of natural fiber-reinforced biopolymer by multi-component laminate. Compos Part B Eng 44:112–119. https://doi.org/10.1016/j.compositesb.2012.07.005
18. Nurazzi NM, Asyraf MRM, Khalina A, Abdullah N, Aisyah HA, Rafiqah SA, Sabaruddin FA, Kamarudin SH, Norrrahim MNF, Ilyas RA, Sapuan SM (2021) A review on natural fiber reinforced polymer composite for bullet proof and ballistic applications. Polymers (Basel) 13:646. https://doi.org/10.3390/polym13040646
19. Pereira AC, de Assis FS, Garcia Filho FDC, Oliveira MS, Lima ES, Lopera HAC, Monteiro SN (2019) Evaluation of the projectile's loss of energy in polyester composite reinforced with fique fiber and fabric. Mater Res 22:20190146. https://doi.org/10.1590/1980-5373-mr-2019-0146
20. Garcia Filho FDC, Monteiro SN (2019) Piassava fiber as an epoxy matrix composite reinforcement for ballistic armor applications. JOM 71:801–808. https://doi.org/10.1007/s11837-018-3148-x
20. da Luz FS, Garcia Filho FC, Oliveira MS, Nascimento LFC, Monteiro SN (2020) Composites with natural fibers and conventional materials applied in a hard armor: a comparison. Polymers (Basel) 12:1920. https://doi.org/10.3390/polym12091920

Natural Fiber and Nanoparticles Reinforced Natural Fiber for Structural Composite Applications

C. Yogin Soodesh and Banasri Roy

Abstract The plant based natural fibers (mostly made of cellulose, hemi cellulose, and lignin) provide several advantages over the traditional inorganic fibers including their low density, good thermal insulation and mechanical properties, reduced tool wear, unlimited availability, low price, and biodegradability. Hence the cellulose micro/nano fibers have evident potential to be utilized as environment friendly reinforcement in composites. Natural fibers reinforced with inorganic nanoparticles can further enhance the mechanical properties of the fiber and could be used as an alternative material to replace synthetic fibers. This short paper will discuss methods of the preparation, physio-chemical and mechanical properties of the nanoparticle reinforced natural fibre.

Keywords Nanoparticles · Natural fibers · Reinforced · Composites

1 Introduction

In recent days sustainability plays a major role in protecting the environment. To achieve this sustainability, material selection in design and manufacture of these sustainable products instigate in the field of engineering and technology. Natural fibers are group of such materials which are often selected due to their environment friendly characteristics rather than choosing synthetic fiber. Natural fiber are the fibrous plant materials produced as a result of photosynthesis. These are also referred to as vegetable, biomass, photomass, phytomass, agromass, solarmass or photosynthetic fibers [1]. Utilization of agricultural by products, wastes, or residues as natural fibres becomes increasingly popular due to its wide availability and efficient economic status. Natural fibres possess enhanced properties such as low density, good thermal insulation, various mechanical properties etc., than in synthetic fibers.

C. Y. Soodesh · B. Roy (✉)
Department of Chemical Engineering, BITS Pilani, Pilani 333031, India
e-mail: broy78945@gmail.com

C. Y. Soodesh
e-mail: h20210028@pilani.bits-pilani.ac.in

S. B. Singh et al. (eds.), *Fiber Reinforced Polymeric Materials and Sustainable Structures*, Composites Science and Technology, https://doi.org/10.1007/978-981-19-8979-7_11

As we all know that agricultural development comes along with waste due to intensive farming practices which is badly affecting the rural and mainly the global environment.

Reportedly in India the total amount of crop residues generated and burned in the year 2017–2018 were 516 and 116 million tonnes, respectively. Estimated 176.1 Tg of CO_2, 10 Tg of CO, 313.9 Gg of CH_4, 8.14 Gg of N_2O, 151.14 Gg of NH_3, 813.8 Gg of NMVOC.453.4 Gg of PM 2.5 and 935.9 Gg of PM were emitted in the indo- gigantic plains (Delhi, Haryana and Punjab) due to this stubble burning [2, 3]. The national policy of management of crop residue (NPMRC) under the ministry of agricultural trying their best to stop the residue burning. We must ensure to follow the sustainable management practices of crop residue which includes but not limited to composting, production of biochar, in- situ management with mechanical intensification, initiation to biogas plants, etc. Hence the solution could be to develop an effective implementation of sustainable management practices with interventions, innovations and policies [2].

Far-reaching research has been conducted on conventional composite materials to optimize their mechanical behaviour and reliability. Researchers have been developing an efficient concept to replace synthetic fibres with the natural ones to evaluate and maximize the performance of structural composite applications. The synthetic fibers are not only non-renewable, poor insulator, and deleterious to health but also the preparation methods of the synthetic fibers lead to high emissions rates and high consumption of energy [3]. Therefore, from sustainable point of view natural materials are very much needed to replace the synthetic fibers. Nanoparticles reinforced natural fibers shows many applications in different fields because of larger surface area, and greater aspect ratio with fascinating properties [4]. These environmentally friendly composites offer new technology and business opportunities in number of industrial sectors such as aerospace, automotive, electronics, biotechnology, etc. This paper contemplates to investigate natural fibre and nanoparticles reinforced natural fibre-based composite with concern to their preparation, mechanical properties, and applications.

2 Natural Fibre

Natural fibers can be extracted from plants, animals and minerals. The plant fibers are made up of constituents like cellulose, lignin, hemicellulose, pectin, waxes and water-soluble substances. Another general term is “lignocellulosic fibers” or LCFs: meaning being lignin and cellulose containing. The amount of cellulose, a semi crystalline polysaccharide component, present depend on the age of the plant [5]. Whereas lignin is an untidy, cross-linked polymer. The presence of lignin makes the fiber more rigid. There is a vast range of natural fibers which can be used for reinforcement and fillers. LCFs are of three categories depending on the part they are extracted from. A classification of LCFs is shown in Fig. 1. There are 6 major

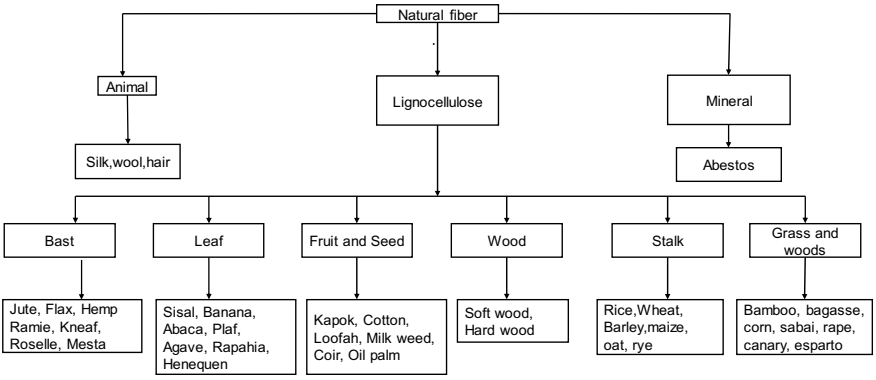

Fig. 1 Classification of lignocellulosic natural fibers [1, 5]

types of lignocellulose fibers namely; bast fibers, leaf fibers, fruit fibers, grass fibers, straw fibers and other types (wood and roots etc.).

3 Physio-Chemical Properties Lignocellulosic Natural Fibers

The properties depend on the plant nature, locality (how it grows and where it grows), geographic area, climatic conditions, the age of the plant, and the most important is the extraction method. The main chemical content in the plant is water. On the dry basis all plant cell wall consists of cellulose and hemicellulose that are present with the lignin with small amount of protein starch and inorganics. The chemical compositions vary from plant to plant and also within the different parts of the same plant [6]. The growth of good aspect ratio Jute/ golden fibers, typically 1–4 m long and 17–20 μm diameter needs optimum temperature of 18–33 °C, minimum moisture of 250 mm and the optimum soil pH of 6.6–7.0 for a yield of 2200 kg/hectare [7]. In the other hand a fiber leaf with high lignin content called Abaca grows well in the tropical weather (25–29 °C, 200 mm minimum moisture and soil pH 5.2–6.4), shows good mechanical strength, and a high yield of 3000 kg/hectare [1]. A linear chain of a hydro glucose substance containing the alcoholic hydroxyl groups is present in the plant fibers which makes it hydrophilic in nature. This hydrophilic nature affects the interfacial bonding between the hydrophobic polymer matrix and the fiber [3, 4].

Physical properties of the fibres depend on shapes, sizes, orientation and thickness of the plant cell walls. Length and width indicate the strength of the fibres which enables us to choose the suitable fiber for our specific usage. Fiber with low crystallinity and low degree of polymerization tend to have low strength and high chemical reactivity. The fibers with low multi fibrillar angle (MFA), which depends

on the crystallinity and orientation of micro fibrils, show lower strain compared to fibers with high MFA under the same mechanical stress [8, 9].

4 Mechanical Properties of Lignocellulosic Fibers

Long fibres of high aspect ratios, high crystallinity and MFA values exhibit good elongation at break point and reduces the composite damage. The specific modulus (elastic modulus per mass density of a material) of the natural fibers are observed to be equivalent or better compared to that of the synthetic fibers [10]. Table 1 shows the mechanical properties of some lignocellulosic and synthetic fiber used for the composite. Natural fibers are becoming increasingly important in composite production due to their high tensile strength, elongation, and stiffness. Lower-density natural fibers results in a great potential for reinforcement in light weight structural composites. Other reason could be the better economic aspects of the jute, hemp, sisal, abaca, coir, etc., which tends to overcome and replace the synthetic fibers. Many researchers have found many varieties of natural fiber equivalent to the mechanical strength of the synthetic fiber.

Table 1 Typical properties of some commonly studied natural fibre and synthetic fibres

Fiber	Source	Density (g/cm^3)	Tensile strength (σ/MPa)	Tensile modulus (E/GPa)	Specific modulus (approx.)	Elongation (%)	Moisture content (%)	Refs.
Natural fiber								
Coir	Fruit	1.2–1.5	98–230	3–6	4	15–51	10	[11]
Cotton	Seed	1.5–1.6	287–800	6–13	6	3–10	33–34	[11]
Flax	Stem	1.53	745–1145	44–61	35	2.07	7	[12]
Hemp	Stem	1.48	690	70	47	1.6	8	[13]
Jute	Plants	1.3	393–773	27	21	1.5–1.8	12	[13]
Keanf	Stem	1.4–1.5	223–930	15–53	24	1.5–2.7	6.2–20	[11]
Ramie	Stem	1.5	560	25	17	2.5	12–17	[13, 14]
Sisal	Leaf	1.3–1.5	363–700	9–38	17	2–7	12.32	[11, 15]
Wood pulp	Others	1.5	1000	40	27	4.4	0–20	[16]
Synthetic fiber								
Aramid	–	1.4	3000–3150	63–37	46	3.3–3.7	–	[13, 16]
Basalt	Mineral	2.7	2130	93	47	2	–	[12]
Carbon fiber	–	1.8	4330	231	129	1.8	–	[12]
E-glass	–	2.5–2.6	2000–3500	70–76	29	1.8–4.8	–	[11]
S-glass	–	2.5	4570	86	34	2.8	–	[13]

5 Extraction Process of Natural Fibers

The extraction method is very crucial during the processing of natural fibers. The most common and old methods are dew and water retting processes, whereas currently the modish ways are the mechanical extraction and chemical treatments which reduce long processing times and also provides better properties of natural fiber [17].

In dew retting process, the parts of the plants are evenly slices and scattered on the field in the presence of bacteria, sunlight, and atmospheric air which break down the cellular tissues and adhesives that surround the fiber. This paves the way for the separation of individual substances that surrounds the fiber. This economical process is mostly used for the production of blast fiber in industries. In water retting process the bunches of plants parts are soaked/submerged in water [18], in which water penetrates to the central part of the stems and the cells and results in bursting of outer layer of the plants. This process of extraction generates low quality fibers not suitable for industries [19]. Table 2 summarizes the extraction methods in brief.

Table 2 Comparison of the extraction process

Extraction methods	Description	Duration	Adv.	Disadv.	Refs.
Dew retting	Plants are cut and spread evenly on grassy fields, in order to breakdown the cellullar tissues and adhesieve substances that are around the fibers by the action of bacteria, sunlight, air and dew	2–3 weeks	Limited resources use	Poor quality fibers, fibers are contaninated with soil and fungi	[20–22]
Water retting	Plants part are subersed in water and obsreved periodically	7–14 days	Retting time is less and uniform prosucts are formed	High cost, environmental concerns, requiers high water treatment maintenance	[23, 10, 24]
Mechanical extration	Fibers hammmering and separated with a hammer mill or/and decorticator	Depending on production fibers	Large quantities produced in short time	High cost High maintenance	[25, 26]

6 Chemical Treatments and Modification of Natural Fibers

The main drawback of natural fibers as reinforcement in composites is their hydrophilic nature which results in poor interfacial interaction between the fibers and matrix and results in poor mechanical properties [27]. Difference constituents of the fibres are sensitive to different range temperature and affect the thermal stability of the composites. To enhance the effectiveness of the interfacial bonding certain modification treatments with different chemicals, reactive additives and coupling agents like alkaline, saline, peroxide, benzoylation, KMnO4, acetylation and stearic acid are attempted on natural fibers [28]. These types of treatments mainly remove the non-cellulosic substance, reduce the hydrophilic nature, and improves adhesion of the natural fibers within the composites. Additionally, these treatments result in increasing the thermal stability of the composite reinforced with natural fiber. Table 3 summarises the effects of the general chemical treatments.

Apart from the chemical treatments mentioned above some other surface treatments also applied on the natural fibers to improve the surface performance (Fig. 2). Surface treatments modify the surface and also the fiber strength [36]. The most commonly used methods are:

(1) Plasma treatment—surface etching: It improves the surface roughness of plant fiber.
(2) Vacuum UV irradiation treatment: widely accepted to remove the impurities improves good adhesion and bio-compatibility.
(3) Ozone treatment: due to the surface oxidation of fiber the mechanical properties are maintained.
(4) Corona treatment: enhanced the acidity and the basicity of the fiber surface.
(5) γ-ray and laser treatment: To increase the strength of the fibers.

Composite reinforced with natural fiber have developed significant processing advantages. Certain orientation of the fibers in the matrix can enhance the stability and load bearing properties of the composites.

7 Applications of the Natural Fibers in Structural Composites

Natural fiber-reinforced composites (NFRCs) are a composite material consisting of a polymer matrix embedded with high strength natural fibers like jute, oil palm, sisal, kenaf and flax etc. have gained interest as an alternative to metals and synthetic fiber because of its growing demand for its light weight and reduced carbon footprints. In 2015, 95% of the fibers used in structural composites were glass fiber [37]. Compared to glass fibers, natural fibre showed many advantages as clear from Fig. 3. Reinforcement provides strength, rigidity, and supports the structural load, whereas the matrix allows to maintain the position and orientation of the reinforcements.

Table 3 Chemical treatments methods

Treatments	Chemical used	Effects	Refs.
Alkaline treatments	NaOH	Non efficient fiber surface area for adhesion. Therefore, Fiber become more uniform, removes amorphous contents, hemicellulose & lignin results in rough surface and strong link after the treatment	[29, 30]
Saline treatments	1% NaOH 1% silane 96% ethanol	Presence of micropores reduces the linkage b/w fiber surface and matrix. It results Higher strength and modulus property are achieved	[27, 31]
Acetic acid treatments	Acetyl group CH_3CO	Excessive moisture content is present Improved moisture resistance properties, reports 50% higher thermal properties, 25% higher tensile and flexural properties after the treatment	[27, 32]
Benzoylation treatment	Benzoyl chloride	More reactive hydroxyl OH groups are exposed on fiber surface More hydrophobic, reports higher thermal stability, improvised tensile properties	[33]
Peroxide treatment	Alkali pre-treatment then benzoyl or dicumyl peroxide	Low interfacial adhesion properties post treatment it improves the tensile properties	[34]
Maleate coupling agent	Malic anhydride, polypropylene	Intense hydrophobic nature is absorbed 72%high flexural strength, water absorption tendency is reduced after treatment	[35]
Potassium permanganate treatment	$KMnO_4$ in acetone solution	Low thermal stability is in turn resulted to observe enhanced chemical interlocking and also high thermal stability	[33]

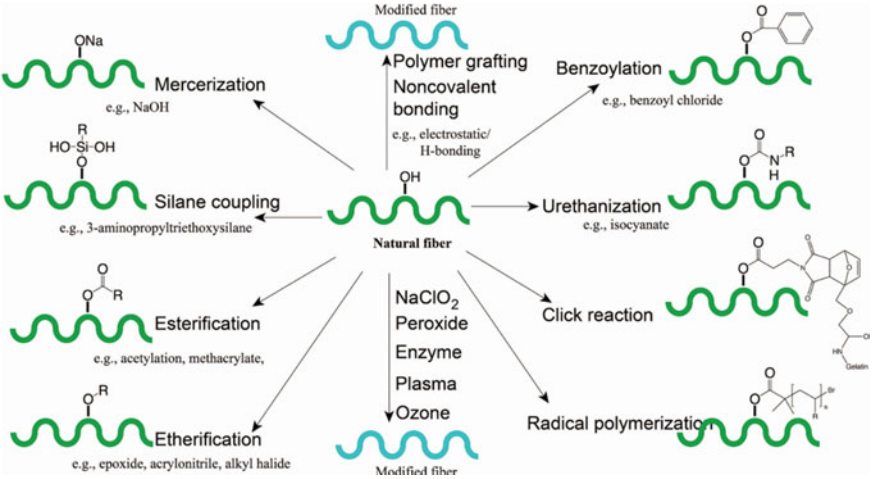

Fig. 2 Treatment and modification of natural fiber [12]

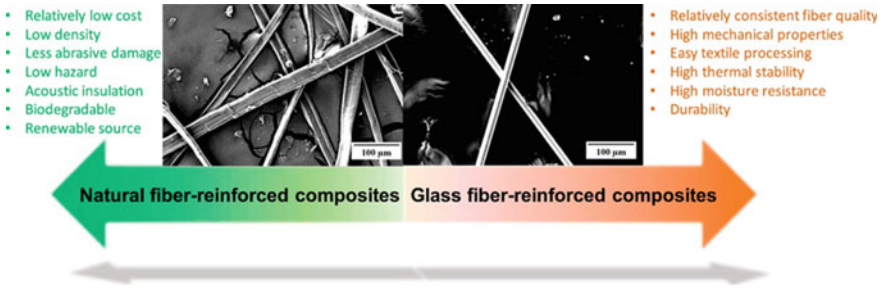

Fig. 3 Relative comparison between natural fiber for composite manufacture [12]

The constituents of the composites retain their individual physical and chemical properties but together they produce higher efficiency of the materials [38].

8 Mechanical Properties of Natural Fiber Reinforced Composites

Natural fibers are not thermally stable at ≥200 °C selection of the polymers is an important factor for composite manufacturing [39]. Extensive research is going on using both thermoplastic and thermoset polymers. Some of the most common natural Polymer based structural composites are as follows:

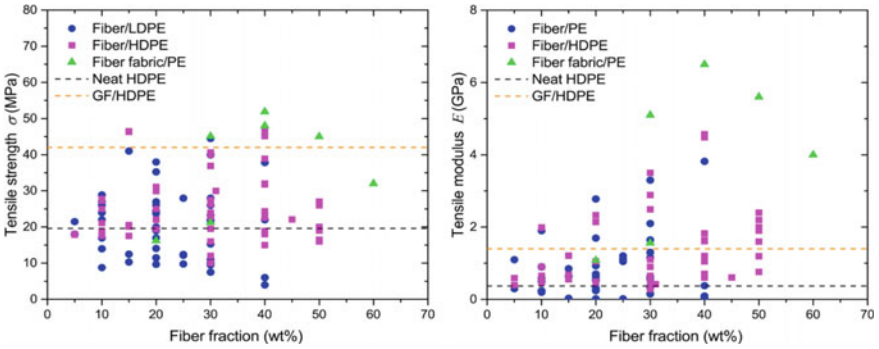

Fig. 4 The properties such as tensile strengths and moduli of natural fiber reinforced polypropylene composites [41]

1. Natural fiber reinforced polypropylene (PP) composite: PP, widely used for its good processing facility, suitability, affordability, low heat disorientation temperature, transparency. The tensile properties of natural fiber/PP composites exhibit wide distribution which can increase the elastic modulus and tensile properties of the matrix. NFRC's with fiber content higher than 30 wt % have attained higher tensile modulus values. A study of bamboo fiber/PP composite demonstrated better physical and chemical compatibility parameters compared to that of the glass fiber/PP composite. Whereas the glass fiber exhibits higher interfacial bonding strength in the composite as shown in Fig. 4 [40]. The properties such as tensile strengths and moduli of natural fiber reinforced polypropylene composites. The black dotted line shows properties of neat PP (σ of 28 M and E of 0.69 GPa) and the orange line shows the properties of 20% wt.% long glass fibers reinforced composites which is used from the Ford Motor company [41].These results concluded that the anisotropic nature of natural fiber is likely the primary reason for its interfacial properties.
2. Natural fiber-reinforced Polyethylene (PE) composites: The 40 wt.% kenaf fiber mat/HDPE composite shows tensile strength (50 MPa cm^3/g), tensile modulus (6.3 GPa cm^3/g), flexural strength (72.9 MPa cm3/g), and flexural modulus (3.9 GPa cm^3/g), comparable to the 40 wt.% discontinuous glass fiber/HDPE composite (Fig. 5). The properties like tensile strengths (σ) and the moduli (E) of natural fiber reinforced polyethylene. The black dotted line represents the pure HDPE (σ of 19.6 MPa and E of 0.74 GPa) and the orange represents the properties of 20 wt.% glass fiber reinforced composite (σ of 42 MPa and E of 1.4 GPa) [42]. A similar case of flax/PE composite shows good tensile strength of 180–280 MPa and tensile modulus of 15-22GPa cm^3/g [43].
3. Natural fiber-reinforced Polylactic acid (PLA): PLA is known for good physical and mechanical properties. Natural fiber/PLA composites demonstrate higher tensile strength and moduli compared to 20 wt.% glass fiber/PLA composite [44]. Composite made from wood pulp sheets compressed with PLA film attained significantly improved tensile properties (σ of 121 MPa and E of 10.5 GPa) with

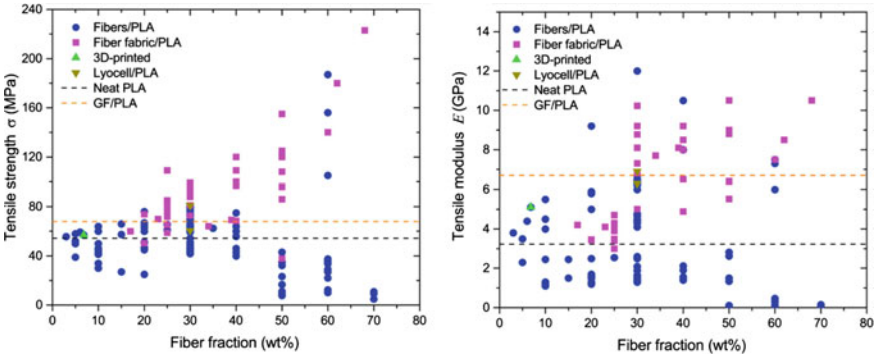

Fig. 5 The properties like tensile strengths (σ) and the moduli (E) of natural fiber reinforced polyethylene [42]

respect to pristine PLA (σ of 60 MPa and E of 3.5 GPa). A 44 vol% unidirectional flax/PLA composite shows a specific tensile strength of 252.3 MPa cm^3/g and modulus of 14.9 GPa cm^3/g which is slightly superior to the 43–50 vol% woven glass fiber-reinforced epoxy (Fig. 6) [45]. The black dotted line represents the pure PLA (σ of 54.36 MPa and E of 3.23 GPa) and the orange represents the properties of 20 wt.% glass fiber reinforced composite (σ of 67.9 MPa and E of 6.7 GPa) [46].

In different studies, the effects of fiber types, compositions, tensile and flexural strengths, fracture toughness, as well as impact resistance on the mechanical properties of NFRCs have been investigated. Most NFRC's synthesised using the common polymer matrices have shown the maximum tensile strength and moduli in the range of 20–140 MPa and 1–10 GPa, respectively. There are several factors associated with the fibers and polymers which makes the processing of the NFRC's

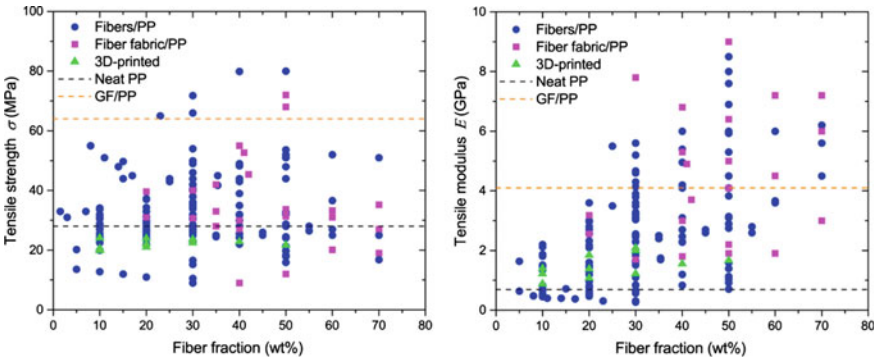

Fig. 6 The properties like tensile strengths (σ) and the moduli (E) of natural fiber reinforced polylactic acid [46]

difficult. Several strategies have implemented to negate such disappointing factors and discussed below.

9 Strategies of Enhancing the Performance of NFRC's

1. Fiber hybridization: Generally, hybridization is defined as combination of two or more fibers into a common matrix. Hybridization seeks to balance fiber compositions to achieve sustainability, low cost and improved performances of NRFCs. This strategy offers a new opportunity for wide applications of the composite materials. New products of certain specification that are to be achieved can be designed with the help of this method [47]. Required properties of the commercially available products could be compared and the combination/design could be formulated according to the predestined specifications of the composites. Hybridization of natural and synthetic fibers such as jute and glass fiber composites boost the mechanical properties by three-fold and six-fold respectively. For example, 30 wt.% pineapple leaf hybridised with recycled bamboo, fiber/PLA composite demonstrated strength, modulus and flexural strength improvement over neat PLA by 66.1, 216, and 66%, respectively [48]. This hybridization with PLA can produce fully biodegradable composite materials.
2. Incorporation of nano cellulosic fillers: lignocellulosic nanofillers such as cellulose nanocrystals (CNCs) and cellulose nanofibrils (CNFs), have emerged as a novel reinforcing material due to their high surface area, high crystals stiffness, strength and good aspect ratio. For examples CNF/HDPE composite has achieved tensile strength of 43 MPa where as for the pristine HDFC tensile strength is 22 MPa. Also, the young's modulus has enhanced from 1.1 for the HDFC matrix to 2.0 GPa for the composite with some decrease in the strain. The impact strength and flexural strength has increased [49]. Addition of 40 wt.% CNF in cellulose acetate butyrate composite increased the tensile strength from 2.07 GPa to 11 GPa [41]. However, the aggregation of nanocellulose in the matrix could be a challenge for manufacturing high-performance nanocellulose composites.
3. Advancement of conventional manufacturing processes: In case of all the methods involved in composites fabricating, the general processing parameters such as moulding temperature, pressure, compression time etc., are the important factors significantly impact the mechanical properties of NFRCs. Studies show that the high processing temperature and pressure have good impact on the rheological properties and also to the infusion of the fiber to the matrix. A twin-screw processing method offers a continuous fibrillation of fiber compounding with the PP [50].
4. Emergence of additive manufacturing of NFRCs: New generation processing like 3D printing have revolutionized the composites manufacture industries. Compared to the traditional process 3D printing has many advantages like fast manufacture, customizable composite geometry, reduced thermal degradation,

saving of expensive tools cost. In case of a 6 vol % jute/PLA composite fabricated using 3D printing tensile strength and modulus are reported to increase 134 and 157%, respectively compared to the same composite synthesised by a conventional method [46]. In addition to the enhanced mechanical strength many other advancements enable to expand the methodology of 3D printing substantially for NFRCs.

5. Exploration of new emerging fibers: At present the production of major natural fibers is expected to reach a level of 40 million tons/year in the middle of twenty-first century and will grow about 3% annually [51]. Among the new emerging fibers, the characterization shows feasible physical, mechanical, thermal and morpho-logical features. Overall, the balance between the synthetic and natural fibers there is a better view in terms of the environment-friendly sustainability, high quality and economy seen in the natural fibers. In handbook of naturals fibers Kozowski R et al. have reported some new and futuristic natural fibers namely Okra fibers, Mesocarp fibers, ficus fibers Pomelo fruit fibers and many more. [51] Hence new fibers must emerge in order to upgrade the advancements in the area of composites.

9.1 Nanoparticles Reinforced Natural Fiber

Natural fibers compared to the man-made synthetic fibers have gained a lot of interest these days in numerous ways as discussed above. However, there are some challenges such as the structure of the fiber, poor mechanical properties (tensile strength, elongation, flexural properties etc.), hydrophilicity [52], low thermal stability and low adhesion with the matrix which slows down the bonding during aging [53], etc., which controls the usage of natural fiber in various structural composite applications. Reportedly nanoparticle modification/reinforcement may be helpful to enhance hydrophobicity of the natural fibers and enhances also the thermal and mechanical properties [52].

10 Preparation of Nanoparticle Reinforced Natural Fibers

Chowdary et al. [54] reported the first attempt to study the properties of copper nano particles (CuNPs) loaded oil palm empty fruit bunch (EFB) fiber/polyester resin composites. The CuNPs was synthesized and embedded in the fibers to make it rigid and strong (Fig. 7). Several kinds of composites were developed from this nanoparticle reinforced fiber; characterized and the material properties are studied [54].

Copper chloride and ascorbic acid was added in PVA solution and then aqueous solution of sodium borohydride added drop wise with stirring. This CuNPs dispersion is stored. The EFB fiber was treated with 20% (3-Chloro-2-hydroxypropyl)

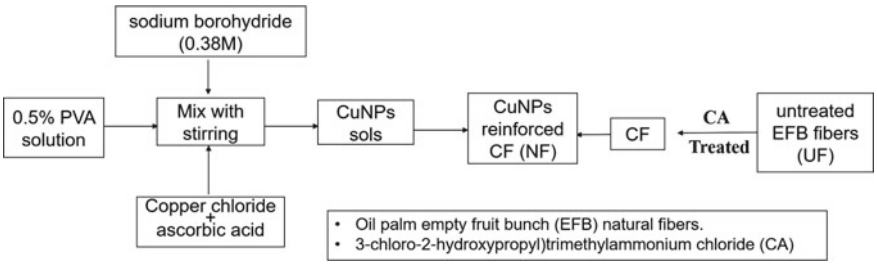

Fig. 7 Synthesis of CuNPs EFB reinforced polyester resin composites [54]

trimethylammonium chloride (CA) solution in a water bath and mix with the CuNPs dispersion. The CuNPs reinforced natural fiber was removed from the bath, rinsed with water, and dried in ambient temperature.

Xia et al. fabricated the composites using inorganic nanoparticles impregnation (INI) process. An in-situ INI process was used to introduce calcium carbonate nanoparticles to the kenaf fibers (Fig. 8) [55]. This process provides good compatibility between natural fiber and matrices. The aim was to extend the pressure during the impregnation process in order to improve the performance of the effective loading efficiency.

Chopped Kenaf bast fibers (50.8 mm length) was treated with 5% w/v NaOH solution in a hermetical reactor at 160 °C and 0.69 MPa for one hr. The dried retted fiber was treated with 0.1 mol/L $CaCl_2$ solution in a hermetical reactor at 100 °C under different pressure from 0.69 to 13.8 MPa for 0.5 h and then treated with 0.1 mol/L Na_2CO_3 soln. at 100 oC [55].

Chen et al. reported on the synthesis of nanoparticle (CNT or SiO_2) reinforced bagasse cellulose powder using N-methyl morpholine N oxide (NMMO) solution and fiber was extruded using a capillary extruder (Fig. 9) [56].

The bagasse cellulose power was mixed with 50% aqueous NMMO and CNT or SiO_2 nanoparticle (0.1 wt.%) and ultrasonicate for 1 h. Then the mixture was dried in a rotavapor at 100 °C The composite fiber was prepared using an advance capillary extrusion rheometer, dried at 100 °C for 2 h, conditioned at 25 °C for 48 h.

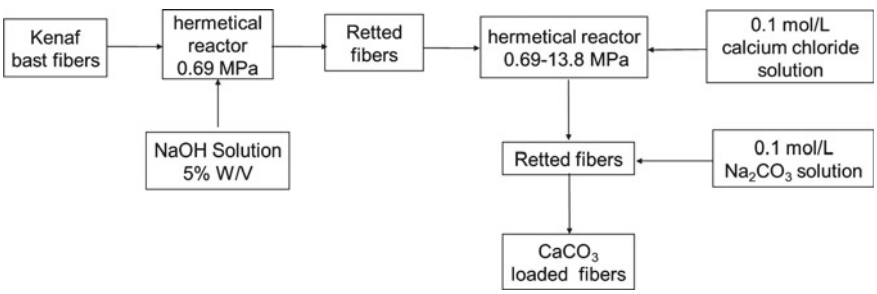

Fig. 8 Flowchart of preparation of $CaCO_3$ loaded fiber composites [55]

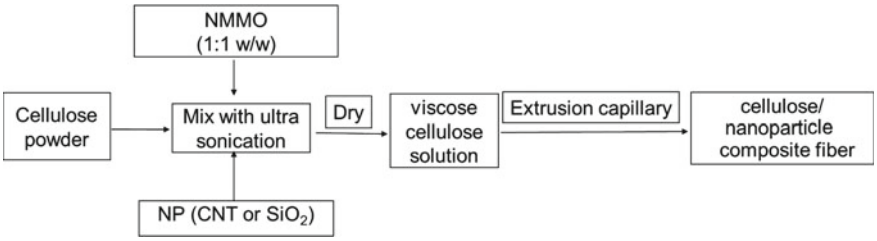

Fig. 9 Flowchart of preparation of nano materials and cellulose-NMMO-water solutions [56]

11 Mechanical Properties of Nanoparticle Reinforced Natural Fibers

Chowdary et al. [54] developed several types of composites by hand mixing method using the CuNPs loaded fibers. The nanocomposites were characterized by using Fourier transform infrared spectroscopy (FTIR), field emission scanning electron microscopy (FESEM), x-ray diffractometer (XRD), differential scanning calorimetry (DSC), tensile strength test, etc. Addition of CuNPs in the fibers improve longevity of the nanocomposite [47]. In another work Sherief et al. grafted functionalized copper nanoparticles (FCuNPs) onto flax fibers and investigated the effects of this structural modification on the mechanical properties of the flax fiber/epoxy model composites (Fig. 10). FCuNPs reinforced fiber showed a decrease in moisture absorption and 25% improvement of tensile strength in the composite since the fiber surface adhesion characteristics were improved. FESEM and XRD analyses showed that the durability of the CuNPs impregnated fiber was improved [57].

Xia et al. [55] observed that at 13.8 MPa external pressure impregnation of calcium carbonate content in kenaf fibers increased by 76.7% and fiber porosity decreased by 70%. This $CaCO_3$ impregnated fibers enhanced the modulus of elasticity, modulus of

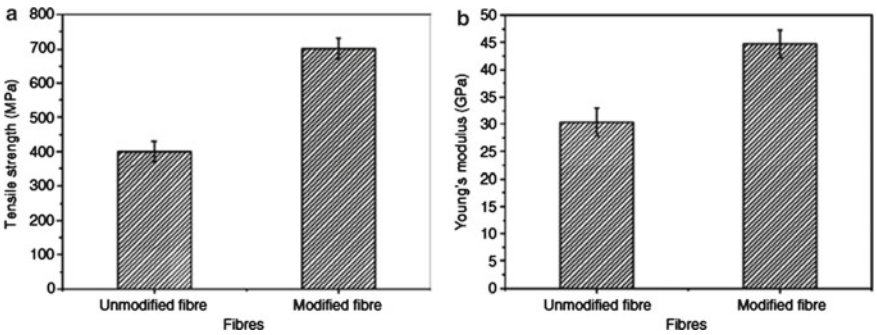

Fig. 10 Tensile strength and tensile modulus of unmodified and copper nanoparticles modified flax fibers [57]

rupture and tensile strength of the composites 43, 79 and 86%, respectively compared with the un-treated fiber/polyester composites as clear from the Fig. 11 [49].

Chen et al. [56] studied the effectiveness of nanoparticles as cellulose fillers on the thermal and mechanical properties of the cellulose/nanoparticle fiber composites. Nanoparticle addition enhances the tensile strength and modulus of the cellulose fiber significantly [49]. Adding a small number of nanoparticles to fill in the wood cellulose matrix resulted in an increase of the cellulose fiber tensile strength and modulus by 14% and 6% respectively, and a decrease of cellulose glass transition temperature (Fig. 12).

However, the chemistry, size or shape of the nanoparticles did not affect the mechanical properties of the reinforced composites much.

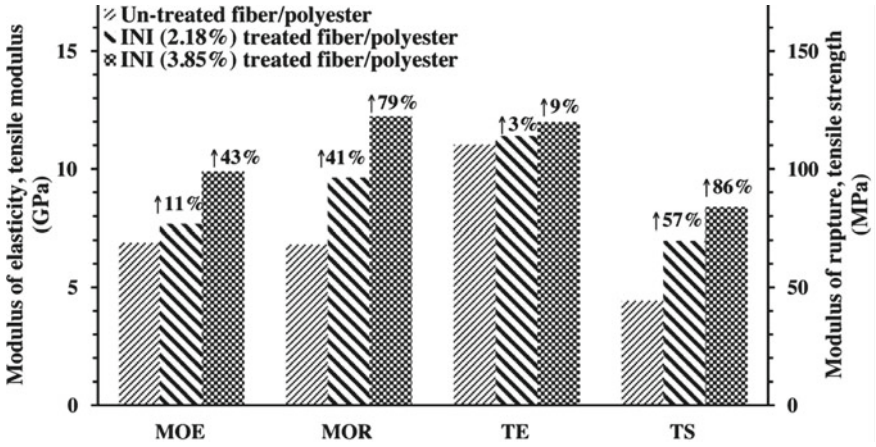

Fig. 11 Comparison of mechanical properties of fiber/INI treated composites [55]

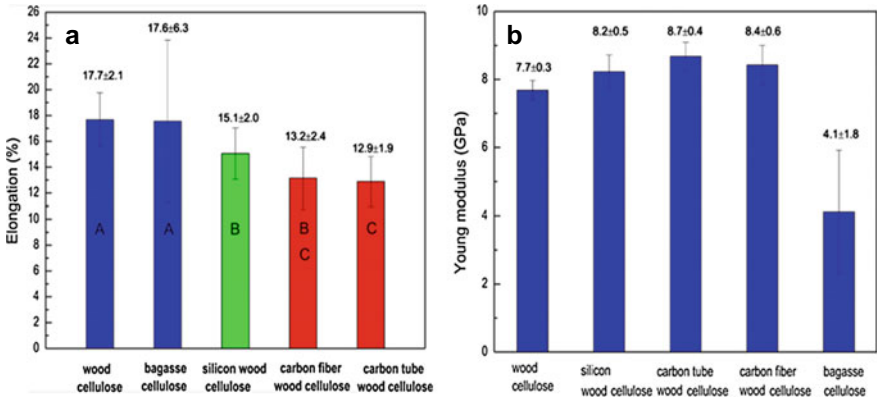

Fig. 12 **a** Comparison of pure and nano cellulose fiber elongation of fiber elongation, and **b** comparison of fiber modulus [56]

The size, shape, and type of nano materials showed little effect on the tenacity and modulus of the nano composite cellulose fibers. The TGA data showed that there was no significant difference of the onset decomposition temperature between the pure cellulose fiber and the cellulose/nanoparticle composite fibers. The glass transition temperatures of the cellulose/nanoparticle composite fibers determined by DSC were lower than that of the pure cellulose fiber.

12 General Applications

Natural fibers reinforced composites are emerging very fast to compete the metal or ceramic fiber based composite materials applied in various kinds of structural industries like automotive, electronic, marine, aerospace, sports goods, etc. Usage of such materials will bring new revolution in the upcoming days which is mostly related to their unique properties.

The use of natural fibres for structural applications is not modern. People in India and other south Asian countries have been using the natural fibers (such as jute, straw, bamboo, grass, etc.) for household applications; making ropes, bags, mats, mixed straws with mud to build walls in villages for long time. Currently, natural *fi*bre reinforced polymer (NFRP) composites have been widely used in automotive and building industries. Fibers such as flax, banana, kenaf, straw, coir, jute are treated and reinforced with soil, cement, fly ash, plaster of Paris and various polymers to find its applications in thermal insulation materials and masonry [14]. For composite building materials natural fibers composites show better sustainability than the commonly used building materials. In the architecture sector these composites are fabricated for manufacturing sunscreens, cladding, walling and flooring etc. Automotive and aircraft industries are using natural fiber composites for their interior application such as insulation, ceiling panels and also as soundproofing materials [15]. The natural fibers such as flax, hemp, sisal and wool are used in Mercedes-Benz components for its door panel, engine encapsulation, trunk applications [58]. Volvo company uses fibers like hemp, jute, rapeseed, wood for the applications for seat padding, natural foams, dashboards and ceilings [59]. Similarly, Audi automotive uses flax and sisal fibers for the seat back, door panels and spare tire liners [60]. There a several other applications and the efforts are being made for the use of natural fibers in automotive industries. Mostly all the major automotive companies have used bio-based composites in various applications [61]. In the field of medical and pharmaceutical cotton and sugarcane fibers are used in antimicrobial and drugs manufacturing areas with the matrix such as oregano oil, poly (3-hydroxybutyrate-co-3- hydroxyvalerate), starch, PLA, etc. [62]. The natural fiber reinforced composites are used in packing materials, dielectric materials, marine materials and in many more. Wood cellulose fibers are reinforced with cobalt sulphide and carbon fibers in battery manufacture [63]. Current researches are focused on developing, characterizing and studying the application of nano particle reinforced natural fiber/polymer composites.

13 Conclusions

From the environmental point of view the natural fibers and nanoparticles reinforced natural fibers could be considered as excellent substitute of the synthetic fibers for the structural composite applications. The extracted raw fibers offer lower abilities and incompatible for the applications. Hence, their modifications are essential. Nanoparticle reinforcement of the natural fiber improves polymer matrix adhesion qualities and offers enhanced mechanical properties of the natural fiber and also for its composites. Researchers are developing new strategies in these technologies so that one day the natural fiber becomes the sustainable and renewable resources in various fields and sectors of the composite applications.

Acknowledgements The authors are grateful for the financial support from SERB Power Fellowship (project no SPF/2021/000001) for this work.

References

1. Rowell RM (2008) Natural fibres: types and properties. In: Properties and performance of natural-fibre composites, Elsevier, pp 3–66. https://doi.org/10.1533/9781845694593.1.3
2. Bhuvaneshwari S, Hettiarachchi H, Meegoda J (2019) Crop residue burning in India: policy challenges and potential solutions. Int J Environ Res Public Health 16(5):832. https://doi.org/10.3390/ijerph16050832
3. Fitzgerald A et al (2021) A life cycle engineering perspective on biocomposites as a solution for a sustainable recovery. Sustainability 13(3):1160. https://doi.org/10.3390/su13031160
4. Hosseini SB (2017) A review: nanomaterials as a filler in natural fiber reinforced composites. J Nat Fibers 14(3):311–325. https://doi.org/10.1080/15440478.2016.1212765
5. Ramu P, Kumar CJ, Palanikumar K (2019) Mechanical characteristics and terminological behavior study on natural fiber nano reinforced polymer composite—a review. Mater Today: Proc 16, 1287–1296 https://doi.org/10.1016/j.matpr.2019.05.226
6. Hoareau W, Trindade WG, Siegmund B, Castellan A, Frollini E (2004) Sugar cane bagasse and curaua lignins oxidized by chlorine dioxide and reacted with furfuryl alcohol: characterization and stability. Polym Degrad Stab 86(3):567–576. https://doi.org/10.1016/j.polymdegradstab.2004.07.005
7. Pickering KL, Efendy MGA, Le TM (2016) A review of recent developments in natural fibre composites and their mechanical performance. Compos Part A Appl Sci Manufact vol 83. Elsevier Ltd, pp 98–112. https://doi.org/10.1016/j.compositesa.2015.08.038
8. Reddy N, Yang Y (2009) Properties of natural cellulose fibers from hop stems. Carbohyd Polym 77(4):898–902. https://doi.org/10.1016/j.carbpol.2009.03.013
9. Gowda TM, Naidu ACB, Chhaya R (1999) Some mechanical properties of untreated jute fabric-reinforced polyester composites. Compos Part A Appl Sci Manufact 30(3):277–284. https://doi.org/10.1016/S1359-835X(98)00157-2
10. Jawaid M, Abdul Khalil HPS (2021) Cellulosic/synthetic fibre reinforced polymer hybrid composites: a review. Carbohydr Polym 86(1):1–18. https://doi.org/10.1016/j.carbpol.2011.04.043
11. Dittenber DB, GangaRao HVS (2012) Critical review of recent publications on use of natural composites in infrastructure. Compos A Appl Sci Manuf 43(8):1419–1429. https://doi.org/10.1016/j.compositesa.2011.11.019

12. Li M et al (2020) Recent advancements of plant-based natural fiber–reinforced composites and their applications. Compos Part B Eng vol 200. Elsevier Ltd. https://doi.org/10.1016/j.compositesb.2020.108254
13. John MJ, Anandjiwala RD (2008) Recent developments in chemical modification and characterization of natural fiber-reinforced composites. Polym Compos 29(2):187–207. https://doi.org/10.1002/pc.20461
14. Li M et al Recent advancements of plant-based natural fiber-reinforced composites and their applications. [Online]. Available http://energy.gov/downloads/doe-public-access-plan
15. Bekele AE, Lemu HG, Jiru MG (2022) Experimental study of physical, chemical and mechanical properties of enset and sisal fibers. Polym Testing 106:107453. https://doi.org/10.1016/j.polymertesting.2021.107453
16. Holbery J, Houston D (2006) Natural-fiber-reinforced polymer composites in automotive applications. JOM 58(11):80–86. https://doi.org/10.1007/s11837-006-0234-2
17. Mahjoub R, Yatim JM, Sam AR, Hashemi SH (2014) Tensile properties of kenaf fiber due to various conditions of chemical fiber surface modifications. Construct Build Mater vol 55, pp 103–113. https://doi.org/10.1016/j.conbuildmat.2014.01.036.
18. Sunny T, Pickering KL (2022) An overview of alkali treatments of hemp fibres and their effects on the performance of polymer matrix composites. Alkaline Chem Appl, IntechOpen, 2022. https://doi.org/10.5772/intechopen.100321
19. Jankauskienė Z, Butkutė B, Gruzdevienė E, Cesevičienė J, Fernando AL (2015) Chemical composition and physical properties of dew- and water-retted hemp fibers. Ind Crops Prod 75:206–211. https://doi.org/10.1016/j.indcrop.2015.06.044
20. Bacci L, di Lonardo S, Albanese L, Mastromei G, Perito B (2011) Effect of different extraction methods on fiber quality of nettle (Urtica dioica L.). Text Res J 81(8):827–837. https://doi.org/10.1177/0040517510391698
21. Antonov V, Marek J, Bjelkova M, Smirous P, Fischer H (2007) Easily available enzymes as natural retting agents. Biotechnol J 2(3):342–346. https://doi.org/10.1002/biot.200600110
22. Jankauskiene Z, Butkute B, Gruzdeviene E, Cesevičiene J, Fernando AL (2015) Chemical composition and physical properties of dew- and water-retted hemp fibers. Ind Crops Prod 75:206–211. https://doi.org/10.1016/j.indcrop.2015.06.044
23. Toriz G, Gatenholm P, Seiler BD, Tindall D (2005) Cellulose fiber-reinforced cellulose esters: Biocomposites for the future
24. Sanjay MR, Siengchin S, Parameswaranpillai J, Jawaid M, Pruncu CI, Khan A (2019) A comprehensive review of techniques for natural fibers as reinforcement in composites: preparation, processing and characterization. Carbohydr Polym vol 207. Elsevier Ltd, pp 108–121. https://doi.org/10.1016/j.carbpol.2018.11.083
25. Sathishkumar TP, Navaneethakrishnan P, Shankar S, Rajasekar R (2013) Characterization of new cellulose sansevieria ehrenbergii fibers for polymer composites. Compos Interfaces 20(8):575–593. https://doi.org/10.1080/15685543.2013.816652
26. Lee CH, Khalina A, Lee S, Liu M (2020) A comprehensive review on bast fibre retting process for optimal performance in fibre-reinforced polymer composites. Adv Mater Sci Eng vol 2020. Hindawi Limited. https://doi.org/10.1155/2020/6074063
27. Kabir MM, Wang H, Lau KT, Cardona F (2012) Chemical treatments on plant-based natural fibre reinforced polymer composites: an overview. Compos B Eng 43(7):2883–2892. https://doi.org/10.1016/j.compositesb.2012.04.053
28. Sepe R, Bollino F, Boccarusso L, Caputo F (2018) Influence of chemical treatments on mechanical properties of hemp fiber reinforced composites. Compos B Eng 133:210–217. https://doi.org/10.1016/j.compositesb.2017.09.030
29. Xu Y, Kawata S, Hosoi K, Kawai T, Kuroda S (2009) Thermomechanical properties of the silanized-kenaf/polystyrene composites. Express Polym Lett 3(10):657–664. https://doi.org/10.3144/expresspolymlett.2009.82
30. John M, Thomas S (2008) Biofibres and biocomposites. Carbohyd Polym 71(3):343–364. https://doi.org/10.1016/j.carbpol.2007.05.040

31. Pothan LA, Thomas S (2003) Polarity parameters and dynamic mechanical behaviour of chemically modified banana fiber reinforced polyester composites. Compos Sci Technol 63(9):1231–1240. https://doi.org/10.1016/S0266-3538(03)00092-7
32. Kommula VP, Reddy KO, Shukla M, Marwala T, Reddy EVS, Rajulu AV (2016) Extraction, modification, and characterization of natural ligno-cellulosic fiber strands from napier grass. Int J Polym Anal Charact 21(1):18–28. https://doi.org/10.1080/1023666X.2015.1089650
33. Saravanakumar SS, Kumaravel A, Nagarajan T, Moorthy IG (2014) Effect of chemical treatments on physicochemical properties of *Prosopis juliflora* fibers. Int J Polym Anal Charact 19(5):383–390. https://doi.org/10.1080/1023666X.2014.903585
34. Bledzki AK, Mamun AA, Lucka-Gabor M, Gutowski VS (2008) The effects of acetylation on properties of flax fibre and its polypropylene composites. Express Polym Lett 2(6):413–422. https://doi.org/10.3144/expresspolymlett.2008.50
35. Yang H-S, Kim H-J, Park H-J, Lee B-J, Hwang T-S (2007) Effect of compatibilizing agents on rice-husk flour reinforced polypropylene composites. Compos Struct 77(1):45–55. https://doi.org/10.1016/j.compstruct.2005.06.005
36. Abdelmouleh M, Boufi S, Belgacem MN, Duarte AP, Salah AB, Gandini A (2004) Modification of cellulosic fibres with functionalised silanes: development of surface properties. Int J Adhesion Adhesives 24(1):43–54. https://doi.org/10.1016/S0143-7496(03)00099-X
37. Thomason J, Jenkins P, Yang L (2016) Glass fibre strength—a review with relation to composite recycling. Fibers 4(4):18. https://doi.org/10.3390/fib4020018
38. Naskar AK, Keum JK, Boeman RG (2016) Polymer matrix nanocomposites for automotive structural components. Nat Nanotechnol 11(12):1026–1030. https://doi.org/10.1038/nnano.2016.262
39. Mochane MJ et al (2019) Recent progress on natural fiber hybrid composites for advanced applications: a review. Express Polym Lett 13(2):159–198. https://doi.org/10.3144/expresspolymlett.2019.15
40. Thomason JL (2010) Dependence of interfacial strength on the anisotropic fiber properties of jute reinforced composites. Polym Compos 31(9):1525–1534. https://doi.org/10.1002/pc.20939
41. Lila MK, Singhal A, Banwait SS, Singh I (2018) A recyclability study of bagasse fiber reinforced polypropylene composites. Polym Degrad Stab 152:272–279. https://doi.org/10.1016/j.polymdegradstab.2018.05.001
42. AlMaadeed MA, Ouederni M, Khanam PN (2013) Effect of chain structure on the properties of Glass fibre/polyethylene composites. Mater Design 47, 725–7302. https://doi.org/10.1016/j.matdes.2012.11.063.
43. Ouali AA et al (2017) Natural unidirectional sheet processes for fibre reinforced bioplastics, pp 060005. https://doi.org/10.1063/1.5016725.
44. Du Y, Wu T, Yan N, Kortschot MT, Farnood R (2014) Fabrication and characterization of fully biodegradable natural fiber-reinforced poly (lactic acid) composites. Compos B Eng 56:717–723. https://doi.org/10.1016/j.compositesb.2013.09.012
45. Couture A, Lebrun G, Laperrière L (2016) Mechanical properties of polylactic acid (PLA) composites reinforced with unidirectional flax and flax-paper layers. Compos Struct 154:286–295. https://doi.org/10.1016/j.compstruct.2016.07.069
46. Huda M, Drzal L, Mohanty A, Misra M (2006) Chopped glass and recycled newspaper as reinforcement fibers in injection molded poly(lactic acid) (PLA) composites: a comparative study. Compos Sci Technol 66(11–12):1813–1824. https://doi.org/10.1016/j.compscitech.2005.10.015
47. Guna V, Ilangovan M, Ananthaprasad MG, Reddy N (2018) Hybrid biocomposites. Polym Compos 39:E30–E54. https://doi.org/10.1002/pc.24641
48. Shih Y-F, Chang W-C, Liu W-C, Lee C-C, Kuan C-S, Yu Y-H (2014) Pineapple leaf/recycled disposable chopstick hybrid fiber-reinforced biodegradable composites. J Taiwan Inst Chem Eng 45(4):2039–2046. https://doi.org/10.1016/j.jtice.2014.02.015
49. Sato A, Kabusaki D, Okumura H, Nakatani T, Nakatsubo F, Yano H (2016) Surface modification of cellulose nanofibers with alkenyl succinic anhydride for high-density polyethylene

reinforcement. Compos A Appl Sci Manuf 83:72–79. https://doi.org/10.1016/j.compositesa.2015.11.009
50. Suzuki K, Okumura H, Kitagawa K, Sato S, Nakagaito AN, Yano H (2013) Development of continuous process enabling nanofibrillation of pulp and melt compounding. Cellulose 20(1):201–210. https://doi.org/10.1007/s10570-012-9843-9
51. Kozłowski RM, Mackiewicz-Talarczyk M, Barriga-Bedoya J (2020) New emerging natural fibres and relevant sources of information, vol. 1. 2020. https://doi.org/10.1016/B978-0-12-818398-4.00022-0
52. Dolez PI, Arfaoui MA, Dubé M, David É (2017) Hydrophobic treatments for natural fibers based on metal oxide nanoparticles and fatty acids. Procedia Eng 200:81–88. https://doi.org/10.1016/j.proeng.2017.07.013
53. Anugrahwidya R, Armynah B, Tahir D (2021) Bioplastics starch-based with additional fiber and nanoparticle: characteristics and biodegradation performance: a review. J Polymers Environ 29(11). Springer, pp 3459–3476. https://doi.org/10.1007/s10924-021-02152-z
54. Chowdhury MNK, Beg MDH, Khan MR (2013) Biodegradability of nanoparticle modified fiber reinforced polyester resin nanocomposite. Procedia Eng 68:431–438. https://doi.org/10.1016/j.proeng.2013.12.203
55. Xia C, Shi SQ, Cai L, Nasrazadani S (2015) Increasing inorganic nanoparticle impregnation efficiency by external pressure for natural fibers. Ind Crops Prod 69:395–399. https://doi.org/10.1016/j.indcrop.2015.02.054
56. Chen JY, Sun L, Negulescu II, Xu B (2017) Fabrication and evaluation of regenerated cellulose/nanoparticle fibers from lignocellulosic biomass. Biomass Bioenerg 101:1–8. https://doi.org/10.1016/j.biombioe.2017.03.024
57. Sherief Z, Xian G, Thomas S, Ajith A (2017) Effects of surface grafting of copper nanoparticles on the tensile and bonding properties of flax fibers. Sci Eng Compos Mater 24(5):651–660. https://doi.org/10.1515/secm-2014-0462
58. Akampumuza O, Wambua PM, Ahmed A, Li W, Qin XH (2017) Review of the applications of biocomposites in the automotive industry. Polym Compos 38(11):2553–2569. https://doi.org/10.1002/pc.23847
59. Faruk O, Bledzki AK, Fink H-P, Sain M (2014) Progress report on natural fiber reinforced composites. Macromol Mater Eng 299(1):9–26. https://doi.org/10.1002/mame.201300008
60. Saxena M, Pappu A, Haque R, Sharma A (2011) Sisal fiber based polymer composites and their applications. In: Cellulose fibers: bio-and nano-polymer composites. Berlin, Heidelberg: Springer Berlin Heidelberg, 589–659. https://doi.org/10.1007/978-3-642-17370-7_22
61. Koronis G, Silva A, Fontul M (2013) Green composites: a review of adequate materials for automotive applications. Compos B Eng 44(1):120–127. https://doi.org/10.1016/j.compositesb.2012.07.004
62. Tavares TD, Antunes JC, Ferreira F, Felgueiras HP (2020) Biofunctionalization of natural fiber-reinforced biocomposites for biomedical applications. Biomolecules 10(1):148. https://doi.org/10.3390/biom10010148
63. Yuan H, Wang F, Li S, Lin Z, Huang J (2020) A cellulose substance derived nanofibrous CoS–nanoparticle/carbon composite as a high-performance anodic material for lithium-ion batteries. New J Chem 44(5):1846–1857. https://doi.org/10.1039/C9NJ05587H

Free Vibration, Mechanical and Damping Properties of Woven Jute FRP Composites with the Effect of Stacking Arrangements

S. Senthilrajan, N. Venkateshwaran, Rajini Nagarajan, Sikiru Oluwarotimi Ismail, P. Sivaranjana, and Suchart Siengchin

Abstract Currently, the demand for vibration damping, lightweight and environmentally friendly material is increasing in automotive and aerospace sectors. Due to this quest, the use of eco-friendly fibrous material has gained importance for its use as a reinforcement in polymeric matrix composite. Therefore, in this present investigation, woven jute fiber mats or layers were added to pure polyester resin to form various composite samples, using compression molding technique. Five different samples were fabricated: neat polyester resin plate and 2–5 woven jute/polyester composites, denoted as NPRP, 2WJPC, 3WJPC, 4WJPC and 5WJPC samples, respectively. The natural frequencies and viscoelastic behaviours of the various samples were examined by free vibration test. From the free vibration test, both natural frequencies and damping factors were obtained. From the results obtained, it was evident that 4WJPC sample exhibited the maximum natural frequencies of 32.96, 231.9 and 659.2 Hz

S. Senthilrajan
Department of Mechanical Engineering, A.V.C.College of Engineering, Tamilnadu Mayiladuthurai-609301, India

N. Venkateshwaran (✉)
Department of Mechanical Engineering, Rajalakshmi Engineering College, Tamilnadu Chennai-602105, India
e-mail: venkatcad@yahoo.com

R. Nagarajan (✉)
Department of Mechanical Engineering, Kalasalingam Academy of Research and Education, Virdhunagar-626126, Tamilnadu, India
e-mail: rajiniklu@gmail.com

S. O. Ismail
Department of Engineering, Centre for Engineering Research, School of Engineering and Computer Science, University of Hertfordshire, Hatfield AL10 9AB, England, UK

P. Sivaranjana
Department of Chemistry, Kalasalingam Academy of Research and Education, Virdhunagar-626126, Tamilnadu, India

S. Siengchin
Department of Mechanical and Process Engineering, The Sirindhorn International Thai-German Graduate School of Engineering (TGGS), King Mongkut's University of Technology North Bangkok, 1518 Wongsawang Road, Bangsue, Bangkok 10800, Thailand

S. B. Singh et al. (eds.), *Fiber Reinforced Polymeric Materials and Sustainable Structures*, Composites Science and Technology, https://doi.org/10.1007/978-981-19-8979-7_12

under modes I, II and III, respectively. Also, the natural frequency of 4WJPC sample was 40% higher than that of NPRP. Therefore, it was evident that the addition of woven jute fiber mat has a significant and good influence on the composite natural frequency. Comparison between experimental and theoretical analysis was carried out and found closely related with each other. Applicably, woven jute fiber mat reinforced polyester composite can be used as a vibration absorbing material (damper), low cost and efficient engineering structure.

Keywords Natural frequency · Damping factor · Woven jute fiber mat · Vibration damping

1 Introduction

Fiber reinforced polymer (FRP) composite materials find their relevance in various automotive structural application over past two decades, due to their higher strength-to-weight ratio, design capability, durability, higher corrosion and wear resistances. Due to the adverse environmental impact of the polymers reinforced with mainly glass and carbon fibers, several studies are being carried out across the world to replace them with natural fiber reinforced composites [1–5]. Reinforcing elements of the natural fiber composites include, but are not limited to the following natural fibers: jute, sisal, flax, banana, rice husk, cotton, bamboo and hemp. They possess inherent properties, such as biodegradability, equivalent specific strength and stiffness, low cost, renewability and non-corrosive nature. Researchers focus on these natural fibers as reinforcements for various applications [6–8]. Recently, the natural fiber reinforced composites-based applications are increasing in automotive sector, aircraft and construction industries, due to their excellent properties of low density, corrosion resistance, less environmental impact, ease of processing method and less cost, when compared with glass, kevlar and carbon (synthetic) fibers [9–11]. Biodegradable polymer composites were estimated to grow at 16% per annum [12].

Several studies have been conducted on numerous natural fiber reinforced composites. To start with, Amico et al. [13] examined the mechanical properties of sisal, glass and hybrid of sisal and glass woven mat composite. From their results, it was concluded that the stacking sequence and hybridization influenced the mechanical properties of the composites. Sapuan et al. [14] investigated into the mechanical properties of woven banana/epoxy composite. They also studied the statistical analysis, using the ANOVA results. Jacob et al. [15] studied the woven sisal and natural rubber composite. They carried out surface modification, using mercerization, salinization and thermal treatments for sisal woven, and concluded that the water absorption was observed to be lowered, due to the fiber surface treatments. Pothan et al. [16] carried out investigation into sisal fabric/polyester resin composite. They fabricated the composite by resin transfer molding technique. They used different weave structures, such as plain, twill and mat. From their experimental results, they analyzed the mechanical properties of the composites. The result analysis revealed that the

woven sisal fibers possessed 32% in volume showed better mechanical properties than the rest of the composites. Venkateshwaran et al. [17] reported the mechanical and water absorption behaviors of woven jute/banana hybrid composites. They concluded that the hybridization influenced the mechanical properties. However, it showed less effect on water absorption behavior. Ahmed et al. [18] considered the influence of hybridization of glass fiber and jute fabric on low-velocity impact behavior and damage tolerance capability of the composites. Drop weight hammer was used for the investigation of impact behaviour. C-scan method was used to study the delamination and damage extent area of the composites. From the results obtained, it was concluded that jute fabric composite exhibited a better absorption capability than jute/glass hybrid composite. Also, damage tolerance capacity was lower than that of jute/glass hybrid composites. Rajesh et al. [19] compared the mechanical behavior of the braided and conventional woven composites. The results obtained were compared with randomly oriented natural fiber composite, which depicted that the braided yarn composites produced better mechanical properties than other types of the composites.

In addition, Rajini et al. [20] reported the mechanical and free vibration properties of montmorillonite clay dispersed woven coconut sheath composites. From their investigation, it was observed that the stacking sequence and alkali treatment contributed to the better mechanical and free vibration behaviours achieved. Ettai et al. [21] studied the vibration damping characteristics of short hemp fiber thermoplastic composites. The results showed that the 30 wt% of noil hemp fiber with 2.5 wt% anhydride-grafted polyethylene octane exhibited the highest damping ratio. Similarly, Chandradass et al. [22] experimented the effect of nanoclay addition on vibration properties of glass fiber reinforced vinlylester composite. From the results obtained, it was observed that the addition of organically modified clay increased the natural frequency of the composite. Ganesa et al. [23] carried out the free vibration behavior of glass fiber/vinyl ester treated and untreated composites. It was evident from their results that NaOH treated glass fiber reinforced composite had better values than HCL treated and untreated glass fiber composites. The damping ratio of the alkali treated composite was higher than untreated glass fiber composite. Ahmed et al. [24] focused on the vibration and damping behavior of composite structure by varying the ply angle of the fiber. They concluded that the outer laminate angle orientation had a significant effect on the inner laminate. Rajesh et al. [25] studied on mechanical, vibration and dynamic mechanical behavior of the nanoclay added banana/jute hybrid intra-ply woven composite. In this investigation, addition of nanoclay improved the mechanical properties of the composites and also increased the storage modulus and glass transition temperature. From the free vibration results obtained, addition of nanoclay up to 2 wt% increased the natural frequency of the composite. Rajesh et al. [26] analyzed the woven fiber/polyester resin composite. They prepared different woven fabrics, such as plain, twill, basket, randomly orientated sisal fiber and unsaturated polyester resin composites. They used rice husk as a filler to enhance the properties. From the results obtained, it was concluded that the basket woven composite showed better stiffness and strength, while the natural filler increased the vibration behavior.

Moving forward, Rajesh et al. [23] studied the free vibrational characteristics of banana/sisal/polyester composite. They used random oriented fiber. From the results obtained, it was concluded that the surface treatment increased the mechanical and vibration behavior of the composites. Vaziri et al. [27] conducted vibration analysis of cantilever beam using fast Fourier transform analyzer and the results showed that the fiber length and volumetric fraction influenced the vibration and mechanical properties of the composites. Rajeshkumar et al. [28] investigated into the vibration characteristics of phoenix species fiber/polyester resin reinforced composite beams. The results depicted that the highest natural frequency was obtained with 30 mm fiber length composite beam. Bennet et al. [29] carried out vibration analysis of a *Sansevieria cylindrica*/coconut sheath/polyester composite. The results showed a better natural frequency of the alkali-treated and silane-treated composites than the untreated. Lei et al. [30] studied the effect of woven structures on the vibration characteristic of glass fabric/epoxy composite plates. The results showed that the fiber volume content and yarn architectures had significant effects on the storage modulus, damping properties and frequencies of the composites. In addition, they recommended interlocked woven structure, because of its better properties when compared with the plain-woven. Rajesh et al. [25] researched on the viscoelastic properties and vibration characteristics of woven banana/jute hybrid composites. In like manner, Pothan et al. [31] investigated into the woven banana, glass fiber and polyester composites. Their results showed that two-layer composite enhanced or produced better tensile properties. Rajesh et al. [32] reported that the free vibration behavior and dynamic mechanical analysis of natural fiber composites and compared them with conventional and knitted composites. They concluded that the intra-ply laminate provided better results in terms of storage modulus and loss factor. Also, an addition of fabric yarn enhanced modal analysis more than other samples.

Based on the aforementioned extensive reported results from literature, the present work was done to fill the revealed research gap on influence of stacking arrangements vibration damping of 2–5 woven jute fiber mats/layers reinforced polyester composites, fabricated by compression molding technique. This is rarely and scarcely reported. Hence, this study addressed this gap both experimentally and analytically to benefit composite researchers, designers, manufacturers and users, as quest for optimization of properties and better application of natural fiber-based composites increase.

2 Experimental Details

2.1 Materials Used

Woven jute fiber mat of 300 × 300 mm and isophthalic polyester resin were used as reinforcement and matrix in the present study, respectively. The reinforcement and matrix were purchased from a local dealer at Chennai, Tamilnadu, India. The

Table 1 Different types of sample systems and their notations

S. No	Description of sample systems	Sample
1	Neat polyester resin plate	NPRP
2	2 Jute woven layer/polyester composite	2WJPC
3	3 Jute woven layer/polyester composite	3WJPC
4	4 Jute woven layer/polyester composite	4WJPC
5	5 Jute woven layer/polyester composite	5WJPC

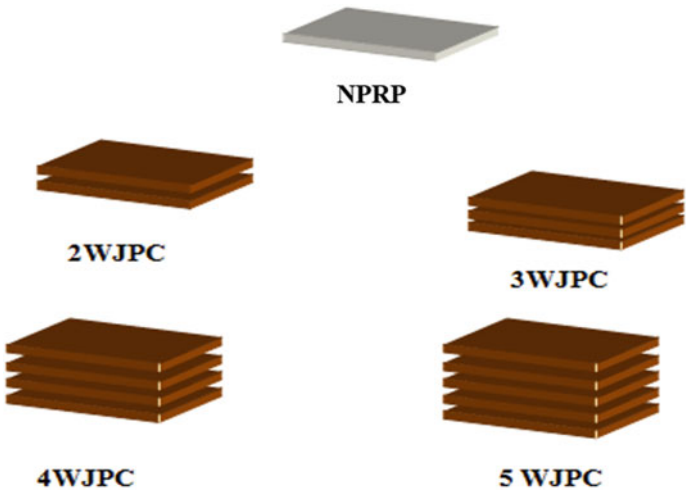

Fig. 1 Schematic illustration of the various sample systems used

composite laminates were fabricated under four different categories by increasing the number of woven mats from 2 to 5, using compression molding technique at a room temperature. After curing, the mold was taken from compression molding machine. The composite was removed from the mold and later cut into samples for flexural, short beam shear strength and free vibration tests, according to their respective ASTM standards. Various types of sample systems used and their notations are presented in Table 1. The samples are also schematically shown in Fig. 1, as fabricated.

2.2 Flexural Test

To evaluate the flexural strengths and moduli of the various five samples, three-point bending test was conducted by using Zwick/Roell universal testing machine. The flexural test set-up followed the ASTMD-790 standard with a test speed of 2 mm/min. For each type of sample, five similar samples were tested and the average

values were reported. The obtained values of moduli were used to evaluate the natural frequency theoretically, as later expressed in Eq. (3).

2.3 Inter-Laminar Shear Strength

Inter-laminar shear strength (ILSS) was performed according to ASTM D2344 standard. The short beam shear test was carried out with the sample length that was 6 times the thickness and the span length was 4 times the sample thickness. The width of the sample was 2 times the sample thickness. Five similar samples were tested for each sample type and then short beam shear strength was calculated by using Eq. (1).

$$F_{sbs} = \frac{0.75xP_{max}}{bxt} \tag{1}$$

where F_{sbs}= Short beam strength (MPa),
P_{max}= Maximum load observed during the test (N),
b = Sample width (mm), and,
t = Sample thickness (mm).

2.4 Free Vibration Test

The free vibration test was conducted in the cantilever mode with a sample size of 250 × 25 × 3 mm^3. An 8778A500sp accelerometer was fixed at one point on the cantilever and impulse was given at predetermined points with Model 1H-01 impulse hammer. NI-9233 data acquisition software was used to store the output data of the accelerometer and impact hammer. The DEWSoft 7.1.1 software was used for time signal conversion, using a fast Fourier transform. With the help of the curve fitting techniques, modal identification function was generated, which showed the peaks of the natural frequencies. The natural frequency and damping ratio were estimated from the amplitude *versus* frequency and acceleration *versus* time plots, respectively. The damping ratio (ζ) was determined using the logarithmic decrement formula, as expressed in Eq. (2).

$$\xi = \frac{1}{2\pi j} \ln \frac{X_i}{X_{i+j}} \tag{2}$$

where X_i represents the peak acceleration of the *ith* peak and X_{i+j} denotes the peak acceleration of the peak *j* cycles after *ith* peak. The experimental set-up for the free vibration test is shown in Fig. 2.

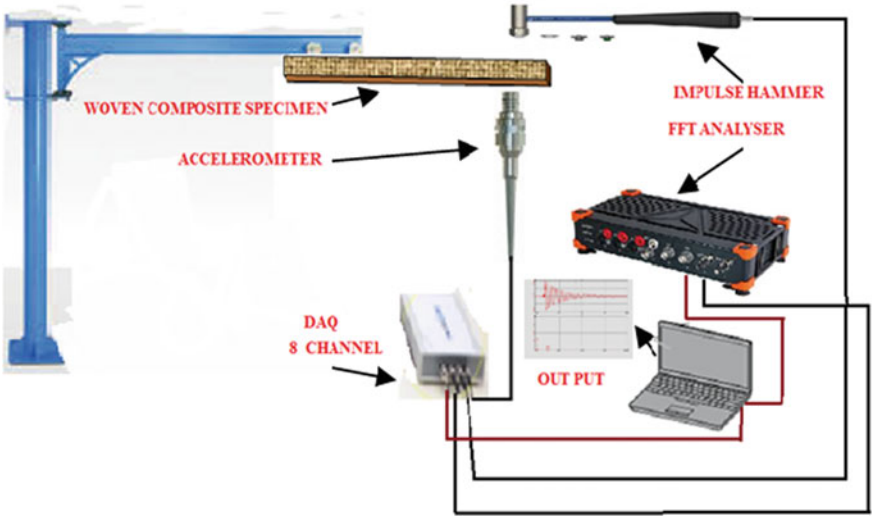

Fig. 2 Schematic illustration of the free vibration test set-up

2.5 Theoretical Modal Analysis

The theoretical natural frequency of cantilever beam was obtained from the Euler–Bernoulli model, as given in Eq. (3) [22]

$$\omega 1 = (\beta L)^2 \sqrt{\frac{EI}{\rho A L^4}} (\text{rad/sec}) \tag{3}$$

where E = Modulus of the beam (MPa),
I = Moment of Inertia (mm^4),
ρ = Density of composites (kg/mm^3),
A = Cross-sectional area of the cantilever beam (mm^2),
L = Length of the beam (mm), and.
β = Determined from the boundary conditions ($\beta = 1.875^2$ and 4.694^2).

3 Results and Discussion

3.1 Flexural Modulus

The influence of stacking 2–5 woven jute fiber mats/layers on the flexural modulus of various composite samples as well as neat polyester matrix were obtained according to the ASTMD-790 standard. Figure 3 shows the average moduli for the various

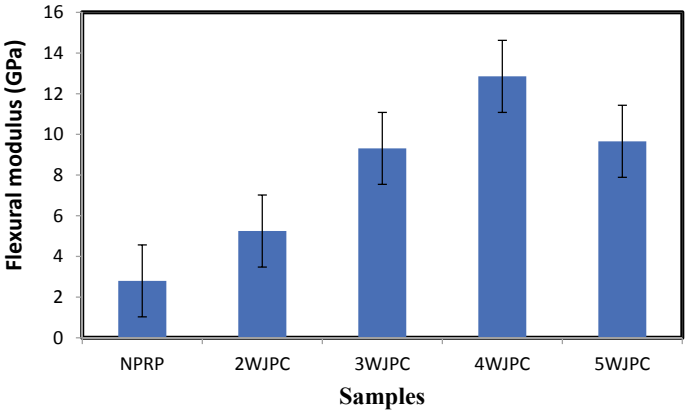

Fig. 3 Flexural moduli of the various samples

stacking sequences of the composite samples and NPRP. It was observed that the 4WJPC sample has the maximum modulus of 12.853 GPa, which was 78% higher than that of the NPRP.

3.2 Inter-Laminar Shear Strength

The ILSS plays a dominant role in estimating the adhesion between the reinforcement and matrix of a composite material. The short beam shear strength was calculated, using Eq. (1) for the various samples used. Figure 4 depicts the ILSS values of the various samples. It was observed that an increase in the number of woven jutes fiber layers caused an increase in the ILSS of the composite samples till a threshold value was achieved with addition of 4 layers, thereafter the ILSS decreased. In addition, it was observed that the 4WJPC sample has the maximum ILSS of 6.035 MPa and this value was calculated to be 40.62% higher than that of the matrix. The improvement in the ILSS was attributed mainly to the better interfacial strength/adhesion between the jute fiber mat and polyester matrix. However, the addition of 5 layers/mats to the matrix decreased the ILSS property of the 5WJPC sample, due to the poor interfacial adhesion between the fiber and matrix. This implied that the addition of woven jute fiber mat has a significant influence on the ILSS of the composite samples. For mat type of reinforcement, ILSS plays a major role in determining the properties of the composite, especially against delamination.

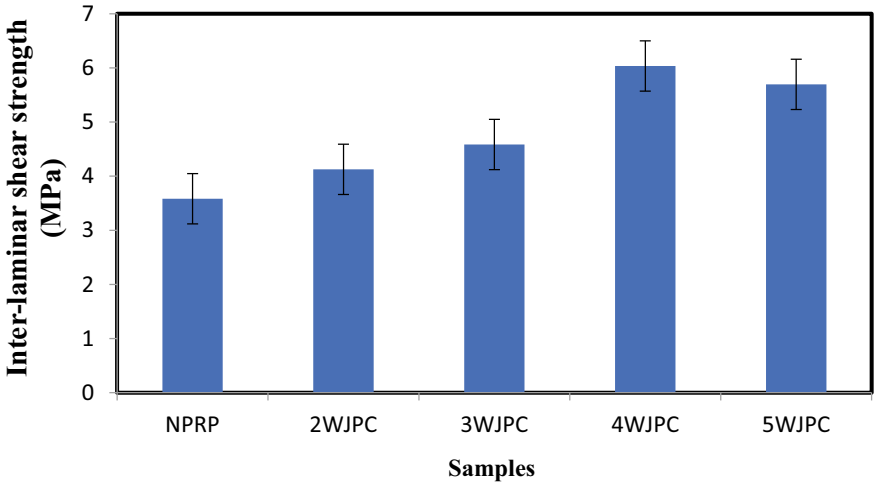

Fig. 4 Short beam shear strengths of the various samples

3.3 Free Vibration Test

Free vibration test (FVT) was carried out on the various samples used under cantilever mode. A sample plot of frequency *versus* time and amplitude *versus* time for the NPRP and 4WJPC sample are shown in Figs. 5a and b, respectively. The peak from the frequency *versus* time plot provided the natural frequencies at modes I, II and III. Table 2 presents the natural frequencies of the various samples under modes I, II and III. In mode I, from the results obtained, the natural frequency of the NPRP was 13.43 Hz. Furthermore, from Table 2, it is evident that the natural frequency increased with the addition of woven jute fiber mats. The maximum value of natural frequency of 32.96 Hz was obtained for the 4WJPC sample material. Similarly, the mode II frequency of resin was 119.6 Hz. Whereas, frequency of 231.9 Hz was recorded for 4WJPC sample. The experimental results thus obtained from free vibration tests were compared with the theoretical values that were obtained by using Eq. (3). Table 2 shows the comparison of the experimental and theoretical values of the natural frequencies at modes I, II and III, damping factors along with the moduli and short beam shear strengths of all the various samples (Table 3).

From the results presented in Table 3, it is further observed that the increase in the natural frequency and damping factor of the composite material depended on the modulus of the composite, ILSS, fiber-matrix interfacial bonding and the laminate arrangement [23]. Furthermore, the natural frequency of the woven fiber mat reinforced composite could depend on the fiber yarn orientation, gap and crimp [32]. In addition, it showed that the 5WJPC sample recorded a lower frequency, due to further addition of a layer. Hence, it suggested that a decrease in the fiber aspect ratio caused a resultant reduction in the modulus and thereby the frequency of the composite samples.

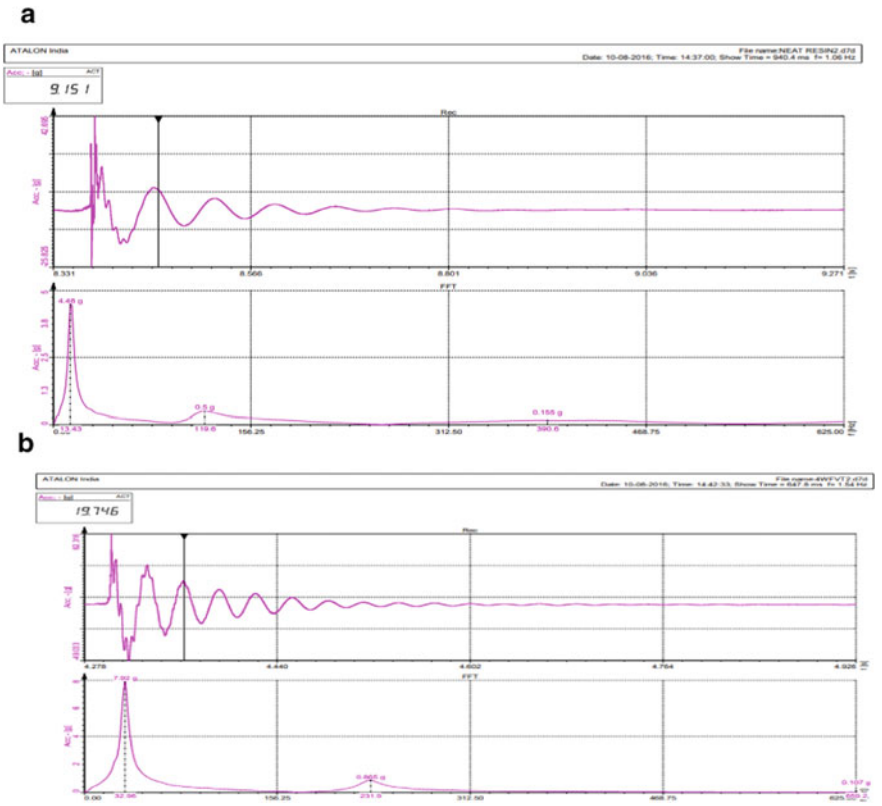

Fig. 5 **a** NPRP: (i) frequency versus time and (ii) acceleration versus time **b** 4WJPC: (i) frequency versus time and (ii) acceleration versus time

Table 2 Experimental and theoretical natural frequencies and damping factors of the various samples for all modes

Sample	Natural frequencies (Hz)						Damping factor (ξ)		
	Experimental			Theoretical					
	Mode								
	I	II	III	I	II	III	I	II	III
NPRP	13.43	119.6	390.6	20.75	121.50	221.30	0.07041	0.05122	0.04324
2WJPC	19.53	128.2	262.5	9.86	133.10	173.02	0.04187	0.03642	0.04215
3WJPC	21.97	158.7	277.1	19.90	142.75	349.25	0.04829	0.03923	0.04213
4WJPC	32.96	231.9	659.2	28.15	176.46	494.20	0.04865	0.05683	0.04682
5WJPC	20.75	159.9	473.6	37.60	235.68	659.20	0.03334	0.027328	0.0315

Table 3 Mechanical properties of the various samples

Sample	Mechanical properties	
	Flexural modulus (GPa)	Short beam shear strength (MPa)
NPRP	2.796	3.583
2WJPC	5.247	4.586
3WJPC	9.312	5.996
4WJPC	12.835	6.035
5WJPC	9.659	4.127

The damping ratios (**ξ**) of the various samples were obtained, using Eq. (2). The average damping ratios of all the various samples are presented in Fig. 6, considering modes I, II and III. It was observed that the 2WJPC sample recorded the lowest damping factor. This result showed that the addition of woven jute fiber mat decreased the damping factor of the composite, due to the absorption of energy, which was dissipated during the vibration. The 4WJPC sample recorded the highest damping factor among the composite samples, due to a better interfacial interaction between fiber and matrix. Also, this was previously evident from the ILSS results obtained. The 5WJPC samples recorded less damping factors in all the three bending modes considered, due to interaction between the fiber and low matrix as well as a resistance of free molecular mobilization [32]. Summarily, the addition of woven jute fiber mat to polyester resin increased the damping property of the composites.

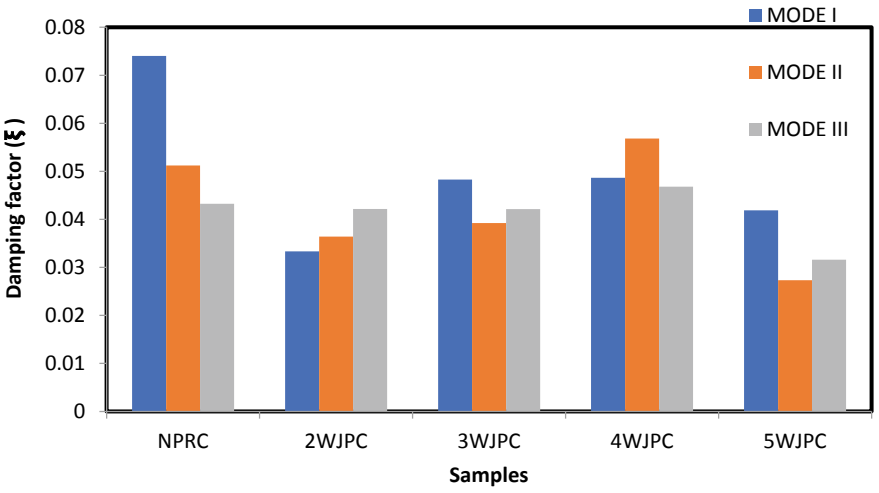

Fig. 6 Damping factors of the various samples

Table 4 ANOVA test for natural frequency of woven jute fiber composites for modes I, II and III

Properties	Model term	Sum of square	Degree of freedom	Mean square	F-value	Prob level	Reject equal means ($\alpha = 0.05$)	Power ($\alpha = 0.05$)
Natural frequency	Between	392,974.7	2	196,487.3	20.6971	0.00013	Yes	0.99947
	Within	113,921.8	12	9493.484	–			
	Adjusted Total	506,896.5	14					
	Total		15					

3.4 Analysis of Variance

The results obtained from ANOVA of natural frequency of modes I, II and III are shown in Table 4.

ANOVA simply described source of variation in frequency as per between and within groups. The p-value used was less than 0.05. Also, from Table 4, it can be concluded that the F-critical was lesser than F-value. Therefore, there was null hypothesis, which can be rejected, while accepting alternative hypothesis, which implied that there was significant effect of layer sequence on the natural frequency of the composite. ANOVA does not reveal the differences between the means of layer arrangement. For this purpose, Tukey–Kramer's method was employed. This method provides 95% accuracy level**.** From Table 5, it is observed that the method provided joint simultaneous confidence intervals for all pairwise differences between the means. Also, its reports also provided the multiple comparison of p-values. This was the significance level at which this difference became significant, using the Tukey–Kramer multiple comparison procedure.

4 Conclusions

The effects of reinforcing polyester resin with 2–5 jute woven mats on vibration damping and viscoelastic behaviors of the resultant composite samples have been extensively analysed, using both experimental and analytical methods. From the results obtained, the following concluding remarks can be deduced.

- The 4WJPC sample has the maximum natural frequencies of 32.96, 231.90 and 659.20 under modes I, II and III, respectively. With addition of woven jute fiber mat, the natural frequency of the composite increased, 40% higher than that of NPRP. However, 5WJPC sample produced the lowest damping factor at all modes, when compared with other samples. This was attributed to absence of better fiber-matrix interfacial adhesion.

Table 5 Tukey–Kramer's method for natural frequency

Tukey–Kramer's all pairs simultaneous confidence intervals of mean difference and p-value						
Response of modes I, II and III						
Term A						
Alpha = 0.050, Error term = S(A), DF = 12, MSE = 9,493,484, Critical value = 37,727						
Comparison groups	Count	Mean	Lower 95.0% Simult. C.I	Mean difference	Upper 95.0% Simult. C.I	P-value
Mode I	5	21.728				
Mode II	5	159.66	−302.322	−137.932	26.45803	0.10466
Mode III	5	412.60	−555.262	−390.872	−226.482	0.00010
Mode II	5	159.66				
Mode I	5	21.728	−26.45803	137.932	302.3220	0.10466
Mode III	5	412.60	−477.330	−252.940	−88.54997	0.00386
Mode III	5	412.60				
Mode I	5	21.728	226.4820	390.872	555.2620	0.000010
Mode II	5	159.66	88.54997	252.940	417.3300	0.003860

- From the ANOVA results obtained from the natural frequencies of modes I, II and III, the p-value was less than 0.05 and F-critical was lesser than F-value. Therefore, there was null hypothesis. It can be rejected, while alternative hypothesis was accepted. This implied that there was significant effect of layer sequence on the natural frequency of the composite. Therefore, Tukey-Kramer's method was suggested for alternative hypothesis, which provided an accuracy level of 95% and multiple comparison of p-values.
- Lastly, from experimental and theoretical comparison, both 2WJPC and 4WJPC experimental results agreed with Guth model, at lower frequencies than others. This can be attributed to the absence of constraints in the effect of fiber-matrix adhesion and heterogeneous composite structure.

Acknowledgements We hereby acknowledge and sincerely appreciate unalloyed supports from the managements of the following institutions: A.V.C. College of Engineering, Mayiladuthurai, Rajalakshmi Engineering College, Chennai as well as the Kalasalingam Academy of Research and Education Tamil Nadu, India.

Data Availability The raw/processed data required to reproduce these findings cannot be shared at this time as the data also forms part of an ongoing study.

References

1. Zhang C, Garrison TF, Madbouly SA, Kessler MR (2017) Recent advances in vegetable oil-based polymers and their composites. Prog Polym Sci 71:91–143. https://doi.org/10.1016/j.progpolymsci.2016.12.009
2. Thakur VK, Thakur MK, Gupta RK (2014) Raw natural fiber–based polymer composites. Int J
3. Drzal LT, Mohanty AK, Misra M (2001) Bio-composite materials as alternatives to petroleum-based composites for automotive applications. Magnesium 40:1–3
4. Krishnasamy S, Thiagamani SMK, Muthu Kumar C et al (2019) Recent advances in thermal properties of hybrid cellulosic fiber reinforced polymer composites. Int J Biol Ma cromol 141:1–13. https://doi.org/10.1016/j.ijbiomac.2019.08.231
5. Senthilkumar K, Siva I, Rajini N, Jeyaraj P (2015) Effect of fibre length and weight percentage on mechanical properties of short sisal/polyester composite. Int J Comput Aided Eng Technol 7:60–71
6. Faruk O, Bledzki AK, Fink H, Sain M (2014) Progress report on natural fiber reinforced composites. Macromol Mater Eng 299:9–26
7. Senthilkumar K, Saba N, Rajini N et al (2018) Mechanical properties evaluation of sisal fibre reinforced polymer composites: A review. Constr Build Mater 174
8. Thiagamani SMK, Krishnasamy S, Muthukumar C et al (2019) Investigation into mechanical, absorption and swelling behaviour of hemp/sisal fibre reinforced bioepoxy hybrid composites: effects of stacking sequences. Int J Biol Macromol 140:637–646. https://doi.org/10.1016/j.ijbiomac.2019.08.166
9. Sanjay MR, Arpitha GR, Naik LL et al (2016) Applications of natural fibers and its composites: an overview. Nat Resour 7:108–114
10. Krishnasamy S, Muthukumar C, Nagarajan R et al (2019) Effect of fibre loading and Ca(OH) 2 treatment on thermal, mechanical, and physical properties of pineapple leaf fibre/polyester reinforced composites. Mater Res Express 6:085545. https://doi.org/10.1088/2053-1591/ab2702
11. Thiagamani SMK, Krishnasamy S, Siengchin S (2019) Challenges of biodegradable polymers: an environmental perspective. Appl Sci Eng Prog x:1. https://doi.org/10.14416/j.asep.2019.03.002
12. Mohanty AK, Misra M, Hinrichsen G (2000) Biofibres, biodegradable polymers and biocomposites: an overview. Macromol Mater Eng
13. Amico SC, Angrizani CC, Drummond ML (2008) Influence of the stacking sequence on the mechanical properties of glass/sisal hybrid composites. J Reinf Plast Compos 29:179–189. https://doi.org/10.1177/0731684408096430
14. Sapuan SM, Leenie A, Harimi M, Beng YK (2006), Mechanical properties of woven banana fibre reinforced epoxy composites. Mater Des 27:689–693. https://doi.org/10.1016/j.matdes.2004.12.016
15. Jacob M, Varughese KT, Thomas S (2006) A study on the moisture sorption characteristics in woven sisal fabric reinforced natural rubber biocomposites. J Appl Polym Sci 102:416–423
16. Pothan L, a., Mai YW, Thomas S, Li RKY, (2008) Tensile and flexural behavior of sisal fabric/polyester textile composites prepared by resin transfer molding technique. J Reinf Plast Compos 27:1847–1866. https://doi.org/10.1177/0731684408090342
17. Venkateshwaran N, ElayaPerumal A (2012) Mechanical and water absorption properties of woven jute/banana hybrid composites. Fibers Polym 13:907–914
18. Ahmed KS, Vijayarangan S, Rajput C (2006) Mechanical behavior of isothalic polyester-based untreated woven jute and glass fabric hybrid composites. J Reinf Plast Compos 25:1549–1569. https://doi.org/10.1177/0731684406066747
19. Rajesh M, Pitchaimani J (2017) Mechanical properties of natural fiber braided yarn woven composite: comparison with conventional yarn woven composite. J Bionic Eng 14:141–150

20. Rajini N, Jappes JW, Rajakarunakaran S, Jeyaraj P (2012) Dynamic mechanical analysis and free vibration behavior in chemical modifications of coconut sheath/nano-clay reinforced hybrid polyester composite. J Compos Mater. https://doi.org/10.1177/0021998312462618
21. Etaati A, Mehdizadeh SA, Wang H, Pather S (2014) Vibration damping characteristics of short hemp fibre thermoplastic composites. J Reinf Plast Compos 33:330–341
22. Chandradass J, Kumar MR, Velmurugan R (2007) Effect of nanoclay addition on vibration properties of glass fibre reinforced vinyl ester composites. Mater Lett 61:4385–4388
23. Rajesh M, Pitchaimani J, Rajini N (2016) Free vibration characteristics of banana/sisal natural fibers reinforced hybrid polymer composite beam. Procedia Eng 144:1055–1059. https://doi.org/10.1016/j.proeng.2016.05.056
24. Maher A, Ramadan F, Ferra M (1999) Modeling of vibration damping in composite structures. Compos Struct 46:163–170
25. Rajesh M, Jeyaraj P, Rajini N (2016) Mechanical, dynamic mechanical and vibration behavior of nanoclay dispersed natural fiber hybrid intra-ply woven fabric composite. In: Nanoclay reinforced polymer composites. Springer, pp 281–296
26. Rajesh M, Singh SP, Pitchaimani J (2018) Mechanical behavior of woven natural fiber fabric composites: effect of weaving architecture, intra-ply hybridization and stacking sequence of fabrics. J Ind Text 47:938–959
27. Vaziri M, Vaziri A, Kadam SS (2013) Vibration analysis of a cantilever beam using FFT analyzer. Int J Adv Eng Technol 4:112–115
28. Rajeshkumar G, Hariharan V (2014) Free vibration characteristics of phoenix Sp fiber reinforced polymer matrix composite beams. Procedia Eng 97:687–693. https://doi.org/10.1016/j.proeng.2014.12.298
29. Bennet C, Rajini N, Jappes JTW et al (2015) Effect of the stacking sequence on vibrational behavior of Sansevieria cylindrica/coconut sheath polyester hybrid composites. J Reinf Plast Compos 34:293–306
30. Lei X, Rui W, Yong L, Jin L (2011) The effect of woven structures on the vibration characteristics of glass fabric/epoxy composite plates. Def Sci J 61:
31. Pothan L, a. (2005) The Static and Dynamic Mechanical Properties of Banana and Glass Fiber Woven Fabric-Reinforced Polyester Composite. J Compos Mater 39:1007–1025. https://doi.org/10.1177/0021998305048737
32. Rajesh M, Pitchaimani J (2018) Dynamic mechanical and free vibration behavior of natural fiber braided fabric composite: comparison with conventional and knitted fabric composites. Polym Compos 39:2479–2489

Experimental Study of Flexure and Shear Parameters for Glass Fiber Reinforced Polymer Rebars Concrete Beams

S. B. Darji and D. R. Panchal

Abstract Glass Fiber Reinforced Polymer (GFRP) is a non-corrosive material. Recently, GFRP rebars have been introduced in the construction industry as a replacement for steel rebars in order to avoid the problem of corrosion in steel. In this research, 15 full-sized reinforced concrete (RC) beams have been casted using GFRP and steel both as longitudinal reinforcement material as well as stirrup material. The flexural performance of GFRP rebar RC beams has been compared with steel rebar RC beams. Some of the beams have been prepared without stirrups in order to study the significance of stirrups in resisting shear forces. It was found that RC beams with GFRP rebar as longitudinal reinforcement and steel as stirrup material were able to withstand the maximum load. The provision of steel stirrups improved the load-carrying capacity by more than 40%. The deflection of GFRP rebar RC beams was observed to be 4–5 times more as compared to conventional RC beams.

Keywords Digital dial gauge · Flexure test · GFRP rebar · Reinforced concrete beam

1 Introduction

Steel has been used as a reinforcement material in RC structures for decades. However one of the major drawbacks of using steel as reinforcement material is its susceptibility to corrosion. Over the period of time, a huge amount of money needs to be invested in reconstructing/retrofitting structures due to corrosion of steel reinforcement. Recent advances in construction materials have led to the development of GFRP materials. These materials are non-corrosive in nature and hence can be used as an alternative to steel as a reinforcing material. Besides being non-corrosive,

S. B. Darji (✉) · D. R. Panchal
Department of Applied Mechanics and Structural Engineering, MSU Baroda, Vadodara 390001, India
e-mail: sbdarji-appmech@msubaroda.ac.in

D. R. Panchal
e-mail: drpanchal-appmech@msubaroda.ac.in

S. B. Singh et al. (eds.), *Fiber Reinforced Polymeric Materials and Sustainable Structures*, Composites Science and Technology, https://doi.org/10.1007/978-981-19-8979-7_13

it is also lightweight (around 20% weight of steel), non-conductive, and has almost double the tensile strength of steel. The only downside to it is the lack of ductility [1] and the non-availability of pre-manufactured fiber reinforced polymer (FRP) stirrups [4]. Along with GFRP rebars, Carbon Fiber Reinforced Polymer (CFRP), Basalt Fiber Reinforced Polymer (BFRP), Aramid Fiber Reinforced Polymer (AFRP), etc. are other types of non-corrosive rebar materials. However, the GFRP rebar is most popular due to its ease of availability and cost-efficiency. Also, the bond strength of GFRP rebars was found to be nearly the same as that of steel rebars [5]. The low ductility of GFRP can be managed if the beams are designed with an appropriate reinforcement ratio [2]. ACI 440.1R-15 [1] specify that GFRP rebars have been used in the construction of roads, bridges, offshore structures, etc. for several decades in various countries. Also, they have already developed design codes and guidelines for using Fiber Reinforced Polymer (FRP) rebars as reinforcements in RC structures, however, India is lagging behind in developing such guidelines due to a lack of research in this domain.

Construction practices and research in abroad have shown that GFRP rebars have been proved effective as reinforcing material in RC structures. This research work has been done to test the performance of GFRP rebars as reinforcing material in India and to encourage more research in this direction.

2 Experimental Procedure

2.1 Test Specimen and Procedure

In this study, a total of 15 full-sized RC beams were tested. The beams considered were 230 mm wide, 300 mm deep, and 1200 mm long. With these considered dimensions, beams when designed as per IS 456-2000 [3], achieved a flexural strength of 46.27 kNm and shear strength of 140.21 kN. A theoretical failure load of 280.42 kN was obtained. The spacing of the stirrups was kept such that the flexure and shear failure occurs at the same load. A total of 5 different types/categories of beams were cast each having 3 specimens. The elevation and cross-section of the typical beam is shown in Fig. 1. The nomenclature of the beams intends to reflect its main attribute. Beams with steel longitudinal reinforcement and steel stirrups were denoted as ‘SS’ category, beams with GFRP longitudinal reinforcement and GFRP stirrups were termed as ‘FF’ category. Beams with GFRP longitudinal reinforcement and steel stirrups were labelled in the ‘FS’ category. Beams with steel longitudinal reinforcement and no stirrups were termed as ‘S’ category and similarly beams with GFRP longitudinal reinforcement and no stirrups were considered as ‘F’ category. The next number indicates the number of specimens in that category. For instance, FS3 indicates the third specimen of the beam having GFRP rebars as longitudinal

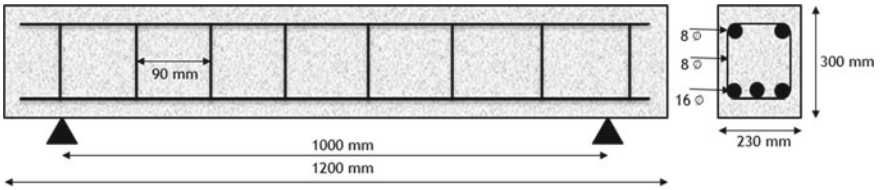

Fig. 1 Elevation and cross-section of beams

reinforcement with steel stirrups. A 4-point bend test was performed on each beam specimen. The beam was simply-supported with an effective span of 1000 mm. The load was applied in a gradually increasing manner and deflection at the center of the span was measured using a digital dial gauge.

2.2 Material Properties

The reinforcement cage of GFRP rebar with GFRP stirrups was prepared in an identical fashion as of steel reinforcement cage, as shown in Fig. 2. It should be noted that the GFRP stirrups were prepared by heating and bending GFRP rebars. As the GFRP rebars were prepared using thermoset resin, it's not ideal to reheat them. However, due to the lack of availability of pre-manufactured bent stirrups in the market, heating, and bending was the only viable option. M20 grade of concrete was used for this study. The tensile properties of the GFRP and steel rebar were provided by the manufacturer. The tensile strength of 8 mm and 16 mm diameter GFRP rebar were 860 MPa and 724 MPa respectively and that of 8 mm and 16 mm diameter steel rebar were 576 MPa and 535 MPa respectively.

Fig. 2 GFRP reinforcement cage

3 Test Results

Entire casting work was completed in three batches and the average concrete strength achieved was 26.66, 27.73, and 27.11 N/mm^2 respectively. The load vs mid-span deflection curves for various categories of the beam are shown in Fig. 3. In SS type specimens, micro flexural cracks were observed with increment in load. Major shear cracks were formed around 200 kN and the average failure load of the beams came out to be 280 kN with an average deflection of 1.67 mm. For FF type of specimens, flexural and shear, both types of cracks were observed with increment in load. The beams failed at an average load of 227 kN in shear at an average deflection of 2.59 mm, achieving less strength than SS type beams. FS category of beams achieved maximum average strength of 337 kN. The beams showed the development of both flexural and shear cracks with incremental loading and an average deflection of 5.22 mm was obtained at failure. S and F type specimens showed large shear cracks due to the absence of stirrups. S and F type of beams failed in shear at an average load of 242 kN and 233 kN respectively obtaining an average deflection of 1.09 mm and 4.83 mm respectively. The failure pattern of different categories of beams has been displayed in Fig. 4.

4 Conclusion

Based on the results obtained after the testing, the following conclusions could be drawn.

1. As the beams fail in shear, the failure load of ‘S’ and ‘F’ types of beams was found to be nearly identical.
2. Failure loads of ‘F’ and ‘FF’ specimens were nearly identical. This indicates that the provision of GFRP stirrups did not have much of an impact.
3. When steel stirrups were provided with GFRP reinforcements, the failure load increased by 44.6%. Hence achieved maximum strength amongst all types of beams.
4. Using GFRP rebars as longitudinal reinforcement, when GFRP stirrups were replaced by steel stirrups the failure load increased by 48.5%.
5. The failure load of ‘FS’ type of specimen was found to be 20% more as compared to the failure load of conventional ‘SS’ type of specimens.
6. Beams reinforced with GFRP rebars showed 4–5 times more deflection as compared to beams reinforced with steel rebars.
7. All the specimens failed under shear as the beam falls under medium deep beam category.

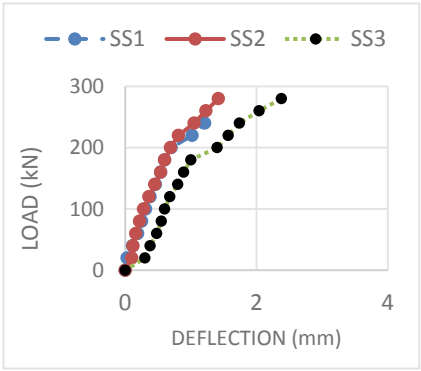

(a) SS beam

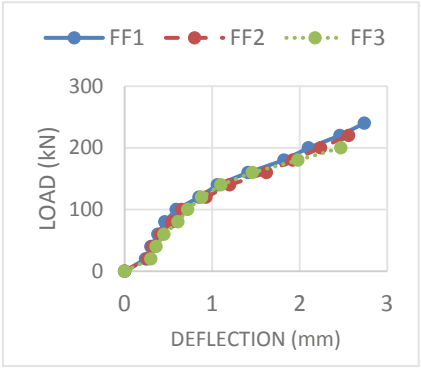

(b) FF beam

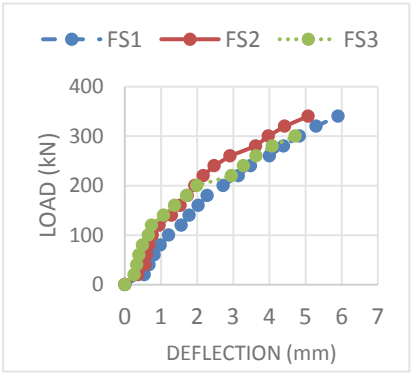

(c) FS beam

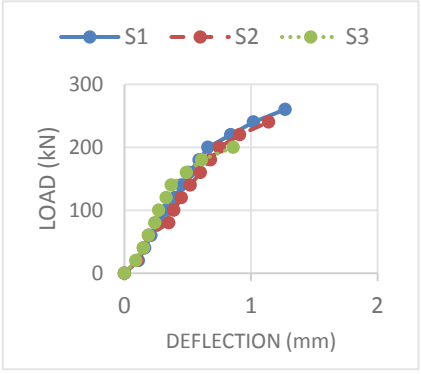

(d) S beam

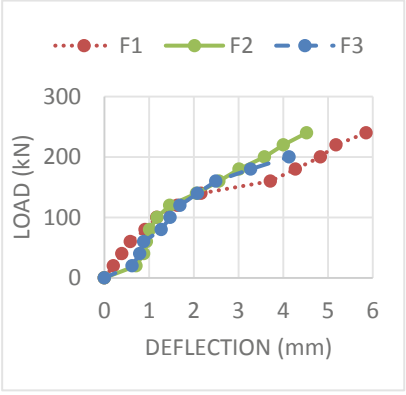

(e) F beam

Fig. 3 Load versus deflection curve of beam specimen

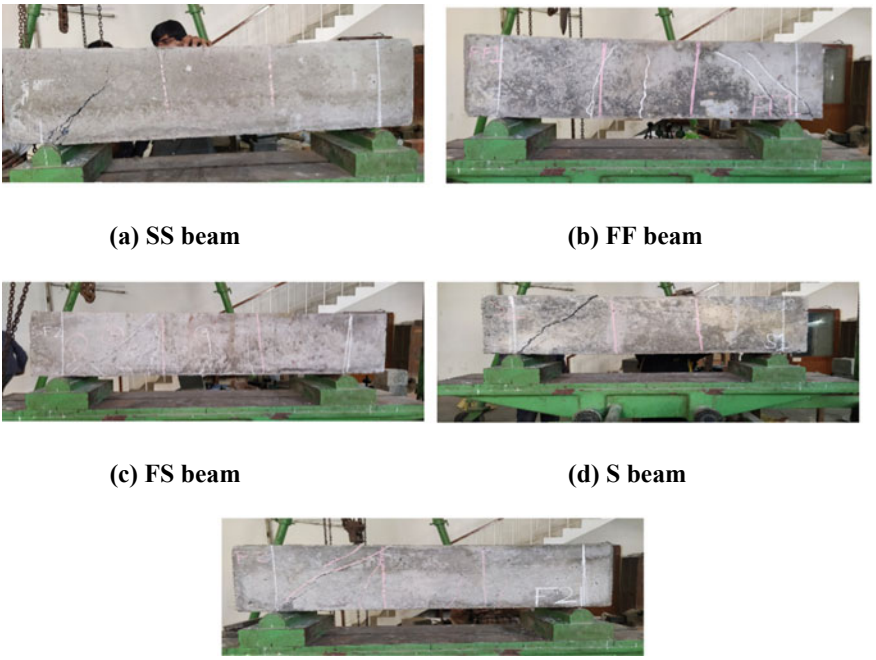

(a) SS beam **(b) FF beam**

(c) FS beam **(d) S beam**

(e) F beam

Fig. 4 Failure pattern of beam specimen

Acknowledgements The authors wish to express their appreciation for AGNI FIBER BOARDS PVT. LTD., Vadodara, for providing GFRP rebar specimens and properties related to it.

References

1. ACI 440.1R-15 (2015) Guide for the design and construction of structural concrete reinforced with fiber-reinforced polymer bars. ACI Committee 440, American Concrete Institute, Farmington Hills, Michigan
2. . El Zareef MA, El Madawy ME (2018) Effect of glass fiber rods on ductile behavior of reinforced concrete beams. Alexandria Eng J 57:4.71–4.79
3. IS 456:2000 (2000) Indian Standard Plain And Reinforced Concrete—Code of Practice, Bureau of Indian Standards, New Delhi
4. J Duic S Das 2018 Performance of concrete beams reinforced with basalt fibre composite rebar Constr Build Mater 176 470 481
5. A Rolland M Quiertant A Khadour S Chataigner K Banzarti P Argoul 2018 Experimental investigations on the bond behaviour between concrete and FRP reinforcing bars Constr Build Mater 173 136 148

Tailoring Properties of Electric Arc Furnace Slag Based Geopolymer Through Fly Ash Incorporation

Anant Mishra and Mukund Lahoti

Abstract Geopolymers are novel binders and are sustainable alternatives for conventional Portland cement. Geopolymers have emerged as a phenomenon of exceptional interest for the construction industry due to their excellent mechanical properties and sustainability in the past few years. A significant factor in producing geopolymers is the selection of the precursors. In this study, electric arc furnace slag (EAFS) obtained as waste from the steel industry is used as the precursor, and the influence of fly ash (FA) on the properties of the developed geopolymer is investigated. Scanning electron microscopy (SEM), X-Ray diffraction (XRD), and X-ray fluorescence (XRF) are used for material characterization and for analysing the microstructural development.

Keywords Geopolymer · Fly-ash · EAF-slag · Alkali activator

1 Introduction

Production of conventional cement is an energy-intensive and non-sustainable process. During cement production, 5–7% of global CO_2 emissions is released, which is one of the significant sources of climate change [1]. India as a developing nation, has a huge demand for developing infrastructure, making it the second-largest cement market next to China across the globe [2]. In the year 2020–21, India had a cement production capacity of 537 million tons (Mt), nearly 7.1% of gross production worldwide [3]. Hence, there is a vital need to develop a cement-free binder. In this context, much research has already been thru to use supplementary binder for construction purposes. Geopolymers are also one of the stable forms of supplementary binder developed through complex chemical reactions formed after alkali activation [4–6].

A. Mishra · M. Lahoti (✉)
Department of Civil Engineering, BITS Pilani, Pilani 333031, India
e-mail: Mukund.lahoti@pilani.bits-pilani.ac.in

A. Mishra
e-mail: p20190420@pilani.bits-pilani.ac.in

S. B. Singh et al. (eds.), *Fiber Reinforced Polymeric Materials and Sustainable Structures*, Composites Science and Technology, https://doi.org/10.1007/978-981-19-8979-7_14

Besides, steel constitutes the backbone of the construction industry, and India is again the second largest country in steel production (1896.4 Mt. in 2022) with a growth rate of 2.2% [7]. Steel slag is a waste generated after smelting crude steel and is associated with severe environmental issues due to the presence of heavy metals, which induces health hazards in the biosphere [8]. Electric arc furnace slag (EAFS) is generated by melting scrap steel and pig iron [9]. Production of steel through the EAF route consumes 57%, 87%, and 67.5% less iron ore, coal, and limestone, respectively, compared to the integrated route [10, 11]. Industrial by-products such as fly ash (FA), silica-fume, bottom ash, blast furnace slag, and rice husk ash, are already being used as supplementary binder and have given promising results in terms of mechanical strength and durability [12–14]. However, very few studies have focused on using electric arc furnace slag (EAFS) as a source for geopolymer.

In this context Ozturk et al. [15] produced EAFS geopolymer mortar with comprehensive testing by varying the sodium silicate to sodium hydroxide (NaOH) ratio (SS:SH) as 1, 1.5, and 2, NaOH molarity as 4, 6, and 8 M), curing temperature as 40 and 80 °C, relative humidity conditions as 45 and 98% and curing time as 6 and 12 h. The highest strength of 22 MPa was achieved when SS:SH was kept 2, NaOH molarity 6 M, curing temperature 80 °C, relative humidity 98%, and curing time 12 h. Apithanyasai et al. [16] produced geopolymeric brick by alkali-activation of ambient cured EAFS along with FA as a binder incorporating waste foundry sand and experimentally investigated the mechanical and environmental assessment. Four mixes were analyzed by fixing the FA (30%), NaOH (8 M), SS:SH (2.5), and varying the different EAFS (10, 20 and 30%) and waste foundry sand (70, 60, 50, and 40%). The specimen reported the best strength of 25.8 MPa. Zaharaki et al. [17] developed EAFS based geopolymer paste with different molarity 8, 10, and 12 M of sodium hydroxide (NaOH). These specimens were exposed to high temperature curing conditions, resulting in 75 MPa of compressive strength. A similar study is performed by Rashad et al. [18] in which partial replacement of EAF slag with fly ash was done to produce a high-strength paste. The specimens were exposed for elevated curing at 40 °C for 6 h, with a fixed alkali to binder ratio of 0.3 and replacement levels (0.15, 30, 45, and 60%). The highest strength of 72 MPa was reported at 90 days with 70% EAFS and 30% FA.

From the above works of literature, it can be observed that EAF slag is a highly potential precursor for developing high strength geopolymer cured at elevated temperature. However, minimal studies are done for using EAF as a sole or part precursor and FA as a modifier, hence more research is needed to understand the influential parameters for developing EAFS-FA geopolymer. In this regard, this study aims to experimentally investigate the effect of different silicate modulus on oven-cured EAFS-FA based geopolymer.

2 Experimental Program

2.1 Materials

EAFS is an industrial waste generated while smelting the crude steel through the EAF route. The surface area and specific gravity of the EAFS is 350 m^2/kg and 3.17, respectively. FA is a waste generated after the combustion of coal. For this study class F FA [19] with surface area and specific gravity of 450 m^2/kg and 2.5 respectively was used. The general view and composition are shown in Fig. 1 and Table 1. The composition was obtained through Malvern Panalytical Epsilon1 XRF spectrometer.

For the activation of precursor, 98.8% pure 40 g/L NaOH pellets were dissolved in distilled water for 24 h forming 10 M sodium hydroxide solution prepared one day before mixed with sodium silicate (Na_2O = 15.50%, SiO_2 = 31%, H_2O = 53.5%, specific gravity = 1.56, baume = 51, and weight ratio = 2.0) in 1:2 mass ratio. XRD patterns of EAFS and FA as shown in (Fig. 2) were obtained at room temperature using a Rigaku MiniFlex II X-ray diffractometer. EAFS mainly consists of quartz, magnetite, fluorite and gehlenite. FA dominantly shows the phases of quartz, mullite, magnetite, and hematite.

Scanning electron microscopy was performed using Apreo LoVac FEI, on both EAFS and FA to gain insight into their microstructure. As shown in Fig. 3, EAFS contains irregular, elongated, and non-defined particle shapes and a dominantly agglomerated morphology. However, FA contains spherical-shaped particles with varied diameters.

Fig. 1 **a** EAF slag and **b** fly ash

Table 1 Chemical composition of class F fly ash and EAFS

% Chemical composition	SiO_2	Al_2O_3	Fe_2O_3	CaO	K_2O	SO_3	P_2O_5	TiO_2	Cr_2O_3	MnO	LOI
EAFS	29.3	5.5	7.4	49.5	4.1	0.9	–	1.2	0.6	0.7	0.6
Fly ash	54.7	26.6	8.7	2.5	2.1	0.2	1.1	3.5	–	0.1	2.2

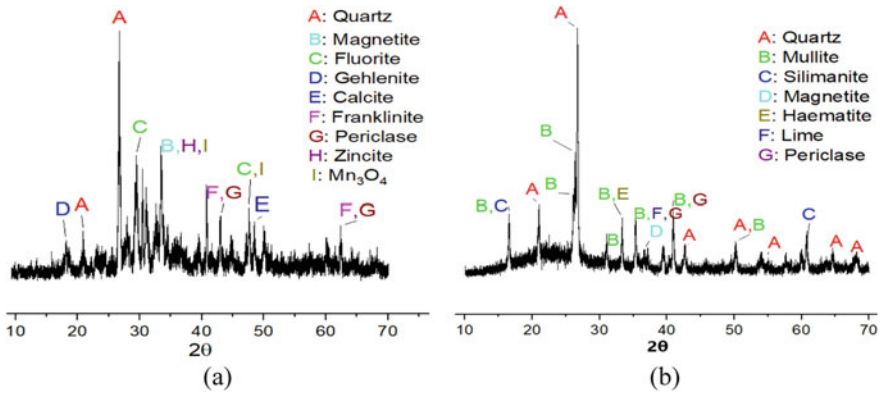

Fig. 2 XRD patterns of **a** EAF slag and **b** fly ash

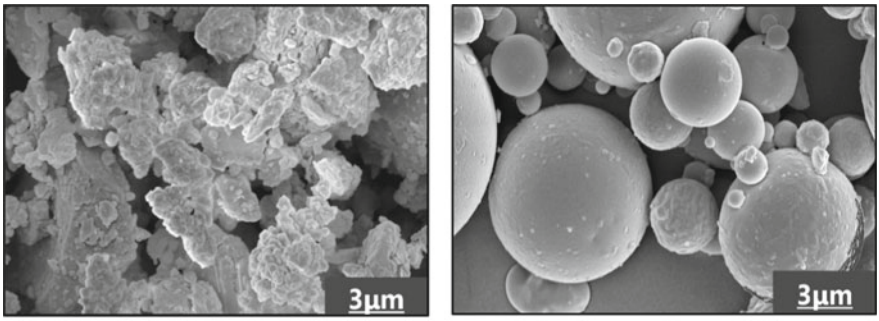

Fig. 3 SEM images of (a) EAF slag and (b) Fly Ash

2.2 Sample Preparations and Mixtures

Four different replacements (0%, 25%, 50%, and 100%) of EAFS with FA paste cubes were cast to investigate the effects of SS:SH on the microstructural changes of EAFS based geopolymer. The first was a control mix with 100% EAFS designated as E100, followed by E75, E50, and E25.

The samples were prepared in three steps: (1) dry mixing of EAFS and fly ash for about 2 min in the mixer; (2) slowly mixing the alkaline activator solution in the dry powder for about 5 min; (3) pouring the blended paste in 50 mm cube molds and vibrating it for 1 min and leveled the top surface. The molded samples are then covered with airtight plastic bags and placed in oven at 80 °C for 24 h. After heat curing for 24 h, samples are de-mold, and kept in airtight containers (to prevent moisture loss) at ambient temperature till further testing. In accordance to ASTM C 109 [20], the compressive strength of the pastes were performed after 28 days

using advanced compression testing machine and flowability was assessed by flow test table just after preparation of paste corresponding to ASTM C230-83 [21].

After testing for compressive strength, SEM was done on the small solid part of the specimens after proper cleaning and coated with thin gold layer for the analysis of developed strength.

3 Results and Discussion

3.1 Mechanical Strength

Four sets of geopolymeric pastes were prepared by replacing EAFS with FA in 0–75% by mass and by varying SS:SH from 1.5, 2.0, and 2.5 while keeping the same heat curing conditions and alkali to binder ratio of 0.40.

Mechanical strength of the casted geopolymeric cubes exhibited an increasing trend when SS:SH was increased from 1.5 to 2 and replacement of EAFS by FA reached 75%. It ranges from 15 to 46 MPa, which significantly influences. The reason for the lowest strength at SS:SH equal to 1.5 could be due to incomplete polymer bond formation within the blend. Several studies [21, 22] reported that a ratio range of 1.5–2.5 gave sufficient compressive strength; however, SS:SH 2.5 gave greater strength in this study. This could be because the reaction was able to proceed due to the availability of enough Na_2SiO_3, which coagulates and acts as a transitional substance or additive that enhanced the dissolution of ions during polymerization developing a Na_2O-Al_2O_3-SiO_2-H_2O (N-A-S-H) gel. The further increase in SS:SH ratio up to 3 slightly reduced the mechanical strength as excessive Na^+ ions might hinder the precipitation phase from coming into contact with the precursor and the alkaline activator [22].

In Fig. 4, it is also observed that, strength is significantly affected by the replacement of EAFS with FA. The sample E100 possesses the lowest strength when compared to E25; this could be due to the glassy nature of FA particles as they act as a micro-aggregate which makes the matrix dense reduces porosity and shrinkage. In addition to this as shown in Fig. 5, N-A-S-H gel generated from FA and C-A-S-H gel from EAFS are combinedly responsible for the denseness of matrix and strength development [18, 23, 24].

3.2 Flowability

As shown in Fig. 6 a decreasing flow trend was observed with an increasing portion of activator. The fluidity decreases as increase in the SS:SH ratio and EAFS content

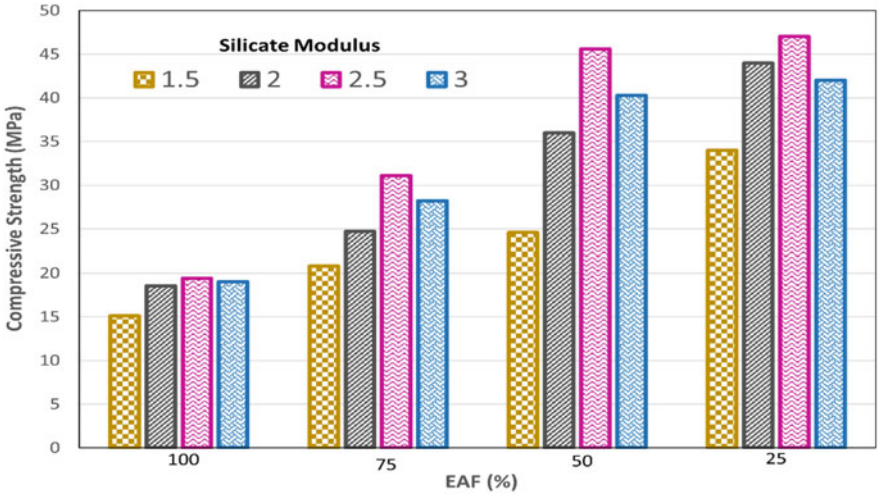

Fig. 4 Variation of 28-day compressive strength with EAFS replacement with different SS:SH ratios

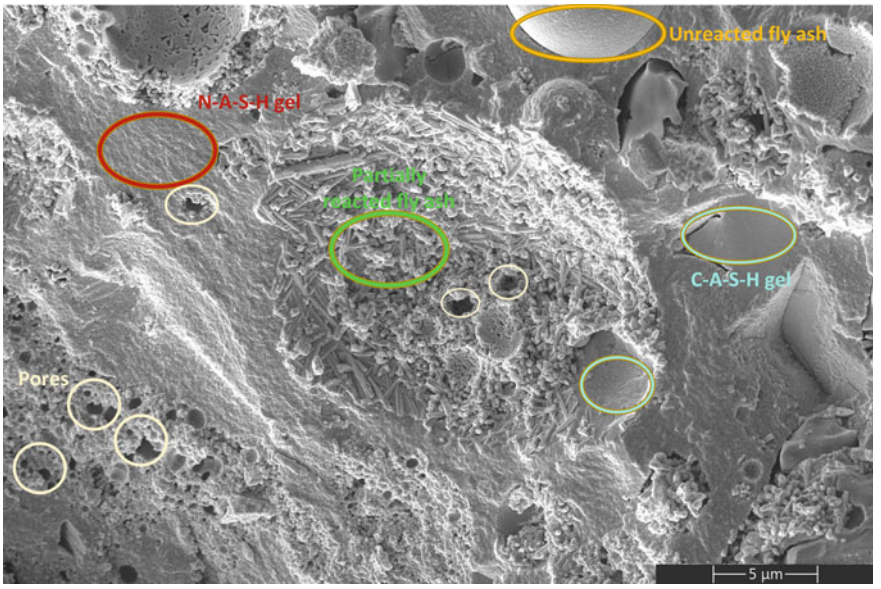

Fig. 5 SEM image of EAFS-FA geopolymer

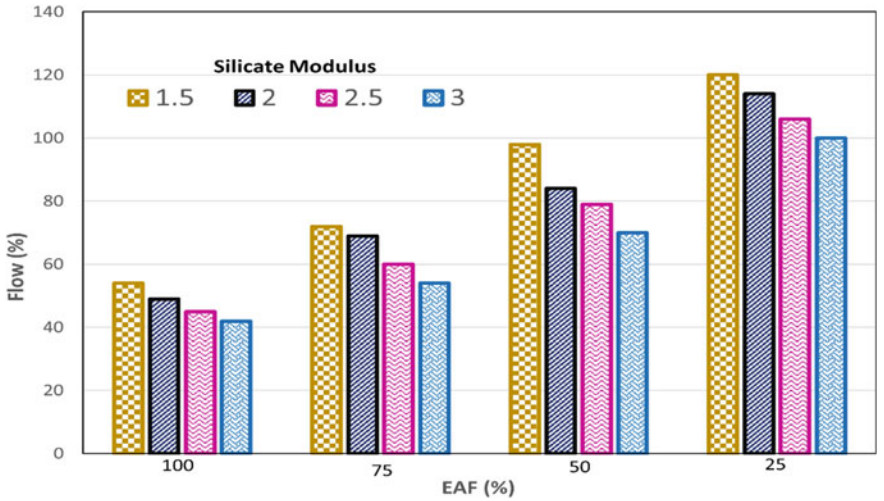

Fig. 6 Effect of FA and SM on flowability of the mixture

in the matrix. FA particles are spherical in shape that provides interparticle lubrication and improves the workability. However, the high content of SiO_3 decreases the flowability due to its viscosity [25].

4 Conclusions

This study investigates the effects of different SS:SH ratios and EAFS replacements on EAFS-FA blended geopolymer. The study led to some useful conclusions, most important of which are mentioned below:

The SS:SH ratios are the influential parameters for developing the compressive strength of alkali-activated EAFS-FA geopolymer paste.

Flowability is directly proportional to the replacement levels and with the compressive strength. However, flowability is inversely proportional to SS:SH but directly proportional to compressive strength.

FA particles are spherical in shape, which results in better workability.

An optimum SS:SH ratio is required for initiating the reaction as excessive silica ion disrupts the alkali mobility and excessive sodium ion imparts the efflorescence on the surface of the paste.

The compressive strength of the developed geopolymer is due to both N-A-S-H gel and C-A-S-H gel.

Declaration of Competing Interest The authors declare that they have no known competing financial interests or personal relationships that could have appeared to influence the work reported in this paper.

References

1. BC McLellan RP Williams J Lay A Riessen Van GD Corder (2011) Costs and carbon emissions for geopolymer pastes in comparison to ordinary portland cement J Clean Prod 19(9–10):1080–1090 https://doi.org/10.1016/j.jclepro.2011.02.010
2. "April 2021," African J Hosp Tour Leis 10(2) (2021). https://doi.org/10.46222/ahhtl.197707 20.000
3. UC Mishra S Sarsaiya A Gupta (2022) A systematic review on the impact of cement industries on the natural environment. Environ Sci Pollut Res. https://doi.org/10.1007/s11356-022-186 72-7
4. Dadsetan S, Siad H, Lachemi M, Mahmoodi O, Şahmaran M (2022) Geopolymer binders containing construction and demolition waste
5. Provis JL (2018) Alkali-activated materials. Cem Concr Res 114:40–48 https://doi.org/10. 1016/j.cemconres.2017.02.009
6. Duxson P, Fernández-Jiménez A, Provis JL, Lukey, GC, Palomo A , Deventer Van JSJ (2007) Geopolymer technology: The current state of the art. J Mater Sci 42(9) 2917–2933 https://doi. org/10.1007/s10853-006-0637-z
7. W. S. Association, "PRESS RELEASE—public policy paper release, Climate change and the production of iron and May 2021
8. Shilar FA, Ganachari SV, Patil VB, Nisar KS, Abdel-Aty AH, Yahia IS (2022) Evaluation of the effect of granite waste powder by varying the molarity of activator on the mechanical properties of ground granulated blast-furnace slag-based geopolymer concrete. Polymers (Basel) 14(2). https://doi.org/10.3390/polym14020306
9. Li X , Sun W, Zhao L, Cai J (2018) Material metabolism and environmental emissions of BF-BOF and EAF steel production routes. Miner Process Extr Metall Rev 39(1):50–58. https:// doi.org/10.1080/08827508.2017.1324440
10. World Steel Association (2011) Steel and raw materials, vol 15, no 4, pp 710–739 [Online]. Available: https://worldsteel.org/dms/internetDocumentList/fact-sheets/Fact-sheet_ Raw-materials2011/document/Factsheet_Raw%20materials2011.pdf
11. Steel G, Report W (2019) Green steel by EAF route: a sustainable value chain in the EU circular economy scenario, vol 32, no 2, pp 16
12. Tripathy A, Acharya PK (2022) Characterization of bagasse ash and its sustainable use in concrete as a supplementary binder—a review. Constr Build Mater 322(December 2021):126391. https://doi.org/10.1016/j.conbuildmat.2022.126391
13. Alamgir Kabir AISM, Johnson Alengaram U, Jumaat MZ, Sharmin A Influence of molarity and chemical composition on the development of compressive strength in POFA based geopolymer mortar. Hindawi Publishing Corporation. https://doi.org/10.1155/2015/647071
14. Gooi S, Mousa AA, Kong D (2020) A critical review and gap analysis on the use of coal bottom ash as a substitute constituent in concrete. J Clean Prod 268:121752. https://doi.org/10.1016/ j.jclepro.2020.121752
15. Ozturk M, Bankir MB, Bolukbasi OS, Sevim UK (2019) Alkali activation of electric arc furnace slag: Mechanical properties and micro analyses. J Build Eng 21(October 2018):97–105. https:// doi.org/10.1016/j.jobe.2018.10.005
16. Apithanyasai S, Supakata N, Papong S (2020) The potential of industrial waste: using foundry sand with fly ash and electric arc furnace slag for geopolymer brick production. Heliyon 6(3):e03697. https://doi.org/10.1016/j.heliyon.2020.e03697
17. Zaharaki D, Galetakis M, Komnitsas K (2016) Valorization of construction and demolition (C&D) and industrial wastes through alkali activation. Constr Build Mater 121:686–693 https:// doi.org/10.1016/j.conbuildmat.2016.06.051
18. Rashad AM, Khafaga SA, Gharieb M (2021) Valorization of fly ash as an additive for electric arc furnace slag geopolymer cement. Constr Build Mater 294:123570. https://doi.org/10.1016/ j.conbuildmat.2021.123570

19. ASTM C618-19 (2019) Standard specification for coal fly ash and raw or calcined natural Pozzolan for use as a mineral admixture in Portland cement concrete. American Society for Testing and Materials, West Conshohocken, PA
20. ASTM C109/C109M-02 (2020) Standard test method for compressive strength of hydraulic cement mortars. Annual B. ASTM Standard, vol 04, p 9
21. ASTM C230 (2010) standard specification for flow table for use in tests of hydraulic cement 1. Annual B. ASTM Standard, no. Note 2, pp 4–9
22. Hwang CL, Huynh TP (2015) Effect of alkali-activator and rice husk ash content on strength development of fly ash and residual rice husk ash-based geopolymers. Constr Build Mater 101:1–9. https://doi.org/10.1016/j.conbuildmat.2015.10.025
23. Rashad AM (2015) Influence of different additives on the properties of sodium sulfate activated slag. Constr Build Mater 79:379–389. https://doi.org/10.1016/j.conbuildmat.2015.01.022
24. Song W (2020) Efficient use of steel slag in alkali-activated fly ash-steel slag-ground granulated blast furnace slag ternary blends. Constr Build Mater 259:119814. https://doi.org/10.1016/j.conbuildmat.2020.119814
25. Zhang P, Gao Z, Wang J, Guo J, Hu S, Ling Y (2020) Properties of fresh and hardened fly ash/slag based geopolymer concrete: a review J Clean Prod 270:122389. https://doi.org/10.1016/j.jclepro.2020.122389

Numerical Investigation of Nonlinear Guided Wave Propagation in a Functionally Graded Material

Mohammed Aslam and Jaesun Lee

Abstract Functionally graded materials (FGM) have recently received extensive attention for their exceptional mechanical properties. This paper presents the nonlinear interaction of the guided waves with micro-crack in an FGM plate. For this purpose, a 2D finite element model of an FGM plate composed of ceramic and metal mixture is developed. The effective gradient of the properties is expressed by a continuous polynomial law as a function of the thickness. The simulation results showed that the generation of higher harmonics provides a sensitive means for micro-crack detection in FGM plates. Moreover, the amplitudes of the harmonics increase with the increase in micro-crack length.

Keywords Functionally graded materials · Guided waves · Micro-crack · Nonlinear ultrasonics

1 Introduction

Bio-inspired composite materials with varying physical characteristics have recently attracted the interest of many engineers and researchers. These materials are also called functionally graded materials (FGM) which can solve the problems associated with stress channelling and stress peeling effects compared to the conventional layered composites [1, 2]. Due to the superior performance of FGM and the continuous development of technology, it has been widely used in biomedical, optics, aerospace, civil engineering, automotive, and various other fields [3].

In recent years, guided waves in FGM structures have received much interest for non-destructive testing. Several numerical and analytical methods have been developed to study guided wave propagation in plate structures made of FGM.

M. Aslam (✉)
School of Civil Engineering, REVA University, Bengaluru 560064, India
e-mail: pcaslam4@gmail.com

J. Lee
School of Mechanical Engineering, Changwon National University, Changwon, South Korea
e-mail: jaesun@changwon.ac.kr

S. B. Singh et al. (eds.), *Fiber Reinforced Polymeric Materials and Sustainable Structures*, Composites Science and Technology, https://doi.org/10.1007/978-981-19-8979-7_15

Zhu et al. [4] developed a recursive formulation of the reverberation-ray matrix to investigate the dispersion behaviour of waves in the FGM plates. Gravenkamp et al. [5] used the scaled boundary finite element method (SBFEM) to calculate dispersion characteristics in plate structures. The technique applies to homogeneous plates, layered composites, and plates with continuously varying material parameters in the thickness direction. Amor et al. [6] employed the Peano-Series method for solving Lamb wave modes of lowest-order propagating in FGM plates made of aluminium nitride. Kuznetsov [7] studied the propagation of harmonic Lamb waves in plates made of FGM with transverse inhomogeneity using the modified Cauchy six-dimensional formalism. Dispersion curves for FGM isotropic plates with different kinds of exponential inhomogeneity are obtained and compared with those for homogenised isotropic plates. Malik et al. [8] presented a new approach for directly calculating group velocity curves using the wave and finite element (WFE) method. The WFE scheme exploits the periodicity of the structure to extract the group and phase velocity curves.

The guided waves have emerged as an active system capable of exciting the structure in a prescribed manner. Guided waves offer the advantage of large-area inspection with a minimum number of installed sensors [9]. Damage detection based on guided waves can be either linear on nonlinear. In the linear method, the wave characteristics like amplitude, time-of-flight, and dispersion are then analysed from the sensor signal to get information regarding the damage. However, linear methods require baseline data to compare with the existing data. Also, the changing environment and operational conditions affect the damage detection procedures [10]. Recent studies show that the nonlinear ultrasonic methods are advantageous compared to linear methods. This method does not depend on baseline data and is more sensitive to microcracks/fatigue cracks. The nonlinearity can be either due to material nonlinearity or contact nonlinearity [11–13].

This work investigates the interaction of primary guided waves with a microcrack in the FGM plate numerically. The nonlinearity considered in this study is due to breathing crack, which generates contact acoustic nonlinearity. The sensitivity of primary Lamb wave modes in detecting microcracks having different lengths is also studied. Numerical modelling of FGM structures is complicated because the mechanical properties of FGM vary throughout the boundary gradient smoothly. Strong mathematical background with knowledge of elasticity, mechanics, and extensive programming/scripting skills is required to develop and solve complex models. This work uses a simplified approach to model FGM using the commercially available software package Abaqus. The modelling aspects are discussed in the subsequent sections.

2 Finite Element Modelling

The geometry of the FGM plate considered for the study is shown in Fig. 1. The total length of the plate is 1 m.

The plate is made of a chrome-ceramic mixture. The lower surface of the plate consists of chrome (cr) alone, whereas the top surface of the plate is composed of only ceramic (cer). The material property is shown in Table 1. The effective material property (α^{eff}) of FGM possesses the following form:

$$\alpha^{eff} = \left(\alpha^{cer} - \alpha^{cr}\right)\left(\frac{y+h}{2h}\right)^{n} + \alpha^{cr} \tag{1}$$

where 2 h (12 mm) is the thickness of the plate, α denotes the material property, and n is the coefficient of the gradient. The typical profiles of the material property (density) that vary with thickness are shown in Fig. 2.

The FGM plate is assumed to be in plane strain condition. A four-node bilinear plane strain quadrilateral element (CPE4R) is used to mesh the FGM plate. The finite element model is discretised such that there are 15–20 elements per wavelength so

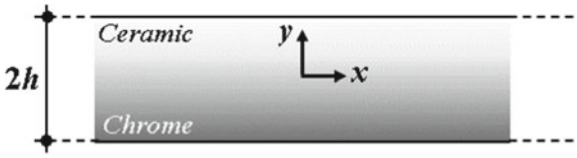

Fig. 1 Geometry of the FGM plate

Table 1 Material properties of FGM plate

Material	Density (kg/m^3)	Young's modulus (GPa)	Poisson's ratio
Ceramic	3900	299.86	0.27
Chrome	7190	248.04	0.21

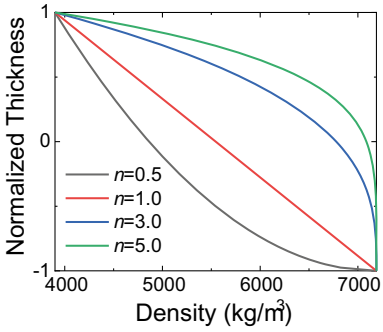

Fig. 2 Profile of density

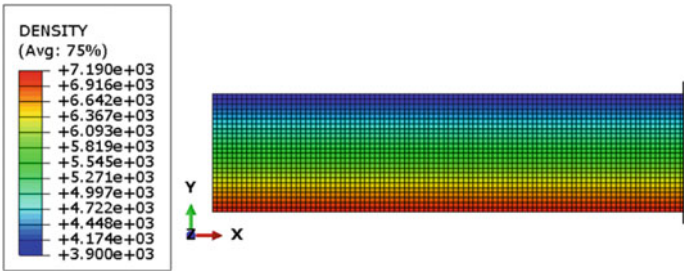

Fig. 3 Distribution of density across the thickness

that a good spatial resolution of the propagating wave is achieved. The time increment for explicit dynamic analysis is chosen based on the Courant-Friedrich-Levy criteria [14]. The fundamental Lamb wave modes are excited by applying a uniform force at the end of the plate. An 8-count Hanning windowed sinusoidal tone burst is used to excite Lamb wave modes.

To obtain a dimensional dependent property is not directly available in any package. However, it is possible to generate the required distributed property as a function of other values, which is only a function of position. The material properties such as density, Young's modulus, and Poisson's ratios are first defined as a function of temperature. The coefficient of thermal expansion is then set to zero to eliminate thermal stresses. The temperature values for each node are defined as a function of position (dimension). This makes material properties depend only on position. The density distribution across the thickness obtained through simulation is shown in Fig. 3.

3 Results and Discussion

The group velocities obtained by the finite element method (FEM) are compared with the available results. The coefficient n for the FGM plate is taken as 1. Figure 4 shows the comparison of group velocities. The maximum frequency considered for the current study is limited to 200 kHz to cut off higher wave modes. It is observed that the finite element solutions are in good agreement with the group velocity dispersion curves.

The displacement distribution of the Lamb wave modes is explored at a given frequency. The displacement profile of longitudinal (U1) and transverse (U2) components across the thickness for A_0 and S_0 wave modes is presented in Fig. 5. The mode shapes are plotted for ceramic, chrome, and FGM ($n = 1$) plates when the plate is excited with a central frequency of 100 kHz. It is observed that the U1 displacement under A_0 mode and the U2 displacements under S_0 mode are antisymmetric about the central plane of the plate for ceramic and chrome plates. However, FGM plates show a slightly inverse symmetry with respect to a deviated axis away from the geometrical

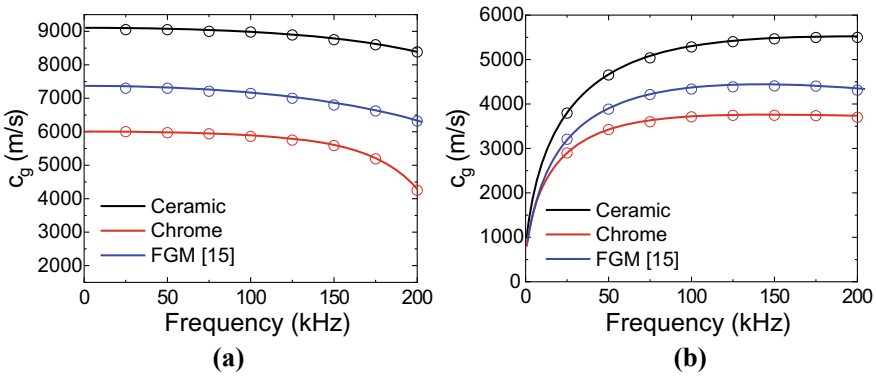

Fig. 4 Comparison of group velocities **a** S_0 mode, **b** A_0 mode (solid line [15], symbols—FEM)

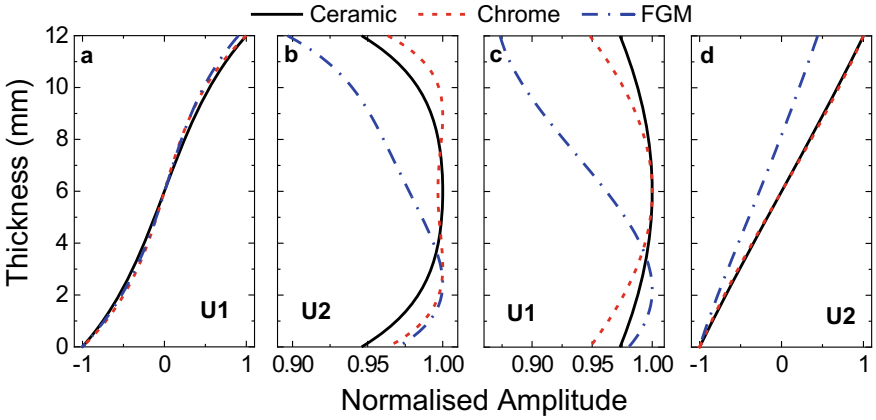

Fig. 5 Normalised displacement amplitudes of lamb wave modes **a** A_0 mode—U1, **b** A_0 mode—U2, **c** S_0 mode—U1, **d** S_0 mode—U2

axis of symmetry. Similarly, for ceramic and chrome plates, the U1 displacement in S_0 mode and U2 displacement A_0 is found to be symmetric with respect to the central axis of the plate. Whereas, for the FGM plate, the displacement components are not symmetric with respect to the central axis of the plate.

3.1 FGM Plate with a Microcrack

The interaction of primary guided waves with a microcrack in the FGM plate is then investigated numerically. The schematic diagram indicating the location of the microcrack and sensors (S1, S2, …) are shown in Fig. 6. For simulating contact

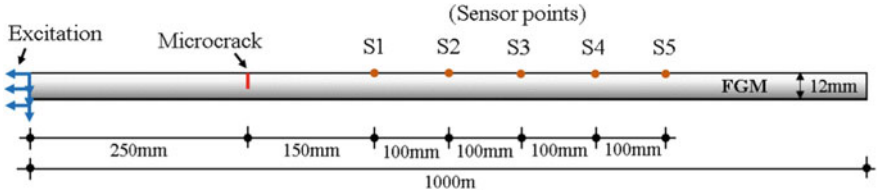

Fig. 6 FGM plate with a microcrack

acoustic nonlinearity, the crack in the plate is modelled as a seam crack. The details regarding the modelling aspects can be referred to our previous work [16]. Four different crack length to thickness ratios ($a/2h$) are considered for the study.

The displacement (U1) response in the time-domain and frequency-domain for different cases when the FGM plate is excited at a frequency of 100 kHz is shown in Fig. 7. It is observed that the waveform gets slightly distorted due to the presence of a microcrack. The shape of the wave packet changes considerably with increases in crack length. The same is reflected in the frequency domain. From Fig. 7b, it is understood that no harmonics are generated in the case of a healthy plate. However, for damaged plates, higher harmonics are generated in addition to the excitation frequency. It is also seen that the amplitude of harmonic components increases with an increase in crack length.

The use of the relative acoustic nonlinearity parameter is effective in characterising damage [11, 12]. The parameter is defined as A_2/A_1^2, where A_1 and A_2 are the amplitudes of the fundamental and second harmonic frequency components, respectively. The variation of this parameter is analysed for the FGM plate with different crack lengths. Figure 8a shows the variation of the relative nonlinearity parameter with respect to $a/2h$. It is observed that the relative amplitude increases with an increase in crack length for both the wave modes. The variation of the relative amplitude as a function of the propagation distance is plotted in Fig. 8b. Based on the

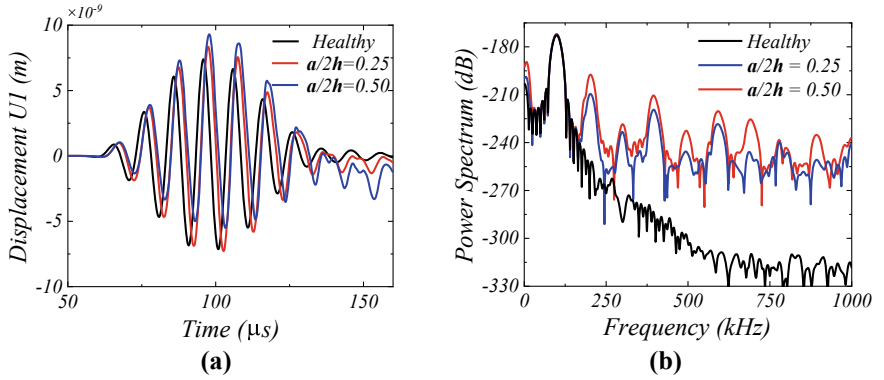

Fig. 7 Displacement (U1) response in **a** time-domain and **b** frequency-domain

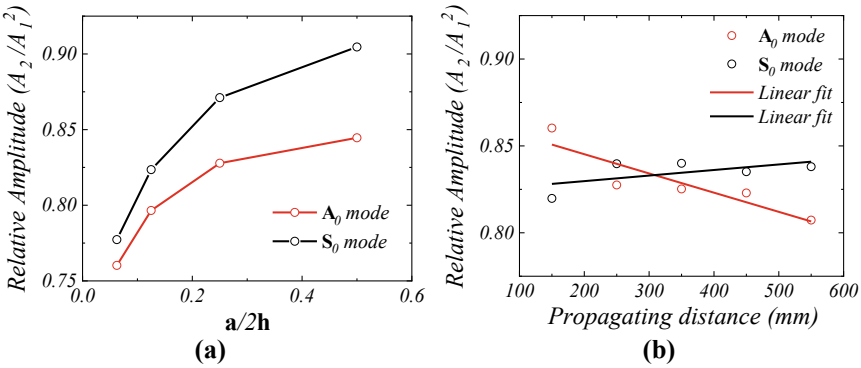

Fig. 8 Relative acoustic nonlinearity parameter as a function of **a** crack length to thickness, **b** propagating distance

linear fit, the relative amplitude increases with an increase in propagation distance for S_0 mode, whereas for A_0 mode, the relative amplitude decreases.

4 Conclusion

The nonlinear guided wave technique is investigated to detect microcracks in FGM plates. The interaction of primary Lamb waves with the microcrack of various lengths is performed using finite element simulations. The results indicate that higher harmonic generation provides a sensitive tool for detecting microcracks in FGM plates. Also, the acoustic nonlinearity parameter showed an increasing trend with an increase in the length of the micro-crack. The current study also introduces a simplified approach to modelling the FGM, which does not require deep knowledge of mathematical models and provides high accuracy.

References

1. Boggarapu V, Gujjala R, Ojha S, Acharya SK, Chowdary S, Gara DK (2021) State of the art in functionally graded materials. Composite Struct 262:113596
2. Lyu Y, Zhang J, Song G, Liu M, Wu B, He C (2019) The dispersion curves and wave structures of Lamb waves in functionally graded plate: theoretical and simulation analysis. AIP Conf Proc 2102:050020
3. Garg A, Belarbi M-O, Chalak HD, Chakrabarti A (2021) A review of the analysis of sandwich FGM structures. Composite Struct 258:113427
4. Zhu J, Ye GR, Xiang YQ, Chen WQ (2011) Recursive formulae for wave propagation analysis of FGM elastic plates via reverberation-ray matrix method. Compos Struct 93:259–270

5. Gravenkamp H, Song C, Prager J (2012) A numerical approach for the computation of dispersion relations for plate structures using the scaled boundary finite element method. J Sound Vib 331:2543–2557
6. Amor MB, Salah IB, Ghozlen MHB (2015) Propagation behavior of lamb waves in functionally graded piezoelectric plates. Acta Acustica United Acustica 101:435–442
7. Kuznetsov SV (2018) Lamb waves in functionally graded plates with transverse inhomogeneity. Acta Mech 229:4131–4139
8. Malik MK, Chronopoulos D, Ciampa F (2021) Direct calculation of the group velocity for two-dimensional complex, composite and periodic structures using a wave and finite element scheme. Appl Sci 11:4319
9. She G-L (2021) Guided wave propagation of porous functionally graded plates: the effect of thermal loadings. J Therm Stresses 44:1289–1305
10. Olisa SC, Khan MA, Starr A (2021) Review of current guided wave ultrasonic testing (GWUT) limitations and future directions. Sensors 21:811
11. Zhu W, Xiang Y, Liu C-J, Deng M, Ma C, Xuan F-Z (2018) Fatigue damage evaluation using nonlinear lamb waves with quasi phase-velocity matching at low frequency. Materials 11:1920
12. Ding T, Zhu W, Ma C, Xiang Y, Deng M, Xuan F-Z (2021) Influence of cyclic-loading induced fatigue micro-crack growth on generation of nonlinear ultrasonic lamb waves. J Nondestr Eval 40:1–12
13. Aslam M, Bijudas CR, Nagarajan P, Remanan M (2020) Numerical and experimental investigation of nonlinear lamb wave mixing at low frequency. J Aerospace Eng 33(4):04020037
14. Duczek S, Joulaian M, Düster A, Gabbert U (2014) Numerical analysis of lamb waves using the finite and spectral cell methods. Int J Numer Methods Eng 99:26–53
15. Benmeddour F, Moulin E, Assaad J, Dupont L (2013) Numerical investigation of the functionally graded materials by the interaction of the plate guided waves with discontinuities and cracks. Proc Meetings Acoust 19:030074
16. Aslam M, Nagarajan P, Remanan M (2021) Defect localisation using nonlinear lamb wave mixing technique. J Nondestr Eval 40:1–12

Effect of High Temperatures on Stiffness of Water Quenched Reinforced Concrete Columns Supplemented with Steel Fibers

K. Ratna Tej Reddy and M. K. S. S. Krishna Chaitanya

Abstract This paper aims to present the effect of temperature on stiffness and the rate of deterioration of stiffness between steel fiber reinforced concrete and reinforced concrete columns that were exposed to a temperature range of 500 to 800C, and on attainment the specimens were cooled by water with a time delay of 60 min and 180 min correspondingly. The study was carried out on 16 column specimens of which 8 were made of steel fiber reinforced concrete and again of which 4 were water cooled after an 60 min post attainment of the desired temperature, while the remaining 4 were water cooled after 180 min post attainment of the desired temperature. The same allocation was made for the other set of 8 columns with an only difference of being made out of just reinforced concrete instead of steel fiber reinforced concrete. Both the sets were heated to temperatures of 500, 600, 700 and 800C and quenched in water completely for 3 min.

Keywords Stiffness · Reinforced column · Destructive test · High temperature · Steel fiber

1 Introduction

The severity of natural disasters such as earthquakes and cyclones has increased in tandem with the advancement of structural safety in the current period of architecture. Even man-made disasters such as building fires and explosions have been kept under control thanks to active fire protection measures such as modern fire extinguishing technologies, faster emergency response times, and the use of high-strength concrete to withstand abrupt explosive loads. Passive fire prevention strategies, such as building the structure to withstand temperature stresses and having a

K. Ratna Tej Reddy (✉)
Department of Civil Engineering, Vignan Institute of Information Technology, Visakhapatnam 530049, India
e-mail: drratnatejreddy@gmail.com

M. K. S. S. Krishna Chaitanya
Department of Civil Engineering, Anil Neerukonda Institute of Technology and Sciences, Bheemunipatnam, Visakhapatnam 531162, India

S. B. Singh et al. (eds.), *Fiber Reinforced Polymeric Materials and Sustainable Structures*, Composites Science and Technology, https://doi.org/10.1007/978-981-19-8979-7_16

longer resilience to post-fire mishaps, such as collapsing, are given less emphasis. To support the above argument, the Plasco Building collapse in Tehran on January 19, 2017, costed the lives of 26 individuals, 16 of whom were firefighters, as a result of an explosion followed by fire. The behavior of concrete after a fire is an area that demands attention because the structure's strength has been compromised, making it more liable to collapse.

Steel fibers have proved to significantly improve the strength of plain concrete. Steel fibers in reinforced concrete have always produced better results in terms of tension and shear forces, but this study aims to throw some light on the behavior of steel fiber reinforced and normally reinforced concrete columns in compression that were exposed to high temperatures of 500 to 800C.

A comparable study looked at the mechanical performance of 300 fiber reinforced concrete specimens manufactured with different types of fibers made of steel, glass and polypropylene with varying percentages. The results showed an increase in compressive strength, load carrying capacity, and improved load deformation resistance as well as an increase in time before the first crack [1].

Steel fibres were found to improve the strength and mechanical properties of concrete in studies. However, several parameters like as aspect ratio, moisture content, shape, volume fractions, and others influence the compressive strength of concrete due to the presence of steel fibres [2].

Furthermore, another study found that adding steel fibres to concrete specimens improves bond strength and prevents brittle failure. The irregularly orientated steel fibres prevent the spread of randomly formed cracks, which frequently occur in shear planes and are ductile cracks [3].

2 Experimental Program

2.1 Methodology

A total of 16 column specimens were cast, of which 8 being supplemented with 1% steel fibres and the rest being produced without steel fibres. Each specimen containing steel fibres was set to a specific temperature (500, 600, 700, 800 °C), with two time delays (60 min and 180 min) post attainment of the set temperature. the temperature was maintained the same until the end of delay for water cooling. These 8 fibre reinforced specimens are then compared to non-fiber reinforced counterparts that have been exposed to similar conditions.

3 Specimen Details

The specimens were cast using a collapsible mold made of 18 mm thick water proof plywood. The column samples have a length of 1200 mm and a cross section of 150 × 150 mm; these parameters were selected for the test configuration using modal analysis [4, 5].

Cement and Aggregates: The concrete of M20 grading, with 0.48:1:1.3:3.33 mix proportions achieved by following IS 10262–2009 [6]. The cement used is 43-grade ordinary Portland cement (OPC) that complies with IS 8112–1989 [7]. Crushed stone that passed through an IS 20 mm sieve and was held on an IS 4.75 mm sieve was used as coarse aggregate, and river bed sand that corresponds to IS 383–1970 grading zone II is utilised as fine aggregate.

Fibers: The use of steel fibres decreases spalling and improves heat resistance [6, 7]. In addition, the fibres in concrete increase the capacity to deform, which reduces spalling. Flat crimped steel fibres with a length of 42 mm and a thickness of 0.7 mm were utilised in this study, because as per other studies, the size, shape, and aspect ratio of fibres affects their resistance to being pulled out of the matrix, compromising bond strength [8]. In comparison to straight or round fibre profiles, the crimped profile of the fibre gives superior anchoring in the concrete matrix.

The shape of the fibre, as well as the strength of the concrete matrix, has a significant impact on the energy absorption characteristic, i.e. concrete toughness [9]. The amount of fibres added to concrete has a direct and considerable impact on the strength, toughness, workability, and practicality of the final result. Unlike many previous studies [10–13] that used a high percentage of fibres by volume, which was impractical on site [14], this study used 1% steel fibres by volume, which was determined with the help of literature from previous studies [10–13] that explored the parameters and complications.

Steel Reinforcement: The reinforcement cage is built of Fe 415 grade steel, with four 8 mm diameter bars as main reinforcement and six mm diameter ties at 85 mm centre to centre in the centre and 42.5 mm centre to centre at the ends, with a 20 mm cover.

4 Test Setup

The cast specimens were cured in curing tanks for 28 days before being heated in an electrical furnace designed exclusively for large specimen heating according to ISO 834 requirements [15]. The furnace is made up of three parts, one of which is a control panel that regulates the temperature. The chamber and a retractable base that rests on a track are the final two components. The chamber is surrounded on three sides by coils, and the retractable base is coated with a refractory brick substrate that holds the specimens in place. The furnace is shown in Fig. 1 with the specimens on the refractory bed.

Fig. 1 Specimens from furnace

The heated column specimens are then quenched in water to cool down (as seen in Fig. 2). A universal testing machine (UTM) capable of applying a maximum load of 1000 kN is used in the laboratory to measure the load deformation behaviour of column samples shown in Fig. 3. Figure 4 shows how the deformation corresponding to the load applied to the column specimen is measured using a dial gauge. Although previous research for flexural stiffness of concrete specimens [14] used various approaches for measuring stiffness, such as ASTM C1018 or JSCE SF-4, this work took a more traditional approach by using a UTM to construct the load deflection curve.

Fig. 2 Quenching specimen in water

Fig. 3 Dial gauge for deformation

Fig. 4 Placing the specimen in UTM

5 Results and Discussions

5.1 Stiffness

Simply defined as the rigidity of an object—the magnitude to which it resists deformation in response to an applied force. The modulus of elasticity, E_c, which is the ratio of stress to strain within elastic limit, is an important parameter to describe the structural behaviour of concrete components. At high temperatures, the modulus experiences a permanent reduction in its value. Like the strength parameter, several factors influence the value of the modulus of elasticity in laboratory specimens tested at high temperatures. The major factors include the temperature, supplementation of fibers, exposure duration and method of cooling. When conventional concrete is

exposed to elevated temperatures, it begins to experience dehydration reactions in the hydrated cement paste, resulting in possible thermal incompatibilities between paste and aggregate, and eventually leading to physiochemical deterioration of the aggregate. Typically, such degradation is accompanied by a decrease in the compressive strength, and the stiffness (modulus of elasticity) of the concrete. The compressive strength affects the load-carrying capacity of a structural component while the stiffness is influenced by the deformation and load distribution.

Stiffness of a material can be determined by knowing the slope of the curve obtained from load and deformation values. The character of the slope determines the stiffness of the material, steeper slope is a result of higher stiffness and vice versa. The slope 'm' has been obtained from the linear trendline's equation, $y = mx + c$ and translated in to percentage of reduction in stiffness with respect to the corresponding control specimen at room temperature considered to be at it maximum stiffness at 100%. From the load deformation plots the slope of the curve of fiber reinforced concrete at room temperature represented by red dashed line is steeper than that of the conventional RCC specimens at room temperature denoted with blue dotted line with slopes 167.8 and 153.1 respectively. These curves will be seen repeatedly further in the results to show the relative difference with respect to the curves of heated specimens in various charts presented under Appendix 1. It is also imperative to understand that the initial and the final readings of the load and deformation are excluded to avoid initial displacement errors. Doing so helps to consider the purest form of load deformation behaviour undergone by the specimen. In addition to that, the rate of reduction of stiffness is computed for fiber reinforced and reinforced specimens at different temperatures. It is expressed in percentage drop per minute for specimens exposed up to 60 min and 180 min. For convenience all specimens are named W5001, FW6003 etc. which translate to W-being water cooled RC columns, FW–being water cooled SFRC column, 500–being the temperature and 3 being exposure duration in hours.

5.2 Effect of Temperature on Stiffness of SFRC Columns Heated from 500 to 800 °C, with an Exposure Duration of 60 Min and Quenched in Water

With reference to Fig. 5 from the appendix and Table 1 at 500 °C it can be observed that the slope 'm' of heated SFRC column is 123.3, which is due to a reduction of 26.5% w.r.t. SFRC control specimen but, considerably better than that of RC column heated at 500 °C which has a slope of 72.7 i.e. a 52.5% reduction in stiffness w.r.t. its RCC control specimen. The addition of steel fibres mitigated the loss in stiffness in concrete due to temperature by nearly 50%. But when heated SFRC column compared with column at room temperature the decrease in stiffness is more. However, the slope of the curve of SFRC column at 500 °C and RC column at room temperature seemed to be similar with close 'm' values of 123.3 and 153.1 respectively. The rate of

Table 1 Slope of curve, m

Temp. (°C)	SFRC specimens			RCC specimens		
	Control	60 min	180 min	Control	60 min	180 min
500	167.8	123.3	66.8	153.1	72.7	47.3
600	167.8	87.3	28	153.1	69.2	61.2
700	167.8	51.7	25.9	153.1	32.6	39
800	167.8	31.2	24.1	153.1	25.7	31.1

Table 2 Reduction in slope of curve w.r.t. corresponding control samples, (%)

Temp. (°C)	SFRC specimens			RCC specimens		
	Control	60 min	180 min	Control	60 min	180 min
500	100	26.5	60.2	100	52.5	69.1
600	100	48.0	83.3	100	54.8	60.0
700	100	69.2	84.6	100	78.7	74.5
800	100	81.4	85.6	100	83.2	79.7

reduction of stiffness for SFRC columns are 0.4% per minute and 0.3% per minute for 60 min and 180 min exposure duration respectively. However, for RC specimens it is 0.9% per minute and 0.4% per minute. This shows that the presence of steel fibre slowed down the pace of reduction of stiffness.

At 600 °C the column with steel fibers showed a significant reduction of 48% in the slope of its curve with respect to the SFRC column at room temperature shown in the Fig. 6 (Appendix 1). While the slope of the RC control column compared to the RC column at 600 °C there is a reduction of 54.8% in the stiffness of the heated sample represented in Table 2, hinting that steel fibers has a slight effect at this temperature.

At 700 °C, from the Fig. 7 (Appendix 1) the slope of both SFRC and RC curves reduced due to high temperature. Nonetheless the SFRC column slightly exhibited better stiffness with respect to it RC counterpart with a 69.2% and 78.7% reductions respectively. And lastly at 800 °C from Fig. 8 (Appendix 1) the slope of the curves of both SFRC and RC specimens exhibited no difference with near equal reductions of 81.4% and 83.2% respectively. This determines that at very high temperatures the presence of fibers has no effect on stiffness of the specimen. This can also be extended to the effect of fibers on rate of reduction of stiffness, from Table 2, there doesn't seem to be much difference in percentages at both 700 and 800 °C exposed for 60 min.

5.3 *Effect of Temperature on Stiffness of SFRC Columns Heated from 500 to 800 °C, with an Exposure Duration of 180 Min and Quenched in Water*

From the Fig. 9 (Appendix 1) and Table 1 at the temperature of 500 °C, the slope m of the curve is at 66.8 of heated SFRC specimen is far less by 60.2% than the SFRC specimen at room temperature. Similar observation is seen in heated RC specimens with a gentler slope relative to ambient RC specimen. The temperature from 500 °C and above has a significant effect on the specimens making it seem like a phase change in the concrete's mechanical properties, however, heated SFRC column performed significantly well with respect to RC column at 500 °C. Seen in Fig. 10 (Appendix 1) at 600 °C, the curves related to heated SFRC and RC specimens have a variation in slope m of 28 and 61.2 respectively. In addition to that the curves at 700 and 800 °C seemed to be fixated at the similar gradient irrespective of further rise in temperature with m value of 25.9 for SFRC specimen and 39 for RC specimen for 700 °C and 24.1 and 31.1 at 800 °C. Also to be noted the percentage of drop in stiffness is similar for samples heated at these temperatures for both SFRC and RC columns. For 700 and 800 °C the drop is 84.6% and 85.6% respectively depicted in Table 2. But for RC specimens the drop in percentage is 74.5 and 79.7% at 700 and 800 °C respectively.

The same phenomenon is observed at temperatures 700 and 800 °C with a very minimal difference in slope of heated SFRC and RC specimens as seen in Figs. 11 and 12 (Appendix 1) respectively. Interestingly, heated SFRC column did not have an advantage over RC columns at both 700 and 800 °C as the loss in stiffness in SFRC column is higher compared to RC columns. This reversal of loss in stiffness may be attributed to the effect of temperature on the steel fibre's stiffness as it reduces with increase in temperature.

5.4 *Rate of Reduction in Stiffness in Percentage Per Minute*

The rate of reduction of stiffness is expressed in percentage lost per minute in concrete specimens in Table 3. At 500, 600, 700 and 800 °C with an exposure duration of 60 min, the percentile drop per minute for SFRC specimens is 0.4, 0.8, 1.2 and 1.4 respectively. The drop is gradual with a difference of 0.2% with every 100 °C increment. On the other hand, at the same temperatures the RC specimens exhibited 0.9, 0.9, 1.3 and 1.4% drop per minute, which is slightly higher than the SFRC specimens. On a parallel comparison between SFRC and RCC specimens, at 500 °C the rate of reduction of stiffness of SFRC specimen exposed for 60 min or one hour performed better with 0.4% per minute than its RCC counterpart with 0.9% per minute. For 600 °C the rate of reduction is minute with a difference of 0.1% between SFRC and RCC specimens. Interestingly, a similar observation has been made for 700 and 800 °C with a minute difference of 0.1% and no difference respectively. The same trend is seen in specimens exposed for 180 min or 3 h duration with negligible

Table 3 Rate of reduction of stiffness, Percent per minute

Temp. (°C)	SFRC specimens		RCC specimens	
	60 min	180 min	60 min	180 min
500	0.4	0.3	0.9	0.4
600	0.8	0.5	0.9	0.3
700	1.2	0.5	1.3	0.4
800	1.4	0.5	1.4	0.4

difference in the rate of reduction of stiffness. It is safe to say that the steel fiber in the concrete columns slowed the rate of reduction in stiffness.

6 Conclusions

The results of experimental work on concrete columns enhanced with steel fibres are presented in this paper. The behaviour of steel fibre reinforced concrete columns that were heated between 500 °C and 800 °C for 60 min and 180 min separately and then cooled by water. Because concrete is a non-homogeneous material, it is difficult to predict its behaviour, particularly in extreme circumstances. Nonetheless, using current literature as a guide and closely monitored experimental work, it is feasible to quantify and, more importantly, analyse the patterns of the plots, which directly illustrate the behaviour of concrete under various settings and aid in its prediction.

1. The stiffness of the fibre reinforced specimen is better than conventional concrete specimen.
2. SFRC specimens heated to 500 °C exhibited minor loss of 26.5% in stiffness on the other hand the RC specimens underwent a loss in stiffness of 52.5%.
3. At 600 and 700 °C the retention of stiffness due to steel fibres started to deplete and didn't have much variance w.r.t. RC counterparts.
4. At 800 °C the contribution of steel fibers to retain the stiffness is nearly zero.
5. Lastly, for 180 min exposure beyond 500 °C, the loss of stiffness of SFRC specimen was greater than the RC specimens. The reversal in behaviour may be due the effect of temperature on the individual fibres.
6. A gradual drop in percentage of the rate of reduction, i.e. 0.2% is observed for every increment of 100 °C.
7. Comparing the rate of reductions of SFRC and RC specimens, the results are not promising, with a insignificant difference of 0.1%, considering the presence of steel fibres.

Appendix 1

See Figs. 5, 6, 7, 8, 9, 10, 11 and 12.

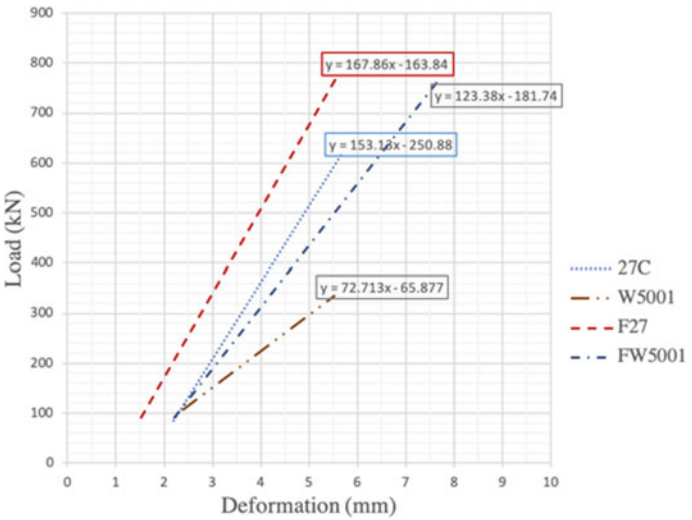

Fig. 5 Variation of load deformation of SFRC specimens exposed to 500C for 1 h and quenched in water

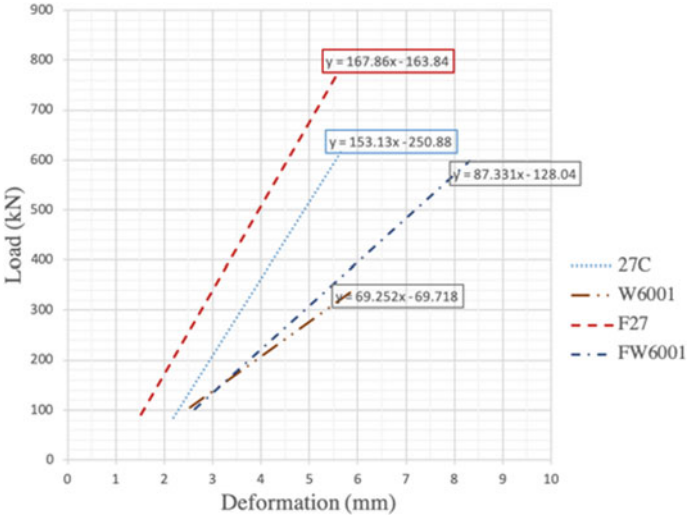

Fig. 6 Variation of load deformation of SFRC specimens exposed to 600C for 1 h and quenched in water

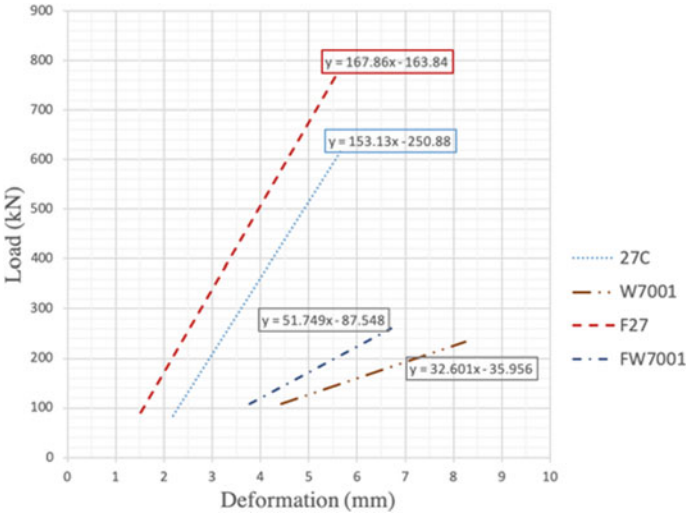

Fig. 7 Variation of load deformation of SFRC specimens exposed to 700C for 1 h and quenched in water

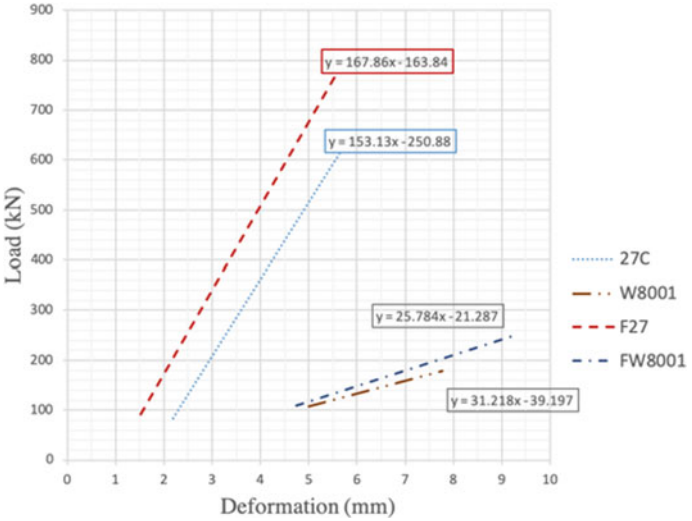

Fig. 8 Variation of load deformation of SFRC specimens exposed to 800C for 1 h and quenched in water

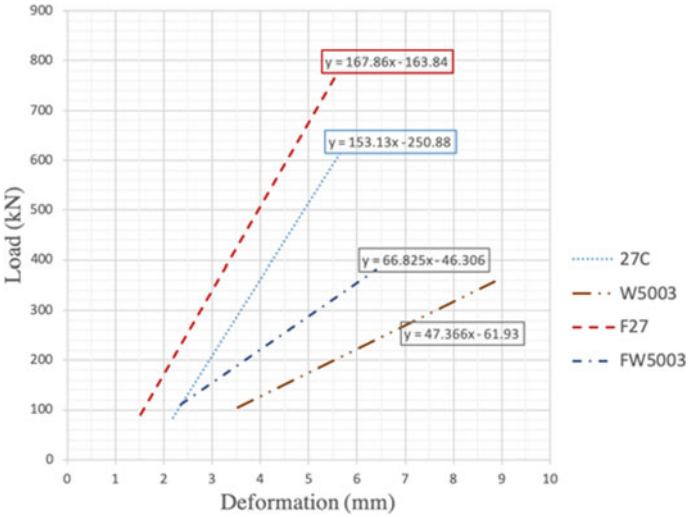

Fig. 9 Variation of load deformation of SFRC specimens exposed to 500C for 3 h and quenched in water

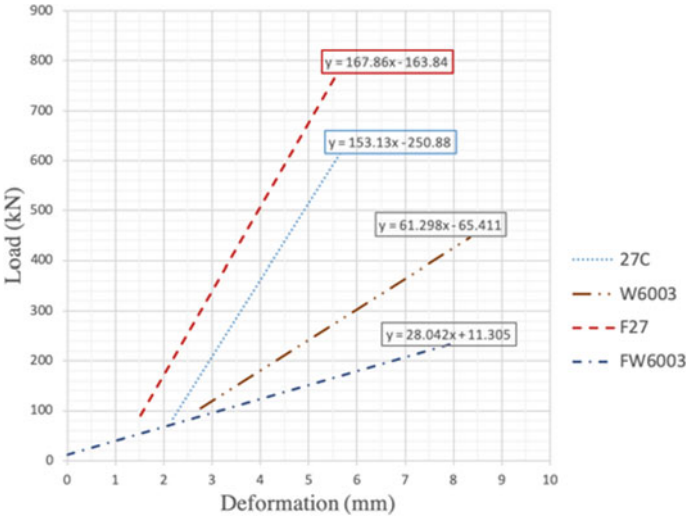

Fig. 10 Variation of load deformation of SFRC specimens exposed to 600C for 3 h and quenched in water

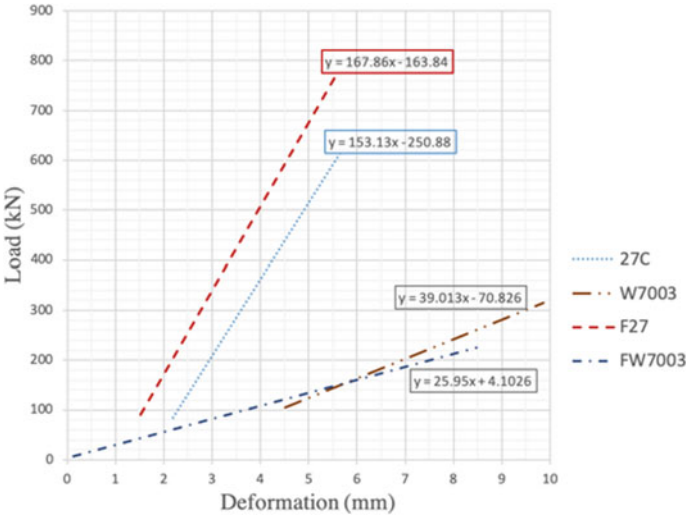

Fig. 11 Variation of load deformation of SFRC specimens exposed to 700C for 3 h and quenched in water

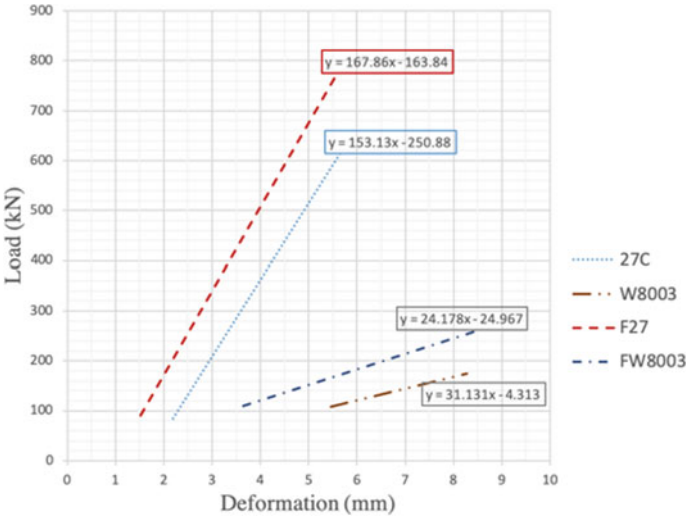

Fig. 12 Variation of load deformation of SFRC specimens exposed to 800C for 3 h and quenched in water

References

1. Keikhaei K (2012) Properties of concretes produced by single and combined hooked end discontinuous discrete steel fibres. Thesis submitted to Eastern Mediterranean university, Institute of Graduate Studies and Research, Department of Civil Engineering, Famagusta, North Cyprus

2. Chalioris CE, Sifri EF (2011) Shear performance of steel fibrous concrete beams. In: The twelfth East Asia-Pacific conference on structural engineering and construction. China
3. Selvam M, Sakthieswaran N, Shiny Brintha G, Ganesh Babu O (May 2016) A review—shear and pullout behaviours of steel fiber reinforced concrete on elevated temperature. Int J Res Appl Sci Eng Technol 4(5):772–774
4. Srinivasa Rao K, Potha Raju M (2010) Residual strength of heated reinforced cement concrete columns. ICFAI Univer J Struct Eng 3(1):54–69
5. IS 456-2000, Indian standard code of practice for plain and reinforced concrete (4th revision), Bureau of Indian standards, New Delhi
6. Kodur VKR, Cheng FP, Wang TC (2003) Effect of strength and fibre reinforcement on the fire resistance of high strength concrete column. ASCE J Struct Eng 129(2):253–259
7. Kodur VR (2003) Fiber reinforcement for minimizing spalling in HSC structural members exposed to fire, Innovations in fiber-reinforced concrete for value. ACI Spec Publ, SP 216:221–236
8. Narayanan R, Kareem-Palanjian AS (1984) Effect of fibre addition on concrete strength. Indian Concr J 58:100–103
9. Soroushian P, Bayasi Z (1991) Fiber type effects on the performance of steel fiber reinforced concrete. ACI Mater J 88(2):129–134
10. Yusof MA et al (2011) Mechanical properties of hybrid steel fibre reinforced concrete with different aspect ratio. Aust J Basic Appl Sci 5(7):159–166
11. Mohan KSR, Sumathi (2015) Study on the strength and durability characteristics of high strength concrete with steel fibers. Int J Chem Tech Res CODEN (USA): IJCRGG ISSN: 0974-4290 8(1):241–248
12. Ranyal A, Kamboj J (2016) Effect of addition of different type of steel fibres on the mechanical aspects of concrete—a review. Int J Civil Eng Technol 7(5):33–42
13. Gustafsson J, Noghaba K (1997) Steel fibers as shear reinforcement structural engineering, vol 2. Lulea University of Technology, Lulea, pp 220–226
14. Nataraja MC, Dhang N, Gupta AP (2000) Toughness characterization of steel fiber reinforced concrete by JSCE approach. Cem Concr Res, USA 30(4):593–597
15. Fire resistance tests-elements of building construction, international standard ISO 834. International Standard Organization, Geneva, Switzerland (2014)

Impact of Clay and Non-clay Microfines on Various Concrete Properties

Kusum Rathore, Vinay Agrawal, Ravindra Nagar, and Nipurn Agrawal

Abstract High amounts of microfines (particles less than 75 μm in size) are unavoidable in sand manufacturing. In addition, due to the manufacturing process and clayey soil strata in rocks, sometimes clay intermingles with manufactured sand (M-sand). Therefore, it is necessary to identify clay and non-clay microfines in M-sand. The present study uses a methylene blue value (MB-value) test for differentiating clay and non-clay particles. Furthermore, the current research examines the effect of clay and non-clay microfines on concrete workability, mechanical strength, and abrasion resistance. Results showed that the MB-value of M-sand is affected by the clay microfines but not by the non-clay sandstone microfines. Clay particles significantly decrease the workability of concrete. Microfines of clay improve the mechanical strength up to an MB-value of 6. Beyond that, a higher superplasticizer dose used to achieve workability deteriorates the strength. Abrasion resistance of concrete also decreases with increase in clay particles.

Keywords Concrete · Clay · Microfines · Methylene blue value (MB-value)

K. Rathore (✉) · V. Agrawal · R. Nagar
Department of Civil Engineering, Malaviya National Institute of Technology, Jaipur, Rajasthan 302017, India
e-mail: 2017rce9049@mnit.ac.in

V. Agrawal
e-mail: vagarwal.ce@mnit.ac.in

R. Nagar
e-mail: rnagar.ce@mnit.ac.in

N. Agrawal
Department of Civil Engineering, Birla Institute of Technology and Science, Pilani, Rajasthan 333031, India
e-mail: f20201765@pilani.bits-pilani.ac.in

S. B. Singh et al. (eds.), *Fiber Reinforced Polymeric Materials and Sustainable Structures*, Composites Science and Technology, https://doi.org/10.1007/978-981-19-8979-7_17

1 Introduction

Concrete is among the most consumed materials on the earth, and river sand is the prime constituent of concrete. Industrialization and urbanization have led to the shortage of quality river sand. River sand is obtained from river beds. Excessive sand mining may cause erosion of river beds and coastlines that lead to flooding, destroy the natural habitat of aquatic life, alter the river bed, and affect the quality and quantity of water [1]. Because of higher costs and limited supply, sand mafias are generated, and low-quality sand is utilized in construction. Therefore it is beneficial both economically and environmentally to use waste or recyclable materials in concrete to make it more sustainable and resource-efficient.

Due to the shortage of river sand nowadays, manufactured sand (M-sand) is utilized in making concrete. M-sand is different from natural sand in shape, surface texture, particle size grading, and high amounts of microfines [2]. Microfines are particles smaller than 75 μm [3]. M-sand is obtained by crushing the rocks. Sometimes, clay minerals get mixed with the M-sand due to clayey soil strata in rocks. Clay is considered a deleterious material in concrete. The presence of clay in concrete affects its fresh and hardened properties [3]. Clay affects the water demand of concrete due to its higher surface area, reduces the paste-aggregate bond, and the normal hydration process of cement also gets affected [4]. Many authors have reported the positive impact of adding stone fines in concrete [5–8]. To avoid the detrimental effects of clay, it is necessary to identify whether microfines are clay particles or non-clay stone fines. Various standards (BS EN 933-9:2009, AASHTO TP 57 2006, ASTM C1777-20) identify the MB-value test to determine the presence or absence of clay in fine aggregate. However, none of the specified codes defines the limiting MB value of microfines. Limiting the powder content in concrete destroys the positive impact of the addition of fines.

Although some research is available on the effect of clay and non-clay microfines on concrete workability, mechanical strength, and drying shrinkage, there is a strong need for a comparative and detailed study of the impact of clay and non-clay microfines in concrete. Most of the studies which were done in the past used limestone M-sand and stone powder for evaluating the effect of clay-doped stone fines in concrete. Petrography of parent rock effect the shape and surface texture of the M-sand, which subsequently affects the water demand and strength properties of concrete. Therefore in the current study, keeping in view the sustainability objective, locally available sandstone quarry waste was used in making the M-sand. Sandstone microfines of the same petrography and kaolin clay were incorporated as 1, 3, 5, 7 and 10% by weight of fine aggregate. The effect of non-clay and clay particles on the MB value of M-sand, workability, mechanical strength, and abrasion resistance of concrete was determined.

2 Experimental Work

2.1 Raw Materials

In this study, Portland pozzolana cement is used. The specific gravity of PPC is 2.89, and 28 days compressive strength is 36.25 MPa as per IS1489 (Part 1): 1991 [9]. Locally available basalt coarse aggregate of 10 mm and 20 mm nominal maximum size is used. The fine aggregate used in the current study is M-sand made of quarry waste of sandstone. The physical properties of M-sand are given in Table 1. Particle size distribution data of fine aggregate is shown in Table 2. Originally it consisted of 16% microfines. These microfines were removed by dry sieving. After sieving, the remaining microfine content was 6%, and it was considered as M-sand with no fines. Sandstone microfines of the same petrography are used as non-clay particles. Locally available kaolin clay is used in this study. Content of clay and sandstone microfines are 0, 1, 3, 5, 7 and 10% by weight of fine aggregate. Clay was first oven-dried at 100 °C for 24 h and then sieved through a 75 μm IS sieve. The mineralogical composition of kaolin and sandstone M-sand determined by X-Ray Fluorescence (XRF) is given in Table 3. Superplasticizer Glenium Sky 777 is used to maintain workability. Regular tap water is used for mixing the raw materials for concrete.

Table 1 Physical properties of fine aggregate

Apparent density (kg/m^3)	Water absorption (%)	Microfine content (%)	Sand grading zone	Fineness modulus	MB Value (g/kg)	Bulk density loose (kg/m^3)	Bulk density packed (kg/m^3)
2600	1.1	6	2	2.46	0.5	1543.33	1725

Table 2 Particle size distribution of fine aggregate

Sieve size	10	4.75	2.36	1.18	0.6	0.3	0.15	0.075
% Passing's	100	99.05	89.25	74.25	57.25	25.55	8	2.3

Table 3 Mineralogical composition of kaolin and sandstone M-sand

Specimen	SiO_2	Al_2O_3	Fe_2O_3	MgO	CaO	Na_2O	K_2O	P_2O_5	LOI
Kaolin	46.51	36.59	2.57	0.06	0.05	0.30	0.41	0.14	13.1
M-sand	91.21	1.62	3.44	0.5	0.25	0.7	1.35	0.10	0.5

2.2 Mix Proportion and Test Methods

In this study, for checking the effect of clay and non-clay microfines in concrete, sandstone microfines and kaolin clay were used as 0, 1, 3, 5, 7 and 10% by weight of M-sand. Concrete mix proportioning was done for M30 grade of concrete as per IS: 10262-2019. The water to cement ratio of 0.40 was constant for all the mixtures. Quantities of cement, sand, and coarse aggregate used were 370 kg/m^3, 679 kg/m^3, and 1248 kg/m^3, respectively. 10 mm and 20 mm nominal maximum size coarse aggregate were used in equal proportion. The slump was in the range of 100 ± 20 mm for all the mixes. Details of the various tests performed are as follows:

MB Value- This test was done following the guidelines of BS EN 933-9: 2009. For this test, 30 ± 0.1 g of microfines were mixed with 500 ml of distilled water into a beaker. This mix was stirred for 5 min at 600 r/min. After that, 5 mL of methylene blue dye was added, and the solution was stirred for another 1 min. A stain test was performed by putting a drop of the mixture on filter paper. If the test mixture absorbs all the dye, a blue stain with a colourless halo appears on the filter paper. If the test is positive spot appears with a blue halo. This procedure is repeated by adding the methylene blue dye to the mixture until a blue halo appears. The test set-up is shown in Fig. 1. The following equation calculates the MB value:

$$\text{MB value} = \frac{\text{V}}{\text{M}} \times 10 \text{ g/kg}$$

Here, V is the quantity of methylene blue dye added, and M is the mass of the sample in grams.

Workability—A slump test was used to ascertain the workability of fresh concrete following the guidelines of IS 1199: 1959.

Compressive and flexural strength—7 and 28 days compressive strength and 28 days flexural strength were determined using IS 516: 1959 [10]. Compressive strength test was performed on cube specimen of 100 mm dimension and average of three cube strength was taken as final strength. Flexural strength was determined on

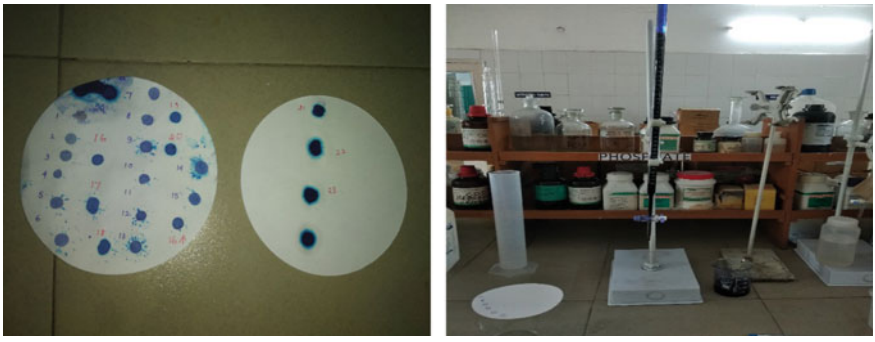

Fig. 1 MB-value test

100 × 100 × 500 mm beam specimen, and an average of three results were taken as final flexural strength.

Abrasion resistance test was performed on 28 days water cured and oven-dried cubes of 100 mm dimension. Depth of abrasion was determined following the protocol IS 1237: 2012 [11].

3 Results and Discussions

3.1 Impact of Clay and Non-clay Particles on MB Value of M-sand

Figure 2 shows that the MB value of M-sand increases slowly with the increase of the content of non-clay fines of sandstone. For every 1% increase in microfine content, the rise in MB-value is less than 0.1. It indicates that non-clay sandstone microfines absorb much less methylene blue dye, and raising the sandstone microfine content has a minor effect on the methylene blue value of M-sand. To see whether the clay particles influenced the MB-value of M-sand kaolin was used in the same weight proportion as sandstone microfines. Figure 3 displays that when there were no clay fines, the MB-value of M-sand was less than 1. Replacement of sandstone fines with 1% clay fines rapidly increased the MB-value to 2.5 g/kg. Further replacement linearly increased the MB-value. For 10% clay inclusion MB-value was 9.5 g/kg. It shows that clays absorb more methylene blue than sandstone microfines. These results also indicate that the MB-value test is suitable for differentiating clay and non-clay particles.

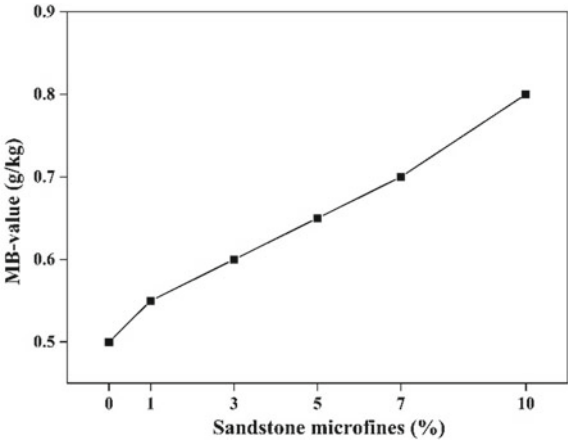

Fig. 2 Impact of sandstone microfines on MB-value of M-sand

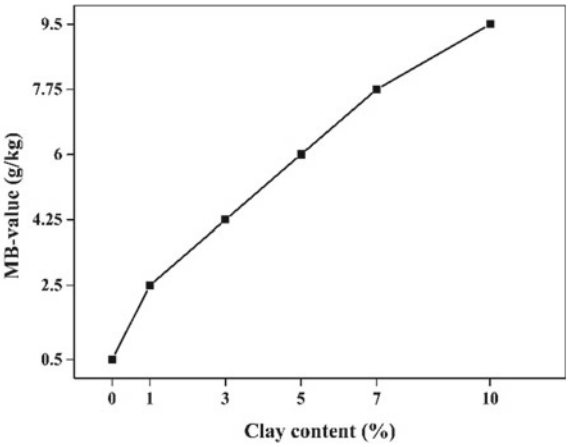

Fig. 3 Impact of clay microfines on MB-value of M-sand

3.2 Impact of Clay and Non-Clay Microfines on Concrete Workability

The impact of clay and non-clay particles on concrete workability was determined by varying the superplasticizer dosages to get a constant slump of 100 ± 20 mm. Figure 4 shows the amount of superplasticizer used when clay and non-clay microfines are used in concrete. The inclusion of non-clay sandstone microfines in concrete raises the superplasticizer demand gradually. This rise is due to the high specific surface area of sandstone microfines. The maximum superplasticizer dose used was for 10% microfine content, and it was 34.5% more than the control concrete. On the other side, clay microfines significantly affected concrete workability. Only a 1% addition of clay fines increased the superplasticizer dosage to 20%. For 7% and 10% clay content, superplasticizer dosages were 151% and 213% more than the control concrete. Delayed setting time was also observed with 7% and 10% clay inclusion. Due to the large specific surface area and layered structure of clay particles, their water requirement is more. Clays also have a higher capability for cation exchange. The cations in the clay may be exchanged with the organic compounds present in the superplasticizer, making it less available for the cement paste. Norvell et al. [3] and Beixing et al. [12] also reported increased water or superplasticizer demand when clay fines were used in concrete.

3.3 Impact of Clay and Non-clay Microfines on the Mechanical Strength of Concrete

Figures 5 and 6 show that including non-clay sandstone microfines in concrete increases the concrete's 7 and 28 days compressive strength and 28 days flexural

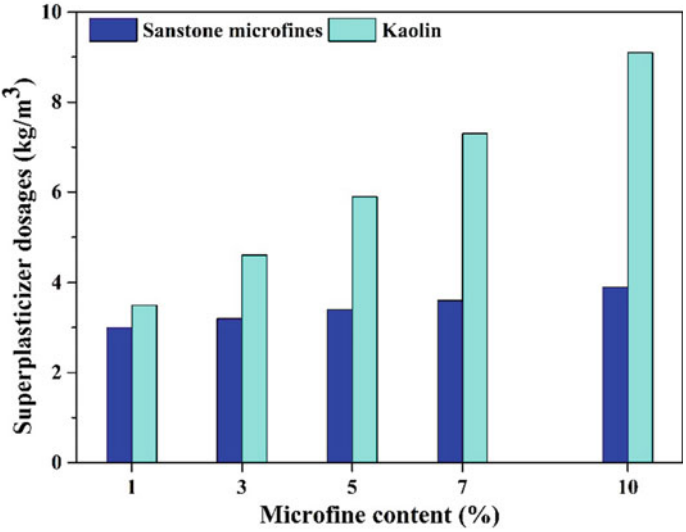

Fig. 4 Impact of variation of clay and non-clay microfines on superplasticizer dosage of concrete

strength. These non-clay particles act as micro fillers to concrete, densify the concrete matrix, and help in the hydration of cement by providing additional nucleation sites. Adding up to 5% kaolin clay does not affect the 7 and 28 days of concrete compressive and flexural strength as clay plays a role in filling the voids, but fines decrease the compressive strength beyond this addition of clay. Twenty-eight days compressive strength of concrete with clay content 7% and 10% was 3% and 10% less than the control concrete. Figure 7 displays that 28 days flexural strength remained unaffected till 5% clay content, and it gives an almost similar increase in strength as obtained by the addition of non-clay microfines, but it decreased by 4% and 9.5% for 7% and 10% clay content. Mechanical strength decrease beyond 5% clay may result from higher superplasticizer dosage to achieve the target workability. Higher superplasticizer dosage delays setting time and increases air void content in concrete, which subsequently decreases concrete's mechanical strength.

3.4 Impact of Clay and Non-clay Microfines on Abrasion Resistance of Concrete

Surface abrasion is a vital durability property of concrete. However, the wearing of the concrete surface makes it prone to other forms of concrete deterioration, such as cracking and corrosion of reinforcement [13]. Figure 8 shows that the wear depth decreases due to the addition of non-clay sandstone fines, while the inclusion of clay fines increases the wear depth. Clay microfines are softer than stone microfines, and

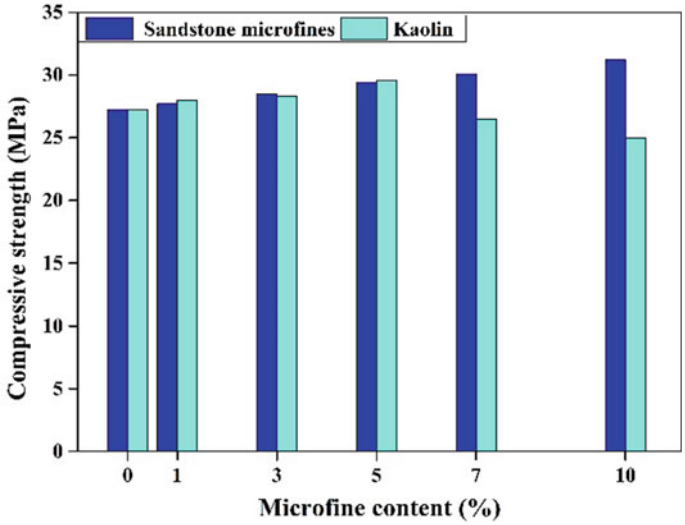

Fig. 5 Impact of variation of clay and non-clay microfines on 7 days compressive strength of concrete

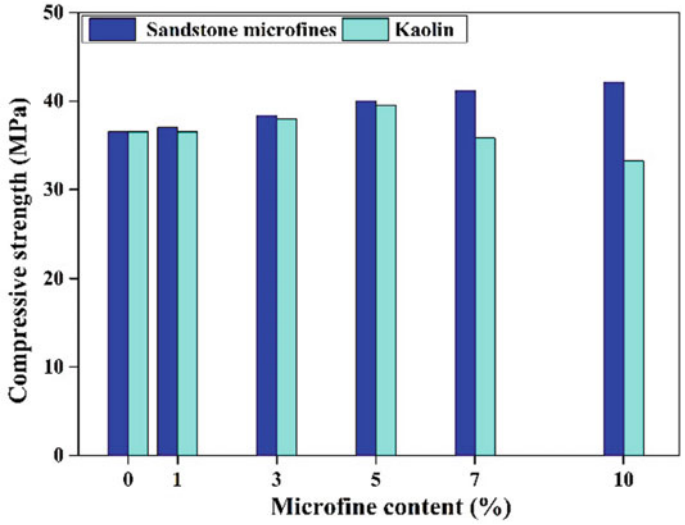

Fig. 6 Impact of variation of clay and non-clay microfines on 28 days compressive strength of concrete

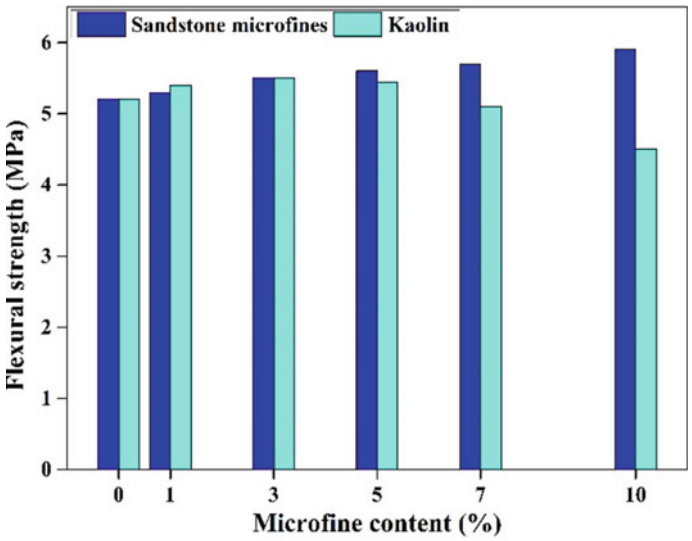

Fig. 7 Impact of variation of clay and non-clay microfines on 28 days flexura strength of concrete

they get easily worn off by rubbing or friction. Compressive strength loss is also responsible for the increased depth of wear of mix containing 7% and 10% clay microfines.

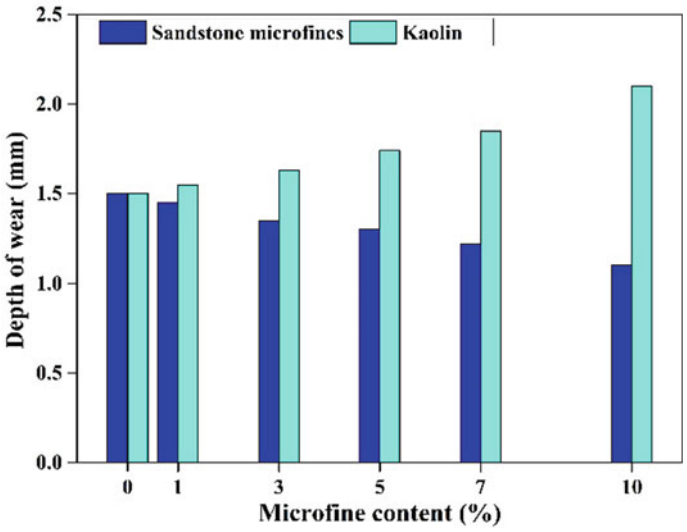

Fig. 8 Impact of variation of clay and non-clay microfines on depth of wear of concrete

4 Conclusions

This study was conducted to check the effect of clay and non-clay microfines in concrete. Sandstone powder and kaolin clay were used as non-clay and clay fines. Based on the test for MB-value, workability, mechanical strength and abrasion resistance of concrete following conclusions were made:

1. The methylene blue value test is a suitable and easy method for quickly determining the presence of clay in the fine aggregate.
2. Clay and non-clay particles decrease concrete workability, but clay particles significantly affect workability.
3. Mechanical strength of concrete with non-clay fines increases with increasing microfine content for the levels studied. However, mechanical strength parameters increase up to 5% clay content, and beyond this, strength reduces due to a higher dosage of superplasticizer used for achieving the required workability.
4. Resistance of concrete to abrasion increases with the increasing non-clay microfines in concrete, while the inclusion of soft clay fines decreases the abrasion resistance.

References

1. Padmalal D, Maya K (2014) Sand mining environmental impacts and selected case studies. https://doi.org/10.1007/978-94-017-9144-1_9
2. Li B, Ke G, Zhou M (2011) Influence of manufactured sand characteristics on strength and abrasion resistance of pavement cement concrete. Constr Build Mater 25:3849–3853. https://doi.org/10.1016/j.conbuildmat.2011.04.004
3. Norvell JK, Stewart JG, Juenger MCG, Fowler DW (2007) Influence of clays and clay-sized particles on concrete performance. J Mater Civ Eng 19:1053–1059. https://doi.org/10.1061/(ASCE)0899-1561(2007)19:12(1053)
4. Wang J, Yang Z, Niu K, Ke G, Zhou M (2009) Influence of MB-value of manufactured sand on the shrinkage and cracking of high strength concrete. J Wuhan Univ Technol Mater Sci Ed 24:321–325. https://doi.org/10.1007/s11595-009-2321-z
5. Rathore K, Agrwal V, Nagar R (2020) Green concrete: using quarry waste of sandstone as fine aggregate with high levels of microfines. Mater Today Proc 32:728–733. https://doi.org/10.1016/j.matpr.2020.03.463
6. Basu P, Skariah B, Chandra R, Agrawal V (2021) Properties of sustainable self-compacting concrete incorporating discarded sandstone slurry. J Clean Prod 281:125313. https://doi.org/10.1016/j.jclepro.2020.125313
7. Katz A, Baum H (2006) Effect of high levels of fines content on concrete properties. ACI Mater J 103:474–82. https://doi.org/10.14359/18226
8. Quiroga PN, Ahn N, Fowler DW (2007) Concrete mixtures with high microfines. ACI Mater J 104:328–9. https://doi.org/10.14359/18680
9. Bureau of Indian Standard (BIS) (1991) Portland pozzolana ement-specification. IS 1489(Part 1) (3rd revision). New Delhi, India
10. IS 516 (2018) Method of tests for strength of concrete. Bureau of Indian Standards Dehli. https://doi.org/10.3403/02128947

11. BIS:1237-2012 (2012) Cement concrete flooring tiles–specification. Bureau of Indian Standards
12. Beixing L, Mingkai Z, Jiliang W (2011) Effect of the methylene blue value of manufactured sand on performances of concrete. J Adv Concr Technol Japan Concr Inst 9:127–132. https://doi.org/10.3151/jact.9.127
13. Safiuddin M, Scott B (2015) Abrasion resistance of concrete–design, construction and case study. Concr Res Lett 6:136–148

Evaluating Accuracy of Correlation Expressions from Literature for Estimation of Concrete Strength from Ultrasonic Pulse Velocity

Arun, Kapilesh Bhargava, P. K. Panda, and K. Mahapatra

Abstract In this article, the strategy for evaluation of compressive strength of concrete from non-destructive and partially destructive testing on the existing structures or cubes is reviewed. It is essential for condition assessment and health monitoring of the existing structures to fulfil the requirements of periodic assessment, reviewing present structural health and condition of the structures. Among the non-destructive tests, ultrasonic pulse velocity (USPV) and rebound hammer (RHM) tests are normally used for qualitative assessment, whereas core test (semi-destructive) is used for quantitative strength assessment. Subsequently, the forms of correlation expression best suited for evaluation of compressive strength of concrete from USPV were ascertained from the correlation expressions of USPV and core strength from the literature. From the results, it was concluded that for the considered dataset, linear correlation model would be best suited for evaluation of concrete compressive strength from USPV. This study would be very useful as a reference for engineers engaged in condition assessment and re-evaluation exercises of existing concrete structures.

Keywords Ultrasonic pulse velocity · Concrete strength · Correlation · Accuracy

1 Introduction

For existing concrete structures, condition assessment has emerged as an important activity with the modern concrete buildings aging across the world. To reduce further damage to the aged/damaged structures, non-destructive tests (NDT), such as ultrasonic pulse velocity (USPV) and rebound hammer (RHM) tests, are preferred over destructive ones (pull-out core tests). For the purpose of estimation of the in-situ

Arun (✉) · P. K. Panda · K. Mahapatra
Directorate of Construction, Services and Estate Management, Mumbai 400094, India
e-mail: arun@dcsem.gov.in

K. Bhargava
Engineering Services Group, Bhabha Atomic Research Centre, Mumbai 400094, India

Homi Bhabha National Institute, Mumbai 400094, India

S. B. Singh et al. (eds.), *Fiber Reinforced Polymeric Materials and Sustainable Structures*, Composites Science and Technology, https://doi.org/10.1007/978-981-19-8979-7_18

strength of concrete from these NDT results, it is generally recommended that correlation expressions should be developed for the particular structure under scrutiny. However, for various constraints, such exercise is not often feasible and thereby, the correlation expression/s are selected from the literature. The Indian Standard [1] available for interpretation of USPV results indicates a possible variation of 20% from the actual strength, when estimated from USPV. Before application to the actual structure, it would be recommended to evaluate the expression/s using some available experimental data, with regards to the accuracy of the predicted concrete strength from NDT results.

There are numerous correlation expressions available in literature for the estimation of concrete strength from the USPV data. Different researchers have selected different forms of equations for representing the relationship between USPV and concrete strength, which include linear relationships [2, 3], exponential relationships [4–6] and power law relationship [7], etc. These expressions are having wide coverage in terms of the USPV and concrete strength values.

In this paper the aforementioned linear, exponential and power law relationships have been selected for the evaluation of their accuracy against experimental data. The experimental data used for the evaluation purpose was selected from the published literature and would be described in more detail in subsequent sections of this paper.

2 Review of Literature

The Indian standard [1] on application of USPV for evaluation of concrete strength in existing structures suggest development of regression equations with experimental data taken from the same structure/group of structures. However, such exercise could be constrained due to several reasons, such as, limitations arising due to resources (funds/time), advanced age or deteriorations observed in structure, or from functional considerations. There have been several studies reported in the literature, wherein, authors have attempted to develop regression relationships between the USPV and the concrete strength. Studies include those conducted on laboratory tests on concrete cubes/cylinders [7], and also actual tests carried out on existing concrete structures [3, 6]. It must be noted that the grade of concrete varied in reference literatures from 5 to 55 MPa [6, 7].

For the present study, as mentioned before, six different equations have been selected as listed below.

Shariati et al. [2] selected the linear form for development of correlation expression and for concrete strength recording, they carried out compression tests on concrete cubes of 150 mm side length. The loading speed for 150 mm side length cube was 13.5 kN/s; the compressive strength of hardened concrete was determined by using specimens tested at 1, 3, 7, and 14 day intervals [2]. Two specimens were tested and the averaged results for each strength test at each age were used [2]. Following equation was proposed:

$$f = 15.533 * V - 34.358 \tag{1}$$

Dauji et al. [3] selected the linear form for development of correlation expression between the USPV from structures at site for which the grade of concrete was 20 MPa, and proposed Eq. (2) for the same:

$$f = 22.980 + 1.625 * V \tag{2}$$

Raouf and Ali [4] selected the exponential form for development of correlation expression between USPV and concrete core strength obtained from 650 test results collected from the results of students, the experimental mixes and others taken from the tested cubes which were send to National Centre for Construction Labs and proposed Eq. (3) for the same:

$$f = 2.016 * e^{0.61*V} \tag{3}$$

Popovics et al. [5] selected the exponential form for development of correlation expressions between USPV and core strength data. They used Klieger experimental results in 1957 for a mathematical comparison for use of direct ultrasonic velocity (DUPV) and surface ultrasonic waves (SUPV), respectively, for strength estimation [5]. The best fit formula for the relationship between concrete strength and direct ultrasonic velocity (DUPV) for the seventh day experimental results by Klieger [5] is presented by Eq. (4) as given below:

$$f = 0.0028 * e^{0.0021*V} \tag{4}$$

Turgut [6] also selected the exponential form for development of correlation expression between the USPV and concrete core strength obtained from 30 reinforced structures with their ages vary between 28 days and 36 years old. The densities of concrete cores vary between 1.88 and 2.60 gr/cm^3. The cores were obtained from columns, shear or retained walls in the concrete structures; the size of cores was 100 mm × 200 mm [6]. All cores were drilled horizontally through the thickness of the concrete elements. The values of the ultrasonic pulse velocities lay within 1.8 and 5.0 km/s; the concrete cube strengths varied between 5.0 and 55.0 MPa [6]. Turgut [6] proposed Eq. (5) as given below:

$$f = 0.3161 * e^{1.03*V} \tag{5}$$

Bhosale and Salunkhe [7] selected the power law form for development of correlation expression between the USPV and compressive strength from cores extracted from samples of slab at laboratory for which the grade of concrete was 20 MPa, 25 MPa and 30 MPa and proposed Eq. (6) for the same:

$$f = 0.0297 * V^{4.8586} \tag{6}$$

In all the above-mentioned relationships given by Eq. (1)–(6), 'V' is the USPV in km/sec., and 'f' is the concrete cube compressive strength in MPa. The accuracy of these expressions would be evaluated with the experimental data selected from studies reported in literature, and these would be described in the next section.

3 Experimental Data for Evaluation

For this study two sets of experiments have been selected from literature. Turgut [6] reported experimental data of USPV on cores obtained from vertical elements of structure (columns and walls) and the corresponding compressive strength values of concrete cores. The range of USPV was 1.8–5.0 km/sec. and that for the concrete strength was 5–55 MPa. The descriptive statistics of the data from this experiment is presented in Table 1 and the histograms for the USPV and concrete strength for the same are presented in Figs. 1 and 2, respectively. In the figures 'PDF' indicates probability density function.

Bhosale and Salunkhe [7] reported experimental data of USPV from slab samples, and the corresponding strength values of concrete obtained on cores taken from slabs in laboratory. The range of USPV was 3.84–4.16 km/sec. and that for the concrete strength was 24.71–36.06 MPa. The descriptive statistics of the data from this experiment is presented in Table 1, and the histograms for the USPV and concrete strength for the same are presented in Figs. 3 and 4, respectively.

Readers may note that the standard distributions applicable for concrete data, namely Normal and Log-normal distributions were fit to the experimental concrete strength data and the goodness of fit was checked by the statistical tests: Chi-squared

Table 1 Statistical descriptors for experimental data: USPV and core strength

Statistic	Data set 1 actual structure: Turgut [6]		Data set 2 laboratory samples: Bhosale and Salunkhe [7]	
	USPV (km/sec)	Core strength (MPa)	USPV (km/sec)	Core strength (MPa)
Number of Samples	71	71	30	30
Range	1.8–5.0	5–55	3.84–4.16	24.71–36.06
Mean	3.40	19.910	4.02	30.940
c.o.v	0.217	0.618	0.022	0.115
C_s	0.258	0.887	−0.523	−0.365
C_k	2.04	3.326	2.17	1.783

c.o.v. = Coefficient of Variation
C_s = Coefficient of Skewness
C_k = Coefficient of Kurtosis

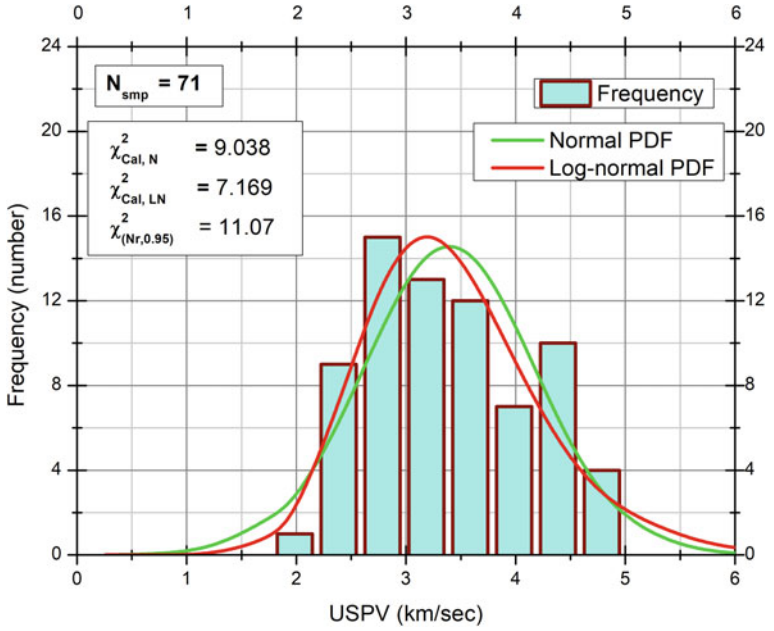

Fig. 1 Histogram and PDF of USPV for experimental data of Turgut [6]

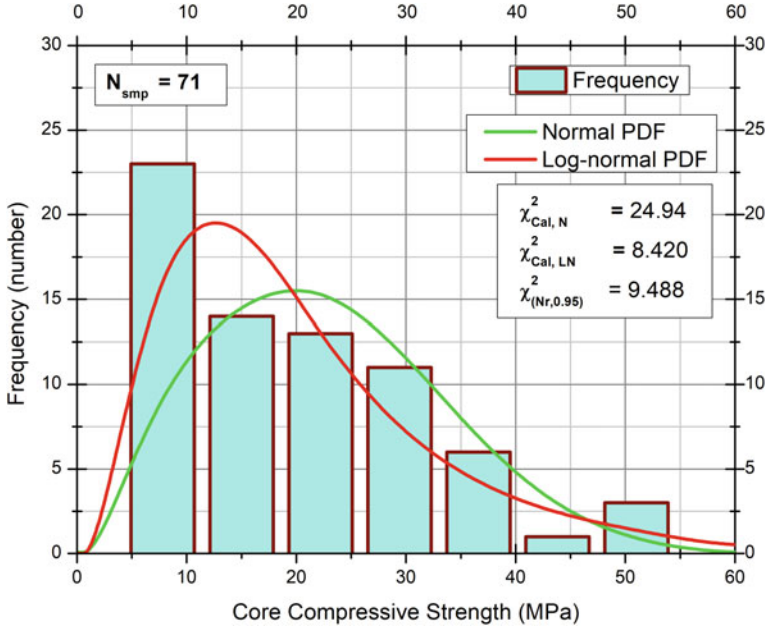

Fig. 2 Histogram and PDF of concrete strength of experimental data of Turgut [6]

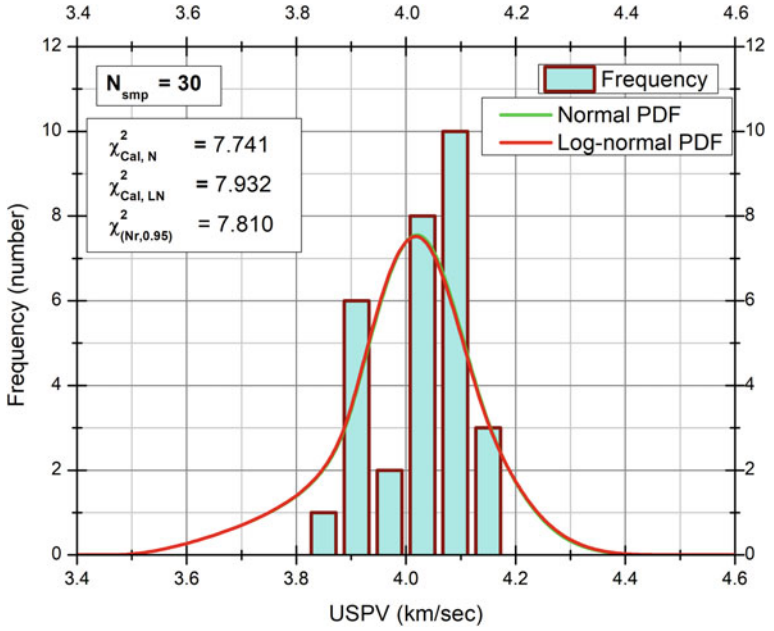

Fig. 3 Histogram and PDF of USPV for experimental USPV data of Bhosale and Salunkhe [7]

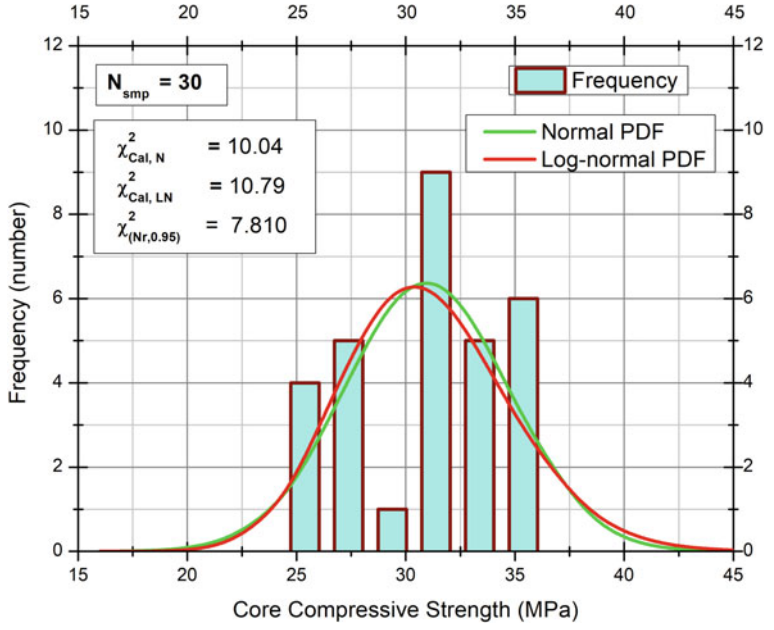

Fig. 4 Histogram and PDF of concrete strength for experimental data of Bhosale and Salunkhe [7]

Table 2 Probabilistic models for core strength results

Dataset	Probability distribution	Calculated value		Reference value [9]	
		χ_{cal}^2	D_{cal}	$\chi_{(N,\,0.95)}^2$	$D_{(n,\,0.95)}$
Turgut [6]	Normal	24.94	0.180	9.488	0.161
	Log-normal	8.42	0.097		
Bhosale and Salunkhe [7]	Normal	10.04	0.050	7.810	0.246
	Log-normal	10.79	0.103		

test and K-S test [8, 9]. In each of the figures (Figs. 2 and 4), the corresponding probability distributions have been plotted over the histograms for visually appreciating the fits. The numerical values of Chi-squared and K-S tests for the data sets have been reproduced in Table 2.

In Table 2, χ_{cal}^2 = calculated value of Chi-square; $\chi_{N,0.95)}^2$ = Chi-square value taken from standard Chi-square tables corresponding to 'N' degrees of freedom and 5% level of significance; D_{cal} = maximum of absolute values of the n differences between observed PDF and the hypothesized PDF evaluated for the observed 'n' samples; $D_{(n,\,0.95)}$ = value obtained from standard distribution table corresponding to 'n' samples and 5% level of significance.

4 Evaluation of Accuracy of Different Correlations

This study pertains to evaluation of the accuracy of different forms of correlation expressions between USPV and concrete strength with respect to experimental data. For the purpose of accuracy, two statistical metrics have been selected: the coefficient of correlation and the standard error of estimate. The correlation coefficient has been evaluated between the actual experimental strength and the strength predicted from the corresponding USPV using the respective equations by using Eq. (7), and the corresponding standard error would be given by Eq. (8) provided below.

$$r = \sqrt[1/2]{\sum \left(Y_{pre} - Y_{mean}\right)^2 / \sum \left(Y_{exp} - Y_{mean}\right)^2} \tag{7}$$

$$s = \sqrt[1/2]{\sum \left(Y_{pre} - Y_{exp}\right)^2 / (N-1)} \tag{8}$$

where, N is the number of samples; Y_{mean} is the mean of the experimental values of the parameter; Y_{pre} and Y_{exp} are the predicted and experimental values of the parameter

Thus, in this study, the accuracy of the correlation expressions from literature has been comprehensively evaluated using two quantitative metrics, namely, coefficient of correlation and standard error.

5 Discussion of Results

The results of the statistical distribution fitting have been presented in Table 2, and Figs. 2, 3 and 4. For the site experimental data of Turgut [6] for concrete strength, Normal distribution is rejected by both Chi-square and K-S tests, whereas the Log-normal distribution is acceptable by both the tests. This observation is supported by the long right-hand tail of the histogram as shown in Fig. 2. It is found that the histogram for the laboratory experimental data of Bhosale and Salunkhe [7] appears to be bimodal as shown in Fig. 4. Chi-squared test rejects both the Normal and Log-normal distribution, whereas the K-S test finds both to be acceptable for concrete strength. It is well-known that the concrete strength data tends to follow Log-normal distribution due to higher frequency near the median and the lower frequency towards the high values of strength.

Presently the accuracies of the correlation models selected from literature are examined with the statistical metrics (coefficient of correlation and standard error) are listed in Tables 3 and 4. Considering the correlation coefficient and the standard error values obtained for the site data, it is observed from Table 3 that the linear regression model of Shariati et al. [2] provides the best prediction, with the other linear model of Dauji et al. [3] along with the exponential model of Raouf and Ali [4] being the next best ones. This indicates that for actual existing structures, a linear regression model between the USPV and concrete strength would provide good approximation for the purpose of prediction and that the exponential model might be considered as well.

It is noted in Table 4 pertaining to the laboratory experimental data that again linear correlation model emerges as the best model, with Dauji et al. [3] model being the best from consideration of the correlation coefficient and standard error, along with Shariati et al. [2] coming a close second. In case of laboratory data, however, the exponential model of Popovics et al. [5] comes third best with both the correlation coefficient and the standard error poor compared to Shariati et al. [2]. Therefore, it can be stated from this study that for laboratory data, the linear regression should be favoured when developing prediction equations for concrete strength as a function of USPV.

Table 3 Comparison of various correlation models with site experimental data of Turgut [6]

Equation no.	Correlation model	Researchers	$r_{xy}{}^2$	$s_{yx}{}^2$ (MPa)
1	Linear models	Shariati et al. [2]	0.760	18.7
2		Dauji et al. [3]	0.762	30.38
3	Exponential regression model	Raouf and Ali [4]	0.760	26.04
4		Popovics et al. [5]	0.564	14.28
5		Turgut [6]	0.721	30.31
6	Power regression model	Bhosale and Salunkhe [6]	0.723	39.38

Table 4 Comparison of various correlation models with laboratory experimental data of Bhosale and Salunkhe [7]

Equation no.	Correlation model	Researchers	r_{xy}^2	s_{yx}^2 (MPa)
1	Linear models	Shariati et al. [2]	0.815	12.67
2		Dauji et al. [3]	0.815	12.23
3	Exponential regression model	Raouf and Ali [4]	0.811	61.2
4		Popovics et al. [5]	0.797	17.82
5		Turgut [6]	0.807	124.44
6	Power regression model	Bhosale and Salunkhe [6]	0.808	28.94

6 Concluding Remarks

In this article, the suitability of a particular form of correlation expression between USPV and compressive strength of concrete has been checked by applying it on a variety of experimental data taken from the literature. Evaluation of concrete strength as a function of USPV by different forms of correlation models suggested that linear correlation model is most suitable for both on-site and laboratory experimental data considered in this study. The estimated value of concrete strength based on USPV measurements can thus be utilized for re-evaluation exercises of existing concrete structures.

References

1. IS 516 (2018) (Part5/Sec. 1), Hardened concrete—methods of test, part 5 non-destructive testing of concrete, section 1 ultrasonic pulse velocity testing, Bureau of Indian Standards, New Delhi
2. Shariati M, Ramli-Sulong NH, Mohammad Mehdi Arabnejad KH, Shafigh P, Sinaei H (2011) Assessing the strength of reinforced structures through ultrasonic pulse velocity and Schmidt rebound hammer test. Sci Res Essays 6(1):213–220
3. Dauji S, Bhalerao S, Srivastava PK, Bhargava K (2019) Conservative characteristic strength of concrete from non-destructive and partially destructive testing. J Asian Concr Fed 5(1):25–39
4. Raouf Z, Ali ZM (1983) Assessment of concrete characteristics at an early age by ultrasonic pulse velocity. J Build Res 2(1):31–44
5. Popovics S, Joseph LR, John SP (1990) The behaviour of ultrasonic pulses in concrete. Cem Concr Res 20(2):259–270
6. Turgut P 2004 Research into the correlation between concrete strength and UPV values. NDT.net 9(12):1–5. https://www.ndt.net/article/v09n12/turgut/turgut.htm
7. Bhosale N, Salunkhe PA (2016) To establish relation between destructive and non-destructive tests on concrete. Int J Eng Res Gen Sci 4(2):634–644
8. Ranganathan R (1999) Structural reliability: analysis and design. Jaico Publishing House, Mumbai
9. Soong TT (2004) Fundamentals of probability and statistics for engineers. Wiley, New York

Bending Analysis of Laminated Composite Cylindrical Shell Using Fifth Order Shear Deformation Theory

M. Shinde Bharti and S. Sayyad Atteshamuddin

Abstract In the present study, a fifth order shear and normal deformation theory is extended for the bending analysis of laminated composite cylindrical shells. The effect of transverse normal and shear deformations is included to predict the displacement and stresses. The governing equations are derived using principle of virtual work, and solved by using Navier's technique. The accuracy and efficacy of the present theory is checked by comparing the present results with those available in the literature.

Keywords Cylindrical shell · Laminated composite · Shear deformation

1 Introduction

Structural components made up of fiber reinforced composite material are having a wide applications in the field of aerospace, marine, automobile, civil, etc. Composite materials are having the attractive properties like high strength-to-weight ratio, lightweight, high stiffness-to-weight ratio. Therefore, the static, free vibration and buckling analysis of cylindrical shells made up of fibrous composite materials is the active area of research among researchers. In past decades, Kirchoff [1] has developed a classical shell theory (CST) for thin shells, and a first order shear deformation theory (FSDT) is developed by Mindlin [2] for analysis of shells. But due to limitations of CST and FSDT, many researchers have developed the higher order shear deformation theories (HSDT) using different polynomial function satisfying the zero transverse shear stress condition at top and bottom of the shell to predict the accurate static, free vibration and buckling behavior of cylindrical composite shells.

Reddy [3] developed a third order shear deformation theory for the static analysis of shells. Bhimaraddi and Chandrashekhara [4] developed a 3D elasticity solution for static analysis of cylindrical shell. A generalized higher-order shear deformation theory is presented by Mantari and Soares [5] for static and dynamic analysis of

M. Shinde Bharti (✉) · S. Sayyad Atteshamuddin
Department of Structural Engineering, Sanjivani College of Engineering, Kopargaon, Maharashtra, India
e-mail: shindebhartist@sanjivani.org.in

S. B. Singh et al. (eds.), *Fiber Reinforced Polymeric Materials and Sustainable Structures*, Composites Science and Technology, https://doi.org/10.1007/978-981-19-8979-7_19

laminated composite shells. Recently, Sayyad and Ghugal [6] presented a general shell theory for the stress analysis of laminated composite and sandwich cylindrical shells. In this paper, fifth order shear and normal deformation theory is extended for the static analysis of laminated composite cylindrical shell. The theory consider the effect of both transverse shear and normal deformation to predict the transvers shear stresses, also the expansion of polynomial shape function is upto fifth order for the accurate prediction of displacement and stresses. Principle of virtual work is used to derive the nine governing equations. Navier's analytical solution is used to solve governing equations for a simply supported laminated composite cylindrical shells. The present theory satisfy the zero shear stress at top and bottom of the shell surface. The present displacement and stresses are compared with the other theories available in literature.

2 Cylindrical Shell Under Consideration

The simply supported cylindrical shells having a width a in x-direction, breadth b in y-direction and thickness h in z-direction is considered in the present study. The geometry and co-ordinate system in the cylindrical shell is as shown in the Fig. 1. Figure 1 shows the geometry and principle axes in the spherical shell at the mid-plane. The shell is made up of multiple layers of laminas of same thickness.

2.1 Displacement Field

The displacement field of the present theory is as follows,

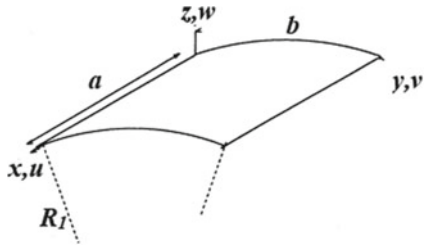

Fig. 1 Geometry and co-ordinate system of cylindrical shell

$$
\begin{aligned}
u(x, y, z) &= \left(1 + z/R_1\right)u_0(x, y) - z w_{0,x} + f_1(z)\phi_x(x, y) + f_2(z)\psi_x(x, y) \\
v(x, y, z) &= v_0(x, y) - z w_{0,y} + f_1(z)\phi_y(x, y) + f_2(z)\psi_y(x, y) \\
w(x, y, z) &= w_0(x, y) + f_1^{'}(z)\phi_z(x, y) + f_2^{'}(z)\psi_z(x, y) \\
f_1(z) &= z - \frac{4z^3}{3h^2},\ f_2(z) = z - \frac{16z^5}{5h^4},\ f_1^{'}(z) = 1 - \frac{4z^2}{h^2}, \\
f_2^{'}(z) &= 1 - \frac{16z^4}{h^4},\ f_1(z) = -\frac{8z}{h^2},\ f_2(z) = -\frac{64z^3}{h^4}
\end{aligned}
\tag{1}
$$

where, *u, v* and *w* are in-plane and transverse displacements and u_0, v_0, w_0 are the displacements in the mid-plane of the shell in *x*, *y* and *z* direction respectively. The parameters $\phi_x, \phi_y, \phi_z, \psi_x, \psi_y, \psi_z$ represents the shear slopes occurred in the mid-plane displacements in *x, y, z* direction after deformation.

2.2 Stress–Strain Relationships

The normal and shear strains are expressed as,

$$
\begin{Bmatrix} \varepsilon_x \\ \varepsilon_y \\ \varepsilon_z \end{Bmatrix} = \begin{Bmatrix} \partial u/\partial x + w/R_1 \\ \partial v/\partial y \\ \partial w/\partial z \end{Bmatrix}, \quad \begin{Bmatrix} \gamma_{xy} \\ \gamma_{xz} \\ \gamma_{yz} \end{Bmatrix} = \begin{Bmatrix} \partial u/\partial y + \partial v/\partial x \\ \partial w/\partial x + \partial u/\partial z - u_0/R_1 \\ \partial w/\partial y + \partial v/\partial z \end{Bmatrix} \tag{2}
$$

Further, the stress–strain relationship can be written using, the Hooke's law as,

$$
\overline{\sigma} = \overline{Q}_{ij}\overline{\varepsilon} \tag{3}
$$

where, $\overline{\sigma}$ represents a stress vector; $\overline{\varepsilon}$ represents a strain vector; $\overline{Q}_{ij}$ represents a stiffness matrix ($i, j = 1, 2, 3, 4, 5, 6$).

3 Governing Equations

The governing equations for the bending analysis can be obtained using the principle of virtual work expressed as,

$$
\int_{dv} \sigma_{ij}\,\delta\varepsilon_{ij}\,dv - \int_{dA} q(x, y)\delta w\,dA = 0 \tag{4}
$$

where, δ is variational operator. Therefore, substituting the stress–strain values the governing equations can be expressed as,

$$
\begin{aligned}
&\boldsymbol{\delta u_0} : -A_{x,x} - A_{xy,y} = 0\\
&\boldsymbol{\delta v_0} : -A_{y,y} - A_{xy,x} = 0\\
&\boldsymbol{\delta w_0} : -B^b_{x,xx} - B^b_{y,yy} - 2B^b_{xy,xy} + A_x \big/ R_1 = q\\
&\boldsymbol{\delta \phi_x} : -B^{S1}_{x,x} - B^{S1}_{xy,y} + C^{S1}_x = 0\\
&\boldsymbol{\delta \psi_x} : -B^{S2}_{x,x} - B^{S2}_{xy,y} + C^{S2}_x = 0\\
&\boldsymbol{\delta \phi_{y:}} : -B^{S1}_{y,y} - B^{S1}_{xy,x} + C^{S1}_y = 0\\
&\boldsymbol{\delta \psi_y} : -B^{S2}_{y,y} - B^{S2}_{xy,x} + C^{S2}_y = 0\\
&\boldsymbol{\delta \phi_z} : -C^{S1}_{x,x} - C^{S1}_{y,y} + D_{xs1} \big/ R_1 + D_{ys1} \big/ R_2 + D^{S1} = 0\\
&\boldsymbol{\delta \psi_z} : -C^{S2}_{x,x} - C^{S2}_{y,y} + D_{xs2} \big/ R_1 + D_{ys2} \big/ R_2 + D^{S2} = 0
\end{aligned}
\tag{5}
$$

where, expressions for stress resultants can be derived from following relations.

$$
\begin{aligned}
&\left(A_x,\ A_y,\ A_{xy}, B^b_x,\ B^b_y,\ B^b_{xy}\right) = \int_{-h/2}^{h/2} \left[\sigma_x,\ \sigma_y,\ \tau_{xy}, z\sigma_x,\ z\sigma_y,\ z\tau_{xy}\right] dz\\
&\left(B^{S_1}_x,\ B^{S_1}_y, B^{S_1}_{xy},\right) = \int_{-h/2}^{h/2} \left\{\left[f_1(z)\left(\sigma_x,\ \sigma_y,\ \tau_{xy}\right)\right]\right\} dz\\
&\left(B^{S_2}_x,\ B^{S_2}_y B^{S_2}_{xy}\right) = \int_{-h/2}^{h/2} \left\{\left[f_2(z)\left(\sigma_x,\ \sigma_y,\ \tau_{xy}\right)\right]\right\} dz\\
&\left(C^{S_1}_x,\ C^{S_1}_y,\ C^{S_2}_x, C^{S_2}_y\right) = \int_{-h/2}^{h/2} \left\{\left[f_1^{'}(z)\left(\tau_{xz}, \tau_{yz}\right)\right], \left[f_2^{'}(z)\left(\tau_{xz}, \tau_{yz}\right)\right]\right\} dz\\
&\left(D^{S_1}, D^{S_2}\right) = \int_{-h/2}^{h/2} \left[\{\sigma_z\left[f_1(z),\ f_2(z)\right]\},\right] dz\\
&\left(D_{xS1}, D_{xS2}\right) = \int_{-h/2}^{h/2} \left[\left\{\sigma_x\left[f_1^{'}(z),\ f_2^{'}(z)\right]\right\}\right] dz\\
&\left(D_{yS1}, D_{yS2}\right) = \int_{-h/2}^{h/2} \left[\left\{\sigma_y\left[f_1^{'}(z),\ f_2^{'}(z)\right]\right\}\right] dz
\end{aligned}
\tag{6}
$$

4 Navier's Solution Scheme

To obtain the analytical solutions for the governing equations stated in Eq. (5). The Navier's analytical technique is used. The simply supported boundary conditions are as follows,

Along the edges $x = 0$ and $x = a$	Along the edges $y = 0$ and $y = b$
$v_0 = w_0 = \phi_y = \psi_y = \phi_z = \psi_z = 0$ $M_x^b = M_x^{S1} = M_x^{S2} = N_x = 0$	$u_0 = w_0 = \phi_x = \psi_x = \phi_z = \psi_z = 0$ $M_y^b = M_y^{S1} = M_y^{S2} = N_y = 0$

The expression for Navier solution can be written as,

$$\begin{aligned}
(u_0,\ \phi_x,\ \psi_x) &= \sum_{m=1,3,5}^{\infty} \sum_{n=1,3,5}^{\infty} (u_1,\ \phi_{x1},\ \psi_{x1})\cos\alpha x\ \ \sin\beta y \\
\left(v_0,\ \phi_y,\ \psi_y\right) &= \sum_{m=1,3,5}^{\infty} \sum_{n=1,3,5}^{\infty} \left(v_1,\ \phi_{y1},\ \psi_{y1}\right)\sin\alpha x\ \ \cos\beta y \\
(w_0,\ \phi_z,\ \psi_z) &= \sum_{m=1,3,5}^{\infty} \sum_{n=1,3,5}^{\infty} (w_1,\ \phi_{z1},\ \psi_{z1})\sin\alpha x\ \ \sin\beta y \\
q(x, y) &= \sum_{m=1,3,5}^{\infty} \sum_{n=1,3,5}^{\infty} q_0 \sin\alpha x \sin\beta y
\end{aligned} \tag{7}$$

where, $\alpha = m\pi/a,\ \ \beta = n\pi/b$; $u_1,\ \phi_{x1},\ \psi_{x1}, v_1,\ \phi_{y1},\ \psi_{y2}, w_1,\ \phi_{z1},\ \psi_{z1}$ are the unknown parameters. Substituting the Eq. (7) in the Eq. (5) the resulting equation can be expressed in matrix form as,

$$[K]\{\Delta\} = \{f\} \tag{8}$$

where $[K]$ is stiffness matrix, $\{\Delta\}$ is the vector of unknowns, $\{f\}$ is the force vector.

5 Illustrative Examples

In the present study the displacement and stresses in laminated composite cylindrical shells is presented and compared with Reddy's PST (Parabolic Shell Theory) [3], Bhimaraddi and Chan-drashekhara's 3D elasticity [4] and Mindlin's FSDT (First Order Shear Deformation Theory) [2].

$$E_1 = 36.0885\,\text{GPa}, \quad E_2 = 26.2818\,\text{GPa},$$
$$G_{12} = 4.9033\,\text{GPa}, G_{31} = 4.4130\,\text{GPa}, \tag{9}$$
$$G_{23} = 4.0208\,\text{GPa}, \quad \mu_{12} = \mu_{13} = \mu_{23} = 0.105$$

The displacement and stresses are presented using following non-dimensional forms,

$$\overline{w} = w\,E\big/q_0\,a, \quad \overline{\sigma}_x = \sigma_x\big/q_0, \quad \overline{\tau}_{zx} = \tau_{zx}\big/q_0 \tag{10}$$

The static analysis of the cylindrical shell considering both transverse shear and transverse normal effect, is highly recommended by researchers in there research. Therefore considering this recommendations in the present study a fifth order shear and normal deformation theory is applied for static analysis of laminated composite cylindrical shell. Table 1 shows the comparison of displacement and stresses in isotropic, 0 °/90 °, 0 °/90 °/0 ° cylindrical shells at $h/a = 0.1$. The present results are compared with the Reddy [3], Mindlin [2], Bhimaraddi and Chandrashekhara [4]. From Table 1 it is observed that the present displacement and in-plane stresses are in excellent agreement with the 3D elasticity solution presented by Bhimaraddi and Chandrashekhara [4]. The results of transverse shear stresses $\overline{\tau}_{xz}$ are obtained using constitutive relation and therefore underestimates the 3d elasticity results given by Bhimaraddi and Chandrashekhara. Figures 2 and 3 shows the through thickness variation of the in-plane and shear stresses in (0 °/90 °) and (0 °/90 °/0 °) cylindrical shells respectively.

6 Conclusions

In the present paper, the bending analysis of simply supported laminated composite cylindrical shell is presented. The present displacement and stresses are found to be in excellent agreement with the 3D solution given by Bhimaraddi and Chandrashekhara [4]. Also, the present theory satisfies the zero shear stress condition at top and bottom surfaces of the shells.

Table 1 Displacements and stresses in laminated composite cylindrical shells with different R/a values ($h/a = 0.1$, $a/b = 1$)

		R/a	Model			
			Present	Reddy [3]	Mindlin [2]	Bhimaraddi and Chandrashekhara [4]
			FOSNT	PST	FST	3D elasticity
Isotropic	$\overline{w}$	5	28.877	28.756	28.508	29.003
		10	29.497	29.390	29.130	29.379

(continued)

Table 1 (continued)

		R/a	Model			
			Present	Reddy [3]	Mindlin [2]	Bhimaraddi and Chandrashekhara [4]
		20	29.639	29.552	29.290	29.445
	$\overline{\sigma}_x$	5	21.098	20.808	20.620	21.138
		10	20.769	20.532	20.342	20.719
		20	20.475	20.277	20.088	20.413
	$\overline{\tau}_{xz}$	5	2.3081	2.3132	2.3193	2.3455
		10	2.3632	2.3642	2.3699	2.3787
		20	2.3775	2.3773	2.3830	2.3847
0 °/90 °	$\overline{w}$	1	38.886	35.358	35.020	41.340
	$\overline{\sigma}_x$	1	25.114	17.198	17.030	23.700
	$\overline{\tau}_{xz}$	1	1.1865	1.4140	1.4284	1.7763
0 °/90 °/0 °	$\overline{w}$	1	36.400	35.097	34.743	40.823
	$\overline{\sigma}_x$	1	22.189	21.246	21.031	23.987
	$\overline{\tau}_{xz}$	1	1.0116	1.6189	1.6382	1.8290

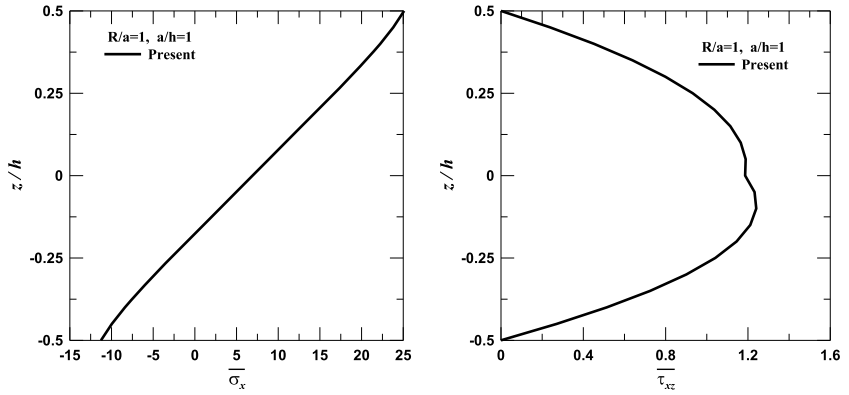

Fig. 2 Through-the-thickness profiles of in-plane stress and shear stress for two-ply (0 °/90 °) laminated shells

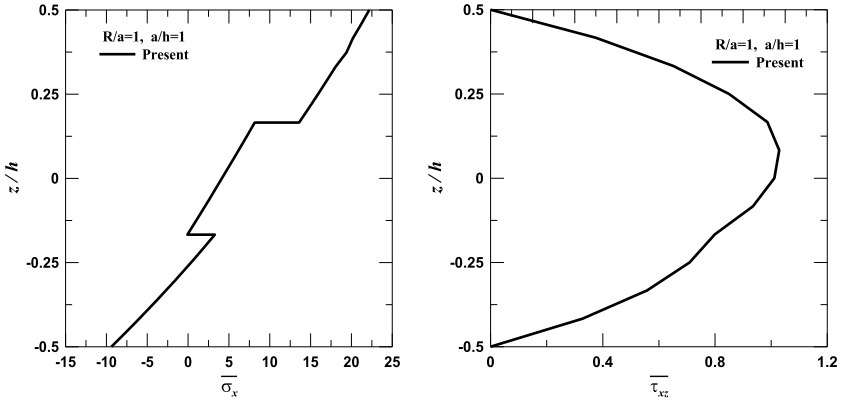

Fig. 3 Through-the-thickness profiles of in-plane stress and shear stress for three-ply (0 °/90 °/0 °) laminated shells

References

1. Kirchhoff GR (1850) Uber das Gleichgewicht und die Bewegung einer Elastischen Scheibe. J Reine Angew Math (Crelle) 40:51–88
2. Mindlin RD (1951) Influence of rotary inertia and shear on flexural motions of isotropic, elastic plates. ASME J Appl Mech 18:31–38
3. Reddy JN (1984) A simple higher-order theory for laminated composite plates. J Appl Mech 51(4):745–752
4. Bhimaraddi A, Chandrashekhara K (1992) Three-dimensional elasticity solution for static response of simply supported orthotropic cylindrical shells. Compos Struct 20:227–235
5. Mantari JL, Soares CG (2012) Analysis of isotropic and multilayered plates and shells by using a generalized higher-order shear deformation theory. Compos Struct 94:2640–2656
6. Sayyad AS, Ghugal YM (2020) Stress analysis of laminated composite and sandwich cylindrical shells using a generalized shell theory. Composite Mater Eng 2(2):103–124

Performance Characteristics and Economical Evaluation of Various Types of Nanomaterial Concrete

H. Da Raghavendra Prasad, S. C. Sharma, and Nagaraj Sitaram

Abstract In this study, a concrete cube was created by partially replacing Ordinary Portland Cement (OPC) with Nano Materials such as Multi-walled Carbon Nano Tubes (MWCNTs), Titanium Di Oxide (TiO2), and Copper Oxide (CuO) at various percentages. MWCNTs were replaced by OPC by 0.01, 0.025, 0.05, and 0.075%, TiO2 by 0.25, 0.5, 0.75, and 1 percent, and CuO by 0.5, 1, 1.2, 1.5, and 2%. Using Nano Materials gives more compressive strength than normal concrete cubes, and MWCNT outperforms TiO_2 and CuO. Simply to reduce cement usage Fly ash was used while the compressive strength and amount of Nano Materials remained constant. As much as 39% Ordinary Portland Cement can be replaced with up to 35% MWCNTs and Fly Ash, 35% TiO_2 and Fly Ash, and up to 34% CuO and Fly Ash. According to the cost analysis, TiO_2 with Fly Ash costs 26.77Rs to prepare a single cube with a maximum replacement of 35% of OPC, while MWCNTs and CuO with Fly Ash cost 146.86 and 42.51Rs to prepare a single concrete cube with a maximum replacement of 39 and 34%, respectively, and normal OPC concrete cubes require 27.98 Rs. In OPC concrete, almost TiO2 cube preparation took a 10% reduction when compared to Normal Concrete cube. In this work, the carbon score was calculated, and the maximum carbon emission reduction up to By replacing cement with MWCNTs and Fly Ash, OPC concrete cube can be reduced by 35%. As a result, we concluded that TiO2 with Fly Ash Nano Material concrete is the most cost-effective when compared to MWCNTs and CuO with Fly Ash. When compared to TiO_2 and CuO with Fly Ash, MWCNTs with Fly Ash provide the greatest replacement and carbon emission reduction.

H. Da Raghavendra Prasad
Department of Civil Engineering, CERSSE, Jain University, Bangalore 562112, India

S. C. Sharma
Department of Mechanical Engineering, Jain University, Bangalore 562112, India

N. Sitaram (✉)
Department of Civil Engineering, East Point College of Engineering and Technology, Bangalore 560049, India
e-mail: naghydro@gmail.com

S. B. Singh et al. (eds.), *Fiber Reinforced Polymeric Materials and Sustainable Structures*, Composites Science and Technology, https://doi.org/10.1007/978-981-19-8979-7_20

Keywords Nano material concrete cube · Replacement for cement · Cost analysis · Carbon score

1 Introduction

Cement is a material which is used the most in construction to withstand load. Due to its vast use the emission of carbon towards the atmosphere is increasing day by day. To withstand these issues we need to reduce use of cement by replacing cement with some other materials which shows the properties of cement. Nowadays research on nano materials is going widely in all the areas. So in this work partial replacement of cement with the selected nano materials has been done with which the cost and strength analysis also carried out for economical construction [1]. Researchers replaced GGBS as a replacement for cement results in which increase its strength [2]. Three different mineral admixtures were used as partial replacement in different percentages to cement to prepare self compacting concrete results in compressive strength of 60 MPa [3]. Concrete mixtures was prepared by using alkali resistant glass fiber in which the results in increased compressive strength from 57.85 to 66.6 MPa [2]. In this work concrete compressive strength with coal bottom ash fineness brings about 12.7 and 5.8% increase in strength compare for controlling mix in water and seawater for about 180 days [1]. In this work fifteen mixtures with different percentages of fiber and silica fume have used results in increment in split tensile strength and flexural strength [4]. Partially replacing coal bottom ash in concrete leads to the development of compressive strength up-to 11.32 and 13.92% on comparison to regular mix [5]. In this research plastic waste in different proportion (40, 50, 60 and 70%) was used as partial replacement for cement results in properties and the compressive strength also rises with rise in percentage of plastic waste content [6]. Different nano materials with different percentages have been used in this compressive strength is increased up to 0.05% replacement with MWCNTs, TiO_2 and CuO.

2 Tests on Materials

2.1 Tests on Fresh Concrete Prepared by Ordinary Portland Cement (OPC)

Fresh has been tested using Ordinary Portland Cement (OPC) with Fine and Coarse Aggregate and with different concrete percentages of cement replaced with Nano Materials (Fig. 1 and Tables 1, 2, 3, 4, 5 and 6).

As mentioned in the Table 7 various tests for fine aggregates and coarse aggregates have been performed with river sand of particle size lesser than 4.75 mm and crushed stone with particle size above 4.75 mm (Fig. 2).

Fig. 1 Tests on cement

Table 1 Tests on ordinary Portland cement (OPC) with Multi-walled carbon nano tubes (MWCNTs) at different % weight to cement

S. No.	Tests	Result				Standard values
		0%	0.1%	0.25%	0.5%	
1	Fineness (%)	8.5	8.6	8.65	8.62	<10
2	Specific gravity	3.15	3.12	3.1	3.16	<3.19
3	Consistency (%)	32	33	30	31	25–35
4	Initial and final setting time (min)	32 and 589 min	35 and 580 min	35 and 576 min	38 and 553 min	>30 <600 min

Table 2 Tests on ordinary Portland cement (OPC) with titanium di oxide (TiO2) at different % weight to cement

S. No.	Tests	Result				Standard values
		0%	0.1%	0.25%	0.5%	
1	Fineness (%)	8.5	8.3	8.4	8.43	<10
2	Specific gravity	3.15	3.1	3.03	3.12	<3.19
3	Consistency (%)	32	30	32	31	25–35
4	Initial and final setting time (min)	32 and 589 min	31 and 582 min	30 and 580 min	33 and 569 min	>30 <600 min

2.2 Tests on Fresh Concrete

Table 8 shows the result for M20 grade concrete with different percentage of Nano materials replaced to cement (Table 9).

Table 3 Tests on Portland Pozzolana cement (PPC) with copper oxide (CuO) at different % weight to cement

S. No.	Tests	Result				Standard values
		0%	0.1%	0.25%	0.5%	
1	Fineness (%)	8.5	8.7	8.6	8.8	<05
2	Specific gravity	3.15	3.12	3.14	3.14	<3.19
3	Consistency (%)	32	31	32	31	25–35
4	Initial and final setting time (min)	32 and 589 min	32 and 594 min	31 and 580 min	34 and 574 min	>30 <600 min

Table 4 Tests on Portland Pozzolana cement (PPC) with multi-walled carbon nano tubes (MWCNTs) at different % weight to cement

S. No.	Tests	Result				Standard values
		0%	0.1%	0.25%	0.5%	
1	Fineness (%)	3.8	3.8	3.82	3.84	<05
2	Specific gravity	3.05	3.06	3.06	3.12	<3.19
3	Consistency (%)	28	29	28	31	25–35
4	Initial and final setting time (min)	32 and 584	33 and 586	35 and 586	36 and 592	>30 <600

Table 5 Tests on Portland Pozzolana cement (PPC) with titanium di oxide (TiO_2) at different % weight to cement

S. No.	Tests	Result				Standard values
		0%	0.1%	0.25%	0.5%	
1	Fineness (%)	3.8	3.8	3.8	3.7	<05
2	Specific gravity	3.05	3.05	3.06	3.05	<3.19
3	Consistency (%)	28	28	28	27	25–35
4	Initial and final setting time (min)	35 and 583	36 and 589	35 and 589	38 and 590	>30 <600

Table 6 Tests on Portland Pozzolana cement (PPC) with copper oxide (CuO) at different % weight to cement

S. No.	Tests	Result				Standard values
		0%	0.1%	0.25%	0.5%	
1	Fineness (%)	3.8	3.8	3.7	3.9	<05
2	Specific gravity	3.05	3.05	3.12	3.09	<3.19
3	Consistency (%)	28	27	29	29	25–35
4	Initial and final setting time (min)	32 and 589	32 and 588	34 and 589	35 and 591	>30 <600

Table 7 Tests on aggregates

S. No.	Material	Tests	Result	Remarks
1	Fine aggregate	Specific gravity	2.32	Around 2.65
2		Water absorption	1.43%	0.3–3%
3		Sieve analysis	2.84	Fineness modulus
1	Coarse aggregate	Specific gravity	2.56	Around 2.65
2		Water absorption	1.65%	0.3–3%
3		Sieve analysis	3.56	Fineness modulus
4		Impact load test	24.3%	Varies on materials

Fig. 2 Tests on aggregates

Table 8 Tests on fresh concrete using ordinary Portland cement

S. No.	Nano material	Tests	Result				Standard values
			OPC				
			0%	0.1%	0.25%	0.5%	
1	MWCNTs	Slump test	35 mm	35 mm	32 mm	31 mm	25–125 mm
2		Compaction factor	0.85	0.82	0.85	0.90	0.7–0.95
1	TiO_2	Slump test	35 mm	36 mm	36 mm	35 mm	25–125 mm
2		Compaction factor	0.85	0.82	0.87	0.89	0.7–0.95
1	CuO	Slump test	35 mm	35 mm	36 mm	36 mm	25–125 mm
2		Compaction factor	0.85	0.84	0.86	0.86	0.7–0.95

Table 9 Tests on fresh concrete using Portland Pozzolana cement

S. No.	Nano material	Tests	Result				Standard values
			PPC				
			0%	0.1%	0.25%	0.5%	
1	MWCNTs	Slump test	29 mm	30 mm	30 mm	30 mm	25–125 mm
2		Compaction factor	0.87	0.88	0.90	0.85	0.7–0.95
1	TiO_2	Slump test	29 mm	29 mm	31 mm	30 mm	25–125 mm
2		Compaction factor	0.87	0.88	0.89	0.90	0.7–0.95
1	CuO	Slump test	29 mm	30 mm	31 mm	30 mm	25–125 mm
2		Compaction factor	0.87	0.87	0.88	0.87	0.7–0.95

3 Results and Discussion

3.1 Comparison of Compressive Strength OPC and PPC Using Different Nano Materials

Compressive Strength test for M20 grade concrete cube has been conducted for different percentages of Nano materials replaced to cement after 7, 14 and 28 days of curing (Figs. 3, 4 and Tables 10, 11).

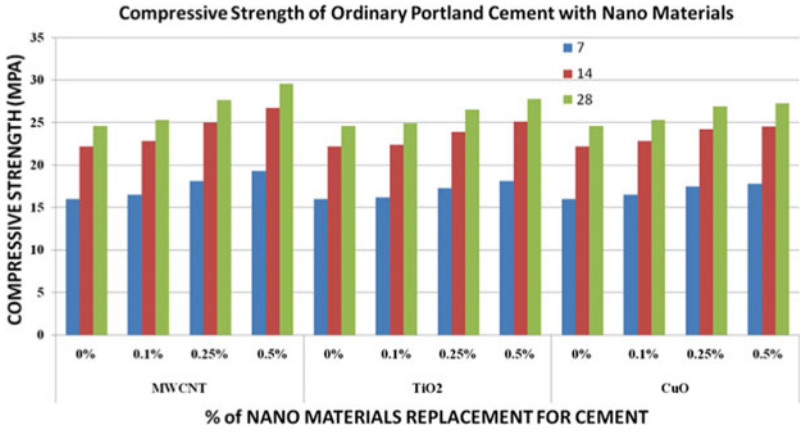

Fig. 3 Compressive strength for concrete cubes using ordinary Portland cement

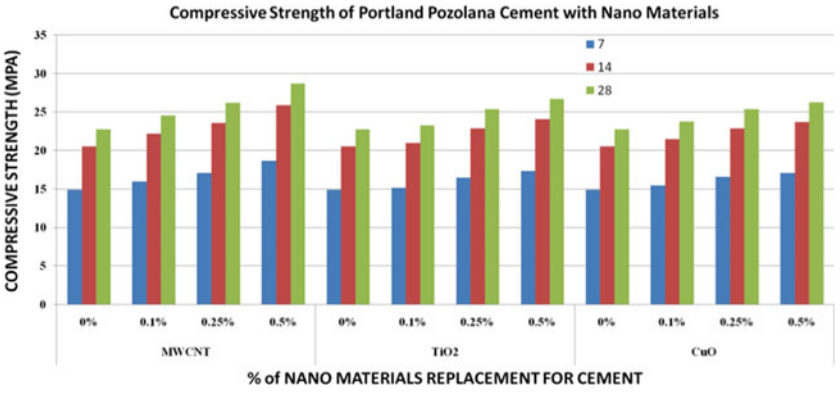

Fig. 4 Compressive strength for concrete cubes using Portland Pozzolana cement

3.2 Weight of Nano Materials and Cement Used per Cube

In our project we have used M20 grade concrete with the different percentages of 0, 0.1, 0.25 and 0.5% and the resulted table has been shown (Table 12).

At the end of the table it is clearly shown that as we apply more percentage of nano materials the compressive strength of cement increases when compare to Titanium Di Oxide and Copper Oxide, MWCNT gives more compressive strength.

Table 10 Compressive strength for concrete cubes using Ordinary Portland cement

S. No.	Material	Days	Percentage replacement			
			Compressive strength (MPA)			
			0.1%	0.25%	0.5%	0%
1	MWCNT	7	16.5	18.1	19.3	16.0
2		14	22.8	25.0	26.7	22.2
3		28	25.3	27.7	29.6	24.6
1	TiO2	7	16.2	17.3	18.1	16.0
2		14	22.4	23.9	25.1	22.2
3		28	24.9	26.5	27.8	24.6
1	CuO	7	16.5	17.5	17.8	16.0
2		14	22.8	24.2	24.57	22.2
3		28	25.3	26.9	27.3	24.6

Table 11 Compressive strength for concrete cubes using Portland Pozzolana cement

S. No.	Material	Days	Percentage replacement			
			Compressive strength (MPA)			
			0.1%	0.25%	0.5%	0%
1	MWCNT	7	16.0	17.1	18.7	14.9
2		14	22.2	23.6	25.9	20.6
3		28	24.6	26.2	28.7	22.8
1	TiO2	7	15.2	16.51	17.4	14.9
2		14	21.0	22.9	24.1	20.6
3		28	23.3	25.4	26.7	22.8
1	CuO	7	15.5	16.6	17.1	14.9
2		14	21.5	22.9	23.7	20.6
3		28	23.8	25.4	26.3	22.8

3.3 Cost Analysis Using Ordinary Portland Cement (OPC)

In the Table 13 the cost for cement which is used to prepare a single concrete cube has been shown.

From the Table 13 the cost of cement has been shown for the preparation of single concrete cube. As it clearly shows that the amount is decreases due to the increase in Nano Materials.

Table 12 Weight of nano materials and cement used per cube

Nano materials	% of nano materials to cement	Weight of cement (g)	Weight of nano materials (g)
MWCNTs	0	1149	0
	0.1	1147.8	1.2
	0.25	1146.1	2.9
	0.5	1143.2	5.8
TiO2	0	1149	0
	0.1	1147.8	1.2
	0.25	1146.1	2.9
	0.5	1143.2	5.8
CuO	0	1149	0
	0.1	1147.8	1.2
	0.25	1146.1	2.9
	0.5	1143.2	5.8

Table 13 Cost analysis of cement used

Nano materials	% Replacement of cement	Weight of cement (g)	Cost of cement	Total cost for cement (Rs)
MWCNTs	0	1149	430.00 Rs per 50 kg	9.88
	0.1	1147.8		9.87
	0.25	1146.1		9.85
	0.5	1143.2		9.83
TiO2	0	1149		9.88
	0.1	1147.8		9.87
	0.25	1146.1		9.85
	0.5	1143.2		9.83
CuO	0	1149		9.88
	0.1	1147.8		9.87
	0.25	1146.1		9.85
	0.5	1143.2		9.83

3.4 Cost Analysis of Nano Materials Used

In the Table 14 we have discussed about the cost of Nano Materials which have been used for the preparation of single concrete cube as a partial replacement for cement in various percentages.

At the end of the table we can conclude that TiO_2 is a much economical nano material in comparison to the other two nano materials.

Table 14 Cost analysis of nano materials used

Nano materials	% Replacement of cement	Cost of nano materials	Weight of nano materials (g)	Total cost (Rs)
MWCNTs	0	1,23,000.00 Rs per Kg	0	0
	0.1		1.2	147.6
	0.25		2.9	356.7
	0.5		5.8	713.4
TiO2	0	500.00 Rs per Kg	0	0
	0.1		1.2	0.6
	0.25		2.9	1.45
	0.5		5.8	2.9
CuO	0	750.00 Rs per Kg	0	0
	0.1		1.2	0.9
	0.25		2.9	2.175
	0.5		5.8	4.35

Table 15 Cost analysis of aggregates used

Weight of fine aggregates (g)	Cost of fine aggregates	Total cost (Rs)
2680	0.95 Rs PER KG	2.55
Weight of coarse aggregates (g)	Cost of coarse aggregates	Total cost in Rs
4150	0.85 Rs PER KG	3.52
Total cost of aggregates		
6.07 Rupees/Cube		

3.5 Cost Analysis of Aggregates Used

In the Table 15 the cost of aggregates is calculated.

At the end of the table we can see that the total cost of the aggregates used is Rs 6.07.

3.6 Total Cost of Materials Used

The table and graph below discusses about the total cost and compressive strength of the nano material (MWCNTs) (Figs. 5 and 6).

From the Tables 16, 17 and 18 and graphs we can clearly see that as the price of the cement with 0.50% replaced Nano material is 729.3 and gives a compressive strength of 29.6 for MWCNTs, price of the cement with 0.50% replaced Nano material is 18.8

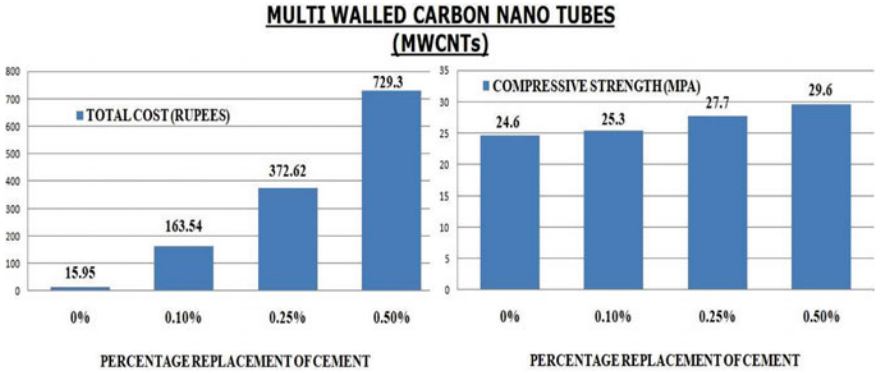

Fig. 5 Total cost of materials with compressive strength (MWCNTs)

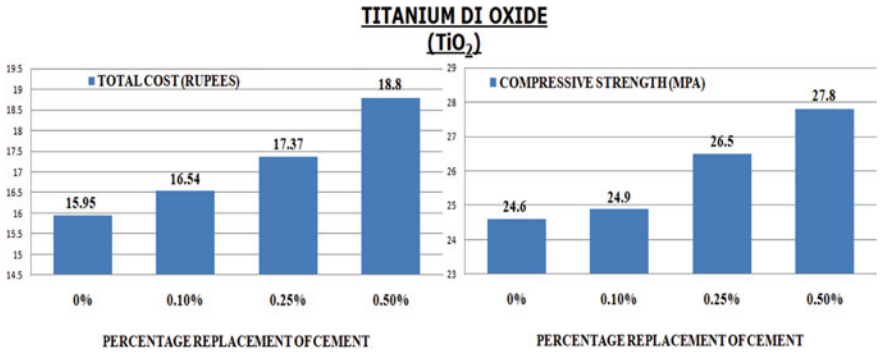

Fig. 6 Total cost of materials with compressive strength (TiO_2)

and gives a compressive strength of 27.8 for TiO_2 and finally the price of the cement with 0.50% replaced Nano material is 20.25 and gives a compressive strength of 27.3 so we can conclude that TiO_2 is much more economical and gives more strength in comparison to the other nano materials (Fig. 7).

Table 16 Total cost of materials with compressive strength (MWCNTs)

Nano materials	% Replacement of cement	Total cost in Rs	Compressive strength (MPA)
MWCNTs	0	15.95	24.6
	0.1	163.54	25.3
	0.25	372.62	27.7
	0.5	729.30	29.6

Table 17 Total cost of materials with compressive strength (TiO_2)

Nano materials	% Replacement of cement	Total cost in Rs	Compressive strength (MPA)
TiO2	0	15.95	24.6
	0.1	16.54	24.9
	0.25	17.37	26.5
	0.5	18.80	27.8

Table 18 Total cost of materials with compressive strength (CuO)

Nano materials	% Replacement of cement	Total Cost In Rs	Compressive Strength In MPA
CuO	0	15.95	24.6
	0.1	16.84	25.3
	0.25	18.10	26.9
	0.5	20.25	27.3

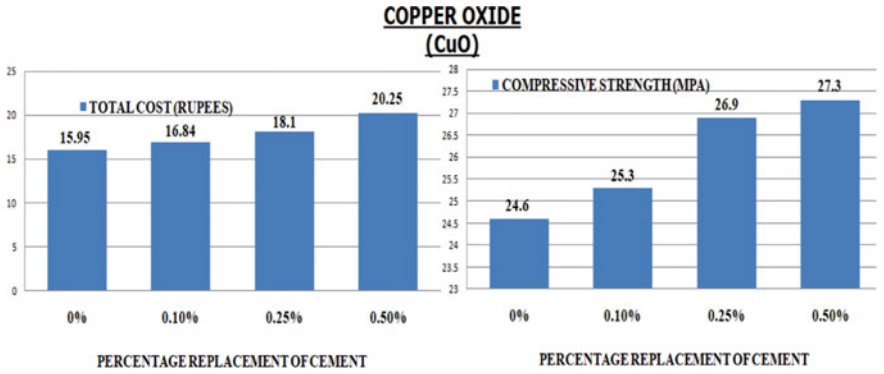

Fig. 7 Total cost of materials with compressive strength (CuO)

3.7 Carbon Emission Calculation for Ordinary Portland Cement (OPC)

As per the literature survey the manufacture of cement produces 0.9 pounds of CO_2 for every pound. That means for every 1 kg of cement will produce 0.9 kg of CO_2 as per the data collected from Portland Cement Association (PCA).

From the Table 19 it shows that the CO_2 emission is decrease when the increase in percentage of Nano Materials used (Fig. 8).

From the Table 19 and graph it shows that the 5.22 g of carbon reduction by reducing cement usage for the preparation of 1 concrete cube using nano materials up to 0.5% with increase in compressive strength.

Table 19 Carbon score versus compressive strength

Nano materials	% Replacement of cement	Weight of cement (g)	Weight of nano materials (g)	Carbon score (g)	Compressive strength (MPA)
MWCNTs	0	1149	0	0	22.8
	0.1	1147.8	1.2	1.08	24.6
	0.25	1146.1	2.9	2.61	26.2
	0.5	1143.2	5.8	5.22	28.7
TiO2	0	1149	0	0	22.8
	0.1	1147.8	1.2	1.08	23.3
	0.25	1146.1	2.9	2.61	25.4
	0.5	1143.2	5.8	5.22	26.7
CuO	0	1149	0	0	22.8
	0.1	1147.8	1.2	1.08	23.8
	0.25	1146.1	2.9	2.61	25.4
	0.5	1143.2	5.8	5.22	26.3

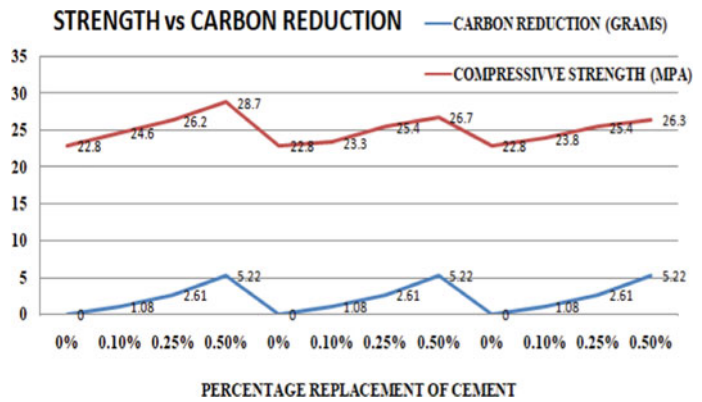

Fig. 8 Carbon score versus compressive strength

4 Conclusion

From the above discussions it can be concluded that Titanium Di Oxide (TiO_2) will give Economical when compare to Multi Walled Carbon Nano Tubes (MWCNTs) and Copper Oxide (CuO) as the cost of Titanium Di Oxide (TiO_2) is comparatively lesser than that of Multi Walled Carbon Nano Tubes (MWCNTs) and Copper Oxide (CuO). When it comes to strength analysis MWCNT gives higher strength compare to TiO_2 and CuO and reduction in carbon emission happens with reduction in cement usage compare to different nano materials with increase in compressive strength.

References

1. Mallisa H, Turuallo G (2017) The maximum percentage of fly ash to replace part of original Portland cement (OPC) in producing high strength concrete. Presented at the AIP Conf Proc
2. Mohammed Abdul Samee MAS, Ahmed MAS, Kaiser M, Safiuddin M (2017) Partial replacement of cement in concrete with fly ash and micro silica. SSRG Int J Civil Eng 4(4)
3. Monkman S, MacDonald M (2017) On carbon dioxide utilization as a means to improve the sustainability of ready-mixed concrete. J Clean Prod 167:365–375
4. Yakovlev GI et al (2017) Modification of cement matrix using carbon nanotube dispersions and nanosilica. Proc Eng 172:1261–1269
5. Yu X, Kang S, Long X (2018) Compressive strength of concrete reinforced by TiO2 nanoparticles. Presented at the AIP Conf Proc
6. Raghavendra Prasad NS (2021) Performance of nano materials for the strength development in concrete cube used as partial replacement for cement at different temperatures. Mater Today Proc 45:7253–7258
7. Ashwini BVB (2020) Effect of multiwall carbon nano tube incorporation on mechanical properties of concrete with partial replacement of cement with fly ash. Int J Eng Res Technol 9(9)
8. Raghavendra Prasad NS, Bairwa L, Mamgain A, Harish CS (2021) Performance evaluation of different types of nano concrete for sustainable construction. J Xidian Univ 15(6)
9. Yildirim M, Derun EM (2018) The influence of CuO nanoparticles and boron wastes on the properties of cement mortar. Materiales de Construcción 68(331)
10. Garcia VJ, Marquez CO, Zuniga-Suarez AR, Zuniga-Torres BC, Rios-Gonzalez PJ (2021) Mechanical and electrical properties of MWCNTs—high early strength cement—mortars composite: dispersion of CNTs and effect of chemical admixtures. An Acad Bras Cienc 93(3):e20200924

Performance of GGBS and SBA in Compressed Stabilized Earth Blocks

Apurwa D. Yawale and Subhash V. Patankar

Abstract Today with the rapidly increasing population and their housing demand, the whole world has been victimized by critical consequences of global warming and climate change. From simple to complex construction, materials being used not only consume massive energy and resources during their life cycle but also deteriorate the environment, releasing an enormous amount of dust, solid waste, and harmful gases. With an intention to provide an immediate solution in the form of sustainable alternative materials, compressed stabilized earth block (CSEB) is chosen in this study where in CSEB basic material used is soil. The performance of Ground Granulated Blast furnace Slag (GGBS) and Sugarcane Baggase Ash (SBA) used in CSEB is checked on the basis of density, water absorption and compressive strength. Specimens of size 190 mm × 90 mm × 90 mm were cast with 8% of cement in addition to the earth along with the addition of GGBS and SBA with varying percentages of 5, 10 and 15% each. The results showed that the CSEB blocks made by using GGBS or SBA have good strength characteristics as compared to conventional bricks. CSEB blocks made by using GGBS show higher strength as compared to SBA.

Keywords Compressed stabilized earth block · GGBS · SBA · Water absorption · Compressive strength

A. D. Yawale (✉)
Department of Structural Engineering, SRES's College of Engineering, University of Pune, Kopargao, Maharashtra 423601, India
e-mail: yawaleapurvast@sanjivani.org.in

S. V. Patankar
Department of Civil Engineering, SRES's College of Engineering, University of Pune, Kopargao, Maharashtra 423601, India
e-mail: patankarsubhashcivil@sanjivani.org.in

S. B. Singh et al. (eds.), *Fiber Reinforced Polymeric Materials and Sustainable Structures*, Composites Science and Technology, https://doi.org/10.1007/978-981-19-8979-7_21

1 Introduction

Shelter is one of the basic needs of humans, especially for the lower-income groups. Lack of resources and the ever-increasing cost of materials have motivated engineers to find new alternatives to conventional building materials. Cost reduction in the housing sector especially with the lower-income sections can be achieved by innovating new construction materials, which can be locally made, and with ease of construction [1]. On the other hand, the production process of these materials is highly energy-intensive, non-eco-friendly and acts as a source of waste generator. It is reported that the Indian construction industry alone is responsible for 22% of the total green house gases emitted into atmosphere [2]. A brick kiln emits about 70–282 g of carbon dioxide, 0.001–0.29 g of black carbon, 0.29–5.78 g of carbon monoxide per kilogram of brick fired depending on type of kiln and fuel used for firing [3]. These all-environmental issues are giving way for development of Compressed stabilized earth block (CSEB). Among sustainable construction techniques, stabilized earth seems to be noteworthy. CSEBs are manufactured by compressing a wet soil mixture and cement in a manually operated press to get a high-density block. The amount of cement to be used will depend on the composition of the soil. Sandy soil requires 5–9% cement by volume while silty soil needs 8–12%, and clayey soil requires 12–15% cement as a stabilizer but cement content of more than 15% is uneconomical [1]. Higher cement dosages lead to more cementitious material available to establish water-insoluble bonds with the silt and sand particles and hence lead to higher strength for CSEB [4]. The improvement in strength with cement occurs mainly due to the formation of hydration product C–S–H (calcium silicate hydrate) gel which is formed due to hydration reactions. With the increasing amount of cement, more C–S–H gels are produced which combine the soil particles, thereby increasing the strength. The binding of sand particles and the self-hydration products of the cement contributes to the early strength of the blocks [5]. Shekhar and Nayak [6] studied the combination of cement-granulated blast furnace slag (GBFS) as a stabilizer and concluded that CSEBs prepared with the addition of 6% cement and 20% GBFS with lateritic soil can be used in the construction of a load-bearing wall. Alam et al. [7] analyzed the performance of cement, gypsum, lime and straw as a stabilizer and stated that 4% cement along with the addition of 1% straw by weight is a cost-effective solution to ensure durable earthen construction. James et al. [8] investigated the combination of cement and sugarcane bagasse ash (SBA) for making CSEBs and reported that 4% cement along with 8% SBA meets the strength requirement prescribed by Indian Standard. Elahi [9] carried out a study to find the effectiveness of cement and FA for producing satisfactory CSEBs in terms of strength and durability. Akinwumi [10] investigated the effects of a stabilizing soil with shredded waste plastic to produce compressed earth bricks (CEB). Danso et al. [11] investigated the microstructure and mechanism of fiber reinforced soil blocks with addition of agricultural waste fibers. Khadko [12] studied the environmental impacts of building construction and justifies suitability of rammed earth as an ideal sustainable housing both in terms of environmental and structural stability. Muntohar [13], utilized lime and rice husk ash for

soil stabilization produced considerable strength gain and improves other geotechnical properties of the stabilized soils. Palanisamy and Kumar [14] focused on use of more sandy soil sieved from the raw earth available at the site and quarry dust by replacing river sand for making unburnt bricks. However, the addition of Waste like Fly Ash GGBS and SBA reduced the weight of blocks, and as such, making the system more environment friendly [15, 16]. Moreover, industrial waste can fill the voids between soil particles and it tends to make the soil-waste mix uniform which promotes the hydration reaction of cement. These hydrated products remain wrapped by the soil particles and the bonding capacity of the soil–cement matrix is significantly improved which tends to increase the strength of the blocks prepared with waste addition [17, 18].

In the present study, the performance of various industrial waste like GGBS and SBA along with cement in the manufacture of CSEBs on the basis of density, water absorption, and dry and wet compressive strength have been investigated.

2 Material and Methodology

2.1 Materials

In the present investigation, the soil used was taken from one of the borrow areas of Samrudhi Mahamarg near the bank of Godavari River, at the depth of 0.40–0.80 m below the ground surface. Table 1 shows the physical properties of Soil used in the production of CSEB block.

Ordinary Portland cement of 53 grade was used as a stabilizing agent. Table 2 shows the physical properties of cement tested in the laboratory.

The SBA was collected from Sanjivani Sugar Factory, Kopargaon while GGBS was collected from JSW Cement Ltd, Pune. The properties of Soil, SBA, and GGBS are tabulated in Table 3. It is observed that the GGBS contains very fine particles

Table 1 Properties of soil

Properties of soil	Test result (%)
Particle size distribution	
Gravel	4.72
Sand	21.96
Silt and clay	73.32
Atterberg's limits	
Liquid limit	31
Plastic limit	15
Plasticity index	16
Optimum moisture content	12

Table 2 Properties of cement

Physical properties of cement	Result
Standard consistency (%)	28.50%
Soundness (Le-Chatelier App.) (mm)	2.31
Initial setting time (min)	115
Final setting time (min)	385
Compressive strength @ 3 days (MPa) @ 7 days (MPa)	30.50 43.33

while SBA contains courser particles but it is similar to the particle size distribution of soil (Table 4).

Procedure for development of compressed stabilized earth blocks (CSEBs):

The soil sample was broken down and then sieve through to a size passing through a 4.75 mm sieve. As the Compressive strength of CSEB increases with the addition of cement and application of desired pressure. Through the literature survey, it is observed that 8% of cement achieves good strength of the block. So in the present investigation cement quantity was kept constant at 8% by weight.

To obtain the best Cement–waste reactivity, GGBS and SBA each of 5, 10, and 15% by weight were used along with soil and 8% cement. The optimum quantity of water required to cast a suitable block was carried out using various trials for optimum pressure of 17 kg/cm^2.

Mixing of dry materials like soil, GGBS or SBA, and cement was done in a metal tray so as to give a homogeneous mix. The requisite quantity of potable water was

Table 3 Properties of SBA and GGBS

S. No.	Properties	Soil	SBA	GGBS
1	Color	Muddy	Grey	White
2	Loose bulk density (kg/m^3)	1500	510	1031
3	Compact bulk density (kg/m^3)	1740	677	1615
4	Fineness modulus	2.8	2.16	0.49
5	Specific gravity	2.52	0.49	2.90

Table 4 Chemical composition of GGBS and SBA

Chemical constituent	Mass percentage (%)	
	SBA	GGBS
SiO_2	73	35.47
Al_2O_3	6.7	19.36
Fe_2O_3	6.3	0.8
CaO	2.8	33.25
MgO	3.2	8.69

then added to this mix by spraying and then turned over many times until all the required water was added. The amount of water that is required to obtain a good quality block was determined by making a good intact ball without sticking to the hand from initial trials. The process is repeated until all the particles are uniformly wetted. Then the materials were placed in a mould of area 190 mm × 90 mm and 160 mm deep without compaction then mould was placed in a compression machine and applied constant pressure of 17 kg/cm^2 as shown in Fig. 1. After application of desired pressure for 1.5 min, the depth of the specimen was maintained at 90 mm. After demolding the specimen, moist curing was done by covering the specimens with a plastic sheet at room temperature for 7, 14, 21, and 28 days (Fig. 2) depending on the test period. This method can prevent loss of moisture of about 1–3% prior to the test for assuring pozzolanic reaction in the soil stabilization system.

Fig. 1 Hand operated press

Fig. 2 Curing of blocks

3 Result and Discussion

3.1 Water Absorption and Bulk Density

After a period of 28 days of moist curing, five samples for each composition were tested for water absorption similar to conventional bricks [19, 20]. Before immersion of sample in water dry weight was taken and find out dry bulk density for 5, 10 and 15% addition of waste (GGBS and SBA) in CSEB block. Figure 3 shows the performance of CSEB blocks using various percentages of industrial waste like GGBS and SBA on the basis of water absorption and also compared with locally available bricks. It is observed that as the percentage of GGBS increases from 5 to 15%, water absorption decreases with an increase in density while with the addition of SBA, water absorption increases with a decrease in density. It might be due to the higher content of Calcium and fineness of GGBS while SBA contains courser particles and presence of more moisture.

But as compared to conventional bricks, water absorbed by CSEB block using GGBS is up to 11.04% while using SBA maximum water absorption is 15.90% which is less than water absorption by conventional brick (up to 20%) (Fig. 4).

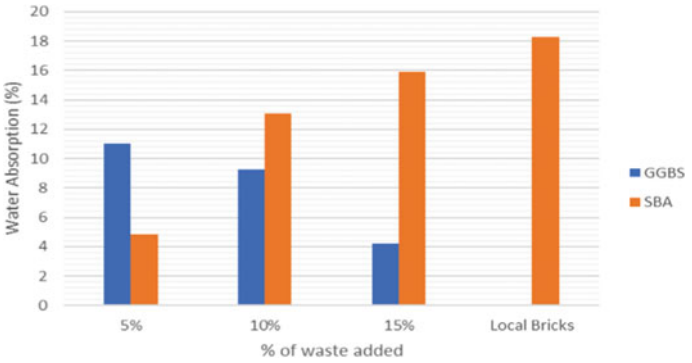

Fig. 3 Effect of adding GGBS and SBA along with soil in CSEB

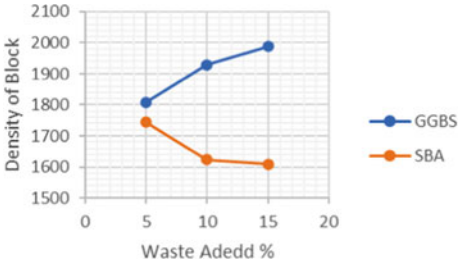

Fig. 4 Effect of waste addition on density of CSEB blocks

3.2 Compressive Strength

In the preliminary investigation if no cement was added to CSEB maximum strength obtained for 5% a Sugarcane Bagasse Ash is 1.8 MPa while with 20% GGBS strength reaches 4 MPa. As shown in Fig. 5. But CESB was not satisfied with the water absorption test. Most of the blocks are dissolved in water during the water absorption test.

So, as per past research, 8% cement was added for making CSEB for further investigation. As cement content is very less it is necessary to check the compressive strength in dry and wet conditions after aspecified curing period.

Compressive strength of the soil, Cement and waste mix CSEB specimens for different curing period is illustrated in Figs. 6 and 7. As GGBS content increases from 5 to 15 compressive strength also increases but rate of gain of strength is more from 7 to 14 days of moist curing while increases with reducing the rate from 14 to 28 days. It is also observed that for a lower percentage of GGBS optimum strength can be achieved at the curing period of 14 days while for 15% of GGBS need 28 days of curing period. As SBA is porous and courser material as compared to GGBS therefore compressive strength reduces with an increasing percentage of SBA. Beyond 21 days of moist curing, comp strength is not much desirable.

The wet compressive strength of the Soil, Cement, and Waste mix CSEB specimens was tested after finding a water absorption test for 14, 21, and 28 days of moist curing. Figure 7 shows the effect of the addition of 5, 10, and 15% of GGBS on the compressive strength of the CSEB by maintaining 8% Cement content under wet conditions.

The wet compressive strength of the Soil, Cement and Waste mix CESB specimens were tested after finding water absorption test for 7, 14, 21, and 28 days of moist curing. Figures 7 and 8 show the effect of the addition of 5, 10, and 15% of GGBS on the compressive strength of the CESB by maintaining 8% Cement content under wet conditions.

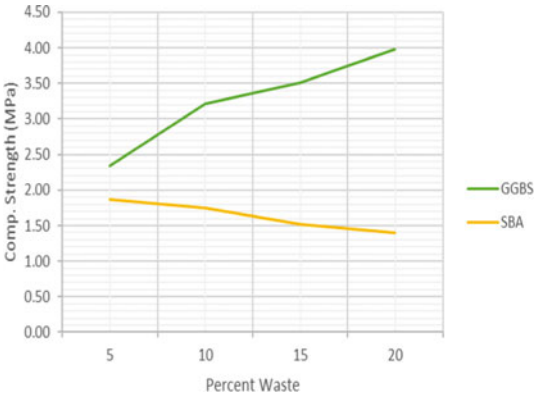

Fig. 5 Effect of waste addition on dry compressive strength of CSEB

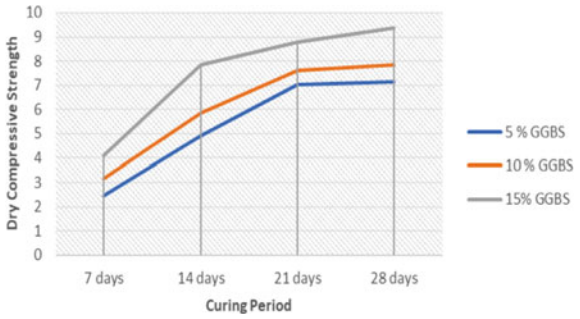

Fig. 6 Effect of GGBS addition dry compressive strength of CSEB

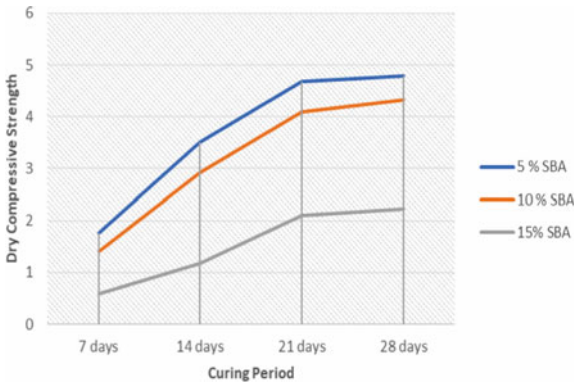

Fig. 7 Effect of SBA addition dry compressive strength of CSEB

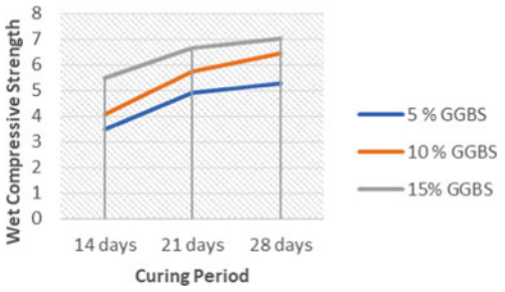

Fig. 8 Effect of GGBS addition wet compressive strength of CSEB

It is observed that the percentage of GGBS content increases compressive strength is also increases at all curing periods. But the rate of gain of strength at 5% GGBS is linearly increases up to 21 days of moist curing thereafter no change in strength. A somewhat similar trend has been observed for 10% GGBS content. While at 15% GGBS content, there is a considerable gain in strength beyond 21 days of moist curing. This might be due to higher calcium content cured under moist curing (Fig. 9).

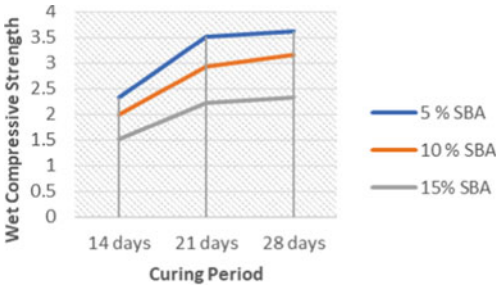

Fig. 9 Effect of SBA addition wet compressive strength of CSEB

3.3 Load Carrying Capacity of Masonary

It observed from above result that best results of compressive strength obtained of CSEB blocks with 15% GGBS and 5% SBA addition along with soil and 8% cement. So three masonry cast using 15% GGBS CSEB blocks, 5% SBA CSEB blocks and locally available burnt bricks. Comparison were made after curing the masonry for 7 days (Fig. 10).

The structural behavior of all masonry under compressive load is similar to conventional masonry. However, Fig. 11 shows the masonry of GGBS block achieves a maximum load than conventional masonry while Masonry with SBA blocks achieves nearly the same load as that of Conventional.

4 Conclusion

This study was carried out to assess the suitability of easily available Sugarcane Bagasse Ash (SBA) and GGBS along with 8% cement for the production of satisfactory CSEBs with soil. The conclusions drawn based on the various tests performed for this study are:

- Performances of Earth Block in compressive strength improved by mixing the soil with cement, and become better by adding GGBS up to 15% while for SBA it is up to 5%.
- The compressive strength test result for 21 days curing and 28 days curing is nearly same. It concludes that at 21 days of curing max strength can be achieved.
- The addition of SBA and GGBS mixture ratio decreased the ability of the compressed stabilized earth to absorb water. The compressed-stabilized earth meets the requirement of the Indian Standard for production of Earth Block.
- In general, the compressive strength due to submersion in water remains 60–70% of the normal (dry) compressive strength specimen.

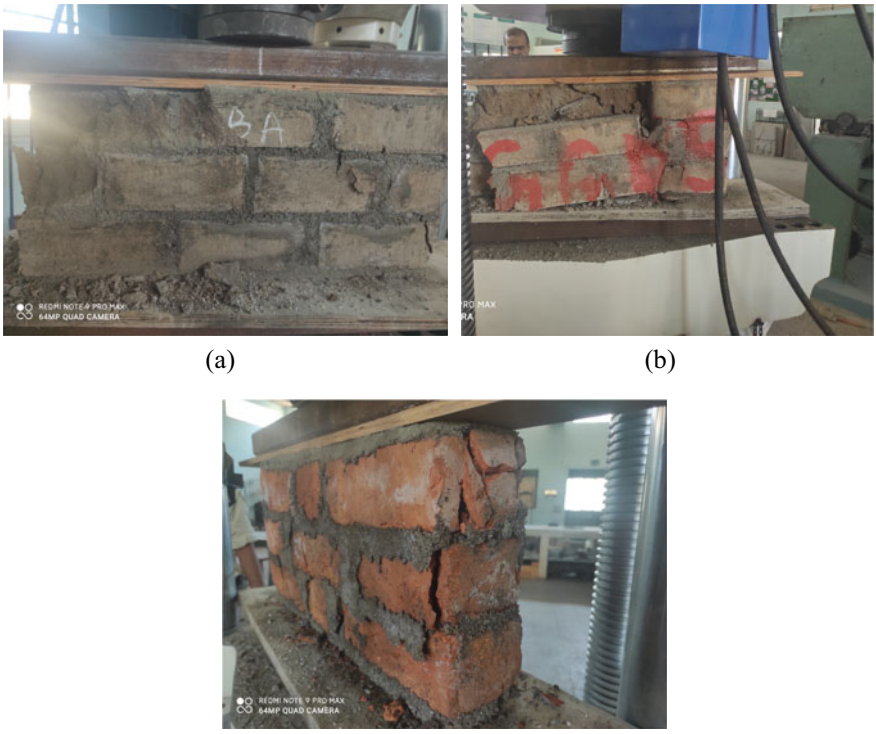

Fig. 10 Failure pattern of CSEB blocks using **a** SBA, **b** GGBS and **c** brick Masonry

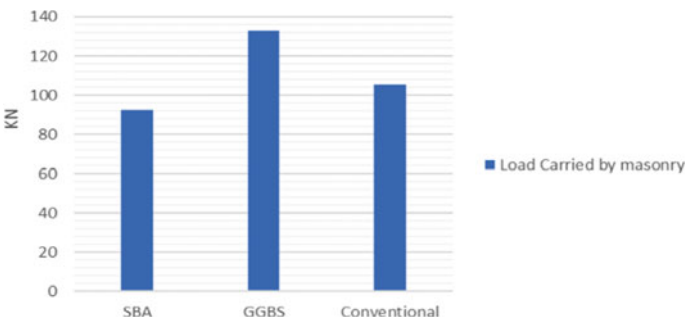

Fig. 11 Comparison of conventional brick masonry with waste added CSEB blocks masonry

- In locally available bricks for heating coal is used which creates pollution But when we use SBA and GGBS we can reduce waste and also reduce environmental pollution.
- Hence CSEB blocks are economical and environmental friendly.

References

1. Sekhar DC, Nayak S (2018) Utilization of granulated blast furnace slag and cement in the manufacture of compressed stabilized earth blocks. Constr Build Mater 166:531–536
2. Anant M, Patel A (2018) Toward sustainable brick production: an overview. Constr Build Mater 165:112–125
3. Nagaraj HB, Shreyasvi C (2016) Compressed stabilized earth blocks using iron mine spoil waste—an explorative study. In: International high-performance built environment conference—a sustainable built environment conference 2016 series (SBE16); Proc Eng 180:1203–1212
4. Walker P, Stace T (1997) Properties of some cement stabilised compressed earth blocks and mortars. Mater Struct 30:545–551
5. Palanisamy P, Kumar PS (2018) Effect molarity in geopolymer earth brick reinforced with fibrous coir wastes using sandy soil and quarry dust as fine aggregate. Case Stud Constr Mater. https://doi.org/10.1016/j.cscm.2018.01.009
6. . Nagaraj HB, Sravan MV, Arun TG, Jagadish KS (2014) Role of lime with cement in long-term strength of compressed stabilized earth blocks. Int J Sustain Built Environ 3:54–61
7. James J, Pandian PK, Deepika K, Manikanda VJ, Manikandan V, Manikumaran P (2016) Cement stabilized soil blocks admixed with sugarcane bagasse ash. J Eng 2016:1–9
8. Alam I, Naseer A, Shah AA (2015) Economical stabilization of clay for earth buildings construction in rainy and flood prone areas. Constr Build Mater 77:154–159
9. Elahi TE, Shahriar AR, Kausar Alam M, Zoynul Abedin Isaac M (2020) Effectiveness of sawdust ash and cement for fabrication of compressed stabilized earth blocks. Constr Build Mater 259:120568
10. Akinwumi II, Domo-Spiff AH, Salami A (2019) Marine plastic pollution and affordable housing challenge: shredded waste plastic stabilized soil for producing compressed earth bricks. Case Stud Constr Mater 11:e00241
11. Danso H, Brett Martinson D, Ali M, Williams JB (2016) Mechanisms by which the inclusion of natural fibres enhance the properties of soil blocks for construction. J Compos Mater:1–11; Khadka B, Shakya M (2016) Comparative compressive strength of stabilized and unstabilized rammed earth. Mater Struct 49:3945–3955
12. Muntohar AS (2011) Engineering characteristics of the compressed-stabilized earth brick. Constr Build Mater 25:4215–4220. https://doi.org/10.1016/j.conbuildmat.2011.04.061
13. Reddy BVV, Kumar PP (2011) Cement stabilised rammed earth. Part B: compressive strength and stress–strain characteristics. Mater Struct 44:695–707
14. Zhang Z, Wong YC, Arulrajah A, Horpibulsuk S (2018) A review of studies on bricks using alternative materials and approaches. Construct Build Mater 188:1101–1118
15. Elahi TE, Shahriar AR, Islam MS (2021) Engineering characteristics of compressed earth blocks stabilized with cement and fly ash. Constr Build Mater 277:122367s
16. IS-1725 (1982) Soil based blocks used in general building construction. Bureau of Indian Standards
17. Malhotra SK, Tehri SP (1996) Development of bricks from granulated blast furnace slag. Constr Build Mater 10:191–193
18. Madurwar MV, Mandavgane SA, Ralegaonkar RV (2014) Use of sugarcane bagasse ash as brick material. Curr Sci 107:1044–1051
19. IS 1077 (1992) Indian standard common burnt clay building bricks—specification
20. IS 3495: (Parts 1 to 4) (1992) Methods of tests of burnt clay building bricks
21. Islam MS, Elahi TE, Shahriar AR, Nahar K, Hossain TR (2020) Strength and durability characteristics of cement-sand stabilized earth blocks. J Mater Civ Eng 32(5):04020087. https://doi.org/10.1061/(ASCE)MT.1943-5533.0003176

Influence of Fire on Steel Reinforcement of R.C.C Elements

Mahipal Burdak and Tarun Gehlot

Abstract Repair and rehabilitation of fire damaged buildings is a popular topic due to the growth in large building fires. This is a specialized field that calls for expertise in a variety of areas such as concrete technology,, structural analysis and repair materials. The whole method for restoring a fire damaged house is thoroughly examined in this study report. Warming the steel reinforcement bars to temperatures of 100, 300, 600, and 900 °C for six samples permitted to acknowledge how fire affected the bars. The heated specimens were rapidly cooled by chilling in the air and, in most cases, quenching in water. Scanning electron microscope (SEM) is used to look at grain size and structure at the microscopic level, while Universal testing machine (UTM) is being used to look at changes in mechanical qualities. When cooled under normal conditions, the temperature has little to no impact on flexibility. By heating the reinforcing bars, the mechanical properties may be altered without affecting the chemical components.

Keywords Fire · Steel reinforcement · RCC · Temperature · SEM · UTM

1 Introduction

Due to the rising frequency of building fires, studies and research have been conducted on the repair and maintenance of fire damaged buildings. Studying these related areas has attracted a lot of resources. The civil industry is particularly interested in the subject of creating a structure that could be rebuilt after it has been devastated by fire. We are completely aware that fires may be devastating in terms of lives lost, families split up and livelihoods destroyed.

The strength and durability repair of fire damaged concrete under post-fire curing was demonstrated by Chi-Sun Poon et al. A unique method for assessing concrete that has been burned down has been put forth by Wei Meing et al. N. R. Short et al. looked at the application of colour image analysis to evaluate concrete that has been

M. Burdak (✉) · T. Gehlot
Department of Structural Engineering, MBM University Jodhpur Rajasthan, Jodhpur, India
e-mail: mahipalburdak@gmail.com

S. B. Singh et al. (eds.), *Fiber Reinforced Polymeric Materials and Sustainable Structures*,
Composites Science and Technology, https://doi.org/10.1007/978-981-19-8979-7_22

burned. A. Y. Nassif et al. looked at how quickly cooling concrete after a fire affected its stiffness properties [1–3].

Kohail et al. [4] developed a numerical model to forecast the mechanical characteristics and durability of RC columns subjected to fire. The model's conclusions were contrasted with the observed experimental results in order to determine whether the recommended model was accurate. Ahmed and Bhuiyan [5] Developed simplified approach which may underperform the residual capacity for Beams when they have been subjected to fire for a prolonged period of time, it was found whenever the post-fire residual capacity of Beams generated from Finite element analysis was contrasted to that obtained using the simplified technique [4, 5].

Durga et al. [6] employed 3D nonlinear transient thermal decomposition finite element modelling, the impact of fire at elevated temperatures on the beam, columns with different cover widths, and slabs of varied thicknesses has been studied. A new technique for merging steel-BFRP bars with different BFRP sheet angles, such as divergence and convergence, was presented by Salehi et al. in [7]. Once the load–displacement charts were finished, the seismic properties of RC frames are compared, and the best method and model are displayed [6, 7].

Our study has the following goal.

- To look at how fire affects reinforcing bars that have been heated to different temperatures, quenched in water, and afterwards cooled to room temperature.
- Conduct tensile strength testing using a Universal Testing Machine to look into the unique variances in the mechanical properties of the bars.
- Analyzing the microstructure of the bars with a scanning electron microscope (SEM).

2 Experimental Work

12 mm-diameter TMT bars were employed as test specimens. The length of all 54 bars was reduced to 40 cm. Six specimens' mechanical properties were assessed using UTM before they were heated at room temperature, and the outcomes were compiled. Without being disturbed, each of the 12 samples was warmed for an hour in the electrical furnace at temperatures of 100°, 300°, 600°, and 900 °C. Following heating, 6 of the 12 specimens at each temperature were placed aside to cool normally at room temperature. The other six were quenched in water for fast cooling. The mechanical properties of these specimens were then tested using UTM, & SEM microstructure analysis was performed on them. When the 12 mm steel bar was cut to a length of 40 cm, its gauge length was 60 mm. The combined tensile strength and flexural strength approach used in tensile testing is ASTM D-638 and ISO 527. Scanning electron microscopy was carried out using the JSM-6480LV at magnifications of 5 μ (×5000) and 10 μ (×1000) (×1000). The specimens are 12 mm in diameter and 10 mm in length. An electric furnace is used to heat the specimens. The greatest temperature this furnace can attain is 1000 °C. The furnace has an inside depth of 45 mm. The furnace is initially turned on to warm it up to the required temperature,

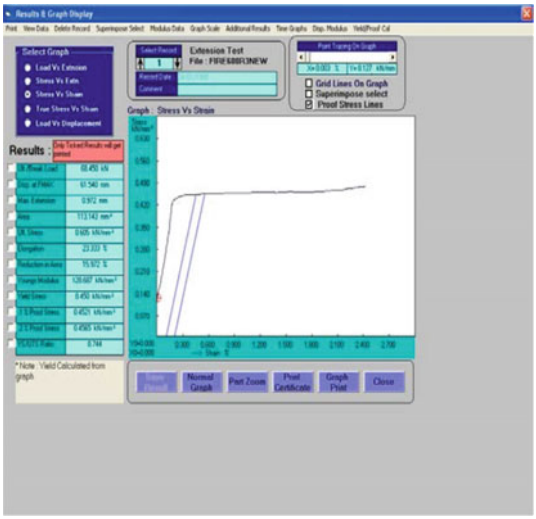

Fig. 1 Outputs of tensile test

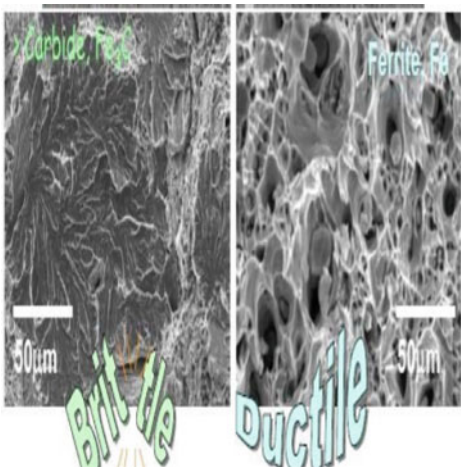

Fig. 2 Steel bars at SEM

and after it reaches that degree. The specimens are heated for one hour, following which three are quickly cooled in water, while the remaining three are left to cool naturally. The three water-quenched specimens are taken out after 15 min. Each time, 6 bars are kept at 100, 300, 600, and 900 °C (Figs. 1 and 2).

3 Results and Discussions

See Tables 1 and 2.

Table 1 Results for rapid cooling conditions

S. No.	Temperature in ° C	Ultimate load (KN)	Ultimate stress (KN/mm^2)	Yield stress (KN/mm^2)	Max. extension (mm)	Elongation (%)	0.2% proof stress
1	Room temp. 27	67.2	0.582	0.465	1.62	28.2	0.464
2	100	66.21	0.583	0.465	1.64	14	0.460
3	300	65.3	0.581	0.452	1.421	31	0.43
4	600	68.4	0.605	0.454	0.970	23.6	0.458
5	900	78.5	0.691	0.468	0.201	11.8	0.539

Table 2 Results for ordinary cooling conditions

S. No.	Temperature in °C	Ultimate load (kN)	Ultimate stress (kN/mm^2)	Yield stress (kN/mm^2)	Max. extension (mm)	Elongation (%)	0.2% proof stress (KN/mm^2)
1	Room temp. 27	67.2	0.591	0.461	1.60	28.1	0.468
2	100	66.3	0.589	0.443	1.135	30.4	0.450
3	300	63.1	0.572	0.431	1.10	28.9	0.428
4	600	64.8	0.571	0.483	0.72	27.41	0.441
5	900	65.8	0.583	0.469	0.68	26.9	0.432

4 Discussion

As seen in Fig. 3, the microstructure of the bar is what causes the ultimate load to initially reduce from and then subsequently rise. The grain size shrinks at high temperatures. When reinforcement bars are rapidly cooled by quenching, it is seen that extreme temperatures exceeding 900 °C have a considerable negative impact on their ductility (Fig. 6). The effect of temperature on ductility in the same condition when cooled under normal conditions (Fig. 11) is not significant. The specimen's maximum load carrying capacity was lower than shown in Fig. 7 for the specimen without heating. Figures from the SEM examination (Figs. 12, 13, 14, 15 and 16) demonstrate that the mechanical characteristics of reinforcement bars can be altered at high temperatures without changing their composition (Figs. 4, 5, 8, 9 and 10).

5 Conclusion

Investigating the impact of fire on reinforcement bars exposed to temperatures of 100, 300, 600, and 900 °C, immediately quenched in water, and normally chilled in ambient temperature, it was found that the ductility of fast cooled bars upon warming to extreme temps of 900 °C.

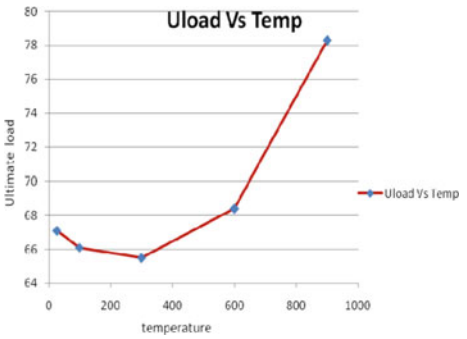

Fig. 3 Temperature verses ultimate load (for rapid cooling)

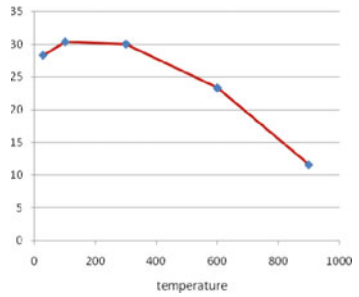

Fig. 4 Temperature verse % elongation (for rapid cooling)

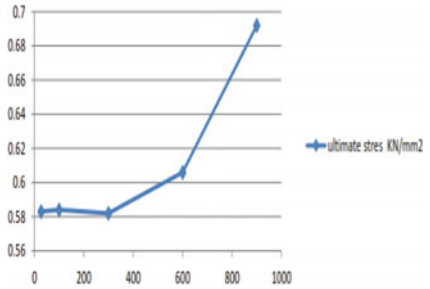

Fig. 5 Temperature versus ultimate stress (for rapid cooling)

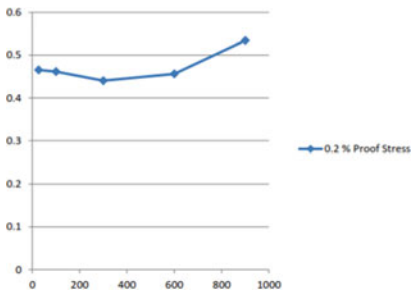

Fig. 6 0.2% proof stress versus temperature (for rapid cooling)

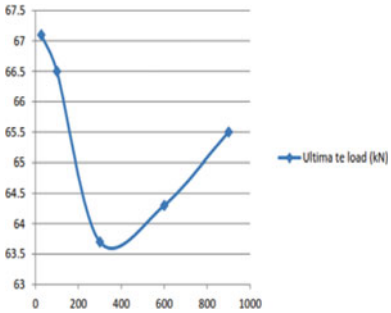

Fig. 7 Temperature verse ultimate load (for ordinary cooling)

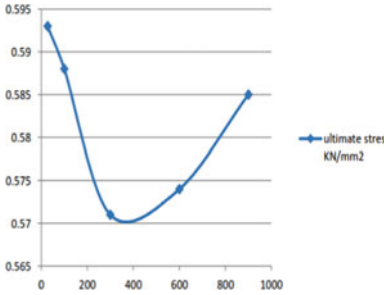

Fig. 8 Temperature verse ultimate stress (for ordinary cooling)

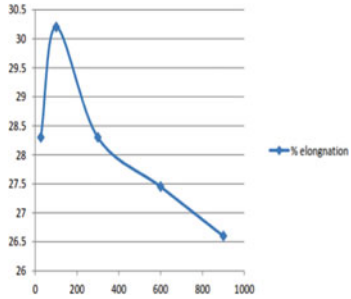

Fig. 9 Temperature verses elongation (for ordinary cooling)

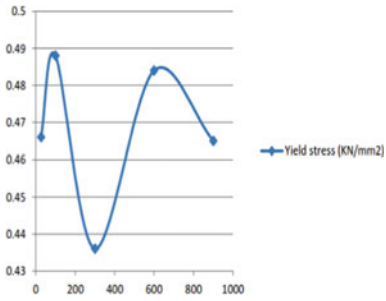

Fig. 10 Temperature verse yield stress (for ordinary cooling)

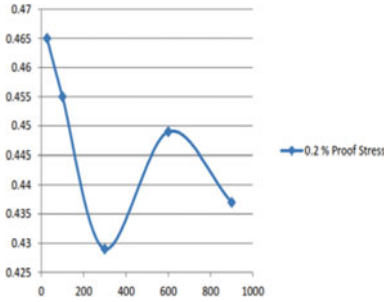

Fig. 11 Temperature verse 0.2% proof stress (for ordinary cooling)

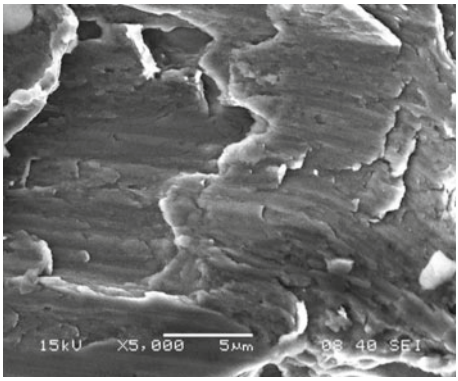

Fig. 12 100 °C ordinary cooling at magnification of 5 µ

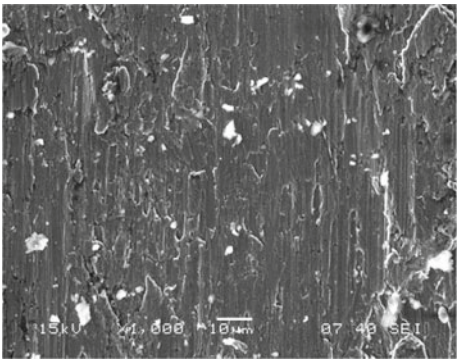

Fig. 13 100 °C ordinary cooling at magnification of 10 µ

Tensile tests of the bars utilizing a Universal Testing Machine indicate a rise in ultimate load and a drop in percent of elongation of the specimen, indicating a significant decline in ductility of the sample.

The bars' microstructure was examined using scanning electron microscope (SEM), which revealed that severe heating causes changes in the microstructure without changing the chemical composition. This might have an adverse effect on the structure.

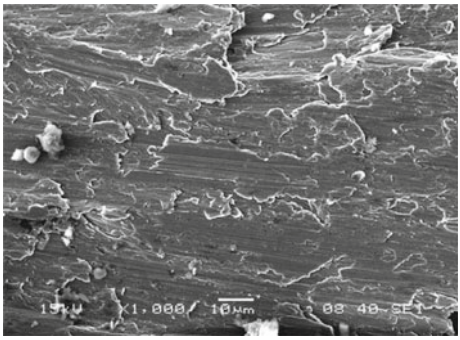

Fig. 14 300 °C ordinary cooling at magnification of 10 μ

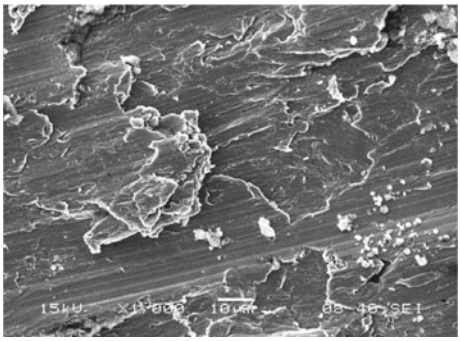

Fig. 15 300 °C rapid cooling at magnification of 10 μ

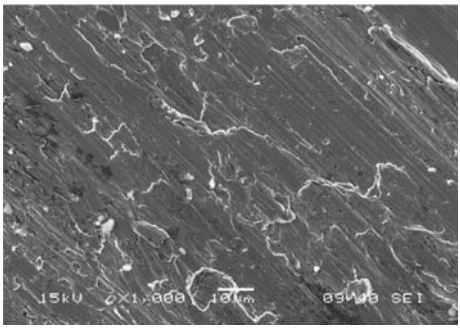

Fig. 16 900 °C ordinary cooling at 10 μ

References

1. Poon C-S, Azhar S, Anson M, Wong Y-L (2000) Strength and durability recovery of fire-damaged concrete after post-fire-curing. Honkong Polytechnic University
2. Lin W-M, Lin TD, Powers-Couche LJ. Microstructure of fire-damaged concrete
3. Short NR, Purkiss JA, Guise SE (2001) Assessment of fire damaged concrete using colour image analysis. Constr Build Mater 15(1):9–15
4. Awad Y, Kohail M, Khalaf MA, Ali YA (2022) Effect of fire extinguishing techniques on the strength of RC columns. Asian J Civ Eng:1–11

5. Bhuiyan MH, Ahmed S (2022) Post-fire residual capacity of reinforced concrete beam. In: Advances in civil engineering. Springer, Singapore, pp 117–126
6. Venkatesh C, Sonali Sri Durga C, Durga S, Muralidhararao T (2021) Evaluation of fire impact on structural elements using ANSYS. J Build Pathol Rehabil 6(1):1–5
7. Salehi R, Akbarpour A, Shalbaftabar A (2020) Fire evaluation of RC frames strengthened with FRPs using finite element method. Am J Eng Appl Sci 13(4):610–626

Static and Dynamic Mechanical Properties of Graphene Oxide and Fly Ash Based Concrete

P. V. R. K. Reddy and D. Ravi Prasad

Abstract Graphene oxide (GO) has been recognized as one of the most potential nanomaterial for reinforcement in cementitious composites due to its extraordinary properties. In the present investigation, the static and dynamic mechanical characteristics of GO and fly ash based concrete (FA-GO-Concrete) have been studied experimentally. The static characteristics have been determined by conducting a compressive strength test and dynamic properties such as fundamental natural frequencies and damping ratios of FA-GO-Concrete beams in free-free conditions were measured using the impact hammer technique. In this paper, the influence of GO addition at 0.15% and variation of fly ash content at 0, 10, 20 and 30% as a replacement of cement was studied. The experimental findings showed that the addition of GO and replacement of fly ash increased the compressive strength and fundamental natural frequencies, whereas reduced the damping ratio of FA-GO-concrete compared to the control concrete. The damping ratios of FA-GO-Concrete increased with fly ash content increment, while the fundamental natural frequencies were reduced with fly ash content increment with respect to the GO-Concrete. The static and dynamic elasticity modulus of FA-GO-Concrete were also determined. It has been found that the desired dynamic properties can be achieved by adding GO and partially replacing the cement with fly ash.

Keywords Graphene oxide · Fly ash · Static mechanical · Dynamic mechanical

1 Introduction

Since concrete was used in constructions for decades, its availability and versatility around the world have made it the most commonly used material [1, 2]. In general, ordinary concrete or standard grade concrete could no longer meet the requirements

P. V. R. K. Reddy (✉) · D. Ravi Prasad
Department of Civil Engineering, NIT, Warangal 506004, India
e-mail: pvrkr@student.nitw.ac.in

D. Ravi Prasad
e-mail: raviprasad@nitw.ac.in

S. B. Singh et al. (eds.), *Fiber Reinforced Polymeric Materials and Sustainable Structures*, Composites Science and Technology, https://doi.org/10.1007/978-981-19-8979-7_23

because of environmental conditions and the structural complexity of offshore structures, hydraulic structures, bridges, dams, and high-rise buildings [3]. In spite of this, high-strength concrete or ordinary concrete is absolutely brittle in nature because of its ratio of compressive strength and tensile or flexural strength [4]. Researchers have studied various methods to overcome this drawback, including adding steel fibers and rebars to concrete, adding supplementary mineral admixtures, and applying fibre-reinforced polymers to strengthen members externally [5]. The above methods can significantly improve the tensile behaviour and ductility, but the brittleness and related microcracks are still completely inevitable. Recently, nanotechnologies have been integrated into the production process of cementitious composites, incorporating a small amount of nanomaterials to improve the mechanical and durability characteristics [6]. Nanomaterials like nano-silica, carbon nanofibers, carbon nanotubes, graphene and their byproducts are very widespread. The chemistry of cement and graphene oxide (GO), which is a graphene derivative, has improved the microstructural and mechanical characteristics of cementitious composites [7, 8]. It is further reported that the incorporation of GO in cementitious composites could refine the pore structure, resulting in the improvement of strength and durability [9–13]. In general, concrete structures are exposed to vibration forces, which include impact loads resulting from dynamic shocks produced by the movement of vehicles. An external force of a particular frequency for a specified amplitude applied to a system can lead to harmonic excitation depending on the dynamic or impact load and the type of structure. If the frequency of the external excitations matches the fundamental frequencies of the system, resonance can also occur. As a result, it is important to examine the dynamic characteristics of concrete structures at typical mode shapes in order to attenuate vibration and decrease resonance [14, 15]. It was concluded that the main concept of vibration monitoring for concrete structural damage analysis relies on dynamic properties and not on the concrete structural geometry; Subsequently, the dynamic response characteristics of the structure will change significantly [16]. In concrete, dynamic characteristics, such as dynamic rigidity modulus, dynamic elastic modulus, and dynamic Poisson's ratio, are important properties that can be determined by its dynamic characteristics, which have a different value from its static mechanical characteristics [16]. The research work mentioned above has investigated the static characteristics of various cementitious composites. However, there is a scarcity of literature on the investigation of dynamic characteristics of GO and fly ash based concrete. The prime objective of this investigation is to study the impact of GO and fly ash on static and dynamic mechanical characteristics. The static properties were determined by conducting a compressive strength test and dynamic characteristics such as fundamental resonant frequencies and damping ratio of FA-GO-Concrete beams in free-free conditions were measured using the impact hammer technique. The characteristics of plain cement concrete were also investigated to determine the impact of fly ash and GO on concrete and for comparison.

Table 1 Technical parameters of GO

Average lateral dimension (μm)	Thickness (nm)	Purity (%)	Number of layers	Surface area (m^2/g)	Bulk density (g/cm^3)
~ 5–10	~ 0.8–2	~ 99	1–4	110–250	0.122

2 Experimental Program

2.1 Materials

53 grade ordinary Portland cement (OPC) conforming to IS:269-2015, fly ash of Class F conforming to IS:3812 (Part 1)-2013, fine aggregates and coarse aggregates (CA) conforming to IS:383-2016, superplasticizer of Polycarboxylate ether based (PCS) conforming to IS:9103-2018 are the materials employed in this experimental study.

Table 1 shows the technical specifications of commercially available GO, which was employed as a nanomaterial. Ultrasonication was employed to disperse GO in water at 4 mg/mL concentration. SEM, EDX, XRD, and FTIR studies were used to characterise GO powder, as shown in Fig. 1. The surface morphology of GO is wrinkled and folded, as seen in the SEM image (Fig. 1a). Elemental composition (Fig. 1b) reveals that GO is composed of 73.14% C, 26.45% O and 0.46% S. The XRD pattern (Fig. 1c) shows that the diffraction peak occurred at $2\theta = 12.6°$ with an interplannar distance of 0.702 nm. The presence of oxygenated functionalities on the surface of GO is shown by the FTIR spectra (Fig. 1d).

2.2 Concrete Specimens Preparation

A GO dosage of 0.15% by weight of binder material was used to examine the effect on concrete of various fly ash replacement percentages of 0, 5, 20, and 30%. In addition, concrete that is absence of both fly ash and GO is referred to as control concrete (M1) for the purpose of comparison. Concrete that contains GO but does not contain fly ash is referred to as GO-concrete (M2), and concrete that contains both fly ash and GO is referred to as FA-GO-concrete (M3, M4, M5). Table 2 presents the mix proportions of concrete.

2.3 Test Procedure of Static Mechanical Properties

The compressive strength of the concrete mixtures was evaluated by employing cubes with dimensions of 100 mm on each side. The apparatus used in the compressive strength tests, the test was performed in accordance with the guidelines provided in IS:516-2021. The samples were evaluated after 7 and 28 days of curing. For each

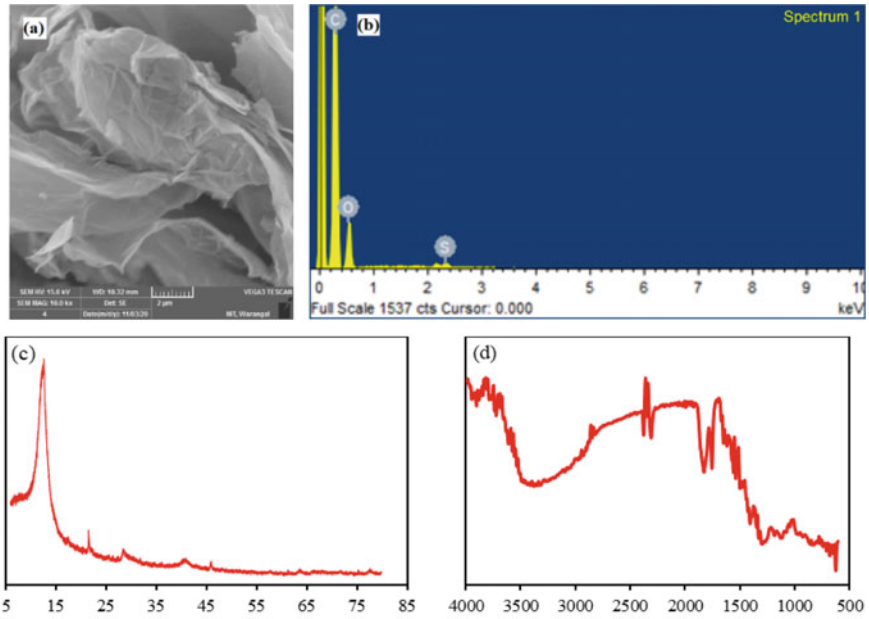

Fig. 1 Micro characterisation of GO **(a)** SEM, **(b)** EDX, **(c)** XRD, **(d)** FTIR

Table 2 Mix proportions of concrete

S. No.	Mix ID	GO (%)	OPC (kg)	Fly ash (kg)	Sand (kg)	CA (kg)	W/C ratio	PCS (%)
1	M1	0	380	0	845	1051	0.44	0.5
2	M2	0.15	380	0	845	1051	0.44	0.5
3	M3	0.15	342	38	845	1051	0.44	0.5
4	M4	0.15	304	76	845	1051	0.44	0.5
5	M5	0.15	266	114	845	1051	0.44	0.5

strength measurement, three identical specimens were evaluated, and the average results were presented.

2.4 Test Procedure of Dynamic Mechanical Properties

The dynamic characteristics of all concrete mixes were determined by using prismatic beams of size 100 mm × 100 mm × 500 mm according to ASTM C215-19. The fundamental natural frequencies and damping ratio of each specimen were examined under free-free conditions. The dynamic characteristics of FA-GO-Concrete were

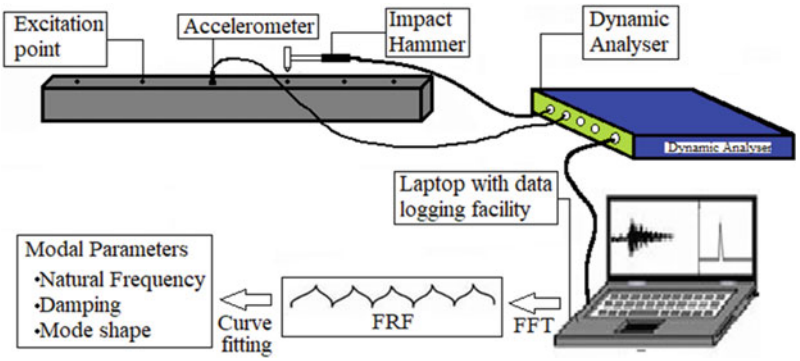

Fig. 2 Schematic view of a dynamic test setup

evaluated by casting and testing 15 prisms. A dynamic analyzer and impact hammers were used to test all specimens. The analyzer uses a forced transducer to excite the specimen and an accelerometer to collect the responses. The frequency response function is carried out using the data collected from the accelerometer. In the present investigation, the fundamental resonant frequencies range between 1 and 10,000 Hz. Figure 2 shows the schematic illustration of dynamic test setup.

3 Results and Discussions

3.1 Static Mechanical Properties

The compressive strength test was performed on all concrete mixes at curing ages of 7 and 28 day, and the findings are reported in Table 3. Compressive strength is an important property for concrete, and it is a qualitative indicator for other characteristics of concrete at hardened state. The compressive strength findings showed that the concrete with the addition of GO at 0.15% and fly ash replacements up to 20% is almost as strong as the control concrete. When compared to control concrete, the concrete with 0.15% GO and 20% replacement of fly ash increased compressive strength by 19.7% and 28.5%, respectively, at 7 and 28 days. In comparison with GO-Concrete, fly ash as a cement replacement in FA-GO-concrete reduced compressive strength. When compared to the control concrete, the compressive strength of FA-GO-Concrete enhanced by 51.5%–7.0% with fly ash content replacements ranging from 0 to 30%. The findings show that adequate fly ash and GO concentration significantly increased the compressive strength of control concrete.

According to Indian standards, Static modulus of elasticity is also determined from the compressive strength, as presented in Table 3. IS:456 suggests the static elasticity modulus of concrete expression as follows:

Table 3 Compressive strengths of all concrete mixes

Mix	Compressive strength (MPa)/increase rate (%)		Static elastic modulus (GPa)/increase rate (%)
	7 days (%)	28 days (%)	
M1	30.9/0	41.1/0	32.04/0
M2	49.6/60.6	62.2/51.6	39.44/23.1
M3	40.6/31.4	58.0/41.2	38.07/18.82
M4	36.9/19.7	52.8/28.5	36.32/13.36
M5	25.5/− 17.5	43.9/7.0	33.14/3.43

$$E_{static} = 5000\sqrt{fck} \tag{1}$$

The elasticity modulus follows a similar pattern to the compressive strength. With a partial replacement of fly ash of 0–30%, the static elasticity modulus of FA-GO-Concrete improved by about 23.1–3.4% compared to the static elasticity modulus of control concrete.

3.2 Dynamic Mechanical Properties

Transverse, longitudinal and torsional resonant frequencies were determined for all concrete mixes in respective directions as per ASTM C215-19. The dynamic characteristic values attained for all concrete mixtures are shown in Table 4. The experimental results revealed that the fundamental resonant frequencies of all vibration modes are increased in concrete mixes with the addition of GO and partial replacements of fly ash content compared to the control concrete, whereas resonant frequencies decreased in FA-GO-Concrete with the replacements of fly ash with respect to the GO-concrete. Dynamic elastic modulus and rigidity modulus have been determined from the fundamental transverse frequencies and torsional frequencies according to the ASTM standards. The dynamic poissons ratio was also calculated and shown in Table 4. The suggested equations are as follows:

$$E_{dynamic} = CMn^2 \tag{2}$$

$E_{dynamic}$ is dynamic elasticity modulus, M is mass of the specimens in kg, n is fundamental resonant frequency of transverse mode in Hz, C is equal to 0.9464 (L^3T/bt^3), L, b, t are length, width and depth of the specimens in m, and T is correction factor.

$$G_{dynamic} = BM\left(n''\right)^2 \tag{3}$$

$G_{dynamic}$ is dynamic rigidity modulus, n'' is fundamental resonant frequency of torsional mode in Hz, B is (4LR/A) in m^{-1}, R is shape factor equal to 1.183, A

Table 4 Dynamic properties of all concrete mixes

Mix	Transverse resonant frequency (Hz)	Longitudinal resonant frequency (Hz)	Torsional resonant frequency (Hz)	Dynamic elasticity modulus (GPa)	Dynamic rigidity modulus (GPa)	Dynamic poissons ratio
M1	1575	4325	2580	46.51	19.69	0.18
M2	1698	4667	2742	54.06	22.24	0.22
M3	1681	4611	2716	52.98	21.82	0.21
M4	1664	4565	2702	51.92	21.59	0.20
M5	1624	4495	2655	49.45	20.85	0.19

is specimen cross-sectional area in m^2. The dynamic Poisson's ratio is as follows:

$$\mu = (E/2G) - 1 \tag{4}$$

The findings clearly showed that incorporation of GO and replacement of fly ash enhanced the dynamic elasticity modulus of FA-GO-Concrete. It was found that the dynamic elasticity modulus was enhanced by about 16.2–6.3% for the FA-GO-Concrete with the partial replacement of fly ash ranging from 0 to 30% in comparison to the control concrete. The natural frequency and damping ratio were measured at various mode shapes, and the findings are reported in Table 5. The frequency response function and mode shapes of all concrete mixes are presented in Fig. 3. In comparison with the control concrete, damping ratio of concrete prismatic specimens with GO and partial replacement of fly ash content decreased. In comparison to GO-concrete, the damping ratio increased in FA-GO-Concrete with the replacement of fly ash. The fundamental transverse frequencies of FA-GO-Concrete with partial replacement of fly ash by 0–30% were enhanced by 7.8–3.1%, in comparison to the fundamental transverse frequency of control concrete. It is observed that the relation between $E_{dynamic}$ and E_{static} is linear and shown in Fig. 4. The determination coefficient R^2 value for this analysis was 0.942, indicating a strong linear relation between the dynamic and static elastic modulus. From the analysis, the following equation was proposed to determine static modulus of elasticity from the dynamic elasticity modulus of in GPa.

$$E_{\text{static}} = 1.075\, E_{\text{dynamic}} - 19 \tag{5}$$

Table 5 Transverse frequencies and damping ratios at different mode shapes

MIX	Mode-1		Mode-2		Mode-3	
	Transverse frequency	Damping ratio	Transverse frequency	Damping ratio	Transverse frequency	Damping ratio
M1	1575	0.97	3748	0.52	6312	0.43
M2	1698	0.60	3991	0.41	6671	0.34
M3	1681	0.63	3940	0.42	6584	0.34
M4	1664	0.72	3909	0.42	6555	0.35
M5	1624	0.78	3854	0.46	6461	0.41

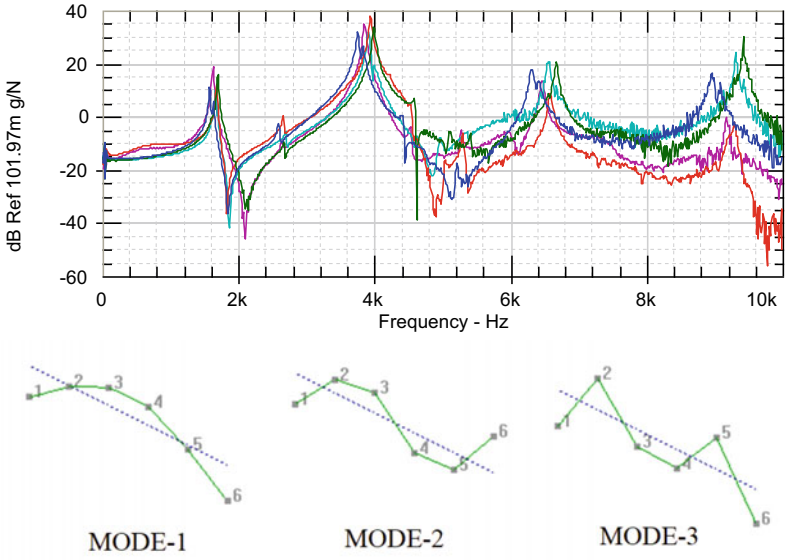

Fig. 3 Frequency response function and mode shapes of all concrete mixes

4 Conclusions

A comprehensive investigation of the static and dynamic characteristics of concrete with the GO addition and the replacements of fly ash was performed. The following are the conclusions:

1. The addition of GO to a concrete mix and partial replacements of fly ash resulted in a noteworthy improvement in compressive strength. When compared to the control concrete, the compressive strengths of FA-GO-Concrete were enhanced by 51.5–7.0% with a fly ash content of 0–30%.
2. The addition of GO and replacement of fly ash improved the static elasticity modulus of FA-GO-Concrete. The static elastic modulus of FA-GO-Concrete

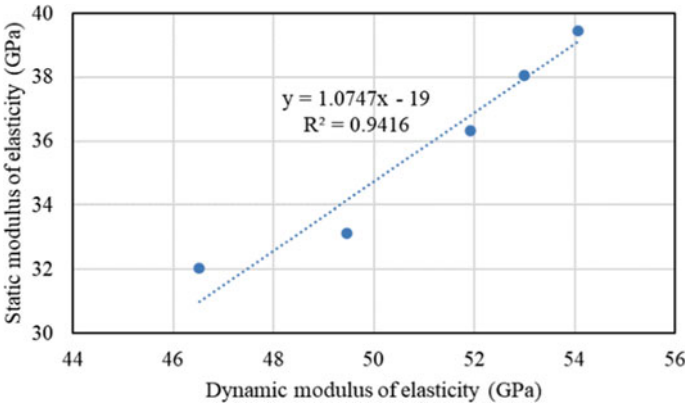

Fig. 4 Relation between dynamic and static elastic modulus

with partial replacement of fly ash of 0–30% was enhanced by around 23.1–3.4%, when compared to the static elastic modulus of control concrete.

3. The damping ratio of FA-GO-Concrete was reduced with the addition of GO and partial replacement of fly ash content compared to the control concrete. The damping ratio of FA-GO-Concrete with fly ash replacement of 0–30% decreased by 19.6–38.2% compared to the control concrete.
4. The fundamental natural frequency of FA-GO-Concrete increased with the addition of GO and the replacement of fly ash content in comparison to the control concrete. The fundamental transverse frequencies of FA-GO-Concrete with partial replacement of fly ash were increased by 7.8–3.1% compared to the fundamental transverse frequency of control concrete.
5. The addition of GO and the replacement of fly ash improved the dynamic elastic modulus and dynamic poissons ratio of FA-GO-Concrete. In comparison with the control concrete, the dynamic elasticity modulus of the FA-GO-Concrete with partial replacement of fly ash was improved by about 16.2–6.3%.

References

1. Sivakumar A, Santhanam N (2007) A qualitative study on plastic shrinkage cracking in high strength hybrid fiber reinforced concrete. Cem Concr Compos 29:575–581
2. Senthil Kumar A, Natesan S (2004) Effect of polypropylene addition on restrained shrinkage cracking of cement composites. J Inst Eng Div:100–106
3. Harun T (2009) Statistical analysis for mechanical properties of polypropylene fiber reinforced light weight concrete containing silica fume exposed to high temperature. J Mater Des 30:3252–3258
4. Bard A et al (2006) Statistical variations in impact resistance of polypropylene fiber reinforced concrete. Int J Impact Eng 32:1907–1920
5. Radhika S, Prasad R (2018) Mechanical and dynamic properties of polypropylene fiber reinforced concrete. Struct Integr Assess Proc ICONS:361–374

6. Perumalsamy B, Chong K (2006) Nanotechnology and concrete: research opportunities. In: Proceedings of the ACI session on nanotechnology of concrete: recent developments and future perspectives, pp 15–28
7. Samuel C et al (2014) Nano reinforced cement and concrete composites and new perspective from graphene oxide. Constr Build Mater 73:113–124
8. Zhu P et al (2015) Mechanical properties and microstructure of a graphene oxide–cement composite. Cem Concr Compos 58:140–147
9. Han Y (2015) Study on properties of cement based composites based on graphene. Low Temp Arch Technol 2:4–6
10. Reddy PVRK, Ravi Prasad D (2022) Graphene oxide reinforced cement concrete—a study on mechanical, durability and microstructure characteristics. Fullerenes, Nanotubes Carbon Nanostruct. https://doi.org/10.1080/1536383X.2022.2141231
11. Reddy PVRK, Prasad DR (2022) Investigation on the impact of graphene oxide on microstructure and mechanical behaviour of concrete. J Build Rehabil 7:1–10. https://doi.org/10.1007/s41024-022-00166-1
12. Reddy PVRK, Prasad DR (2022) A study on workability, strength and microstructure characteristics of graphene oxide and fly ash based concrete. Mater Today Proc 62:2919–2925. https://doi.org/10.1016/j.matpr.2022.02.495
13. Reddy PVRK, Ravi Prasad D (2022) Synergetic effect of graphene oxide and fly ash on workability, mechanical and microstructural properties of high-strength concrete. Jordan J Civ Eng 16:507–517
14. Reddy PVRK, Ravi Prasad D (2023) The role of graphene oxide in the strength and vibration characteristics of standard and high-grade cement concrete. J Build Eng 63:105481. https://doi.org/10.1016/j.jobe.2022.105481
15. Orak S (2000) Investigation of vibration damping on polymer concrete with polyester resin. Cem Concr Res 30:171–174
16. Zheng L, Huo XS, Yuan Y (2008) Experimental investigation on dynamic properties of rubberized concrete. Constr Build Mater 22:939–947

Development of Coal Ash for Structural Applications

Mainak Ghosal

Abstract There are various beneficial aspects of coal ash, especially when used in cement and concrete. Coal ash is a waste or pollutant from thermal power industries which is classified as pond ash, bottom ash, and fly ash. With climate change and its consequences no longer a myth, our paper reports the various studies that have been conducted to examine the advantageous effects of Fly ash utilization as an additive in cement, admixture in concrete and partial replacement of cement in concrete.

Keywords Ash · Cement · Coal · Concrete

1 Introduction

Coal ash is a waste of coal-based thermal power plants. It is a waste material as from the past it had faced disposal problems. India ranks 4th in the world in the production of coal ash after USSR, USA and China [1]. Though there are Class C and Class F (AASHTO M 295, ASTM C 618) coal or fly ashes, India produces ashes mainly of Class F or low-lime type. Due to the high % of fly ash content in Indian coal, the country's current annual production of Fly ash is approximate to the tune of 250M.T, out of which less than 50% is utilized. If the country's declared objective of 100% fly ash utilization is to be achieved, then there is no other option but to look out for newer and more sophisticated pastures for bulk use. From the very beginning of the nineteenth century, a virtual vision existed that Fly Ash may substitute cement in the concrete industry. The concept of higher cement means greater strength and durability has not proved true in the true sense as the structures exposed to different climatic conditions in India have a different say. To make concrete strong and durable at a lower cost, use of supplementary cementitious materials like fly ash needs to be enhanced. In India during the mid-seventies and early eighties, engineers/scientists responsible

M. Ghosal (✉)
Consulting Engineers Association of India (E & NE Region), Kolkata 700014, India
e-mail: mainakghosal2010@gmail.com

Engineering Colleges Under MAKAUT, Bidhannagar, West Bengal 700064, India

IIEST, Shibpur, Howrah, West Bengal 711103, India

S. B. Singh et al. (eds.), *Fiber Reinforced Polymeric Materials and Sustainable Structures*, Composites Science and Technology, https://doi.org/10.1007/978-981-19-8979-7_24

for making standards/specifications/codes understood the useful properties of the ash and necessary provisions were made in various standards such as IS: 456-1976-Code of Practice for Plain and Reinforced Concrete, IS; 1489(Part1)-1976-Specifications for Portland Pozzolana Cement, IS: 2250-1981-Code of practice for preparation of masonry mortar and recently in January 2016, IS:383-2016-Coarse & Fine aggregates for Concrete, etc. However, fly ash utilization failed to make an impact resulting in low-quality ash with high unburnt-carbon content and less finesse, because adequate technologies for the collection of fly ash at thermal power stations were not available and awareness too was negligible. In the eighty's era of superpower thermal stations (capacity greater than 1000 MW) came up & with it came the concept of 'Bottom Ash' cropped up. 'Bottom ash' is the coarser material amongst the ashes with better geotechnical properties, which falls into furnace bottom in modern large thermal power plants and constitutes about 20% of the total ash content of the coal fed in the boilers. In view of the substantial amount of bottom ash generated each year from the 80s and already accumulated mixed with pond ash, it merits immediate attention. Also, because of improved efficiency of boilers and coal mills resulted in good quality ash (consisting of both fly ash and bottom ash), partial replacement of fine aggregates (sand/stone) through these ashes is also being thought off due to ongoing restrictions on the use of quarrying river sand because of environmental/ecological concerns of soil erosion in the river-bed altering the course of the river and banks' slope-stability causing floods and also due to the dwindling supply of stone/sand day by day, as mining being banned in most of the states. Herculean challenges are being faced in obtaining quality stone aggregates which conform to the norms that aggregates should be clean, hard, strong, dense, non-porous and durable pieces of crushed stone, crushed gravel, natural gravel or a combination with sand should be natural sand or crushed stone, crushed gravel and combination as per Grading of Zone I, II or III but most project specifications following the same.

Table 1 of IS: 383-2016 recommends the use of Bottom Ash as a partial replacement of Coarse Aggregates.

Table 1 Extent of utilization Cl 4.2.1

S. No.	Type of aggregate	Maximum utilization		
		PCC	RCC	Lean concrete Less than M15
(1)	(2)	(3)	(4)	(5)
(i) *Coarse aggregate*				
(a) Iron slag aggregate (%)		50	25	100
(b) Steel slag aggregate		25%	Nil	100%
(c) Recycled concrete aggregate (%)		25	20	100
(d) Recycled aggregate		Nil	Nil	100%
(e) **Bottom ash (from thermal power plants)**		**Nil**	**Nil**	**25%**
(ii) *Fine aggregate*				

Today cement concrete has 4 essential ingredients- cement, aggregates (fine and coarse), water, and admixtures in place of classically 3 ingredients cement, aggregates, and water. Fly ash which is also called mineral admixture thus finds use in many of the recent cementitious applications. In India, though various standards published by the Bureau of Indian Standards (BIS) limit the fly ash content to 35% max., in actual practice it is still in a very nascent stage let alone enhancing the fly ash % like the developed countries. In the area of road construction, Indian Roads Congress (IRC) has also released standards for use of fly ash in Roller Compacted Concrete (RCC) roads. But there remains a need to publish relevant standards for use of fly ash in RCC Dams though RDSO has literature pertaining to the use of Coal Ash in Railway embankments [2]. It may be pointed out here that due to the heavy axle loads of rails and very tight safety tolerances prevailing in Railways, fly ash can't be directly used in railway projects. This paper analyses the numerous pieces of research that have been conducted to examine the effects of the use of Fly Ash as an additive in cement, admixture in concrete, and as a replacement of cement in concrete.

2 Brief Description

It is now a known fact, especially after the pandemic that climate change and its consequences are no more a myth. The worst is yet to come and ultimately this needs to be arrested. Recent reports suggest that the average atmospheric CO_2 concentration is 410 ppm, 50% higher than in the pre-industrial era. This has manifested in Super cyclones, continued drought, untimely floods, sudden wildfires/landslides, melting of ice and glaciers or avalanches. Are we destined to end up with a 3° world a far cry from 2° or 1.5°? With the cement sector accounting for an approximate 3% CO_2 emissions the use of fly ash as a partial replacement for cement should prove a viable alternative material/technology sustained for the long run. The two types of fly ash used in the cement construction are described as follows.

2.1 Class F fly Ash

The burning of harder, older anthracite, and bituminous coal typically produces Class F fly ash. This fly ash is pozzolanic in nature and contains less than 20% lime (CaO). Possessing pozzolanic properties, the glassy silica and alumina of Class F fly ash require a cementing agent, such as Portland cement, quicklime, or hydrated lime, with the presence of water in order to react and produce cementations compounds. Alternatively, the addition of a chemical activator such as sodium (water glass) to a Class F ash can lead to the formation of a geopolymer. As stated before, these Class F types are generally found in India.

2.2 Class C Fly Ash

Fly ash produced from the burning of younger lignite or sub-bituminous coal, in addition to having pozzolanic properties, also has some self-cementing properties. In the presence of water, Class C fly ash will harden and gain strength over time. Class C fly ash generally contains more than 20% lime (CaO). Unlike Class F, self-cementing Class C fly ash does not require an activator. Alkali and sulfate (SO4) contents are generally higher in Class C fly ashes.

1. Effect of Fly Ash on Concrete

Though a large number of significant results have been reported on the use of fly ash in concrete [3–8], however, there is not much literature available on the use of fly ash as a partial replacement of fine aggregates [3, 4, 9], with even less literature on the use of bottom ash [6, 10–12] as partial replacement of fine aggregate.

2. Effect of Bottom Ash on Concrete

An experimental investigation of various fresh and hardened properties of concrete was reported. Tests were conducted on mixes of natural sand (known as control mix), bottom ash, and mixes having equal volumes of natural sand and bottom ash. Also, mixes were developed using high-range water-reducing admixtures. The results indicated that the mixing water requirement increases rapidly when bottom ash is used in the concrete, also the inclusion of bottom ash has no significant influence on the entrapped air content and setting times of fresh concrete. Due to the higher water requirement and yield, the compressive strength properties of the bottom ash and combined bottom ash and natural sand mixtures are lower than those of the control samples [10].

An investigation was also carried out on the behavior and long-term durability of Laboratory-made roller-compacted concretes containing bottom ash as fine aggregate for the properties like fresh properties and strength, stiffness, and deformation characteristics [6, 11]. It was observed that samples containing dry bottom ash offered excellent strength, stiffness, and deformation properties, considering the range of cement factors used. Laboratory-made roller compacted concretes with various combinations of cement (Type I and Type V for sulfate-resistant concrete), lignite dry bottom ash, and crushed limestone coarse aggregate was tested to ascertain the suitability of this type of concrete for pavement applications. The analysis of the test results leads to the conclusion that durable concrete can be produced with the high-calcium dry bottom ash used in this investigation. Resistance to sulfate attack, rapid freezing, and thawing, and wear improved with increases in cement and/or coarse aggregate contents. Length changes due to external sulfate attack varied from 0.0388%, whereas no mass loss or reduction in strength was found in any of the test samples. Abrasion testing under wet conditions was consistently worse than under dry conditions. After 300 rapid freezing and thawing cycles, the mixture proportions of this investigation displayed a maximum mass loss of 2.3% and a minimum durability factor of 91.2%.

A study on the influence of Bottom Ash Replacements as Fine Aggregate on the Property of Cellular Concrete was conducted with various Foam contents. River sand was replaced by bottom ash from a power plant in Thailand at the rates of 0, 25, 50, 75, and 100% by volume. Compressive strength, density and water absorption of foam concrete were tested at 7, 14 and 28 days respectively, and the paper reports that the density of cellular concrete decreased while the water absorption increased with an increase in replacement level of bottom ash [12].

One very relevant study shows that grinding CBA from coal can be sustainably utilized in cementitious composites or mortar as a substitute material to tackle today's violent environments [13]. The strength and thermal properties of concrete containing high calcium and water absorptive fine aggregate from well-graded Bottom Ash (BA) as a partial sand replacement (control mix (CM) 0%, BM5: 5%, BM10: 10%, BM15: 15%, and BM20: 20%). The 15% replacement showed the highest compressive strength at 28 days along with the split tensile and flexural strength and thermal conductivity results [14].

This Paper deals with Coal Bottom Ash (CBA) affecting the cracking of concrete beams. Concrete specimens were grouped into four distinct combination replacements by half (50%) and full (100%) of coarse and fine CBA aggregate with the addition of 20% fly ash to the cement amount [15]. The beams were thus subjected to a cyclic load testing procedure to evaluate the cracking mechanism. The experimental results revealed that though the compressive strength of all groups achieved the targeted strength of 30 MPa at 28 days, the splitting tensile and flexural strengths decreased with the increment in the volume of CBA in the design mixture.

Results of a comprehensive experimental investigation on the use of bottom ash in cement and concrete, both as a pozzolanic additive and as a replacement of natural sand as a fine aggregate have been reported [16]. In this series of tests, bottom ash partly substituted natural sand as fine aggregate to promote the sustainability of a green environment. At appropriate replacement levels by bottom ash, the workability, compressive strength and durability of substituted concrete were greater than with natural sand alone.

This paper presents the experimental investigations carried out to study the mechanical properties of concrete where various percentages (30, 50 and 70%) replacement of coarse aggregates with pre-washed municipal solid waste incineration (MSWI) bottom ash [17]. The results obtained reveal that not more than 50% replacement is possible and prewashing is a must where slower strength development is noticed along with higher development at later ages (Fig. 1).

Fig. 1 Coal ash aggregates, both coarse and fine (also called 'coal mill rejects') displayed by students of IIEST, Shibpur at the 3rd Asia Pacific Conference on '*Dry Extraction and Effective Utilization of Bottom Ash and Technological Advances in other Coal Combustion Products and Emissions in Thermal Power Plants'* held on 17–18th March 2017 at Hotel Pride Plaza, Kolkata organized by Coal Ash Institute of India (CAII)

3 Conclusion

Ministry of Road Transport and Highways restricts the maximum use of fly ash in road pavements to 20% (as shown in Fig. 2) which is very unsustainable and the limit needs to be raised. Recently revised IS: 383-2016 has permitted the use of Bottom Ash and the research back-up as discussed in this paper stresses the fact that though fly ash that concrete mix of grades M 15 and M 20 may be effectively designed with substitution as high as 60% for fly ash and 50% for bottom ash, but higher grades require different technologies and methodologies and should be promoted at any cost. Similarly, there is a strong need to review the restriction of the use of fly ash in concrete to 35% in IRC:112-2011. Though very little literature [18] report coal ash's excellent compatibility with nanomaterials and nanotechnology, much research needs to be carried out in this particular area to develop the concrete mix's grade as a synergy between the two. Also as reported in the literature reviews, effective coal ash utilization on cement concrete brings us a more durable and sustainable concrete. So, in persuasion with India's response to climate change, our enhanced commitment at COP 26 (2021) was to achieve *Panchamitra* i.e., net-zero CO_2 emissions by 2070—a holistic and comprehensive approach that may be made possible with fly ash blending.

MINISTRY OF ROAD TRANSPORT & HIGHWAYS
SPECIFICATIONS FOR ROAD AND BRIDGE WORKS
(Fifth Revision)

601 DRY LEAN CEMENT CONCRETE SUB-BASE

601.3.3 Cement Content

The cement content in the dry lean concrete shall be such that the strength specified in Clause 601.3.4 is achieved. The minimum cement content shall be 150 kg/cu.m of concrete. In case flyash is blended at site as part replacement of cement, the quantity of flyash shall not be more than 20 percent by weight of cementitious material and the content of OPC shall not be less than 120 kg/cu.m.

602 CEMENT CONCRETE PAVEMENT

6023.2 Cement Content

When Ordinary Portland Cement (OPC) is used the quantity of cement shall not be less than 360kg/cu.m. In case fly ash grade I (as per IS:3812) is blended at site as part replacement of cement, the quantity of fly ash shall be upto 20 percent by weight of cementitious material and the quantity of OPC in such a blend shall not be less than 310 kg/cu.m. The minimum of OPC content, in case ground granulated blast furnace slag cement blended, shall also not be less than 310 kg/m³. If this minimum cement content is not sufficient to produce concrete of the specified strength, it shall be increased as necessary by the contractor at his own cost.

Fig.2 MORT&H's specification regarding the use of fly ash

References

1. Senapati MR (2011) Fly ash from thermal power plants—waste management and overview. Curr Sci 100(12):1791–1794
2. Study report on use of coal ash in railway embankment, report number GE: 0–S005, geotechnical engineering directorate. Research Designs and Standards Organization, Lucknow, Feb 2006
3. Al-Manaseer AA, Hang MD, Nasser KW (1988) Compressive strength of concrete containing fly ash, brine and admixture. ACI Mater J:109–116
4. Haque MN, Day RL, Langan BW (1989) Realistic strength of air-entrained concretes with and without fly ash. ACI Mater J:241–247
5. Swamy RN, Sami ARA, Theodorakopoulos DD (1983) Early strength fly ash concrete for structural application. ACI Mater J:414–422
6. Siddique R (2004) Performance characteristics of high volume class F fly ash concrete. Cem Concr Res 34:487–493
7. Sivasundram V, Malhotra VM (2004) High performance high volume fly ash concrete. Ind Concr J:13–21
8. Naik TR, Ramme BW (1989) High strength concrete containing large quantities of fly ash. ACI Mater J:111–116
9. Maslehuddin M, Al-Mana AI, Shamim M, Saricimen H (1989) Effect of sand replacement on the early age strength gain and long term corrosion resisting characteristics of fly ash concrete. ACI Mater J:58–62
10. Swami RN, Alli SAR, Theodorakepoulos DD (1983) Early strength fly ash concrete for structural application. ACI Mater J:414–422
11. Sivasundram, Malhotra VM (2004) High-performance high volume fly ash concrete. Ind Concr J:13–21
12. Onprom P, Chaimoon K, Cheerarot R (2015) Influence of bottom ash replacements as fine aggregate on the property of cellular concrete with various foam contents. Adv Mater Sci Eng 2015:11. https://doi.org/10.1155/2015/381704
13. Al Biajawi MI, Embong R, Muthusamy K, Ismail N, Obianyo II (2022) Recycled coal bottom ash as sustainable materials for cement replacement in cementitious. Compos Rev Constr Build Mater 338. https://doi.org/10.1016/j.conbuildmat.2022.127624
14. Abdullah MJ, Beddu S, Manan TSBA, Syamsir A, Naganathan S, Kamal NLM, Mohamad D, Itam Z, Yee HM, Yapandi MFKM, Nazri FM, Shafiq N, Isa MH, Ahmad A, Rasdi NW (2022)

The strength and thermal properties of concrete containing water absorptive aggregate from well-graded bottom ash (BA) as partial sand replacement. Constr Build Mater 339. https://doi.org/10.1016/j.conbuildmat.2022.127658
15. Hasim AM, Shahid KA, Ariffin NF, Nasrudin NN, Zaimi MNS, Kamarudin MK (2022) Coal bottom ash concrete: mechanical properties and cracking mechanism of concrete subjected to cyclic load test. Constr Build Mater 346. https://doi.org/10.1016/j.conbuildmat.2022.128464
16. Muthusamy K, Rasid MH, Jokhio GA, Budiea AMA, Hussin MW, Mirza J (2020) Coal bottom ash as sand replacement in concrete: a review. Constr Build Mater 236. https://doi.org/10.1016/j.conbuildmat.2019.117507
17. Zhang T, Zhao Z (2014) Optimal use of MSWI bottom ash in concrete. Int J Concr Struct Mater 8:173–182. https://doi.org/10.1007/s40069-014-0073-4
18. Ghosal M, Chakraborty AK (2018) Issues affecting the applicability aspects of nanomaterials in cement construction, advances in concrete, structural and geotechnical engineering, book chapter on ACSGE-2018 proceedings, organized by BITS-Pilani. Publisher-Bloomsbury, pp 373–378

Strength Characteristics of Warm Mix Asphalt Using Brickdust as a Mineral Filler

Shiva Kumar Mahto and Sanjeev Sinha

Abstract Warm mix asphalt (WMA) gained attractive properties due to its lowering production temperature and also added benefits in reducing the gas emissions in the environment as compared to that of hot mix asphalt (HMA). This article presents the usage of brickdust (BD) in the preparation of Warm mix asphalt (WMA) by wax-based technology. The effect of brick dust filler was varied from 25 to 100% replacement by the weight of the natural stone dust (NSD) filler. Cylindrical specimens were prepared using Marshall mix design and dense bituminous macadam (DBM) gradation was adopted by Ministry of Road Transport and Highways (Morth-5 revision) guidelines. Prepared specimens were exposed to Marshall Stability, volumetric properties, and indirect tensile strength (ITS) test. The results showed improved performance with the addition of brick dust into mixes. Stability and ITS were increased from 25 to 75% stone dust replacement and a decrease in strength is observed with 100% replacement. The optimum brick dust content in the warm mix was found at 75% replacement of stone dust by gaining maximum stability and tensile strength.

Keywords Warm mix asphalt · Sasobit · Brickdust · Marshall properties

1 Introduction

In the last decade, the use of warm-mix asphalt has been dominant due to its lower production temperature and less gas emission in the environment as compared to that of hot mix asphalt (HMA). The warm mixes prepared by different technologies have not only been useful in reducing mixing temperature but also attributes to low fuel consumption and increases longer haul distance. There are several methods in which three main technologies are followed in practice water-based technologies, organic wax-based additive and chemical additives [1]. The literature surveys reported that

S. K. Mahto (✉) · S. Sinha
Department of Civil Engineering, NIT Patna, Bihar 800005, India
e-mail: shivam.phd19.ce@nitp.ac.in

S. Sinha
e-mail: sanjeev@nitp.ac.in

S. B. Singh et al. (eds.), *Fiber Reinforced Polymeric Materials and Sustainable Structures*,
Composites Science and Technology, https://doi.org/10.1007/978-981-19-8979-7_25

the organic wax-based technology has been the foremost technology in attaining high strength and durability. It is also observed that the overall performance such as moisture susceptibility, rutting, cracking and fatigue behaviour has been significantly higher and stiffer than any other techniques [2–7].

1.1 Background

The use of organic wax such as Sasobit wax, paraffin wax, asphaltan-B has been significantly influenced the production of warm mixes at lower temperatures. Subsequently, it enhances the strength, moisture resistance and cracking properties in the preparation of warm mixes [8–10]. The fatigue and rutting behaviour also found to be improved in WMA prepared using this technology with suitable material [3, 11]. The sasobit wax has a melting temperature of 90–116 °C and it is easily miscible with bitumen at 115 °C which changes the viscosity of the binder and is capable of coating the aggregates at low temperatures [12, 13]. The use of different waste materials such waste engine oil, reclaimed asphalt pavement (RAP), plastic waste, recycled aggregates has been a great success using this technology [3–16]. The inclusion of filler such as lime, nano hydrated lime, copper slag, fly ash has been reported that has greatly influenced the strength and resistance to moisture damage in warm asphalt mixtures [17, 18].

Asphalt mix mainly comprises of coarse aggregates, fine aggregates, filler and bitumen as a binder. The role of mineral filler is to fill the gap between the coarse and fine aggregates. Different fillers have different properties such as pozzolana, cementitious etc. These physical properties of such material imparts additional stiffness into the asphalt mixes. India has more than 100,000 brick industries which high quantity of brick dust nearby such areas. These can be harmful to soil for cultivation. However, in the literature, the study with the use of brick dust is not observed with warm mix asphalt mixtures. The present study focuses on the utilization of brick dust in the construction of flexible pavement mixes using warm mix technology. Here in the state of Bihar, an Eastern part of India, comprises many brick manufacturers and the residue of brick dust from these industries has been hazardous to humans and the environment [19]. This motivated to make use of brick dust in the warm mixes using sasobit as an additive for binder preparation. The objective of the study is to evaluate the effect of brick dust (BD) at different contents by exposing it to moisture damage tests.

2 Materials and Methods

2.1 Materials

Aggregates: The aggregates with a nominal size of 26.5 mm were used in the study. The gradation was adopted from Morth, 2013 guidelines. Dense Bitumen Macadam (DBM) grade 2 was adopted for the study. The aggregates were obtained from the nearby stone quarry located in Gaya district, Bihar, India. The physical properties and gradation adopted for mixes are as shown in Table 1 and Fig. 1.

Table 1 Physical properties of the aggregates

S. No.	Test name	Value	IS code	Standard values for Bituminous concrete (MoRTH)
1	Specific gravity	2.84	ASTM C128-01	2.5–3.2
2	Aggregate impact test, %	8.087	ASTM C131 M	Max 24%
3	Los Angeles value, %	15.65	ASTM C 131	Max 30%
4	Flakiness, %	23.65	ASTM 4791-10	Max 30%
5	Elongation, %	24.12	ASTM 4791-10	Max 30%
6	Combined index, %	27.28	ASTM 4791-10	Max 35%
7	Aggregate crushing value, %	18.34	ASTM D 5821	Max 30%
8	Soundness test, %	2.68	ASTM C88-13	Max 12%
9	Water absorption, %	0.15	ASTM D 7172-14	Max 2%

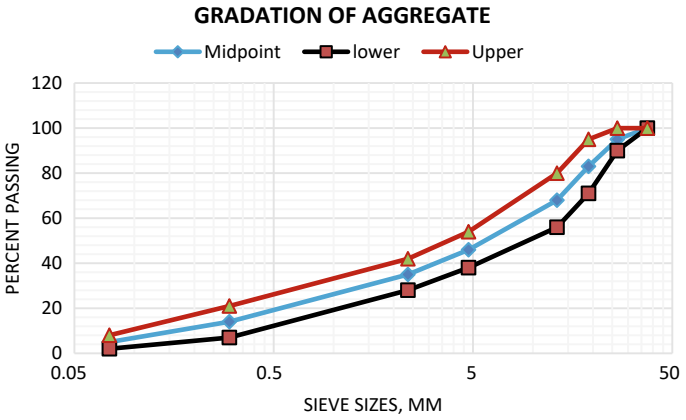

Fig. 1 Gradation of the aggregate adopted

Table 2 Physical properties of Bitumen and Sasobit

S. No.	Test name	Results	Sasobit	Limits as per IS 73	Code
1	Penetration	54	–	Min 45	ASTM D5
2	Softening point	48	82–105	Min 47	ASTM D36
3	Ductility value	95	–	≥ 75	ASTM D113-99
4	Flash and fire temp	221	–	220	ASTM D 92
5	Stripping value	2%	–	< 4	ASTM D 4469-17
7	Specific gravity value	1.01	0.86	0.97–1.02	ASTM D70-03
8	Kinematic viscosity at 135 °C, cSt	395 cSt	13 cSt	Min 350	ASTM D21710

2.2 Binder

The viscosity grade VG 30 is used as a Bitumen binder in the study and sasobit wax was used as an additive for form mix preparation. The wax was obtained from KPL international limited Mumbai. The physical properties of binder and wax are as shown in Table 2.

3 Methodology

The Sasobit wax was added at 3% for binder preparation which aids in reducing the viscosity of bitumen [20, 21]. It is to be noted that for filler material, the percentage passing of 2–8% is required in the preparation of these mixes. Brick dust was obtained from the local manufacturer, and it was varied from 25 to 100% at 25% increment by the weight of the maximum filler material content in order to evaluate the moisture sensitivity for its utility in the construction of flexible pavements. Marshall mix design was used as per the guidelines of Asphalt Institute manual series II (MS-2). Marshall Stability, Retained Marshall stability and indirect tensile strength. Figure 2 shows the methodology adopted.

4 Results and Discussions

The cylindrical specimens were prepared, and the optimum bitumen content (OBC) was obtained for all the mix variants. The OBC for natural stone dust was high and the inclusion of BD into mixes reduces the asphalt content required and also influences the strength of the mixes. Figure 3 shows the OBC variation.

It is observed that the OBC decreases with the increase in the brickdust content. A reduction of 8.33% was observed with the inclusion of BD in the mixes. This might

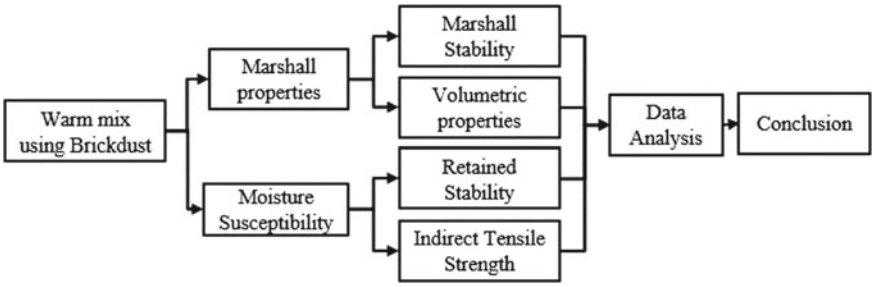

Fig. 2 Methodology adopted

Fig. 3 Variation in OBC of the mixes

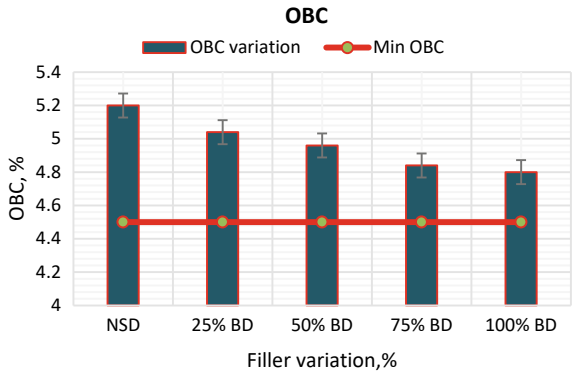

be due to the fine particles that may lead to expanding the bitumen particles and may act as an asphalt extender function [22].

4.1 Marshall Stability and Retained Marshall Stability

The Marshall stability was evaluated for the mixes prepared which were conditioned at 60 °C and stability test was carried out under static loading of 50 mm/minute. For retained stability, the samples were conditioned at 60 °C up to 24 h and thereafter subjected to Marshall stability testing. The results are represented in Figs. 4 and 5 respectively.

The stability was found to be significantly with the increase in the BD content and further increase with higher leads to decrease in the stability value. The maximum stability was found to be at 75% BD addition and an increase of 17.84% was found as compared with control mix. The similar trend was also followed in the RMS value. It is to be noted that a value having more than 80% retained stability are better resistance to moisture and appropriate for the mixes as Morth guidelines. Almost all

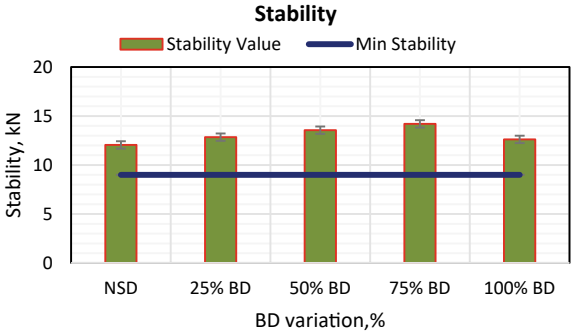

Fig. 4 Stability plot

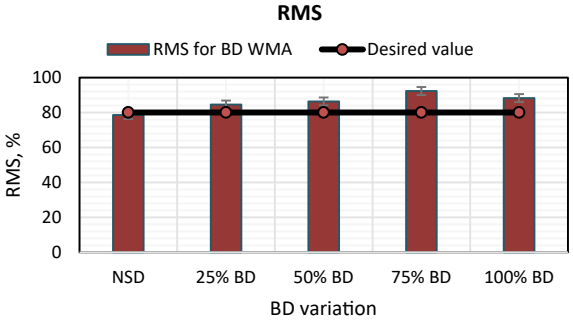

Fig. 5 Retained stability plot

the mixes were able to exceed this value except the mix with NSD was less than that of 80% which indicates that the mix was less resistance to moisture damage.

4.2 Volumetric Properties

The voids in mineral admixture and voids filled with bitumen (VFB) was evaluated for all the mixes. It can be used to assess the void that remains in the mixes after the compaction. Figures 6 and 7 shows the volumetric properties of the WMA mixes.

It is noticed that the inclusion of the BD has greatly influenced the void-bitumen phenomenon in the mixes. The VFB for all the mixes was found to be in the range of 68–76%. As per the recommendation of Morth the VFB must be in the range of 65–75 and min 12% for the VMA. The mix with 100% BD replacement was found to exceed the value of VFB and less than the minimum required of VMA content.

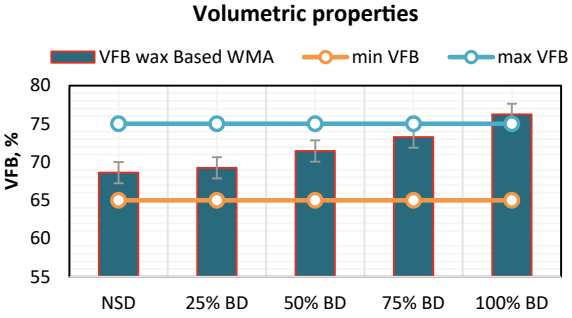

Fig. 6 Voids filler with bitumen in all the mix variants

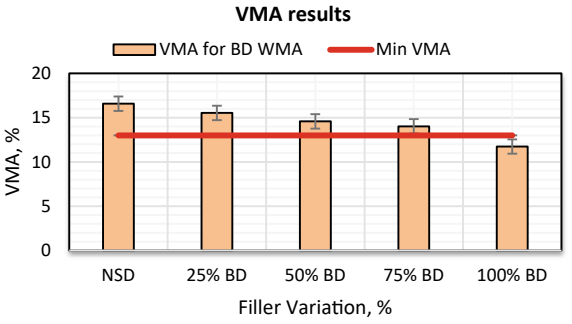

Fig. 7 Indicates the VMA in the mixtures

4.3 Marshall Quotient (MQ)

The MQ represents the stiffness of the asphalt mixtures. It is the ratio of stability to flow. The higher stiffness represents the mixes are more resistivity to the loads. Figure 8 represents the MQ value.

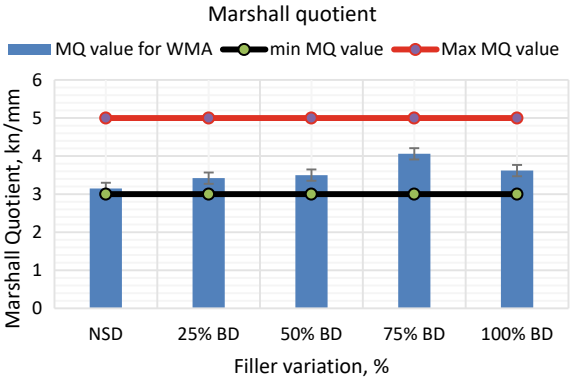

Fig. 8 Marshall quotient plot

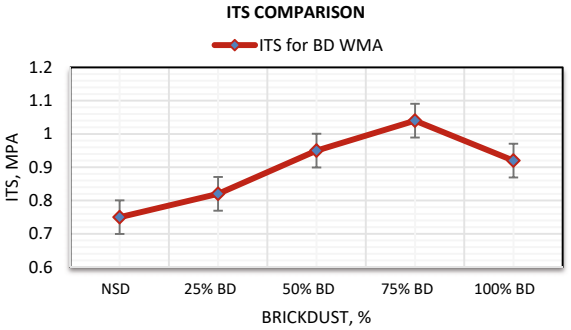

Fig. 9 Indirect tensile strength test plot

The Morth recommends having the Marshall Quotient value in the range of 3–5. If the mix attains the higher value within this range it can perform better resistance. It can be seen that the maximum MQ value was obtained for the mix prepared at 75% replacement of BD with NSD and thus it can be said that the mix at this content can resist more loads without deformation for long periods.

4.4 Indirect Tensile Strength (ITS)

The ITS can be determined the load applied diametrically on the cylindrical specimen at the rate of 50 mm/min. It is followed as per ASTM D6931. Figure 9 shows the ITS plots for all the mixes.

It is seen that the mixes attained significantly increased value with the addition of brick dust into the mixes. The ITS was having a maximum value of 75% BD content. It can be one of the parameters to assess the rutting parameter. The maximum ITS value may have less rut depth in the mixes.

5 Conclusion

The warm mix is produced at lower temperatures and the performance can be comparable with the conventional hot mixes with several advantages. The moisture damage is one of the factors which stands for demerits in these mixes. The inclusion of proper additives can minimise this problem. In the current study, the Brickdust was varied at different percentages as a replacement for the natural stone dust filler. The addition was sasobit wax to decrease the mixing temperature up to 30 °C. It is noticed that the addition of the BD in the mixes performs better. The strength was significantly higher than that of control WMA. The Marshall Quotient and indirect tensile strength were significantly higher at 75% BD for the NSD replacement. It can be concluded that the addition of 75% brickdust provided high stability and stiffness to the warm

mixes. Therefore, it can be an optimum quantity as a replacement for stone dust in these mixes. However, more studies are required to assess the other performance tests such as rutting, cracking and fatigue failure.

References

1. IRC (2019) IRC SP 101 2019 guideline for warm mix asphalt. J Chem Inf Model 53(9):1689–1699
2. Piccone G, Loprencipe G, Almeida A, Fiore N (2020) Evaluation of the performance of a warm mix asphalt (WMA) considering aged and unaged specimens. Coatings 10(12):1–17. https://doi.org/10.3390/coatings10121241
3. Dinis-Almeida M, Afonso ML (2015) Warm mix recycled asphalt—a sustainable solution. J Clean Prod 107:310–316. https://doi.org/10.1016/j.jclepro.2015.04.065
4. Batari A, Aman MY, Saeed SM, Ahmed TY, Chinade AU (2017) Rutting assessment of crumb rubber modifier modified warm mix asphalt incorporating warm asphalt additive. Int Res J Eng Technol 04(02):1239–1244. Available https://irjet.net/archives/V4/i2/IRJET-V4I2242.pdf
5. Yousefi A, Behnood A, Nowruzi A, Haghshenas H (2021) Performance evaluation of asphalt mixtures containing warm mix asphalt (WMA) additives and reclaimed asphalt pavement (RAP). Constr Build Mater 268. https://doi.org/10.1016/j.conbuildmat.2020.121200
6. Behl A, Kumar G, Sharma G, Jain PK (2013) Evaluation of field performance of warm-mix asphalt pavements in India. Proc Soc Behav Sci 104:158–167. https://doi.org/10.1016/j.sbspro.2013.11.108
7. Kumar R, Saboo N, Kumar P, Chandra S (2017) Effect of warm mix additives on creep and recovery response of conventional and polymer modified asphalt binders. Constr Build Mater 138:352–362. https://doi.org/10.1016/j.conbuildmat.2017.02.019
8. Xiao F, Jordan J, Amirkhanian SN (2009) Laboratory investigation of moisture damage in warm-mix asphalt containing moist aggregate. Transp Res Rec J Transp Res Board 2126(1):115–124. https://doi.org/10.3141/2126-14
9. Silva HMRD, Oliveira JRM, Peralta J, Zoorob SE (2010) Optimization of warm mix asphalts using different blends of binders and synthetic paraffin wax contents. Constr Build Mater 24(9):1621–1631. https://doi.org/10.1016/j.conbuildmat.2010.02.030
10. Merusi F, Caruso A, Roncella R, Giuliani F (2010) Moisture susceptibility and stripping resistance of asphalt mixtures modified with different synthetic waxes. Transp Res Rec 2180:110–120. https://doi.org/10.3141/2180-13
11. Roma TIS et al (2020) Evaluating the performance of warm mix asphalt incorporating evaluating the performance of warm mix asphalt incorporating recycled asphalt pavement treated bases recycled asphalt pavement treated bases. Transp Res Proc 45:716–723. https://doi.org/10.1016/j.trpro.2020.02.106
12. Jamshidi A, Othman M, You Z (2013) Performance of warm mix asphalt containing Sasobit Ò: state-of-the-art. Constr Build Mater 38:530–553. https://doi.org/10.1016/j.conbuildmat.2012.08.015
13. Mohi I, Mir MS (2020) Study of warm mix asphalt using reclaimed asphalt pavement and copper slag: a review, vol 362, pp 355–362
14. Ronald Fabrice PK, Abejide SO, Adedeji JA, Hassan Mostafa MM (2020) Evaluating the performance of warm mix asphalt incorporating recycled asphalt pavement treated bases. Transp Res Proc 45:716–723. https://doi.org/10.1016/j.trpro.2020.02.106
15. Mosa AM, Jawad IT, Salem LA (2018) Modification of the properties of warm mix asphalt using recycled plastic bottles, vol 31, no 9, pp 1514–1520
16. Mohi I, Din U, Shafi M (2021) Laboratory study on the use of reclaimed asphalt pavement and copper slag in warm mix asphalt pavements using waste engine oil as a rejuvenator. Int J Pavement Res Technol 0123456789. https://doi.org/10.1007/s42947-021-00036-y

17. Diab A, You Z (2014) Rheological properties of short-term aged foamed asphalt modified with nano hydrated lime. In: CICTP 2014 safe, smart, sustainable multimodal transportation system—proceedings of the 14th cota international conference on transportation professional, pp 1043–1050. https://doi.org/10.1061/9780784413623.101
18. Woszuk A, Bandura L, Franus W (2019) Fly ash as low cost and environmentally friendly fi ller and its effect on the properties of mix asphalt. J Clean Prod 235:493–502. https://doi.org/10.1016/j.jclepro.2019.06.353
19. Issar S (2018) Bricks or food ? Bihar's construction conundrum, pp 1–9
20. Wasiuddin NM, Selvamohan S, Zaman MM, Guegan MLTA (2007) Comparative laboratory study of sasobit and aspha-min additives in warm-mix asphalt. Transp Res Rec 1998:82–88. https://doi.org/10.3141/1998-10
21. Liu K, Zhang K, Wu J, Muhunthan B, Shi X (2018) Evaluation of mechanical performance and modification mechanism of asphalt modified with graphene oxide and warm mix additives. J Clean Prod 193:87–96. https://doi.org/10.1016/j.jclepro.2018.05.040
22. Wagaw F, Emer P, Quezon T, Geremew A (2018) Evaluation of the performance of brick dust as a filler material for hot asphalt mix design : a case study in Jimma zone. Int J Eng Sci 7(3):64–72. https://doi.org/10.9790/1813-0703026472

Concrete Compressive Strength Prediction Using Boosting Algorithms

Shreyas Pranav, Mukund Lahoti, and Muthukumar Gopalarathnam

Abstract This study proposes intelligent machine learning (ML)-based methods for concrete compressive strength prediction by utilizing a publicly available dataset. The methods employed are the XGBoost, CatBoost and TabNet algorithms. A total of 1030 data points are collected wherein the independent input variables are the amounts of the different components of the concrete mix design and the output variable is the compressive strength at different curing ages. The proposed boosting algorithm approaches are contrasted with a few other popular ML techniques used in this field, such as logistic regression, classification and regression tree, and artificial neural networks. It is found that XGBoost and CatBoost show significantly lower mean errors between predicted values and actual observations of the compressive strength than the contemporary architectures, while TabNet is not so efficient. TabNet's lower efficiency of prediction can be attributed to the relatively small dataset that was used for this study.

Keywords Concrete compressive strength · Prediction · Machine learning · Artificial intelligence

1 Introduction

Concrete is the most established construction material in the world primarily because of its good mechanical properties combined with long-term durability and sustainability. To develop comprehensive design guidelines for concrete, it is essential to understand and monitor the mechanical properties of concrete. Among the different concrete mechanical properties, compressive strength is the most basic as well as the

S. Pranav (✉) · M. Lahoti · M. Gopalarathnam
Department of Civil Engineering, BITS Pilani, Pilani 333031, India
e-mail: p20140720@pilani.bits-pilani.ac.in

M. Lahoti
e-mail: mukund.lahoti@pilani.bits-pilani.ac.in

M. Gopalarathnam
e-mail: muthug@pilani.bits-pilani.ac.in

S. B. Singh et al. (eds.), *Fiber Reinforced Polymeric Materials and Sustainable Structures*, Composites Science and Technology, https://doi.org/10.1007/978-981-19-8979-7_26

most important, because it directly determines structure safety. However, predicting the compressive strength of concrete is a challenging task, because concrete is a complex matrix made up of different, and sometimes variable kinds of materials: coarse and fine aggregates, cement, water, fly ash, blast furnace slage, admixtures, and these ingredients are arbitrarily distributed over the entire matrix. Such a complex framework makes precise prediction of the compressive strength a challenging task [1, 2]. Usually, the most straightforward means to know the compressive strength of concrete is by performing experimental investigation. Typically, cube or cylinder samples are cast based on a pre-determined mix design and then kept for curing for a specified duration. Thereafter, the compressive strength can be obtained easily by use of a standard compressive testing machine [3–5]. However, this approach typically requires 28 days for each sample, making the process difficult to rely on for large-scale studies involving multiple mix designs. Seeing this, researchers have proposed some experimental regression-based approaches for concrete compressive strength estimation based on a given mix design [6–8]. Unfortunately, the relation between concrete mix design and compressive strength is strongly nonlinear, making it tough to arrive at an exact regression expression. Yet another way to predict concrete performance is through numerical simulation [9, 10]. However, as previously mentioned, the combination of random distribution of mix constituents and nonlinearity makes it challenging to precisely simulate concrete and its behavior [1, 11]. With the advent of artificial intelligence (AI), machine learning (ML) has emerged as a popular approach to predict different aspects of concrete strength. Machine learning is a sub-discipline of artificial intelligence, and can be used for achieving various goals such as image classification, text analysis, clustering, etc. Compressive strength prediction is one such application of the regression function of ML. In contrast with traditional regression, machine learning regression uses algorithms that have the ability to 'learn' from the input data and give accurate outputs, and this is a clear benefit over traditional regression [12]. Till date, several ML methods have been used for predicting compressive strength, with artificial neural network (ANN) and support vector machine (SVM) being the most prominent. For example, Siddique et al. [13] used ANN for compressive strength estimation of self-compacting concrete with bottom ash, while Uysal and Tanyildizi [14] also used ANN to predict the compressive strength of self-compacting concrete at elevated temperature conditions. Dantas et al. [15] and Duan et al. [16] also employed a similar ANN for concrete incorporating construction waste and recycled concrete aggregate respectively. Chou et al. [17, 18] explored various ML approaches to estimate the concrete compressive strength, including ANN and SVM. Aiyer et al. [19] proposed a modified version of SVM, called least square SVM, to this area of research. Pham et al. [20] further bettered the least square SVM using metaheuristic optimization, predicting the compressive strength of high-performance concrete. Omran et al. [21] evaluated the precision of several data mining techniques in estimating the compressive strength of environment-friendly concrete. Chithra et al. [22] explored the use of ANN in estimating the compressive strength of concrete blended with nano-silica and copper slag. Naderpour [23] also used ANN to estimate the compressive strength of environment-friendly concrete. Ashrafian [24] utilized heuristic regression for

predicting compressive strength and ultrasonic pulse velocity of fiber-reinforced concrete. Zhang et al. [25] predicted the compressive strength of concrete using the random forest technique; they also examined the significance of each input variable.

In this paper, we applied three boosting algorithms, XGBoost, CatBoost and TabNet for predicting the compressive strength of concrete. 1030 sets of concrete compressive strength data are collected, and sorted in such a way that the mix design components and curing duration are the independent variables and the compressive strength is the output variable. The performance of all these algorithms is compared to popularly used prediction algorithms in this field, such as Artificial Neural Netowrks (ANN), Support Vector Machines (SVM), Classification and Regression Tree (CART) and Logistic Regression (LR). The comparison is done on the basis of Root Mean Squared Error (RMSE), Mean Absolute Error (MAE) and Mean Absolute Percentage Error (MAPE).

2 Methodology

2.1 Dataset

Machine learning algorithms typically require huge amounts of training data to be efficient, often in tens of thousands. However, it is not practical to gather such a vast dataset for a field such as compressive strength prediction. Still, to have a reasonably accurate prediction model, we have assimilated 1030 concrete compressive strength datapoints. In fact, this dataset was first assimilated by Yeh [26], and has already been used for other machine learning applications [18]. The mix design components which comprise the independent variables for this study are: cement, water, coarse aggregates, sand, superplasticizer, ground granulated blast furnace slag and fly ash. The compressive strengths have been obtained by preforming standard procedures on 150 mm height cylinder specimens [26]. A few statistical metrics such as mean, standard deviation etc. of the experimental parameters are listed in Table 1.

2.2 Machine Learning for Regression

We use various state-of-the-art machine learning models for tabular data to perform the task of concrete strength predictions, namely TabNet, XGBoost, and CatBoost models. We compare the performance of these models with other studies and show that these models perform very well compared to older models.

XGBoost. XGBoost (Extreme Gradient Boosting) is a gradient boosting machine learning algorithm, first introduced by a group of data scientists at the University of Washington. It is widely used as a machine learning technique for tabular data. It can be generally used for classification and regression tasks. It uses decision tree as the

Table 1 Statistical information related to the dataset used for compressive strength prediction

Parameter	Unit	Minimum	Maximum	Mean	SD	Type
X_1: cement	kg/m^3	102.00	540.00	281.17	104.51	Input
X_2: water	kg/m^3	121.75	247.00	181.57	21.36	Input
X_3: coarse aggregate	kg/m^3	801.00	1145.00	972.92	77.75	Input
X_4: fine aggregate	kg/m^3	594.00	992.60	773.58	80.18	Input
X_5: super-plasticizer	kg/m^3	0.00	32.20	6.20	5.97	Input
X_6: blast-furnace slag	kg/m^3	0.00	359.40	73.90	86.28	Input
X_7: fly ash	kg/m^3	0.00	200.10	54.19	64.00	Input
X_8: curing time	days	1.00	365.00	45.66	63.17	Input
Y: compressive strength	MPa	2.33	82.60	35.82	16.71	Output

base learning model. The algorithm sequentially adds decision trees to predict the residual of the past models and sums the prediction of all trees to produce the final output. We use XGBoost as a regression model to predict the strength of concrete using predictor variables. A few advantageous features of XGBoost are as follows:

- Parallelization
- Non-linearity
- Scalability
- Cross-validation
- Regularization.

CatBoost. The CatBoost is a gradient boosting method, similar to XGBoost. It is a boosting algorithm which supports multiple categories of data, and thus the name CatBoost. It provides implicit support for categorical variables and provides very high-quality results on general tabular data tasks. It can be used for both classification and regression applications. A few advantageous features of CatBoost are as follows:

- Boosting schemes lead to good quality without tuning of parameters.
- Quick and scalable due to the use of symmetric tress.
- Ease of use—R and python supported.

TabNet. TabNet (Tabular Net) is a recently proposed state-of-the-art deep network for tabular data. It provides explainable and high-quality predictions. It is an attention-based model which uses sequential attention mechanism to extract quality information from data. TabNet works for both supervised and unsupervised tasks. It is a deep-learning model, and generally requires huge amount of data to perform well. A few advantageous features of TabNet are as follows:

- Can encode varied data types such as images along with table data.
- There is no need for feature engineering; TabNet chooses the best features and is readily interpretable as well.

Table 2 Results of various models on the concrete data in terms of RMSE, MAE and MAPE

Reference	Algorithm	RMSE	MAPE (%)	MAE
Proposed models	CatBoost	4.76	13.55	3.08
	XGBoost	4.00	9.89	2.68
	TabNet	23.13	46.03	17.34
Chou et al. [17, 18]	ANN	7.95	20.84	6.19
	SVM	5.59	12.03	12.05
	CART	7.84	20.66	5.86
	LR	10.11	29.89	7.87
	CART + SVM + LR	5.08	11.97	3.52

2.2.1 Results

The full dataset is split into 90% training and 10% testing randomly. Compressive strength prediction is done for the three proposed machine learning algorithms and the performance is tabulated in Table 2. The performance is measured using RMSE, MAPE and MAE.

RMSE is Root Mean Square Error (RMSE) and can be calculated using Eq. 1.

$$RMSE = \sqrt{\frac{\sum_{i=1}^{n}\left(x_i - x_i'\right)^2}{N}} \tag{1}$$

where x_i is actual observation and x_i' is predicted observation. N is the total number of observations.

MAE stands for Mean Absolute Error and can be calculated using Eq. 2.

$$MAE = \frac{\sum_{i=1}^{n}\left|x_i - x_i'\right|}{N} \tag{2}$$

MAPE is Mean Absolute Percentage Error and can be calculated using Eq. 3.

$$MAPE = \frac{1}{n}\sum_{i=1}^{n}\left|\frac{x_i - x_i'}{x_i}\right| \tag{3}$$

Lower the value of these metrics, better the performance; generally, models are optimized to minimize MAE or MSE (Mean Squared Error).

It can be observed from Table 2 that the CatBoost and XGBoost algorithms perform better than all previous models, due to significantly lower RMSE, MAE and MAPE values. TabNet is not performing well due to less amount of available training data. XGBoost is the most preferable out of all three because it has the least RMSE, MAPE and MAE values. The XGBoost algorithm performs better than even the CART + SVM + LR model proposed by Chou et al. [17, 18]. Thus, both

XGBoost and CatBoost can and should be further utilized in concrete strength prediction applications. Figure 1 also shows the correlation between the model-predicted compressive strength using XGBoost, CatBoost and TabNet, and the experimentally obtained values from various literature sources. It can be noticed that the TabNet algorithm does not perform as satisfactorily as the XGBoost and CatBoost algorithms in modelling the compressive strength of concrete.

3 Conclusions

This study aimed at improved concrete compressive strength prediction using intelligent machine learning (ML)-based techniques by utilizing a publicly available dataset. We have used the state-of-art XGBoost, CatBoost and TabNet algorithms for the same, and achieved good performance improvement in prediction of strength. A total of 1030 data records were used to train and test the efficiency of the different models. Performance was measured using three statistical measures: RMSE, MAE and MAPE. The boosting algorithms performed better than the existing algorithms in terms of all these measures in general. It can be concluded that these algorithms, particularly the XGBoost algorithm, can be used and deployed for prediction purposes in strength prediction applications with reasonable confidence. Plots showing the predicted and tested values of compressive strength also showed that XGBoost and CatBoost are good representative models, while TabNet is not as effective.

As a consequence of the exceptional performance of XGBoost and CatBoost in compressive strength prediction, further research should explore the use of these models for other aspects of mechanical strength prediction, such as tensile strength, flexural strength etc. It should also be explored for predicting the strengths of other construction materials and other combinations of materials not considered in this study. One limitation of this study is that only a few types of concrete mixes are considered in the dataset, namely concrete with blast furnace slag and concrete with fly ash. However, many other materials have been used in concrete mixtures which need to be taken into account. In fact, when more such input variables are included and the size of the dataset increases, it is expected that the performance of these models will further improve.

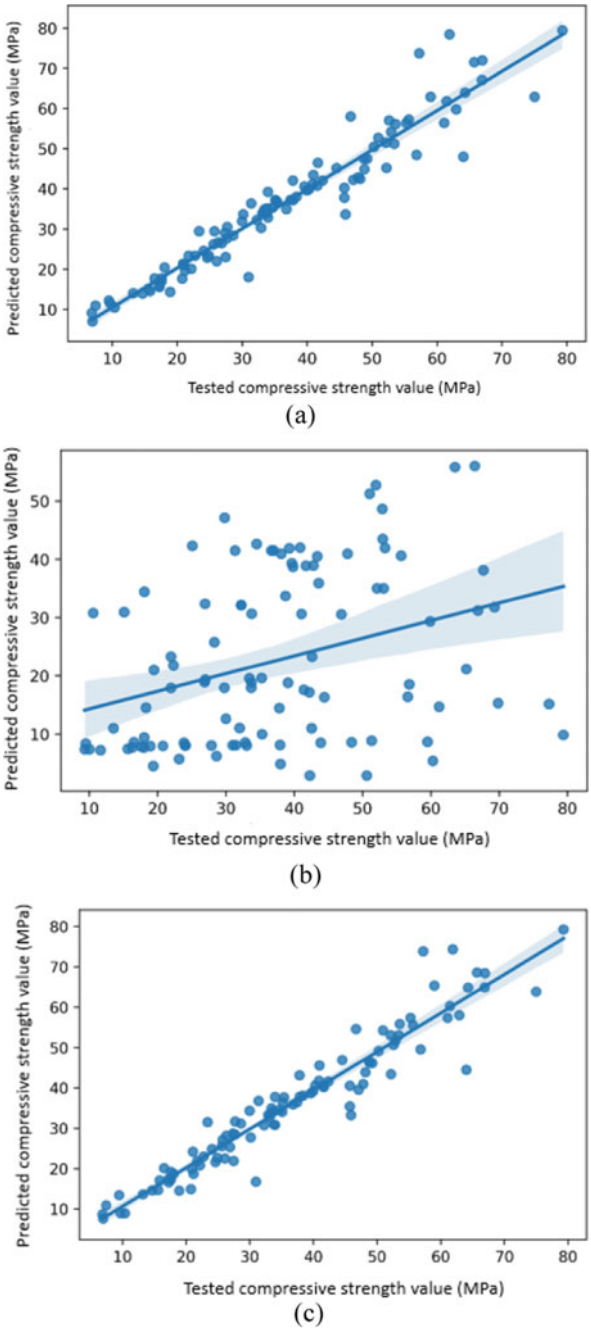

Fig. 1 Correlation plots between the predicted and experimentally obtained values of the compressive strength using **a** XGBoost, **b** TabNet and **c** CatBoost algorithms

References

1. Feng D-C, Li J (2016) Stochastic nonlinear behavior of reinforced concrete frames. II: numerical simulation. J Struct Eng 142:4015163. https://doi.org/10.1061/(ASCE)ST.1943-541X.0001443
2. Feng D, Ren X, Li J (2016) Stochastic damage hysteretic model for concrete based on micromechanical approach. Int J Non-Lin Mech 83:15–25. https://doi.org/10.1016/j.ijnonlinmec.2016.03.012
3. Bischoff PH, Perry SH (1991) Compressive behaviour of concrete at high strain rates. Mater Struct 24:425–450
4. Lessard M, Chaalla O, Aitcin P-C (1993) Testing high-strength concrete compressive strength. ACI Mater J 90:303–308
5. Shi H, Xu B, Zhou X (2009) Influence of mineral admixtures on compressive strength, gas permeability and carbonation of high performance concrete. Constr Build Mater 23:1980–1985. https://doi.org/10.1016/j.conbuildmat.2008.08.021
6. Bharatkumar BH, Narayanan R, Raghuprasad BK, Ramachandramurthy DS (2001) Mix proportioning of high performance concrete. Cement Concr Compos 23:71–80. https://doi.org/10.1016/S0958-9465(00)00071-8
7. Bhanja S, Sengupta B (2002) Investigations on the compressive strength of silica fume concrete using statistical methods. Cement Concr Res 32:1391–1394. https://doi.org/10.1016/S0008-8846(02)00787-1
8. Zain MFM, Abd SM (2009) Multiple regression model for compressive strength prediction of high performance concrete. J Appl Sci 9:155–160. https://doi.org/10.3923/jas.2009.155.160
9. De-Cheng F, Xiao-Dan R, Jie L (2018) Softened damage-plasticity model for analysis of cracked reinforced concrete structures. J Struct Eng 144:4018044. https://doi.org/10.1061/(ASCE)ST.1943-541X.0002015
10. Feng D-C, Wang Z, Wu G (2019) Progressive collapse performance analysis of precast reinforced concrete structures. Struct Des Tall Special Build 28:e1588. https://doi.org/10.1002/tal.1588
11. Feng D-C, Xie S-C, Deng W-N, Ding Z-D (2019) Probabilistic failure analysis of reinforced concrete beam-column sub-assemblage under column removal scenario. Eng Failure Anal 100:381–392. https://doi.org/10.1016/j.engfailanal.2019.02.004
12. Salehi H, Burgueño R (2018) Emerging artificial intelligence methods in structural engineering. Eng Struct 171:170–189. https://doi.org/10.1016/j.engstruct.2018.05.084
13. Siddique R, Aggarwal P, Aggarwal Y (2011) Prediction of compressive strength of self-compacting concrete containing bottom ash using artificial neural networks. Adv Eng Softw 42:780–786. https://doi.org/10.1016/j.advengsoft.2011.05.016
14. Uysal M, Tanyildizi H (2012) Estimation of compressive strength of self compacting concrete containing polypropylene fiber and mineral additives exposed to high temperature using artificial neural network. Constr Build Mater 27:404–414. https://doi.org/10.1016/j.conbuildmat.2011.07.028
15. Dantas ATA, Batista Leite M, de Jesus Nagahama K (2013) Prediction of compressive strength of concrete containing construction and demolition waste using artificial neural networks. Constr Build Mater 38:717–722. https://doi.org/10.1016/j.conbuildmat.2012.09.026
16. Duan ZH, Kou SC, Poon CS (2013) Prediction of compressive strength of recycled aggregate concrete using artificial neural networks. Constr Build Mater 40:1200–1206. https://doi.org/10.1016/j.conbuildmat.2012.04.063
17. Jui-Sheng C, Chien-Kuo C, Mahmoud F, Ismail A-T (2011) Optimizing the prediction accuracy of concrete compressive strength based on a comparison of data-mining techniques. J Comput Civ Eng 25:242–253. https://doi.org/10.1061/(ASCE)CP.1943-5487.0000088
18. Chou J-S, Tsai C-F, Pham A-D, Lu Y-H (2014) Machine learning in concrete strength simulations: multi-nation data analytics. Constr Build Mater 73:771–780. https://doi.org/10.1016/j.conbuildmat.2014.09.054

19. Aiyer BG, Kim D, Karingattikkal N, Samui P, Rao PR (2014) Prediction of compressive strength of self-compacting concrete using least square support vector machine and relevance vector machine. KSCE J Civ Eng 18:1753–1758. https://doi.org/10.1007/s12205-014-0524-0
20. Anh-Duc P, Nhat-Duc H, Quang-Trung N (2016) Predicting compressive strength of high-performance concrete using metaheuristic-optimized least squares support vector regression. J Comput Civ Eng 30:6015002. https://doi.org/10.1061/(ASCE)CP.1943-5487.0000506
21. Omran BA, Chen Q, Jin R (2016) Comparison of data mining techniques for predicting compressive strength of environmentally friendly concrete. J Comput Civ Eng 30. https://doi.org/10.1061/(ASCE)CP.1943-5487.0000596
22. Chithra S, Kumar SRRS, Chinnaraju K, Alfin Ashmita F (2016) A comparative study on the compressive strength prediction models for high performance concrete containing nano silica and copper slag using regression analysis and artificial neural networks. Constr Build Mater 114:528–535. https://doi.org/10.1016/j.conbuildmat.2016.03.214
23. Naderpour H, Rafiean AH, Fakharian P (2018) Compressive strength prediction of environmentally friendly concrete using artificial neural networks. J Build Eng 16:213–219. https://doi.org/10.1016/j.jobe.2018.01.007
24. Ashrafian A, Taheri Amiri MJ, Rezaie-Balf M, Ozbakkaloglu T, Lotfi-Omran O (2018) Prediction of compressive strength and ultrasonic pulse velocity of fiber reinforced concrete incorporating nano silica using heuristic regression methods. Constr Build Mater 190:479–494. https://doi.org/10.1016/j.conbuildmat.2018.09.047
25. Zhang J, Ma G, Huang Y, Sun J, Aslani F, Nener B (2019) Modelling uniaxial compressive strength of lightweight self-compacting concrete using random forest regression. Constr Build Mater 210:713–719. https://doi.org/10.1016/j.conbuildmat.2019.03.189
26. Yeh I-C (1998) Modeling of strength of high-performance concrete using artificial neural networks. Cement Concr Res 28:1797–1808. https://doi.org/10.1016/S0008-8846(98)00165-3

Rehabilitation and Retrofitting of Reinforced Concrete Structures Using Fiber Reinforced Polymers-Experiments

G. R. Reddy

Abstract Structures get distressed or health of the structures gets deteriorated with the time. Also demand on the structures may increase with the time. Good examples to mention are moving loads on the bridges, seismic loads on the structure etc. To take care of these aspects, structures have to be revisited frequently and assessed for its strength and serviceability status. If these requirements are not met, the structure needs to be rehabilitated to meet the initial design intent and retrofitted if the load demand increases. Conventionally after proper repair, steel jacketing, concrete jacketing, bracing etc. are adopted to rehabilitate and retrofit the structure. However, recently Fiber Reinforced Polymers (FRP) is taking the lead materials for rehabilitation and retrofitting of structures especially Reinforced Concrete structures. Along with fundamental procedure of FRP rehabilitation and retrofitting, details of testing as built and rehabilitated/ retrofitted structure are discussed in this paper. Importance of key parameters such as setting time, anchoring, workmanship etc. to achieve the target strength and ductility are also discussed. Brief explanation on modelling and analysis of tested as built and retrofitted structure is provided.

1 Introduction

One set of Structures referred to here are RCC residential buildings, office buildings, schools, hospitals, auditoriums, bridges etc. Another set of structures are referred to are historical stone masonry and brick masonry. The later one generally falls into one of the definition of sustained structures where as the first set may not be due to the

G. R. Reddy (✉)
VJTI, Mumbai, India
e-mail: grrddy@yahoo.com

NITK, Surathkal, India

University of Mumbai, Mumbai, India

BARC, Mumbai, India

HBNI, Mumbai, India

S. B. Singh et al. (eds.), *Fiber Reinforced Polymeric Materials and Sustainable Structures*, Composites Science and Technology, https://doi.org/10.1007/978-981-19-8979-7_27

durability and less service life. The definition considered for sustained structure is a structure designed using resources efficiently and has longer life. Good examples are heritage structures which are built using natural materials such as stones and clay bricks. Also natural mortars used to bond bricks and stones. The structures are designed for normal loads such as dead weight, live loads, imposed loads, thermal loads and accidental loads such as Blast loads, extreme winds, earthquake loads, Fire loads which has certain return period. In addition, the structure will interact with environment and its life gets affected may be due to carbonation, corrosion etc. The corrosion and accelerated corrosion due to carbonation are not issues in historical structure. The environment interactions are different in the first set of structures and it is more severe. It may be due to two major materials such as concrete and steel which have different load resistance and environment resistance. To repair, rehabilitate and retrofit such structures aiming to extend the life, Fiber Reinforced Polymers (FRP) is the good option and have good load resistance and have good resistance for environmental interactions. Mechanical properties of various fibers are shown in Table 1. FRP composites consists of high strength fibers embedded in the matrix of polymer resin. The fiber provide the load carrying capacity and the matrix is to ensure sharing of load among fibers and protect the fibers from environment. The FRP is further classified as laminates and fiber wraps. The former one is used for resisting flexure loads and later is used confinement to increase shear and axial capacity.

To understand the effectiveness of FRP strengthening, experiments were performed [1] on RC beam-column joints before and after repair. The joints first tested till failure under cyclic loads and then repaired and strengthened with FRP and retested. The wrapping the concrete structural elements will improve the confinement and hence increase in strength as shown in Fig. 1a and is similar to effect of the confined steel. It is essential to note that the wrapping will be effective only when the concrete has lateral deformation the obvious behaviour of concrete when start loading. When there is a need to increase the flexural capacity, it is achieved by using FRP laminates similar to the reinforcement. It is located generally near the surface of the concrete of structural elements. Both the confinement and flexure effects are clearly shown in Fig. 1b, c.

Based on the understanding of the effect of FRP strengthening, A full scale Ordinary Moment Resisting RC structure was tested as shown in Fig. 2a till failure. The load deflection characteristics are shown in the Fig. 2b. The same structure was

Table 1 Mechanical properties of fibres and steel

Property	E-glass	Carbon-HS	Basalt	Aramid Kevlar-29	Steel
Density (g/cc)	2.55	1.75	2.7	1.44	7.8
Young's modulus (GPa)	69	221	89	83	210
Tensile strength (Mpa)	3450	3100	4840	3620	–

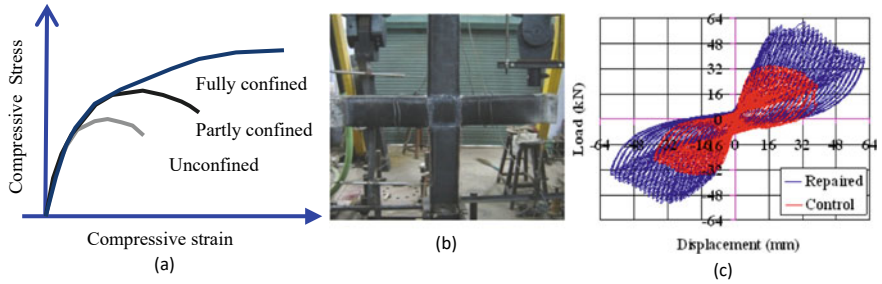

Fig. 1 Effect of FRP rehabilitation on RCC structural component

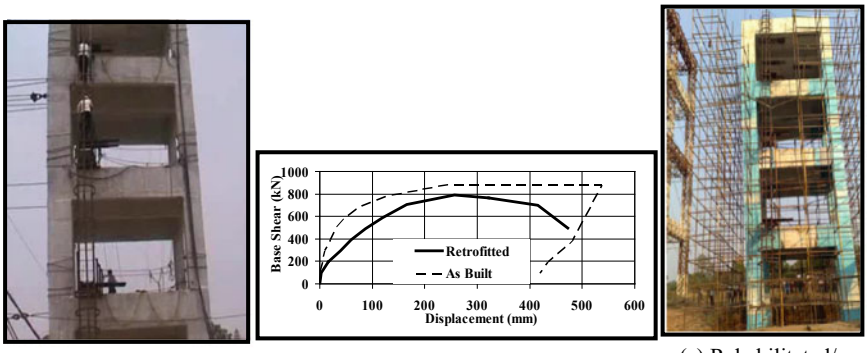

(a) As built Structure (b) Capacity (c) Rehabilitated/ Retrofitted Structure

Fig. 2 Full scale testing of RCC structures for its capacity original and rehabilitated/retrofitted with FRP

repaired and rehabilitated/Retrofitted with FRP as shown in Fig. 2c and further tested till failure. The achieved capacity is also shown in Fig. 2b.

2 Overall Design and Configuration of the Structure

The structure is a replica of a part of an existing office building. All the geometry details of the building are maintained as that of existing building and is shown in Fig. 3. Roof plan and typical floor plans are also shown in Fig. 3. However, original structure has ductile detailing as per IS 13920, where as the test structure has non-ductile detailing and detail of reinforcement is modified accordingly. Figure 3 also shows the foundation along with rock anchors to avoid rocking and sliding while loading the structure till failures. In total, 144 numbers of 1500 mm long high strength (bolts) rock anchors were used with 700 mm embedment in concrete and 800 mm in

rock. The rock anchors were inserted in pre-drilled holes in the rock and the holes are then grouted with non-shrinkable epoxy mortar grout.

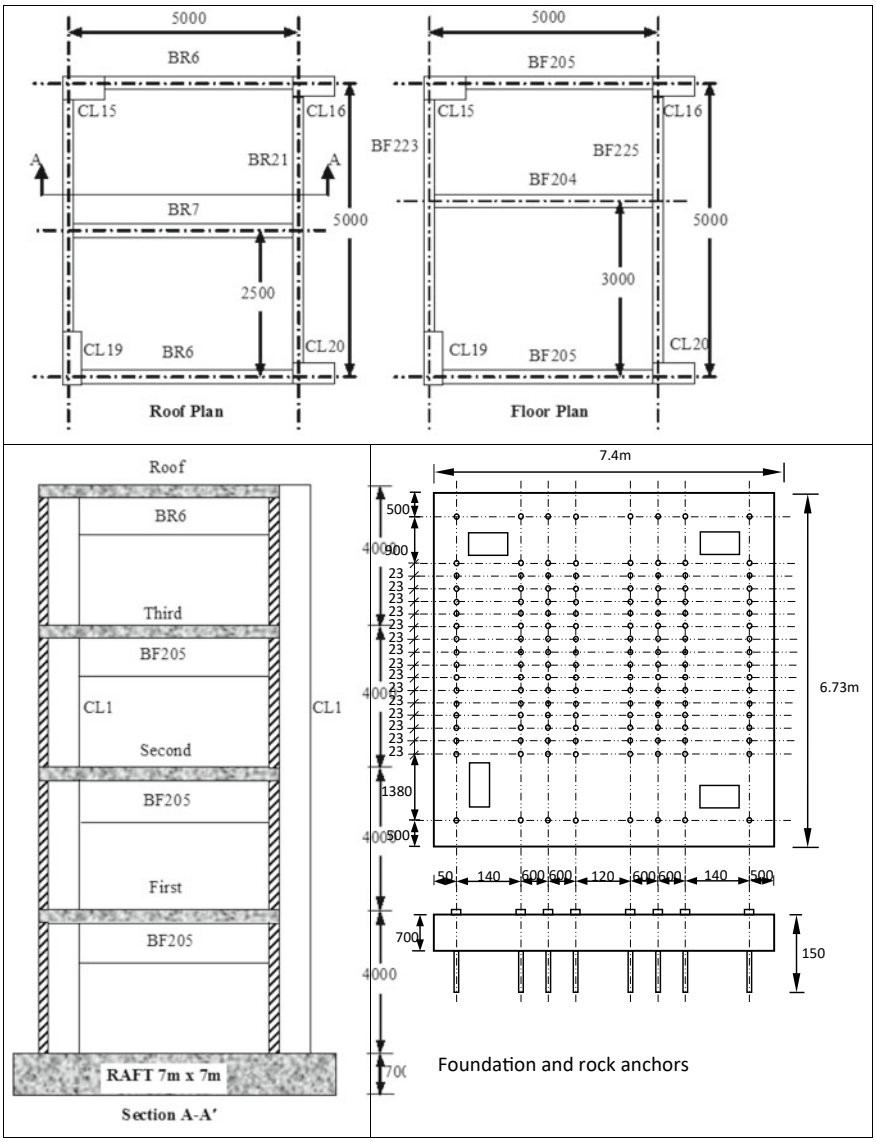

Fig. 3 Floor plans, elevation and foundation details of the structure tested

Table 2 Average concrete cube strengths

Location	Compressive strength in Mpa	Location	Compressive strength in Mpa	Location	Compressive strength in Mpa
Raft	32.88	1st–2nd Floor	33.30	3rd floor	29.86
Raft to 1st floor	28.86	2nd floor	31.09	3rd to 4th floor	31.24
1st floor	27.73	2nd to 3rd floor	32.24	4th floor (roof)	30.56

3 Material Properties

The material used in the design was of Concrete grade: M20 ($f_{ck} = 20$ MPa) and Reinforcement: HYSD ($f_y = 415$ MPa). However, The average concrete cube strengths taken from various locations are given in Table 2.

The test was conducted at tower testing facility of Central Power Research Institute, Bangalore, India. Electro Mechanical winches were used to apply load in pre defined pattern with four units at roof, three units at third floor, two units at second floor and one units at first floor. Load monitored using tension type load cells. Displacements were monitored using theodolites and laser sensors. To measure the strains in the reinforcement, strain gauges were used, to measure the strains on the surface, strain gauges, dial gauges and LVDTs were used as shown in Fig. 4.

24 strain gauges on first and fourth floor levels and 32 strain gauges at second and third floor levels were provided. Electrical resistivity based surface mounted strain gauges with a gauge length of 120 mm were installed on the top surface of beam and inner surface of the column. Therefore, in order to obtain average surface strains over a gauge length, at the base of the columns, dial gauge potentiometers were installed on the tension side of all the four columns. Although, digital theodolites were the main instrument to read the displacements at various levels, in order to have more confidence in the readings, laser based displacement measuring devices were used in parallel.

4 Testing

The load on the structure was applied by means of pulling the structure using cables with a constant ratio of 1:2:3:4 always maintained between the loads at 1st floor: 2nd floor: 3rd floor: 4th floor. However, one major limitation of the test facility was that the test needed to be performed under load-control mode. The load was applied remotely by means of high strength cables passing through pulleys using electro mechanical winches. The loads transferred through each cable was monitored using tension type load cells. The load on the structure was gradually increased in the steps

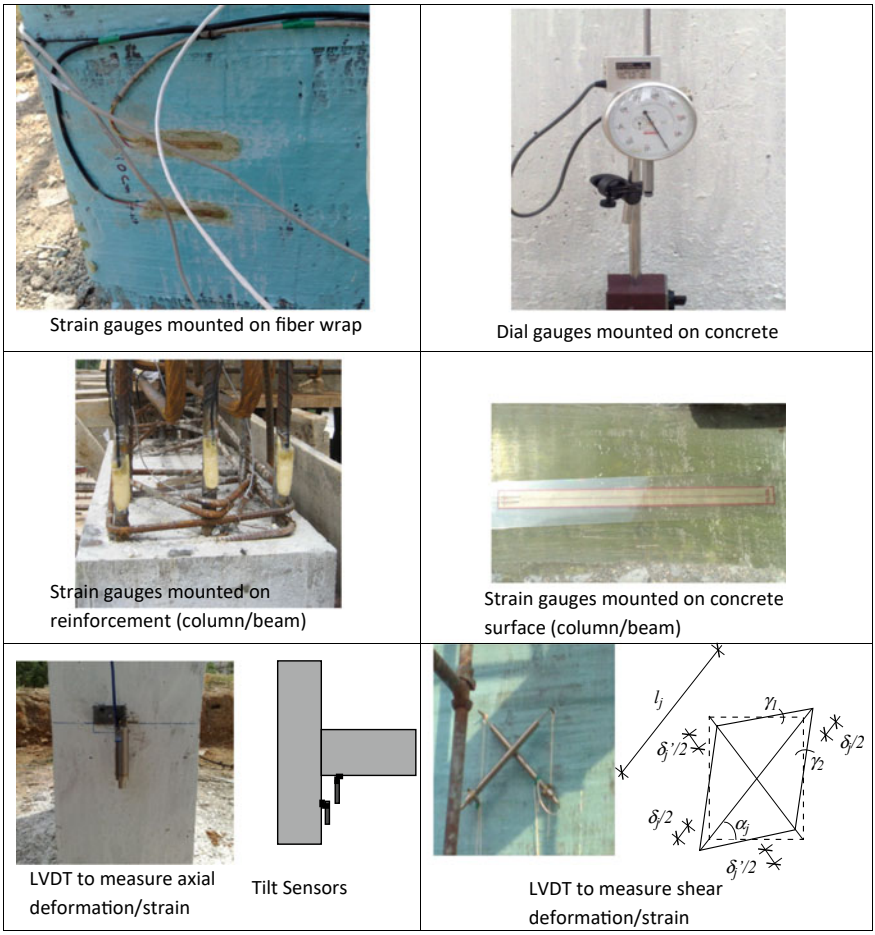

Fig. 4 Various instruments used to measure strains

of one ton at 1st floor, which resulted in a corresponding load step of 2ton at 2nd floor, 3ton at 3rd floor and 4ton at 4th floor resulting in a load step of 10t in Base shear. The base shear in the first step was 10t, in the second step 20t and so on till failure.

5 Test Results

The structure behaved linearly till a base shear value of around 300 kN. At this point the flexural tension cracks at the base of the columns started to get generated and the structure displayed a reduced stiffness. After reaching a base shear value of approx

500 kN, the cracks at the base of the columns opened wider and failures at other locations namely beams and beam-column joints started to show up. As a result the stiffness of the structure further went down, as can be seen from the pushover curves shown in Fig. 5. After reaching the base shear values of 700 kN, the joints of the structure displayed rapid degradation and the inter-storey drift increased rapidly. On further increase in the lateral load, the structure displayed a very soft behavior with large displacement increase for the small increase in the base shear. On reaching a base shear of 90t (882.90 kN), i.e. 9t load at first floor, 18t at second floor, 27t at third floor and 36t at fourth floor, the structure started undergoing increasing displacement at constant load. It was observed that as the displacement increases, the contribution of relative displacement between third and fourth floor reduces, which is attributed to the joint failure at the third floor level.

The dial gauges read the total extension over a gauge length, which was then converted to average surface strains at the base of the columns and plotted as shown in Fig. 6. Again, it can be seen that the average strains rise linearly with base shear till a base shear of approximately 400–500 kN thereafter rising at a higher rate. The rate of increase of strain becomes very high after a base shear of 700 kN. As expected and seen from failure modes, the column CL 19 displays minimum values of strains.

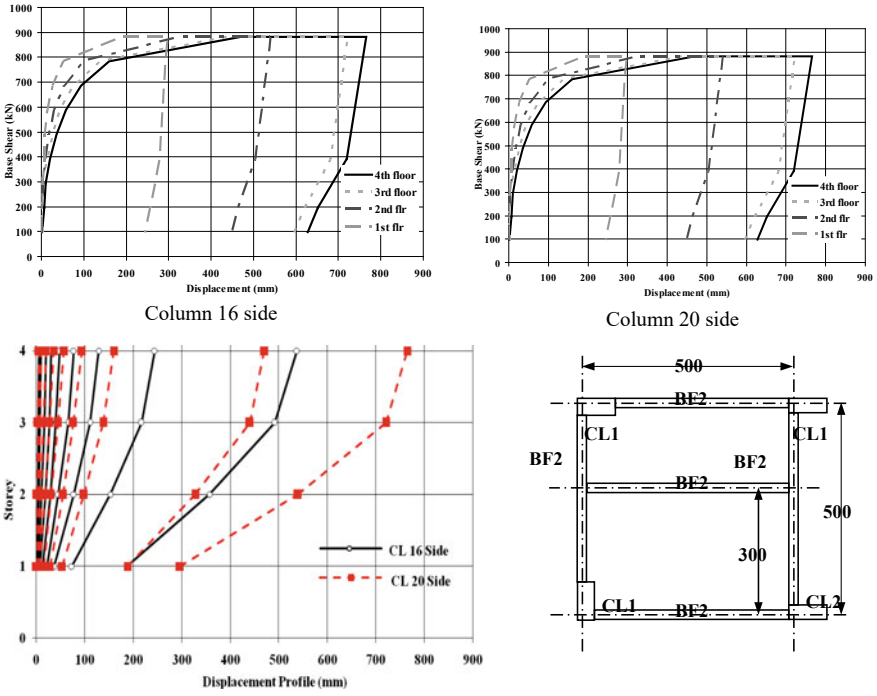

Fig. 5 Displacement profiles at column 16 and 20 locations

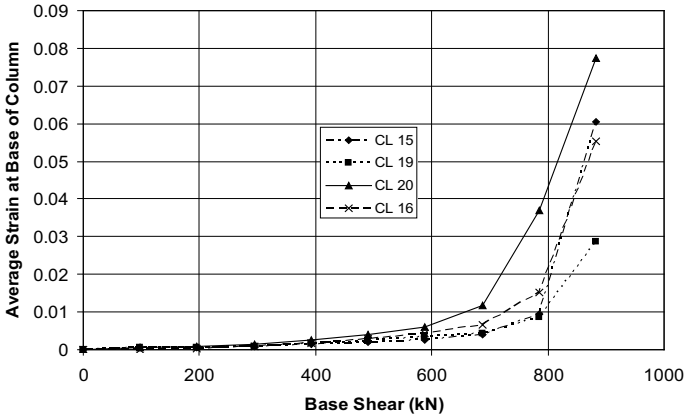

Fig. 6 Average surface strains at the base of the columns

The average beam bar strain of beams BF 205 are plotted in Fig. 7 for 1st, 2nd, 3rd and 4th floor levels of the structure. The plot clearly shows that as the base shear increased, the average beam bar strain increased almost linearly up to a base shear value of 50 t and thereafter going in the non-linear range. The maximum strains were obtained for 1st floor levels as expected and the strain gauges at that level broke after the yielding of the reinforcement bars. These strain gauges could read only up to a base shear of 70t.

Figure 8 show various failure modes and patterns observed during the experiment. Figures 8a, b show the failure of bottom storey columns on compression side, namely columns CL16 and CL20 respectively. As the lateral load was increased on the structure, columns CL 16 and CL20 underwent increasing compressive forces

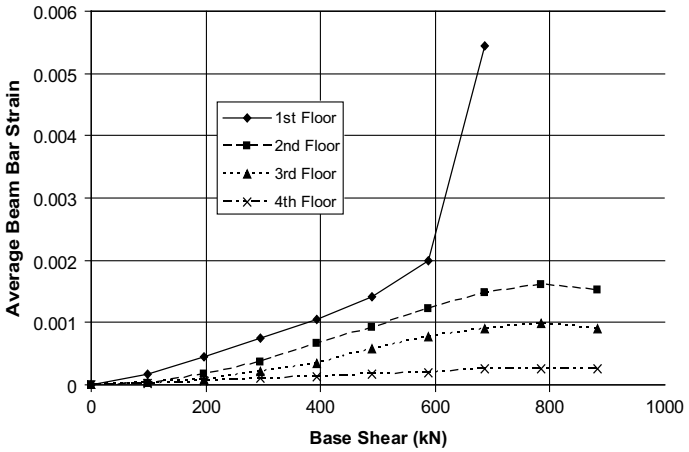

Fig. 7 Average beam bar strains

combined with bending moment. Thus, due to this combined axial compression and bending, the column section started to show tension cracks on the rear face. On further increase in the loads, which resulted in increase in both bending moment as well as axial forces on the column, these tension cracks grew further along the depth of the section demonstrating the shifting of neutral axis towards the front face of the columns. Due to the shift of neutral axis, less area was available to resist higher compressive forces. Consequently, crushing of concrete on front face of the column commenced and the state of the columns at the failure is depicted in Fig. 8a, b.

Figure 8c, d shows the failure modes of the beam in flexural and flexure-shear mode while testing and after the test with the loose concrete removed. These figs show the end of the beam BF 205 connected to CL 15 at 1st floor. Figure 8d shows the status of the beam after all the loose concrete was removed and the clear beam hinging could be well appreciated with lot of spalling on compression and tension faces of the beams. Figure 8e show the torsional failure of beam transverse to the direction of loading during the test. Figure 8f shows the failure of joint of CL 19 at first floor while testing. In this case, the column depth (400 mm) was much smaller than beam depth (1000 mm) and also the beam eccentricity was high since the beam of width 230 mm was flushed with the face of the column with the width of 900 mm. Figure 8g show diagonal shear crack in the joint of CL20, 2nd floor during the test with flexural and flexure-shear cracks in the beam and bond failure of the tension reinforcement. Figure 8h shows the failure of joint of CL 19 at 2nd floor level, which shows the beam bar bursting out of the joint. Such a failure can, in general, be prevented if proper confining reinforcement is provided in the joint core.

6 Experiments on Retrofitted Structure

Once the structure was tested till failure, the loads were removed. The unloaded structure had certain permanent deformations. The structure was pulled back to its original position and the sections were built up with micro-concrete to make up for the spalled concrete. The thin cracks were grouted with epoxy based grout system. The repair work was performed by M/s Binyas Contech Pvt. Ltd. Bangalore.

The contribution of original reinforcement inside the sections was assumed as 50% of original and no slip criterion was considered because of assumption of anchorage due to insertion of laminates in columns/beams and due to wrapping.

The carbon laminates were used to make up for the loss of reinforcement in the section and carbon and glass fiber sheets were used for confinement and shear strengthening. In general, international codes such as ACI440.R, Eurocode 8, Fib Bulletin 14 were followed for design of retrofitting with certain modifications such as no-slip assumption. The experience of the earlier tests conducted on repaired and retrofitted beam-column joints at IIT Bombay was utilized to recommend the retrofitting. Columns were retrofitted with two layers of 400 gsm C-sheet up to 1.2 m from the face of the raft.

Fig. 8 Various failure modes and patterns observed during the experiment

Step 1: **Beam lamination**: Application of laminates on top and bottom faces of beams BF 205 by inserting into columns up to a length of 1 m from the face of the column (Fig. 9a).

Step 2: **Column lamination**: Application of laminates only on inner face of the columns up to a length of 750 mm from the face of the beam/slab (Fig. 9b).

Step 3: **Column Longitudinal sheeting**: Application of C-sheets on outer face of the column with fibers along the longitudinal axis of the column up to a distance of 1 m from the face of the beam/slab (Fig. 9c).

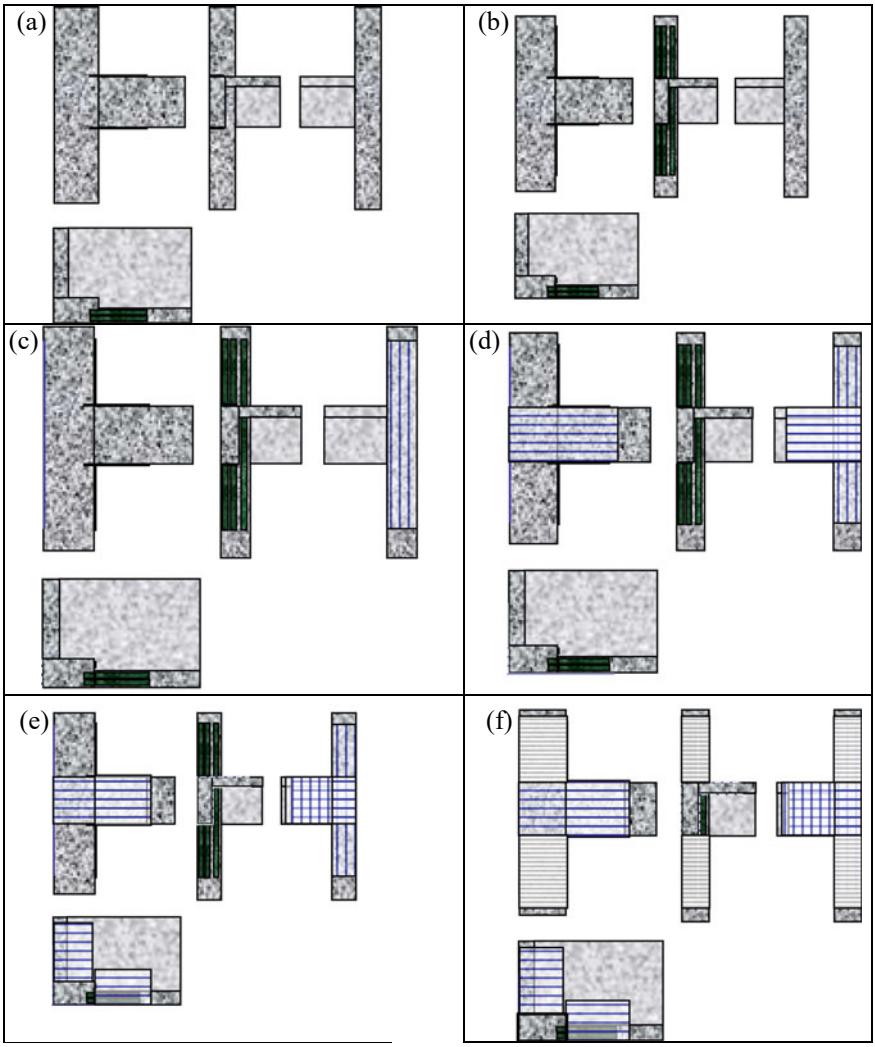

Fig. 9 Details of FRP retrofitting of various elements of RCC structure

Step 4: **Joint Sheeting**: Application of C-sheet on joint face with horizontal fibers up to a distance of 1 m from the face of the column (Fig. 9d).

Step 5: **Slab sheeting**: Application of C-sheets on beams with fibers along longitudinal axis for beams BF 205 and fibers transverse to longitudinal direction for beams BF 223 and 225 coming up to the slab (Fig. 9e).

Step 6: **Column wrapping**: Application of G-sheets on columns with fibers oriented transverse to the longitudinal axis of the columns (Fig. 9f).

Table 3 provides the quantitative details FRP retrofitting of the structure.

7 Application of Retrofitting

The repair of the structure tested earlier, by micro-concreting and epoxy grouting was performed by M/s Binyas Contech Pvt Ltd. The application of fiber sheets was performed by M/s R&M international Pvt Ltd. Figure 9 shows the application of Fiber Reinforced Composites on different parts of the structure and Fig. 10 shows the overall view of the repaired and retrofitted structure.

8 Experimental Results

As mentioned earlier, the test facility allowed the experiment to be conducted essentially under load-control mode. As a result, in the first phase experiment on the as-built structure, the pushover curve did not yield any post-peak softening. In order to obtain the post-peak degradation in the pushover curve for the retrofitted structure, once the load reached the peak load, the load was released after some time and then again increased. Thus, essentially, small cycles around the peak were given. In this way, the gradual degradation of the structure in the post peak region could be obtained experimentally. The Pushover curve obtained from the experiment is shown in Fig. 11.

9 Failure Patterns

Photograph in Fig. 11 shows the overall failure mode of retrofitted structure. The different failure modes observed for the retrofitted structural components and elements are given in Fig. 12. In can be seen that the failures are mainly due to poor performance of repair method adopted for strengthening. It may be due to insufficient time given for curing. It also may be residual local strain or deformations. The failure modes of the RCC portion of elements and components are same as shown in Fig. 8 of the original structure. It shows, that repair did not regain original concrete characteristics. Also the wrapping could not confine the concrete to original level.

Table 3 Quantitative retrofitting details of FRP

Column 16 and 20 1st floor: Beam lamination: 2 – 100 × 1.4 Column lamination: 2 – 100 × 1.4 + 1 – 50 × 1.4 Column longitudinal sheeting: 2 layer 400 gsm C-sheet Joint sheeting: 2 layer 400 gsm C-sheet Slab sheeting: 2 layer 400 gsm C-sheet Column wrapping: 1 layer 900 gsm Glass sheet	Column 16 and 20 2nd floor: Beam lamination: 3 – 50 × 1.4 Column lamination: 1 – 100 × 1.4 + 2 – 50 × 1.4 Column longitudinal sheeting: 2 layer 400 gsm C-sheet Joint sheeting: 2 layer 400 gsm C-sheet Slab sheeting: 2 layer 400 gsm C-sheet Column wrapping: 1 layer 900 gsm Glass sheet
Column 16 and 20 3rd floor: Beam lamination: 2 – 50 × 1.4 Column lamination: 3 – 50 × 1.4 Column longitudinal sheeting: 1 layer 400 gsm C-sheet Joint sheeting: 1 layer 400 gsm C-sheet Slab sheeting: 1 layer 400 gsm C-sheet Column wrapping: 1 layer 900 gsm Glass sheet	Column 15 1st floor: Beam lamination: 2 – 100 × 1.4 Column lamination: 2 – 100 × 1.4 + 1 – 50 × 1.4 Column longitudinal sheeting: 2 layer 400 gsm C-sheet Joint sheeting: 2 layer 400 gsm C-sheet Slab sheeting: 2 layer 400 gsm C-sheet Column wrapping: 1 layer 900 gsm Glass sheet
Column 15 2nd floor: Beam lamination: 3 – 50 × 1.4 Column lamination: 1 – 100 × 1.4 + 2 – 50 × 1.4 Column longitudinal sheeting: 2 layer 400 gsm C-sheet Joint sheeting: 2 layer 400 gsm C-sheet Slab sheeting: 2 layer 400 gsm C-sheet Column wrapping: 1 layer 900 gsm glass sheet	Column 15 2nd floor: Beam lamination: 3 – 50 × 1.4 Column lamination: 1 – 100 × 1.4 + 2 – 50 × 1.4 Column longitudinal sheeting: 2 layer 400 gsm C-sheet Joint sheeting: 2 layer 400 gsm C-sheet Slab sheeting: 2 layer 400 gsm C-sheet Column wrapping: 1 layer 900 gsm glass sheet

(continued)

Table 3 (continued)

Column19 1st floor: Beam lamination: 2 – 100 × 1.4 Column lamination: 2 – 100 × 1.4 + 1 – 50 × 1.4 Column longitudinal sheeting: 2 layer 400 gsm C-sheet Joint sheeting: 2 layer 400 gsm C-sheet Slab sheeting: 2 layer 400 gsm C-sheet Column wrapping: 1 layer 900 gsm Glass sheet	Column 19 2nd floor: Beam lamination: 3 – 50 × 1.4 Column lamination: 1 – 100 × 1.4 + 2 – 50 × 1.4 Column longitudinal sheeting: 2 layer 400 gsm C-sheet Joint sheeting: 2 layer 400 gsm C-sheet Slab sheeting: 2 layer 400 gsm C-sheet Column wrapping: 1 layer 900 gsm Glass sheet
Column 19 3rd floor: Beam lamination: 2 – 50 × 1.4 Column lamination: 3 – 50 × 1.4 Column longitudinal sheeting: 1 layer 400 gsm C-sheet Joint sheeting: 1layer 400 gsm C-sheet Slab sheeting: 1layer 400 gsm C-sheet Column wrapping: 1 layer 900 gsm glass sheet	No retrofitting was prescribed for fourth floor/roof

Fig. 10 Structural elements, components and system after retrofitting with FRP techniques and micro concreting

Figure 12a–c shows same failures of beam as shown in Fig. 8c, d due to the modes of the beam in flexural and flexure-shear. Figure 12d–f shows the join failures similar to that in Fig. 8f. Figure 12g, h shows the similar failure as shown in Fig. 8h due to the beam bar bursting out of the joint. Figure 12i shows the column failure at the foundation/raft level. Had the wrap is removed like other locations, similar failure as seen in Fig. 8a, b.

10 Practical Observations on Retrofitting

Repair and retrofitting of concrete structures with FRP is susceptible to workmanship and quality of application. The retrofitting of the structure was done professionally but due to some practical and technical reasons such as inaccessibility to certain areas, certain flaws remained. The following observations were made on the retrofitting:

i. At some places, where the concrete had spalled, proper micro-concreting and injection grouting could not be properly done due to practical difficulties

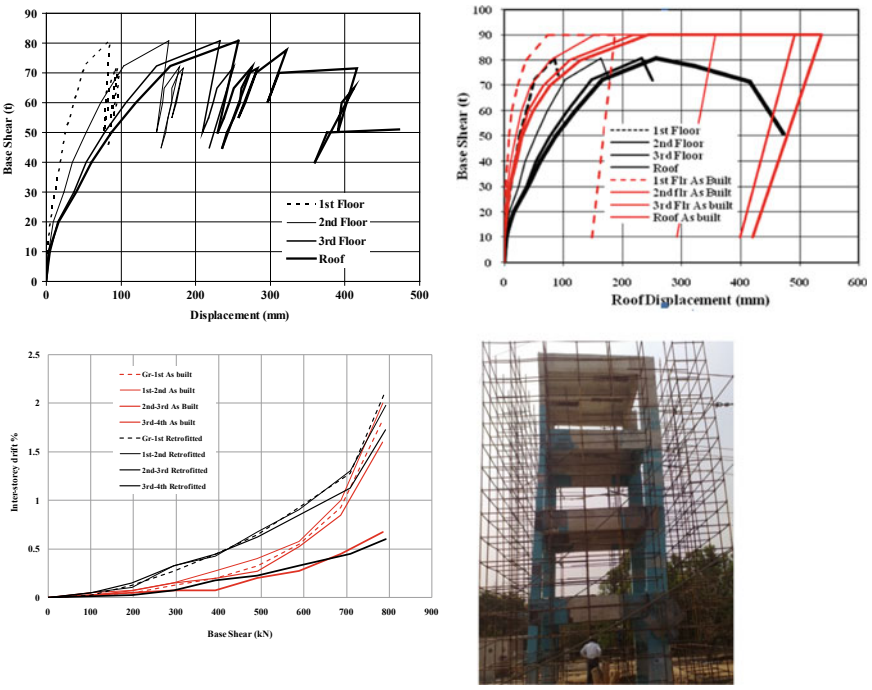

Fig. 11 Load deflection characteristics and drifts evaluated after retrofitting

ii. The laminates at the critical locations such as column ends and beam ends were not anchored
iii. Fine rounding of corners and removal of all undulations could not be 100% achieved due to practical problems.

11 Post Test Analysis Results

Various Assumptions made on different parameters are explained as follows.

Strength of the concrete

The extent of recovery of strength of concrete cannot be judged with certainty, here as an engineering judgment the strength of concrete in retrofitted specimen is considered as 0.8 times the strength of concrete in original structure.

Strength of reinforcing bars inside the concrete:

As seen in the test and observed from the strain data shown in Fig. 7 the rebars had yielded during the first test. At the plastic hinge length locations such as column base and beam ends, the strains in the rebars reached quite high values. Though, the structure was pulled back before retrofitting and re-testing, certain amount of plastic strain remained in the rebars. Furthermore, it was observed that at critical locations, bond cracks to the extent of lateral spalling had appeared, leading to bond slip. Based

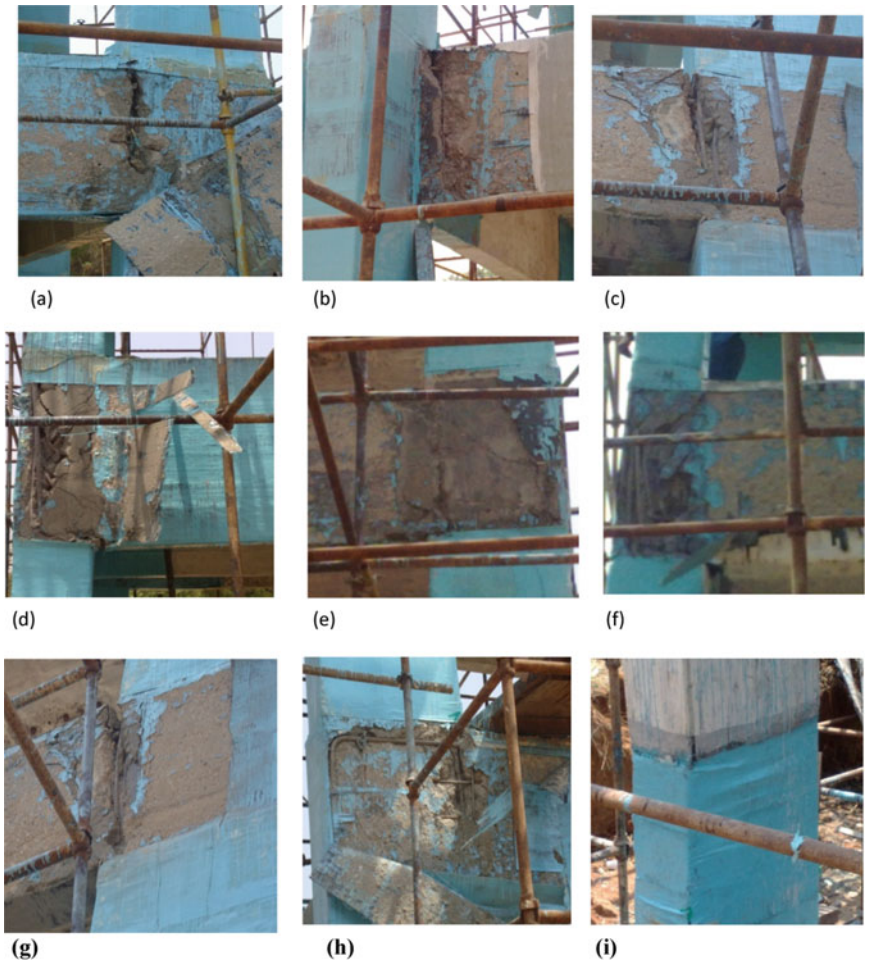

Fig. 12 Failure models of retrofitted structure components

on high rebar strains and bond slip behavior, the contribution of reinforcement was considered as 50% of the original for column base and 1st floor beams (that suffered very high damage), while the same was considered as 80% of the original for other locations.

Contribution of laminates:

The experiments at beam-column joint level performed under the BRNS project [5] on "Upgradation of Concrete Structures with Fiber Reinforced Composites" displayed that when the laminates are partially inserted in the ends, they are not able to develop their full strength. Based on the results of those tests, 80% of the full contribution of the laminates is considered.

Stiffness:

The experiments at beam-column joint level performed under the BRNS project [5] displayed that following the repair and retrofit philosophy as followed in this work, the stiffness of the retrofitted specimen is approximately 50% of the original stiffness. Similar phenomenon was also observed in the full scale test on retrofitted structure (Fig. 10). Therefore, 50% of the stiffness of original structure was assumed in this case.

12 Determination of Hinge Properties

The hinge properties were calculated by the procedures described in [2]. The material properties for the FRP used for retrofitting are given in Table 2. The stress-strain curve for all types of fiber composites is linear till failure. Kindly note that the properties provided in Table 4 are taken from material supplier and are differed from those given in Table 1.

The post test analysis for the structure was performed using commercial software SAP2000 by modelling the structure as described in annexure. The beams and columns of the structure were modeled as 3D beam (frame) elements, with six degrees of freedom at both nodes. Frame members are modeled as line elements connected at points (joints). The slabs were modeled using four-noded quadrilateral shell elements. To capture the inelastic behavior of members, flexural springs (moment-rotation), shear springs (shear force–deformation) and torsional springs (torsional moment-rotation) were modelled. The joint deformation characteristics were modeled using the joint model explained in [2]. The hinge characteristics, once obtained, were assigned to the frame members. The hinges assigned on a typical joint of the structure in the program and their physical significance is displayed in Fig. 12. Since the loading was uni-directional, no joint hinges were provided for the transverse beams of the joints. Three cases were analyzed, with different types of nonlinear hinges modelled (Fig. 14).

1. Model with moment and shear hinges only (Model 1)
2. Model with torsional hinges along with moment and shear hinges (Model)

Table 4 Properties of fiber composites

Material	Effective thickness (mm)	Tensile strength (MPa)	Tensile modulus (GPa)	Ultimate strain
Carbon fiber wrap	0.23	3790	230.0	0.017
Carbon plate Composite	1.40	2790	155.1	0.018
Glass fiber wrap	0.34	1960	70.0	0.028

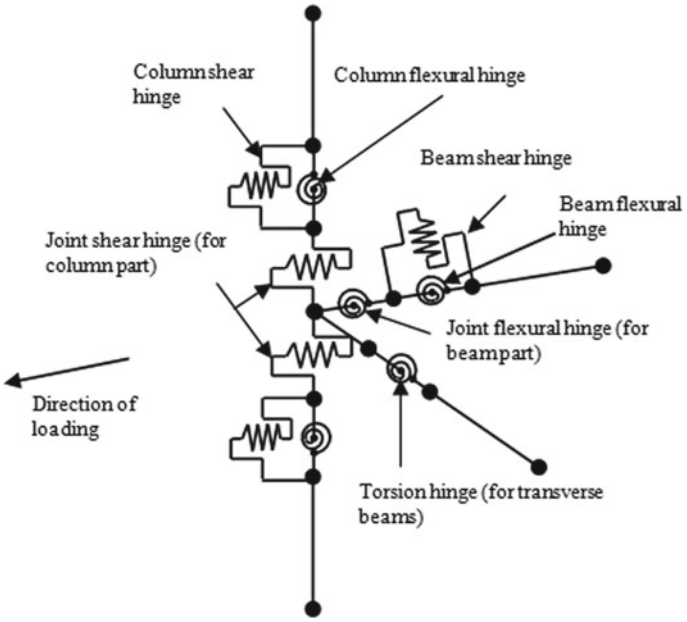

Fig. 13 Hinge model of typical beam column joint of the structure

3. Model with joint characteristics along with torsional, moment and shear hinges (Model 3).

Load deflection characteristics of retrofitted structure is shown in Fig. 13. It can be seen that the numerically obtained displacement shape for Models 1 and 2 display a parabolic shape for the structure and do not match the experimentally observed profile. This discrepancy is attributed to the rigid behavior of the joints. However, in the experiment, due to the failure at joint levels, the displacement of the roof level was much less than would be expected in the case of shear building behavior. In order to simulate this phenomenon, modeling of joint nonlinearities becomes extremely important and therefore explains why the deflected shape obtained from Model 3 matches closely the experimentally observed one. Thus, it can be concluded that the third model could simulate almost all types of failure modes that were observed in the experiment, since not only the base shear, but also the deflected shape of the structure could be successfully captured.

13 Conclusions and Discussions

Experiment was conducted on a full-scale RC framed structure which was a replica of a substructure of an existing office building. The structure was constructed with non-seismic detailing.

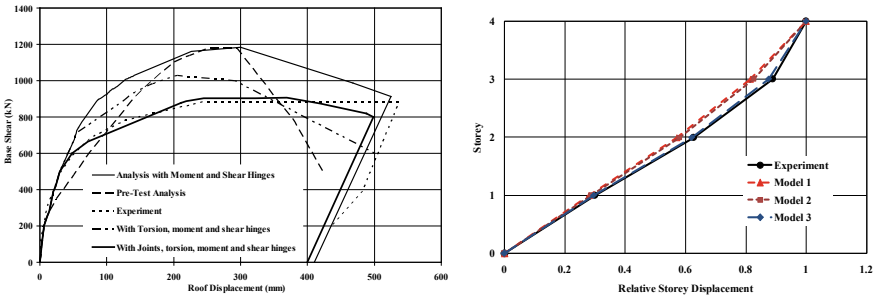

Fig. 14 Load deflection characteristics of retrofitted structure

The failure patterns clearly displayed the vulnerability of RC buildings with non-conforming detailing to fail in undesirable failure mechanisms such as joint shear failures, bond failures etc. Although the structure displayed large variety of failure mechanisms, the damage mostly was concentrated in the joint region or at the beam/column interfaces with wide flexural cracks along with bond failures.

Retrofitting of the damaged structure was carried out using FRP composites. Failure modes and test results of retrofitted structure revealed that while performing retrofitting design, one needs to understand the state of the structure by detailed NDT and evaluate element and joint characteristics in both linear as well as nonlinear range by analysis.

Another very important aspect of repair and retrofitting is the workmanship. Surface preparation by removal of old loose concrete, pouring of new concrete and its bonding with old concrete, rounding off sharp corners etc. are few important aspects. Also, proper care should be taken to bond the FRP sheets and laminates to the original structure.

It has been shown that in order to capture the overall behaviour of RC structures, neglecting the inelasticity in the joints can lead to inaccurate results.

The analysis of the retrofitted structure was based on several assumptions considering the residual material properties in the retrofitted structure and significant engineering judgement based on test results of beam-column joints tested under BRNS projects were used to reach the conclusion. However, based on the assumptions and following the procedure detailed in this paper, a good agreement between experimental and numerical results was found for retrofitted structure as well.

14 Annexure

Step by step procedure to evaluate capacity of the structure is explained considering two storey plane frame structure as shown in Fig. 15.

The element stiffness matrices of frame structural elements such as column and beam considering bending deformations are given as follows.

Fig. 15 Idealised 2D frame

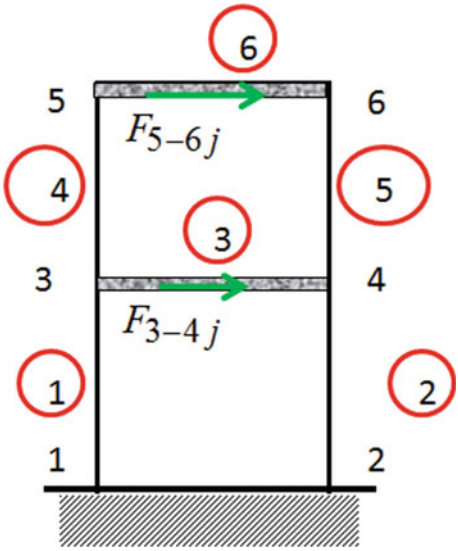

i. Euler theory

$$\begin{bmatrix} 12\,C_i & 6L_1C_i & -12\,C_i & 6L_1C_i \\ & 4L_i^2C_i & -6L_1C_i & 2L_i^2C_i \\ & & 12\,C_i & -6\,L_1C_i \\ \text{Symmetric} & & & 4\,L_i^2C_i \end{bmatrix}$$

where $C_i = \frac{EI_{yi}}{L_i^3}$

ii. Timoshenko theory

$$\begin{bmatrix} 12\,C_1 & 6L_1C_1 & -12\,C_1 & 6L_1C_1 \\ & (4+\varphi_{y1})L_1^2C_1 & -6L_1C_1 & (2-\varphi_{y1})\,L_1^2C_1 \\ & & 12\,C_1 & -6\,L_1C_1 \\ \text{Symmetric} & & & (4+\varphi_{y1})\,L_1^2C_1 \end{bmatrix}$$

$$\text{where} \quad \varphi_{yi} = \frac{12EI_{yi}}{GA_{syi}L_i^2} \quad C_i = \frac{EI_{yi}}{L_i^3(1+\varphi_{yi})}$$

where

L_i	Length of the i-th beam element
Iyi	Moment of inertia of i-th beam element about z-axis
Asyi	Shear area of the i-th beam element along y-axis
E	Modulus of elasticity
G	Modulus of rigidity

In the case to consider axial and torsional deformations in beam or column the following stiffness matrices can be added suitably.

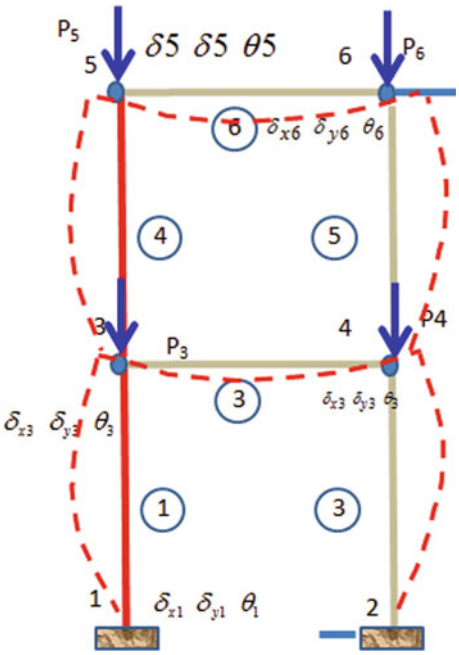

Fig. 16 Deformations under normal loads

$$\begin{bmatrix} \frac{AE}{L_i} & -\frac{AE}{L_i} \\ -\frac{AE}{L_i} & \frac{AE}{L_i} \end{bmatrix} \text{ and } \begin{bmatrix} \frac{GJ}{L_i} & -\frac{GJ}{L_i} \\ -\frac{GJ}{L_i} & \frac{GJ}{L_i} \end{bmatrix}$$

1. Assemble element stiffness matrix.
2. Solve for deflections as shown in Fig. 16, forces and moments for normal loads $[K]\{x\} = \{p\}$.
3. Store the forces and moments.
4. Solve for displacements (Fig. 17) considering 10 kN lateral force at top and middle level.
5. Evaluate forces and moments. Add forces and moments of normal loads.
6. Check state of stress in concrete and steel. If concrete cracks, modify the moment of Inertia of section neglecting the area of tensile stress exceeding yield stress,
7. Go to step 4 and solve for the load increment with say 10 kN.
8. Repeat step 4–7 till steel yield.
9. Then release the degree of freedom at node 1 if yields and assemble stiffness matrix with rotational stiffness, shear stiffness and torsional stiffness at hinge locations as shown in Fig. 18 which is obtained from element non-linear characteristics as shown below. In the case of RC elements while evaluating non linear stiffness bond slip and buckling of bars need to be considered. Note that same treatment should be given for all the hinges formed.
10. Solve for deflections, forces and moments. Newton–Raphson technique may be adopted to ensure the equilibrium an few iterations need to be performed.

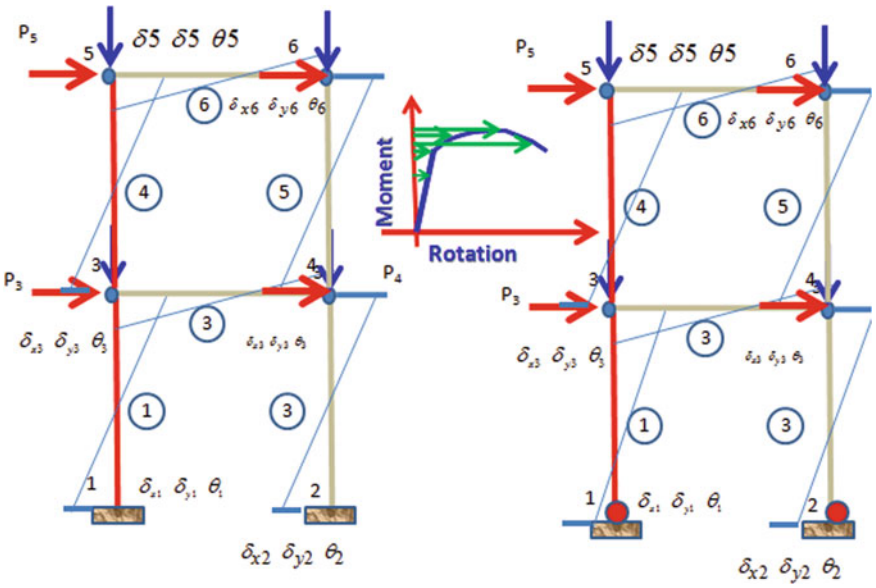

Fig. 17 Deformations and hinge formations due to lateral loads

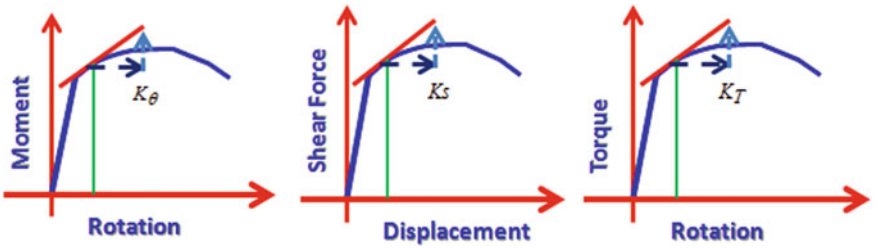

Fig. 18 Hinge characteristics of structural elements and joints

Check the values are with in element performance limits by adding normal load values.

11. Check the stresses and strains in the concrete and steel.
12. Check the rotations are drifts are within limits (performance limits targeted. If not repeat step 4–10.

Acknowledgements The work presented in this paper is out of contributions of persons from various organisations such as Bhabha Atomic Research Centre, Mumbai, Central Power Research Institute, Bangalore, R&M International and M/s Binyas Contech Pvt. Ltd. Bangalore. Their efforts and contributions are acknowledged and without them this work would have not performed. Also the moral support and Participation form Indian Institute of Technologies, National Institute of

Technologies, Indian Institute of Science, Thapar Institute of Technology, Atomic Energy Regulatory Board, Nuclear Power Corporation of India Limited, Structural Engineering Research Centre and other institutes is highly appreciated.

References

1. Reddy GR, Hari Prasd M, Varma AK (2019) A text book of seismic design, structures, piping systems and components. Springer, New York
2. Sharma A, Reddy GR, Vaze KK (2013) Pushover experiment and analysis of four storey full scale reinforced concrete structure before and after retrofitting. Bhabha Atomic Research Centre
3. Kessler E, Gadow R, Straub J (2016) Basalt, glass and carbon fibers and their fiber reinforced polymer composites under thermal and mechanical load. AIMS Mater Sci 3(4):1561–1576
4. Balaguru PN (2005) Construction of fiber reinforced polymer (FRP) jackets for the protection of pier caps. Construction report, RI-RU6862
5. Board research in nuclear sciences project on "upgradation of concrete structures with fiber reinforced composites" project No. 05. Submitted by IIT Bombay (2006)
6. ACI 440.R (2008) Guide for the design and construction of externally bonded FRP systems for strengthening concrete structures. American Concrete Institute
7. Eurocode 8 Earthquake resistant design of structures—part 1: general rules and rules for buildings (ENV 1998-1-1/2/3). CEN Technical Committee 250/SC8, Berlin, Germany

Construction Technology for Integral Bridges with Basalt Fiber-Reinforced Polymer Prestressing Tendons

Vasant A. Matsagar

Abstract Conventional structural materials are being replaced by advanced composite materials owing to their superior mechanical properties. Basalt fiber-reinforced polymer (BFRP) is the latest fiber-reinforced polymer (FRP) composite material introduced as reinforcement and pre-stressing tendons for reinforced concrete (RC) and pre-stressed concrete (PSC) structures. On the other hand, with the increasing demand on flyovers and bridges in city spaces, planning and design must address faster constructions of aesthetically appealing slender bridges, which are making joint-less, i.e., integral bridges popular. Therefore, beginning from designing the components required for the use of the BFRP in pre-stressing operations to establishing design procedure of the BFRP-PSC members of integral bridges are required. Evaluating mechanical properties of the BFRP rods/ tendons is challenging using the existing mechanical testing methods due to their relatively lower transverse direction strength. This creates issues not only in characterization of the BFRP in laboratory conditions but also on-field pre-stressing application in integral bridges. Hence, development of a proper anchor with optimum size for the BFRP rods is crucial. Hence, expansive cement grout-based anchor is developed, tested, and assessed, by studying the parameters affecting the gripping behavior and optimizing the anchor design based on the finite element (FE) analysis. Then again, understanding of the thermo-mechanical behavior of the BFRP composites is needed for practical and cost-effective applications in integral bridges, experiencing thermal stresses throughout their service-life. Characterization and assessment of performance of the BFRP rods at elevated temperatures is investigated through extensive experimental and analytical studies. Consequently, a semi-empirical constitutive law for predicting the thermo-mechanical behavior of FRP composites is proposed and validated with experimental results. The proposed model is original, generic, and flexible, and is based on typical characteristics of the composite, eliminating the requirement for conducting the tension test at elevated temperatures. Experimental investigations are carried out to assess the flexural performance of the BFRP-pre-stressed concrete (PSC) beams designed as over-reinforced, under-reinforced, and significantly under-reinforced, as

V. A. Matsagar (✉)
Department of Civil Engineering, Indian Institute of Technology (IIT) Delhi, Hauz Khas, New Delhi 110 016, India
e-mail: matsagar@civil.iitd.ac.in

S. B. Singh et al. (eds.), *Fiber Reinforced Polymeric Materials and Sustainable Structures*, Composites Science and Technology, https://doi.org/10.1007/978-981-19-8979-7_28

well as the non-pre-stressed concrete beams, for developing design philosophy for the BFRP-reinforced/ pre-stressed concrete members. The assessment is made based on the flexural strength, serviceability satisfaction, safety factor against failure, and deformability/ ductility. The efficacy of the partial pre-stressing of the beams in a multi-layered system of tendons is investigated, and an alternative source of ductility is introduced by allowing the tendons to rupture sequentially in a progressive manner. Furthermore, the flexural analysis of the tested beams is carried out based on the available code provisions for complimenting the experimental findings. Ductility evaluation of concrete beams pre-stressed with the FRP tendons is conducted, wherein the effect of the partial pre-stressing, layering of the tendons, addition of sacrificial rebars, and functionally-graded concrete (FGC) is elaborated. The finite element analysis (FEA) testified the efficacy of the introduced techniques in improving the ductility of the FRP-pre-stressed members. To investigate on the efficacy of using the BFRP pre-stressing tendons in integral bridges, the BFRP tendons are used for the design of conventional and integral bridges, and a comparative assessment is carried out with steel-pre-stressed conventional bridges. It is concluded that employing both the techniques of using the non-corroding BFRP tendons and the proposed integral form of bridges is a promising technology in bridge construction. Apart from that, the natural fiber composites, being cost effective and environment-friendly, are investigated for possible use in post-tensioning of RC beams. The successful utilization of such natural fibers in structural applications may result in more sustainability in construction industry.

1 Introduction

1.1 General

There has been a growing need to construct slender and aesthetically appealing flyovers and bridges in shorter duration due to space constraints and increasing road traffic in cities all over the world. This, coupled with the recent advancements in science and technology has led to a shift in attention towards composite structural materials due to its enhanced mechanical properties, relatively greater durability, and sustainability standards as compared to the conventional constructional materials. One such material that has been in the limelight is the Basalt Fiber-Reinforced Polymer (BFRP) which has been proposed to replace reinforcing steel and pre-stressing cables/ tendons in the reinforced concrete (RC) and pre-stressed concrete (PSC) structures, respectively.

1.2 Integral Bridges

The bridges in which the superstructure and its pier/abutment are built monolithically are known as integral bridges, i.e., without bearings. These bridges eliminate the problems arising out of installation and maintenance requirements when expansions joints are present, and also result in increased structural efficiency and better ride quality. They are also aesthetically appealing due to slender sections and accommodate greater clearance underneath the bridge for traffic flow due to reduced depth of girder. The following are some of the advantages of integral bridges:

i. Reduced initial construction cost due to absence of expansion joints and bearings which are typically associated with high prices;
ii. Reduced construction time required as installation of bearings is rather a tedious task;
iii. Prevention of ingress of salts from deicing on the deck when minimal of them exist; and
iv. Unsusceptible to differential settlement and pier buckling due to the integrity of members.

A major disadvantage of integral bridges is the accumulation of stresses due to lack of stress release points. Therefore, it is especially important that the stresses generated by eliminating release points are adequately addressed so that cracks do not develop on the structure due to thermal expansion and contraction as well as thermal deformations do not occur. Although there are a few countries that have developed some guidelines and recommendation on the usage of the FRP composites in bridge design and construction, there are no fully developed codes that can be directly adopted for the design of FRP-reinforced/pre-stressed bridges due to inadequate data and field experience.

1.3 Basalt-Fiber Reinforced Polymer (BFRP)

The BFRP is an inorganic material which is manufactured by melting natural volcanic basalt rocks at elevated temperature. The quarried basalt rocks are crushed and washed before melting it at 1400 °C. Then it is ejected through nozzles of diameter 9 to 13 μm to form basalt fibers. Basalt fibers are used along with resin (30 to 40% of FRP composite) to manufacture lightweight and state-of-the-art composite materials that are cost-effective as compared to the carbon fiber-reinforced polymer (CFRP) and offering superior performance as compared to the glass fiber-reinforced polymer (GFRP).

Figure 1 shows in generic sense the stress–strain curve of the BFRP in comparison to the conventional steel and other FRP composites. From Fig. 1, the following important conclusions can be drawn:

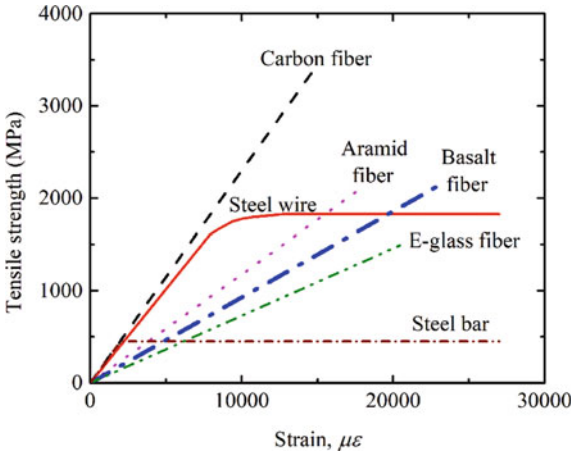

Fig. 1 Stress–strain curves of steel and fiber-reinforced polymer composites

i. The BFRP has higher tensile strength and higher modulus of elasticity when compared to electrical glass (E-glass FRP).
ii. With significant enhancement in production technology over time, the BFRP has achieved ultimate tensile strength of about 2100 MPa and modulus of elasticity of 90 MPa.
iii. The BFRP possesses higher strength by over 500% while having only 33% its density, when compared to the commonly used low carbon steel reinforcement.

1.4 Applications of FRP Composites

The FRP composites have varying applications in civil engineering structures. It is most commonly used as an internal reinforcement in rigid pavements, buildings, bridges, etc. It is also used to strengthen an existing structure in flexure by bonding the FRP sheets/plates with epoxy resin on the tension face and in shear by bonding it to the exterior of beams in the shear zone. The use of the GFRP in construction of bridges for the first time goes back to 1971 in the USA. It was later used as an internal reinforcement along with steel cables for the pre-stressing of Ulenbergstrasse Bridge in Germany in 1986 [2]. It is expected that various components of the FRP bridges will remain in service for a longer period since the FRP bars are resistant to corrosion. The comparison of life-cycle costs of reinforced concrete and fiber-reinforced concrete bridges has shown that the total costs including the initial capital, maintenance cost, disposal, and replacement costs of the FRP bridges are less than half the total costs per square meter of the RC bridges [2].

1.5 Anchoring System for FRP Tendons

Although the FRP materials have superior tensile strength in the longitudinal direction, they are weak in transverse direction and hence require a different pre-stressing set up from that of conventional steel cables. The allowable pre-stress for FRP tendons as per the American Concrete Institute is 65% of its ultimate tensile strength while it is 75% for conventional steel. Further, the losses in pre-stress resulting from creep and relaxation are different for FRP tendons. Therefore, in order to conduct laboratory experiments and utilize the FRP tendons in pre-stressing, the proper design of its anchoring system is extremely important. It has been experimentally proven that the behavior of cement grouted FRP anchors in pull-out are affected by factors such as the surface conditions of the tendons, properties of the cement grout used, and the stiffness of the steel sleeves. The friction coefficient between the surface of the FRP tendon and the cement grout controls the bond strength, and the distribution of bond stress is determined by the length of anchor provided.

1.6 Structural Members Reinforced/Pre-Stressed with FRP Materials

The vulnerability of conventional steel to corrosion that gives rise to durability issues, and its considerably high density led to the search for a substitute material in the form of fiber-reinforced polymer composites. Although the FRP composites have successfully overcome the limitations of conventional steel, they do come with their own shortcomings. The FRP composites are non-ductile in nature, and therefore, it is not desirable to have under-reinforced design as recommended for the common reinforced concrete structures, while at the same time, over-reinforced design also does not necessarily ensure that the structural member will have adequate ductility to avoid sudden collapse. Experimental investigations have shown that the solution to the ductility problem is to provide FRP bars and tendons in layers and allow the structure to fail by rupture of the tendons in progressive manner. Further, to effectively utilize the high tensile strength of this material, it is recommended that the BFRP tendons be pre-stressed which will ensure that the high deflection and increased crack width, the result of high elastic lengthening caused by low elastic modulus of BFRP, is avoided.

2 Anchor Design for Basalt Fiber-Reinforced Polymer Tendons

2.1 General

The optimization of design of anchor for basalt fiber reinforced polymer is critical due to its low strength in transverse direction. The anchor system designed for the BFRP tendons should be able to impart adequate clamping force to prevent slippage while at the same time not to cause premature failure of the grips due to the relatively low transverse strength of the BFRP composite. In absence of guidelines, little to no research has been carried out to optimize the anchor design. Therefore, this section is devoted to development of the most economical and optimal size of anchor through experiments using expansive cement grout. Finite element simulations are carried out for the proposed anchor to validate the experimental results and the anchors are tested for efficiency in the laboratory.

2.2 Analytical Study

It is necessary that the anchor developed using expansive cement grout is able to produce expansive pressure and transfer it to the tendons in an analogous way as hydrostatic pressure. The bond stress and frictional coefficient between the grout material and the tendon can be determined with the help of pull-out tests. The pull-out load is a function of the sum of resistance offered by bond stress and friction, and it is given by Eq. (1) [6].

$$T = UL(\tau_0 + \mu P) \tag{1}$$

where, T is pull-out load in Newton; U is circumference of the tendon in millimeters; L is length of the anchor in millimeters; τ_0 is bond stress in MPa; μ is coefficient of friction; and P is gripping pressure.

The property of expansive cement is modeled using a combination of analytical and experimental methods. The analytical method considers the anchor as a cylinder with a thick wall which is experiencing internal pressure caused by the expansion of cement. The governing differential equation for plane strain condition is given [7] in Eq. (2).

$$r\left(\frac{d^2\sigma_r}{dr^2}\right) + 3\left(\frac{d\sigma_r}{dr}\right) = 0 \tag{2}$$

The general solution of Eq. (2) gives,

$$\text{Radial stress, } \sigma_r(r) = \frac{P_i r_i^2 - P_o r_o^2 + \left(\frac{r_i r_o}{r}\right)^2 (P_o - P_i)}{r_o^2 - r_i^2} \tag{3}$$

$$\text{Hoop stress, } \sigma_\theta(r) = \frac{P_i r_i^2 - P_o r_o^2 + \left(\frac{r_i r_o}{r}\right)^2 (P_o - P_i)}{r_0^2 - r_i^2} \tag{4}$$

$$\text{Longitudinal axial stress, } \sigma_z = -2v \frac{P_i r_i^2 - P_o r_o^2}{r_o^2 - r_i^2} \tag{5}$$

where, P_i is the internal pressure; P_o is the external pressure; r_i is the inner radius; r_o is the outer radius; r is the radius where stresses are obtained.

2.3 Experimental Study

Pull-out tests were performed on several specimens of the BFRP rods of 8 mm diameter to study the gripping behavior. The anchor system consisted of a BFRP rod enclosed in a mild steel sleeve with expansive cement grout in between. The key properties of the BFRP rod and the expansive cement grout were provided by the manufacturers. When the expansive cement grout, poured inside the anchor, hardens, it generates internal pressure on the inner surface on the steel sleeve and an external pressure on the outer surface of the BFRP rod. The anchors were instrumented with strain gauges to measure the hoop strain generated by the internal pressure on the steel sleeves with the help of DT85 Series 3 data acquisition device.

The flowchart in Fig. 2 shows the important steps that were followed to develop an optimal anchor system for the BFRP. For more accurate results, four different sets of anchors were made, each set consisting of two anchors of 60 and 150 mm lengths, and they were used to test four samples of the BFRP rods. Figure 3 is a diagrammatic representation of the new anchor developed.

In this anchor, the hoop strain measured at mid-length on the outer surface of steel sleeves are found to vary with respect to time, increasing from zero during casting to maximum at 90 h. Similarly, the hoop strain values show an increasing trend with increase in size of the samples. The pull-out tests revealed that the specimen failed by slippage of the BFRP rods in the shorter of the two anchors. Since the anchor was closed from the loading end to prevent slippage at the interface of steel sleeve and the expansive cement grout, slippage occurred at the interface of the expansive cement and the BFRP rod. Highest pull-out load corresponds to the anchor with the least grout thickness which is mainly due to the reduction in confinement with increasing cross-section.

The grip length of the anchor should naturally be such that it is able to withstand the ultimate tensile load of the BFRP rod without any slippage. The resistance to slipping is offered by bond and frictional resistances, wherein, the bond resistance is associated with the chemical composition of the material, and the frictional resistance

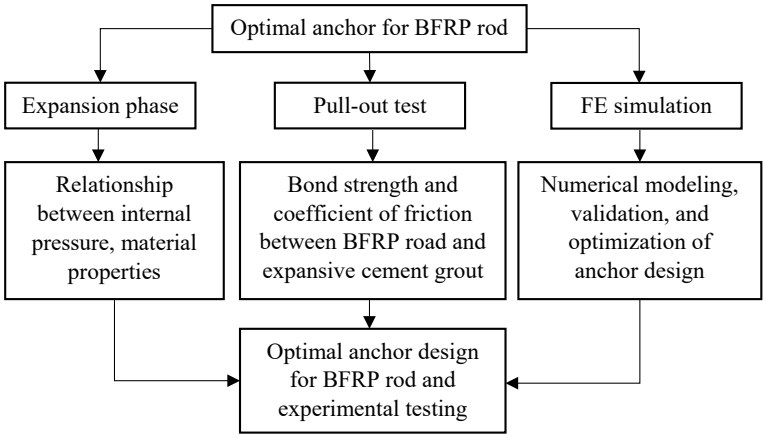

Fig. 2 Flowchart of important steps to develop optimum BFRP anchor [7]

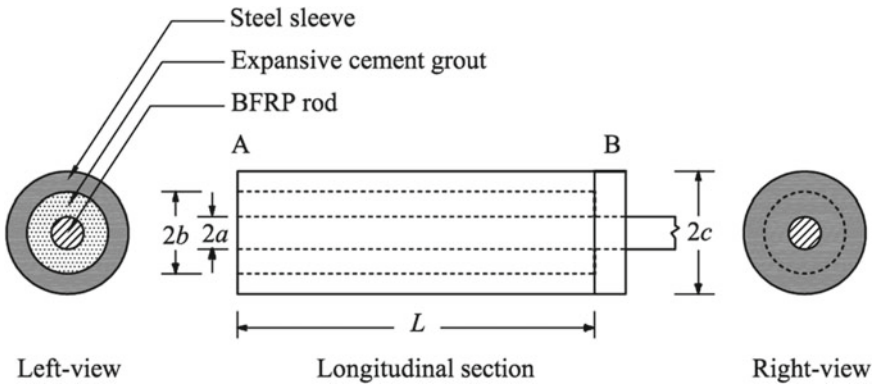

Fig. 3 Diagrammatic representation of the anchor [3]

varies with varying size of the anchor as it is dependent on the geometry of the anchor. Therefore, a change in the length of the anchor changes both the slippage resistance components, and hence, requires optimization to ensure that it is economical as well as being structurally sound.

2.4 FE Simulations

In finite element (FE) modelling, steel sleeve is considered elasto-plastic and the BFRP rod is considered linear elastic with orthotropic behavior. The expansive cement grout is modelled as concrete damaged-plasticity (CDP) model. The contact

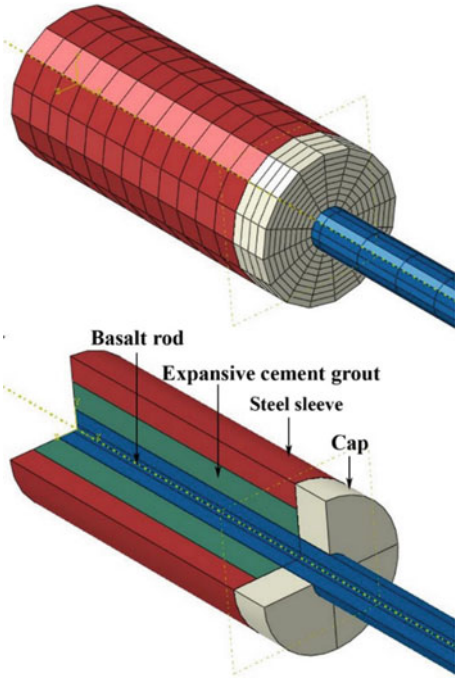

Fig. 4 Finite element model of the anchor [3]

properties that were obtained from the pull-out tests must be correctly defined as it bears utmost significance in numerical simulation, especially so for the contact surface between the expansive cement grout and the BFRP rod. The anchor is modeled in FE Software, ABAQUS®, as shown in Fig. 4.

The FE model results is then validated against the experimental and analytical results, and is adopted for optimizing the design of anchor upon founding dependable. The anchor developed is also tested by conducting tension test of the BFRP rods to check its efficiency. It is seen through the analysis that the gripping pressure and the diameter of the rod are inversely related, i.e., the gripping pressure decreases with increase in diameter of the rod. The reason is because the increase in diameter of rod causes the thickness of confinement to reduce. Further, it is also understood that the gripping pressure increases initially with increasing grout thickness but then starts to decrease after a certain point, and this is attributed to the fact that the initial increase in volume of grout causes it to expand thereby increasing the gripping pressure, and then further increase in the thickness of grout causes the confinement to reduce resulting in decrease in gripping pressure.

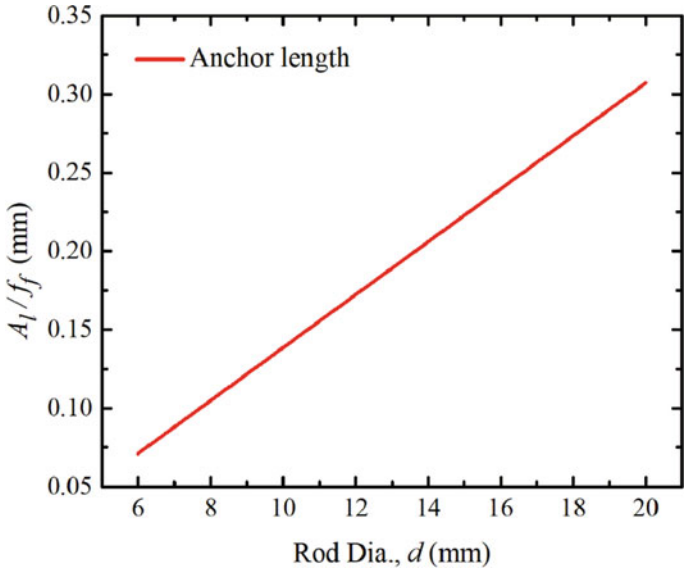

Fig. 5 Relation between rebar diameter (d) and the ratio of anchor length (A_l) to the ultimate tensile strength of the BFRP rod (f_f) [3].

2.5 Optimal Anchor

An anchor that does not slip and can safely withstand the ultimate tensile strength of the rebar while also considering the economy by using the least amount of material is desirable as an optimal anchor. The length of the anchor varies with the diameter of the rebar, and it can be obtained from Fig. 5. From the current study, the following anchor was found to be the optimal anchor for 8 mm diameter the BFRP rebar with 1200 MPa tensile strength:

Optimal Anchor: inner diameter = 16 mm, outer diameter = 24 mm, and length of steel sleeve = 125 mm.

3 Performance of the BFRP at Elevated Temperatures

3.1 General

There has been extremely limited research conducted so far about the mechanical properties and the performance of the BFRP at elevated temperatures since they have been only recently introduced in the industry. However, FRP composites are generally known to exhibit rapid loss of strength and stiffness at elevated temperatures due to its low temperature deflection point. In order to investigate the response of the BFRP

rods at elevated temperatures in the laboratory, the members that are reinforced/pre-stressed using the BFRP rods are subjected to fire, up to 450 °C, and tension test has been carried out, followed by establishment of a constitutive relationship between the variation in temperature and the degradation of its mechanical properties. There was a marginal degradation of mechanical properties of the BFRP rods at 300 °C, and a loss of about 43% of its tensile strength was recorded when the temperature reached 400 °C. The BFRP rods lost all of its tensile strength at 450 °C.

3.2 Experimental Investigations

The following prerequisite tests are carried out to determine the basic properties of the BFRP rod:

i. Determination of Fiber Content of the BFRP rod

It is important to know the fiber content of the BFRP rod because it influences the performance of the material at elevated temperatures. The average fiber content, determined through scanning electron microscopy (SEM), was 80.1%.

ii. Dynamic mechanical thermal analysis (DMTA)

The DMTA test is conducted on the BFRP rod to obtain the glass transition temperature (T_g) of the resin matrix. This is done by subjecting the BFRP specimen to a small oscillating force as a function of temperature and time. The glass transition temperature (T_g) of the material was found to be 171.7 °C.

iii. Thermo-gravimetric analysis

The thermo-gravimetric analysis has been used to measure the thermal stability of the BFRP rods, wherein, the variation in the weight of the material is recorded with changing temperature. The analysis showed that the variation in the degradation of the weight is related to the resin content. The decomposition temperature (T_d) of the sample was found to be 423.7 °C.

iv. Tension test at ambient temperature

The tension test on the BFRP rods at ambient temperature provides a basis for investigating the effects on the tensile strength and elastic modulus of the BFRP rods at elevated temperature. Due to the unavailability of high-temperature extensometers to measure the modulus of elasticity at elevated temperature, it becomes necessary to measure the modulus of elasticity by utilizing the total deflection of the sample and compare it with the one given by extensometers at ambient temperature. As the results obtained based on the total deflection of the sample varied on average by only 6.9% as compared to the value obtained using extensometers, the method based on total elongation is considered appropriate for measuring the modulus of elasticity of the BFRP rods at elevated temperature.

With the results of the prerequisite tests available, the tension test on the BFRP rods at elevated temperature is carried out. Three samples each are tested at various levels of temperature ranging from 35 to 450 °C, except at the critical temperature of 400 °C where six identical samples are tested for higher reliability of results.

As it can be seen from Fig. 6, the degradation in the tensile strength of the BFRP rods at elevated temperature occur in three distinct phases with linear variation having unique slopes. Whereas, the degradation of the modulus of elasticity of the BFRP rods occur in two phases, also linear with two distinct slopes. There is a marginal deviation of tensile strength up to a temperature of 150 °C, losing only 4% of the ambient tensile strength. From 200 to 400 °C, there has been a notable degradation, losing over 40% of its residual strength. It is worth noting that this range of temperature starts just above the transition temperature of 171.7 °C. From 400 to 450 °C, the tensile strength is degraded dramatically with only 13% residual strength at 450 °C. From room temperature to 250 °C, only 3% of the reference value of the tensile modulus of elasticity has been degraded. Beyond 250 °C the degradation rate increased and reached to 25% of the original value.

The BFRP rods exposed to elevated temperatures (35, 250, and 450 °C) were also investigated through scanning electron microscope which showed that the bonding between the fibers and the resin matrix start to deteriorate with rise in temperature. The following SEM images show lumps of resin deposited on the surface of the

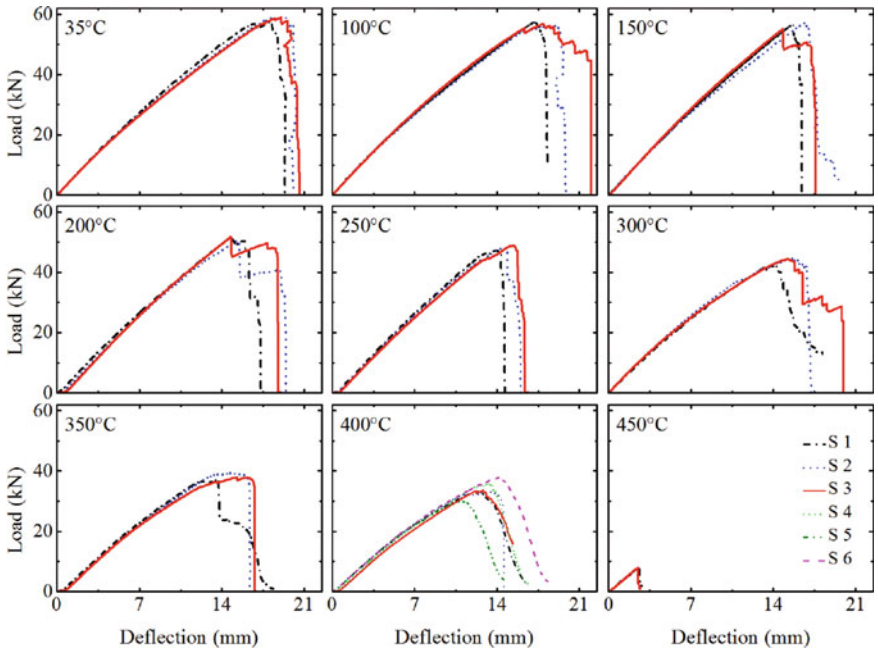

Fig. 6 Load–deflection curves for the BFRP rods at different temperatures [2]

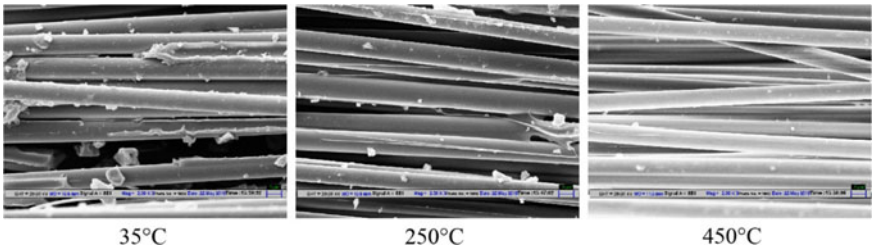

Fig. 7 SEM images of the BFRP rods at elevated temperatures [2]

rods at room temperature and beginning to soften at 250 °C followed by complete disappearance of the resin from the surface at 450 °C (Fig. 7).

3.3 Constitutive Law in Thermo-Mechanics

Based on the investigations and the data obtained experimentally, a semi-empirical law incorporating the effects of fraction of fiber volume, transition temperature of glass, and decomposition temperature of resin has been proposed to estimate the degradation of mechanical properties of the BFRP rods at elevated temperature, which is given by Eq. (6):

$$P(T) = P_0\left(A - B\exp\left\{\left[\frac{T - T_0}{T_d}\right]^C\right\}\right) \tag{6}$$

where, A, B, and C are the coefficients that are a function of fraction of fiber volume, V_f; glass transition temperature, T_d; and decomposition temperature of resin, T_g.

4 BFRP Reinforced and Pre-Stressed Concrete Beams

4.1 General

In this section, the performance of the BFRP-reinforced and pre-stressed concrete beams is evaluated in flexural behavior, with analysis of flexural strength, safety, serviceability, and ductility assessment. For this purpose, twelve separate beams are studied under four different series of design, namely, over-reinforced concrete beams (without pre-stressing), over-reinforced PSC beams, under-reinforced PSC beams, and significantly under-reinforced PSC beams. Figure 8 shows the geometric and reinforcement details of the beams experimentally studied for assessing the

performance of the BFRP reinforced and pre-stressed concrete beams under flexural loading condition.

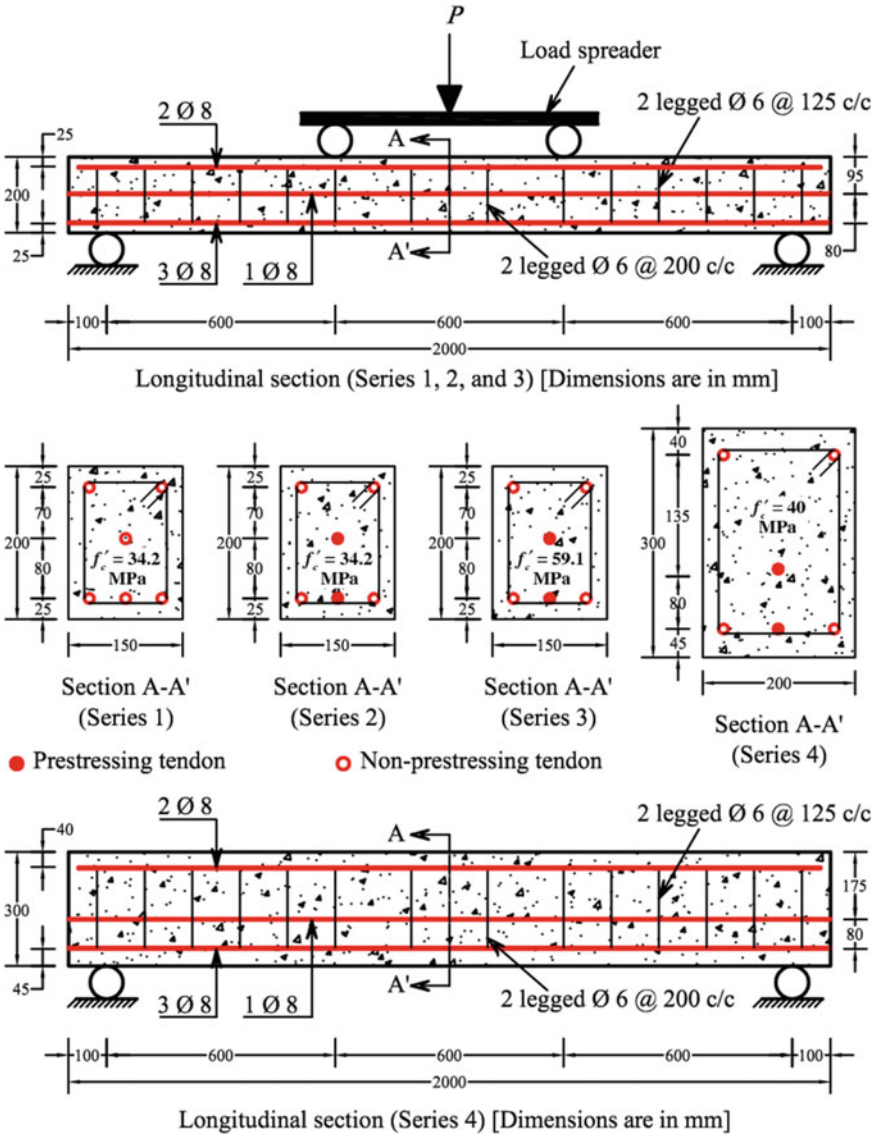

Fig. 8 Geometric and reinforcement details of the beams studied [4]

4.2 Experimental Investigations

The beams were cast with M30 (Series 1 and 2), M50 (Series 3), and M35 (Series 4) grades of concrete. For the purpose of pre-tensioning the BFRP tendons, the anchors blocks designed in Sect. 2 were used during application of pre-tensioning force using a hydraulic jack from the live end of the member. The beams under Series 2, 3, and 4 were pre-tensioned at 30%, 35%, and 60%, respectively. In order to ensure that accurate pre-tensioning force is applied, the pre-tensioning process was monitored simultaneously with the observations from load cells and strain gauges mounted on the BFRP tendons, and the total elongation and a gauge mounted on the hydraulic pump. A strain gauge was also instrumented on the top surface of the beams to measure the compressive strains developed.

The BFRP beams were tested under laboratory setup of four-point test apparatus with loads applied monotonically over two points using a load-spreader. A linear variable differential transformer (LVDT) was used to measure the deflection undergone by the beam and a sensor was used for detecting the cracks at mid-span of the beam, in addition to visually monitoring the beams for initiation and propagation of cracks and their patterns. The load–deflection relationships of the beams are bilinear with different slopes before and after cracking. This is due to the diminishing flexural rigidity caused by the development of cracks on the tension face of the beams.

As the first series of beams were over-reinforced without pre-stressing, the failure was governed by crushing of concrete, which was then followed by successive rupture of subsequent layers of the BFRP reinforcements, observing the failure load of 72.1 kN. For the second series also, with over-reinforced design and having the same compressive strength of concrete but having been partially pre-stressed, the load-carrying capacity increased to 76.1 kN and the failure was still governed by compression of concrete followed by rupture of the BFRP rods. In the third series, which was under-reinforced and pre-stressed at 35% of the ultimate tensile strength of the BFRP tendons, the failure was governed by rupture of the BFRP rods with a failure load of 85.6 kN. This is attributed to the fact that the beams were cast with higher grade of concrete which allowed full contribution of the BFRP reinforcements towards the flexural strength of the beam. The fourth series, being significantly under-reinforced and pre-stressed to 60%, the failure was governed by the rupture of the layers of the BFRP tendons/reinforcements in a progressive manner in three stages. The first rupture of the pre-stressed tendons was seen to occur in the lowest layer, followed by the rupture of tendons closer to the neutral axis, and finally the un-pre-stressed BFRP rods in the lower layer. The load-carrying capacity for the flexural members in the fourth series was 121.8 kN.

The strain measurements obtained from the strain gauges mounted on the BFRP tendons and the compression fiber of the beams reveal that compressive strain in the top fiber has reached the yield strain (0.003) for the first and the second series. The compressive strain is lower than that the yield strain for Series 3, and much lower than the yield strain for the fourth series. Therefore, the strain responses confirm that

the failure of the members was as anticipated for each series depending on whether they are under or over-reinforced.

For deflection check, the service loads are obtained from the flexural strength by dividing it by reduction factor of 0.7 and a load factor of 1.7. The deflection undergone by the beams under the service loads are checked against the permissible deflection, $\left(\frac{L}{240}\right)$. It is observed that the beams that are over-reinforced and are not pre-stressed or are marginally pre-stressed, and having lower compressive strengths (Series 1 and 2), have undergone deflection greater than the permissible value and hence do not meet the serviceability requirement. On the other hand, beams with higher grade of concrete and pre-stressed to greater extent, undergo lesser deflections, with the least deflection when the beam is significantly under-reinforced and pre-stressed to 65% of the ultimate tensile strength of the tendons. This shows that the under-reinforced design with pre-stressing satisfies the deflection criterion reasonably well.

The beams that are not pre-stressed fared poorly in terms of crack width with cracks more than the permissible crack width [4]. The over-reinforced section experienced crack widths lesser than the permissible value, while the under-reinforced sections with pre-stressing exhibited least amount of crack widths. Also, the beams that were not pre-stressed had the lowest cracking load whereas the pre-stressed beam with significant under-reinforced section exhibited the highest cracking load.

The deformability factor is defined as the ratio of deflection parameter at ultimate load to the deflection parameter at cracking load [3]. Following this definition, the deformability indices for each of the series under consideration is calculated. It is noted that the deformability index is higher for over-reinforced sections, that is with higher reinforcement ratio to balanced ratio: $\left(\frac{\rho_f}{\rho_b}\right)$. The ratio of cracking load to ultimate load, $\left(\frac{P_{cr}}{P_u}\right)$ indicates whether the serviceability criterion is met, wherein, lower $\frac{P_{cr}}{P_u}$ means poor serviceability performance and vice-versa. Figure 9 shows the variation of deformability index and $\frac{P_{cr}}{P_u}$ with respect to $\frac{\rho_f}{\rho_b}$.

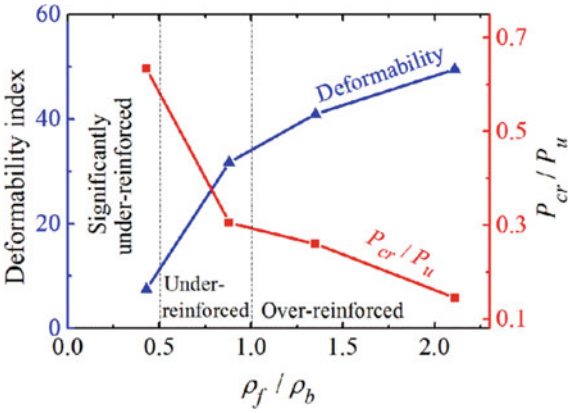

Fig. 9 Variation of deformability index and $\frac{P_{cr}}{P_u}$ with respect to $\frac{\rho_f}{\rho_b}$

5 Flexural Analysis of BFRP-Reinforced and Pre-Stressed Concrete Beams

5.1 General

It is important to conduct flexural analysis because the information related to cracking load and the ultimate load can be obtained from this analysis which is required for the evaluation of serviceability and modes of failure of the beams. Further, estimation of load–deflection values and behavior is also crucial in assessment of ductility of the members.

This section focusses on the flexural analysis of the BFRP-reinforced/ pre-stressed beams by following the recommendation of the American Concrete Institute (ACI) in accordance with ACI PRC-440.1-15 (2015), as well as preceding research involving similar materials such as the glass fiber-reinforced polymers (GFRP). The calculation of flexural strength based on the assumptions given in ACI has been detailed by Alraie [2]. Specifically, the following are the objectives of this section:

i. Analysis of the BFRP-reinforced/pre-stressed beams tested in Sect. 4, calculation of cracking and ultimate load-carrying capacities and comparison with experimental results;
ii. Estimation of load-deflection response and comparison with experimental results; and
iii. Conduct finite element analysis (FEA) and validate numerical results with experimental outcomes.

5.2 Analysis of Beams

The process of flexural analysis of the BFRP-reinforced/pre-stressed concrete beams consists of the following steps:

(a) Calculation of pre-stress losses

The short-term pre-stress losses in the BFRP pre-stressed beams occur due to elastic shortening whereas the long-term losses occur due to shrinkage, creep, and relaxation of tendons.

These losses are calculated as follows:

- Loss due to elastic shortening is given by, $\Delta f_{es} = m f_{cp}$
- where, $m = \frac{E_f}{E_{ct}}$ is the modular ratio; E_f is the elastic modulus of the BFRP tendons; E_{ct} is the elastic modulus of concrete at pre-stress transfer stage; and f_{cp} is the compressive stress in concrete at the tendon level.
- Loss due to shrinkage of concrete is given by, $\Delta f_s = \varepsilon_s E_f$, where $= \varepsilon_s = 0.0006$.
- Loss of stress due to creep in the BFRP tendons is calculated as, $\Delta f_{cr} = 0.0358 f_{pt}$; where, f_{pt} is the initial pre-stress.

- Loss of stress due to relaxation of the BFRP tendons is calculated as, $\Delta f_{cr} = 0.0636 f_{pt}$ for 50% initial pre-stress.

(b) Check for stresses due to permanent loads

This check is performed for top and bottom fiber stresses, which are induced due to the permanent loads such as pre-stressing force and the dead loads.

(c) Calculation of balanced ratio

The balanced ratio (ρ_b) is given by,

$$\rho_b = 0.85\beta_1 \frac{f_c^{'}}{f_{fu}} \frac{\varepsilon_{cu}}{\varepsilon_{cu} + \varepsilon_{fu} - \varepsilon_{pmt}} \tag{7}$$

where, β_1 is the ratio of depth of the equivalent rectangular stress block to the depth of neutral axis, given by, $\beta_1 = 0.85 - 0.05\frac{f_c^{'} - 27.5}{6.9}$; $f_c^{'}$ is the compressive strength of concrete; f_{fu} is the tensile strength of the BFRP tendons; ε_{cu} is the ultimate tensile strain of the BFRP; and ε_{pmt} is the initial pre-stressing strain in the lowest tendon.

(d) Calculation or reinforced ratio

Equation (8) is used to calculate the reinforcement ratio (ρ) as follows:

$$\rho = \frac{\sum_{i-1}^{p} A_{fi}\alpha_i}{bd_m} \tag{8}$$

where, A_{fi} is the cross-sectional area of the tendon; α_i is the ratio of stress in a tendon at balanced condition to the ultimate tensile strength of the tendon $= \frac{f_{bi}}{f_{fu}}$; b is the width of beam; d_m is the distance of the bottommost pre-stressing tendon from the extreme compression fiber; and p is the total number of tendons.

(e) Calculation of cracking moment

The cracking moment is given by,

$$M_{cr} = \left(f_r + \sum \sigma_{bp}\right) S_b \tag{9}$$

where, f_r is the modulus of rupture of concrete; S_b is the section modulus corresponding to extreme bottom fiber; and $\sum \sigma_{bp}$ is the resultant compressive stress at extreme bottom fiber due to pre-stressing forces.

(f) Calculation of depth of neutral axis (n)

The depth of neutral axis is calculated with uniform design approach as follows: For significantly under-reinforced section,

$$n = k_u d_u \tag{10}$$

where,

$$k_u = \frac{-B + \sqrt{B^2 - 4AC}}{2A} \tag{11}$$

$$A = \frac{bd^2}{2} f_{fu}\left(1 - \frac{f_{mpt}}{f_{fu}}\right)\frac{E_c}{E_f} \tag{12}$$

$$B = \left[F_{pe}d_m + \varepsilon_f d_m\left(\sum_{i=1}^{q} A_{fi}E_{fi}\right)\right] \tag{13}$$

$$C = -\left[F_{pe}d_m - \varepsilon_f\left(\sum_{i=1}^{q} A_{fi}E_{fi}h_i\right)\right] \tag{14}$$

For under-reinforced section,

$$n = k_u d_u \tag{15}$$

where,

$$k_u = \frac{-B \pm \sqrt{B^2 - 4AC}}{2A} \tag{16}$$

$$A = 0.85 f_c^{'} b\beta_1 d_m^2 \tag{17}$$

$$B = -\left[A + F_{pe}d_m + \varepsilon_f d_m\left(\sum_{i=1}^{q} A_{fi}E_{fi}\right)\right] \tag{18}$$

$$C = \left[F_{pe}d_m + \varepsilon_f\left(\sum_{i=1}^{q} A_{fi}E_{fi}h_i\right)\right] \tag{19}$$

For over-reinforced section,

$$n = k_u d_u \tag{20}$$

where,

$$k_u = \frac{A + \sqrt{A^2 + 4B}}{2} \tag{21}$$

$$A = \frac{\left[\left(\sum_{j=1}^{m} A_f E_f \varepsilon_{pji}\right) - \varepsilon_{cu}\left(\sum_{j=1}^{q} A_{fj}E_{fj}\right)\right]}{0.85 f_c^{'} b\beta_1 d_m^2} \tag{22}$$

$$B = \frac{\varepsilon_{cu}\left(\sum_{j=1}^{q} A_{fj} E_{fj} h_j\right)}{0.85 f_c^{'} b \beta_1 d_m^2} \tag{23}$$

where, f_{mpi} is the initial effective pre-stress in the bottommost tendon; E_c is the modulus of elasticity of concrete; E_f is the modulus of elasticity of the BFRP tendons; A_f is the cross-section area of the BFRP tendons; ε_f is the difference between ultimate rupture strain and the initial pre-stressing strain of the lowest tendon; A_{fj} is the cross-sectional area of the BFRP tendons in a layer, j; E_{fj} is the modulus of elasticity of the BFRP tendons in a layer, j; h_i is the distance of the tendons in each layer from the extreme compression fiber; ε_{pji} is the initial pre-stress in a tendon in an individual layer, j; and q is the number of layers of tendons.

(g) Calculation of strains in concrete and the BFRP tendons

For significantly under-reinforced and under-reinforced sections, the strain in a layer of pre-stressed tendons:

$$\varepsilon_{pj} = \left(\varepsilon_{fu} - \varepsilon_{pmi}\right)\frac{\left(d_j - n\right)}{\left(d_m - n\right)} + \varepsilon_{pji} \tag{24}$$

The strain in a layer of non-pre-stressed tendons:

$$\varepsilon_{nj} = \left(\varepsilon_{fu} - \varepsilon_{pmi}\right)\frac{\left(h_j - n\right)}{\left(d_m - n\right)} \tag{25}$$

The strain on the extreme compression fiber of the concrete:

$$\varepsilon_c = \left(\varepsilon_{fu} - \varepsilon_{pmi}\right)\frac{(n)}{\left(d_m - n\right)} \tag{26}$$

For over-reinforced sections, the strain in a layer of pre-stressed tendons:

$$\varepsilon_{pj} = \frac{0.003}{n}\left(d_j - n\right) + \varepsilon_{pji} \tag{27}$$

The strain in a layer of non-pre-stressed tendons:

$$\varepsilon_{nj} = \frac{0.003}{n}\left(h_j - n\right) \tag{28}$$

where, d_j is the depth of pre-stressing tendon in an individual layer form the extreme compression fiber; h_j is the depth of non-pre-stressing tendon in an individual layer form the extreme compression fiber; ε_{pji} is the initial pre-stress in a tendon in an individual layer; and n is the neutral axis depth.

(h) Calculation of compressive force in concrete and tensile force in tendons

The compressive force in concrete is calculated as:

$$C_c = 0.85 f_c^{'} b \beta_1 bn \tag{29}$$

The tensile force in pre-stressed tendons:

$$F_{pj} = E_f \varepsilon_{pj} A_{fpj} \tag{30}$$

The tensile force in non-pre-stressed tendons:

$$F_{nj} = E_f \varepsilon_{nj} A_{fnj} \tag{31}$$

where, A_{fpj} is the cross-section area of pre-stressed tendons of layer, j; and A_{fnj} is the cross-section area of non-pre-stressed tendons of layer, j.

(i) Moment of resistance:

$$M_u \left[\left(\frac{T + C_c}{2} \right) (d - \overline{d}) \right] \tag{32}$$

where, T is the total tensile force in tendons; C_c is the compressive force in the compression zone of concrete; d is the effective depth of centroid of the tendons, and $\overline{d}$ is the depth of the centroid of the rectangular stress block of concrete from the top fiber.

(j) Deflection calculation

The deflection at the mid-span of a pre-stressed beam is given by:

$$\Delta = \frac{Px}{24 E_c I_e} \left(3L^2 - 4x^2\right) + \frac{P D^2 x}{10 G_c I_e} - \frac{F_p \left(d_p - y_e\right) L^2}{8 E_c I_e} \tag{33}$$

where, F_p is the pre-stressing force; e is the constant eccentricity; P is the Concentrated load; x is the distance of load from support; L is the span of beam; E_c is the modulus of elasticity of concrete; G_c is the Shear modulus of concrete; and d_p is the distance of centroid of tendons from extreme compression fiber.

5.3 Results of Analysis

The analytical approach elaborated in Sect. 5.2 is found to underestimate results of flexural analysis as compared to the results obtained experimentally and it is more prominent in over-reinforced non-pre-stressed sections, as it is dependent on the way concrete behaves. This is expected due to the assumptions of Whitney's rectangular

stress block. It is also clearly explained in the ACI standards that code provisions provide a conservative approach to flexural analysis. Out of the two methods of obtaining deflection, the ACI method underestimates the deflection as the formula proposed in the code does not account for residual deflection due to cyclic loading, especially for over-reinforced non-pre-stressed design. However, the ACI method does yield reasonable deflection for under-reinforced pre-stressed design due to very low β_d.

5.4 Finite Element Analysis (FEA)

A comprehensive numerical modelling and finite element analysis (FEA) of the BFRP-reinforced/pre-stressed beams were carried out in ABAQUS Software, with the application of material and geometric properties of the beams and the parameters related to their behaviors. The details of modelling and FEA are available from Alraie [2]. The numerical simulation involved three stages, namely, application of pre-stress, application of self-weights, and application of load until failure.

The results of the FEA also indicate that the concrete reaches the ultimate compressive strength for over-reinforced design which further attests the fact that failure is governed by compressive failure of concrete for over-reinforced designs. Similarly, for the under-reinforced and significantly under-reinforced designs, the failure was seen to be governed by tension failure as the compressive strength of concrete remain below its ultimate compressive strengths. The FEA also shows that the area of cracks is substantial in over-reinforced non-pre-stressed design, and it diminishes considerably in significantly under-reinforced pre-stressed design. In general, it can be concluded from the FEA that there is a reasonable degree of agreement between the actual and the analytical and experimental analysis.

6 Ductility of FRP-Reinforced/PRE-Stressed Beams

6.1 General

A significant shortcoming of the fiber-reinforced polymer (FRP) composites is their non-ductile nature which means that they are unable to undergo plastic deformation. The FRP composites rupture suddenly and without giving prior warning, endangering lives of occupants. While some codes/ standards recommend designing the FRP-reinforced/pre-stressed structures over-reinforced in order to utilize the relatively higher ductility of concrete, the study by Alraie et al. [6, 7] focused on the prediction of non-linear response of members reinforced/pre-stressed with the FRP composites in under-reinforced design. In doing so, the beams were expected to lose stiffness

in a progressive manner due to successive rupture of the FRP tendons by acquiring pseudo-ductility.

In this section, under-reinforced beams pre-stressed with FRP material, were analyzed and finite element (FE) simulation were conducted to study whether they actually exhibit progressive failure. Different numbers of tendons were provided in layers with varying pre-stressing ratios and sectional properties and as well as inclusion of a sacrificial rebar which was supposed to provide warning. The specific objectives behind undertaking the present study had been:

i. To assess the ductility of the FRP-pre-stressed beams that are designed as under-reinforced sections, as per energy dissipation approach;
ii. To introduce pseudo-ductility in the FRP-pre-stressed beams by providing FRP tendons in layers with sacrificial rebar; and
iii. To use functionally-graded concrete to compensate for uneconomic multi-layered system of FRP tendons.

It is established eventually through the analyses and the FE simulations conducted that when beams are partially or fully pre-stressed with the FRP tendons distributed in layers across the section, it results in improvement in their ductility.

6.2 Analysis from Energy Perspective

The analytical approach elaborated in Sect. 5 is followed for conducting the flexural analysis, subsequent to which ductility is evaluated from the load–deflection curves thus obtained. The ratio of inelastic energy to the total energy is defined as ductility, and it is given by the areas under the load–deflection curve.

$$EnergyRatio = \frac{E_{in} + E_{in(addl)}}{E_{esc} + E_{in} + E_{in(addl)}} \tag{34}$$

where, E_{in} is initially absorbed inelastic energy (before reaching ultimate capacity); $E_{in(addl)}$ is additionally absorbed inelastic energy (after reaching ultimate capacity); and E_{esc} is elastic energy. A beam is considered ductile when the energy ratio is greater than 75%, semi-ductile when the energy ratio is 7074% and brittle when the energy ratio is less than 70%. Non-linear analysis of cracked section for the FRP-pre-stressed beams was conducted as per ACI-specified and other simplified method as reported by Alraie [2]. In order to obtain the non-linear load–deflection curve, the change of moment of inertia after cracking of the beam was used. The results obtained were validated with the experimental and FE analysis outputs.

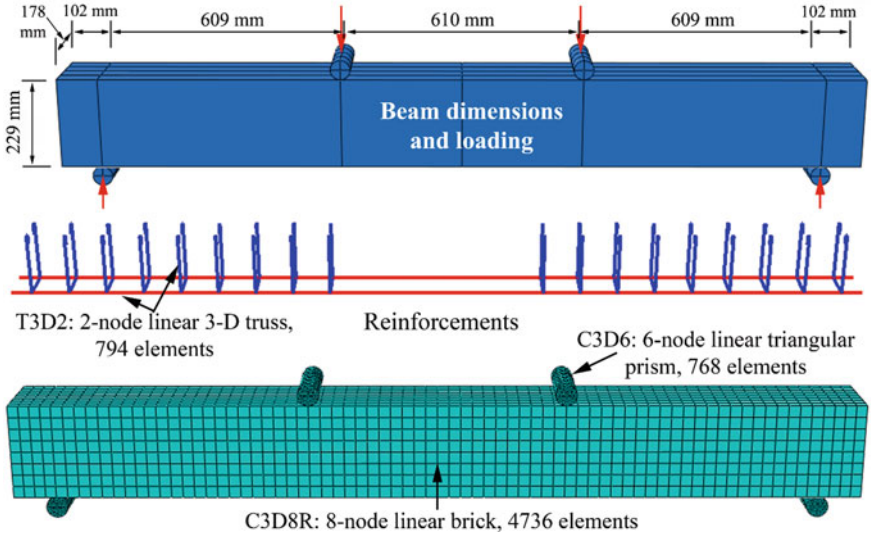

Fig. 10 Finite element model of beam in ABAQUS® [3]

6.3 Validation of Analysis and Comparison of Results

The analysis is carried out for different materials as internal reinforcement, i.e., carbon fiber-reinforced polymer (CFRP), glass fiber-reinforced polymer (GFRP), and basalt fiber-reinforced polymer (BFRP). The work that has already been conducted by numerous researchers previously are studied and used for validating the analytical results, which are further corroborated with separate finite element analysis (FEA) conducted. The FEA is carried out using ABAQUS® Software by modelling three different beams which have been experimentally investigated in previous works by other researchers. Figure 10 shows a FE model of one of the three beams selected for the study. The comparison of the results obtained from the three different approaches, i.e., analytical, experimental that obtained from literature, and the FEA conducted here show that the outputs concur very well with reasonably low difference in terms of load- and moment-carrying capacities [2].

6.4 Proposed Model for Assessment of Ductility

A beam of suitable cross-section that is pre-stressed with the CFRP reinforcements is selected such that the shear arm ratio, $\frac{x}{d} \geq 2.7$. Choosing such geometric proportion ensures that the failure is governed by flexure and not by shear criterion, whereas, earlier results are considered for $\frac{x}{d} = 4.06$. It is also worth noting that the tendons are arranged in multiple layers, i.e., distributed across the cross-section depth. The

CFRP tendons are used to study the effects of multiple layers of tendons, and the BFRP rods are used for analysis with partial pre-stressing. The details of the beam analyzed are as follows:

Beam cross-section: 400 mm × 610 mm, effective depth: 575 mm, length of beam: 7 m, grade of concrete: 80 MPa, modulus of elasticity of concrete: 36,595 MPa, tensile strength of concrete: 5.57 MPa, ultimate tensile strength of CFRP tendons: 1800 MPa, modulus of elasticity of CFRP tendons: 1,24,000 MPa, area of CFRP rebar: 836 mm^2, ultimate tensile strength of the BFRP tendons: 966.4 MPa, modulus of elasticity of the BFRP tendons: 48,675.7 MPa, area of the BFRP rebar: 1672 mm^2, and position of load: 2333 mm.

6.5 Numerical Results

6.5.1 Layering of Tendons

First, the CFRP tendons are arranged in a single layer and are studied for pseudo-ductility with varying pre-stressing ratios, taken as a percentage of the ultimate tensile strength of the CFRP tendons. It was noted that the elastic energy changes marginally with changing pre-stressing ratio and attains highest value of only 42.1%, which is classified as being brittle. Figure 11 presents the load–deflection curve, elastic (E_{in}) and inelastic (E_{esc}) energies, and energy ratio of 42.1%, for 50% pre-stressing ratio. Here, ε_c is the compressive strain in the concrete top fiber at failure.

Next, the same number of CFRP tendons are arranged in 2- and 3-layered system and are investigated for pseudo-ductility. It was observed that the energy ratio for was 70% for 2-layered CFRP tendons which can be classified as semi-ductile, and it increased to 79.3% for 3-layered CFRP tendons that can be classified under ductile nature. The reason for the increase in ductility in multiple layered tendons, as discussed earlier, is due to the progressive rupture of the tendons which contributes to higher inelastic energy to the system. It was also seen that the highest ductility corresponded to 30% pre-stressing ratio, which is because of the fact the reserve strength of the tendons reduces with increasing pre-stressing ratio. Figure 12 presents the load–deflection curves, elastic and inelastic energies and energy ratios, for 50% pre-stressing ratio, for 2- and 3-layered tendons.

Although, providing the tendons in layers show great promise in terms of improving the ductility characteristics, it has an inverse relationship with the load-carrying capacity, i.e., the load-carrying capacity of the member decreases with increasing number of layers of tendons. The reason for this reduction in the load-carrying capacity is that some reinforcement located in the upper part of the section does not contribute to the flexural capacity. The tendons on the bottom layer, by virtue of its larger distance from the neutral axis, rupture well before the tendons in the upper layer have achieved their ultimate tensile strengths. Therefore, the solution to the reducing load-carrying capacity with increasing number of layers of tendons may be recommended in the form of functionally-graded concrete.

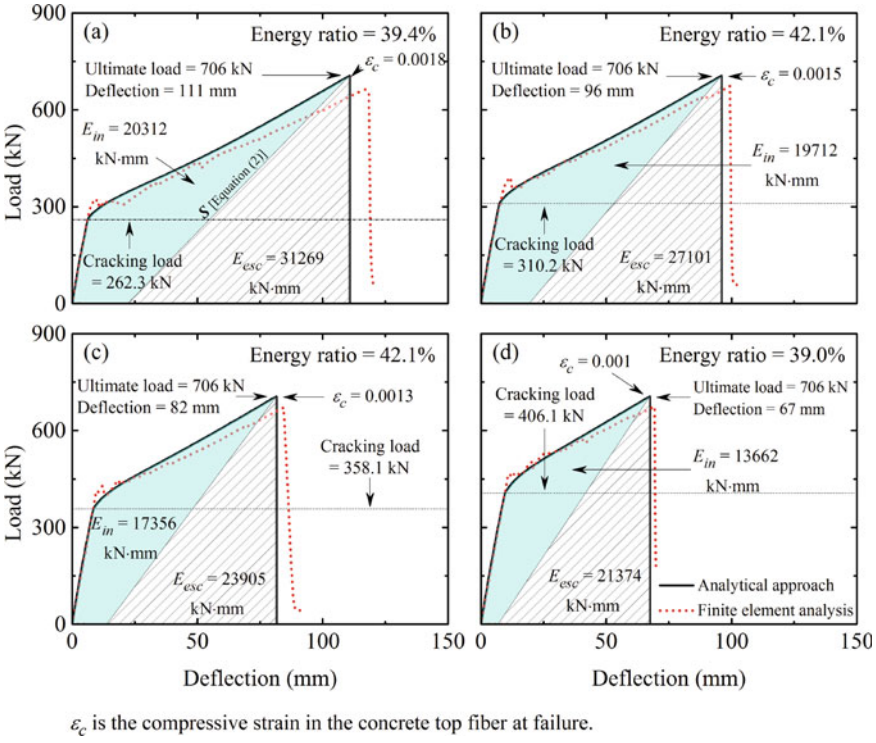

ε_c is the compressive strain in the concrete top fiber at failure.

Fig. 11 Load–deflection curve and energy ratio for 50% pre-stressing ratio [7]

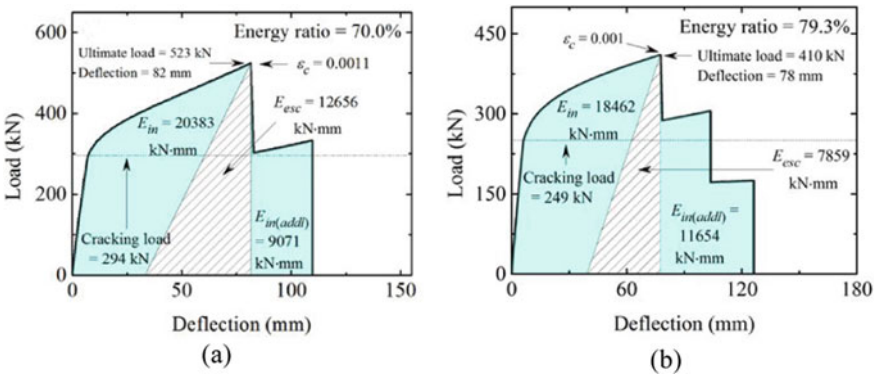

Fig. 12 Load–deflection curve and energy ratio for 50% pre-stressing ratio for **a** 2-layers and **b** 3-layers of tendons [5]

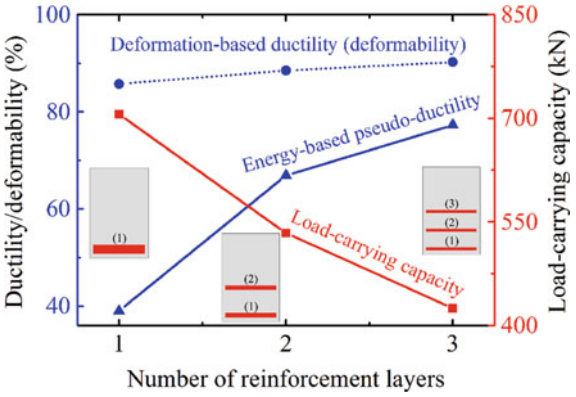

Fig. 13 Relationship between ductility, load-carrying capacity, and number of layers of tendons [7]

Using functionally-graded concrete with a warning rebar pre-stressed to a higher pre-stressing ratio helps achieve high energy ratio and a load-carrying capacity similar to that of a single layered system. It is also observed that the flexural strength keeps increasing after the failure of the warning rebar by almost 6% which allows sufficient warning time before total collapse. Figure 13 shows how the ductility and load-carrying capacity of a flexural member vary with respect to number of layers of tendons in the cross-section.

6.5.2 Partial Pre-Stress

Similar to the concept of arrangement of tendons in layers, partial pre-stressing is carried out to avoid sudden failure by regulating the pattern of failure. When both pre-stressed and non-pre-stressed reinforcement are provided in a single layer, the ones that are pre-stressed rupture first and the non-pre-stressed rebars take over and provide the flexural strength.

The analysis for partial pre-stressing is conducted on the BFRP tendons, where both partially stressed and fully stressed beams are assessed. A partially pre-stressed beam is the one in which the tendons in a layer are stressed to different magnitudes; whereas, a fully pre-stressed beam is the one in which all the tendons in a layer are stressed to equal magnitude. For the purpose of this analysis, a beam with two pre-stressing magnitudes has tendons stressed at 40 and 0% of ultimate tensile strength. For a beam with three pre-stressing magnitudes, some tendons are stressed at 30% and others at 40%, while the non-pre-stressed ones are at 0% of the ultimate tensile strength. Finally, for a beam with four pre-stressing magnitudes, tendons are stressed at 30, 45, and 60% and the non-pre-stressed tendons are at 0%.

It was observed that the energy ratio increases with increasing pre-stressing ratio and attain ductile behavior at 60% pre-stressing ratio. The reason behind this is, the reserve strengths of non-pre-stressed rebars increases with increasing pre-stressing ratio. An additional inelastic energy is introduced with increased deflection which

ultimately leads to high energy ratio. The increase in pre-stressing ratio is also found to reduce the load-carrying capacity because when the pre-stressed tendons rupture before the non-pre-stressed rebars, the beam reaches its load-carrying capacity. The non-pre-stressed tendons partly contribute to the flexural strength until collapse, hence improving the ductility.

7 BFRP Tendons in Integral Bridges

7.1 General

Integral bridges have been getting increasingly popular as they eliminate the need for expansion joints and bearings which are sources of deterioration, requiring repeated maintenance, facilitate ingress of chemicals, lubricants, deicing salts, etc. and lead to corrosion that ultimately reduce the durability of the structure. The issue of durability is even more pronounced in pre-stressed structures as they are slender and lead to lower section capacities. Therefore, in this section investigation on the possibility of using the BFRP tendons in integral bridges is presented to address the aforementioned issues and compare the results of conventional steel pre-stressed concrete (PSC) bridges.

7.2 Analysis of Integral Bridges

A major difference between conventional and integral bridges is how they respond to actions such as temperature variation, creep and shrinkage of concrete, and deformation. The horizontal deformation is partially restrained in the integral bridges as they are in contact with both the foundation and the fill. The interaction between (a) the foundation and the bridge and (b) the fill and the bridge play a crucial role in determining the effects of actions and deformation. This renders independent analysis of the members of the integral bridges impractical.

It is particularly important to correctly assess ground stiffness in the analysis and design of integral bridges otherwise it might lead to underestimation of secondary forces, moments, and effects of variation in temperature. The stresses due to parasitic action are also influenced by the coefficient of expansion due to variation in temperature and the modulus of elasticity of concrete. Therefore, if it is felt that the integral system is incapable of tackling stresses generated by parasitic action, the structure may be designed as a quasi-integral bridge.

It has been proven through research by Schlaich et al. [8] that optimizing the form of integral bridges results in slender as well as robust structure. One of the recommended techniques for the purpose is to follow the bending moment profile for the shape of the girder which also leads to economic design.

7.3 Design of Bridges

Four different bridges with combinations two different forms and two different pre-stressing materials have been studied in order to determine the most optimized form of bridge and the material for pre-stressing to overcome durability issues as a result of corrosion. The following are the combinations studied:

i. Simply-supported bridge with steel as pre-stressing material (SSB_Steel)
ii. Simply-supported bridge with the BFRP as pre-stressing material (SSB_BFRP)
iii. Integral bridge with steel as pre-stressing material (IB_Steel)
iv. Integral bridge with the BFRP as pre-stressing material (IB_BFRP)

Structural design basis as per the guidelines of AASHTO, British, and Euro-codes have been prepared for the design of the four bridges.

Methodology for Analysis and Design

The methodology of design of the BFRP-reinforced/pre-stressed girders is quite different from that of the steel reinforced/pre-stressed girders. Since conventional steel is highly ductile, designers recommend under-reinforced sections so that the tendons yield before the brittle concrete does, which allows sufficient time for giving warning and prevents catastrophic collapse. However, in case of the BFRP-reinforced/pre-stressed girders, both the concrete and the pre-stressing materials are highly brittle which poses grave concern of not receiving warning prior to failure. Therefore, using the BFRP material in design may require arrangement of tendons in multiple layers as opposed to a single layer and adopting over-reinforced design philosophy otherwise. Increasing the reserve strain and deflection capacity by reducing the initial strain is one of the most effective techniques to achieve ductility in the BFRP-reinforced/pre-stressed girders.

Loads and Load Combination

The four bridges detailed in Sect. 7.3 are all subjected to same loading except dead load contributed by the self-weight of the members and the varying line of action of pre-stressing forces due to varying depth of girders. The following loads are considered:

i. Dead and Superimposed Loads
ii. Vehicular Live Load as per Eurocode 1-Part 2 (2003)
iii. Braking and Traction Loads as per Eurocode
iv. Wind Load
v. Temperature Variation as per Eurocode 1 (2003)
vi. Temperature Gradient Variation as per Eurocode 1 (2003)
vii. Seismic Loads as per Eurocode 8 (2005)
viii. Snow Load

The load combinations are formed as per the recommendations of codes where both serviceability and ultimate limit states are considered for the bridges.

Table 1 Geometric and material properties of the bridges

	Type of bridge			
	(SSB_Steel)	(SSB_BFRP)	(IB_Steel)	(IB_BFRP)
Grade of concrete in girder	C70/C80	C70/C80	C70/C80	C70/C80
Grade of concrete in deck	C35/C45	C35/C45	C35/C45	C35/C45
Grade of concrete in abutment	C30/C37	C30/C37	C30/C37	C30/C37
Type of material for strand	Steel	BFRP	Steel	BFRP
Modulus of elasticity of tendon (GPa)	195	48	195	48
Ultimate tensile strength of tendon (MPa)	1860	1200	1860	1200
Jacking stress applied (MPa)	1395	780	1395	780
Width at support (mm)	740	740	740	740
Width at 10 m from support (mm)	400	400	400	400
Width at mid-span of girder (mm)	400	400	400	400
Depth at support (mm)	1800	1600	2000	1800
Depth at 10 m from support (mm)	1950	1750	1150	950
Depth at mid-span of girder (mm)	2100	1900	1450	1250
Thickness of slab (mm)	300	300	300	300

Bridge Design Details

The two bridges designed with conventional steel tendons are post-tensioned with 4 cables in two layers. Each cable is made up of 22 strands of 140 mm^2 cross-sectional area. The other two bridges are also post-tensioned but with 4 BFRP cables in 2 layers. Also, each BFRP cable is made up of 44 strands of 115.5 mm^2 cross-sectional area. The cable profiling is maintained same for both the steel and BFRP-pre-stressed bridges with respect to the soffit of the girder. The geometric and material properties are given in Table 1.

The bridges are modeled and analyzed in Midas Civil 2019 software. Figure 14 shows the longitudinal section of the four different bridges designed.

Self-Weight (Dead Load) Comparison

The cross-section of the girder obtained through design for the four bridges are compared used to obtain the dead load (self-weight) and are compared with each other. It was observed that the simply-supported bridge with conventional steel as pre-stressing tendons had the highest self-weight while the integral bridge with the BFRP pre-stressing tendons had the lowest self-weight. This is testimony of the lightweight superstructure obtained when the bridge is designed integrally using the BFRP tendons for pre-stressing.

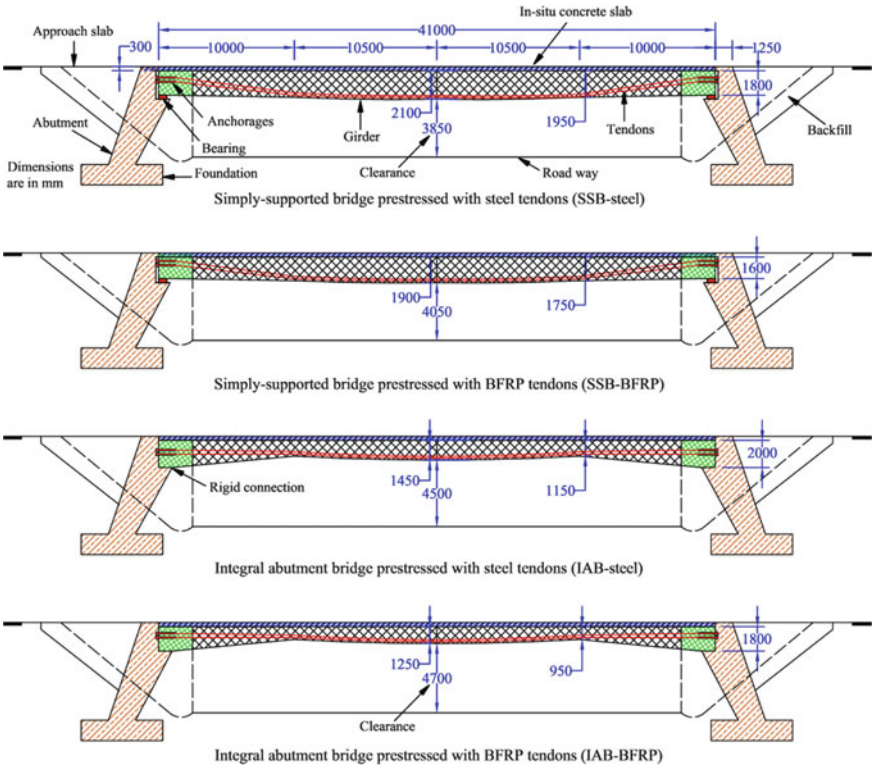

Fig. 14 Longitudinal section of the four different bridges designed (modified from Schlaich et al. [8] and reported in Alraie [2])

Deflection under Live Load

The transverse (vertical direction) deflection values of the girders are compared with each other, and it is seen that the integral bridge with the BFRP pre-stressing tendons have a lower value of deflection as compared to the simply-supported steel pre-stressed bridge and simply-supported BFRP-pre-stressed bridge. The integral steel-pre-stressed bridge has the lowest deflection value which is expected due to its superior integrity and greater girder depth (higher flexural rigidity).

Bending Moment Diagrams of Girders

Figure 15 shows the bending moment diagrams of all four bridges at the center of the girder. The bending moment diagram shown is due to all probable loads that are expected on the bridge. It is seen that the simply-supported steel-pre-stressed bridge has the highest sagging moment whereas the integral BFRP-pre-stressed bridge has the lowest moment.

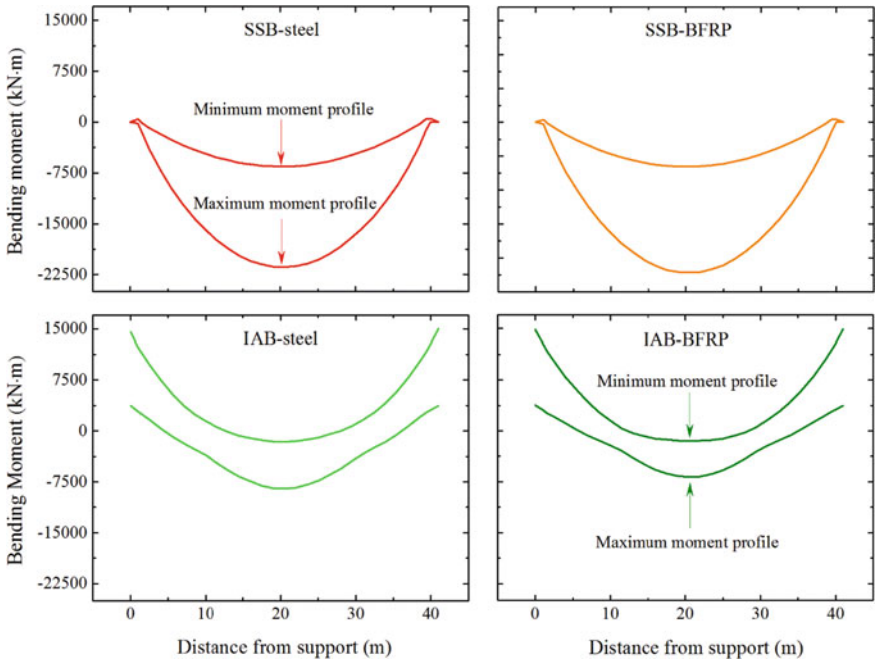

Fig. 15 Bending moment diagrams [2]

Top Fiber Stress Diagrams

Figure 16 shows the stress experienced at the top fiber and it is found to be highest in case of the integral BFRP-pre-stressed bridge. The reason for the high stress is due to the lowest section depth of the girder. However, the stress is found to be within the limit permitted typically by the codes.

7.4 Aesthetic Appeal

Since the integral BFRP-pre-stressed bridge is slender in design and offers the highest traffic clearance underneath the bridge as seen from the 3-D view of the girders in Figure 17, it is found to be the most aesthetically pleasing bridge structure.

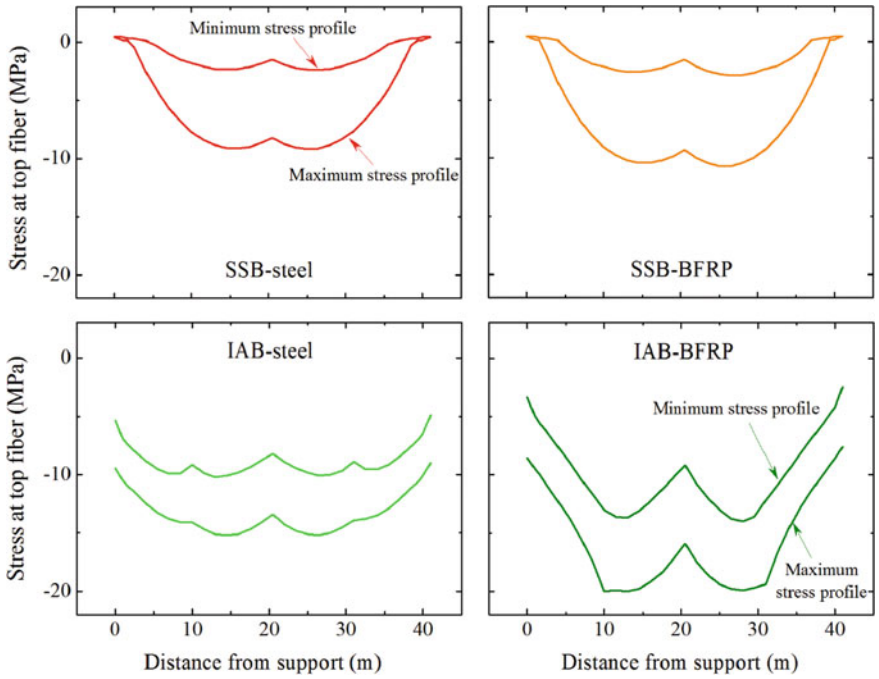

Fig. 16 Stress diagram at top fiber [2]

8 Conclusion

8.1 Optimal Anchor

The gripping pressure increases with increasing thickness of cement grout in expansive cement grout up to a certain point and then shows decreasing trend. Also, the gripping pressure has an inverse relationship with the diameter of rebar and the design of anchor is influenced more by the length than the cross-sectional dimension which only influences the resistance offered by friction while the length influences the bond resistance in addition to the frictional resistance. Therefore, the optimal anchor is the one with the thinnest cross-section.

8.2 Performance of the BFRP Rebar at Elevated Temperature

Only a marginal deviation of tensile strength is seen when temperature is raised up to 150 °C, where there is a loss of about 4% of the tensile strength. With rise in temperature beyond 150 °C–400 °C a notable degradation in tensile strength occurs,

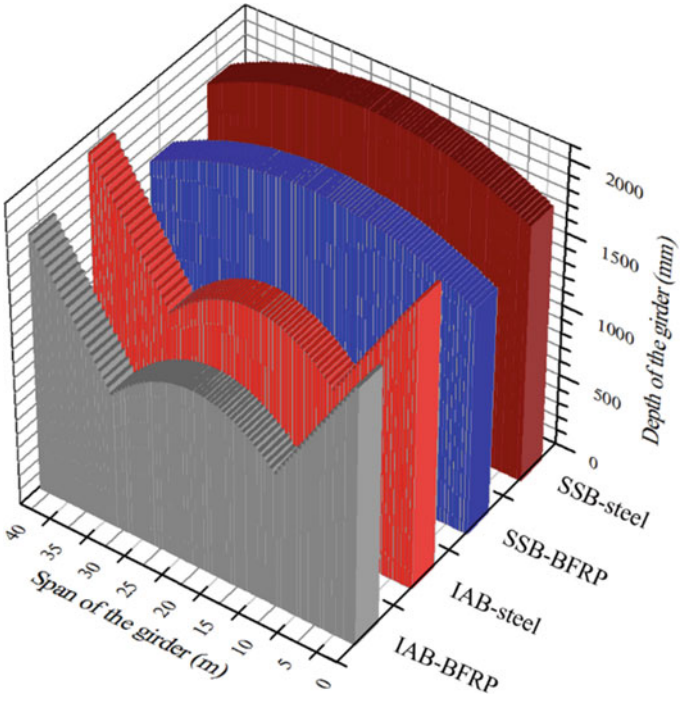

Fig. 17 3-D view of the girders [2]

losing over 40% of its residual strength. From 400 °C–450 °C, the tensile strength is degraded drastically with only 13% residual strength at 450 °C. On the other hand, the modulus of elasticity of the BFRP rods degrade at a lesser rate, retaining about 97% of its ambient tensile modulus at 250 °C and 75% at 450 °C.

Overall, the BFRP rod when tested at elevated temperature performs remarkably well as compared to other competing materials owing to its high glass transition temperature and high resin decomposition temperature as well as its high fiber content. The proposed constitutive model to estimate the degradation in tensile strength is original and comprehensive that helps predict the thermo-mechanical characteristics accurately.

8.3 Design Philosophy

The beams that are not pre-stressed and designed as over-reinforced perform below par in serviceability. However, it shows promise as far as ductility is concerned with high deformability index and an increased reserve strength. The same beams when pre-stressed improve in both serviceability requirement and ductility with about 6% increase in load-carrying capacity as compared to the non-pre-stressed beams. When

the beams are designed as under-reinforced with pre-stressing, the members are able to meet the serviceability requirement with enhanced performance as compared to the over-reinforced design. The energy-based evaluation, however, reveal that the failure is brittle in nature. Finally, the significantly under-reinforced section with pre-stressing performed extremely well in serviceability, though the ductility still remained an issue. The findings of the investigation proves that pre-stressing the BFRP tendons improves its performance in terms of enhanced flexural strength and serviceability performance. In order to overcome the issue of ductility in both over- and under-reinforced design, it is recommended that the BFRP tendons be provided in multiple layers with partial pre-stressing which is expected to allow sequential rupture of the tendons and hence achieve an acceptable ductility performance.

8.4 Ductility

When the tendons are placed in a single layer, the failure undergone by the member is found to be brittle in nature. Providing the tendons in layers results in improvement in ductility with an exceptional energy ratio in a 3-layered tendon arrangement. However, the disadvantage of providing the tendons in multiple layers is obviously the reduced load-carrying capacity of the member. The solution to restore the load-carrying capacity equivalent to a single-layered system is providing functionally-graded concrete with a warning rebar in the design of the BFRP-pre-stressed beams which increases both ductility and load-carrying capacity.

8.5 BFRP Pre-Stressed Integral Bridges

The integral bridges not only eliminate need for providing and maintenance of bearings as well as expansion joints but are also aesthetically pleasing and are more durable relatively. Application of the BFRP tendons to pre-stressed integral bridges is a viable replacement for corrosion-prone steel pre-stressed bridges. The BFRP-pre-stressed bridges offer the lowest self-weight due to slender sections. They also deflect less as compared to the steel pre-stressed bridges, and have a lesser amount sagging moment at mid-span.

Acknowledgements The present book chapter merely summarizes in the form of this self-review on the research work conducted since a decade on construction technology for integral bridges with basalt fiber-reinforced polymer (BFRP) prestressing tendons at Indian Institute of Technology (IIT) Delhi and reported through several scholarly publications referenced erstwhile. The technical inputs, data, and information received from Dr Ali Alraie, Mr Nikhil Garg, Mr Gaurav Swami, Prof. Dr Dipti Ranjan Sahoo, Dr-Ing. Andreas Apitz, Dr-Ing. Arndt Goldack, Prof. Dr sc. techn. Mike Schlaich, and Prof. Dr-Ing. Bohumil Kasal are gratefully acknowledged.

References

1. ACI PRC-440.1–15 (2015) Guide for the Design and Construction of Structural Concrete Reinforced with Fiber-Reinforced Polymer Bars. ACI Committee 440, American Concrete Institute (ACI), Farmington Hills, Michigan (MI), USA
2. Alraie A (2022) Construction technology for integral bridges with basalt fiber-reinforced polymer prestressing tendons. Doctoral Thesis, Indian Institute of Technology (IIT) Delhi
3. Alraie A, Matsagar V (2021) Design approach for concrete beams prestressed with high-strength basalt fiber-reinforced polymer tendons. The Indian Concr J 95(1):19–32
4. Alraie A, Matsagar V (2023) Flexural performance of basalt fiber-reinforced polymer prestressed concrete beams. Am Concr Inst (ACI) Struct J 120(1):1–16. https://doi.org/10.14359/51736123
5. Alraie A, Garg N, Matsagar V (2021) Pseudo-ductility through progressive rupture of basalt fiber-reinforced polymer tendons in partially prestressed functionally-graded concrete beam. In: Singh SB, Sivasubramanian MVR, Chawla H. (eds) Emerging trends of advanced composite materials in structural applications, composites science and technology, Springer, Singapore, pp 97–126
6. Alraie A, Garg N, Matsagar V, Goldack A, Schlaich M (2022) Pseudo-ductility through progressive failure of multi-layered carbon fiber-reinforced polymer (CFRP) prestressed concrete beams. Struct Eng Int J, pp 1–16. https://doi.org/10.1080/10168664.2022.2056863
7. Alraie A, Sahoo DR, Matsagar V (2021) Development of optimal anchor for basalt fiber-reinforced polymer rods. J Compos Constr (ASCE) 25(3):04021011
8. Schlaich M, Apitz A, Goldack A (2018) Form optimized CFRP reinforced and post-tensioned integral concrete bridge using precast girders. Tomorrow's Megastructures, 40th IABSE symposium, international association for bridge and structural engineering (IABSE), 19–21 September, Nantes, France